Atomistic Modelling of the Structure and Kinetics of Silica-based Sol-Gel Processes

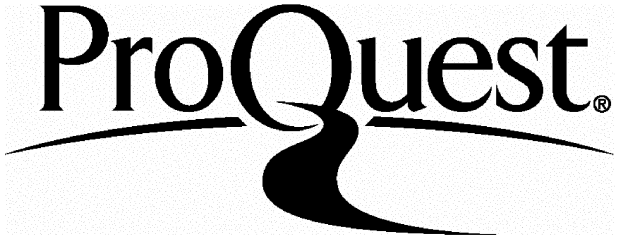
José Carlos G. Pereira

ProQuest Number: 10055871

All rights reserved

INFORMATION TO ALL USERS
The quality of this reproduction is dependent upon the quality of the copy submitted.

In the unlikely event that the author did not send a complete manuscript
and there are missing pages, these will be noted. Also, if material had to be removed,
a note will indicate the deletion.



ProQuest 10055871

Published by ProQuest LLC(2016). Copyright of the Dissertation is held by the Author.

All rights reserved.
This work is protected against unauthorized copying under Title 17, United States Code.
Microform Edition © ProQuest LLC.

ProQuest LLC
789 East Eisenhower Parkway
P.O. Box 1346
Ann Arbor, MI 48106-1346

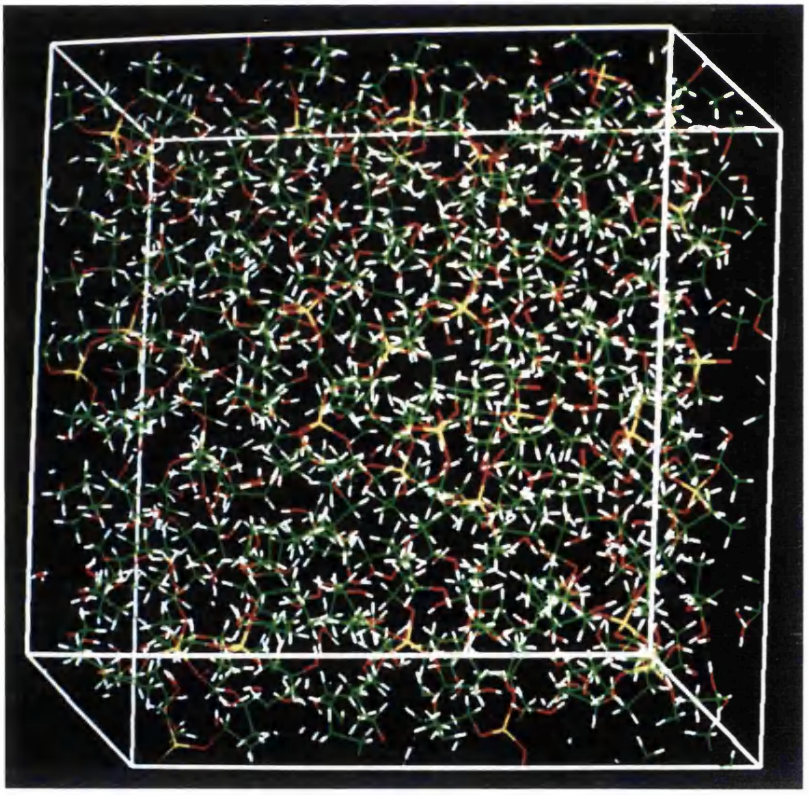
The Royal Institution of Great Britain,
Davy Faraday Laboratory,
London.

University College London,
Department of Geological Sciences,
London.

Instituto Superior Técnico,
Departamento de Engenharia de Materiais,
Lisboa.

Thesis submitted for the degree of Ph.D.
University of London.
April 1997

You may say I'm a dreamer
but I'm not the only one...
John Lennon



Contents

Abstract 1

Acknowledgements 2

I Sol-Gel Processes 3

1 History 4

2 Technological importance 8
2.1 Advantages and disadvantages . . . 8
2.2 Applications . . . 10
2.2.1 Monoliths . . . 11
2.2.2 Coatings . . . 14
2.2.3 Membranes . . . 16
2.2.4 Powders . . . 16
2.2.5 Aerogels . . . 17
2.2.6 Biological . . . 17
2.2.7 Preservation . . . 19

3 Basic principles 20
3.1 General . . . 20
3.2 Precursors . . . 21
3.3 Hydrolysis . . . 28
3.3.1 Inductive effects . . . 28
3.3.2 Catalysis . . . 29
3.3.3 Solubility . . . 31
3.3.4 Water/alkoxide ratio . . . 32
3.3.5 Isotopic studies . . . 33
3.3.6 Chain effects . . . 33
3.3.7 Transesterification and reesterification . . . 36
3.4 Condensation . . . 36
3.4.1 Solubility . . . 37
3.4.2 Electrostatics . . . 38
3.4.3 Polymerisation . . . 40
3.4.4 Catalyst role . . . 44

3.4.5 Temperature effects . . . 45
3.4.6 Pressure effects . . . 46
3.4.7 Chemical additives . . . 47
3.5 Kinetic models . . . 47
3.5.1 Branching Theory model . . . 49
3.5.2 Functional Group model . . . 50
3.5.3 Bicomponent model . . . 51
3.5.4 Nearest Neighbour model . . . 53
3.5.5 Statistical model . . . 55
3.6 Growth models . . . 56
3.6.1 Kinetic models . . . 56
3.6.2 Monomer-cluster models . . . 57
3.6.3 Cluster-cluster models . . . 58

4 Sol-Gel bibliography **61**
4.1 General references . . . 61
4.2 Topical references . . . 62
4.3 Current references . . . 63

II Atomistic Modelling **64**

5 History **65**

6 Ab-Initio theory **67**
6.1 Density Functional theory . . . 67
6.2 Functionals . . . 71
6.3 Basis Sets . . . 73
6.4 Atomic charges . . . 74
6.5 Optimisation . . . 75
6.6 COSMO model . . . 77

7 Molecular Mechanics theory **80**
7.1 Molecular Dynamics . . . 80
7.2 Long range interactions . . . 86
7.3 Pressure and temperature . . . 88
7.4 NVT and NPT ensembles . . . 89
7.5 Properties . . . 92

8 Atomistic Modelling bibliography **95**
8.1 General references . . . 95
8.2 Current references . . . 96

III Ab-Initio Studies 97

9 Small clusters 98
9.1 Introduction . . . 98
9.2 H_2O, H_3O^+, OH^- and H_2O--H_2O . . . 100
9.3 CH_3OH and CH_3CH_2OH . . . 106
9.4 $Si(OH)_4$ and $Si_2O(OH)_6$ . . . 109
9.5 $Si(OCH_3)_4$ and $Si(OCH_2CH_3)_4$ . . . 114
9.6 $Al(OH)_4^-$, $Al_2O(OH)_6^{2-}$ and $AlSiO(OH)_6^-$ . . . 117
9.7 Conclusions . . . 119

10 Different conformations 121
10.1 Introduction . . . 121
10.2 Intramolecular effects . . . 122
10.3 Cyclisation effects . . . 128
10.4 Ring effects . . . 134
10.5 Conclusions . . . 140

11 Silicate clusters 141
11.1 Introduction . . . 141
11.2 Branching effects . . . 143
11.3 Branched rings . . . 147
11.4 Double rings . . . 152
11.5 Large rings . . . 157
11.6 Silicate clusters data . . . 159
11.7 Conclusions . . . 164

12 Silicate reactions 166
12.1 Introduction . . . 166
12.2 Silicate clusters precursors . . . 167
12.3 Kinetic model . . . 168
12.4 Silicate clusters evolution . . . 175
12.5 Conclusions . . . 180

13 Sol-Gel clusters 182
13.1 Introduction . . . 182
13.2 Structure . . . 183
13.3 Charge distribution . . . 189
13.4 Reaction energies . . . 190
13.5 Conclusions . . . 194

14 Solvated clusters 195
14.1 Introduction . . . 195
14.2 Solvated water and methanol . . . 196
14.3 Solvated TMOS . . . 197
14.4 Solvated monomer . . . 198
14.5 Solvated dimer . . . 198

14.6 Energy 200
14.7 Conclusions 200

15 Reaction mechanisms **203**
15.1 Introduction 203
15.2 Data on protonated species 204
15.3 Formation of protonated species 206
15.4 Reactions of protonated species 209
15.5 Condensation S_N2 and *Lateral Attack* mechanisms 209
15.6 Hydrolysis S_N2 mechanism 214
15.7 Conclusions 217

IV Molecular Mechanics studies **219**

16 Cutoff-based liquids **220**
16.1 Introduction 220
16.2 Density versus partial charges 221
16.3 Dipoles versus partial charges 223
16.4 Energy versus partial charges 224
16.5 RDF versus partial charges 227
16.6 MSD versus partial charges 228
16.7 Intramolecular equilibration 235
16.8 Forcefield dependence of density 243
16.9 Density versus cutoff 244
16.10 Density versus equilibration time 244
16.11 Density versus system size 245
16.12 Energy fluctuation versus timestep 246
16.13 Execution time versus cutoff 246
16.14 Conclusions 248

17 Cutoff-based solutions **249**
17.1 Introduction 249
17.2 Forcefield 250
17.3 Mixture effects 251
17.4 Aggregation effects 252
17.5 Density and energy 259
17.6 Conclusions 261

18 Ewald sum-based liquids **264**
18.1 Introduction 264
18.2 Forcefield 265
18.3 Ewald sum 267
18.4 Density 270
18.5 Potential and kinetic energy 271
18.6 Enthalpy of vaporisation 275
18.7 Specific heat 281

18.8 Radial distribution function 282
18.9 Mean square displacement 290
18.10 Diffusion coefficient 294
18.11 Conclusions 294

19 Ewald sum-based solutions **296**
19.1 Introduction 296
19.2 Reactive interactions 297
19.3 Monomer and dimer aggregation 301
19.4 Density and energy 304
19.5 Short data collection times 308
19.6 Short run times 308
19.7 Solvation effects 308
19.8 Conclusions 313

V Final Remarks **314**

20 Discussion **315**
20.1 Chemistry of silica in solution 315
20.2 Atomistic modelling 323

Bibliography **327**

List of Figures

1.1 Limeplaster ancient sculpture 5
1.2 Precious Opal 6

2.1 Temperature diagram 9
2.2 Sol-gel cracking 10
2.3 Gel-silica mirror 12
2.4 Ultraviolet transmission 12
2.5 Infrared transmission 13
2.6 Thermal expansion 13
2.7 Window coating 14
2.8 Refractive index versus TiO_2 and porosity 15
2.9 Reflectance diagram 15
2.10 Tricomponent aerogels 17
2.11 Aorts Si content 18

3.1 Drying and sinterisation 21
3.2 Structure of metal alkoxides 22
3.3 Alkoxide oligomerization 24
3.4 DMDES, MTES and TEOS behaviour 26
3.5 Organic-inorganic copolymer 28
3.6 Inductive effects 29
3.7 pH rate profile 29
3.8 Hydrolysis of different silanes 30
3.9 TEOS-water-ethanol phase diagram 31
3.10 Solvent effects 33
3.11 Gelation time vs water and alcohol concentration 34
3.12 Hydrolysis of TEOS species 35
3.13 Silification of wood 37
3.14 Temperature and pH dependence on solubility 38
3.15 Size dependence on solubility 39
3.16 Ionised species in solution 39
3.17 Silica polymerisation 40
3.18 Silicate species 41
3.19 Silicate anions 42
3.20 TMOS and TEOS polymer growth 42
3.21 Stober silica powders 44

3.22 pH condensation trends 45
3.23 Sol-gel pressure trends 46
3.24 Drying control additives 47
3.25 DCCAs microstructural influence 48
3.26 Sol-gel species 48
3.27 Branching Theory kinetic model 50
3.28 Functional Group kinetic model 52
3.29 Bicomponent kinetic model 53
3.30 Statistical kinetic model 56
3.31 Fractal growth models 57

7.1 MD energy conservation 83

9.1 H_2O, H_3O^+, OH^- and H_2O--H_2O clusters 102
9.2 Methanol and Ethanol Molecules 106
9.3 $Si(OH)_4$ and $Si_2O(OH)_6$ clusters 109
9.4 $Si(OCH_3)_4$ and $Si(OCH_2CH_3)_4$ Alkoxides 116
9.5 $Al(OH)_4^-$, $Al_2O(OH)_6^{2-}$ and $AlSiO(OH)_6^-$ Clusters 117

10.1 DF-BHL/DNP data for $Si(OH)_4$ conformations 124
10.2 DF-BLYP/TNP data for $Si(OH)_4$ conformations 125
10.3 DF-BHL/DNP data for $Si_2O(OH)_6$ conformations 126
10.4 DF-BLYP/TNP data for $Si_2O(OH)_6$ conformations 127
10.5 DF-BHL/DNP data for $Si_3O_2(OH)_8$ conformations 129
10.6 DF-BLYP/DNP data for $Si_3O_2(OH)_8$ conformations 130
10.7 Data for $Si_4O_3(OH)_{10}$ conformations 132
10.8 Data for $Si_5O_4(OH)_{12}$ conformations 133
10.9 Data for $Si_3O_3(OH)_6$ conformations 135
10.10 Data for $Si_4O_4(OH)_8$ conformations 137
10.11 Data for $Si_8O_{12}(OH)_8$ conformations 138

11.1 TMOS-based system gas chromatographic analysis 142
11.2 TEOS-based System ^{29}Si NMR Analysis 143
11.3 DF-BHL/DNP data for $Q_2^2Q_2^1$ and $Q_3^1Q_1^3$ 144
11.4 DF-BHL/DNP data for $Q_3^2Q_2^1$, $Q_3^1Q_1^3Q_1^2$ and $Q_4^1Q_1^4$ 146
11.5 DF-BHL/DNP data for $Q_2^2Q_1^3Q_1^1$ and $Q_3^2Q_1^3Q_1^1$ 148
11.6 DF-BHL/DNP data for $Q_2^2Q_1^3Q_1^2Q_1^1$, $Q_2^2Q_2^1Q_1^4$, $Q_2^3Q_2^1Q_1^2c$ and $Q_2^3Q_2^1Q_1^2t$ 150
11.7 DF-BHL/DNP data for $Q_2^3Q_2^2$, $Q_2^3Q_1^3Q_1^2Q_1^1$ and $Q_2^2Q_1^4Q_1^3Q_1^1$ 153
11.8 DF-BHL/DNP data for $Q_4^2Q_1^4$, $Q_2^2Q_2^3Q_1^2e$ and $Q_2^2Q_2^3Q_1^2c$ 156
11.9 DF-BHL/DNP data for Q_5^2 and Q_6^2 158

12.1 Small clusters kinetic evolution 176
12.2 Non-cyclic clusters kinetic evolution 177
12.3 Trimer rings kinetic evolution 178
12.4 Large rings kinetic evolution 179

13.1 [X Y 0] clusters 183

13.2 [X Y 1][0 3 1] clusters 184
13.3 [X Y 1][X Y 1] clusters 185
13.4 [2 1 1][2 1 1] clusters 188

15.1 Lasaga hydrolysis mechanism 204
15.2 Condensation S_N2 mechanism 210
15.3 *Lateral Attack* mechanism 211
15.4 S_N2 and *Lateral Attack* energy evolution 213
15.5 *Lateral Attack* energy across the valley 214
15.6 Condensation energy evolution 215
15.7 First hydrolysis energy evolution 217
15.8 Last hydrolysis energy evolution 218

16.1 Reference RDFs in water 227
16.2 Reference RDFs in methanol 227
16.3 Reference RDFs in ethanol 228
16.4 Cutoff-based RDFs in water 229
16.5 Cutoff-based RDFs in methanol 230
16.6 Cutoff-based RDFs in methanol (Cont.) 231
16.7 Cutoff-based RDFs in ethanol 232
16.8 Cutoff-based RDFs in ethanol (Cont.) 233
16.9 Cutoff-based RDFs in ethanol (Cont.) 234
16.10 Cutoff-based RDFs in ethanol (Cont.) 235
16.11 Cutoff-based RDFs in TMOS 236
16.12 Cutoff-based RDFs in TMOS (Cont.) 237
16.13 Cutoff-based MSDs in water 238
16.14 Cutoff-based MSDs in methanol 238
16.15 Cutoff-based MSDs in ethanol 239
16.16 Cutoff-based MSDs in TMOS 239
16.17 Intramolecular energy in water 240
16.18 Intramolecular energy in methanol 241
16.19 Intramolecular energy in ethanol 241
16.20 Intramolecular energy in TMOS 242
16.21 Intramolecular energy in TEOS 242
16.22 Energy fluctuation versus timestep 247

17.1 Initial configurations 253
17.2 Methanolic solution before mixture 254
17.3 Methanolic solution after mixture 255
17.4 Ethanolic solution before mixture 256
17.5 Ethanolic solution after mixture 257
17.6 Monomer aggregation interactions 258
17.7 Trimer ring aggregation interactions 259
17.8 Aggregation effects 260

18.1 Ewald sum cutoff effects 267
18.2 Ewald sum cutoff effects (cont.) 268

18.3 Ewald sum cutoff effects (cont.) 269
18.4 Ewald sum pressure and temperature effects 271
18.5 Ewald sum pressure and temperature effects (cont.) 272
18.6 Ewald sum pressure and temperature effects (cont.) 273
18.7 Ewald sum-based RDFs in water 283
18.8 Ewald sum-based RDFs in heavy water 283
18.9 Ewald sum-based RDFs in methanol 284
18.10 Ewald sum-based RDFs in ethanol 285
18.11 Ewald sum-based RDFs in ethanol (Cont.) 286
18.12 Ewald sum-based RDFs in TMOS 287
18.13 Ewald sum-based RDFs in TEOS 288
18.14 Ewald sum-based MSDs in water 291
18.15 Ewald sum-based MSDs in heavy water 291
18.16 Ewald sum-based MSDs in methanol 291
18.17 Ewald sum-based MSDs in ethanol 292
18.18 Ewald sum-based MSDs in TMOS 292
18.19 Ewald sum-based MSDs in TEOS 292
18.20 Water phase diagram 293

19.1 Alkoxide reactive interactions 299
19.2 Monomer reactive interactions 300
19.3 Dimer reactive interactions 302
19.4 Monomer and dimer aggregation 303
19.5 Aggregation interactions 305
19.6 Solvation before hydrolysis 311
19.7 Solvation between hydrolysis and condensation 312
19.8 Solvation after condensation 312

List of Tables

2.1 Sol-gel advantages and disadvantages 8
2.2 Silica Optics 11
2.3 Gel optics advantages 11

3.1 Tetraalkoxides 25
3.2 Organoalkoxides 25
3.3 Sol-gel solvents 32
3.4 Long chain effects 34
3.5 Branched chain effects 35
3.6 Gelation characteristics for SiO_2 36
3.7 Transesterification effects 36
3.8 Role of catalysts 44
3.9 Sol-gel temperature trends 46

9.1 H_2O structure and charge distribution 101
9.2 H_2O--H_2O structure and charge distribution 103
9.3 OH^- structure and charge distribution 105
9.4 H_3O^+ structure and charge distribution 105
9.5 Water auto-ionisation energy 105
9.6 Methanol structure and charge distribution 107
9.7 Ethanol structure and charge distribution 108
9.8 $Si(OH)_4$ structure and charge distribution 110
9.9 $Si_2O(OH)_6$ structure and charge distribution 111
9.10 $Si(OH)_4$ condensation energy 114
9.11 TEOS and TMOS structure and charge distribution 115
9.12 $Al(OH)_4^-$, $Al_2O(OH)_6^{2-}$ and $AlSiO(OH)_6^-$ structure and charge distribution . . 118

11.1 [Silicate clusters bond lengths 160
11.2 Silicate clusters bond angles 161
11.3 Silicate clusters charge distribution 162
11.4 Silicate clusters condensation energy 163

12.1 Silicate clusters precursors 169
12.2 Silicate clusters precursors 170

13.1 [X Y 0] clusters structural data 186
13.2 [X Y 1][0 3 1] clusters structural data 187

13.3 [X Y 1][X Y 1] clusters structural data 187
13.4 [2 1 1][2 1 1] conformations data 188
13.5 [X Y 0] clusters charge distribution 189
13.6 [X Y 1][0 3 1] clusters charge distribution 190
13.7 [X Y 1][X Y 1] clusters charge distribution 190
13.8 Monomer hydrolysis 191
13.9 Dimer hydrolysis 191
13.10 Water forming asymmetrical condensation 192
13.11 Water forming symmetrical condensation 192
13.12 Methanol forming asymmetrical condensation 193
13.13 Methanol forming symmetrical condensation 193

14.1 Solvated water data 197
14.2 Solvated methanol data 198
14.3 Solvated TMOS data 199
14.4 Solvated monomer data 199
14.5 Solvated dimer data 201
14.6 Cosmo reaction energies 201

15.1 $Si(OH)_3(H_2O)^+$ and $Si_2OH(OH)_6^+$ data 205
15.2 $Si(OMe)_3(HOMe)^+$, $Si(OH)_3(HOMe)^+$ and $Si(OMe)_3(H_2O)^+$ data 207
15.3 Water ionisation environment dependence 207
15.4 Protonated species formation 208
15.5 Protonated species reactions 209
15.6 Condensation S_N2 attack evolution 211
15.7 Condensation *Lateral Attack* evolution 212
15.8 Protonated species reactions 216

16.1 Cutoff-based simple liquids density 222
16.2 Cutoff-based partial charges 222
16.3 Molecular electric dipole moment 223
16.4 Cutoff-based MD energy in liquids at high pressure 224
16.5 Cutoff-based MD energy in liquids at ambient conditions 225
16.6 Cutoff-based MD energy in liquids at boiling temperature 225
16.7 Cutoff-based internal energy 226
16.8 Cutoff-based diffusion coefficient 240
16.9 Density versus forcefield 243
16.10 Density versus forcefield with Mulliken charges 244
16.11 Density versus cutoff 245
16.12 Density versus equilibration time 245
16.13 Density versus size 246
16.14 Energy fluctuation versus timestep 246
16.15 Execution time versus cutoff 247
16.16 Execution time versus buffer width 248

17.1 Cutoff-based partial charges 251
17.2 Methanolic solutions data 261

17.3 Ethanolic solutions data 262

18.1 Ewald sum-based partial charges 266
18.2 Ewald sum-based simple liquids density 274
18.3 Ewald sum-based water energy 276
18.4 Ewald sum-based methanol energy 277
18.5 Ewald sum-based ethanol energy 278
18.6 Ewald sum-based TMOS energy 279
18.7 Ewald sum-based TEOS energy 280
18.8 Enthalpy of vaporisation in liquids 281
18.9 Specific heat in liquids 282
18.10 Self-diffusion coefficient in liquids 295

19.1 Sol-gel solutions density 306
19.2 Sol-gel solutions energy 307
19.3 Short collecting time density 309
19.4 Short collecting time energy 310
19.5 Short run time density and energy 311

Abstract

This thesis concerns the study of the structural and kinetic aspects of silica-based sol-gel processes, which we investigate using ab-initio and molecular mechanics computer modelling techniques. It is divided into five parts.

The first is a general introduction to sol-gel processes. It contains four chapters, which describe the historical evolution of sol-gel processes, their technological importance, the current scientific background in the chemistry of silica-based processes and a guide to the principal sol-gel bibliography.

The second part is a general introduction to atomistic modelling. It is divided in four chapters. The first is a brief historical overview focusing on the crescent motivation to apply computing methods. The second reviews ab-initio theory. The third is a review of molecular mechanics theory and the fourth is a guide on the main atomistic modelling bibliography.

The third part contains all density functional and Hartree-Fock studies, aiming to elucidate the structural growth and reaction mechanisms occurring in sol-gel processes. It contains seven chapters. Small species are analysed in chapter one to investigate the accuracy of the methods. The role of different silicate conformations is analysed in chapter two. In chapter three, the study of the silicate clusters is completed. All information is gathered in chapter four to create a growth kinetic model. The influence of the alkoxy groups is studied in chapter five. Solvation effects are investigated in chapter six. Hydrolysis and condensation reaction mechanisms are studied in chapter seven.

The fourth part contains all molecular dynamics studies, aiming to create a realistic model to simulate sol-gel processes in solution. It contains four chapters. In the first, a model is developed to simulate liquids in a large range of thermodynamic conditions. This model is used in chapter two to study mixture and aggregation effects in diluted sol-gel solutions. The methodology developed in chapter one is enhanced in chapter three. This model is applied in chapter four to study aggregation and solvation effects in more realistic sol-gel solutions.

The fifth part is an overall discussion with two sections. The first summarises the implications of this work and considers possible directions for future studies. The second contains general considerations about the present and future of computer modelling.

The thesis concludes with an alphabetical list of bibliography covering all references cited in the work.

Acknowledgements

The author is greatly indebted to Instituto Superior Técnico, Dept. Eng. Materiais, Lisboa, and JNICT, Programa Ciência and programa Praxis XXI, Lisboa, for their financial support.

The author wishes to acnowledge the computer time generously given by The Royal Institution, London, on Convex C220, SG Power Challenge *Faraday* and *Rumford* and SG Indigo workstations, by EPSRC, Edinburgh, on Cray T3D *Darwin*, by Daresbury Laboratories, Daresbury, on Intel 8600i, by University College London, Dept. of Geological Sciences, on SG Indigo workstation, by Dr. John Brodholt, UCL, on SG Power Challenge *Slamdunk*, by ULCC, London, on Convex *Neptune* and *Pluto*, by Instituto Superior Técnico, Civil Eng. Dept., Lisboa, on IBM 6000 workstations and by Molecular Simulations Inc., San Diego, on SG Indy workstations. The author is also grateful to INESC, Lisboa. The author wants to acnowledge Dr. Bill Smith and Dr. Tim Forester at Daresbury, who wrote Dl_poly, Dr. Julian Gale at RI, who wrote Gulp and the MSI rcenter staff at San Diego, who support Dmol and Discover. A special acknowledgement to MSI, for a very enrichning working experience at San Diego.

The first personal acknowledgement is for Prof. Richard Catlow and Prof. David Price, the main supervisors of this work. The author wishes to thank, in particular, their inspiring scientific advice, encouragement, patience and eternal good humour. The author would also like to thank Prof. Rui Almeida for his co-supervisition. A work of this dimension is not possible without the help of many coleagues. The author is particularly indebted to Prof. Benedito Cabral at Faculdade de Ciencias, Lisboa, Mr. Alexei Sokol, Dr. Alex Lifshivtz, Dr. Ashley George, Dr. Adrian Smith, Dr. Robin Grimes, Dr. Dewi Lewis, Dr. David Gay, Dr. Robert Bell, Mr. Furio Cora, Mr. Chris Nuttal, Dr. Simon Carling, Mr. Andy Davids, Dr. Richard Oldroyd, Dr. Yuei Mori, Dr. Josef Breu, and Dr. Martin Exner at RI, London, to Mr. Patricia Carvalho, Dr. Luis Santos, Prof. Amaral Fortes, Prof. Fátima Vaz and Prof. Fernanda Margarido at IST, Dept. Eng. Materiais, Lisboa, to Dr. Vessal Behnam, Dr. Clive Freeman, Dr. Ton Van Dalen, Dr. Zhengwei Peng and Dr. Kit Lau, at MSI California, to Dr. David Kitson at MSI UK, to Dr. Steve Marshall at Daresbury Laboratory, to Dr. Julie Altmann at ULCC, London, to Prof. Moitinho de Almeida at IST, Dept. Eng. Civil, Lisboa and Antonio Costa at CIIST, IST, Lisboa. A word of gratitude for Dr. Sasha Shluger at RI, for his encouragment.

The author wants to thank the administrative staff at RI, particularly Edna Raggett, Edmund Corran and Derek Cummings and at UCL, particularly Ron Dudman. A word of recognition for the night staff, namely P. Vickers and F. E. Searbone at UCL, London, and António Gomes, Adelino Leitão and Bernardino Caramelo at IST, Lisboa. A special word of thanks for Mrs. and Mr. José, for their help and tolerance during all this time.

Part I

Sol-Gel Processes

Chapter 1

History

The ability to make ceramic objects, in a controlled way, is the first technological achievement of mankind, evidenced by the earliest fired ceramics discovered to date, the molded figures found in Dolne Vestonice, former Czechoslovakia, and made about 22,000 B.C. [127].

In spite of the evolution in the manufacturing processes, particularly in the Middle East, about 10,000 B.C. (see Figure 1.1), producing limeplaster from limestone, and later during the classic civilisations, ceramics and glasses remained essentially as non noble materials, made essentially to fulfill functional purposes. Only after mastering the technique of producing porcelain, in China, during the Tang dynasty (618-907 A. D.) and much later in Europe, in 1708, in Germany, under the direction of J. F. Bötger [127], ceramic technology received renewed interest and ceramic pieces acquired enormous esthetical and social value.

Many advances have occurred since then in the preparation of powders, forming and methods of densification. Powders may have a crystal chemistry controlled to produce specific physical properties. Glass-ceramics may contain a unique combination of microstructure and phase assemblages not obtainable by traditional ceramic processes. However, they are limited by the constraints on traditional glass-making prior to ceraming and the methods used to transform the powders in commercial ceramic products are not very different from those used by the Chinese, more than a thousand years ago. As pointed out by L. L. Hench [95], for millennia, ceramics have been made with basically the same technology: powders, either natural or man-made, have been shaped into objects and subsequently densified at temperatures close to their temperature liquidus. The technology of making glass has also remained fundamentally the same since prehistory: particles are melted, homogenised and shaped into objects from the liquid.

The limitations of such traditional processing are certainly not important for many conventional applications, but they impose severe constraints on developing sophisticated new materials for electronic, structural, space or medical applications. Modern ceramics obtained by these methods are primarily the products of applied physics and physical metallurgy, relating physical behaviour and microstructure. Major advances in ceramic and glass technology need "ultrastructural control", requiring an application of chemical principles unprecedented in the history of ceramics.

The expression *ultrastructure processing* was coined by analogy with the biological sciences, with the observation of what is termed cellular ultrastructure (after the invention of the electron microscope), and the development of ultrastructural manipulation, studying and controlling events at the cellular and even molecular level, leading to the creation of molecular biochemistry and eventually genetic engineering. Inorganic materials also can now be made to manipulate



Figure 1.1: Limeplaster sculpture, found in Jericho, about 7,000 B.C. [127].

and control the function of cellular membranes and consequently cells [95], thereby reducing the distance between molecular biochemistry and molecular materials chemistry. The emphasis in ultrastructure processing and in sol-gel processes is on controlling the structure and microstructure of the material at the molecular level, namely its homogeneity and its internal surfaces, to obtain materials with unique combinations of physical and chemical properties.

Silicon constitutes approximately 20 at. % of the earth's crust in the form of SiO_2 or the silicates in rocks, minerals and soil constituents. Many natural systems show evidence of silicate hydrolysis and condensation to form polysilicates gels and particles. The precious opal, for example, is formed by amorphous silica particles glued together by a lower-density silicate gel [42]. Repeated hydrolysis and condensation of silica in water, lead to the formation of aqueous polysilicate species that evolve, under appropriate chemical conditions, to form spherical particles of essentially anhydrous silica.

As water is a unique liquid, so is amorphous silica a unique solid [105]. Apart from their technological importance, silica-based sol-gel processes are particularly fascinating for their unique insight into the chemistry of silicon. Manmade synthesis of polysilicate gels from alkoxide precursors closely followed the first preparation of silicon tetrachloride in 1824 [42]. In 1845 Ebelman was able to synthesise $Si(OCH_2CH_3)_4$ by reacting $SiCl_4$ with ethanol, and in the next years he reported the hydrolysis and subsequent condensation of $Si(OCH_2CH_3)_4$, forming silicate solutions from which fibres could be drawn and gels that could be used to produce optical monoliths, if dried for long enough (about one year...) [96].

In 1860 Mendeleyev proposed that the hydrolysis of $SiCl_4$ yields a product ($Si(OH)_4$), that subsequently reacts successively to form high molecular weight polysiloxanes. In spite of these contributions, and some interesting potential applications (like the use of this gel process to



Figure 1.2: Precious Opal, from Fichtelgebirge/RFA, 35x 25 mm [163].

preserve the deteriorating stonework of the Houses of Parliament, in London, proposed by von Hoffmann, in 1861 [245]), these materials remained of interest only for chemists, for almost one hundred years. During the whole nineteenth century, noted chemists like Ostwald and Lord Rayleigh investigated the problem of the periodic precipitation phenomena that lead to the formation of Liesegang rings and the growth of crystals from gels [96]. In 1864 Graham showed that the water in silica gel could be exchanged for organic solvents, thus supporting the theory that the gel consisted of a solid network with continuous porosity.

The 1930s become an important turning point for sol-gel processes, in particular regarding their technological applications and relation with industry. The process of supercritical drying, which during the last 60 years proved to be fundamental in producing aerogels in a reasonably short time, without cracking, was invented by Kistler in 1932. In 1939 W. Geffcken recognised that oxide films could be prepared from alkoxides, and for the first time, the corresponding industrial application was developed by a glass company. Schroeder developed a thin films physics for this process by using many single-oxide and mixed-oxide layers [66]. The characterisation of silica gels as formed by a network structure was already generally accepted in the 1930s, largely due to the work of C. B. Hurd, who showed that they must consist of a entire polymeric network formed by polysilicic acid, enclosing a continuous liquid phase.

Since 1935, mineralogists have become interested in using sol-gel processes to prepare powders which could be used with advantage in studies of solid state equilibria, where homogeneous samples are essential [227]. In the 1960s, R. J. Roy recognised the potential of the method for achieving very high levels of chemical homogeneity in colloidal gels and used it to synthesise a large number of new ceramic oxide compositions, involving mainly Al, Si, Ti and Zr, that could not be made using traditional ceramic powder methods [96].

In 1955 R. K. Iler published the first edition of *The Chemistry of Silica*, a milestone in the understanding of solubility, polymerisation and many other aspects of silica in aqueous systems. His pioneering work led to the commercial development of colloidal silica powders, the colloidal

Ludox spheres. The method was extended in 1968 by Stober, creating the so-called Stober spherical silica powder, with a uniform distribution of particles sizes (see Figure 3.21). At the same time, important but classified scientific and technological work was being carried out by the nuclear-fuel industry, to prepare small spheres of radioactive oxides and thus avoiding the generation of the dangerous dust produced by conventional ceramic methods.

The ceramics industry began to show interest in gels in the sixties. Large scale production of automotive rear-view windows started in 1959 and continued with anti-reflection coatings in 1964 and with sunshielding windows in 1969, based on the $SiO_2 - TiO_2$ system [66]. In 1969, L. Levene and I. M. Thomas, and H. Dislich and P. Hinz, working independently, established the chemical basis for the preparation of multicomponent glasses, glass ceramics and crystalline substances, through controlled hydrolysis and condensation of alkoxides. Since then, any type of multicomponent oxide can be synthesised by the sol-gel process, using the alkoxides of the different elements [66]. In the beginning of the 1970s, ceramic fibres were already being made from metalorganic precursors by several companies, but only in 1975-77, when B.E. Yoldas and M. Yamane demonstrated that indeed monoliths can be made by carefully drying of gels [42], the enthusiasm for sol-gel processes exploded and important financial resources were allocated for research in this area, all over the world.

The sol-gel process, "Glass from the bottle", as it was nicknamed, was attracting more and more interest and the sol-gel research community was already large enough to justify a conference entirely dedicated to the subject, *International Workshop on Glasses and Glass Ceramics from Gels*, held in Padova, Italy, in 1982, where it was recognised that "almost 100 papers have been published" about sol-gel processes. Since then the amount of work and the number of publications has increased extraordinarily fast, together with the number and diversity of applications suggested, in what is certainly, in the end of the 20th century, one of the most promising technologies for the future.

Chapter 2

Technological importance

2.1 Advantages and disadvantages

The main advantages and disadvantages of sol-gel processes, when compared with other technological methods, like high temperature melting, vapour deposition, ceramics from metal-organic polymers or preparation of ultrafine powders of controllable size [157], are presented in Table 2.1 [153].

As the raw materials are liquids at working conditions and after mixing they form low viscosity liquid solutions, homogenisation can usually be achieved, at a molecular level, in a short time. Since the reactants are so well mixed in the solutions, they are likely to be equally well-mixed, at the molecular level, when the gel is formed.

Using synthetic chemicals rather than minerals, as is usually the case in the ceramics industry, guarantees high purity and reproducibility of the final products, an important point when considering the quality control of the whole industrial process.

As hydrolysis and condensation occur even at ambient temperature and pressure, the high temperatures (above Liquidus temperature T_L) required to melt and mix the raw materials in conventional melting processes are not needed. As can be seen in Figure 2.1, even the densification, the stage requiring higher temperatures (close to the glass transition temperature t_g), is usually done at a lower temperature that the annealing required in melting techniques to reduce the strain and defects introduced during the quench of the melt. Low temperature processing is a key advantage, because it allows a much better control of the whole chemical and physical transformations.

From the technological point of view, low temperature saves energy, increases the safety,

Advantages	Disadvantages
Better homogeneity	*Expensive raw materials*
Better purity	*Undesirable residuals*
Lower temperature of preparation	*Large shrinkage during processing*
Better chemical and physical control	*Long processing times*
Better glass products	*Insufficient scientific understanding*

Table 2.1: Principal advantages and disadvantages of sol-gel processing, from J. D. Mackenzie [153].

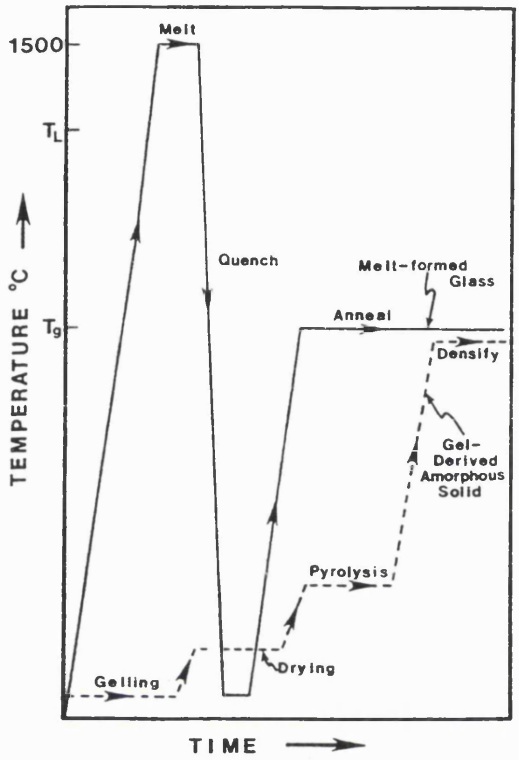


Figure 2.1: Comparison of melt-derived and gel-derived processing as a function of temperature, from Mackenzie [156].

minimises air pollution and reduces the complexity of the industrial plant and consequently the financial investment needed. From the scientific point of view, it tends to minimise evaporation losses and reactions with containers, therefore increasing the reproducibility, and avoids undesirable phase separation and crystallisation processes taking place during the quenching and annealing steps in melt-formed glasses. New non-crystalline solids can thus be produced outside the range of normal glass formation, from which new crystalline phases can subsequently be formed. Organic monomers that decompose or evaporate at high temperatures can be combined with inorganic precursors to create new organic-inorganic materials with unique properties [212].

A large range of experimental parameters, including precursors, solvents, additives, temperature, pressure, time, have a direct influence in the structure, microstructure and general properties of the final products, allowing a enormous freedom to design new methodologies and to control better the final properties required.

Better glass products can be made exploring the special properties of gel [153], as the sol-gel process has the unique advantage of allowing the preparation of the same composition, such as silica, in very different physical forms, fibres, coatings, monoliths, just by varying experimental conditions, essentially those controlling the viscosity of the system [96].

The need for long processing times is by any standard, an important disadvantage of sol-gel processes, as the whole process can take several hours or more probably days to take place. Moreover, the raw materials used in sol-gel processes are comparatively expensive, which make the method unsuitable, from the economical point of view, for ordinary applications, like pro-

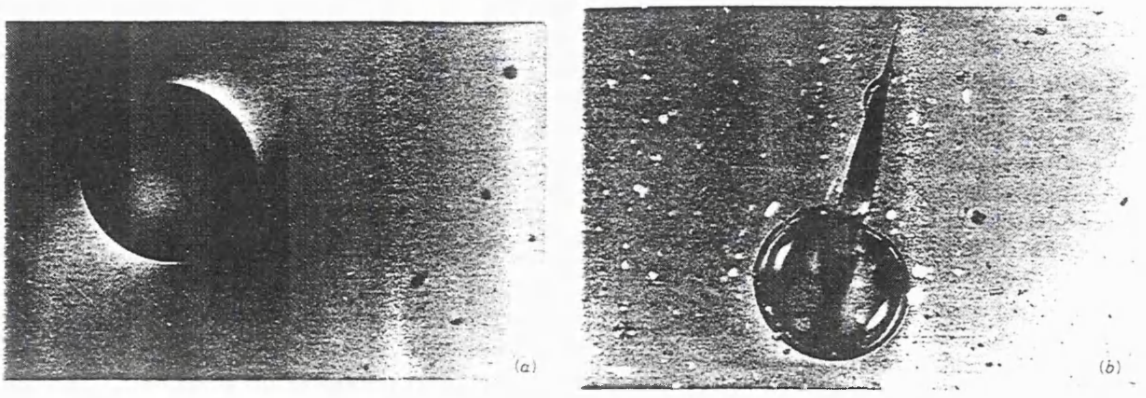


Figure 2.2: Initiating a crack in a sol-gel monolith, from Hench et al. [97].

ducing window glass, for example. Industrial applications of sol-gel processes need also to take into account the health hazards of organic solutions. It is unlikely therefore that sol-gel processes will be used in the future in mass-production of ordinary glass and ceramics, where quantity, implying short processing times and cheap raw materials, instead of quality, is the key factor.

Undesirable residual fine pores, hydroxyl and organic groups, namely solvent, are difficult to remove and may introduce internal strains eventually leading to cracking during gelation and drying. In fact, large shrinkage during processing is potentially a very serious problem in sol-gel processes, often leading to cracking during gelation or drying (see Figure 2.2). However, recent use of critical point drying for aerogels and drying control chemical additives for xerogels, has solved some of the numerous problems associated with the pore evacuation, making it possible to produce large monolithic dried gels routinely and rapidly [98]. Though size scale-up is still one the greatest uncertainties of sol-gel processing, control of drying rates, elimination of casting defects and rigorous atmosphere control can yield large sol-gel optical components.

Although substantial effort in sol-gel fundamental research has been carried out during the last 15 years, a lack of scientific understanding of the many complexities associated with the process still subsists. Without this scientific foundation, exploitation of sol-gel processes will be inefficient.

2.2 Applications

Applications for sol-gel processing derive directly from the low temperature, compositional and microstructural control, combined with the various dimensional shapes that can be obtained directly from the gel state: monoliths, films, fibres and powders.

By the end of 1984, crystalline and noncrystalline oxides from over 50 chemical systems had been already prepared using the sol-gel technique and it was expected that some 200 oxide systems would be studied by the sol-gel method during the next two decades [155].

Both glass and polycrystalline fibres have been made using the sol-gel method. Compositions include TiO_2 and $ZrO_2 - SiO_2$ glass fibres, high purity SiO_2 waveguide fibres and Al_2O_3, ZrO_2, ThO_2, MgO, TiO_2, $ZrSiO_4$ and $3Al_2O_3.2SiO_2$ polycrystalline ceramic fibres [96].

Excellent optical transmission
from the ultraviolet (160nm) to near infrared (3600nm)
Excellent refractive index homogeneity
Isotropic optical properties
Small strain birefringence
Very low coefficient of thermal expansion ($0.55 \times 10^{-6}/°C$)
Very high thermal stability
Very high chemical durability
Small number of bubbles or inclusions
Ability to be polished to high standards

Table 2.2: Silica optics properties, reviewed by L. L. Hench [97].

Improved casting	*Complex geometries*
Light weight optics	*Aspheric optics*
Surface replication	*Internal structure*
Reduced grinding	*Reduced polishing*
Improved properties	*Lower coefficient of thermal expansion*
Lower ultraviolet cutoff wavelength	*Higher optical transmission*
No absorption due to OH band	*Lower solarisation*
Higher homogeneity	*Fewer defects*
Improved impregnation	*Impregnation with organic polymers*
Graded refractive index lenses	*Laser-enhanced densification*
Controlled chemical doping	*Control of variable oxidation states of dopants*

Table 2.3: Potential advantages of gel-silica optics over fused quartz and fused silica components, from Hench et al. [97].

2.2.1 Monoliths

Silica gels containing wide ranges of alkalis, alkaline earths, transition metals and rare earth elements can now be made using drying additives, allowing us to prepare materials with a wide range of optical absorption spectra, index of refraction and dispersion [98]. As reviewed by Hench et al. [97], silica optics are preferred for many optical systems, such as intracavity laser optics, because of the characteristics listed in Table 2.2.

The conventional methods to produce silica glass, *fused quartz* (naturally occurring quartz crystals are melted at high temperatures) and *fused silica* (pure silicon tetrachloride is fused at high temperatures), tend to let substantial amounts either of cation and hydroxyl impurities or water and Cl ion contents in the final glass. Furthermore, the nature of the processes involved makes the direct manufacture of near net shape optics impossible [97]. Sol-gel processes offer the potential for improving many features of silica optics, as listed in Table 2.3.

In particular, net shapes and surfaces can be obtained through casting sols at low temperatures into molds of predetermined configurations, as shown in Figure 2.3. The superior ultraviolet and near infrared optical transmission of gel silica optics when compared with fused silica optics is shown in Figures 2.4 and 2.5. A very low coefficient of thermal expansion is an especially important physical characteristic in a glass intended to be used as a optical component in a laser cavity or together with other glasses in optical waveguides and fibres. Figure 2.6 shows that lower coefficients of thermal expansion can be obtained using sol-gel technology to produce optical silica.

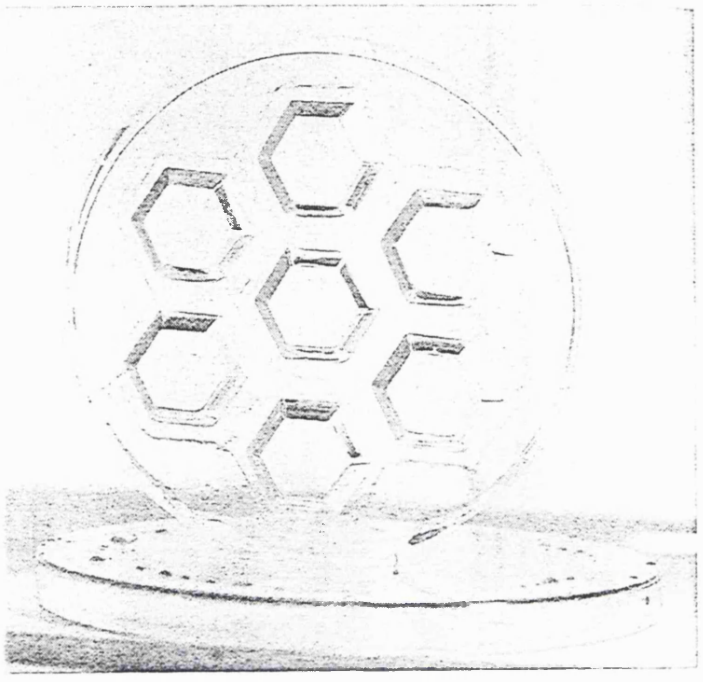


Figure 2.3: Lightweight sol-gel silica mirror with integral faceplate, as shown by Hench et al. [97].

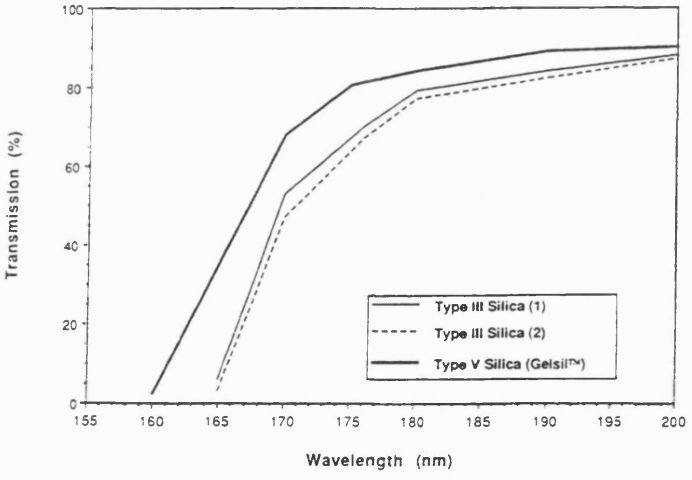


Figure 2.4: Ultraviolet transmission of gel silica, standard silica, and two fused silica glasses, from Hench et al. [97].

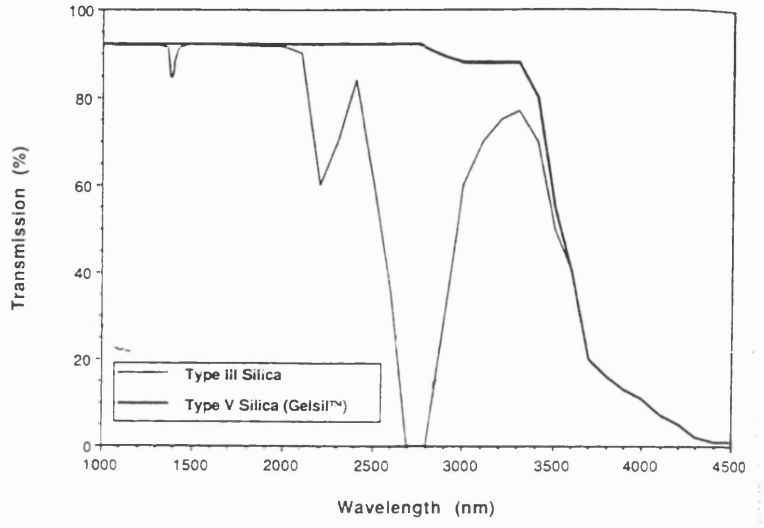


Figure 2.5: Near infrared transmission of gel silica, standard silica, and two fused silica glasses, from Hench et al. [97].

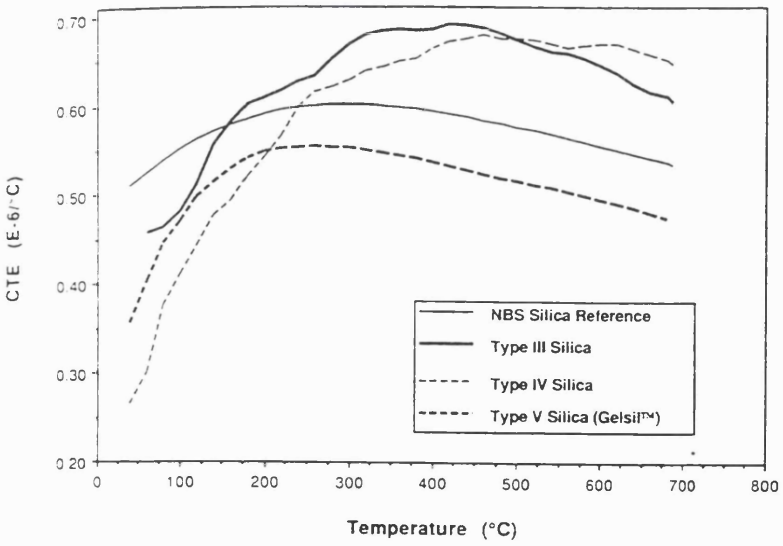


Figure 2.6: Coefficient of thermal expansion of gel silica, standard silica, and two fused silica glasses, from Hench et al. [97].

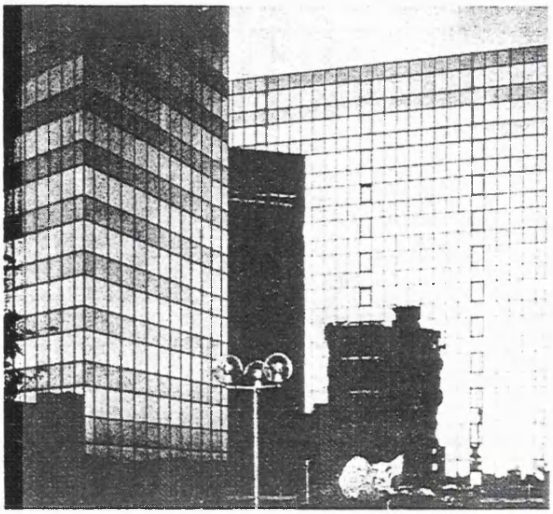


Figure 2.7: Office buildings with sol-gel coated glass windows, Germany [42].

2.2.2 Coatings

Optical coatings alter the reflectance, transmission and absorption of the substrate. Architectural glass, coated with a gel containing TiO_2, to control the reflectance, and Pd, to control absorption [42], is currently applied to office buildings, as shown in Figure 2.7, which appear outwardly uniformly reflective, while light transmission is controlled in accordance with sun exposure, to minimise summer cooling costs (different sides of the building might even have coatings with different transmission, due to different sun exposure). The $SiO_2 - TiO_2$ binary system is particularly suitable because the refractive index for films consolidated at 500^oC increases continuously with TiO_2 content from 1.4 to 2.2, as can be seen in Figure 2.8. Different absorptions and a variety of colored coatings can be produced incorporating different transition metals.

Oxide coatings on glass and silicon substrates have also been used extensively as antireflective surfaces, for example in solar cells, laser optics and photographic lenses, using multiple coating techniques to decrease transmission in a wide spectral region, as shown in Figure 2.9. The reflectance of a surface can be almost completely eliminated when the refractive index of the surface varies smoothly from the value of air to the value of the substrate [42]. The refractive index decreases linearly with porosity, as shown in Figure 2.8, and consequently careful control of the microstructure is necessary to obtain materials with the properties required.

Sol-gel films can protect against corrosion or abrasion, increase strength or provide planarisation (decreasing diffuse and increasing specular reflectance). In silicon-based microelectronics applications, sol-gel films are a low-temperature alternative to thermal SiO_2 and compete with CVD silica [42]. Three major drawbacks of sol-gel films, from the standpoint of abrasion and corrosion resistant layers are: 1) Thick coatings, larger than 1 μ, are difficult to achieve without cracking; 2) Sol-gel films are in general quite brittle; 3) Relatively high temperatures are required to achieve good properties.

However, organically modified systems, that can potentially combine the hardness of ceramics with the toughness of organic polymers, can be deposited in thick layers at low temperatures without cracking [212]. Organically modified silicate films are currently being used as antiscratch

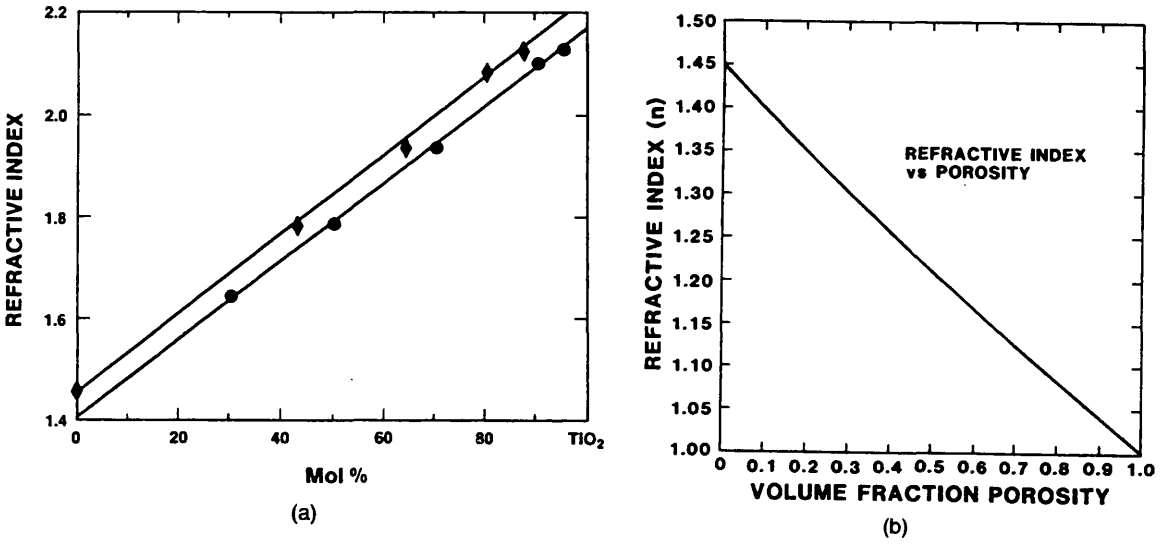


Figure 2.8: Refractive index as a function of: a) x mol% for gel-derived films in the binary system $xTiO_2 - (100 - x)SiO_2$, densified at 450^oC (circles) and 500^oC (diamonds); b) volume fraction porosity [42].

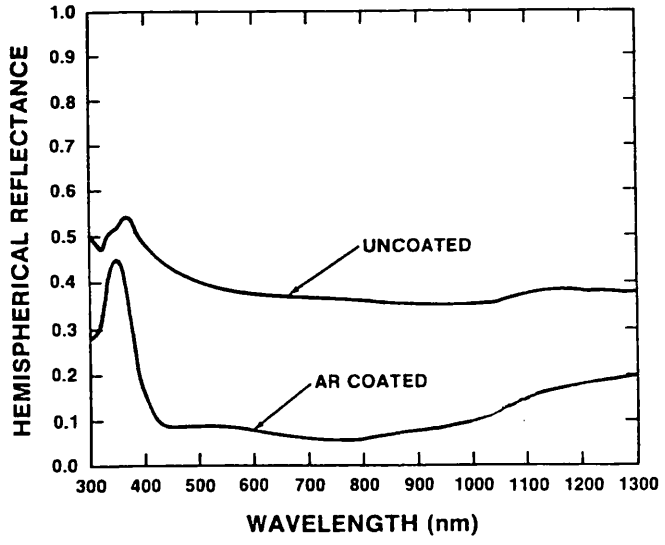


Figure 2.9: Reflectance of uncoated and $SiO_2 - TiO_2$ double layer coated silicon solar cells [42].

coatings on acrylic and polycarbonate windows and lenses [42].

Other applications include electronic thin films, namely high temperature superconductor films and titania films used as photoanodes [42]. Ferroelectric $BaTiO_3$ and several other titanates and zirconates, transition metal oxide gels, namely TiO_2, SnO_2, WO_3 and V_2O_5, with a very high electrical conductivity, can also be currently fabricated [154].

Porous films explore specific features of gels, namely pore volume, surface area and surface reactivity, to achieve specific goals, namely in sensors and catalytic surfaces. As discussed by Brinker et al. [42], zeolite particles with pores between 5 and 10 Å, like ZSM-5, have been embedded in silicate sol-gel matrices with pore size smaller than 4Å, so all molecules larger than nitrogen can be adsorbed only within the zeolite channels. A ZSM-5 zeolite/silicate composite (ZSM-5 pore size = 6 Å) can easily separate propanol (kinetic size = 4.7 Å) from iso-octane (kinetic size = 6.2 Å).

2.2.3 Membranes

High surface areas and small pore sizes characteristic of inorganic gels are properties unattainable by conventional ceramic processing methods. According to Brinker et al. [42], sol-gel membranes also offer several advantages when compared with conventional organic polymer membranes: 1) They can be operated and sterilised at high temperatures; 2) They do not swell or shrink in contact with liquids; 3) They are much more abrasion-resistant. These properties can be exploited in applications such as filtration, separation, catalysis and chromatography. Ultrafiltration and reverse osmosis, microfiltration of water, wine, beverages and ultrafiltration of milk have also been discussed as possible applications [42].

2.2.4 Powders

The fabrication of radioactive solid spheres is historically one of the most important and impressive sol-gel applications. The technique can be processed easily by remote control and, due to liquid processing, it eliminates environmental hazards associated with radioactive dusts, a major problem in the nuclear industry. The process involves dropping spray-formed sol spheres into a column of a heated inert liquid. Internal gelation occurs during passage of the spheres down the column, after which they are collected, washed and fired at the bottom of the columns. UO_2 spheres with diameters ranging from 30 μ to 1200 μ and density in excess of 99% have been routinely fabricated in this continuous process. $UO_2 - PuO_2$ and CeO_2 spheres have been similarly fabricated and the process can be applicable to many other oxides [154]. This internal gelation method has also been applied to prepare ZrO_2-based and other complex oxide spheres, containing high-level radioactive wastes, which are extremely leach resistant [154]. An alternative conventional sol-gel method, using $Si(OEt)_4$ and $Al(OEt)_3$, was also able to produce highly nonleachable pellets, after sintering at only 800^oC [154]. The combination of low volatility of radionuclides, low processing temperatures and low leach rates make the gel-derived glass pellets a potentially attractive high level waste form for long-term storage.

Other applications for powders include catalysis, chromatography, aerosols, pigments, abrasives and fillers.

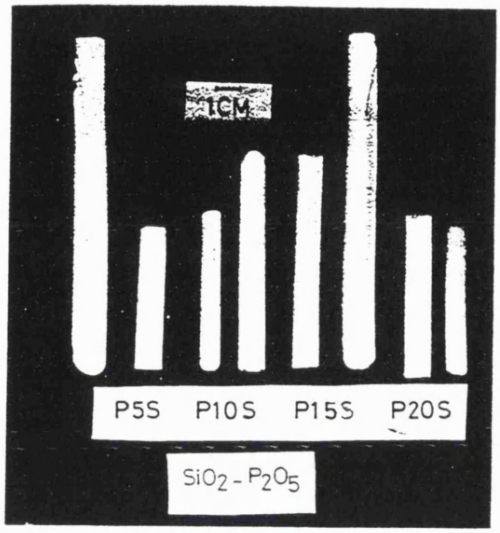


Figure 2.10: Monolithic aerogels in the $SiO_2 - P_2O_5$ binary system, from Woignier et al. [247].

2.2.5 Aerogels

Since they were first produced, in the early 1930s, aerogels have been the subject of increasingly important research, due to their unique properties; and nowadays specific conferences are dedicated exclusively to them. SiO_2-based transparent tiles as large as $20 \times 20 \times 3$ cm^3 [76], and monoliths of complex systems such as $SiO_2 - B_2O_3 - P_2O_5$ [247], shown in Figure 2.10, were produced more than ten years ago. As reviewed by Fricke [76, 75], due to their extremely high porosities (between 85% and 98%, in the porous range 1-100nm), aerogels have extremely low densities, between 0.08 and 0.3 g/cm^3, very small index of refraction (between 1.015 and 1.06), extremely small Young's modulus ($E \approx 10^6 - 10^7 N/m^2$), sound velocities (100-300 m/s, compared with 5×10^3 m/s in silica glass) and thermal conductivities (0.02 W/mK at ambient air pressure and 0.01 if evacuated, the lowest values ever found in powders and solid bodies for the same pressure and temperature [76]).

Aerogels have been used in Čerenkov counters for detection of relativistic particles, at CERN/Geneva and DESY/Hamburg, as the small index of refraction allows the momentum of relativistic particles to be determined in a range which is not covered by compressed gases or by liquids [166]. Because aerogels have high solar transmission and thermal resistance, layers of granulated silica-aerogel between protective glasses have been used to insulate houses, as the radiation passes through but the heat subsequently produced is retained. Small high velocity particles in space can be captured by low density aerogels and gradually decelerated in their porous structure [75], this way acting as a soft wall and reducing considerably the potential damage of the impact. Other possible applications for aerogels include gas filters in 20-100 nm region and substrates for catalytic materials.

2.2.6 Biological

The structures of living organisms are usually made of a rather restricted range of materials but with a great variety of microstructures. Thus most plants are built of cellulose and all vertebrates rely on collagen to withstand tensile forces [47]. Collagen appears as a pure tensile

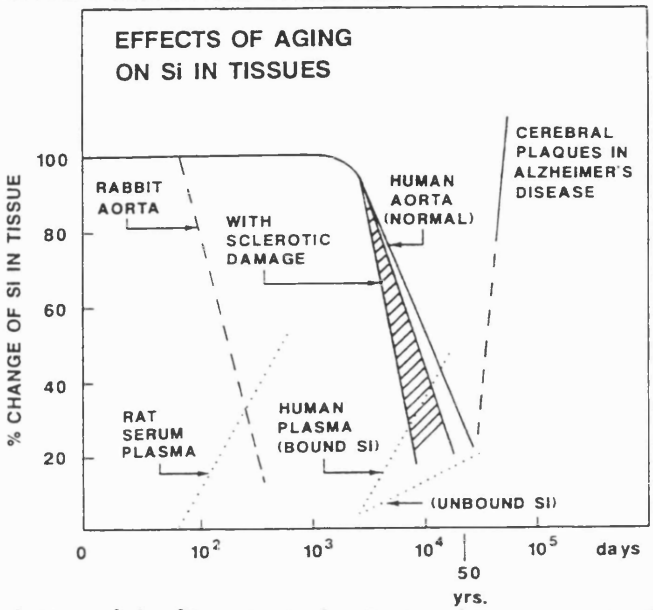


Figure 2.11: Time evolution of the Si content of rodent and human aorts, from Hench et al. [98].

fibre in tendon, a reinforcement for an elastic sheet in skin, and a mineral-reinforced matrix in bone. As Calvert wrote [47], biology seems to have displayed little versatility in the chemistry of structural materials, but shows great subtlety in processing to obtain different microstructures. Manufactured materials tend to follow the opposite trend. They have many different chemical compositions but most are used pure or with a simple reinforcement. Important research is currently being carried on to study how natural materials, like bone and mollusc shell, are actually made, in order to use this knowledge to produce new microstructures using the structural control potentially offered by sol-gel processes.

To understand the mechanisms of the low temperature organic-inorganic processes associated with silica sol and gel formation, aging and drying, might be potentially vital for understanding several biological and biomedical mechanisms, as important as the mineralisation of bone and dentim, plant metabolism and genetic manipulation, arteriosclerosis, tissue bonding of bioactive implants, and mechanisms of precyte evolution, as described by Hench et al. [98]. Figure 2.11 shows the logarithmic decrease in human and rodent aortic Si content with time. This drastic reduction of Si for individuals 10-20 years old, is attributed to the loss of Si bound to a mucopolysaccharide in the wall of the aorta. This loss appears to degrade the integrity of the wall, reduces its elasticity, increases lipid transport across the wall and increase the propensity for forming atherosclerotic plaques, hardening the arteries and in last instance conducting to heart attacks. Human aortas damaged by sclerotic lesions have been reported to have 1/3 less bound silica. The association of a hydroxylated polymerised silica gel surface with bonding of amino acids, collagen, mucopolysaccharides, soft and hard tissues has been studied extensively using special compositions of the glass system $Na_2O - CaO - P_2O_5 - SiO_2$, which indeed develops chemical bonds with living tissues [98]. The consequences of these kind of studies in understand the fundamental issues of life and even prolonging life might be of major significance.

2.2.7 Preservation

Since the nineteenth-century, attempts have been made to preserve stone and sculpture with alkoxysilanes [245] and in the last 20 years the subject has raised considerable research interest, with several books and congresses dedicated to this matter. Although considerable advances have been made in the use of gels derived from alkoxysilanes as consolidants for stone, the results are still neither predictable nor consistent [245], mainly because a fundamental understanding of these consolidants is lacking. Organically modified silicate films are currently being used as coatings to protect medieval glass from corrosion [42].

Chapter 3

Basic principles

3.1 General

Sol-gel processing is a general designation for a broad range of experimental methods aiming to produce high quality amorphous and crystalline solids by preparation of colloidal solutions and subsequent transformation in gels and homogeneous solid materials, as a result of several, carefully controlled, chemical and physical transformations. According to Hench et al. [96], the global process can be divided in several steps: *hydrolysis and condensation*, *gelation*, *aging*, *drying*, *stabilisation* and *densification*.

Hydrolysis and condensation reactions of carefully chosen chemical precursors, in liquid solution, lead to the formation of a *colloid*. A colloid is a two-phase suspension where the particles of the dispersed phase are so small, 1-1000 nm [42], that gravitational forces are negligible and interactions are dominated by van der Walls and Coulombic forces. Due to their small mass and inertia, these particles exhibit *Brownian motion*, moving along random trajectories governed by momentum transference in collisions. A *sol* is a colloidal suspension of solid particles in a liquid, an *emulsion* a colloidal suspension of liquid droplets in a liquid and an *aerosol* a colloidal suspension of particles in a gas: a *fog* if the particles are liquid and a *smoke* if they are solid. A sol formed by suspensions of branched macromolecules is usually called a *polymeric* sol, whereas a sol formed by dense particles is called a *particulate* sol.

Further condensation of the sol aggregates leads to the formation of larger molecules, until a single molecular system extends throughout the liquid solution, completing the *gelation* process. The *gelation point*, when the sol becomes a gel, can therefore be defined microscopically as the degree of reaction at which this single giant molecule is formed, whereas macroscopically it can be defined as the instant at which the system can support a stress elastically.

Several theories have been proposed to describe the gelation process, namely the *classical theory*, developed by Flory [74], the *percolation theory*, reviewed by Zallen [250], where the *percolation threshold* is the model equivalent of the gel point, and more recently, the *fractal theory*, introduced by Mandelbrot [158]. When the chains of a polymeric sol grow randomly or the particles of a particulate sol aggregate, fractal structures may be formed.

The gel structure is best described as a two-phase system formed by the juxtaposition of continuous solid and liquid phases (in the sense that both phases extend continuously throughout the whole system) of colloidal dimensions (in the sense that everywhere in the system the distance between the two phases never exceeds 1000nm).

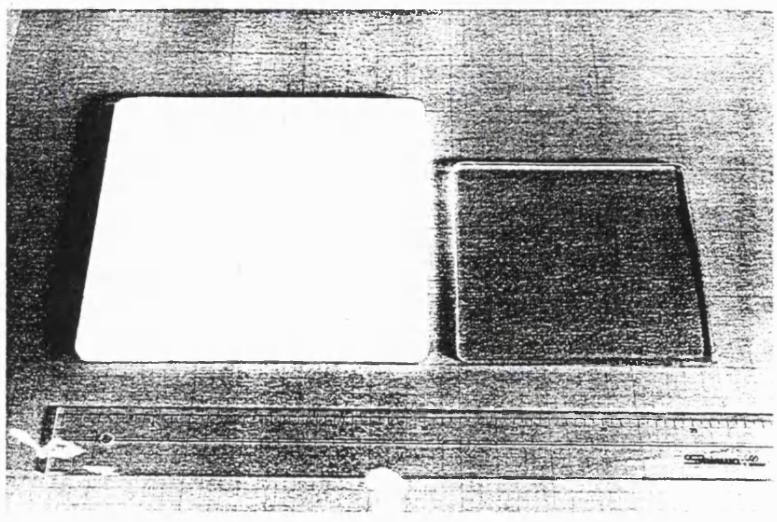


Figure 3.1: Large dried gel plate and corresponding sintered glass [42].

The polycondensation process does not stop at the gelation point and it continues for hours or weeks, during the aging period. The cast gel remains completely immersed in liquid, this way allowing repeated solution and reprecipitation of the structure, to decrease the number of defects and the porosity and to increase the thickness of interparticle necks[96]. A relaxed aged gel must develop sufficient strength to resist cracking during drying.

During drying the liquid is removed from the interconnected pore network. Large capillary stresses can develop during drying when the pores are small, typically < 20 nm [96]. When a gel monolith is dried under hypercritical conditions, the network does not collapse and a low density *aerogel* is produced. Aerogels can have pore volumes as large as 98% and densities as low as 0.08 g/cm^3. When the gel is dried at ambient pressure, *shrinkage* occurs, the volume is often reduced by a factor of 5 to 10 and the monolith is called a *xerogel*. To prevent cracking, *drying chemical controlling additives*, DCCAs, are added. If the pore liquid is primarily alcohol based, the monolith is often called an *alcogel*. Although sol-gel processes are usually carried out using a common solvent, ultrasonic irradiation can be used to promote hydrolysis and condensation [252], producing special gels called *sonogels*.

The subsequent removal of surface reactive groups from the pore network, dehydration or chemical stabilisation, results in a chemically stable ultraporous solid.

Finally the porous gel is sintered at high temperatures, to force its densification and the elimination of the pores. The densification temperature is about 1000^0C, though it depends considerably on the dimensions of the pore network, the connectivity of the pores and its surface area [96]. The glasses thus obtained (see Figure 3.1) ultimately become equivalent to the glasses obtained by conventional melting methods [153, 242, 175] (see also [87, 234], but with much higher degrees of purity and homogeneity.

3.2 Precursors

Metal alkoxides are the most common precursors used in sol-gel processes, essentially because they are easy to manipulate, they are soluble in organic solvents and they react rapidly with wa-

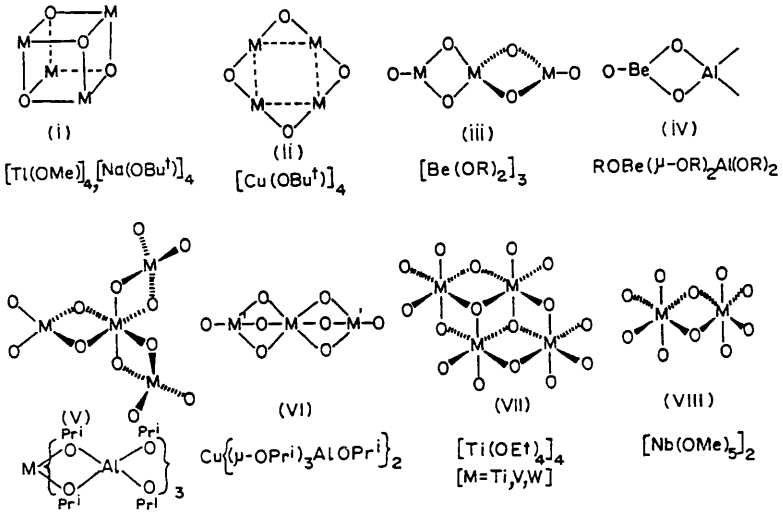


Figure 3.2: Structure of some metal alkoxides, (i) cubanes; (2) planar; (3) bridged trigonal and tetrahedral units; (5)-(viii) bridged tetra- and octa-hedral units, as presented by R. C. Mehrotra [165]. The alkyl groups were omited for simplicity.

ter to produce the hydrolysed species required to continue the aggregation process. Furthermore, they can be easily purified by volatization or crystallisation.

Although metal alkoxides have been known for more than a century, it was not until 1978 that a monograph was published on this topic. In fact, the chemistry of alkoxides of almost all the elements in the periodic table has been elucidated only during the past few decades, due to the efforts of D. C. Bradley [39], R. C. Mehrotra [164, 165, 166] and others, who created a complete new family of chemical compounds, some of which are summarised in Figure 3.2.

Although several different routes have ben proposed to synthesize metal oxides, the commercial products, widely used in sol-gel research, are essentially manufactured by: 1) reactions of metals with alcohols, used to prepare alkoxides of alkali metals, alkaline earths and trivalent metals [39]:

$$M + nROH \longrightarrow M(OR)_n + n/2H_2 \uparrow$$

2) reaction of metal halides with alcohols, used to prepare trivalent and higher valent metals:

$$MCl_n + nROH \longrightarrow M(OR)_n + nHCl \uparrow .$$

Even for those metal halides reacting only partially with alcohols, the reaction can be pushed to completion, using a base like ammonia or alkali alkoxide [164]; 3) reaction of metal halides with sodium alkoxides:

$$MCl_n + nNaOR \longrightarrow M(OR)_n + nNaCl$$

3) alcohol interchange:

$$M(OR)_n + nR'OH \longrightarrow M(OR')_n + nROH$$

If ROH is more volatile than R'OH, the reaction can be driven quantitatively to the right-hand side by fractional distillation.

Bimetalic and higher metallic alkoxides can be prepared by reaction between the constituent alkoxides [164]:

$$M(OR)_m + M'(OR)_n \longrightarrow MM'(OR)_{m+n},$$

by reaction of metal halides with other bimetallic alkoxides:

$$MCl_n + nM'(M''(OR)_n) \longrightarrow M(M''(OR)_n)_m + nM'Cl \downarrow$$

or by more specific reactions.

The physical and chemical properties of *metalorganic* compounds (with metal-oxygen-carbon linkages, different from organometallic compounds, with direct metal-carbon bonds), depend directly on the electronic distribution around the bonds M-O and O-C, which determine if the alkoxides are non-volatile solids, low-volatile polymeric compounds or volatile monomeric covalent liquids, as in the silicon alkoxides.

Molecular association of alkoxides influences the physical and chemical properties of these compounds and may affect the processes which lead to the sol-gel transformation. The oligomerization of metal alkoxides is due to the tendency of the metal to maximise its coordination number and fill its empty d and f orbitals, establishing dative intermolecular bonds accepting the lone pair of oxygen from neighboring alkoxides groups. The degree of association depends of the metal atom, of the alkoxy group, and in some cases of the solvent. Moreover, aging effects may change the oligomerization degree. In general, the degree of association tends to increase with the size of the central atom and to decrease with increasing branching and bulkiness of the alkoxy group, due to steric effects, as can be seen in Table 3.3.

The high volatility of some alkoxides is an important property because it allows us to obtain pure precursors by distillation. However, special attention is necessary in sol-gel solutions containing several precursors, with different volatilities, in order to avoid unwanted changes of composition during the synthesis. Although dependent on many parameters, volatility typically increases with branching and decreases with the size of n-alkyl chains and with the degree of oligomerization [91].

The viscosity of the alkoxides usually follows as expected the opposite trends to that of volatility; but a general rule aiming to describe, even qualitatively, the trends on viscosity of the different oligomeric species has not been found. In thin film and fibre production, the viscosity in solution becomes probably the most critical parameter.

Molecular association, or complexation, as discussed by Dislich [66], is considered to be the first step in the synthesis of multicomponent glasses by the sol-gel route. In fact, the reaction between alkoxides of elements with different electronegativities or which are able to increase the coordination number forming coordination complexes constitutes the basis of the chemistry of double alkoxides [91]:

$$MOR + M'(OR)_n \longrightarrow M[M'(OR)_{n+1}]$$

where M = alkali or alkaline earth metals.

Typical *tetraalkoxysilanes* used in silica-based sol-gel processes are presented in Table 3.1. $Si(OCH_2CH_3)_4$ TEOS (silicon tetraethoxide or tetraethoxysilane or tetraethyl orthosilicate) and $Si(OCH_3)_4$ TMOS (silicon tetramethoxide or tetramethoxysilane or tetramethyl orthosilicate) are the most commonly used precursors in silica-based sol-gel processes, due to their simplicity. They are normally prepared by the Ebelman's technique, reacting tetrachlorosilane with the corresponding alcohol and producing HCl as a by-product:

$$SiCl_4 + CH_3CH_2OH \longrightarrow Si(OCH_2CH_3)_4 + 4HCl$$

Group I	$LiOBu^t$	hexameric
Group II	Be primary alkoxides	infinite polymers
	tertiary alkoxides	dimeric and trimeric
Group III	B lower alkoxides	monomeric
	$Al(OEt)_3$	tetra-hexameric when fresh
		polymeric on aging
	$Al(OPr^i)_3$	dimeric in vapor phase
		trimeric in solution when fresh
		tetrameric on aging
	$Al(OBu^t)_3$	dimeric
	$Ga(OEt)_3$ and higher normal alkoxides	tetrameric
	$Ga(OPr^i)_3$	dimeric
	$Ga(OBu^t)_3$	dimeric
Group IV	Si, Ge	monomeric irrespective of the chain length and branching of alkoxy group
	$Sn(OMe)_4$	highly associated
	Sn *n*-alkoxides	tetrameric
	$Sn(OPr^i)_4$	trimeric
	$Sn(OR^t)_4$	monomeric
Group V	As	monomeric
	Sb	monomeric
	Bi	monomeric
Group VI	S	monomeric
	Se	monomeric
	Tl	monomeric
Transition elements		
Cu(II), Ni(II), Co(II)		polymeric
Mn(II), Cr(II)		polymeric
Cr(III)		polymeric except
$Cr(OBu^t)_3$		dimeric
$Cr(OBu^t)_4$		monomeric
$V(OMe)_4$		trimeric
$V(OEt)_4$		dimeric
$V(n\text{OPr})_4$, $V(n\text{OBu})_4$, $V(n\text{OAm})_4$		1.38, 1.31, 1.27
$V(OR^s)_4$, $V(OR^t)_4$		monomeric
Fe(III) *n*-alkoxides		trimeric
$Fe(OPr^i)_3$, $Fe(OBu^t)_3$		dimeric
$Ti(OMe)_4$		tetrameric
$Ti(OEt)_4$		2.4 depending on environment and concentration
$Ti(OPr^n)_4$, $Ti(OBu^n)_4$		trimeric
$Ti(OPr^i)_4$		1.4
$Zr(OMe)_4$		polymeric
$Zr(OEt)_4$, *n*-alkoxides		3.6
$Zr(OPr^i)_4$		trimeric
$Zr(OAm^s)_4$		dimeric
$Zr(OR^s)_4$, $Zr(OR^t)_4$		monomeric
Ce(IV) *n*-alkoxides		tetrametric
Th(IV) *n*-alkoxides		hexameric
Nb(V), Ta(V) *n*-alkoxides		dimeric (lower in ROH)
Lanthanons		dimeric-tetrameric

Figure 3.3: Oligomerization of alkoxides, as reviewed by M. Guglielmi et al. [91].

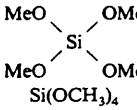
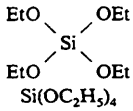
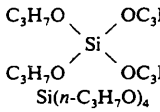
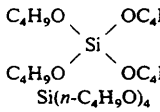
Name	MW	bp	n_D (20°)	d (20°)	η (ctsks)	Dipole Moment	Solubility
 $Si(OCH_3)_4$ tetramethoxysilane TMOS	152.2	121	1.3688	1.02	5.46	1.71	alcohols
 $Si(OC_2H_5)_4$ tetraethoxysilane TEOS	208.3	169	1.3838	0.93	—	1.63	alcohols
 $Si(n\text{-}C_3H_7O)_4$ tetra-*n*-propoxysilane	264.4	224	1.401	0.916	1.66	1.48	alcohols
 $Si(n\text{-}C_4H_9O)_4$ tetra *n*-butoxysilane	320.5	115	1.4126	0.899	2.00	1.61	alcohols
$(MeOCH_2CH_2O)_4Si$ tetrakis(2-methoxyethoxy) silane	328.4	179	1.4219	1.079	4.9	—	alcohols

Table 3.1: Physical properties of typical tetraalkoxysilanes utilised in sol-gel processes [42].

To decrease the *functionality f* of the reactants (its number of active sites) and consequently simplify the structure of the colloidal particles, $R'Si(OR)_3$ *organotrialkoxysilane* and $R'_2Si(OR)_2$ *diorganodialkoxysilane* precursors might be used, where R' represents a non-hydrolysable ligand. Typical *organoalkoxysilanes* used in silica-based sol-gel processes are presented in Table 3.2.

In order to understand better the hydrolysis-condensation of $Si(OC_2H_5)_4$,the reactions of the corresponding three and two functional precursors, methyltriethoxysilane, $(CH_3)Si(OC_2H_5)_3$, MTES, and dimethyldiethoxysilane, $(CH_3)_2Si(OC_2H_5)_2$, DMDES, have been studied, as shown in Figure 3.4 [207].

To control the short-range architecture of the silica networks, multi-center alkoxides like $Si_2O(OCH_3)_6$ (hexamethoxydisiloxane), $Si_3O_2(OCH_3)_8$ (octamethoxytrisiloxane) and the cubic cage $Si_8O_{12}(OCH_3)_8$ can be prepared to produce specific oligomers acting as molecular

Name	Formula	MW	pb (°C)	d ($g\text{-}cm^{-3}$)	Dipole Moment (debyes)	n_D	η (millipoise)
Methyltriethoxysilane	$MeSi(OEt)_3$	178.3	141	0.895	1.72	1.3832	—
Methyltrimethoxysilane	$MeSi(OMe)_3$	136.22	102	0.955	1.6	1.3696	0.5
Methyl tri-*n*-propoxysilane	$MeSi(n\text{-}OPr)_3$	220.4	83	0.88	—	—	—
Phenyltriethoxysilane	$PhSi(OEt)_3$	240.37	112	0.996	1.85	1.4718	—
Vinyltriethoxysilane	$H_2C{=}C(H)\text{-}Si(OEt)_3$	190.31	160	0.903	1.69	1.396	0.7

Table 3.2: Physical properties of typical organoalkoxysilanes utilised in sol-gel processes [42].

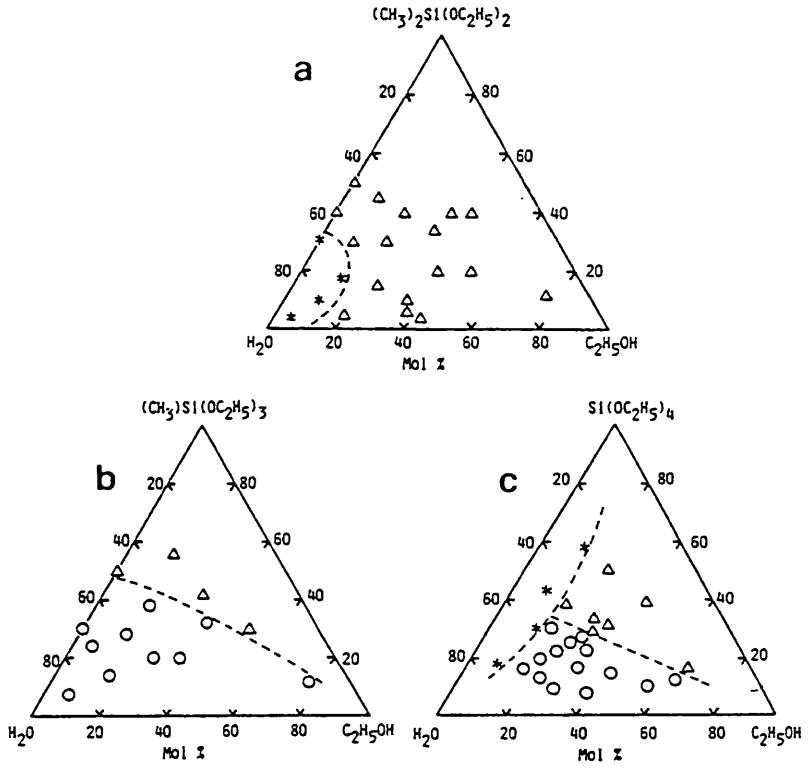


Figure 3.4: Behaviour of (a) DMDES-H_2O-C_2H_5OH, (b) MTES-H_2O-C_2H_5OH and (c)TEOS-H_2O-C_2H_5OH solutions (circum.= homogeneous solution and gelation; triang.= homogeneous solution but no gelation; aster.= immiscible), from Sakka et al. [207].

building blocks. For example, using $Si_2O(Et)_6$, as sol-gel precursor, only even clusters will be produced, assuming that the reverse hydrolysis is relatively unimportant, and consequently $_{29}Si$ NMR studies of the cluster aggregation are greatly simplified [55]. The octamer can be synthesized by the following reactions [42]:

$$Si_8O_{12}H_8 + 8Cl_2 \longrightarrow Si_8O_{12}Cl_8 + 8HCl$$

$$Si_8O_{12}Cl_8 + CH_3ONO \longrightarrow Si_8O_{12}(OCH_3)8 + 8NOCl$$

Combining several different precursors, it is possible to prepare a enormous range of hybrid silicate systems, *organically modified silicates*, with unique properties. In particular, it is possible to produce structures with inorganic precursors such as $Si(OR)_4 + R_2Si(OR)_2$ with precursors like $YR'Si(OC_2H_5)_3$, where R' and Y represent an alkilene and an organofunctional group, respectively. If Y is a polymerisable group, a organic network might be formed in addition to the inorganic one, increasing even further the range of materials that can be produced by these combining techniques. The solubility of the various precursors and their thermal stability at the required temperature, play a key role in the design of such chemical processes.

Schmidt and co-workers [192], have studied the sol-gel transformations occurring to the epoxysilane $(MeO)_3SiC_3H_6OCH_2CHCH_2O$, when allowed to react with $Si(OR)_4$, $Ti(OR)_4$ and $Zr(OR)_4$. Sol-gel processes are usually carried out with acid or basic catalysis. Under acid conditions, epoxides may react with water to form undesirable glycols:

$$(MeO)_3Si(CH_2)_3OCH_2CHCH_2O \longrightarrow (-O)_3Si(OCH_2)_3OCH_2CH(OH)CH_2(OH).$$

Furthermore, the addition of water to systems containing $Ti(OR)_4$ or $Zr(OR)_4$, leads to the precipitation of $Ti(OR)_2$ or $Zr(OR)_2$. Consequently, water has to be added very carefully, to prevent these effects. It is shown that $Ti(OR)_4$ and $Zr(OR)_4$, when combined with the epoxysilne, act in two different ways: as network formers of the inorganic network and as catalysts of the epoxide polymerisation [192].

Epoxysilanes can be used to form simultaneously inorganic and organic networks because the covalent Si-C bonds cannot be broken by hydrolysis. This behaviour is not observed with transition metals, where the more ionic M-C bonds can be easily cleaved by water. Strong complexing agents, SCL, have therefore to be used, like β-diketones and allied derivatives, polyhydroxylated ligands such as polyols, and also α- or β-hydroxyacids, according to C. Sanchez and M. In [208]. The use of these strong complexing ligands in modified systems $M(OR)_{4-n}(SCL)_n$, with M = Ce, Ti, Zr, allows the synthesis of organic-inorganic copolymers of transition metals, as the one represented in the beautiful micrograph of Figure 3.5. The structure and properties of these copolymers depend strongly on the complexation ratio = SCL/M and on the hydrolysis ratio in the initial solution.

Non-alkoxide precursors are sometimes used in sol-gel processes, when it is difficult to obtain the corresponding alkoxide precursor, or when their lower price becomes fundamental to viabilize a potential commercial application. The most used are nitrate and chloride inorganic salts, typically $LiNO_3$, $NaNO_3$, $Ca(NO_3)_3$, $Al(NO_3)_3$ and $AlCl_3$, or organic salts like acetylacetonates and acetats [91]. Use of these precursors involves a different chemistry that leads to different structures and additional problems, like the removal of the anions from the system. A further difficulty when working with nitrates is their tendency to crystallise during the drying of the gel [91].



Figure 3.5: TEM micrograph of an hybrid organic-inorganic copolymer, from C. Sanchez et al. [208].

Soda glass (sodium silicate) was used until 1968 to prepare aerogels, following the reaction:

$$Na_2SiO_3 + 2HCl + nH_2O \longrightarrow SiO_2.H_2O + 2NaCl + (n - x + 1)H_2O.$$

It was replaced by metal alkoxydes because these allow the production of silica aerogels with much larger surface areas, $1500m^2$, than achieved before, $600m^2$ [166].

3.3 Hydrolysis

Metal alkoxides, in general, tend to hydrolyse rapidly when exposed to water, according to the reaction:

$$M - OR + H_2O \longrightarrow M - OH + ROH.$$

Transition metal alkoxides are usually too reactive and they have to be stabilised by adding complexing agents, like carboxylic acids or β-diketones, to avoid fast precipitation [149]. Silicon alkoxides are much less sensitive to hydrolysis, due to the high electronegativity of Si, and acid or base catalysis is usually employed in sol-gel processing, to enhance their reactivity.

3.3.1 Inductive effects

Inductive effects play an important role in the hydrolysis reaction and in sol-gel chemistry in general. As shown on Figure 3.6, the electron withdrawing effect of the most usual substituents attached to silicon increases in the order R, OR, OH and OSi, where R represents an alkyl group. Consequently, in both hydrolysis and condensation reactions, electron providing groups are replaced by electron withdrawing groups.

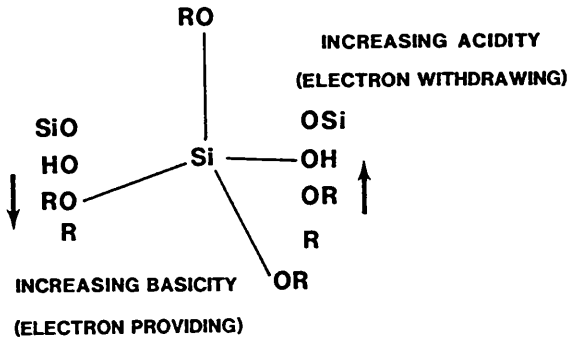


Figure 3.6: Inductive effects of substituents attached to silicon [42].

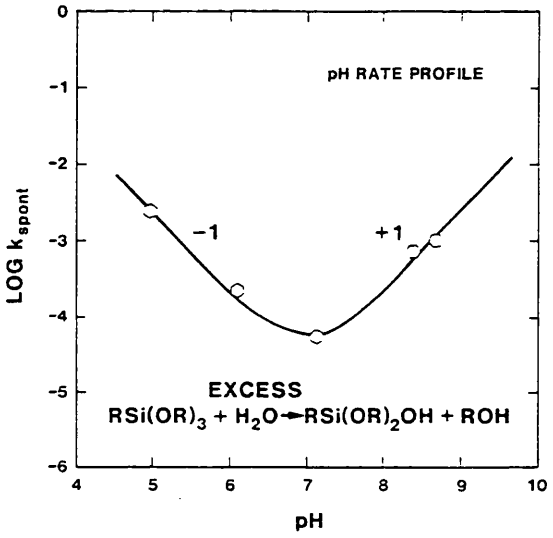


Figure 3.7: pH rate profile for the hydrolysis of a complex alkoxysilane [42].

3.3.2 Catalysis

Mineral acids and ammonia are usually used in sol-gel processing to catalyse the hydrolysis reaction, although several other catalysts are known, like acetic acid, KOH, amines, KF, titanium alkoxides, vanadium and other oxides [42]. Although it has been reported that mineral acids are more effective catalysts than equivalent concentrations of base (see Sakka et al. [206]), this is probably due to the increase in the acidity of silanol groups with the extent of hydrolysis and condensation, that may neutralise basic catalysts. In fact, the rate of hydrolysis seems to increase linearly with the concentration of $[H^+]$ below pH 7 and $[OH^-]$ above pH 7, with slope equal to -1 and +1, as shown in Figure 3.7.

Above pH 7, the hydrolysis mechanism is likely to involve a deprotonated species:

$$Si - OR + OH^- \longrightarrow Si - OH + OR^-.$$

Consequently, each subsequent hydrolysis step should occur faster than the previous one, as OR electron providing groups are being substituted by OH electron withdrawing groups that help to stabilise negative intermediate species.

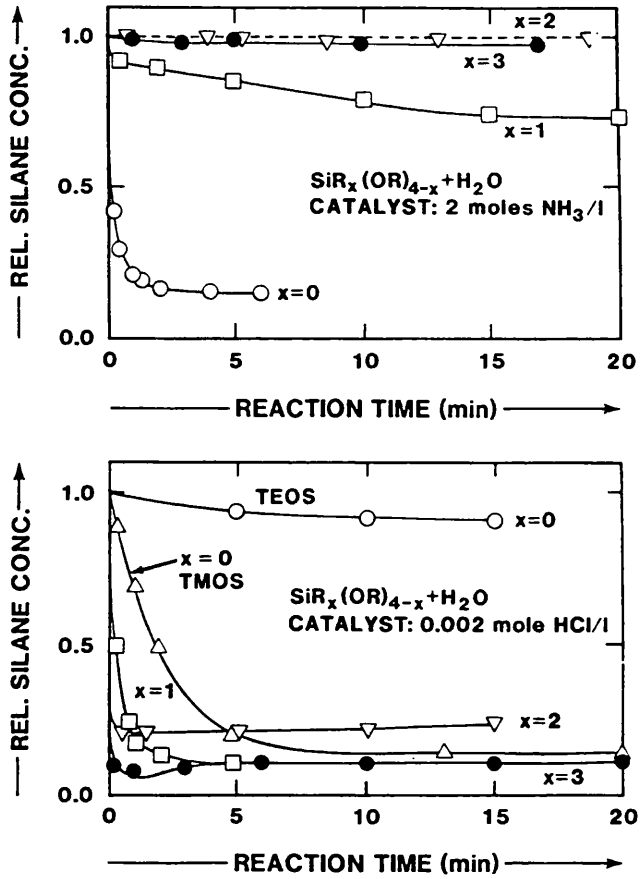


Figure 3.8: Acid- and base-catalysed hydrolysis of different silanes in ethanol: bold cir. $(CH_3)_3SiOC_2H_5$; down tri. $(CH_3)_2Si(OC_2H_5)_2$; squa. $CH_3Si(OC_2H_5)_3$; open cir. $Si(OC_2H_5)_4$; up tri. $Si(OCH_3)_4$ [42].

Below pH 7, the hydrolysis mechanism may involve a protonated species:

$$Si - OR + H_3O^+ \longrightarrow Si - OHR^+ + H_2O,$$

$$Si - OHR^+ + H_2O \longrightarrow Si - OH_2^+ + ROH,$$

$$Si - OH_2^+ + H_2O \longrightarrow Si - OH + H_3O^+.$$

Each subsequent hydrolysis step should therefore be slower than the previous one, as the progressively more electron withdrawing substituents make it more difficult to stabilise the protonated species.

Progressive substitution of ethoxy groups by methyl groups, more electron providing, using methylethoxysilanes, $Si(CH_3)_n(CH_3CH_2O)_{4-n}$ (n increasing from 0 to 3), as precursors, should help to stabilise protonated species and have the opposite effect on deprotonated ones, therefore increasing the hydrolysis rate in acid medium and decreasing it in basic medium. These general trends were indeed observed experimentally, as shown in Figure 3.8.

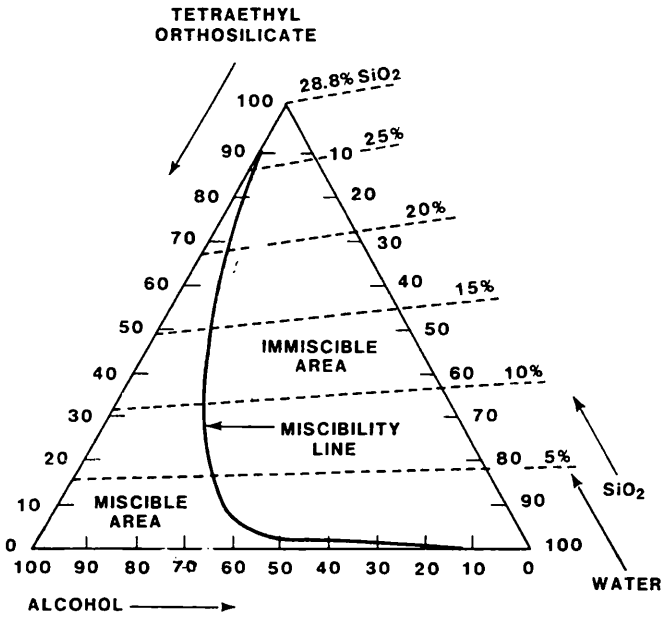


Figure 3.9: TEOS-water-ethanol ternary phase diagram [42].

3.3.3 Solubility

Most alkoxides, in particular TMOS and TEOS, are immiscible with water and a solvent, typically an alcohol, is usually employed to avoid liquid-liquid phase separation. The ternary phase-diagram presented in Figure 3.9 for the most common sol-gel system, $Si(OCH_2CH_3)_4 - H_2O - CH_3CH_2OH$, shows that a significant concentration of ethanol is necessary to avoid the region of immiscibility. In practise this imposes a higher limit on the amount of water that can be added to the solution, for a given alcohol/alkoxide ratio.

Strictly speaking, it is possible to carry out sol-gel precesses without using any solvent, as the alcohol produced during the hydrolysis is enough to remove the initial phase-separation. In fact, ultrasonic agitation has been used, in place of a solvent, to obtain a homogeneous liquid, to produce the so-called sonogels [252]. However, it is presently assumed that for most sol-gel systems, the use of a solvent is desirable [155]. Some of the solvents most commonly used in sol-gel processes are presented in Table 3.3.

Because hydrolysis is catalysed either by OH^- or H_3O^+ ions, solvent molecules that hydrogen bond to hydroxyl or hydronium ions reduce the catalytic activity under basic or acid conditions, respectively. Hydrogen bonding with the solvent may also influence the reaction mechanisms, for example stabilising weak leaving groups [42].

The reverse hydrolysis, reesterification (and in much less extent the reverse condensation), should also depend in a critical way on the solvent used. Using an alcohol with smaller alkyl groups than the alkoxide lead to significant increases in the hydrolysis rate, as important alkyl exchange (transesterification) will occur. In practise, in most experimental sol-gel work, an alcohol with the same alkyl group as the alkoxide is usually used, to avoid increasing even more the chemical complexity of these processes.

The relatively high vapor pressure of the most common solvents proves to be a critical factor in open-system, sol-gel processes, where important weight losses occur during the relatively long

	MW	bp	ρ	n_D	ε	η	μ
Protic							
water H_2O	18.01	100.00	1.000	1.333	78.5	10.1	1.84
methanol CH_3OH	32.04	64.5	0.791	1.329	32.6	5.4	1.70
ethanol C_2H_5OH	46.07	78.3	0.785	1.361	24.3	10.8	1.69
2-ethoxyethanol $C_4H_{10}O_2$	90.12	135	0.93	1.408	—	—	2.08
formamide CH_3ON	45.04	193	1.129	1.448	110	33.0	3.7
Aprotic							
dimethylformamide C_3H_7NO	73.10	152	0.945	1.430	36.7	7.96	3.86
dioxane 1,4 $C_4H_8O_2$	88.12	102	1.034	1.422	2.21	10.87	0
tetrahydrofuran C_4H_8O	72.12	66	0.889	1.405	7.3	—	1.63

bp: °C. n_D: 20°. η: millipoise.
ρ: g/cm^3 at 20°C. Dielectric constant, ε: at 25°C. Dipole moment, μ: debyes.

Table 3.3: Physical properties of solvents commonly used in sol-gel processes [42].

time (hours or even days) necessary for gelation to be completed. This mass transfer, in turn, leads to a important decrease in the specific surface area of the gel, as shown in Figure 3.10, probably with dramatic consequences during the aging and drying stages, where the gel behaviour depends essentially on its microstructure.

3.3.4 Water/alkoxide ratio

The molar ratio water/alkoxide in solution, R, is a key parameter in silica-based, sol-gel chemistry. As each tetrafunctional precursor, like TMOS and TEOS, requires four water molecules to be fully hydrolysed but liberates two during its full condensation, R=2 is enough to complete the sol-gel polymerisation in stoichiometric conditions, though R=4 is necessary to allow full hydrolysis to take place before condensation occurs in a significant amount.

When the amount of water in solution is low, the rate of hydrolysis should increase rapidly with R, as the interactions between alkoxide and water molecules becomes more probable. For large amounts of water, diffusion constraints should no longer be important and hydrolysis should become kinetic-controlled and almost independent of the concentration of water. The condensation rate should decrease steadly with increasing R, because the interaction between the two silanol groups becomes more difficult and the reverse hydration of the siloxane bonds already formed is favoured.

The overall result of these combined effects is shown in Figure 3.11, for various concentrations of solvent. The minimum in each curve represents the region where neither the hydrolysis nor the condensation are seriously affected by the lack or excess of water, respectively. This minimum is slightly shifted to larger R when the concentration of solvent increases, because in these dilute solutions, increasing the amount of water enhances substantially the rate of hydrolysis

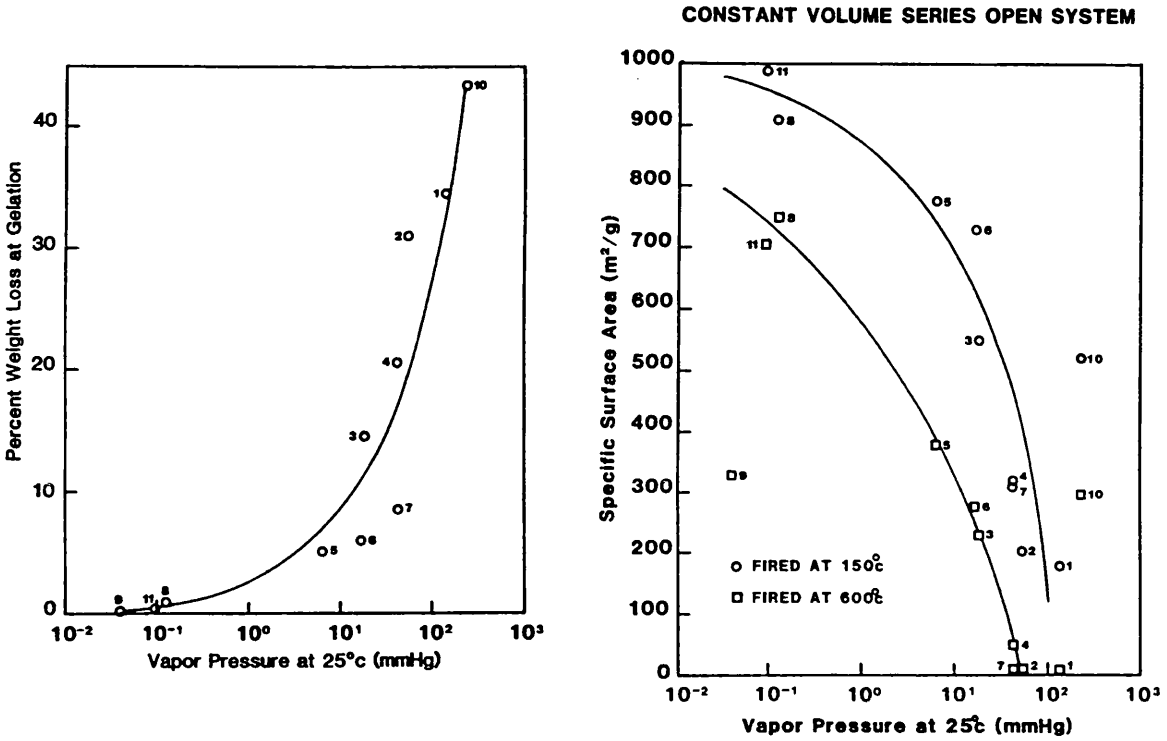


Figure 3.10: a) Weight loss of the solution at gelation and b) Specific surface area of fired gels, as a function of solvent vapor pressure, from Mackenzie [155].

without decreasing as much the rate of condensation. When ($R \gg 2$) the water-producing condensation (requiring two OH groups) is favoured, whereas under stoichiometric conditions ($R \ll 2$), the alcohol-producing condensation (requiring a OR and a OH groups) becomes more important [42].

A detailed analysis of the influence of the water condensation on the hydrolysis reaction can be achieved by following the evolution with time of the various species formed during the hydrolysis of the alkoxide, for different values of R, using ^{29}Si NMR spectroscopy, as shown in Figure 3.12.

3.3.5 Isotopic studies

Isotopic studies with ^{18}O have shown that the reaction of isotopically labelled water with TEOS produces only unlabelled alcohol in both acid- and base-catalysed systems [42], thus supporting the hypothesis of a nucleophilic attack of the oxygen contained in water on the silicon atom:

$$Si - OR + H_2^{18}O \longrightarrow Si -^{18} OH + ROH.$$

The same behaviour is observed in organoalkoxysilanes, $SiR_n(OR)_{4-n}$, with n=1,2 or 3 [42].

3.3.6 Chain effects

The rate of the hydrolysis reaction is very sensitive to steric effects induced by long or branched alkyl chains, as can be seen in Tables 3.4 and 3.5. This effect can be used to advantage in multi-component processing, where metal alkoxides with different reactivities should hydrolyse

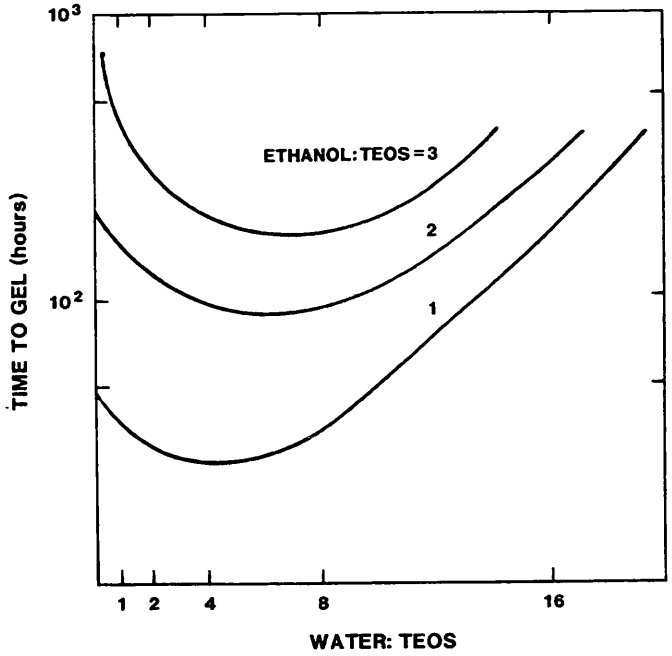


Figure 3.11: Gelation time as a function of the water/alkoxide and alcohol/alkoxide molar ratios, for a TEOS/water/EtOH system [42].

Rate Constant k for Acid Hydrolysis of Tetraalkoxysilanes $(RO)_4Si$ at 20°C.

R	k 10^2 (1 $mol^{-1} s^{-1} [H^+]^{-1}$)
C_2H_5	5.1
C_4H_9	1.9
C_6H_{13}	0.83
$(CH_3)_2CH(CH_2)_3CH(CH_3)CH_2$	0.30

Table 3.4: Long chain effects for acid hydrolysis [42].

approximately at the same time, for homogeneity purposes. This can be achieved either by adding the various precursors at different times to the reactional medium (less reactive first) or by using precursors with more bulky alkoxyl groups attached to more reactive metals. Transesterification may be important, however, in this case, and a complex mixture of the various possible combinations might be formed, hydrolysing at very different rates.

The role of the alkyl groups present in alkoxides and alcohols, in sol-gel reactions, goes, however, far beyond steric and inductive effects only, as can be seen in Table 3.6, for several different combinations of alkoxide/alcohol, always using dilute HCl as the catalyst. The most striking result is the extremely short gelation time obtained for $Si(OOCH_3)_4$, which seems to be due to a strong catalytic effect of the acetate anion CH_3COO^- [155].

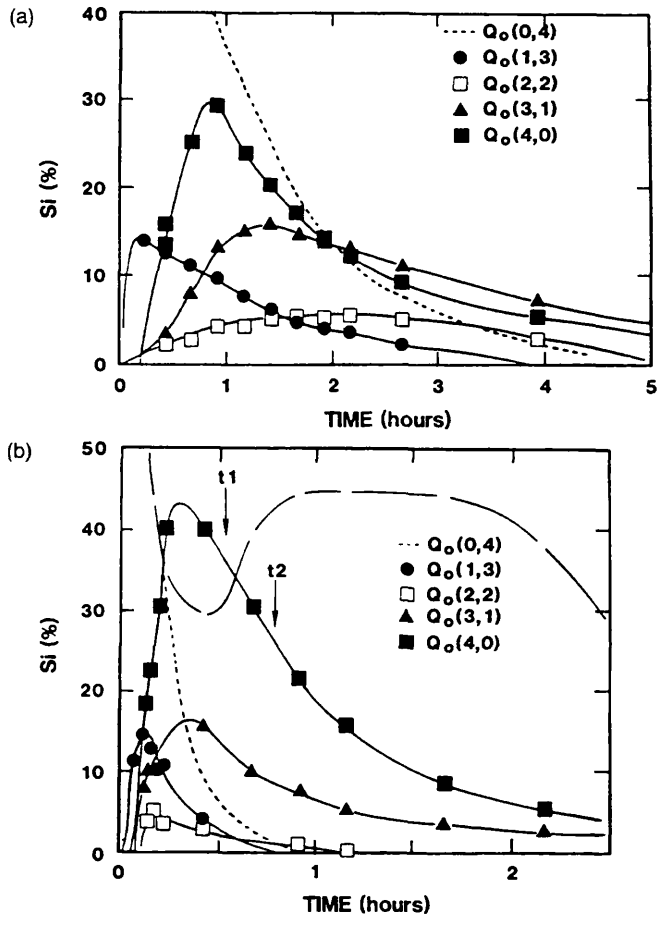


Figure 3.12: Evolution with time of species $Si(OH)_x(OEt)_y$, represented as (x, y), during the acid-catalysed hydrolysis of TEOS, with a) R=3.8 and b) R=10, as determined by ^{29}Si NMR [42].

Rate Constants k (10^2 (1 mol.$^{-1}$ s^{-1} [H$^+$]$^{-1}$)) for Acid Hydrolysis of Alkoxyethoxysilanes $(RO)_{4-n}$ Si$(OC_2H_5)_n$ at 20°C.

	R			
n	C_6H_{13}	$CH_3CH(CH_3)CH_2$ $\diagdown$ CH $\diagup$ H_3C	$CH_3(CH_2)_5$ $\diagdown$ CH $\diagup$ H_3C	$CH_3CH(CH_3)CH_2$ $\diagdown$ CH $\diagup$ $CH_3CH(CH_3)CH_2$
0	0.8	—	—	0.030
1	1.1	—	—	—
2	5.0	0.15	0.095	0.038
3	5.0	—	—	—

Table 3.5: Branched chain effects for acid hydrolysis [42].

	Starting		Gelation Characteristics			
			Gelation Time	Initial Volume	Volume Gel pt.	$\frac{V_{Gel}}{V_{initial}}$
Sample	Compounds	Solvent	(hr)	(cm^3)	(cm^3)	(vol%)
(A) (1)	$Si(OCH_3)_4$	C_2H_5OH	152	24.0	16.7	70
(2)	$Si(OC_2H_5)_4$	C_2H_5OH	242	27.7	17.3	63
(3)	$Si(OC_4H_9)_4$	C_2H_5OH	243	36.0	30.6	85
(5)	$Si(OOCCH_3)_4$	C_2H_5OH	1	25.0	25.0	100
(B) (7)	$Si(OCH_3)_4$	CH_3OH	44	16.5	12.0	70
(8)	$SI(OCH_2H_5)_4$	CH_3OH	108	21	14.7	70
(9)	$Si(OC_4H_9)_4$	CH_3OH	64	29.0	27.7	96
(C) (12)	$Si(OCH_3)_4$	n-C_3H_7OH	131	24.2	21.5	89
(13)	$Si(OC_2H_5)_4$	n-C_3H_7OH	246	28.3	23.5	83
(14)	$Si(OC_4H_9)_4$	n-C_3H_7OH	550	37.5	29.5	79

Table 3.6: Gelation characteristics for SiO_2 gels, from Mackenzie [155].

Solvent systems for 1:4:1.89	Gel times
TMOS + MeOH	129 h
TMOS + EtOH	160 h
TEOS + MeOH	168 h
TEOS + EtOH	321 h
TPOS + PrOH	383 h

Table 3.7: Gel times for different silicon alkoxides at 1:4:1.89 silicon:water:acid ratio, from Kelts [126].

3.3.7 Transesterification and reesterification

The different gelation times obtained for the systems TEOS/MeOH and TMOS/EtOH, show that transesterification was not very significant, at this acid concentration (molar ratio HCl/TEOS = 0.07) [155]. However, transesterification often occurs when alkoxides are hydrolysed in alcohols containing different alkyl groups [42]. In fact, the gelation times obtained by Kelts et al. [126] for the same systems but at much higher acid concentrations (HCl/Si = 1.89) are almost equal, as can be seen in Table 3.7, showing that important transesterification occurred. These differences seem to show that the rate of transesterification increases with the concentration of H^+ in solution. Other authors observed transesterification in acid-catalysed conditions but not under base-catalysed conditions [42]. Transesterification seems to be severely reduced when bulky alcohols are employed and seems to occur more readily after partial hydrolysis, thus suggesting important steric constraint effects. Reesterification seems also to occur much faster under acidic than under basic conditions [42].

3.4 Condensation

When silica has been previously dissolved in water at high temperature, pressure or pH or when a solution containing a soluble silicate (like a inorganic salt or a metal akoxide) is hydrolysed,

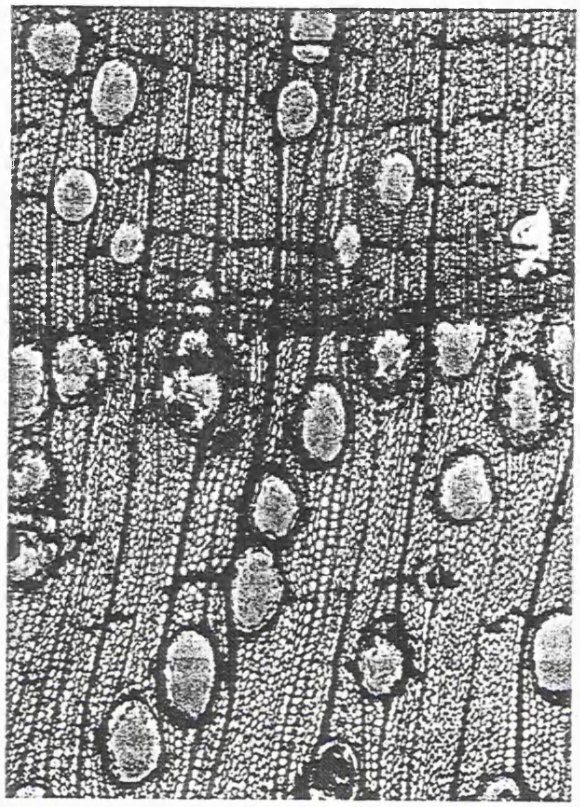


Figure 3.13: Photomicrograph (65x) of a section of silicified wood, from Iler [105].

supersaturated solutions of $Si(OH)_4$ in pure water are formed. Monomeric silica comes out of supersaturated solutions in three ways: 1) As a deposit on a solid surface, where $Si(OH)_4$ condenses with surface MOH groups, where M is a metal that forms a silicate at that pH; 2) As colloidal particles, remaining in suspension, if an insufficient area of a receptive solid surface is available to accept silica rapidly. These may aggregate, forming silica gel, if the concentration of $Si(OH)_4$ is greater than 200-300 ppm [105], or remain in solution, eventually forming opal. Very slow deposition may produce quartz [105]; 3) as biogenic amorphous silica, replicating exactly the detailed structure of organic forms, even after further crystallisation, as the crystals are so small that even submicroscopic structures are retained (see Figure 3.13).

3.4.1 Solubility

There is no evidence that silica is soluble to any appreciable degree in any liquid other than water [105]. The dissolution and deposition of silica in water involves chemical reactions of hydration and dehydration, generally described as:

$$(SiO_2)_n + 2H_2O(SiO_2)_{n-1} + Si(OH)_4$$

For nonporous amorphous silica, the equilibrium concentration of $Si(OH)_4$ at 25°C corresponds to 70 ppm as $SiO-(2)$, the solubility of silica in water at this temperature. Most silica powders and gels, formed by extremely small particles of amorphous silica or by porous aggregates, with

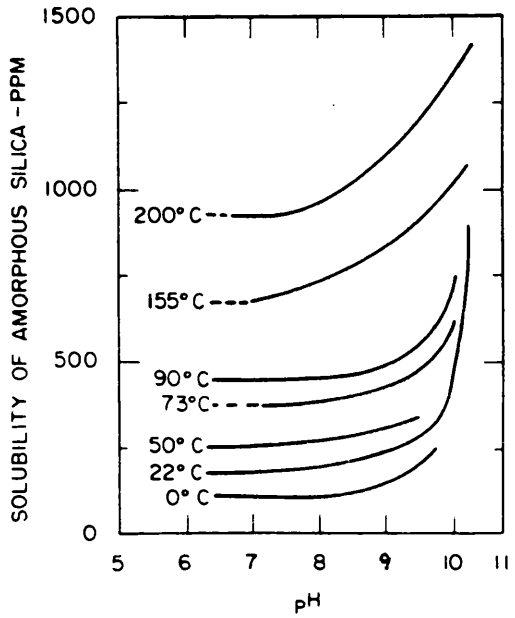


Figure 3.14: Solubility of amorphous silica versus pH at different temperatures, from Iler [105].

SiOH groups at the surface, exhibit a solubility of 100-130ppm SiO_2. Crystalline silica, like quartz, has a much lower solubility, about 6ppm SiO_2 [105].

To understand fully the behaviour of silica systems in solution, it is crucial to take into account how the solubility of silica changes with the physical and chemical conditions of the solution. Solubility of silica increases steadily with pressure, temperature and pH, as can be seen in Figure 3.14. Moreover, according to the radius of curvature, the solubility of silica is higher in convex surfaces and lower in concave ones. Silica tends thus to deposit in the crevice between particles and smaller particles tend to dissolve in favour of larger ones, as seen in Figure 3.15. Impurities like aluminium and some metal ions tend to decrease the solubility of silica [105].

3.4.2 Electrostatics

The electrical characteristics of a colloidal solution, essentially determined by the pH of the medium, play a very important role in the evolution of the system with time. The *isoelectric point* of $Si(OH)_4$, where the electrical mobility of silicate particles is zero, can be estimated to be between pKa and pKb, defined as the negative logarithms of the equilibrium constants for the silica ionisation reactions [105]:

$$Ka : H_3O^+ + Si(OH)_4 \longrightarrow (HO)_3SiOH_2^+ + H_2O$$

$$Kb : Si(OH)_4 + OH^- \longrightarrow (HO)_3SiO^- + H_2O$$

Experimentally, the isoelectric point for $Si(OH)_4$ has been found to be around pH 2.

Because $Si(OH)_4$ is a relatively weak acid, almost all monomeric silicate species remain neutral below pH 8 and only between pH 8 and 12 does $Si(OH)_3O^-$ become the predominant species. As $Si(OH)_3O^-$ is a very weak acid, further deprotonation occurs only above pH 12, where $Si(OH)_2O_2^{2-}$ is the most important species (see Figure 3.16).

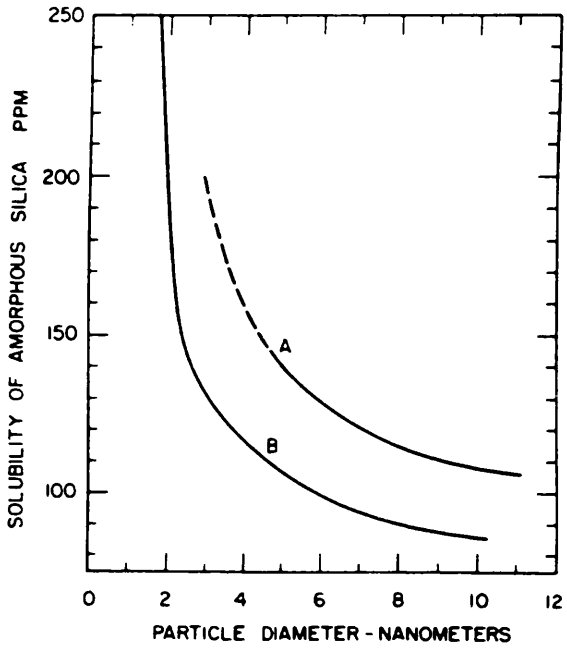


Figure 3.15: Fraction of silica dissolved versus time for particles of indicated initial diameters in nanometers, from Iler [105].

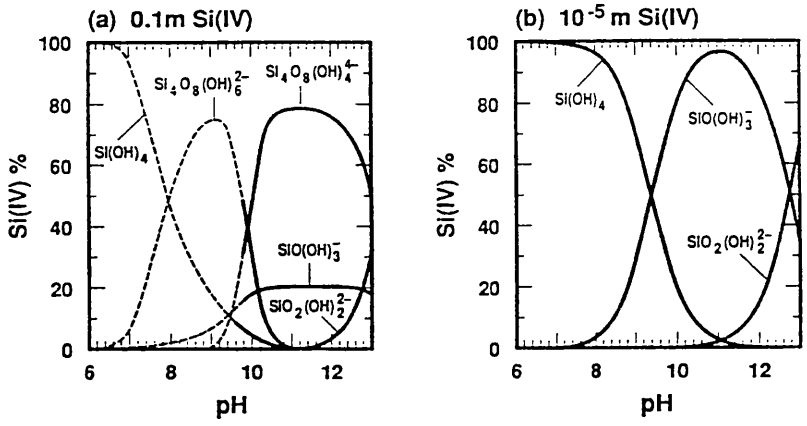


Figure 3.16: Distribution of monomeric ionised species in solution, as a function of pH [42].

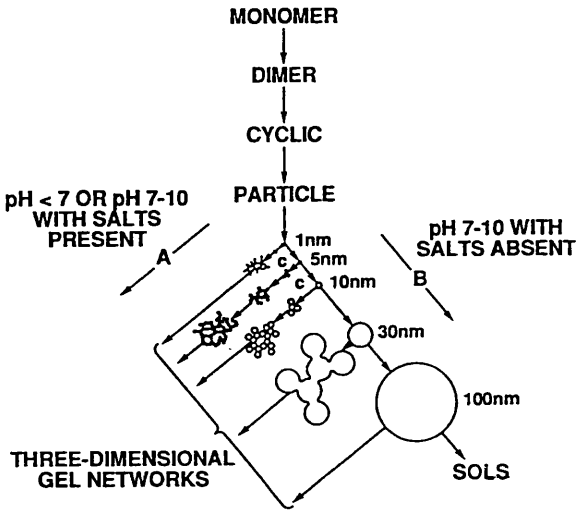


Figure 3.17: Polymerisation behaviour of silica, according to Iler [105]. In basic solution particles grow in size and decrease in number, forming sols, while in acid solution, particles aggregate into three-dimensional networks, forming gels.

3.4.3 Polymerisation

The inorganic polymerisation occurring in silica-based sol-gel processes, results in the water and alcohol condensation of the silanol groups formed during the hydrolysis, with formation of successive linking disiloxane bonds, according to the reactions:

$$Si - OH + OH - Si \longrightarrow Si - O - Si + H_2O,$$

$$Si - OR + OH - Si \longrightarrow Si - O - Si + ROH.$$

According to Iler [105], the global polymerisation process can be divided, in simple terms, in to three stages, as shown in Figure 3.17: 1) aggregation of small clusters to form sol particles; 2) Growth of sol particles; 3) Linking of particles into chains, then networks that eventually extend throughout the liquid medium, forming the gel.

Monomeric silicic acid, $Si(OH)_4$, has never been isolated, but it is soluble and stable in water, at 25^oC, for long periods of time, if the concentration is less than about 100 ppm as SiO_2 [105]. When a solution of monomer is formed at a concentration greater than about 100-200 ppm (the solubility of amorphous silica), and in the absence of solid phase on which the soluble silica might be deposited, the monomer polymerises by condensation to form dimer and higher molecular weight species of silicic acid.

Unlike carbon-based polymers, where chains growth and cross-link by covalent branches or Van der Waals interactions, in silicon-based polymers, highly condensed clusters are formed and particles with 1-500 nm size may be produced.

Silicic acid has a strong tendency to form polymers with a maximum of siloxane bonds and a minimum of SiOH groups [105]. Thus, highly condensed clusters are formed during the earliest stage of polymerisation, namely ring structures, as can be seen in Figures 3.18 and 3.19. These clusters continue growing by further addition of monomers and by linking together, to form larger three-dimensional structures, as depicted in Figure 3.20. These condense internally to the most compact state with SiOH groups remaining on the outside.

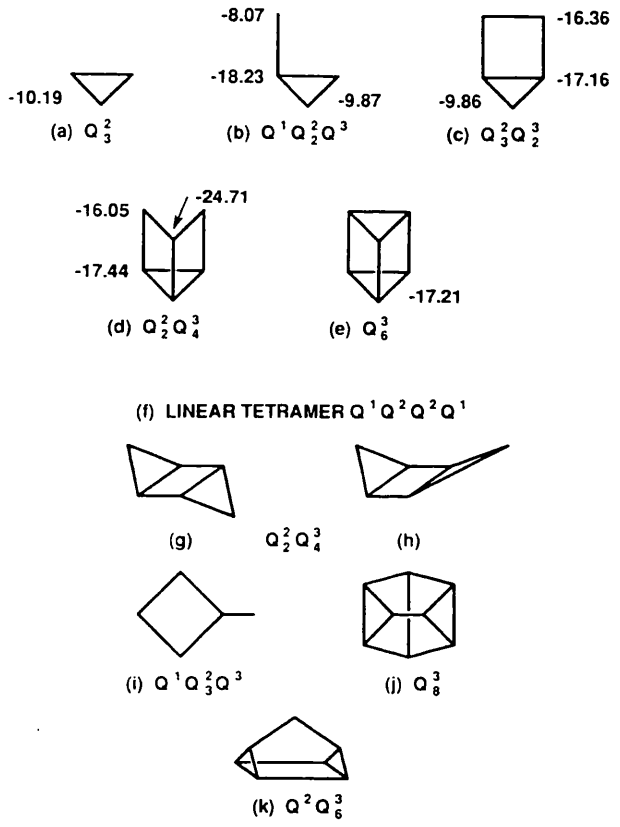


Figure 3.18: Silicate species present in a 1.4 M aqueous potassium silicate (1:1) solution identified by ^{29}Si NMR. Chemical shifts, given in ppm with respect to the monomer resonance, are included for positively identified species [42].

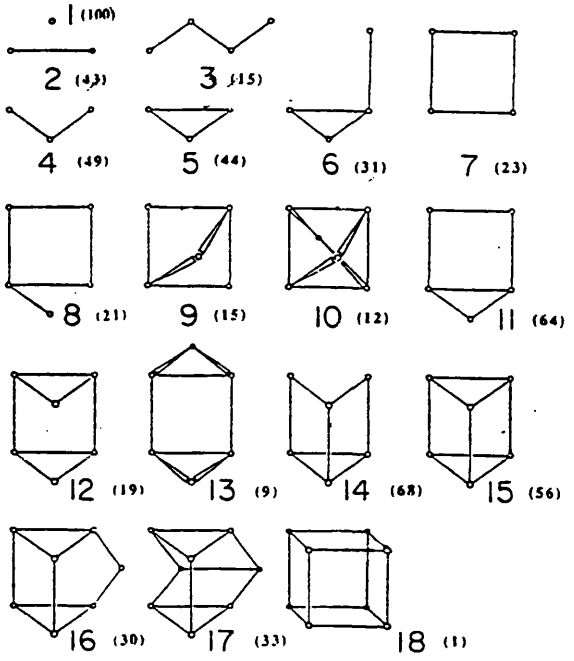


Figure 3.19: Structure of the 18 silicate anions determined by ^{29}Si NMR spectroscopy. The proportion of each species is given in parentheses, relative to the monomer, for a 0.63 M 1.5:1.0 (K:Si) potassium silicate solution [136].

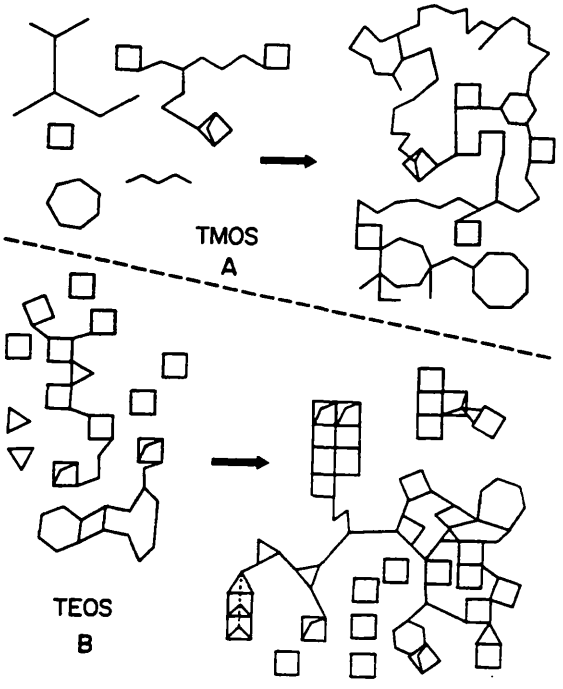


Figure 3.20: Sketch of polymer growth for TEOS and TMOS in a low pH sol-gel reaction, from Kelts [126].

The condensation reaction seems to involve an ionic mechanism, as the rate has a minimum for pH 2, at the isoelectric point of silica, increasing above and below pH 2 with the concentration of OH^- and H^+, respectively.

Above pH 2, the condensation mechanism is likely to involve a deprotonated species, as follows:

$$Si - OH + OH^- \longrightarrow SiO^- + H_2O$$

$$SiO^- + HO - Si \longrightarrow Si - O - Si + OH^-$$

The most stable deprotonated clusters should be the largest ones, due to the electron withdrawing effect of the OSi groups, thus condensation should occur preferentially between highly condensed aggregates and smaller, neutral species.

Below pH 2, the condensation mechanism may involve a protonated species:

$$Si - OH + H_3O^+ \longrightarrow Si - OH_2^+ + H_2O$$

$$Si - OH_2^+ + HO - Si \longrightarrow Si - OH - Si^+ + H_2O$$

$$Si - OH - Si^+ + H_2O \longrightarrow Si - O - Si + H_3O^+$$

The most stable protonated clusters should be the smallest ones, due to the smaller withdrawing effect of the OH groups, thus condensation should occur preferentially between neutral, larger clusters and protonated monomers or end groups on chains. As deprotonated species $SiOSiO^-$ should be more stable than protonated ones $HOSi - OH_2^+$, condensation occurs faster in basic than in acid conditions. As seen before, water consuming and alcohol consuming depolymerisations are also much more important under basic conditions than under acid conditions.

The particles thus formed act as nuclei for further polymerisation, which occurs by essentially three processes: 1) Growth of particles at the expense of silicic acid in solution; 2) an *Ostwald Ripening Mechanism*, where small particles, which are more soluble, dissolve and reprecipitate on larger, less soluble, nuclei, so the particles in solution grow in size and decrease in number. Differences in solubility between particles decrease with size, as curvature effects become less significant. At low pH, where the rate of dissolution and deposition of silica is small, significant differences in solubility are noticeable only between particles smaller than 2 nm and particle growth becomes negligible after a size of 2-4 nm is reached [105]. Above pH 7, where silica solubility is high, significant differences can be found between particles as large as 5 nm, and growth becomes slow only when they reach 5-10 nm. At higher temperatures, even larger particles are produced at this stage, particularly at high pH; 3) At low pH, the silica particles are essentially neutral and thus can collide and aggregate, forming chains and eventually a gel network. The rate of aggregation increases rapidly with concentration, and for concentrations of SiO_2 above 1%, as is usually the case in sol-gel processes, it may start immediately after the beginning of the condensation process, involving not only particles but also oligomers [105]. After the gel network has been formed, the structure becomes stronger as the necks between particles become thicker due to solution and deposition of silica.

At lower concentrations and near the isoelectric point, where the condensation rate is smaller, the monomer is converted largely to discrete particles before they begin to aggregate. At pH around 5-6, both ripening and aggregation mechanisms should occur simultaneously.

Above pH 6-7, particles 1-2 nm in diameter are formed in a few minutes [42]. In this pH range, silica particles are negatively charged and repel each other, so they do not collide and

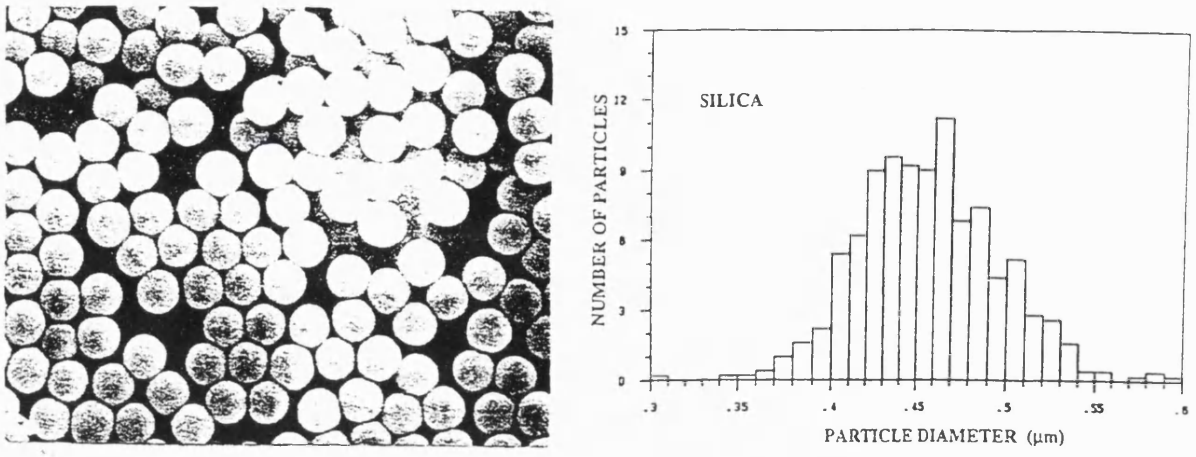


Figure 3.21: SEM micrograph and size distribution of a typical batch of Stober spherical silica powders, from L. L. Hench et al. [96].

Catalyst	Concentration (mole: TEOS)	Gelation Time (hr)
HF	0.05	12
HCl	0.05	92
HBr	0.05	285
HI	0.05	400
HNO_3	0.05	100
H_2SO_4	0.05	106
HOAc	0.05	72
NH_4OH	0.05	107
No catalyst		1000

Catalyst	Volume Shrinkage (%)	25°C Bulk Density (g/cm^3)	Volume Shrinkage (%)	600°C Bulk Density (g/cm^3)	Vickers Hardness
HOAc	84.0	1.32		2.08	666.5
HCl	81.3		85.2	2.06	429
HNO_3	79.9	1.14	85.2	1.82	470
H_2SO_4	71.6		80.0	1.46	224
HF	78.4	0.54	82.7	0.71	75
NH_4OH	67.8	0.49	71.7	0.70	28
No catalyst	87.5	0.95		1.25	

Table 3.8: Gelation times and Vickers hardness for different catalysts, in the system TEOS/water/EtOH, from Mackenzie [155].

aggregation is not possible. Consequently, gelation does not take place and a fully-developed sol is produced, with large, homogeneous particles, present in the solvent, like in the Stober process (see Figure 3.21) or in the method devised to produce nuclear-fuel particles. In this case, aggregation and gelling can still be achieved, by adding a electrolyte to the solution (a salt, like NaCl), concentrated enough to reduce the charge repulsion of the silica particles. The general trends of silica condensation, as a function of pH and composition, are represented schematically in Figure 3.22.

3.4.4 Catalyst role

Systematic studies on the the role of acid or basic catalysts on sol-gel reactions have shown that these effects are much more complex than just the control of the pH of the solution. Results obtained by Mackenzie [155] and presented in Table 3.8 show that HF and $HOAc$, in particular, have a catalysing effect that is much higher than could possibly be expect taking into account only the pH of the solution. Although the apparent initial pH of the solution is much higher for HF and HOAc than for the other acid catalysts considered, namely HCl, HNO_3 and H_2SO_4,

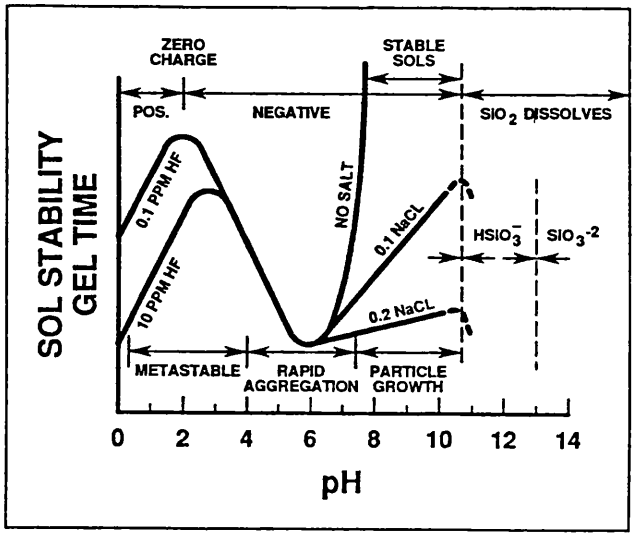


Figure 3.22: Time of gelation in silica condensation, as a function of pH and F^- concentration, from Brinker et al. [42].

the gelation time is much shorter when HF and $HOAc$ have been used. This clearly cannot be explained only by the protonation and deprotonation mechanisms usually proposed to describe acid and basic catalysis and shows that much more complex mechanisms, where the anion plays a important role, must be occurring in solution, at least when these two catalysts are added. This enhancing effect of HF and HOAc has been attributed to the nucleophilic character of F^- and OAc^-, which would atack neutral or even protonated initial reactants, forming penta- or six-coordinated fluor-complexated species [42] which would subsequently decay forming the products. However, no experimental or theoretical information seems to be known about these complex mechanisms. The effect of the acid anion concentration on gelation has been studied by Coltrain et al. [58].

The microstructure, and consequently the physical properties of gels are also dramatically influenced by catalytic effects, as can be seen by inspecting the density and Vickers hardness measured for the various catalyst-based dried gels, given in the same Table: the density increased from $0.70g/cm^3$ for a NH_4OH basic-catalysed gel to $1.3g/cm^3$ for a non-catalysed and to $2.1g/cm^3$ for a HCl acid-catalysed system, whereas the Vickers hardness increased from 75 for a HF-catalysed dried gel to 667 for a HOAc-catalysed one.

3.4.5 Temperature effects

In spite of its obvious influence on the gelation rate and other kinetic and structural aspects, the amount of published information on the effects of temperature on sol-gel processes is rather small, perhaps because most known studies have been carried out in open systems containing highly volatile solvents as MeOH and EtOH, which evaporate rapidly above $25°C$. Table 3.9 shows how quickly the gelation time decreases with temperature, an expected trend as the rates of diffusion and activated reactions are considerably enhanced. It was also reported [155] that a increase in temperature from 54 to $70°C$ led to a decrease of the bulk density of the gel from $1.46g/cm^3$ to $0.98g/cm^3$. In both works, no structural or detailed kinetic investigations were reported. As discussed by Iler, silica solubility in aqueous solutions increases steadly with temperature;

	Gelation Time (hr)		
Temperature, °C	HF	HCl	None
4	48.5	1440	
25	9.2	380	2520
70	0.3	20	27

Table 3.9: Time of gelation for a closed system $TEOS/H_2O/EtOH/Catalyst = 1/4/4/0.05$, as a function of temperature, from Mackenzie [155].

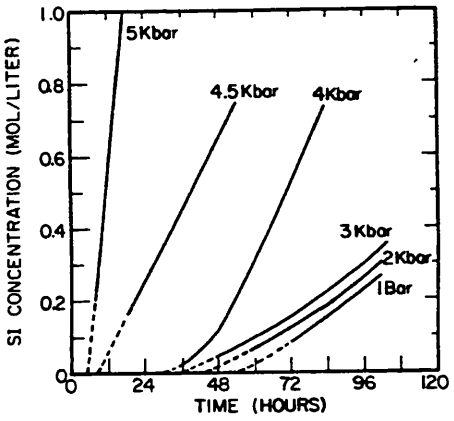


Figure 3.23: Concentration of higher polymer species, as a function of pressure, for a TMOS-based acid-catalysed system. The dashed lines represent extrapolations to zero concentrations, from Jonas [110].

consequently, the Ostwald ripening mechanism becomes progressively more effective for higher temperatures, leading to larger particles and to a larger range of conditions (particularly of pH) where it is significant.

3.4.6 Pressure effects

Most of the sol-gel research reported so far has been carried out at atmospheric pressure and consequently little is known about the influence of pressure on the structure and kinetics of these processes. However, some studies using ^{29}Si NMR and Raman spectroscopies [110], clearly show that pressure is potentially a very important variable in sol-gel processes, as it reduces considerably the time necessary for gelation to occur, (a technologically critical parameter), as depicted in Figure 3.23. Certainly, these kinetic differences should give rise to important structural differences as well. In particular, they might lead to less homogeneous structures, with much higher specific surface areas, due to a smaller evaporation of the solvent and in general to a more strained structure, with more defects and a higher energy. Jonas [110] reported that the size of the polymer particles seem to be smaller when high-pressure is applied. Unfortunately, no systematic experimental studies seem to have been done so far concerning these effects, to check the validity of these predictions and preliminary studies.

Molecule	BP (°C)	Viscosity (cP)	Dipole Moment (debye)	H bond	Gel Time (hr)	$I(R)$
Methanol (M)	65	0.62	1.7	*A*	39	220
Formamide (F)	200	4.32	3.7	*D, A*	20	343
Dimethyl Formamide (DF)	150	1.1	3.8	*D, A*	71	300
Acetonitrile (A)	82	0.37	3.9	*A*	55	450
Dioxane (D)	110	1.44	0	*A*	75	475

Figure 3.24: Physical properties of commonly used DCCAs, from Jonas [110].

3.4.7 Chemical additives

The major problem in the production of large monolithic glasses of high quality is the prevention of fractures during the ageing and drying stages of the sol-gel process. Important microstructural modifications, particularly the pore size distribution, occur when the solvent escapes from within the gel, leading to the formation of important stresses in the silica network with hazardous cracking consequences. Organic drying control additives, DCCAs, such as formamide (NH_2CHO), have been found greatly to facilitate the drying of large monolithic gels, without cracking [110, 17, 184]. Some of the DCCAs most commonly used in current sol-gel research are shown in Table 3.24.

The stabilising effect of DCCAs in the drying of gels has been generally attributed to an increase in the pore radius of the gel, which decreases the stress in the pores enough to resist the drying process. Indeed, nitrogen desorption studies carried out by Artaki et al. clearly show that the pore radius, porosity and specific surface area considerably increase when the concentration of formamide in solution augments, as shown in Figure 3.25.

Kinetic studies have shown that, in neutral conditions, the addition of formamide to the sol-gel solution decreases substantially the hydrolysis rate (by a factor of 6) but increases the condensation rate slightly [185]. Under acidic conditions, the opposite trend was observed, an increase of the hydrolysis rate and a reduction of the condensation rate [42].

3.5 Kinetic models

The complexity of the sol-gel kinetics is clearly evidenced by the rapid increase in the number of species and reactions involved, with the increasing detail of the analysis. Successive hydrolysis of $Si(OR)_4$ can lead to the formation of five different species: one monosilanol, two disilanols, one trisilanol and one tetrasilanol ($Si(OH)_4$), which, in turn, can dimerise by twenty four different reactions [189]. In general, at the nearest functional group, 15 Si species may occur and 165 rate constants are required fully to describe all their possible reactions: 10 different hydrolysis, 55 water condensations and 100 alcohol condensations [121]. These numbers increase even more at the next-to nearest functional group level, where 1365 distinct Si species require a striking number of 199,290 rate constants, divided by 364 hydrolysis, 66,430 water condensations and 132,496 alcohol condensations [121].

To overcome the cumbersome difficulties of such a direct approach and to allow accurate predictions of the evolution with time of the most important species present in solution, several

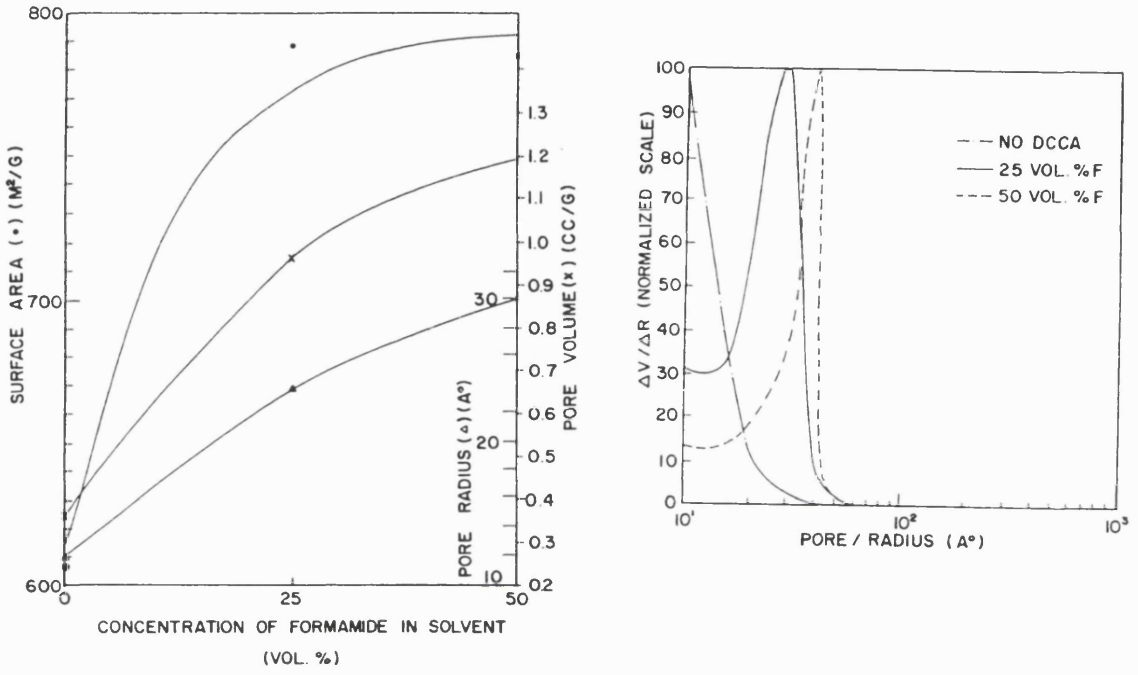


Figure 3.25: Variation of a) the surface area, pore volume and b) the pore size distribution on the gel with the concentration of formamide in a TMOS-based, R=10 solution, from Artaki et al. [17].

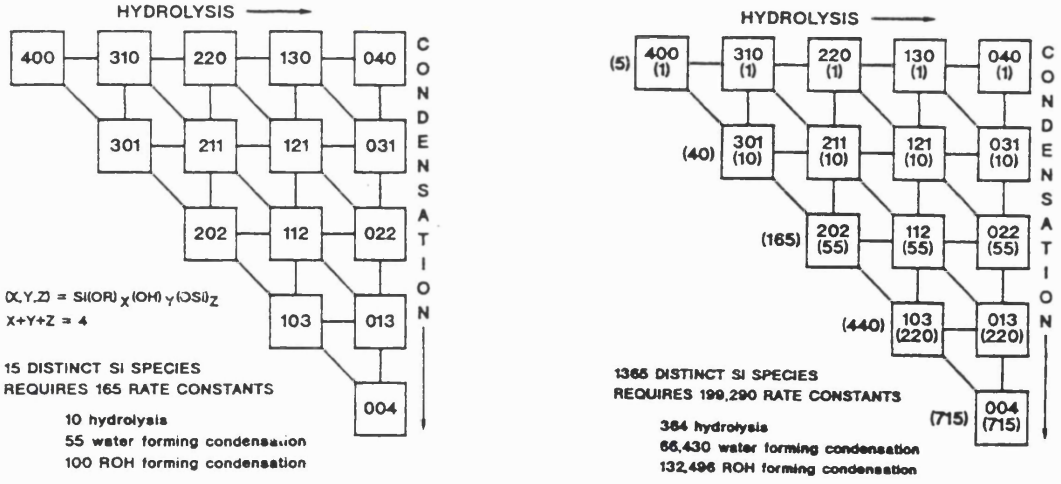


Figure 3.26: Si species and rate constants involved in silica-based sol-gel kinetics for two levels of approximation: a) Nearest functional group; b) next-to-nearest functional group, from Kay et al. [121].

approximate models have been proposed.

3.5.1 Branching Theory model

The branching theory model, presented by Peppas et al. [189], assumes that: 1) the reactivity of each functional group $M\text{-}X(X = OR, OH, OM)$ is independent of its environment; 2) the hydrolysis rate is much faster than the condensation rate. Three rate constants, k_1, k_{-1} and k_p are thus defined to describe the forward and reverse hydrolysis, and the forward water condensation (ignoring therefore the alcohol condensation and the reverse condensations):

$$MOR + H_2O \underset{k_{-1}}{\overset{k_1}{\rightleftarrows}} MOH + ROH$$

$$MOH + MOH \xrightarrow{k_p} MOM + H_2O$$

For mathematical convenience, normalised concentrations P, R are defined relatively to the initial alkoxide and water concentrations, $[MOR]_0$ and $[H_2O]_0$, as follows:

$$P_{MOR} = \frac{[MOR]}{[MOR]_0} \quad P_{MOH} = \frac{[MOH]}{[MOR]_0} \quad P_{MOM} = \frac{2[MOM]}{[MOR]_0}$$

$$P_{H_2O} = \frac{[H_2O]}{[H_2O]_0} \quad R_{H_2O} = \frac{[H_2O]_0}{[MOR]_0} \quad R_{ROH} = \frac{[ROH]_0}{[MOR]_0}$$

$$\text{with } P_{MOR} + P_{MOH} + P_{MOM} = 1 \tag{3.1}$$

Assuming that cyclisation is negligible and the kinetic constants remain constant throughout the reaction, the following rate equations can be derived:

$$\frac{dP_{MOR}}{dt} = [MOR]_0[-k_1 P_{MOR} P_{H_2O} R_{H_2O} + k_{-1} P_{MOH} P_{ROH} R_{ROH}] \tag{3.2}$$

$$\frac{dP_{MOH}}{dt} = [MOR]_0[k_1 P_{MOR} P_{H_2O} R_{H_2O} - 2k_p P_{MOH}^2 + -k_{-1} P_{MOH} P_{ROH} R_{ROH}] \tag{3.3}$$

$$\frac{dP_{H_2O}}{dt} = [MOR]_0[-k_1 P_{MOR} P_{H_2O} R_{H_2O} - k_{-1} P_{MOH} P_{ROH} R_{ROH}] + k_p P_{MOH}^2 \tag{3.4}$$

$$\frac{dP_{ROH}}{dt} = [MOR]_0[k_1 P_{MOR} P_{H_2O} R_{H_2O} - k_{-1} P_{MOH} P_{ROH} R_{ROH}] \tag{3.5}$$

This system of coupled differential equations can be numerically solved, with the initial conditions:

$$P_{MOR} = 1 \quad P_{MOH} = 0 \quad P_{MOM} = 0 \quad P_{H_2O} = 1 \quad P_{ROH} = 1 \tag{3.6}$$

in order to obtain the adimensional concentrations P_{AOR}, P_{AOH} and P_{AOA}, as a function of time. Typical results for this model are presented in Figure 3.27. As shown by Peppas et al. (see Figure 3.27), the quality of the kinetic predictions decreases considerably when the reverse hydrolysis is not considered.

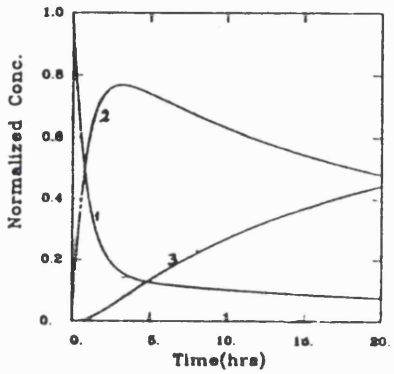


Figure 3.27: Normalised concentration of TEOS (curve 1), silanol (curve 2) and siloxane (curve 3) as a function ot time, obtained with the branching theory kinetic model, by Peppas et al. [189].

3.5.2 Functional Group model

A slightly different approach was presented in the same year (1988), by Assink et al. [20], who advanced the functional group model, which takes into account the forward hydrolysis, water condensation and alcohol condensation, described by three kinetic constants k_H, k_{CW} and k_{CA} (ignoring therefore all the reverse reactions). To conserve the total number of functional groups during the condensation, it is assumed that one SiOH and one SiOR groups react to give two (SiO)Si groups. Consequently k_{CW} and k_{CA} are twice as larger than the number of reactions that actually take place:

$$\begin{aligned} SiOR + H_2O &\xrightarrow{k_H} SiOH + ROH \\ 2SiOH &\xrightarrow{k_{CW}/2} 2(SiO)Si + H_2O \\ SiOH + SiOR &\xrightarrow{k_{CA}/2} 2(SiO)Si + ROH \end{aligned}$$

Like in the previous model, the reactivity depends only of each specific functional group and is independent of its environment. A set of rate equations for the various functional group reactions can thus be written as:

$$\frac{d[SiOR]}{dt} = -k_H[SiOR][H_2O] - \frac{k_{CA}}{2}[SiOH][SiOR] \quad (3.7)$$

$$\frac{d[SiOH]}{dt} = k_H[SiOR][H_2O] - k_{CW}[SiOH]^2 - \frac{k_{CA}}{2}[SiOH][SiOR] \quad (3.8)$$

$$\frac{d[(SiO)Si]}{dt} = k_H[SiOR][H_2O] - k_{CW}[SiOH]^2 - \frac{k_{CA}}{2}[SiOH][SiOR] \quad (3.9)$$

$$\frac{d[H_2O]}{dt} = -k_H[SiOR][H_2O] + \frac{k_{CW}}{2}[SiOH]^2 \quad (3.10)$$

$$\frac{d[ROH]}{dt} = k_H[SiOR][H_2O] + \frac{k_{CA}}{2}[SiOH][SiOR] \quad (3.11)$$

This set of equations can be solved numerically, as shown in Figure 3.28 or be further simplified, considering the specific features of the reactions involved. When the water concentration is not enough to hydrolyse all alkoxides, two limiting cases can be considered. If the hydrolysis is much faster than the condensation then the concentration of alcohol should increase in two stages, first

rapidly, during the incomplete hydrolysis, slower later, when the alcohol condensation occurs. In the opposite case, a single rate of production of alcohol should be observed, controlled by the hydrolysis rate. In fact the first case is always observed and hydrolysis is indeed much faster than condensation. To compare the rate of water and alcohol condensations, two limiting cases may again be considered. If k_{CW} is much larger than k_{CA}, the condensation rate should be proportional to $[SiOH]^2$, whereas in the opposite case it will be proportional to $[SiOH][SiOR]$. As hydrolysis is much faster than condensation, the early time silanol and methoxy functional group concentrations are approximately given by:

$$[SiOH] = [H_2O]_0 \quad [SiOR] = [SiOR]_0 - [H_2O]_0 \tag{3.12}$$

Consequently, by measuring the initial overall condensation rate as a function of the initial water concentration it is possible to determine which, if either, of these limiting cases is applicable. As condensation proceeds, the silanol and methoxy functional group concentrations are given by:

$$[SiOH] = [H_2O]_0 - \frac{1}{2}[(SiO)Si] \tag{3.13}$$

$$[SiOR] = [SiOR]_0 - [H_2O]_0 - \frac{1}{2}[(SiO)Si] \tag{3.14}$$

Substituting these concentrations in the rate equation for (SiO)Si yields:

$$\begin{aligned} \frac{d[(SiO)Si]/dt}{([H_2O]_0 - \frac{1}{2}[(SiO)Si])} &= (k_{CW} - k_{CA})\{[H_2O]_0 - \frac{1}{2}[(SiO)Si]\} \\ &\quad + k_{CA}\{[SiOR]_0 - [(SiO)Si]\} \end{aligned} \tag{3.15}$$

This equation can be further simplified when significant condensation has not yet occurred, where the inequality $[(SiO)Si] \ll [SiOR]_i$ applies. Representing thus by $< [SiOH] >$ the average concentration of the silanol functional group, yields:

$$\frac{d[(SiO)Si]/dt}{< [SiOH] >} = (k_{CW} - k_{CA}) < [SiOH] > + k_{CA}[SiOR]_0 \tag{3.16}$$

Both k_{CW} and k_{CA} can thus be obtained from a plot oh the initial condensation rate divided by $< [SiOH] >$ versus $< [SiOH] >$. Assink et al. [20] obtained the values 0.006 and 0.001 l/(mol min) for k_{CW} and k_{CA}, respectively, whereas k_H was found to be greater than 0.2 l/(mol min). A numerical solution of the functional group model equations, using these rate constants, is presented in Figure 3.28.

3.5.3 Bicomponent model

This model was extended later by Re [201], for a system containing two different alkoxides, and consequently two different functional groups M_1OR and M_2OR. Nine forward reactions need to be considered:

$$\begin{aligned} SiOR + H_2O &\xrightarrow{k_h} SiOR + ROH \\ 2SiOH &\xrightarrow{k_{cw}/2} SiOSi + H_2O \\ SiOR + SiOH &\xrightarrow{k_{ca}/2} SiOSi + ROH \end{aligned}$$

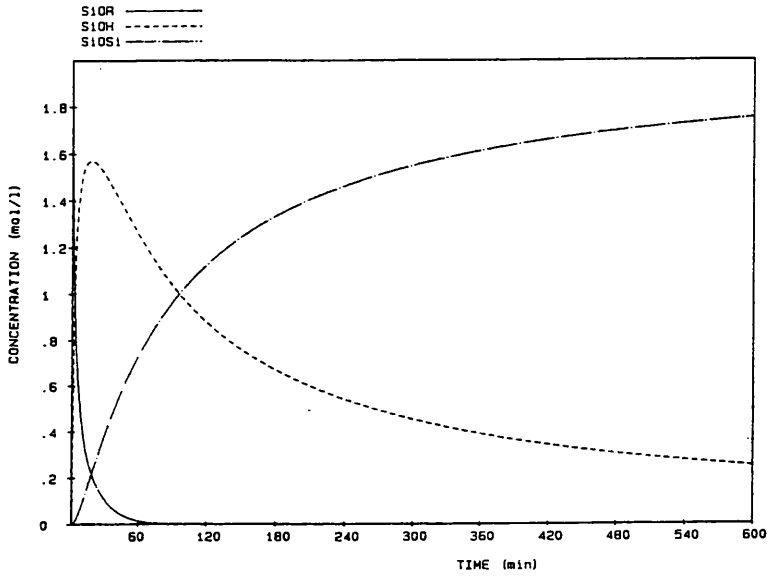


Figure 3.28: Temporal evolution of the groups SiOR, SiOH and SiOSi for TMOS at pH 3 and water/TMOS = 4, with $k_{CW} = 0.006$, $k_{CA} = 0.001$ and $k_{CW} = 0.2$ l/(mol min), obtained with the functional group model, from Rey [201].

$$
\begin{aligned}
MOR + H_2O &\xrightarrow{k_{Mh}} MOH + ROH \\
2MOH &\xrightarrow{k_{Mcw}/2} MOM + H_2O \\
MOR + MOH &\xrightarrow{k_{Mca}/2} MOM + ROH \\
SiOH + MOH &\xrightarrow{k_{MScw}/2} SiOM + H_2O \\
SiOH + MOR &\xrightarrow{k_{MSca1}/2} SiOM + ROH \\
SiOR + MOH &\xrightarrow{k_{MSca2}/2} SiOM + ROH
\end{aligned}
$$

and the corresponding rate expressions for the various species are given by [201]:

$$
\begin{aligned}
\frac{d[SiOR]}{dt} &= -k_h[SiOR][H_2O] - \frac{k_{ca}}{2}[SiOR][SiOH] \\
&\quad -k_{MSca2}[SiOR][MOH] \qquad (3.17) \\
\frac{d[SiOH]}{dt} &= k_h[SiOR][H_2O] - \frac{k_{ca}}{2}[SiOR][SiOH] - k_{cw}[SiOH]^2 \\
&\quad -k_{MSca1}[SiOH][MOR] - k_{MScw}[SiOH][MOH] \qquad (3.18) \\
\frac{d[SiOSi]}{dt} &= k_{cw}[SiOH]^2 + k_{ca}[SiOR][SiOH] \qquad (3.19) \\
\frac{d[MOR]}{dt} &= -k_{Mh}[MOR][H_2O] - \frac{k_{Mca}}{2}[MOR][MOH] \\
&\quad -\frac{k_{MSca1}}{2}[MOR][SiOH] \qquad (3.20) \\
\frac{d[MOH]}{dt} &= k_{Mh}[MOR][H_2O] - \frac{k_{Mca}}{2}[MOR][MOH] \\
&\quad -k_{Mcw}[MOH]^2 - k_{MSca2}[SiOR][MOH]
\end{aligned}
$$

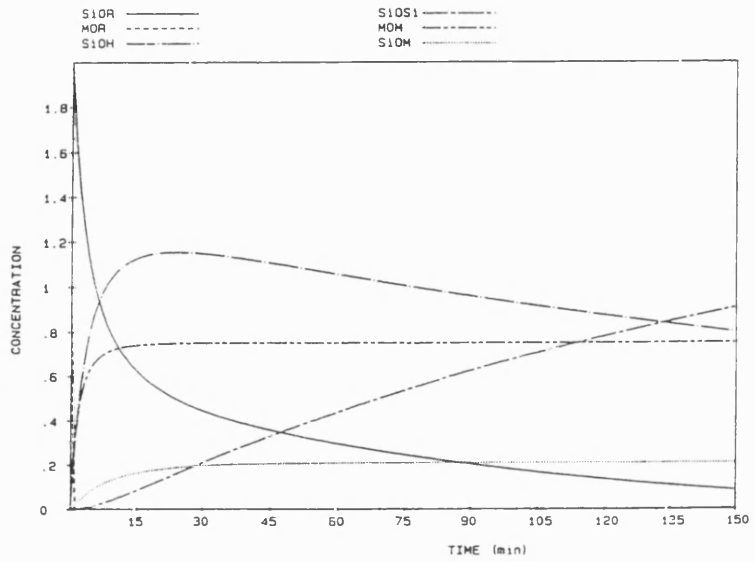


Figure 3.29: Calculated time dependence of the various functional groups for TMOS and M alkoxide analysis at pH 3 with water/TMOS = 4 and M/TMOS = 2, obtained with the bicomponent model, from Re [201].

$$-k_{MScw}[SiOH][MOH] \tag{3.21}$$

$$\frac{d[MOM]}{dt} = k_{Mcw}[MOH]^2 + k_{Mca}[MOR][MOH] \tag{3.22}$$

$$\frac{d[SiOM]}{dt} = k_{MScw}[SiOH][MOH] + k_{MSca1}[SiOH][MOR] + k_{MSca2}[SiOR][MOH] \tag{3.23}$$

$$\frac{d[H_2O]}{dt} = -k_h[SiOR][H_2O] + \frac{k_{cw}}{2}[SiOH]^2 + \frac{k_{Mcw}}{2}[MOH]^2 + k_{MScw}[SiOH][MOH] - k_{Mh}[MOR][H_2O] \tag{3.24}$$

$$\frac{d[ROH]}{dt} = k_h[SiOR][H_2O] + \frac{k_{ca}}{2}[SiOR][SiOH] - k_{Mh}[MOR][H_2O] + \frac{k_{Mca}}{2}[MOR][MOH] + k_{MSca1}[MOR][SiOH] + k_{MSca2}[SiOR][MOH] \tag{3.25}$$

Numerical solutions for this system of nine non-linear coupled differential equations are presented in Figure 3.29. Unfortunately, no reliable experimental data seems to be currently available to compare with them [201].

3.5.4 Nearest Neighbour model

Probably the most elegant kinetic model proposed so far to describe sol-gel kinetics is the nearest-neighbour model, proposed by Kay et al. [121]. It assumes that the reaction conditions around each functional group depend on its nearest neighborus, attached to the same silicon atom, but is independent of the chemical characteristics of the next-to nearest neighborus. Designating by (XYZ) a species with X $SiOR$, Y $SiOH$ and Z $(SiO)Si$ groups (so $X + Y + Z = 4$), all

possible reactions can be described by two hydrolysis equations:

$$(X_i+1),(Y_i-1),Z_i+H_2O \overset{k_{H_{(i+1)}}}{\longrightarrow} \underline{X_i,Y_i,Z_i}+ROH$$

$$\underline{X_i,Y_i,Z_i}+H_2O \overset{k_{H_i}}{\longrightarrow} (X_i-1),(Y_i+1),Z_i+ROH$$

plus two water forming condensation equations:

$$X_i,(Y_i+1),(Z_i-1)+X_j,Y_j,Z_j \overset{k_{CW_{(i+1),j}}}{\longrightarrow} \underline{X_i,Y_i,Z_i}+X_j,(Y_j-1),(Z_j+1)+H_2O$$

$$\underline{X_i,Y_i,Z_i}+X_j,Y_j,Z_j \overset{k_{CW_{i,j}}}{\longrightarrow} X_i,(Y_i-1),(Z_i+1)+X_j,(Y_j-1),(Z_j+1)+H_2O$$

and four alcohol forming equations:

$$(X_i+1),Y_i,(Z_i-1)+X_j,Y_j,Z_j \overset{k^R_{CA_{(i+1),j}}}{\longrightarrow} \underline{X_i,Y_i,Z_i}+X_j,(Y_j-1),(Z_j+1)+ROH$$

$$X_i,(Y_i+1),(Z_i-1)+X_j,Y_j,Z_j \overset{k^H_{CA_{(i+1),j}}}{\longrightarrow} \underline{X_i,Y_i,Z_i}+(X_j-1),Y_j,(Z_j+1)+ROH$$

$$\underline{X_i,Y_i,Z_i}+X_j,Y_j,Z_j \overset{k^R_{CA_{i,j}}}{\longrightarrow} (X_i-1),Y_i,(Z_i+1)+X_j,(Y_j-1),(Z_j+1)+ROH$$

$$\underline{X_i,Y_i,Z_i}+X_j,Y_j,Z_j \overset{k^H_{CA_{i,j}}}{\longrightarrow} X_i,(Y_i-1),(Z_i)+(X_j-1),Y_j,(Z_j+1)+ROH$$

The kinetic equations directly describing these reactions can be rearranged in order to isolate the terms containing $[X_i,Y_i,Z_i]$, $[H_2O]$ and $[ROH]$, yielding for the kinetic master equation of the species (X_i,Y_i,Z_i) [121]:

$$\begin{aligned}\frac{d[X_i,Y_i,Z_i]}{dt} &= \{k_{H_{(i+1)}}[H_2O]\}[(X_i+1),(Y_i-1),Z_i]+\{\sum_j(k_{CW_{(i+1),j}}+k^H_{CA_{(i+1),j}})[X_i,Y_i,Z_i]\}\\ &[X_i,(Y_i+1),(Z_i-1)]+\{\sum_j k^R_{CA_{(i+1),j}}[X_j,Y_j,Z_j]\}[X_i+1),Y_i,(Z_i-1)]\\ &-\{k_{H_i}[H_2O]+\sum_j(k_{CW_{i,j}}+k^H_{CA_{i,j}}+k^R_{CA_{i,j}})[X_j,Y_j,Z_j]\}[X_i,Y_i,Z_i] \qquad (3.26)\end{aligned}$$

and for the temporal evolution of $[H_2O]$ and $[ROH]$:

$$\begin{aligned}\frac{d[H_2O]}{dt} &= -\frac{1}{2}\sum_i\sum_j k_{CW_{i,j}}[X_i,Y_i,Z_i][X_j,Y_j,Z_j]\\ &-\{\sum_i k_{H_i}[X_i,Y_i,Z_i]\}[H_2O] \qquad (3.27)\\ \frac{d[ROH]}{dt} &= \{\sum_i k_{H_i}[X_i,Y_i,Z_i]\}[H_2O]+\\ &\frac{1}{2}\sum_i\sum_j(k^H_{CA_{i,j}}+k^R_{CA_{i,j}})[X_i,Y_i,Z_i][X_j,Y_j,Z_j] \qquad (3.28)\end{aligned}$$

These equations represent an exact theoretical description of the temporal evolution of the 15 (XYZ) chemically distinguishable species at the nearest functional group level. Although this set of equations cannot, in general, be integrated analytically, it can solved numerically to an arbitrary accuracy. In terms of this model, the functional group equations are given by:

$$[SiOR] = \sum_i X_i[X_i, Y_i, Z_i] \quad \frac{d[SiOR]}{dt} = \sum_i X_i \frac{d[X_i, Y_i, Z_i]}{dt} \tag{3.29}$$

$$[SiOH] = \sum_i Y_i[X_i, Y_i, Z_i] \quad \frac{d[SiOH]}{dt} = \sum_i Y_i \frac{d[X_i, Y_i, Z_i]}{dt} \tag{3.30}$$

$$[SiOR] = \sum_i X_i[X_i, Y_i, Z_i] \quad \frac{d[(SiO)Si]}{dt} = \sum_i Z_i \frac{d[X_i, Y_i, Z_i]}{dt} \tag{3.31}$$

3.5.5 Statistical model

The elegance and correctness of the nearest functional group model, which provides a powerful theoretical insight in the kinetics of sol-gel processes, proves to be its main weakness, as in practice it seems almost impossible to measure accurately the 165 kinetic rate constants required for this model. The statistical model represents a compromise between the simplicity of the functional group model and the accuracy of the nearest functional group model, as it assumes that all hydrolysis and condensation rate constants depend only on the functional group reactivity and on a statistical weight factor given by the number of different equivalent reactions that actually may occur. The 165 rate constants are therefore reduced to only 3, given by:

$$k_{H_i} = X_i k_H \quad k_{CW_{i,j}} = Y_i Y_j k_{CW} \tag{3.32}$$

$$k^H_{CA_{i,j}} = X_i Y_j k_{CA} \quad k^R_{CA_{i,j}} = X_i Y_j k_{CA} \tag{3.33}$$

The statistical kinetic equations for $[X_i, Y_i, Z_i]$, $[H_2O]$ and $[ROH]$ can therefore be obtained just by substituting the rate constants thus defined in the general equations of the nearest functional model, yielding [121]:

$$\begin{aligned}
\frac{d[X_i, Y_i, Z_i]}{dt} &= k_H\{(X_i+1)[(X_i+1),(Y_i-1),Z_i] - X_i[X_i, Y_i, Z_i]\}[H_2O] + \\
&\quad k_{CW}\{(Y_i+1)[X_i,(Y_i+1),(Z_i-1)] - Y_i[X_i, Y_i, Z_i]\}\sum_j Y_j[X_j, Y_j, Z_j] + \\
&\quad \frac{k_{CA}}{2}[\{(X_i+1)[(X_i+1), Y_i,(Z_i-1)] - X_i[X_i, Y_i, Z_i]\}\sum_j Y_j[X_j, Y_j, Z_j] + \\
&\quad \{(Y_i+1)[X_i,(Y_i+1),(Z_i-1)] - Y_i[X_i, Y_i, Z_i]\}\sum_j X_j[X_j, Y_j, Z_j]],
\end{aligned} \tag{3.34}$$

$$\frac{d[H_2O]}{dt} = \frac{k_{CW}}{2}\{\sum_i Y_i[X_i, Y_i, Z_i]\}^2 - k_H[H_2O]\sum_i X_i[X_i, Y_i, Z_i], \tag{3.35}$$

$$\frac{d[ROH]}{dt} = k_H[H_2O]\sum_i X_i[X_i, Y_i, Z_i] + \frac{k_{CA}}{2}\sum_i X_i[X_i, Y_i, Z_i]\sum_i Y_i[X_i, Y_i, Z_i]. \tag{3.36}$$

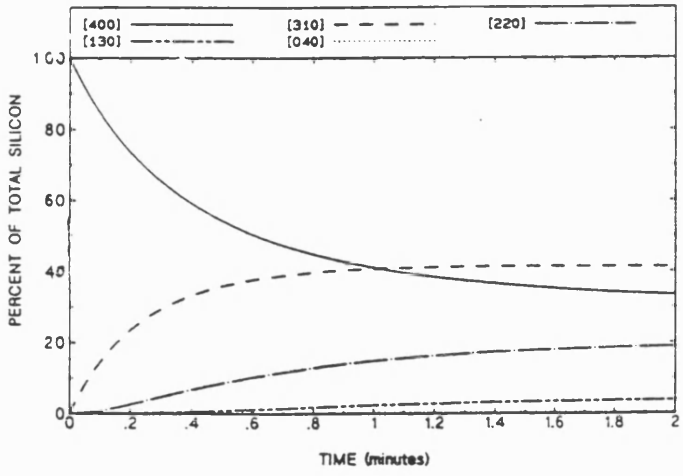


Figure 3.30: Early time dependence for the species (XY0): (400), (310), (220), (130) and (040), obtained with the statistical model, from Kay et al. [121].

Therefore, the time evolution of species [211], for example, is given in this model by:

$$\begin{aligned}\frac{d[211]}{dt} &= k_H(3[301]-2[211])[H_2O]+k_{CW}(2[220]-[211]) \\ &\quad .[SiOH]+\frac{k_{CA}}{2}\{(3[310]-[211])[SiOH]+ \\ &\quad (2[220]-[211])[SiOR]\}. \end{aligned} \tag{3.37}$$

The time evolution for the concentration of the various species was calculated by Assink et al. [121, 18, 19], assuming for the kinetic constants k_H, k_{CW} and k_{CA}, the values previously obtained with the functional group model: 0.2, 0.006 and 0.001 l/mol min, respectively. The early time dependence for species (XY0) is represented in Figure 3.30.

3.6 Growth models

Several models have been proposed, during the last fifty years, to describe the growth processes occurring during carbon and silicon polymerisation in solution, generally grouped into *equilibrium* and *kinetic* models (for a review see Zarzycki [251]). The equilibrium models are essentially the classic *Flory theory* and the *percolation theory*, which simulate the growth process by formulating simple rules to control the addition of new monomers to the silicate clusters. The results of these models are therefore completely deterministic. The kinetic models are based in the same principle but the monomers diffusion and reactivity are determined by random distributions generated in computer simulations. These models describe much better the silica growth than the equilibrium models and are consequently discussed here.

3.6.1 Kinetic models

The kinetic models aim to simulate the dynamics of the growth process, by defining a set of rules to regulate the diffusion and aggregation behaviour of arbitrary fragments representing

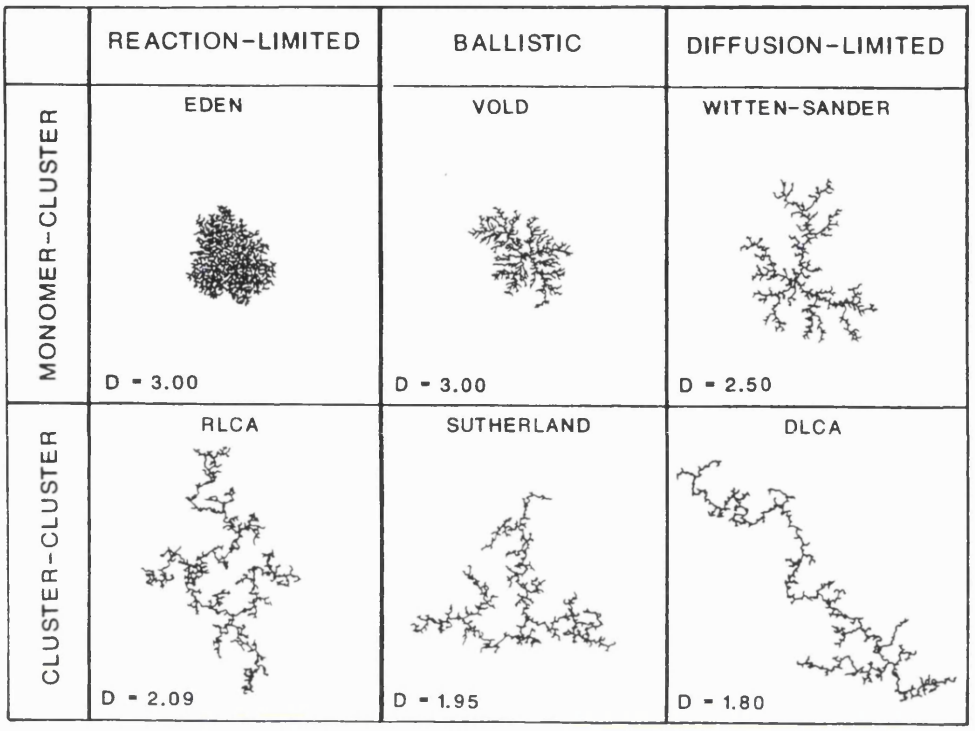


Figure 3.31: Fractal models simulating the silica growth [42].

the species in solution, in this way trying to get insight in the chemical and physical factors that control the process. In all these models, regions of space are arbitrarily defined, sometimes constructed as a lattice (to simplify), where a given number of units (controlled by density) is randomly positioned. The geometrical features of the structures thus obtained, in particular their mass and surface fractal dimensions, can subsequently be measured and compared with experimental measurements. A fractal structure can be characterised by a *mass fractal dimension* d_m (lower than 3, the Euclidean value), according to $M \propto r^{d_m}$, or a *surface fractal dimension* d_s (bigger than 2, the Euclidean value), according to $S \propto r^{d_s}$, where M, S and r represent the mass, the surface and the radius of the particles, respectively (see [210]). As reviewed by Avnir, a extensive set of fractal analyses had been carried out in the last ten years in many different kinds of naturally-occurring materials, using a large range of experimental methods, that include, among others, adsorption surface area/particle size analyses, small angle x-ray scattering, photophysical studies and direct computerised image analysis[21].

3.6.2 Monomer-cluster models

Kinetic models (shown in Figure 3.31) use slightly different approaches to simulate the polymerisation growth: *cluster-cluster*, that occurs in sol-gel acid solutions and in the particle growth; *monomer-cluster*, that occurs in alkaline solutions. In the *Eden* growth, a monomer-cluster model proposed in 1961 by Eden to study the growth of cancers [211], one starts with one occupied position (the seed) and randomly picks and occupies one of the neighbouring sites. This process is repeated over and over, with every empty site around a filled site being a potential point of growth. Eden clusters obtained in this way have uniform interiors and smooth surfaces

relative to their radius. In fact, older inner growth sites tend to be occupied first and deep empty sites in the cluster are therefore rare. Thus, this model is valid when growth occurs from monomers and when the functionality of the monomers is large, as in basic solutions with large water/silica ratio, where condensation tends to occur between large ionised clusters and neutral, less acid, monomers.

At slightly lower pH and water/ratio, where hydrolysis did not completed before condensation starts, the *poisoned Eden* model seems to be more accurate (see [125]). This is a modification of the Eden model, where it is assumed that the monomers are only partly hydrolysed, and consequently only some of the neighbouring sites are effective, according to a previously defined distribution of monomer functionality. The clusters thus produced tend to be porous but the interior is not fractal. The external surface of the clusters is however a fractal, and interestingly enough, d_s, depends not only of the number of poisoned sites but also of its distribution by the monomers. This d_s, ranging from 1.3 to 1.75, in 2D models [211, 124], compares with $d_s = 2.7$, reported for the condensation of TEOS under basic conditions, with water/silica = 2 [211].

The *ballistic* model was developed by Vold, more than 30 years ago, to simulate colloidal aggregation, and like the Eden model, it is a monomer-cluster model leading to dense mass and surface clusters [161]. In this model particles are fired, one at a time, along linear trajectories randomly chosen, in the vicinity of a stationary central particle, where the growth starts. If a mobile particle contacts the stationary particle it sticks at that point and a stationary cluster is formed. Additional monomers are added in the same way until a large aggregate has grown. This model leads to clusters that are slightly more open, with deep channels, than the Eden, but without the fractal characteristics of the poisoned Eden.

An important aspect of both Eden and Vold models is that they are *reaction-limited* models, as monomers do not diffuse in the lattice. In 1981 Witten and Sander proposed a diffusion-limited aggregation model, which provided a basis for a better understanding of a variety of diffusion-limited processes such as random dendritic growth and the flocculation of colloidal systems[160]. In this model, monomers are released one by one from sites arbitrarily far from a central cluster and are allowed to travel randomly until either they stick irreversibly, at first contact, with the growing cluster, or they move too far from it, in which case they are eliminated and a new monomer generated.

Because of their Brownian motion trajectories, which simulate diffusion, monomers cannot penetrate deeply into a cluster without intercepting a cluster arm. The clusters produced by this model are thus mass fractals, with $d_m = 2.5$ [42], though they still have the particle-like shape, characteristic of the monomer-cluster growth. This model helps therefore to describe the SAXS results obtained by Keefer for alkaline TEOS solutions, which show a mass fractal dimension $d_m = 2.84$ for water/silica = 1 [124]. For larger water concentrations, where hydrolysis occurs to a larger extent, only a fractal surface is observed, as in the poisoned Eden model, as branching becomes more important in these conditions.

3.6.3 Cluster-cluster models

Unlike colloidal aggregation in real systems, in monomer-cluster models there is a central, nucleation site, whose approximate location in the final cluster can be found by inspection. The region surrounding the growth site has anomalously high density and density correlations are found in the radial and tangential directions[162]. In cluster-cluster aggregation models there is no unique starting particle and instead, aggregation is assumed to occur in a similar way

throughout all the reacting system. To avoid border effects, periodic boundary conditions are usually applied in cluster-cluster models.

In the diffusion-limited cluster-cluster model, a fraction of non-adjacent sites is randomly occupied, at the start of the simulation. These single particle clusters are then picked at random and moved in the simulation space until they move in the nearest-neighbour positions of other particles and stick together. This aggregation process can be continued until a single large cluster corresponding to the gelation point has been formed, extending throughout the space simulation. The mobility of the clusters can be made equal for all clusters or inversely proportional to their size, to simulate mass effects. Compared to monomer-cluster aggregation, the strong mutual screening of colliding clusters creates very open fractal structures, with a mass fractal dimension as low as 1.80 [42].

As proposed by Meakin [160], the previous model can be modified, to be a reaction-limited model, just by introducing a sticking probability P smaller than 1. Each time a cluster contacts another one, a random number x uniformly distributed between 0 and 1 is generated and aggregation is considered to have occurred only when $x < P$. If aggregation did not occur, the monomer might attempt to move onto an occupied site, in the next step, in which case it is returned to its previous position, where it remains free or attached to the hit cluster, depending on the model. As some rearrangement is allowed in this model before aggregation occurs, the fractal characteristics of the clusters thus produced are less accentuated than in the diffusion-controlled model and d_m increases to 2.01. Consequently, more dilute solutions, where the diffusion-controlled method should become more relevant, should lead to more open structures, with larger mass fractal dimensions.

A cluster-cluster evolution of the ballistic model was proposed some years later by Shuterland. This model starts with an ensemble of single particles. A pair of particles is selected to form a binary cluster and returned to the ensemble. Objects are picked from the ensemble, combined via random linear trajectories and returned to the ensemble. This process is repeated until all of the particles are contained in a large single cluster. The selection of pairs of objects from the ensemble is carried out using probabilities which are dependent on the masses of the two objects [161].

Cluster-cluster growth is expected to occur when no continuous source of monomers is available or when there is no mechanism favouring condensation predominantly between monomers and large clusters. This is the case below pH 2, where hydrolysis is much faster than condensation and therefore fully hydrolysed monomers tend to be produced, which react subsequently to form higher aggregated clusters. The solution become thus rapidly depleted of monomers, which are not compensated by the reverse depolymerisation, which is negligible in these strongly acidic conditions. In fact, experimental evidence has shown that, at pH 1, the concentration of monomers becomes negligible for a time $t \geq 0.01 t_{gel}$, where t_{gel} is the time required for gelation to occur [42]. Condensation tends thus to occur between end groups, where protonation is easier, producing long chains, randomly branched, as described by cluster-cluster models. Because depolymerisation is slow and redistribution reactions are therefore suppressed, no monomers are available to fill in the voids left between the chains and highly open structures are consequently produced.

Cluster-cluster aggregation can be forced, even in alkaline solutions, by using a two-step procedure, where a small amount of water is first added to the solution, so monomers are only partially hydrolysed and condensation produces only oligomers with relatively low molecular weight, which stop growing when all available water and silanol groups have reacted. Addition

of water in excess and catalyst in a second stage, causes all the remaining sites to hydrolyse fast and subsequent condensation occurs primarily between the oligomeric species formed during the first stage. Mass fractal dimensions as low as 1.9 and 2.1 have been measured experimentally for silicate systems produced in acid- and basic-catalysed two-step procedure, respectively [42], in good agreement, thus, with the value 2.1, predicted by the reaction-limited cluster-cluster model described above. The slightly smaller fractal dimension obtained in basic conditions should be attributed to some dissolution and redistribution that occured during the second step, after the basic catalysts were added.

Despite the invaluable contribution given by these equilibrium and kinetic growth models to the understanding of the aggregation processes occurring in solution, they cannot provide any fundamental insight in the chemical and physical aspects of silica growth, due to their non-atomistic, entirely empirical, formulation. In fact, their main advantage, their simplicity, is also their major weakness, and they cannot even attempt to simulate the complexity of silicate systems in solution. This major challenge is reserved for atomistic potential-based classical simulations and in last instance, to full quantum mechanical simulations.

Chapter 4

Sol-Gel bibliography

4.1 General references

During the last twenty years, the number of published works concerning sol-gel processes has increased enormously, covering a range of experimental techniques and new applications that is continuously expanding. It is therefore difficult to have an up-to-date overview of such a large and dynamic research field, particularly in what concerns high-tech and military applications, whose publication is usually severely restricted. Fortunately, considerable effort has been made to publish together the most important works, in the public domain, relative to sol-gel science and sol-gel applications, and to produce general reviews of the most relevant topics in sol-gel processes, with complete reference lists covering a much larger range of works.

The book *Sol-Gel Science: The Physics and Chemistry of Sol-Gel Processing*, published by C. J. Brinker and G. W. Scherer in 1989 [42], is probably the best introduction to sol-gel processes, covering all the most important aspects with great detail and providing a almost exhaustive list of references for each subject. A general review published in 1990 in Chemical Reviews, by L. L. Hench and J. K. West, *The Sol-Gel Process* [96], provides a comprehensive overview of the most important aspects of sol-gel processes and an important list of references. An article published in 1993 in *Pour la Science*, *The gels pour l' optique* [54], gives a simple overview of sol-gel science and technology.

Important articles covering all the key aspects of sol-gel processes, can be found in the proceedings of the *International Workshop on Glasses and Glass Ceramics from Gels*, a biennial meeting held since 1981:

- *Proceedings of the International Workshop on Glasses and Glass Ceramics from Gels*, Padova, Italy, 1981, Ed. V. Gottardi, Journal of Non-Crystalline Solids, 48 (1982)

- *Proceedings of the Second International Workshop on Glasses and Glass Ceramics from Gels*, Würzburg, Federal Republic of Germany, 1983, Ed. H. Sholze, Journal of Non-Crystalline Solids, 63 (1984)

- *Proceedings of the Third International Workshop on Glasses and Glass Ceramics from Gels*, Montpellier, France, 1985, Ed. J. Zarzycki, Journal of Non-Crystalline Solids, 82 (1986)

- *Proceedings of the Fourth International Workshop on Glasses and Glass Ceramics from Gels*, Kyoto, Japan, 1987, Ed. S. Sakka, Journal of Non-Crystalline Solids, 100 (1988)

- *Proceedings of the Fifth International Workshop on Glasses and Glass Ceramics from Gels*,

Rio de Janeiro, Brasil, 1989, Ed. M. A. Aegerter, Journal of Non-Crystalline Solids, 121 (1990)
- *Proceedings of the Sixth International Workshop on Glasses and Glass Ceramics from Gels*, Seville, Spain, 1991, Ed. L. Esquivias, Journal of Non-Crystalline Solids, 147 & 148 (1992)

A series of important meetings, concerning sol-gel science and technology, were held in 1984, 1986 and 1988, sponsored by the Materials Research Society, under the title *Better Ceramics Through Chemistry*, and the proceedings were published in book form:

- *Better Ceramics Through Chemistry*, Eds. C. J. Brinker, D. E. Clark and D. R. Ulrich, Materials Research Society, 32 (1984)
- *Better Ceramics Through Chemistry II*, Palo Alto, California, USA, Eds. C. J. Brinker, D. E. Clark and D. R. Ulrich, Materials Research Society, 73, 822p (1986)
- *Better Ceramics Through Chemistry III*, Reno, Nevada, USA, Eds. C. J. Brinker, D. E. Clark and D. R. Ulrich, Materials Research Society, 121, 838p (1988)

Another important series of meetings took place in 1983, 1985, 1987, 1989 and 1991, with the name *Ultrastructure Processing* and the proceedings were published in book form by John Wiley & Sons:

- *Ultrastructure Processing of Ceramics, Glasses, and Composites*, Eds. L. L. Hench and D. R. Ulrich, John Wiley & Sons, 558p (1984)
- *Science of Ceramic Chemical Processing*, Eds. L. L. Hench and D. R. Ulrich, John Wiley & Sons, 582p (1986)
- *Ultrastructure Processing of Advanced Ceramics*, Eds. J. D. Mackenzie and D. R. Ulrich, John Wiley & Sons (1988)
- *Ultrastructure Processing IV*, Eds. D. D. Uhlmann, M. Weinberg and D. R. Ulrich, John Wiley & Sons (1988)
- *Ultrastructure Processing of Advanced Materials*, Eds. D. D. Uhlmann and D. R. Ulrich, John Wiley & Sons, 718p (1992)

The papers in these collections are essentially review articles written by the leading research groups on each topic. The first sections are usually devoted to sol-gel science, namely structure, kinetics and characterisation, whereas the latter ones are dedicated to sol-gel technology, in particular new materials and applications.

4.2 Topical references

Specific topics in sol-gel processes are discussed at length in several classic books and general reviews. *The Chemistry of Silica*, written by R. K. Iler, published first in 1955 and reedited in 1979 [105] with major modifications, is certainly the main reference for every aspect of the chemistry of silica in aqueous systems. *Metal Alkoxides*, written by D. C. Bradley, R. C. Mehrotra and D. P. Gaur and published in 1978, is usually credited as the general reference concerning the chemistry of alkoxides (references not given explicitly here can be found in Brinker's book).

The chemistry and physics of organic polymers, discussed in the well known book *Principles of Polymer Chemistry*, written by P. J. Flory in 1953 [74], is also relevant for inorganic

polymers, particularly in what concerns the medium and long range processes, like the gelation, which depend little on the chemical details of each particular system. A reportedly excellent introduction to percolation theory, with reference to gelation, is provided in *The Physics of Amorphous Solids*, by R. Zallen, published in 1983.

Peharps one of the most influential books written in the last twenty years, *The Fractal Geometry of Nature*, by B. B. Mandelbrot [158], published in 1983, is the first reference concerning fractal geometry. The application of fractal concepts in materials science is presented in *Fractals*, by J. Feder, published in 1988. The random aggregation of clusters and gelation applying fractal theory is the subject of the P. Meakin review *Models for Colloidal Aggregation* [162], published in 1988 in Annual Reviews in Physics and Chemistry. Important work on the same topic can be found in the collection *On Growth and Form* [161], edited in 1986 by H. E. Stanley and N. Ostrowsky.

Important work concerning the structure of glasses has been presented in the *University Conferences on Glass Science* held at Pennsylvania State University, and the proceedings have been published by Journal of Non-Crystalline Solids:

- *Proceedings of the Sixth University Conference on Glass Science*, Pennsylvania State University, USA, 1981, Eds. G. E. Rindone, C. G. Pantano and W. B. White, Journal of Non-Crystalline Solids, 49 (1982)
- *Proceedings of the Tenth University Conference on Glass Science*, Pennsylvania State University, USA, 1989, Ed. C. G. Pantano, Journal of Non-Crystalline Solids, 120 (1990)

Work specifically on aerogels has been presented and reviewed in the meetings *International Symposium on Aerogels* and the proceedings published under several labels:

- *Aerogels*, Ed. J. Fricke, Springer-Verlag (1986)
- *2nd International Symposium on Aerogels*, Revue de Physique Appliquée, 24 (1989)
- *3rd International Symposium on Aerogels*, Journal of Non-Crystalline Solids, 145 (1992)

A important collection reviewing the principal applications of sol-gel technology was edited in 1988 by L. C. Klein, *Sol-Gel Technology for Thin Films, Fibers, Preforms, Electronics, and Speciality Shapes*, Noyes Publications.

4.3 Current references

The above publications and its references cover most of the fundamental sol-gel research produced during the decade of 80 and before. More recent work can be found in *Journal of Non-Crystalline Solids* and *Journal of Sol-Gel Science and Technology*. Applied research, concerning the practical aspects of sol-gel processes and the development of new applications, is often presented in *Journal of Materials Research*, *Materials Research Bulletin*, *Journal of the American Ceramic Society*, *American Ceramic Society Bulletin* and *Journal of Materials Science*, whereas more fundamental research, concerning the chemical and physical aspects of sol-gel transformations, is published namely in *Physics and Chemistry of Glasses*. *Journal of Chemical Physics*, *Journal of the American Chemical Society*, *Journal of Applied Physics*, *Applied Physics Letters*, *Journal of Materials Chemistry* and *Chemistry of Materials*.

Part II

Atomistic Modelling

Chapter 5

History

Much of the basics of Atomistic Modelling theory was established well before the actual techniques could be implemented. The Ewald sum method was proposed as early as 1926 [11], many years before Molecular Dynamics simulations or indeed any computer simulation could be performed. In the same way, the Møller-Plesset pertubation theory [169] was presented in 1934, when Hartree-Fock calculations were not in the foreseeable horizon, even without MP corrections.

The first quantum mechanical calculation on molecules was attempted by Coulson and Moffatt in the 1950s [50], who tried to calculate the electron structure on a N_2 molecule, reportedly using a mechanical hand calculator. Unfortunately they had to abandon the study after estimating that it would take another 20 years to complete... The first ab-initio calculations, by today's standards, are carried out only in the 1960s (anyway, much before Coulson's calculation would finish!), by Pople (see [195]).

Simulations based on an interatomic potentials approach start in 1953, with the publication of *Equation of State Calculations by Fast Computing Machines* [168], the first Monte Carlo simulation, performed on MANIAC, at Los Alamos, using a algorithm that is still today the basis of the MC technique. This was closely followed by the first Molecular Dynamics simulation, presented in 1957 by Alder and Wainwright, in a two page report, *Phase Transition for a Hard Sphere System* [9], followed two years later by the description of the method [10]. These separate works presented the basic ideas of molecular simulation, establishing a new dimension in scientific calculations. From the conceptual point of view, MC is even more radical than MD, because it lacks the determinism of the latter.

In 1964 Hohenberg and Kohn published the *Inhomogeneous Electron Gas* [101], laying the foundations of Density Functional theory. This was the most influential step in applied quantum mechanics since the development of Hartree-Fock theory (whose first calculations were being attempted by that time), because the range of possible ab-initio applications suddenly increased tremendously. It was thereafter reasonable to consider ab-initio calculations involving large biomolecules, more systematic reaction studies or even crystals with large unit cells.

In 1969 and 1971, the first MC [28] and MD [200] simulations of liquid water took place. The first MD simulation of glass formation, was carried out by Woodcock in 1971 [217], who cooled molten KCl. At the same time, methods to calculate energy gradients in HF calculations were developed for the first time [6]. The first simulation of silica glass is reported in 1976, again by Woodcock et al. [248], in *Molecular Dynamics Studies of the Vitreous State: Simple Ionic Systems and Silica.*

The method of Car and Parrinello, proposed in 1985 in *Unified Approach for Molecular Dynamics and Density Functional Theory* [48], aims to get the best of both classic and quantum worlds, providing the advantages of a molecular dynamics simulation but with the forces and energy calculated every timestep directly from ab initio methods. It is one of the major contributions for computer simulation since the epic days of Metropolis and Alder, but it certainly requires fast computing machines. The CP method will never replace the inter-atomic potentials approach.

Probably the best NPT ensemble algorithm proposed so far, the corrected NPT Hoover ensemble was published only very recently, in 1993 [167]. In the same year, the COSMO model was published by Klamt and Schüürmann [130]. The very rapid progress in computer hardware has been thus acompanied by an ever growing theoretical effort to develop better models. Both are likely to continue in the future.

The term *Ab-initio*, designating both HF and DF methods, is used throughout this work, as *First Principles* is perhaps too general. Strictly speaking, an Ab-initio calculation can hardly be described as a simulation, as it aims to solve an equation, as exactly as possible. The expression *Atomistic Modelling* was therefore coined to designate both equation solution and phase space description approaches. Although historically the term *Molecular Mechanics* has been used to designate essentially Energy Minimisation methods, it will be applied throughout this work in a more general way, to designate all methods based on Classical Mechanics and involving an interatomic potentials approach.

Computer simulation has a valuable role to play in providing accurate results for problems in statistical mechanics, which would be otherwise untractable. This is particularly the case in liquids, which lack the order of crystals and the low interactivity of the gases. On the other hand, ab-initio calculations provide a tool, often unique, to gain insight into the fundamental mechanisms occurring at the atomic level. This is particularly true for reactional solutions.

Atomistic modelling aims to be a third way between theory and the experiment. It offers insights to the experimentalist and assist in the interpretation of new results. It can be used to test theories and to help develop new ones.

Atomistic modelling provides a direct route between the atomic characteristics of the system (energy, structure, charge distribution), and its macroscopic properties, (density, transport coefficients, thermodynamic properties, fractal dimension). It aims therefore to relate the technologically important properties with the mechanisms at their origin, this way helping the experimentalist to improve the process.

This is particularly the case in Sol-Gel processes, where the properties of the materials obtained strongly depend on a very large number of relevant parameters, whose combined influence can hardly be studied, in a reasonable amount of time, using only experimental procedures. Atomistic modelling seems thus to be a very valuable tool to study these chemical and physical processes, in a systematic way, to try to understand their behaviour (which is the scientific motivation), and to determine the best combinations of parameters to be used in experimental work (which provides the technological motivation).

Chapter 6

Ab-Initio theory

The Ab initio results reported in this work include Density Functional calculations, carried out with Dmol 2.1-96.0 from Molecular Simulations Inc., and Hartree-Fock calculations, carried out with Cadpac 5.2 from Cambridge University.

6.1 Density Functional theory

The Density Functional theory is based in two theorems developed by Hohenberg and Kohn [101] and Kohn and Sham [137], which state that all the properties related with the ground state of a molecular system, in principle nondegenerate, can be directly related with the physically meaningful ground state electron density $\rho_0(\vec{r})$.

The well known variational principle for the ground level energy is used to prove that, for a given number n of electrons, moving under the influence of an external potential $V(\vec{r})$ defined by N nucleus, both $V(\vec{r})$ and n are unique functions of $\rho_0(\vec{r})$. As $V(\vec{r})$ and n fix the Hamiltonian of the system, they determine all the properties for the ground state and consequently these are a unique function of $\rho_0(\vec{r})$. Clearly, n is a function of $\rho_0(\vec{r})$, because:

$$n = \int \rho_0(\vec{r}) d\vec{r}$$

To prove that $V(\vec{r})$ is a unique function of $\rho_0(\vec{r})$, a proof by reductio ad absurdum can be used. If there were two external potentials V and V', differing by more than a constant, each giving the same $\rho_0(\vec{r})$ for its ground state, their Hamiltonians H and H' would be different, the same happening with the respective ground state wave functions ψ_0 and ψ_0'. Consequently, designating the ground state energies for each Hamiltonian by E_0 and E_0', the following statements will be true, due to the variational principle:

$$\begin{aligned} E_0 &= <\psi_0|H|\psi_0> \; < \; <\psi_0'|H|\psi_0'> \; = \; <\psi_0'|H'|\psi_0'> + <\psi_0'|H - H'|\psi_0'> \\ &= E_0' + \int \rho_0(\vec{r})(V(\vec{r}) - V'(\vec{r}))d\vec{r} \end{aligned}$$

Similarly:

$$\begin{aligned} E_0 &= <\psi_0'|H'|\psi_0'> \; < \; <\psi_0|H'|\psi_0> \; = \; <\psi_0|H|\psi_0> + <\psi_0|H' - H|\psi_0> \\ &= E_0 + \int \rho_0(\vec{r})(V(\vec{r}) - V'(\vec{r}))d\vec{r} \end{aligned}$$

and summing both expressions, $E_0 + E_0' < E_0 + E_0'$, so the potentials $V(\vec{r})$ and $V(\vec{r})$' cannot be different. Consequently, the wave function of the ground state is itself a function only of the electronic density $\rho_0(\vec{r})$. As the ground state energy assumes its minimum value E_0 for the wave function ψ_0 which properly describes that state, which is directly related with the correct density $\rho_0(\vec{r})$, any other wave function ψ, related with a different density $\rho(\vec{r})$, will lead to a higher value for the energy:

$$E_0 = <\psi_0(\rho_0)|H|\psi_0(\rho_0)> < <\psi(\rho)|H|\psi(\rho)> .$$

Therefore, the energy attains its lowest value, corresponding to the energy of the ground state E_0, for the correct electronic density ρ_0. Defining the global anti-symmetric wavefunction y of the ground state of the system by the Slater determinant of the orthonormal molecular orbitals ϕ:

$$\psi = \frac{1}{\sqrt{n!}}|\phi_1(1)\phi_2(2)...\phi_n(n)|$$

and defining the total energy of the ground system of a molecular system as: $E_t[\rho] = T[\rho] + U[\rho] + E_{xc}[\rho]$, where $T[\rho]$ is the kinetic energy of a system of non interacting particles of density ρ, $U[\rho]$ is the classical electrostatic energy due to the Coulomb interactions and $E_{xc}[\rho]$ includes all the exchange and many-body correlation contributions E_c to the total energy, these can be given by:

$$\begin{aligned}
\rho_0(\vec{r}) &= \sum_i^N |\phi_i(\vec{r})|^2 \qquad T = \sum_i^N <\phi_i(\vec{r})|\frac{-\nabla^2}{2}|\phi_i(\vec{r})> \\
U &= \sum_\alpha^N \sum_{\beta>\alpha} \frac{Z_\alpha Z_\beta}{|\vec{R}_\alpha - \vec{R}_\beta|} + \sum_i^n \sum_\alpha^N <\phi_i(\vec{r})|\frac{-Z_\alpha}{\vec{R}_\alpha - \vec{r}}|\phi_i(\vec{r})> + \\
&\quad + \frac{1}{2}\sum_i^n \sum_j^n <\phi_i(\vec{r}_1)\phi_j(\vec{r}_2)|\frac{1}{\vec{r}_1 - \vec{r}_2}|\phi_i(\vec{r}_1)\phi_j(\vec{r}_2)> \\
E_{xc}[\rho] &= \frac{1}{2}\sum_i^n \sum_j^n <\phi_i(\vec{r}_1)\phi_j(\vec{r}_2)|\frac{1}{\vec{r}_1 - \vec{r}_2}|\phi_i(\vec{r}_2)\phi_j(\vec{r}_1)> + E_c
\end{aligned}$$

As there is no exact expression for $E_{xc}[\rho]$, the simplest approach is to apply the Local Density Approximation, where it is assumed that, for slow varying density, $E_{xc}[\rho]$ can be approximated as:

$$E_{xc}[\rho] = \int \rho(\vec{r})\epsilon_{xc}(\rho(\vec{r}))d\vec{r}$$

where $\epsilon_{xc}(\rho(\vec{r}))$ represents the exchange and correlation energy per electron of a uniform electron gas of density $\rho(\vec{r})$. A good review about the uniform electron gas is presented in Parr and Yang's book [187]. The total energy can then be written as:

$$\begin{aligned}
E_t &= \sum_i^N <\phi_i(\vec{r})|\frac{-\nabla^2}{2}|\phi_i(\vec{r})> - \sum_\alpha^N <\phi_i(\vec{r})|\frac{-Z_\alpha}{\vec{R}_\alpha - \vec{r}}|\phi_i(\vec{r})> + \\
&\quad + \frac{1}{2} <\rho(\vec{r}_1)\rho(\vec{r}_2)\frac{1}{|\vec{r}_1 - \vec{r}_2|}> + \sum_\alpha^N \sum_{\beta>\alpha} \frac{Z_\alpha Z_\beta}{|\vec{R}_\alpha - \vec{R}_\beta|} + <\rho(\vec{r}_1)\epsilon_{xc}(\rho(\vec{r}_1))> \\
&= \sum_i^N <\phi_i(\vec{r})|\frac{-\nabla^2}{2}|\phi_i(\vec{r})> + <\rho(\vec{r}_1)(\epsilon_{xc}(\rho(\vec{r}_1)) + \frac{V_e(\vec{r}_1)}{2} - V_N)> + V_{NN}
\end{aligned}$$

As the energy of the ground state is given by the minimum of the total energy, it can be obtained calculating the first derivative of E_t, subject to the orthonormality constraints for the wave functions ϕ, using a Lagrangian multipliers ϵ_{ij} approach [6]:

$$\frac{\delta E_t}{\delta \rho} - \sum_i^n \sum_j^n \epsilon_{ij} < \phi_i | \phi_j >= 0.$$

This minimisation leads to a set of coupled equations [6]:

$$(-\frac{\nabla^2}{2} - V_N + V_e + \mu_{xc}[\rho])\phi_i = \epsilon_i \phi_i \quad \text{with } \mu_{xc}[\rho] = \frac{\delta(\rho \epsilon_{xc})}{\delta \rho},$$

corresponding to a system of n noninteracting electrons, moving in a potential given by $-V_N + V_e + \mu_{xc}[\rho]$. The total energy obtained when solving these equations, $\sum_i^n \epsilon_i$, can be corrected for the real potential, $\epsilon_{xc}(\rho) + \frac{V_e}{2} - V_N + V_{NN}$, leading finally to the expression, for the ground state energy:

$$E_0 = \sum_i^n \epsilon_i + < \rho(\vec{r}_1)(e_{xc}(\rho) - \mu_{xc}[\rho] - \frac{V_e(\vec{r}_1)}{2}) > + V_{NN}.$$

The various aspects of DF theory are fully discussed in the book of Parr et al. [187] and a general review is presented by Ziegler [253]. In practise, the method is implemented defining each molecular orbital ϕ_i as a linear combination of a given set of primary wave functions. Most DFT implementations have been designed to study crystalline solids, using periodic boundary conditions and plane wave basis sets, with the properties defined by the Bloch theorem. Dmol 2.1-96.0 uses a set of localised atomic orbitals χ_μ:

$$\phi_i = \sum_\mu C_{i\mu} \chi_\mu,$$

defined numerically on a spherical grid as the product of a spherical harmonic function $Y_{ml}(\theta, \phi)$ and a numerical radial part, defined by a set of points (typically 300), from the origin to an outer distance of 5.3 Å(10 Bohr). Each point is described by a function of cubic spline coefficients, to generate first and second order energy derivatives. The terms $-\nabla^2/2$, required for evaluation of the kinetic energy, are also stored as spline coefficients. The global, piece-wise analytic, atomic wave functions χ_μ, are therefore given in each point by:

$$\chi_\mu(\theta, \phi, r) = Y_{ml}(\theta, \phi)(Ar^3 + Br^2 + Cr + D).$$

These atomic basis functions χ_μ are obtained solving the atomic DFT equations using exactly the same procedure, for a single atom of each element, being given by the linear combination of primary wave functions ξ_κ, with a radial part defined also by a function of cubic spline coefficients, chosen to accurately sample the variational field [6]:

$$\chi_\mu = \sum_\kappa C_{\kappa\mu} \xi_\kappa \qquad \xi_\kappa(\theta, \phi, r) = Y'_{ml}(\theta, \phi)(A'r^3 + B'r^2 + C'r + D').$$

Unlike the molecular wave functions ϕ, the atomic wave functions χ_μ are not orthonormal, and consequently, when inserted in the set of Schrodinger equations above defined, these take the

form, after multiplying on the left side by χ_η and integrating:

$$\sum_\mu < \chi_\eta(\vec{r})| - \frac{\nabla^2}{2} - V_N + V_e + \mu_{xc}[\rho]|\chi_\mu(\vec{r}) > C_{i\mu} = \epsilon_i \sum_\mu < \chi_\eta(\vec{r})|\chi_\mu(\vec{r}) > C_{i\mu}$$

$$\sum_\mu H_{\eta\mu} C_{i\mu} = \epsilon_i \sum_\mu S_{\eta\mu} C_{i\mu}.$$

As H depends on the values of the coefficients C, this equation must be solved by a iterative technique, using the following procedure: 1) choose an initial set of coefficients C_{im} 2) construct a set of molecular orbitals ϕ_i using C_{im}; 3) construct $\rho(\vec{r})$ using ϕ_i; 4) construct V_e and μ_{xc} using $\rho(\vec{r})$; 5) obtain new set of coefficients C_{im} solving Schrodinger equation; 6) construct new molecular orbitals ϕ_i; 7) construct new $\rho(\vec{r})$; 8) if new $\rho(\vec{r})$ and old $\rho(\vec{r})$ are different repeat the whole process. To ensure smooth convergence, damping is usually required, for example, $\rho(\vec{r}) = x\rho(\vec{r})$ new $+(1-x)\rho(\vec{r})$ old, with $0 < x < 1$; 9) if $\rho(\vec{r})$ new and $\rho(\vec{r})$ old are equal, evaluate E_0. As the wave functions are numerical, the two sets of integrals defined above have also to be calculated numerically:

$$H_{\eta\mu} = \sum_i \chi_\eta(\vec{r}_i)(-\frac{\nabla^2}{2} - V_N + V_e + \mu_{xc}[\rho])\chi_\mu(\vec{r}_i)w(\vec{r}_i),$$

$$S_{\eta\mu} = \sum_i \chi_\eta(\vec{r}_i)\chi_\mu(\vec{r}_i)w(\vec{r}_i),$$

where $w(\vec{r}_i)$ represents the weight associated with each point of the molecular grid used for the integration (see Becke [30] and Jordá [190], for recent integration schemes).

In Dmol 2.1-96.0 the molecular grid is generated in a spherical pattern around each atomic center, out to 5.3Å, with a number of radial points typically given by $14(Z+2)^{1/3}$ [6], where Z is the atomic number of each atom in the molecule (25 for H, 30 for O, 35 for Si). These radial shells are logarithmic spaced, to treat the rapid oscillations of the molecular orbitals near the nuclei.

The angular points for each r shell increase with the quantum number l and are selected by schemes designed to yield exact angular integration, using quadrature methods and a product-Gauss rule in $cos(\theta)$ and ϕ [6]. The total number of points per atom in the grid is approximately 1000.

Therefore, at the beginning of a calculation, after generating this molecular grid, the program has to interpolate all the atomic quantities, known for each point of the atomic grids, to this new set of mesh points. To accelerate convergence far from the nucleus and to avoid integrating over the nucleus, a partition function is used, defined as:

$$p_\alpha(\vec{r}) = \frac{g_\alpha(\vec{r} - \vec{R}_\alpha)}{\sum_\beta g_\alpha(\vec{r} - \vec{R}_\alpha)} \quad with\ p_\alpha(\vec{r}) = 1 \quad and \int f(\vec{r})d\vec{r} = \sum_\alpha \int f(\vec{r})p_\alpha(\vec{r})d\vec{r},$$

where $g_\alpha(\vec{r} - \vec{R}_\alpha)$ is a function typically large for small $(\vec{r} - \vec{R}_\alpha)$ and small for large $(\vec{r} - \vec{R}_\alpha)$, so $p_\alpha(\vec{r})$ goes to zero near the nucleus and decreases faster far from them. The function $g_\alpha(\vec{r} - \vec{R}_\alpha)$ implemented in Dmol 2.1-96.0 is given by [6]:

$$g_\alpha(\vec{r} - \vec{R}_\alpha) = \rho_\alpha(\vec{r} - \vec{R}_\alpha)[e^{\frac{r_o}{|\vec{r} - \vec{R}_\alpha|}} - 1],$$

where r_o is equal to 0.5 Åand $\rho_\alpha(\vec{r}-\vec{R}_\alpha)$ is the atomic charge density for atom α. The Fock $H_{\eta\mu}$ and overlap $S_{\eta\mu}$ numerical integrals can consequently be rewritten as sums $\sum_\alpha p_\alpha(\vec{r})H_{\eta\mu}$ and $\sum_\alpha p_\alpha(\vec{r})S_{\eta\mu}$:

$$\begin{aligned} H_{\eta\mu} &= \sum_\alpha \sum_i \chi_\eta(\vec{r}_i)(-\frac{\nabla^2}{2} - V_N + V_e + \mu_{xc}[\rho])\chi_\mu(\vec{r}_i)w(\vec{r}_i)p_\alpha(\vec{r}), \\ S_{\eta\mu} &= \sum_\alpha \sum_i \chi_\eta(\vec{r}_i)\chi_\mu(\vec{r}_i)w(\vec{r}_i)p_\alpha(\vec{r}). \end{aligned}$$

The Coulombic potential $V_e(\vec{r})$ is calculated by solving the Poisson equation $-\nabla^2 V_e(\vec{r}) = 4\pi e^2\rho(\vec{r})$, instead of integrating all over the space $V_e(\vec{r}) = \int \frac{\rho(\vec{r}_i)}{|\vec{r}-\vec{r}_i|}d\vec{r}_i$. This approach, devised by Delley [64], requires a analytical representation of the charge density. Instead of a least-squares-fitting procedure, a projection scheme is used. $\rho(\vec{r})$ is partitioned in multipolar components $\rho_{\alpha lm}|(\vec{r}-\vec{R}_\alpha)|$:

$$\rho_{\alpha lm}(|\vec{r}-\vec{R}_\alpha|) = \frac{1}{\sqrt{4\pi}}\frac{1}{\sqrt{2l+1}}\int Y_{lm}(\vec{r}-\vec{R}_\alpha)p_\alpha(\vec{r}-\vec{R}_\alpha)\rho(\vec{r})d\Omega.$$

To accelerate the integration, a partition function $p_\alpha(\vec{r}-\vec{R}_\alpha$ is applied, where $g_\alpha(\vec{r}-\vec{R}_\alpha) = \frac{\rho_\alpha(\vec{r}-\vec{R}_\alpha)}{|\vec{r}-\vec{R}_\alpha|}$. The analytic total density is obtained from the summation over all $\rho_{\alpha lm}$:

$$\tilde{\rho} = \sqrt{4\pi}\int_{\alpha lm}\sqrt{2l+1}Y_{lm}(\vec{r}-\vec{R}_\alpha)\rho_{\alpha lm}(|\vec{r}-\vec{R}_\alpha|).$$

In general, the analytic model density $\tilde{\rho}$, is not exactly equal to the numerical orbital density ρ, due to truncation errors, but these can be controlled by the number of terms used in the projection. The Coulombic potential for each component is then given by [6]:

$$V_{\alpha lm}(\vec{r}) = \vec{r}^{-l-1}\int_o^r \rho_{\alpha lm}(x)x^{l+2}dx + \vec{r}^{\,l}\int_r^\infty \rho_{\alpha lm}(x)x^{l-1}dx$$

and the total potential by:

$$V_e(\vec{r}) = 4\pi\sqrt{4\pi}\sum_{\alpha lm}\frac{1}{\sqrt{2l+1}}Y_{lm}(\vec{r}-\vec{R}_\alpha)V_{\alpha lm}(|\vec{r}-\vec{R}_\alpha|)$$

Dmol 2.1-96.0 is described by its author, Delley, in [64].

6.2 Functionals

In DFT theory, all the conceptual difficulties are isolated in a single term, the exchange and correlation energy, $E_{xc}[\rho]$, and the price to pay for the simplicity and efficiency of the method is mainly the need to develop expressions for this term. Consequently, much work has been done to try to obtain simple and accurate expressions for this purely quantum contribution, with no classic analogue.

Under the Local Density Approximation (LDA), the electron gas model can be used to develop expressions for $e_{xc}(\rho(\vec{r}))$. In Dmol 2.1-96.0, the expressions for the local exchange and correlation functionals developed by von Barth and Hedin (1971) [239], after Hedin and

Lundqvist (1972) [94], and reviewed by Moruzzi, Janak and Williams (1978) [173], are used to calculate separately the exchange and correlation contributions, for both spin restricted and spin unrestricted calculations. Defining r_s as the radius of a sphere with electronic density $\rho(r)$ containing a total charge of one electron:

$$\frac{4}{3}\pi r_s^3 = \frac{1}{\rho(r)}$$

the electron exchange energy is given by [6]:

$$\epsilon_x = -\frac{C_{x1}}{r_s} \quad C_{x1} = \frac{3}{4}(\frac{9}{4\pi^2})^{1/3}$$

and the electron correlation energy comes equal to, for the spin restricted case:

$$\epsilon_c = -0.0225F(\frac{r_s}{21.0}) \quad with\ F(x) = (1+x^3)ln(1+\frac{1}{x}) + \frac{x}{2} - x^2 - \frac{1}{3}$$

and for the spin unrestricted case:

$$\epsilon_c = -0.0225F(\frac{r_s}{21.0}) + [\frac{0.4582}{r_s}(2^{1/3}-1) - 0.0113F(\frac{r_s}{52.9}) + 0.0225F(\frac{r_s}{21.0})f(\frac{\Delta\rho}{\rho})$$

with $\rho(\vec{r}) = \rho_\alpha(\vec{r}) + \rho_\beta(\vec{r})$, $\Delta\rho = \rho_\alpha(\vec{r}) - \rho_\beta(\vec{r})$ and $f(y) = (2^{4/3}-2)^{-1}[(1+y)^{4/3} + (1-y)^{4/3} - 2]$. In a spin unrestricted calculation, it is possible to form two different charge densities, for alpha and beta electrons, and their sum and difference give respectively the total charge density $\rho(\vec{r})$, and the spin density $\Delta\rho(\vec{r})$.

The inaccuracies of the LDA method, particularly in the description of bond energies, are discused namely by Tschinke et al. [231]. Equations for non-local, gradient-corrected, exchange and correlation energy, have been proposed, namely by Becke (1988) [29], Lee et al. (1988) [146] and Vosko et al.(1980) [240]. The Becke total exchange energy is given by:

$$E_x = -C_{x2}\sum_\sigma \int \rho_\sigma^{4/3} d^3\vec{r} - \beta \sum_\sigma \int \rho_\sigma^{4/3} \frac{x_\sigma^2}{1 + 6\beta x_\sigma sinh^{-1} x_\sigma} d^3\vec{r}$$

where the first term is the local exchange energy described above, σ denotes α and β electron spin, and x_σ and C_{x2} are given by:

$$x_\sigma = \frac{|\nabla\rho_\sigma|}{\rho_\sigma^{4/3}} \quad C_{x2} = \frac{3}{2}(\frac{3}{8\pi})^{1/3}$$

The parameter $\beta = 0.0042$ a.u. was determined by fitting the exchange energy of the six noble gas atoms helium through radon [29]. The Lee-Yang-Parr second-order gradient expansion formulas, for the correlation energy, respectively for closed and open shells, are given by [146]:

$$\begin{aligned} E_c &= -a\int \frac{1}{1+d\rho^{-1/3}}[\rho + b\rho^{-2/3}[C_F\rho^{5/3} - 2t_W + (\frac{1}{9}t_W + \frac{1}{18}\nabla^2\rho)]e^{-c\rho^{-1/3}}]d^3\vec{r} \\ E_c &= -a\int \frac{1}{1+d\rho^{-1/3}}[\rho + 2b\rho^{-5/3}[2^{2/3}C_F\rho_\alpha^{8/3} + 2^{2/3}C_F\rho_\beta^{8/3} - \rho t_W + \\ &\quad \frac{1}{9}(\rho_\alpha t_W^\alpha + \rho_\beta t_W^\beta) + \frac{1}{18}(\rho_\alpha\nabla^2\rho_\alpha + \rho_\beta\nabla^2\rho_\beta)]e^{-c\rho^{-1/3}}]d^3\vec{r} \end{aligned}$$

In these equations $t_w(\vec{r})$, $\gamma(\vec{r})$ and C_F are given by:

$$t_W(\vec{r}) = \frac{1}{8}\frac{|\nabla\rho(\vec{r})|^2}{\rho(\vec{r})} - \frac{1}{8}\nabla^2\rho; \quad \gamma(\vec{r}) = 2[1 - \frac{\rho_\alpha^2(\vec{r}) + \rho_\beta^2(\vec{r})}{\rho^2(\vec{r})}]; \quad C_F = \frac{3}{10}(3\pi^2)^{2/3}$$

and the coefficients $a = 0.049$, $b = 0.132$, $c = 0.2533$, $d = 0.349$ were obtained by a fitting procedure, using the Hartree-Fock orbital for the helium atom [146]. The correlation potential, the functional derivative of E_c with respect to $\rho(\vec{r})$, is also given by Lee et al.

6.3 Basis Sets

The five hydrogen radial functions in Dmol 2.1-96.0 were obtained from three atomic DFT calculations [6]: the first for the normal atom of hydrogen, to determine the occupied 1s orbital, the second with a nuclear charge of 1.3, to give additional 1s and 2p functions, slightly more contracted, and the third with a nuclear charge of 4.0, to obtain a further set of 1s and 2p functions, thereby generating an even better description, particularly near the nucleus. Double numerical basis sets, DN and DND, use only the first two functions, 1s+1s, whereas the first 2p function is already included in the DNP basis set, as a polarisation function. The remaining 1s and 2p functions are applied in the so-called extended ENP and triple TNP numerical basis set (strictly speaking, the TNP basis is closer to a hybrid quadruple basis set, so it should match, at least, a fully optimised real triple basis set, and the name is kept here essentially for rapid reference).

The ten radial functions for carbon were obtained after four atomic DFT calculations: the first for the normal carbon atom, to give the occupied 1s, 2s and 2p functions; a second for the C^{2+} cation, where two electrons were removed from the higher 2p energy levels, to obtain a second set of 2s and 2p functions, closer to the nucleus; a third for a nuclear charge +5.0 and a single electron, to give 3d, 2p and 1s highly contracted functions; and the fourth for a nuclear charge +7.0, again with a single electron, to obtain a additional set of 3d and 2p, giving the best possible description near the nucleus, where the molecular wavefunctions are expected to change very rapidly. The DN basis set uses only the first 5 functions, to generate a double representation of the valence shell, 1s+2s+2p+2s+2p, whereas DND and DNP basis sets include 3d, as a polarisation function. The so-called extended ENP and triple-numerical TNP basis sets, contain all ten basis functions.

The ten radial functions for oxygen were obtained in the same way as for carbon, after four equivalent atomic DFT calculations: the first for the normal oxygen atom, to obtain the occupied 1s, 2s and 2p functions, a second for the O^{2+} cation, after removing two electrons from the orbitals 2p, to give another set of more contracted 2s and 2p basis functions, a third one for the hydrogenic O, with a single electron and a +5.0 nuclear charge, to obtain 3d, 2p and 1s basis functions, and a fourth also for a single electron but again with a larger nuclear charge, +7.0, to obtain two further 3d and 2p functions. The double representation of the valence shell required by the double basis set DN is obtained with the first five functions 1s+2s+2p+2s+2p, whereas the first 3d is introduced in DND and DNP basis sets to act as a polarisation function. The four remaining functions, 2p+1s+3d+2p are added in the so-called extended ENP and triple numerical TNP basis sets.

Thirteen radial functions were generated for silicon, by undertaking three atomic DFT calculations: first for the normal silicon atom, to give the occupied 1s+2s+2p+3s+3p five atomic

orbitals; second for the ionic Si^{2+}, removing two alpha electrons from the highest energy 3p orbital and adding a 3d orbital, without changing its occupation to determine additional 3s+3p+3d functions; and third for the ionic excited-state formed when two alpha electrons leave 2s and 2p levels and one is transferred to a formerly empty 3d orbital, forming a Si^{+} ion, in order to obtain another five basis functions, 2s+2p+3s+3p+3d. To generate a double representation of the valence shell of silicon, as required in a DN basis set, the first seven basis functions have to be used, 1s+2s+2p+3s+3p+3s+3p, and the next additional 3d is required to act as a polarisation function in DND, DNP and ENP basis sets. The last five basis functions were implemented to create the so-called triple basis set TNP, to enhance the electronic description near the silicon atoms and in general to improve the quality of the structural and energetic results in silicon-based molecular systems.

Hartree-Fock calculations, corrected by a Møller-Plesset second-order perturbation [169], were done using Cadpac 5.2 with the standard double-zeta $6-31G^{**}$ and triple-zeta $6-311G^{**}$ basis set. Each atomic function is given by the product of the appropriate spherical harmonic and a radial part given by the sum of contracted Gaussian functions. The left figures give the number of Gaussians in each core orbital, while the right ones represent the number of Gaussians in each valence orbital. A single * describes a additional polarisation function for all atoms but H, given by a single Gaussian for the next quantum number l, while a double ** includes also H polarisation functions. The $6-31G^{**}$ atomic wavefunctions for oxygen, for example, are given by:

$$\begin{aligned}
\text{core}: \quad & \chi_{1s} = Y_0^0 \sum_{i=1}^{6} C_i e^{-\alpha_i r^2} \\
\text{inner valence}: \quad & \chi_{2s} = Y_0^0 \sum_{i=1}^{3} C_i e^{-\alpha_i r^2} \qquad \chi_{2p} = Y_m^1 \sum_{i=1}^{3} C_i e^{-\alpha_i r^2} \qquad m = -1, 0, 1 \\
\text{outer valence}: \quad & \chi'_{2s} = Y_0^0 C e^{-\alpha r^2} \qquad \chi'_{2p} = Y_m^1 C e^{-\alpha r^2} \qquad m = -1, 0, 1 \\
\text{polarisation}: \quad & \chi_{3d} = Y_m^2 C e^{-\alpha r^2} \qquad m = -2, -1, 0, 1, 2,
\end{aligned}$$

corresponding to a total of 1+2+2+1 different radial functions and 1+4+4+5 different atomic wavefunctions (the actual coefficients are given in the long compilations edited by Huzinaga [104] and Poirier et al. [193]). An analytic double zeta plus polarisation basis set is therefore formally equivalent to the double numerical plus polarisation basis set discussed above. A good general review about exponential, Gaussian and other analytic basis sets is presented by Wilson [246].

6.4 Atomic charges

Both Mulliken [176] and Hirshfeld population analyses are employed in this work. In the former, a gross population g_μ for each basis function ϕ_μ is obtained dividing equally the overlap contributions between the orbitals involved, ϕ_μ and ϕ_ν, giving:

$$g_\mu = P_{\mu\mu} + \sum_{\mu} \sum_{<\nu} P_{\mu\nu} S_{\mu\nu} \qquad with \sum_{\mu}^{N} g_\mu = n$$

where $P_{\mu\nu}$ are the elements of the density matrix and $S_{\mu\nu}$ are the elements of the overlap matrix. A total gross population g_A for each atom A can now be defined as $g_A = \sum_{\mu \in A} g_\mu$ and the Mulliken charges become simply equal to $q_A = Z_A - g_A$.

The Hirshfeld partition of the charge distribution is based in the deformation density $\rho_d(\vec{r})$, defined as the difference between the molecular and atomic charge densities:

$$\rho_d(\vec{r}) = \rho(\vec{r}) - \sum_A \rho_A(\vec{r} - \vec{R}_A)$$

where $\rho_A(\vec{r} - \vec{R}_A)$ represents the charge density at $\vec{r}$ of atom A centered at $\vec{R}_A$. The deformation density is weighted according to the relative contribution of each atom to the charge at $\vec{r}$:

$$W_A(\vec{r}) = \frac{\rho_A(\vec{r} - \vec{R}_A)}{\sum_B \rho_B(\vec{r} - \vec{R}_B)}$$

The effective atomic charges, dipoles and quadrupoles are then defined as:

$$q(A) = \int \rho_d(\vec{r}) W_A(\vec{r}) d\vec{r}$$

$$\mu_x(A) = \int \rho_d(\vec{r}) W_A(\vec{r})(x - x_A) d\vec{r}$$

$$\theta_{xy}(A) = \int \rho_d(\vec{r}) W_A(\vec{r})(x - x_A)(y - y_A) d\vec{r}$$

6.5 Optimisation

The minimisation of a N-dimensional function, as the geometry optimisation of a molecule, is usually done applying successive one-dimensional line minimisations, until reaching the minimum. Different methods differ only in the choice of the minimisation direction $\vec{h}$. Both the line minimisation and the direction choice can be done either with function information $f()$ only, or with gradient information $\vec{\nabla} f()$.

In the first case, the simplest approach is to minimise successively along the axis directions $\vec{e}_1 ... \vec{e}_N$, but usually this is inefficient. The *direction set (Powel's) methods* aim to construct a set of non-interfering conjugate directions:

1. Given a starting position $\vec{P}_o$, initialise $\vec{h}_i = \vec{e}_i$
2. For $i = 0...N$, minimise along direction $\vec{h}_i$ to obtain $\vec{P}_{i+1}$.
   Copy direction $\vec{h}_{i+1}$ to $\vec{h}_i$.
3. For $i = N$, copy $\vec{P}_N - \vec{P}_o$ to $\vec{h}_N$.
   Minimise along $\vec{h}_N$ and define new $\vec{P}_o$.

To avoid linear dependence between the directions $\vec{h}_i$, these can be reinitialised after N iterations of the basic procedure or more sophisticated Brent's and Powel's algorithms can be used [199].

Predicting chemical structures with ab-initio methods became reasonable in the 1970s, when various methods became available to calculate the derivative of the total energy, decreasing substantially the CPU time required for these calculations. In Density Functional Theory, the derivative of the total energy is given by [6]:

$$E^a = \frac{\delta E}{\delta a} = \sum_i < \phi_i^a | H - \epsilon_i | \phi_i > + E_{HF}^a$$

where E^a_{HF} represents the Hellmann-Feynman force, which gives the derivative in the absence of any orbital relaxation [6]. In Dmol 2.1-96.0 the basis functions are derived analytically, as they are given by angular spherical harmonics and radial cubic splines.

The simplest method that uses gradient information to determine the minimisation directions is the *steepest descent method*:

Minimise along the direction defined by $\vec{P}_i$ and $\vec{\nabla} f(\vec{P}_i)$. Repeat until convergence.

Although reliable, the method is inefficient, because the new search direction is always orthogonal to the previous one. In the *conjugate gradient methods*, a set of conjugate directions is chosen, according to the algorithm:

1. Given $\vec{P}_o$ initialise $\vec{h}_o = \vec{\nabla} f(\vec{P}_o)$.
2. For $i = 0...end$, minimise along direction $\vec{h}_i$.
   Calculate $\vec{g}_{i+1} = -\vec{\nabla} f(\vec{P}_{i+1})$.
   Determine $\vec{h}_{i+1} = \vec{g}_{i+1} + \gamma_i \vec{h}_i$.

where $\gamma_i = \frac{\vec{g}_{i+1}\vec{g}_{i+1}}{\vec{g}_i\vec{g}_i}$ in the *Fletcher-Reeves method* and $\gamma_i = \frac{(\vec{g}_{i+1}-\vec{g}_i)\vec{g}_{i+1}}{\vec{g}_i\vec{g}_i}$ in the *Polak-Ribiere method*, which is apparently better. In these conditions, it can be shown [199] that, for all $i \neq j$, $\vec{g}_i \cdot \vec{g}_j = 0$ and $\vec{h}_i A \vec{h}_j = 0$ (A=Hessian matrix), so all gradients are mutually orthogonal and all directions are mutually conjugate [199].

In the *variable metric methods*, an inverse Hessian matrix A^{-1} is constructed, according to the algorithm:

1. Given $\vec{P}_o$ calculate $\vec{g}_o = -\vec{\nabla} f(\vec{P}_o)$ and initialise $H_o = I$.
2. For $i = 0...end$, calculate $\vec{h}_i = H_i \vec{g}_i$
   Minimise along direction $\vec{h}_i$.
   Calculate $f(\vec{P}_{i+1})$ and $\vec{g}_{i+1} = -\vec{\nabla} f(\vec{P}_{i+1})$.
   Update $H_{i+1} = H_i + U_i$.

In the *Davidon-Fletcher-Powel method*, U_i is equal to:

$$H_{i+1} = H_i + \frac{(\vec{x}_{i+1} - \vec{x}_i) \otimes (\vec{x}_{i+1} - \vec{x}_i)}{(\vec{x}_{i+1} - \vec{x}_i) \cdot (\vec{\nabla} f_{i+1} - \vec{\nabla} f_i)} - \frac{[H_i(\vec{\nabla} f_{i+1} - \vec{\nabla} f_i)] \otimes [H_i(\vec{\nabla} f_{i+1} - \vec{\nabla} f_i)]}{(\vec{\nabla} f_{i+1} - \vec{\nabla} f_i) H_i (\vec{\nabla} f_{i+1} - \vec{\nabla} f_i)}$$

while in the *Broyden-Fletcher-Goldfarb-Shanno method*, which is apparently better, there is another term:

$$(\vec{\nabla} f_{i+1} - \vec{\nabla} f_i) H_i (\vec{\nabla} f_{i+1} - \vec{\nabla} f_i) \vec{u} \otimes \vec{u}$$

where $\vec{u}$ is equal to:

$$\vec{u} = \frac{(\vec{x}_{i+1} - \vec{x}_i)}{(\vec{x}_{i+1} - \vec{x}_i) \cdot (\vec{\nabla} f_{i+1} - \vec{\nabla} f_i)} - \frac{H_i(\vec{\nabla} f_{i+1} - \vec{\nabla} f_i)]}{(\vec{\nabla} f_{i+1} - \vec{\nabla} f_i) H_i (\vec{\nabla} f_{i+1} - \vec{\nabla} f_i)}$$

In these conditions, it can be shown [199] that $\lim_{i\to\infty} H_i = A^{-1}$ and $x_m - x_i = A^{-1}[-\nabla f(\vec{x}_i)]$, where x_m is the minimum, for any current point $\vec{x}_i$ [199]. The variable methods might be slightly more efficient near the minimum than the conjugate methods. In compensation, the conjugate gradient methods are faster (per cycle) and only require intermediate storage of the order of N, while the variable metric methods require a matrix of size $N \times N$.

Ab-initio programs tend to implement variable metric methods, because the number of atoms is small and the number of geometry cycles should be as small as possible. In molecular mechanics programs, the steepest descent methods can be useful in complex systems, very far from the minimum, where the reliability of the method is the most important factor, and conjugate gradient methods are required when the number of atoms involved is very large, for example during the minimisation of a large PBC system.

A constrained optimisation of a function $F(\vec{x})$ subject to a series of n constraints $C_i(\vec{x}) = 0$ can be handled replacing $F(\vec{x})$ by the Lagrangian function:

$$L(\vec{x}, \lambda) = F(\vec{x}) - \sum_{i=1}^{n} \lambda_i C_i(\vec{x})$$

At a stationary point of the function L, $\frac{\delta L}{\delta \lambda_i} = -C_i = 0$ and $\frac{\delta L}{\delta x_j} = \frac{\delta F}{\delta x_j} = 0$, so it is also a stationary point for the function F and all constraints are satisfied. Detailed information about specific optimisation algorithms (implemented in codes as Dmol 2.1-96.0 and Gaussian 82), can be found in Baker's work [26, 24], including determination of transition states [22] and constrained optimisation [23, 25] techniques. Long reviews specifically about determination of transition states by ab-initio methods are presented by Bernardi and by Schlegel in [144].

Annealing methods are used in atomistic modelling, namely in Molecular Dynamics and Monte Carlo, to identify the global minimum in systems with many local minima, where static minimisations are likely to fail. The simplest method is to decrease slowly the temperature and allow the atoms to move to more favourable arrangements. A slightly different approach is to sample the configuration space at high temperature, and then periodically minimise the energy by either, decreasing slowly the temperature to 0 Kelvin or performing a static (quenching) minimisation. All these techniques have been extensively applied during this work, to determine the more stable silicate conformations and to initialise liquid solutions.

6.6 COSMO model

The Conductor-like Screening Model, COSMO, is a continuum dielectric model, where a solute molecule is embedded in a dielectric continuum of permittivity ϵ. The interface between the cavity formed by the solute and the dielectric, the *solvent accessible surface*, has thus a surface charge distribution, arising from the polarisation of the dielectric medium in response to the charge distribution of the solute $\rho(\vec{r})$. The aim of any continuum dielectric model is to determine this screening charge density $\sigma(\vec{r})$, given by classic electrostatics [130, 107] as:

$$4\pi\sigma(\vec{r}) = (\epsilon - 1)\vec{n}(\vec{r})\vec{E}(\vec{r}),$$

where $\vec{n}(\vec{r})$ is the surface normal vector at a point $\vec{r}$ and $\vec{E}(\vec{r})$ represents the total electric field at the inner side of the surface at that point. This can be done by a double iterative procedure, optimising $\sigma(\vec{r})$ for each $\rho(\vec{r})$ and vice-versa, but it is computationally quite expensive and the analytical gradient of the screening energy relatively to the solute geometry cannot be evaluated [130]. For spherical and ellipsoidal cavities, the problem was solved analytically by Onsager [183] but these cavity shapes are quite restrictive for general application.

Basically, the COSMO model calculates the screening charges in a conductor ($\epsilon = \infty$), for arbitrarily shaped cavities, using a non-iterative procedure, and then the dielectric screening

energy and its gradient are scaled by $(\epsilon - 1)/(\epsilon + \frac{1}{2})$, to take into account the dielectric. For strong dielectrics, such as polar liquids, the relative error seems to be quite small, while for weak dielectrics ($\epsilon \approx 1$) the absolute error in the dielectric energy and gradient are almost irrelevant [130].

If the charges Q_i are enclosed by an arbitrary closed surface S the screening charge distribution on S and the screening energy can be found by dividing S into a large number of small fragments S_μ centred at $\vec{t}_\mu$ with constant surface density σ_μ on each segment (Dmol 96.0 typically uses about 160 segments). If $|S_\mu|$ is the area and $q_\mu = |S_\mu|\sigma_\mu$ is the charge of each segment μ, then

$$b_{i\mu} = \frac{1}{|S_\mu|}\int_{S_\mu} |\vec{r} - \vec{r}_i|^{-1} d^2\vec{r}$$

is the interaction of a unit solute charge at $\vec{r}_i$ with a unit screening charge at the segment μ and

$$a_{\mu\nu} = \frac{1}{|S_\mu||S_\nu|}\int_{S_\mu}\int_{S_\nu} |\vec{r} - \vec{r}'|^{-1} d\vec{r} d\vec{r}'$$

is the interaction of unit screening charges at S_μ and S_ν. Writing the interaction between unit solute charges as $c_{ij} = |\vec{r}_i - \vec{r}_j|^{-1}$, the total electrostatic energy E_T and the surface electrostatic potential Φ can be written, in matrix form, as:

$$E_T = \frac{1}{2}\vec{Q}^T C\vec{Q} + \vec{Q}^T B\vec{q} + \frac{1}{2}\vec{q}^T A\vec{q} \quad \Phi(\vec{q}) = B\vec{Q} + A\vec{q}$$

where the vectors $\vec{Q}$ and $\vec{q}$ represent the solute and screening charges and the matrices A, B and C are formed by the elements $a_{\mu\nu}$, $b_{i\mu}$ and c_{ij}, respectively. The screening charge distribution $\vec{q}^*$ that minimises the electrostatic energy is then given by:

$$\frac{d}{dq}E_T|_{\vec{q}^*} = B\vec{Q} + A\vec{q}^* = 0 \quad \vec{q}^* = -A^{-1}B\vec{Q}.$$

This result is equivalent to considering the boundary condition of vanishing potential on the surface of a conductor: $\Phi = 0$. The electrostatic energy of the screening system $E = \frac{1}{2}\vec{Q}^T C\vec{Q} + \vec{Q}^T B\vec{q}$ and the electrostatic solvation energy $\Delta E = \vec{Q}^T B\vec{q}$ become thus equal to:

$$E = \frac{1}{2}\vec{Q}^T(C - BA^{-1}B)\vec{Q} \quad \Delta E = -\frac{1}{2}\vec{Q}^T BA^{-1}B\vec{Q}$$

and the analytic gradient of the dielectric energy with respect to each atomic position $\vec{R}_\alpha$ is given by [130]:

$$\vec{\nabla}_{\vec{R}_\alpha}\Delta E = -\frac{1}{2}\vec{\nabla}_{\vec{R}_\alpha}(\vec{Q}^T BA^{-1}B\vec{Q}) = -\vec{q}^{*T}(\vec{\nabla}_{\vec{R}_\alpha}B)\vec{Q} + \frac{1}{2}\vec{q}^{*T}(\vec{\nabla}_{\vec{R}_\alpha}A)\vec{q}^*.$$

Physically the first part represents the change of Coulomb interaction between the solute charges $\vec{Q}$ and the screening charges $\vec{q}^*$ due to a change of $\vec{R}_\alpha$, while the second part represents the corresponding change in the interaction of the screening charges.

The COSMO electrostatic solvation energy can be included directly in the hamiltonian equations and therefore an electrostatic COSMO contribution is present in every SCF cycle [6]. The direct incorporation of the solvent effects within the SCF procedure and the direct evaluation of the gradients are the major computational advantages of the COSMO scheme. However,

the results depend on the Van der Waals radii used to evaluate the cavity surface, obtained as a superimposition of spheres centered at the atoms [6]. Full details of COSMO theory and implementation in a semi-empirical (Mopac) and ab-initio (Dmol 96.0) codes are presented by Klamt et al. [130] and Andzelm et al. [16] respectively.

The most relevant Ab Initio studies carried out during this work are presented in the third part: *Ab Initio Studies.*

Chapter 7

Molecular Mechanics theory

The Molecular Mechanics results reported in this work include Molecular Dynamics and Energy Minimisation calculations, carried out with Discover 2.9 and Discover 94.0-96.0 from Molecular Simulations Inc., and Molecular Dynamics calculations carried out with Dl_poly 1.1 from Daresbury Laboratories. Throughout this work, the term *Molecular Mechanics* is used to describe all Classical Mechanics methods involving an interatomic potentials approach.

7.1 Molecular Dynamics

Molecular Dynamics is the general name given to a large number of computational methods (see for example Berendsen et al. [35],Tildesley [228] and Gubbins [90]), adopting different mathematical techniques and physical conditions, used to solve the classical equations of motion for a system of N atoms:

$$\vec{f}_i = m_i\ddot{\vec{r}}_i \quad \text{or} \quad \vec{f}_i = \dot{\vec{p}}_i \text{ and } \vec{p}_i = m_i\dot{\vec{r}}_i \quad with\ i = 1...N$$

interacting via a potential V of the form:

$$V(\vec{r}_1, \vec{r}_2 ... \vec{r}_N, t) = V(t) + \sum_i V(\vec{r}_i) + \sum_i \sum_j V(\vec{r}_i, \vec{r}_j) + \sum_i \sum_j \sum_k V(\vec{r}_i, \vec{r}_j, \vec{r}_k) + ...$$

A well established method to solve the first or second order sets of differential equations above defined is the *finite difference method*, where the equations are solved on a step-by-step basis, using the positions, velocities and accelerations of all the atoms at time t to calculate their positions, velocities and accelerations at time $t + \Delta t$. The accuracy of the integration and the cpu time needed to simulate a given real time, increase both for lower timesteps. The larger value of Δt that still produces an acceptable integration error is determined by the magnitude of the truncation error of the algorithm used and by the frequencies of the fastest atomic movements in the atomic system. These are usually vibrational stretching modes, with frequencies not higher than $10^{-14}s^{-1}$, and in practice, timesteps between 10^{-15}s and 10^{-16}s are usually used in MD simulations.

The most used integration algorithms in MD are the direct Verlet methods, as they are fastest and reliable (even for larger timesteps), and the Gear predictor-corrector methods, due to its superior accuracy (at least for smaller timesteps). In a *Gear fourth-order method*, an

estimate of $\vec{r}(t+\Delta t)$, $\vec{v}(t+\Delta t)$, $\vec{a}(t+\Delta t)$ and $\vec{b}(t+\Delta t)$ is first made, using a Taylor series expansion about time:

$$\begin{aligned}
\vec{r}^P(t+\Delta t) &= \vec{r}(t)+\vec{v}(t)\Delta t+\frac{1}{2!}\vec{a}(t)\Delta t^2+\frac{1}{3!}\vec{b}(t)\Delta t^3\\
\vec{v}^P(t+\Delta t) &= \vec{v}(t)+\vec{a}(t)\Delta t+\frac{1}{2!}\vec{b}(t)\Delta t^2\\
\vec{a}^P(t+\Delta t) &= \vec{a}(t)+\vec{b}(t)\Delta t\\
\vec{b}^P(t+\Delta t) &= \vec{b}(t)
\end{aligned}$$

New accelerations can now be calculated for the predicted positions, using the information provided by the potential:

$$\vec{a}^V(t+\Delta t)=-\frac{1}{m}\vec{grad}V(\vec{r}^P)(t+\Delta t)$$

Finally, the difference between the predicted and calculated accelerations, $\vec{\Delta a}(t+\Delta t)=\vec{a}^V(t+\Delta t)-\vec{a}^P(t+\Delta t)$ can now be used to correct all the vectors previously predicted:

$$\begin{aligned}
\vec{r}^C(t+\Delta t) &= \vec{r}^P(t+\Delta t)+c_0\vec{\Delta a}(t+\Delta t)\\
\vec{v}^C(t+\Delta t) &= \vec{v}^P(t+\Delta t)+c_1\vec{\Delta a}(t+\Delta t)\\
\vec{a}^C(t+\Delta t) &= \vec{a}^P(t+\Delta t)+c_2\vec{\Delta a}(t+\Delta t)\\
\vec{b}^C(t+\Delta t) &= \vec{b}^P(t+\Delta t)+c_3\vec{\Delta a}(t+\Delta t)
\end{aligned}$$

This method is very rigorous, for small timesteps, but obliges us to estimate the best coefficients C_i, leading to optimum stability and accuracy of the trajectories, to store $15N$ floating numbers for r^P, v^P, a^P, b^P and a^V. Because the final values for the vectors $\vec{r}(t+\Delta t)$, $\vec{v}(t+\Delta t)$, $\vec{a}(t+\Delta t)$ and $\vec{b}(t+\Delta t)$ are very sensitive to the accuracy of the predictor step, a purely mathematical operation, without using any physical information, the quality of this method decreases rapidly for larger timesteps, above 1.0 fs. The original Verlet algorithm uses the following equations:

$$\begin{aligned}
\vec{r}(t+\Delta t) &= \vec{r}(t)+\vec{v}(t)\Delta t+\frac{1}{2}\vec{a}(t)\Delta t^2\\
\vec{r}(t-\Delta t) &= \vec{r}(t)-\vec{v}(t)\Delta t+\frac{1}{2}\vec{a}(t)\Delta t^2
\end{aligned}$$

which lead, when added, to the equation for advancing the positions:

$$\vec{r}(t+\Delta t)=2\vec{r}(t)-\vec{r}(t-\Delta t)\Delta t+\vec{a}(t)\Delta t^2$$

and when subtracted, to the equation for calculating the velocity:

$$\vec{v}(t)=\frac{\vec{r}(t+\Delta t)-\vec{r}(t-\Delta t)}{2\Delta t}$$

After calculating the positions $\vec{r}(t+\Delta t)$, the new accelerations $\vec{a}(t+\Delta t)$ can be obtained directly from the potential V:

$$\vec{a}(t+\Delta t)=-\frac{1}{m}\vec{grad}V(\vec{r})(t+\Delta t)$$

This method only needs to store 9N floating numbers for $\vec{r}(t)$, $\vec{r}(t-\Delta t)$ and $\vec{a}(t)$, and is faster and more reliable for larger timesteps than the Gear predictor-corrector methods. Although the truncation error when calculating the new positions is only of order Δt^4, the truncation error associated with the determination of the velocities is already of order Δt^2. As in this algorithm the velocities are not used at all to determine the trajectory, this can lead to larger numerical errors in the kinetic energy. To avoid this problem, a slightly modified *Leapfrog Verlet method* was proposed, based in the equations:

$$\vec{v}(t+\frac{1}{2}\Delta t) = \frac{\vec{r}(t+\Delta t)-\vec{r}(t)}{\Delta t} \qquad \vec{a}(t) = \frac{\vec{v}(t+\frac{1}{2}\Delta t)-\vec{v}(t-\frac{1}{2}\Delta t)}{\Delta t}$$

usually written as:

$$\vec{r}(t+\Delta t) = \vec{r}+\vec{v}(t+\frac{1}{2}\Delta t)\Delta t \qquad \vec{v}(t+\frac{1}{2}\Delta t) = \vec{v}(t-\frac{1}{2})\Delta t) + \vec{a}\Delta t.$$

After calculating $\vec{r}(t+\Delta t)$, the new acceleration $\vec{a}(t+\Delta t)$ can be calculated from the potential:

$$\vec{a}(t+\Delta t) = -\frac{1}{m}\vec{grad}V(\vec{r})(t+\Delta t).$$

The velocities at time t can be calculated from the expression:

$$\vec{v}(t) = \frac{\vec{v}(t+\frac{1}{2}\Delta t)+\vec{v}(t-\frac{1}{2}\Delta t)}{2}.$$

This is the integration algorithm implemented in Discover 2.9.8 and Dl_Poly 1.1. Like the original Verlet method, it is simple, fast and needs also just to store 9N floating points, $\vec{r}(t)$, $\vec{v}(t-\frac{1}{2})$ and $\vec{a}(t)$. Nevertheless, this method obliges us to calculate the velocities twice, at time $(t+\frac{1}{2}\Delta t)$, to determine the new positions, and at time t, just to calculate the kinetic energy. A further modification of the original Verlet algorithm is the *Velocity Verlet method*, defined by the equations:

$$\vec{r}(t+\Delta t) = \vec{r}+\vec{v}\Delta t+\frac{1}{2}\vec{a}(t)\Delta t^2 \qquad \frac{\vec{v}(t+\Delta t)-\vec{r}(t)}{\Delta t} = \vec{a}(t+\frac{1}{2}\Delta t) = \frac{\vec{a}(t)+\vec{a}(t+\Delta t)}{2},$$

usually written as:

$$\vec{r}(t+\Delta t) = \vec{r}(t)+\vec{v}(t)\Delta t+\frac{1}{2}\vec{a}(t)\Delta t^2,$$
$$\vec{v}(t+\Delta t) = \vec{v}(t)+\frac{1}{2}[\vec{a}(t)+\vec{a}(t+\Delta t)]\Delta t.$$

In this version of the Verlet algorithm, in order to continue storing only 9N floating point numbers, after calculating all the new positions $\vec{r}(t+\Delta t)$, with the first equation, a new acceleration $\vec{a}(t+\Delta t)$ would have to be determined, for each atom, from the potential $V(\vec{r})(t+\Delta t)$ and a new velocity $\vec{v}(t+\Delta t)$ immediately calculated, using the second equation, before considering the next atom. To determine all the new accelerations at the same time, as is usually required in practise, without increasing the amount of memory required, it is necessary to use before the information contained in the arrays v(t) and a(t) to calculate a unnecessary velocity at mid-step $\vec{v}(t+\frac{1}{2}\Delta t)$ given by:

$$\vec{v}(t+\Delta t) = \vec{v}(t)+\vec{a}(t)\frac{1}{2}\Delta t+\frac{1}{2}\vec{a}(t+\Delta t)\Delta t = \vec{v}(t+\frac{1}{2}\Delta t)+\frac{1}{2}\vec{a}(t+\Delta t)\Delta t,$$

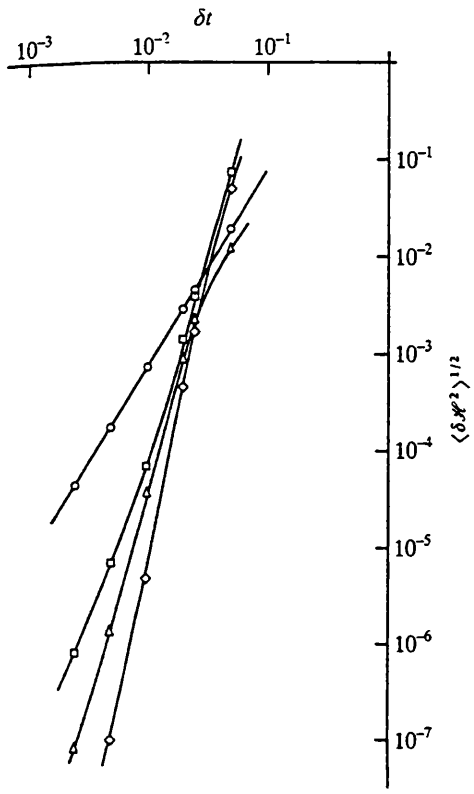


Figure 7.1: Energy conservation as a function of the timestep for a Velocity Verlet (circles), Gear fourth-order (squares), Gear fifth-order (triangles), and Gear sixth-order (diamonds) integration algorithms, using log-log scales. All runs started from the same initial conditions, and proceeded for the same total simulation time [11].

before calculating the new accelerations $\vec{a}(t + \Delta t)$ and calculating finally $\vec{v}(t + \Delta t)$. Like the Leapfrog Verlet algorithm, the Velocity Verlet algorithm also requires the calculation of two velocities per step, and although the velocities obtained using the second method might be slightly more rigorous, in practice both algorithms seem to present the same advantages and disadvantages. By default, Discover 96.0 uses a Velocity Verlet integration algorithm. Other widely used integration algorithms, like the ABM_4, also implemented in Discover 96.0, are explained elsewhere [199]. In Figure 7.1 the Velocity Verlet algorithm is compared with several different order Gear algorithms, regarding the energy conservation as a function of the timestep. The accuracy of common molecular dynamics algorithms is discussed by Macgowan et al. [152] and Rodger [203].

The quality of a molecular mechanics simulation is governed essentially by the quality of the potential V, which contains all the information describing the system. In the last twenty years, a enormous effort have been devoted to increasing the quality of these descriptions of the classical potential and many different equations, parameters and forcefields have been proposed and tested [241] (for implementation see Rittger [202]). The ab-initio forcefield cff91, used in Discover 2.9.8 and 96.0 simulations, developed by Molecular Simulations Inc. [5], is presented below. In Dl_poly 1.1 simulations, the cross-terms were ignored.

$$V = \sum K_2(r - r_0)^2 + K_3(r - r_0)^3 + K_4(r - r_0)^4 +$$

$$\sum K_2(\theta-\theta_0)^2 + K_3(\theta-\theta_0)^3 + K_4(\theta-\theta_0)^4 +$$
$$\sum V_1[1+cos(\phi-\phi_{01})] + V_2[1+cos(2\phi-\phi_{02})] + V_3[1+cos(3\phi-\phi_{03})] +$$
$$\sum K_\chi\chi^2 + \sum F_{rr'}(r-r_0)(r'-r'_0) + \sum F_{\theta\theta'}(\theta-\theta_0)(\theta'-\theta'_0) +$$
$$\sum F_{r\theta}(r-r_0)(\theta-\theta_0) + \sum(r-r_0)[V_1 cos\phi + V_2 cos2\phi + V_3 cos3\phi] +$$
$$\sum(r'-r'_0)[V_1 cos\phi + V_2 cos2\phi + V_3 cos3\phi] +$$
$$\sum(\theta-\theta_0)[V_1 cos\phi + V_2 cos2\phi + V_3 cos3\phi] +$$
$$+\frac{1}{4\pi\epsilon_0}\sum\sum_{i>j}\frac{q_iq_j}{r_{ij}} + \sum\sum_{i>j}[\frac{A_{ij}}{r_{ij}^6} - \frac{B_{ij}}{r_{ij}^9}].$$

The calculation of these last two terms, representing the Coulombic and Van der Waals interactions, are the most time-consuming, because they involve the determination of $\frac{N^2}{2}$ contributions. When the number of atoms N involved in the simulation is too big to consider all interactions, a cutoff has to be introduced for a given distance. Although this is an important approximation, for most of the systems, for cutoffs larger than 9-12 Å, the resulting truncation errors in the total Van der Waals contribution and even in the total Coulombic contribution are small enough not to introduce important changes in the results.

Instead of just cutting the nonbonding potentials for distances larger than the cutoff, a switching function is sometimes used to decrease the potential to zero in a more smooth way, guaranteeing the existence of the first and second derivatives of the potential in the transition region. Although the simulations with Discover 2.98 presented here used this method, apparently a switching function tends to create artifacts in the forces, and as it decreases, in practise, the cutoff used, it was not applied in Dl_poly 1.1.

To decrease the time necessary to calculate the nonbonding forces, the most time consuming task in a MD or MC code, several techniques have been proposed, namely the *Verlet Neighbour List* [57], the *Cell-Neighbour Table* [170] and *Multiple Timestep* [31, 177, 215] methods. In the former, instead of calculating the distance between all the atoms for each timestep, a obviously very time consuming task, a list of neighbours closer than a given distance, necessarily larger than the cutoff, is created for each atom, and is used in the subsequent steps to decide which atoms are under the cutoff distance or not. This list is updated, after about 20 timesteps, or automatically, when the sum of the distances moved by two atoms is larger than the buffer width (defined as the difference between the radius used to create the list and the cutoff), to guarantee that the list always contains all the atoms closer than the cutoff distance. The Cell-neighbour Table methods apply the same principle, dividing the system in small cells and checking to which cell the atoms belong. This method avoids the time-consuming step of creating the VN list and is preferred when the cutoff is much smaller than the cell box.

In the Multiple Timesteps methods, the usual timestep is used just for very small distances, typically closer than 6-8 Å, and a larger timestep, usually 5 to 20 times bigger, is used to calculate the slowly varying but enormously time consuming interactions between this first cutoff and the second, usual cutoff. The equations of motion are integrated exactly in the usual way; the very short interactions, like bond, angle and torsion potentials, responsible for the description, for example, of the high frequency vibrational modes, are determined for every short timestep. In compensation, the nonbonding interactions for distances between the two cutoffs are recalculated only for each long timestep. This method can be combined with a Verlet Neighbour List, to speed up the simulation even more. Unfortunately, the Multiple Time Step methods tend to

create additional fluctuations in the energy, as this changes suddenly every time the slowly varying second region is updated. To compensate this effect, a smooth function could be added, to introduce progressively this change during each short time step, but that would imply an increase in CPU time and also in memory (to store the necessary data). All these techniques are implemented in Dl_poly 1.1 and Discover 96.0, and the VNL is in Discover 2.9.8 also.

Molecular Dynamics, like other techniques, Monte Carlo and Energy Minimisation, can be used to simulate atom clusters in vacuum and condensed matter systems in bulk. In the former case, used for example to study large biochemical systems, like proteins, all the interactions between the atoms present are usually considered. In the second case, as it is not possible to simulate the number of atoms necessary to reasonably describe a bulk environment, the concept of periodic boundary conditions is used, and it is assumed that the system can be contained in a central crystalline cell, surrounded by other identical cells, generated by translational symmetry of the former. A infinite number of cells can, thus, be created in this way, where each atom is a exact copy of one in the primary cell, and although the trajectories of these ghost atoms are not calculated, their interactions with the atoms in the primary cell do contribute to the calculation of the trajectories of these, allowing us to simulate the real bulk conditions in the central cell. When an atom reaches the border of the primary cell, it enters in its neighbour cell and consequently a ghost atom enters in the corresponding position in the real cell.

The periodicity introduced in this way, to simulate bulk systems, is usually welcome in crystalline solid state systems, where several layers of cells around the primary cell are usually considered, using the designated extended convention, but is artificial in amorphous systems like glasses or liquids, where that order does not exist, and consequently, when simulating these systems, the designated minimum image convention is usually used, following which, every atom in the central cell interacts only with the nearest representation, real or copy, of each of the other atoms present in the same cell.

To fulfill this convention, used in all MD simulations carried out in this work, the cutoff has to be smaller than half of the smallest dimension of the cell size, to guarantee that each atomic contribution is counted only once. In compensation, this restriction means also that an atom located, for example, in the centre of the primary cell, does not interact at all with the atoms situated very close to the vertices of the cell. Although the number of interactions not considered in this way can be reduced using cells with a more spherical shape, like a rhombic dodecahedron or a truncated octahedron (both implemented in Dl_Poly1.1), this should not be significant when the number of atoms is largeused. During this work, a cubic cell was always used to simulate bulk liquids, due to its simplicity. The effects of periodic boundary conditions are discussed by Pratt [198].

When molecular systems are being simulated, it is necessary to define a criterion to decide which molecule images are nearest and whether or not a given molecule is located under the cutoff distance. This can be done adopting a group based criterion, as in Discover 2.98, or an atom based criterion, as in Dl-Poly1.1 (in Discover 96.0 both criteria are allowed). In the group based criteria, the position of a switching atom, representing each molecule, is used to determine the distance between two molecules or whether or not a given molecule is under the cutoff distance.

Using this criterion, at a given instant all the interactions with the atoms in a molecule are considered, because the switching atom is slightly under the cutoff distance and the instant after, if the switching atom moves behind the cutoff limit, all those interactions are suddenly completely ignored. In the same way, at a given instant the molecule A is closer to molecule

B than C and all interactions between A and B are considered and all interactions between B and C are ignored. The instant after, one of the three molecules moves slightly and everything changes: all the interactions between A and B are ignored and all interactions between A and C are considered. Modifications like these occur in just one timestep, and consequently important fluctuations in the potential and consequently, total and kinetic energies can be expected when using this criterion for large molecules.

The atom based criterion is conceptually simpler and avoids this switching problems but in compensation is slower, as the comparisons are no longer made between molecules but between all the atoms present in the system. Furthermore, this method tends to create artificial charge layers over the cutoff surface, as the sum of the atomic charges in the cutoff region is, in general, no longer zero.

Molecular Dynamics is essentially a deterministic technique, as usually only the initial velocities are random. In Monte Carlo, however, a truly random generation of new configurations is vital to sample effectively the phase space. High quality and efficient random number generators have been proposed recently by Ishikawa [106], Toral [229] and Lüscher [151].

7.2 Long range interactions

One of the most difficult problems in molecular simulation is the evaluation of the long range forces, particularly the Coulombic interactions, in ionic crystals and polar liquids, which cannot be described properly simply by using a cutoff technique, without increasing, in a unacceptable way, the amount of cpu time needed. The Coulombic force between two atoms separated by 9 Å, the cutoff used in the cutoff-based simulations done in this work, is only 20 times lower than if the two atoms were 2 Å apart, and this decrease is partially compensated by the increasing number of atoms in the shell.

For distances large enough these interactions may compensate each other, as the overall system is neutral, but the intermediate range interactions, which are not accounted when using a cutoff procedure are expected to play an important role in the behaviour of condensed matter molecular systems. Several methods have been proposed to deal with long-range forces, like the reaction field method [237], due to L. Onsager, the particle-particle and particle-mesh algorithm, due to Eastwood, Hockney and Lawrence and a technique for studying dipolar systems, due to Ladd [11], but the most widely used (see for example Adams [7] is the Ewald summation method, due to its simplicity and consequent facility of implementation. A Ewald sum was used in all Dl_poly 1.1 [216] simulations of liquids presented in this work.

Basically, the method assumes that the system contained in the primary unit cell is repeated in all the other cells in space. The total Coulombic energy can then be written as:

$$\mathcal{U}_C = \frac{1}{8\pi\epsilon_0} \sum_{nn'l}{}' \frac{q_n q_{n'}}{r_{nn'l}},$$

with $r_{nn'l} = |\vec{r}_n - \vec{r}_{n'} + \vec{r}_l|$ and $\vec{r}_l = n_1\vec{a}_1 + n_2\vec{a}_2 + n_3\vec{a}_3$. The terms $n = n'$ for $\vec{r}_l = 0$ are evidently excluded from the sum, represented thus as $\sum'$. Writing $\frac{1}{r}$ as a Gaussian integral from 0 to ∞:

$$\frac{1}{r} = \frac{2}{\sqrt{\pi}} \int_0^\infty \exp(-r^2t^2)dt.$$

This can be evaluated separately between 0 and η and between η and ∞:

$$\frac{2}{\sqrt{\pi}}\int_0^{\infty}\exp(-r^2t^2)dt = \frac{2}{\sqrt{\pi}}\int_0^{\eta}\exp(-r^2t^2)dt + \frac{2}{\sqrt{\pi}}\int_{\eta}^{\infty}\exp(-r^2t^2)dt.$$

The second integral can be written as a complementary error function, which tends rapidly to zero:

$$\frac{2}{\sqrt{\pi}}\int_{\eta}^{\infty}\exp(-r^2t^2)dt = \frac{1}{r}erfc(\eta r)$$

In the first integral, $\exp(-r^2t^2)$ can be Fourier transformed:

$$\exp(-r^2t^2) = (\frac{1}{2t\sqrt{\pi}})^3\int_{-\infty}^{\infty}d\vec{K}^3\exp(-K^2/4t^2)\exp(-i\vec{K}\cdot\vec{r}).$$

Integrating in t and replacing the integration in the reciprocal space by a summation over $\vec{K}$ vectores, the first integral becomes equal to:

$$\frac{1}{2\pi^2}\int_{-\infty}^{\infty}d\vec{K}^3\frac{\exp(-K^2/4\eta^2)}{K^2}\exp(-i\vec{K}\cdot\vec{r}) = \frac{4\pi}{NV_c}\sum_{\vec{K}}\frac{\exp(-K^2/4\eta^2)}{K^2}\exp(-i\vec{K}\cdot\vec{r}),$$

where N is the total number of cells with volume V_c. The Coulombic energy can now be expressed as:

$$\begin{aligned} U_C &= \frac{1}{2\epsilon_0 NV_c}\sum_{\vec{K}}\frac{\exp(-K^2/4\eta^2)}{K^2}\sum_{nn'}{}'q_nq_{n'}\exp(-i\vec{K}\cdot(\vec{r}_n-\vec{r}_{n'}))\sum_l'\exp(-i\vec{K}\cdot\vec{r}_l). \\ &+\frac{1}{8\pi\epsilon_0}\sum_{nn'l}{}'q_nq_{n'}\frac{erfc(\eta r_{nn'l})}{r_{nn'l}} \end{aligned}$$

When $\vec{K}$ is a reciprocal lattice vector, represented by $\vec{G}$, the sum $\sum_l'\exp(-i\vec{K}\cdot\vec{r}_l)$, over a complete set of lattice sites is N, if not the sum is zero [53, 108]. To explore this result, it is necessary to complete the sum, adding the missing auto-interaction terms for $l = 0$ and then subtracting them explicitly:

$$\lim_{r\to\infty}\frac{2}{\sqrt{\pi}}\int_0^{\eta}\exp(-r^2t^2)dt = \frac{2}{\sqrt{\pi}}$$

The Coulombic energy is finally given by:

$$\begin{aligned} U_C &= \frac{1}{2\epsilon_0 V_c}\sum_{\vec{G}}{}'\frac{\exp(-G^2/4\eta^2)}{G^2}\sum_{nn'}q_nq_{n'}\exp(-i\vec{G}\cdot(\vec{r}_n-\vec{r}_{n'}) \\ &+\frac{1}{8\pi\epsilon_0}\sum_{nn'l}{}'q_nq_{n'}\frac{erfc(\eta r_{nn'l})}{r_{nn'l}} - \frac{\eta}{4\pi^{3/2}\epsilon_0}\sum_{nn'}q_nq_{n'} \end{aligned}$$

In the sum over the $\vec{G}$ vectors, the terms for $G = 0$ are actually divergent. However, because $\sum_{nn'}q_nq_{n'} = 0$ those terms will cancel each other and they can be omited, denoting this explicitly by writing $\sum'$ [53, 108] (see also [5]).

The slowly convergent Madelung sum of the electrostatic interactions was thus replaced by two rapidly convergent sums, where cutoffs can be applied: one in the real space, the other in

the reciprocal space, plus a constant term. Usually the real sum is calculated using the same cutoff chosen for the Van der Waals and bonding interactions. The reciprocal sum, the most time consuming, due to the sum in $\vec{G}$ and n, n', can usually be calculated considering less than ten vectors in each direction. Theoretical and experimental studies about the optimum value for the parameter η or $\alpha = \eta/L$ (L = cell length) can be found, respectively in [53, 108] and [138]. The extension of the Ewald method for systems with dipole and quadrupole charge distributions is discussed by Ziman [254] and Kittel [129].

7.3 Pressure and temperature

The total energy U can be given as the average of an instantaneous energy $\mathcal{U}$:

$$U = <\mathcal{U}> = <\mathcal{V}> + <\mathcal{K}>$$

where the instantaneous kinetic $\mathcal{K}$ and potential $\mathcal{V}$ energies are defined in the usual way, for a system containing N atoms:

$$\mathcal{U} = \sum_{i}^{N} |\vec{p}_i|^2/2m_i + \mathcal{V}(\vec{r}_1 ... \vec{r}_N)$$

The temperature and pressure may be calculated using the equipartition equations:

$$< p_i \delta\mathcal{U}/\delta p_i >= k_B T \qquad < q_i \delta\mathcal{U}/\delta q_i >= k_B T$$

obtained from the generalised equipartition theorem[11]:

$$< \chi_i \delta\mathcal{H}/\delta\chi_j >= \delta_{ij} k_B T$$

Applying the first equipartition equation to the system above defined and summing for all the $3N$ terms, the average temperature of the system is obtained as a function of the velocity components for all atoms:

$$< \sum_{i}^{N} |\vec{p}_i|^2/m_i >= 2 <\mathcal{K}>= 3Nk_B T$$

An instantaneous temperature $\mathcal{T}$ can thus be defined as:

$$\mathcal{T} = \frac{2\mathcal{K}}{3Nk_B} = \frac{1}{3Nk_B} \sum_{i}^{N} |\vec{p}_i|^2/m_i$$

Applying the second equipartition function to the system and summing for all 3N terms, the temperature is related with the total forces $\vec{f}_i^{tot} = \vec{f}_{int}^{i} + \vec{f}_{ext}^{i}$ acting on each atom:

$$- < \sum_{i=1}^{N} \vec{r}_i \vec{f}_i^{tot} >= 3Nk_B T$$

If $V(\vec{r}_1 ... \vec{r}_N) = 0$ the internal forces $\vec{f}_i^{int}$ are zero and the equation $PV = Nk_B T$ is valid, so the external forces $\vec{f}_i^{ext}$ become equal to:

$$- < \sum_{i=1}^{N} \vec{r}_i \vec{f}_i^{ext} >= 3PV$$

Isolating the calculation of the interactions between all the atoms in a single term, the internal virial $\mathcal{W}$, defined as:

$$\mathcal{W} = \frac{1}{3}\sum_{1=1}^{N} \vec{r}_i \cdot \vec{f}_i^{int} = -\frac{1}{3}\sum_{1=1}^{N} \vec{r}_i \cdot \nabla\vec{\mathcal{V}}(\vec{r}_i) = -\frac{1}{3}\sum_{1=1}^{N} w_i$$

the average pressure of the system is obtained as a function of the average temperature, the volume cell and the internal virial:

$$PV = Nk_B T + < \mathcal{W} >$$

and the instantaneous pressure $\mathcal{P}$ is defined as:

$$\mathcal{P}V = Nk_B\mathcal{T} + \mathcal{W}$$

7.4 NVT and NPT ensembles

Peharps the simplest algorithm proposed so far to simulate constant pressure and temperature conditions, the Berendson method, described in detail in [34], considers two scaling factors λ and μ, defined according to the equations:

$$\lambda = 1 + \frac{\Delta t}{2\tau_T}(\frac{\mathcal{T}}{T_{ext}} - 1) \quad \text{and } \mu = [1 + \frac{\Delta t\beta}{\tau_P}(\mathcal{P} - P_{ext})]^{1/3}$$

In these expressions $\mathcal{T}$ and T_{ext} are the instantaneous and external temperature, $\mathcal{P}$ and P_{ext} are the instantaneous and external pressure, Δt is the timestep, β is the compressibility of the system and τ_T, τ_P are arbitrarily defined relaxation times, in practise used to control the strength of the coupling with the temperature and pressure baths. As the compressibility is coupled with the pressure relaxation time τ_P, no accurate value, defined for each particular system, is necessary to use. In both Discover 2.9.8 and Dl_poly 1.1, β was made equal to $5.0 \times 10^{-5} bar^{-1}$. The parameters λ and μ are calculated each timestep and then used to scale the velocities v_{iK}, the coordinates q_{iK} and the cell parameters a_K according to the equations:

$$v_{ik} = \lambda v_{ik} \quad q_{ik} = \mu q_{ik} \quad a_K = \mu a_k \quad i = 1..N \quad k = x, y, z$$

In the Berendsen approach, the canonical ensemble is described considering only the scaling factor λ.

The Berendsen scaling methods [34] are easy to implement, produce consistent results, even using simple integration methods, like the Verlet algorithms, but do not simulate properly the fluctuations existent in the NVT and NPT ensembles. These fluctuations may be simulated using the extended Hamiltonian methods due to Nose [181], for constant temperature, Parrinello and Rahman [188, 182], for constant pressure conditions. The Nose method can be described defining two different sets of variables, the real variables $\vec{q}_i'$, $\vec{p}_i'$, t' and the virtual variables $\vec{q}_i$, $\vec{p}_i$, t related through an additional degree of freedom s:

$$\vec{q}_i{}' = \vec{q}_i \quad \vec{p}_i{}' = \vec{p}_i/s \quad t' = \int^t \frac{dt}{s}$$

Consequently:

$$\frac{\delta\vec{q}_i{}'}{\delta t'} = s\frac{\delta\vec{q}_i}{\delta t}$$

These transformations can be interpreted as corresponding to a scaling of the time by $dt' = dt/s$. For a system with N particles, with masses m_i and potential energy $V(\vec{q}_i')$, the Hamiltonian of the extended system, including the variable s, is postulated as:

$$H = \sum_{i=1}^{N} \vec{p}_i^2/2m_i s^2 + V(\vec{q}) + p_s^2/2Q + gk_BT \ln s$$

where Q behaves as a mass for the motion of s and p_s represents the conjugate momentum of s, $p_s = Q\delta s/\delta t$. Assuming that the Hamiltonian formalism can be applied with virtual variables, the equations of motion can be written as:

$$\begin{aligned} \frac{\delta \vec{q}_i}{\delta t} &= \frac{\delta H}{\delta \vec{p}_i} = \vec{p}_i/m_i s^2; \qquad \frac{\delta \vec{p}_i}{\delta t} = -\frac{\delta H}{\delta \vec{q}_i} = -\frac{\delta V}{\delta \vec{q}_i} \\ \frac{\delta s}{\delta t} &= \frac{\delta H}{\delta p_s} = p_s/Q; \qquad \frac{\delta p_s}{\delta t} = -\frac{\delta H}{\delta s} = (\sum_{i=1}^{N} \vec{p}_i^2/2m_i s^2 - gk_BT)/s \end{aligned}$$

The Hamiltonian H, the momentum $\sum_{i=1}^{N} \vec{p}_i$ and the angular momentum $\sum_{i=1}^{N} \vec{q}_i \times \vec{p}_i$ are conserved, because:

$$\frac{\delta H}{\delta t} = \sum_{i=1}^{N} (\frac{\delta H}{\delta \vec{p}_i}\frac{\delta \vec{p}_i}{dt} + \frac{\delta H}{\delta \vec{q}_i}\frac{\delta \vec{q}_i}{dt}) + \frac{\delta H}{\delta p_s}\frac{\delta p_s}{dt} + \frac{\delta H}{\delta s}\frac{\delta s}{dt}) = 0$$

and the potential V satisfies the equations:

$$\begin{aligned} \frac{\delta}{\delta t}\sum_{i=1}^{N} \vec{p}_i &= -\sum_{i=1}^{N} \frac{\delta V}{\delta \vec{q}_i} = 0 \\ \frac{\delta}{\delta t}\sum_{i=1}^{N} \vec{q}_i \times \vec{p}_i &= \sum_{i=1}^{N} \vec{q}_i \times \frac{\delta \vec{p}_i}{\delta t} + \frac{\delta \vec{q}_i}{\delta t} \times \vec{p}_i = \sum_{i=1}^{N} -\vec{q}_i \times \frac{\delta V}{\delta \vec{q}_i} = 0 \end{aligned}$$

As the Hamiltonian is conserved, the extended system is in a microcanonical ensemble and the corresponding partition function can be given by:

$$Q = \frac{1}{N!h^{3N}} \int d\vec{p} \int d\vec{q} \int dp_s \int ds\ \delta(H_o(\vec{p}/s, \vec{q}) + p_s^2/2Q + gk_BT \ln s - U)$$

where $H_o(\vec{p}/s, \vec{q})$ represents the Hamiltonian of the physical system, $\sum_{i=1}^{N} \vec{p}_i^2/2m_i s^2 + V(\vec{q})$, and shortened forms $d\vec{p} = d\vec{p}_1 ... d\vec{p}_N$ and $d\vec{q} = d\vec{q}_1 ... d\vec{q}_N$ are used. The partition function can be rewritten in the real variable formulation as:

$$\begin{aligned} Q &= \frac{1}{N!h^{3N} g k_B T} \exp[(\frac{3N+1}{g})U/k_BT] \int dp_s \exp[-(\frac{3N+1}{g}p_s^2/2Qk_BT]) \times \\ &\int d\vec{p}' \int d\vec{q}' \exp[-(\frac{3N+1}{g})H_o(\vec{p}', \vec{q}')/kT] \end{aligned}$$

If g is set equal to $3N+1$, the partition function comes equivalent to that of the physical system in the canonical ensemble, multiplied by a constant. Consequently, to simulate a microcanonical ensemble in the Nose extended system corresponds to simulate a canonical ensemble in the physical system. Under the quasiergodic hypothesis, which relates the time average along the trajectory to the ensemble average, the average of any static quantity A, along the trajectory

determined by the equations of motion above defined, is therefore exactly that in the canonical ensemble [181]:

$$\lim_{t_0\to\infty}\frac{1}{t_0}\int_0^{t_0} A(\vec{p}/s,\vec{q})dt = <A(\vec{p}',\vec{q}')>_{NVT}$$

The NPT algorithm due to Parrinello and Rahman [188] generalizes the constant pressure technique proposed by Andersen [13](see also Heyes [99]), to any external applied stress and to any shape and size variations of the cell. Considering a matrix $H = |\vec{a}_1\vec{a}_2\vec{a}_3|$ formed by the cell vectors $\vec{a}_i$, the metric tensor $G = H^T H$ and the matrix $\sigma = V_c(H^T)^{-1}$ can be defined, where $V_c = \vec{a}_1 \cdot \vec{a}_2 \times \vec{a}_3$. The position $\vec{r}_i$ of a particle i is given by $\vec{r}_i = \xi_i\vec{a}_1 + \eta_i\vec{a}_2 + \zeta_i\vec{a}_3 = H\vec{s}_i$ where $0 \leq \xi_i, \chi_i, \eta_i \leq 1$. The images of $\vec{s}_i$ are at $\vec{s}_i + n_1\vec{a}_1 + n_2\vec{a}_2 + n_3\vec{a}_3$. The time evolution of the $3N+9$ particle and cell variables, when only hydrostatic pressure is applied, is then determined by the Lagrangian [188]:

$$\mathcal{L} = \frac{1}{2}\sum_{i=1}^{N} m_i\dot{\vec{s}}_i^T G\dot{\vec{s}}_i - \sum_{i=1}^{N}\sum_{j>i}^{N} V(\vec{r}_{ij}) + \frac{1}{2}WTr\dot{H}^T\dot{H} - P_{ext}V_c$$

where P_{ext} is the external pressure and W is a mass parameter that determines the pressure relaxation time. The extended hamiltonian is given by:

$$H = \sum_i \frac{1}{2}m_i\vec{v}_i^2 + \sum_{i=1}^{N}\sum_{j>i} V(\vec{r}_{ij}) + \frac{1}{2}WTr\dot{H}^T\dot{H} + P_{ext}\sigma$$

and the equations of motion become equal to:

$$\ddot{\vec{s}}_i = \sum_{j\neq i} m_i^{-1}(V^T/r_{ij})(\vec{s}_i - \vec{s}_j) - G^{-1}\dot{G}\dot{\vec{s}}_i \quad W\ddot{H} = (\pi - P_{ext})\sigma \quad i = 1...N$$

where $V_c\pi = \sum_i m_i\vec{v}_i\vec{v}_i - \sum_i\sum_{j>i}(V^T/r_{ij})\vec{r}_{ij}\vec{r}_{ij}$. When a general stress is applied, the second motion equation has to be replaced by:

$$W\ddot{H} = (\pi - P_{ext})\sigma - H\Sigma$$

where $\Sigma = H_o^{-1}(S - P_{ext})(H_o^T)^{-1}V_c = H_o^{-1}(S-p)\sigma_o$ and H_o represents a reference state of the system (typically $< H >$) and S is the external stress matrix.

This complex set of equations makes this method difficult to implement and time consuming. The algorithm introduced by Hoover and later extended by Melchionna et al. [167] is simpler and can reproduce the NVT and NPT ensembles, allowing to use multiple thermostats, constrained dynamics and a shape-varying cell, like in Parrinello's method. In the NVT ensemble, the equations of motion are given by:

$$\dot{\vec{r}}_i = \frac{\vec{p}_i}{m_i} \quad \dot{\vec{p}}_i = \vec{F}_i - \zeta\vec{p}_i \quad \dot{\zeta} = v_T^2\left(\frac{\mathcal{T}}{T_{ext}} - 1\right)$$

where ζ acts as a frictional coefficient to balance the deviation between the instantaneous and external temperature. In this ensemble, the Helmholtz energy is conserved [167]:

$$A = \sum_i \frac{p_i^2}{2m_i} + U(\vec{r}) + \frac{dNk_BT_{ext}\zeta^2}{2v_T^2} + dNk_BT_{ext}\int^{t'} dt'\zeta(t')$$

The isothermal-isobaric trajectory is generated by the equations:

$$\dot{\vec{r}}_i = \frac{\vec{p}_i}{m_i} + \eta(\vec{r}_i - \vec{R}_0) \quad \dot{\vec{p}}_i = \vec{F}_i - (\eta + \zeta)\vec{p}_i \quad \dot{\zeta} = v_T^2(\frac{\mathcal{T}}{T_{ext}} - 1)$$
$$\dot{\eta} = \frac{v_P^2}{Nk_BT_{ext}} V(\mathcal{P} - P_{ext})\dot{V} = dV\eta$$

where $\vec{R}_0$ is the centre-of-mass of the system, d is the system dimensionality and η acts as a strain-rate factor to balance the deviations of instantaneous and external pressure. The tightness of the temperature and pressure bath is controlled by v_T and v_T parameters. Defining the enthalpy, with contributions for the thermostat and barostat, as:

$$H = K + U + P_{ext}V + \frac{dNk_BT_{ext}}{2}(\frac{\zeta^2}{v_T^2} + \frac{\eta^2}{v_P^2}),$$

it can be shown that the equilibrium distribution function is proportional to $\exp(-\beta H)$, so the NPT ensemble is correctly described. As the Helmholtz energy in the canonical ensemble, the Gibbs energy is conserved in the NPT ensemble: $G = A + P_{ext}V$ [167].

Clearly, the Hoover extended method is a major improvement in the simulation of the NPT ensemble. However, the development of accurate descriptions of the isothermal-isobaric trajectories remain a open field of research, where important contributions might be expected in the future.

7.5 Properties

The transport coefficients measure the time response of a system to a perturbation. Introducing this perturbation in the equations of motion and comparing the equation for the response with the corresponding macroscopic transport equation, the transport coefficient may be identified. Usually it is a infinite time integral of an equilibrium time correlation function (see Gordon's review [86]). In particular, the diffusion coefficient D is given by [11]:

$$D = \frac{1}{3}\int_0^\infty < \vec{v}_i(t) \cdot \vec{v}_i(0) >$$

where $\vec{v}_i(t)$ represents the velocity of the molecule or atom i at an instant t. This time correlation integral can also be given by a corresponding Einstein relation, valid at long times:

$$2tD = \frac{1}{3} < |\vec{r}_i(t) - \vec{r}_i(0)|^2 >$$

where $\vec{r}_i(t)$ gives the position of the molecule or atom i at the instant t. This equation is used in this work to calculate the total D_t and partial D_x, D_y, D_z self-diffusion coefficients.

The pair distribution function, defined as the probability of finding two atoms a distance r apart, relative to the probability expected for a completely random distribution at the same density, can be defined as [11]:

$$g(r) = \rho^{-2} < \sum_i \sum_{j \neq i} \delta(\vec{r}j)\delta(\vec{r}_j - \vec{r}) >= \frac{V}{N^2} < \sum_i \sum_{j \neq i} \delta(\vec{r} - \vec{r}_{ij}) >,$$

where $g(r)$ provides important insight into the structure of liquids and glasses. In particular, the number of atoms N at a distance smaller than r_N can be obtained from:

$$N = 4\pi\rho \int_0^{r_N} r^2 g(r) dr;$$

$g(r)$ can also be used to express the ensemble average of any pair function:

$$< A >=< \sum_i \sum_{j>i} a(r_{ij}) >= \frac{1}{2} N\rho \int_0^{\infty} a(r) g(r) 4\pi r^2 dr$$

In particular, the energy and pressure in a system with only pair interactions may be written as:

$$\begin{aligned} U &= \frac{3}{2} N k_B T + 2\pi N\rho \int_0^{\infty} r^2 v(r) g(r) dr, \\ PV &= N k_B T - \frac{2}{3} \pi N\rho \int_0^{\infty} r^2 w(r) g(r) dr. \end{aligned}$$

In practice, a direct evaluation of these quantities is more accurate and most systems are not described just by pair addictive interactions. However, this formalism can be used to estimate the long-range interactions neglected by the cutoff criteria, which in general are pair addictive. Assuming that $g(r) \approx 1$ at the cutoff distance r_c, which is reasonably true for systems not strongly correlated, the corrected energy and pressure become equal to:

$$\begin{aligned} U &= U_c + 2\pi N\rho \int_{r_c}^{\infty} r^2 v(r) dr, \\ PV &= PV_c - \frac{2}{3} \pi N\rho \int_{r_c}^{\infty} r^2 w(r) dr. \end{aligned}$$

This approach is applied in Dl_poly1.1 to estimate the long-range corrections for the Van der Waals forces.

The specific heat may be calculated directly from the definition, in the NVT ensemble: $c_V = (\frac{\delta U}{\delta T})_V$ and in the NPT ensemble: $c_P = (\frac{\delta H}{\delta T})_P$. c_V can also be calculated, in the NVT ensemble, from the average energy fluctuations $< \delta\mathcal{U}^2 >=< (U - \mathcal{U})^2 >$. Writing the partition function $Q_N(V,T)$ and the Helmholtz free energy A_{NVT} in this ensemble as:

$$Q_N(V,T) = \int \frac{dp^{3N} dq^{3N}}{N! h^{3N}} e^{-\beta \mathcal{U}(p,q)} \qquad A(V,T) = -\frac{1}{\beta} ln Q_N(V,T)$$

both equations can be combined to give the identity:

$$\int \frac{dp^{3N} dq^{3N}}{N! h^{3N}} e^{\beta[A(V,T) - \mathcal{U}(p,q)]} = 1$$

and differentiating with respect to β, a second identity can be obtained:

$$A(V,T) - U(V,T) + \beta(\frac{\delta A}{\delta T})_V = 0$$

Defining the average energy as:

$$U =< \mathcal{U} >= \frac{\int dp^{3N} dq^{3N} \mathcal{U}(p,q) e^{-\beta \mathcal{U}(p,q)}}{\int dp^{3N} dq^{3N} e^{-\beta \mathcal{U}(p,q)}}$$

and using the previous identities, the relation between C_V and $< \delta\mathcal{U}^2 >$ can finally be obtained:

$$< \delta\mathcal{U}^2 >_{NVT} = k_B T^2 C_V$$

A equivalent relation is valid in the NPT ensemble between C_P and the average enthalpy fluctuations $< \delta\mathcal{H}^2 >$ [11]:

$$< \delta\mathcal{H}^2 >_{NPT} = k_B T^2 C_P$$

The most relevant Molecular Mechanics studies carried out during this work are presented in the fourth part: *Molecular Mechanics Studies.*

Chapter 8

Atomistic Modelling bibliography

8.1 General references

Because atomistic modelling is such a new field of investigation, with intensive theoretical research under way, most of the information is dispersed over an increasing number of articles. There are books available on Hartree-Fock and Density Functional theory, but usually they are more concerned with applications and are not oriented to code development.

The book *Computer Simulation of Liquids*, published in 1987 by M. P. Allen and D. J. Tildesley [11] and reprinted several times since then, is still probably the best global reference for Molecular Dynamics and Monte Carlo simulations, with a good list of references, that covers the most important work done until 1985. Other useful compilations are:

- *Computer Modelling of Fluids Polymers and Solids*, Ed. Catlow et al., Kluwer Academic Publishers, (1990)

- *Molecular Liquids, Dynamics and Interaction*, Ed. A. J. Barnes et al., C135 NATO series, (1984)

- *Computer Simulation in Materials Science*, Ed. M. Meyer et al., Kluwer Academic Publishers, (1991)

- *Computer Simulation of Solids, Lecture Notes in Physics*, Ed. Catlow et al.

The book *Density-Functional Theory of Atoms and Molecules*, from 1989, written by R. G. Parr and W. Yang [187], is perhaps the most accessible general reference specifically on Density Functional theory, with commented bibliography. A recent book is *Modern Density Functional Theory: A Tool for Chemistry*, edited by P. Politzer and J. M. Seminario, Elsevier (1994). Other important compilations are:

- *Proceedings of the first NATO Summer School on Density Functional Methods in Physics*, Alcabideche, Portugal, 1983, Ed. R. M. Dreizler and J. de Providencia, Plenum Press (1985)

- *Proceedings of the second NATO Summer School on Density Functional Theory*, Il Ciocco, Italy, 1993, Ed. E. K. Gross and R. M. Dreizler, B337 Nato series, Plenum Press (1995)

The book by J. A. Pople, *Ab-initio Molecular Orbital Theory* [195], published in 1986, is a good general reference for Hartree-Fock theory, with extensive bibliographic coverage. An important collection *Ab Initio Methods in Quantum Chemistry, vols. I and II*, was edited

by K. P. Lawley in 1987, in the series Advances in Chemical Physics [144, 145], with good reviews in basis sets, transition state determination and other subjects. A relatively recent book is *Theoretical Geochemistry: Applications of Quantum Mechanics in the Earth and Mineral Sciences* published in 1992 by J. A. Tossell and D. J. Vaugham [230]. The book *Numerical Recipes in C: the Art of Scientific Computing*, written by W. H. Press et al. in 1988 and reedited in 1992 [199] is already a classic of numerical analysis.

8.2 Current references

Most of the references given above do not cover the extensive theoretical and applied work done during the last ten years. The most relevant theoretical information is usually reported in *Computer Physics Communications*, *Journal of Computational Chemistry*, *Journal of Molecular Physics*, *Journal of Chemical Physics*, *Physical Review Letters* and *Physical Review B*. Applied work can usually be found in *Journal of Physical Chemistry*, *Journal of American Chemical Society*, *Chemical Physics* and *Molecular Simulation*.

Part III

Ab-Initio Studies

Chapter 9

Small clusters

This chapter has essentially two purposes: the first is to study the structure, charge distribution and reaction energies of the small clusters that are particularly relevant in sol-gel processes, like water, methanol, ethanol and the alkoxides most commonly used, $Si(OCH_3)_4$ (TMOS) and $Si(OCH_2CH_3)_4$ (TEOS), the smallest silicate clusters, $Si(OH)_4$ and $Si_2O(OH)_6$, and aluminosilicate clusters, $Al(OH)_4^-$, $Al_2(OH)_6^{2-}$ and $SiAlO(OH)_6^-$. The second purpose is to profit from the extensive data available and small CPU time required for these clusters to compare the accuracy provided by the most common ab-initio methods, Hartree-Fock theory (HF-MP2) and Density Functional theory, for local and non-local functionals, (DF-BHL and DF-BLYP), with different basis sets (6-31G**, 6-311G** and DN, DND, DNP, TNP), SCF and Gradient Tolerances.

9.1 Introduction

Ab initio tests on small clusters are important to estimate the errors in calculations of larger clusters, where extensive accuracy checks cannot be afforded. A comparison between HF and DF is presented by Andzelm et al. [15]. For a range of typical organic and small inorganic molecules, it is claimed that DFT calculations result in equilibrium geometries, vibrational frequencies, bond dissociation energies and reaction energies that are in many cases significantly closer to experiment than those obtained with Hartree-Fock theory. While Hartree-Fock optimised basis sets such as 6-31G** set can be used to obtain good geometries, the accurate prediction of reaction energies requires the use of density functional optimised basis sets. Non-local corrections (as proposed by Becke and Perdew) for the exchange and correlation energies are found to be essential in order to predict reaction energies within a few kcal/mol. Following Altmann [12], DF bonds are slightly too long while HF bonds are slightly too short. In general, both methods seem to give similar geometrical parameters, though HF predictions are more reliable. For Limtrakul [147], DF and HF-MP2 appear to provide results that are generally of comparable quality.

The adsorption of methanol on aluminosilicate cluster representations for zeolites has been investigated by Gale et al. [78], using non-local density functional theory. This study has been further extended for water and ammonia, by the same author [77]. Extensive gas-phase and adsorbed data relatively to the structure, charge distribution, energies and vibrational frequencies of these molecules are also given by Gale.

The structure, energy and charge distribution for a water dimer, in gas phase, are investigated in great detail by Popkie et al. [194] and Umeyama et al. [236], using Hartree-Fock theory. The first work is a study of the energies involved in hydrogen bonding in H_2O, HF, $H_3N - HF$ and other complexes. It presents a substantial review of theoretical and experimental work, in particular for the water dimer. The second paper aims essentially to develop potentials to describe fully hydrogen bonds in Molecular Mechanics MC and MD simulations. Bell et al. [32] presented systematic direct ab initio dynamics studies of proton transfer in hydrogen-bond systems, using several different levels of approximation, HF, HF-MP2 and DF-BLYP using Gaussian basis sets.

The structure and possible decomposition routes for silanol, SiH_3OH, the simplest saturated species containing an SiO bond, is discussed by Gordon [85], at the HF-MP2/6-31G(d,p) level of theory. The energies and structures of related molecules and radicals were also investigated. A study of the vibrational frequency of the donor OH group in the H-bonded dimers of water, methanol and silanol was published recently by Bleiber et al [36] at the HF-MP2 and the HF-MP4 levels of theory. Ab Initio calculations of the interaction of water with silanol, intended as a model for the free hydroxyl of amorphous silica, were reported by Ugliengo et al [233], at the HF-MP2 level of approximation. The silanol dimer has not been observed in the gas phase because of its readiness to yield disiloxane [36]. The lowest potential energy surface of disiloxane Si_2OH_6 was investigated in detail by Luke [150], as a function of the the torsion angles H-Si-O-Si', at the HF-MP2/631G(d,p) level of theory.

The review of Heanry et all [93], appropriately named *The elusive SiO bond*, gives a detailed account of the character of the SiO bond, with a full list of references that covers most of the more important theoretical work published in this subject until 1991. In another review, Gibbs [83] shows that molecular orbital calculations on hydroxyacid molecules with first- and second-row X-cations (Na, Mg, Al, Si, P, S) yield bond lengths and angles that are close to these in chemically similar minerals. In particular, individual bond lengths and angles within a crystal structure, like α-quartz, can be reproduced with reasonable accuracy by MO calculations on a small molecule like $Si_2O(OH)_6$.

Comparison between LDF and HF-MP2 calculations for disiloxane and analogs, with Si substituted by Al, B, P, Ga or Ge are presented by Stave et al. [218], while these aluminosilicates were studied by Mortier et al. [172] and Brand et al. [40] at the HF/STO-3G level of theory. The first work aims to explain the difference in properties of bridging and terminal silanol groups; the second to study the proton affinity of the central bridging sites in Si-O-Al and Si-O-Si. The OH stretching frequencies were found to be much less dependant on cluster size than the proton affinities. The structures, force constants and acidities of molecules structural analogs of disiloxane, $H_3T - O - TH_3$ and the protonated form $H_3T - OH - TH_3$, with T=Si, Al, B and P, have been calculated by Nicholas et al. [180] using restricted Hartree-Fock, with minimal, double- and triple-zeta basis functions. Direct SCF calculations and geometry optimisations for aluminosilicates have been done by Ahlrichs [8], namely for SiH_3OH, $Si(OH)_4$ and $Al(OH)_4^-$.

The Density Functional calculations presented in this chapter and in the next ones were undertaken with Dmol 2.1-96.0, from Biosym Technologies [5], while the Hartree-Fock calculations were undertaken with Cadpac 5.1-5.2, from Cambridge University. We used numerical DN, DND, DNP, ENP and TNP basis sets with Dmol and Gaussian 6-31G** and 6-311G** basis sets with Cadpac (see chapter 6). A local exchange and correlation functional proposed by von Barth-Hedin-Lundqvist, designated as BHL (also described as the Local Density Approximation LDA), and the non-local functional proposed by Becke-Lee-Yang-Parr, designated as BLYP,

have been used with Dmol.

All Hartree-Fock calculations have been corrected by a Møller-Plesset second-order pertubation, designated as MP2. Unless when explicitly stated otherwise, in Dmol calculations we used a SCF tolerance of 10^{-5} a.u. for the electronic density, a gradient tolerance of 0.015 a.u. for each coordinate and a medium grid. In the Cadpac calculations we used a SCF tolerance of 10^{-7} a.u. and a gradient tolerance of 10^{-2} a. u. All are restricted calculations and no symmetry constrains were used (point group C_1).

9.2 H_2O, H_3O^+, OH^- and H_2O--H_2O

The Table 9.1 shows the results for structure and charge distribution calculated for a single molecule of water, for several different levels of approximation. At the DF-BHL/DN level, without any polarisation functions, the HOH angle, 110.2^o, and the dielectric dipole moment, $2.59D$, are clearly too large, when compared with the experimental values: 104.45^o and 1.85 D, respectively.

The inclusion of 3d polarisation functions in the oxygen atom basis (DND) increases considerably the quality of the results, as the HOH angle decreases to 103.6^o, the electric dipole to 1.91 D and the OH bond length to 0.99 Å. Such changes could be expected, as the addition of functions of higher angular quantum number essentially allows for small displacements of the centres of electronic charge from the nuclear positions, which is particularly important in highly polar molecules, with a large charge separation-as in water.

The further addition of 2p polarisation functions to each hydrogen (DNP) improves only slightly the quality of the results obtained for the electric dipole and the HOH angle, as the charge distributed around the hydrogen atoms is small.

The partial charges obtained by a Mulliken gross population analysis are larger when the polarisation functions are included, though the electrical dipole moment is much smaller. This behaviour is not observed in the Hirshfeld partial charges, which depend only on the charge distribution and seem to be very accurate, at this level of approximation. In principle, this variation is due to two factors: the arbitrary "half-half" criterion used in the Mulliken method to divide the overlap terms of the density distribution and the fact that the basis set is obtained from atomic calculations: a standard approach. The electronic distribution in a hydrogen atom is very different from than in a molecule and consequently the atomic basis set for atomic hydrogen should be very different from the basis describing a hydrogen in a molecule. This problem is particularly acute for hydrogen, as in larger atoms the overall charge distribution is much less affected by the chemical environment. Mulliken charges obtained from standard Gaussian-type basis sets, optimised to use with Hartree-Fock or Density Functional, would be probably much more accurate.

The accuracy obtained at the DF-BHL/DNP level of approximation is already very high for this simple molecule, and a further refinement of the basis, to a triple basis set, increases only slightly the accuracy of the OH bond (which becomes 0.97 Å) and increases the HOH angle to 104.8^o. For a single molecule of water, it is not particularly worth applying a non-local exchange and correlation energies. In the non-local DF calculation with a double basis set, the accuracy of the OH bond length actually decreased slightly, when compared with the best local density determinations.

The best calculation presented in this work for water, a non-local density calculation with

H_2O

Method	*Total Energy*	OH *Length*	HOH *Angle*	*Dipole*
BHL/DN	-75.883450	0.99	110.2	2.59
DND	-75.908135	0.98	103.6	1.91
DNP	-75.910391	0.98	103.9	1.86
TNP	-75.923459	0.97	104.8	1.87
BLYP/DNP	-76.441266	0.99	103.8	1.80
TNP	-76.455469	0.97	104.9	1.81
MP2/6-31G**	-76.222449	0.96	103.8	2.11
6-311G**	-76.288612	0.96	102.4	2.10
Exp.	-	0.9584	104.45	1.85
	Hirshfeld Charges		*Mulliken Charges*	
	O	H	O	H
BHL/DN	-0.3380	0.1690	-0.7360	0.3680
DND	-0.3148	0.1574	-0.9390	0.4690
DNP	-0.3026	0.1513	-0.8920	0.4460
TNP	-0.3056	0.1528	-0.4040	0.2020
BLYP/DNP	-0.2867	0.1433	-0.8440	0.4220
TNP	-0.2899	0.1450	-0.3130	0.1560
MP2/6-31G**	-	-	-0.6408	0.3204
6-311G**	-	-	-0.4658	0.2329

Table 9.1: Total energy (Ha), bond length (Å) bond angle and charge distribution for an isolated H_2O molecule, after local DF-BHL, non-local DF-BLYP and HF-MP2 optimisations, using numerical (DN, DND, DNP, TNP) and Gaussian (6-31G**, 6-311G**) basis sets. Experimental values from [77] and [122].

a triple basis set, leads to very precise results for the OH bond angle, the HOH bond angle and the electric dipole moment, only 0.01 Å, 0.4^o and 0.04 D far from the experimental data, respectively. The Hartree-Fock method, at the MP2 level, with a 6-31G** double zeta plus polarisation basis set, leads to a OH bond length that matches the experimental value (0.96 Å), but the dipole moment is too high: 2.11 D. Introducing another valence basis function, in the 6-311G** basis set, does not contribute to improve the results: the HOH angle, in particular, becomes 1^o further from the correct value.

A difficult test for any ab-initio method is to be able to describe the structure and energy of a hydrogen bond. The results presented in Table 9.2, for an isolated water dimer, show important differences between the various ab-initio methods tested. Two geometries are considered: a linear structure with a strong directional bond (as determined experimentally) and a cyclic structure, where two (non-directional) hydrogen bonds can be formed.

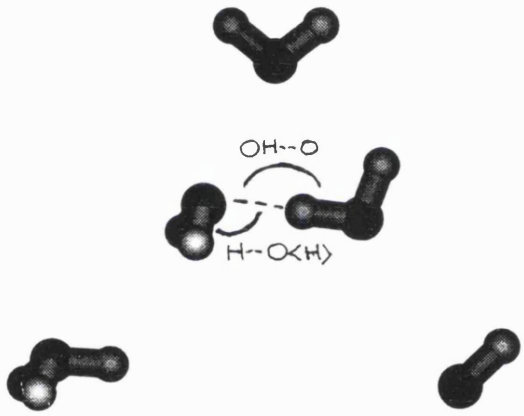


Figure 9.1: Optimised H_2O, H_2O--H_2O, H_3O^+ and OH^- clusters, after ab-initio DFT-BHL/DNP energy minimisation.

All methods predict correctly the greater stability of the linear structure over the cyclic one, by a difference as large as 1.4-1.5 kcal mol^{-1} for DF-BHL/DNP and DF-BLYP/DNP methods, but only 0.2 kcal mol^{-1} for the HF-MP2/6-31G** calculation. This latter difference seems too small, considering that the cyclic structure has never been found experimentally (a simple Maxwell-Bolzmann analysis at 20^oC, considering only these two structures, would predict that as much as 41 % of the dimers would have the cyclic structure).

However, the most striking result is the tendency shown by the Local Density Approximation to overestimate strongly the strength of hydrogen bonds. The predicted H-bond energy, for this level of approximation (-11.3 kcal mol^{-1}), is much higher than the expected value: between -4 and -6 kcal mol^{-1}. Furthermore, the calculated H-bond length (1.71 Å) is too short when compared with the value deduced from experience in gas phase: 1.98-2.00 Å. However, similar O- -H and OH bond lengths were found in ice I_h at 100 K, respectively 1.74 Å and 1.01 Å. A LDA calculation, with a triple basis set (DF-BHL/TNP), leads to a small improvement in the hydrogen bond energy (-9.0 kcal mol^{-1}) but the $O--H$ bond length remains almost unaltered.

A much better agreement with experiment is found when non-local DF with a double basis set is used (DF-BLYP/DNP). The hydrogen bond energy decreases to -6.4 kcal mol^{-1}, which

$H_2O - -H_2O$

Method	*Tot. E*	*Hyd. E*	O-O	O-H	O- -H	OH- -O	H- -O<H>
Linear							
BHL/DNP	-151.83874	-11.3	2.71	1.00	1.71	176.9	106.0
TNP	-151.86124	-9.0	2.71	0.99	1.72	176.6	106.2
BLYP/DNP	-152.89271	-6.4	3.01	0.99	2.02	175.9	116.9
TNP	-152.91782	-4.3	2.98	0.98	2.00	172.7	119.1
MP2/6-31G**	-152.45623	-7.1	2.92	0.96	1.96	169.9	107.3
Cyclic							
BHL/DNP	-151.83657	-9.9	-	0.99	2.00	-	-
BLYP/DNP	-152.89032	-4.9	-	0.99	2.28	-	-
MP2/6-31G**	-152.45590	-6.9	-	0.96	2.20	-	-
Gas (*Linear*)	-	-5.3	2.98	-	-	180	120
Ice I_h (100K)	-	-5.0	-	1.01	1.74	180	120

	Cyc: μ	*Lin*: μ	H_{at}	O_{at}	H_a	O_d	H_{dt}
					Hirsfeld		
BHL/DNP	0.09	2.66	0.1325	-0.3469	0.0685	-0.2176	0.1816
BHL/TNP	-	2.65	0.1343	-0.3467	0.0698	-0.2215	0.1821
BLYP/DNP	0.19	2.59	0.1317	-0.3156	0.0909	-0.2339	0.1635
BLYP/TNP	-	2.44	0.1323	-0.3176	0.0917	-0.2363	0.1650
					Mulliken		
MP2/6-31G**	0.17	2.28	0.3320	-0.6911	0.3104	-0.6269	0.3378

Table 9.2: Total energy (Ha), hydrogen-bond energy (kcal mol^{-1}), bond lengths (Å), bond angles, electric dipole (Debye) and charge distribution for an isolated $H_2O - -H_2O$ water dimer (O_d = donor oxygen; H_{dt} = hydrogens in donor molecule; H_a = acceptor hydrogen; O_{at} and H_{at} = oxygen and hydrogen in acceptor molecule; <H> means the bisector line between the two H_{dt} hydrogens, see Figure 9.1). Experimental values from [89], [46] and [236].

is still 1-2 kcal mol^{-1} higher than the experimental value, and the *O- -H* bond length (2.02 Å) becomes only 0.02-0.04 Å larger than the expected value. A further improvement is achieved when a triple basis set is used (DF-BLYP/TNP): the hydrogen bond energy decreases to -4.3 $kcalmol^{-1}$, close to the -4.5 $kcalmol^{-1}$ limit predicted by the best HF calculations, and the distance between the two oxygen atoms (2.98 Å) matches exactly the experimental value.

In DF-BHL/DNP and HF-MP2/6-31G** calculations, the H- -O-<H> angle (<H> means the bisector line between the hydrogens in the donor molecule, see Figure 9.1) is about 15^o smaller than the experimental prediction, 120^o. However, in both non-local DF calculations, the agreement with experience is excellent, particularly with a triple basis set (DF-BLYP/TNP). For all calculations, the *O- -H-O* angle is relatively close to the predicted value, 180^o, but surprisingly it decreases when the level of approximation increases.

The Hartree-Fock calculation predicts a good value for the *O- -H* hydrogen bond length (1.96 Å) but the corresponding *OH* bond length is too short (0.96 Å) and consequently the *O-O* distance is 0.08 Å shorter than the experimental value: as can be seen for ice I_h or comparing the DF-BLYP/TNP calculations in the water dimer with those in water, an hydrogen bond tends to increase the primary *OH* bond length. The Hartree-Fock value for the hydrogen bond energy is relatively poor, -7.1 $kcalmol^{-1}$, at this level of approximation, when compared with the non-local DF results, with a triple or even double basis set.

In contrast to the cyclic structure, where the charge separation is very small, the linear structure has a large electric dipole moment, which according to the calculations presented here is probably between 2.28 D and 2.44 D for the best HF and DF results. Although a hydrogen bond is essentially a electrostatic interaction, there is some charge transference from the oxygen to the hydrogen, responsible for the large dipole, as can be seen by inspection of the Hirshfeld and Mulliken charges obtained for the various calculations, presented also in Table 9.2.

The results presented in Tables 9.3 and 9.4 for the simplest ions, OH^- and H_3O^+, show almost no differences between the Local and Non-Local Density Functional values. However, the Hartree-Fock/MP2 results are reasonably different. In particular, DF and HF predict very different values for the OH^- electric dipole moment (0.19 D and 0.99 D respectively), which is surprising, considering the simplicity of this ion. However, the H_3O^+ dipole moment is almost the same in all calculations (about 2.25 D), and is probably a reliable value (no experimental data seems to be available to compare).

The difference between DF and HF *OH* bond lengths (about 0.02-0.03 Å) is essentially the same as in water. The experimental value for the *OH* bond length, 0.95 Å, seems to be too short, as this bond should be weaker and consequently longer than in H_2O, where the experimental bond length is 0.96 Å. An increase of about 0.02 Å in the *OH* bond length, is actually predicted in all three calculations for this ion, and the real value should be very close to 0.98 Å, as calculated at the HF-MP2/6-31G** level.

The enthalpy of water auto-ionisation ($2H_20 + \Delta H \rightarrow H_3O^+ + OH^-$), calculated from the heats of formation of H_2O, H_3O^+ and OH^-, at 0 K, is shown in Table 9.5 and compared with the DF and HF results obtained from the total energy of the species involved. The agreement is excellent for both local and non-local DFT calculations but is relatively poor for the Hartree-Fock/MP2 method, which is 33.9 $kcalmol^{-1}$ higher than expected. Even at the MP2 level, the Hartree-Fock energies cannot be considered as very reliable and multi-determinant wavefunction descriptions, demanding a enormous amount of CPU time, are probably necessary to obtain accurate values.

	OH^-		
Method	BHL/DNP	BLYP/DNP	MP2/6-31G**
Energy	-75.295377	-75.822320	-75.528485
OH Length	0.99	0.99	0.97
Hirshfeld			
O	-0.8107	-0.8129	-
H	-0.1893	-0.1871	-
Mulliken			
O	-0.8280	-0.8140	-1.1030
H	-0.1720	-0.1860	0.1030
Dipole	0.16	0.19	0.99

Table 9.3: Total energy (Ha), bond length (Å), electric dipole (Debye) and charge distribution for an isolated OH^- ion.

	H_3O^+			
Method	BHL/DNP	BLYP/DNP	MP2/6-31G**	Exp.
Energy	-76.173169	-76.705321	-76.508973	-
OH Length	1.01	1.01	0.98	0.95
HOH Angle	108.3	108.3	112.6	109
Hirshfeld				
O	0.0503	0.0723	-	-
H	0.3165	0.3092	-	-
Mulliken				
O	-1.0080	-0.9440	-0.4171	-
H	0.6690	0.6480	0.4724	-
Dipole	2.25	2.22	2.26	-

Table 9.4: Total energy (Ha), bond length (Å), bond angle, electric dipole (Debye) and charge distribution for an isolated H_3O^+ ion. Experimental values from [224].

	Auto-ionisation
Method	*Energy*
BHL/DNP	221.0
BLYP	222.7
MP2/6-31G**	255.7
Exp. (ΔH_f^0)	221.8

Table 9.5: Water auto-ionisation energy (kcal/mol), after local DF-BHL, non-local DF-BLYP and HF-MP2 optimisations, using numerical (DNP) and Gaussian (6-31G**) basis sets. Experimental value from [224].

9.3 CH_3OH and CH_3CH_2OH

The structure and charge distribution calculated for methanol and ethanol are presented in Tables 9.6 and 9.7. The Local Density Approximation, with a DNP basis set (DF-BHL/DNP), can describe accurately these molecules because there are no hydrogen bonds involved. For methanol, the maximum difference between the optimised angles and the values derived experimentally is 2.5^o (HCO angle). The bond lengths are approximately 0.02 Å larger than the experimental values.

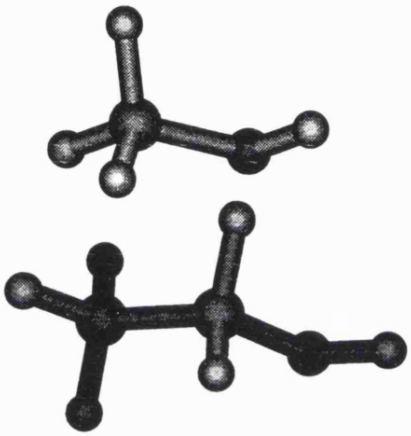


Figure 9.2: Optimised CH_3OH and CH_3CH_2OH molecules, after ab-initio DFT-BHL/DNP energy minimisation.

For ethanol, the agreement between local and non-local DF and Hartree-Fock calculations is excellent as regards the bond angles: the maximum differences to HF values were 1.1^o for the DF-BHL method (CCH angle) and 0.9^o at the DF-BLYP level (HC_2H angle). The ethanol bond lengths calculated with DFT are larger than the HF values, particularly for the bonds involving the oxygen atom. With LDA the OH bond is 0.03 Å larger than expected and in the Non-Local Approximation the OH and OC bonds are 0.03 Å and 0.04 Å larger, respectively. All the other differences are smaller or close to 0.02 Å, for both Local and Non-Local Density methods, which is probably the accuracy that can be expected for these levels of approximation. The most significant inaccuracies might be attributed to a lower quality of the oxygen atomic basis functions. To achieve a accuracy of 0.02 Å or lower with DFT when compared with HF, it would be necessary to use a triple basis set, as in water, though such calculations were never performed.

At the DF-BHL/DNP level, the electric dipole moment im methanol (1.59 D) is in reasonable agreement with the value determined experimentally: 1.70 D. The Mulliken population analysis shows, however, a exaggerated concentration of charge in the valence 2p and polarisation 3d functions of the carbon atom, removed from the alkyl hydrogens, that results in a Mulliken partial charge even more negative for C than for O. This unrealistic charge distribution is not observed in the Hirshfeld charges, which conform well with what could be expected, from a chemical point of view. When non-local exchange and correlation energies are added, the electric dipole (1.63 D) and the Mulliken charges become slightly better, but in compensation the OH and CO bond lengths become 0.03^o larger than the experimental values. The best results were

	CH_3OH			
Method	BHL/DNP	BLYP/DNP	MP2/6-31G**	Exp.
Energy	-114.85895	-115.72633	-115.38984	-
Length				
CH	1.11	1.10	1.09	1.094
CO	1.42	1.45	1.42	1.421
OH	0.98	0.99	0.96	0.963
Angle				
H_gCH_g	108.4	109.8	108.3	108.5
HCO	109.7	106.1	112.6	107.2-129.9
COH	108.0	107.2	107.6	108.0
Hirshfeld				
C	-0.0674	-0.0285	-	-
O	-0.2201	-0.2238	-	-
H_C	0.0438	0.0380	-	-
H_O	0.1561	0.1431	-	-
Mulliken				
C	-0.6980	-0.5760	-0.0606	-
O	-0.6500	-0.6850	-0.5704	-
H_C	0.2870	0.2800	0.1032	-
H_O	0.4870	0.4450	0.3214	-
Dipole	1.59	1.63	1.76	1.70

Table 9.6: Total energy (Hartree), bond lengths (Å), bond angles, electric dipole (Debye) and charge distribution for an isolated CH_3OH molecule (H_g = gauche hydrogens in the methyl group). Experimental values from [195], [78] and [122].

	CH_3CH_2OH		
	BHL/DNP	BLYP/DNP	MP2/6-31G**
Energy	-153.83282	-155.03003	-154.58206
Length			
C_2H	1.10	1.10	1.09
C_3H	1.11	1.10	1.09
CO	1.42	1.46	1.42
OH	0.99	0.99	0.96
CC	1.50	1.53	1.51
Angle			
$H_gC_3H_g$	108.1	108.7	108.9
HC_2H	106.9	108.3	107.4
CCH	111.2	110.8	110.1
CCO	107.2	107.4	107.0
HCO	110.5	110.0	110.8
COH	107.9	107.8	107.8
Hirshfeld			
C_3	-0.1355	-0.1013	-
C_2	-0.0232	0.0080	-
H_3	0.0490	0.0386	
H_2	0.0354	0.0284	
O	-0.2142	-0.2212	-
H_O	0.1551	0.1416	
Mulliken			
C_3	-0.9880	-0.9020	-0.3396
C_2	-0.3990	-0.3340	0.0570
H_3	0.3340	0.3120	0.1195
H_2	0.2820	0.2800	0.0874
O	-0.6700	-0.7070	-0.5714
H_O	0.4910	0.4490	0.3207
Dipole	1.51 (trans)	1.58 (trans)	1.62 (trans)
Exp.(trans-gauche)	1.44-1.68	"	"

Table 9.7: Total energy (Hartree), bond lengths (Å), bond angles, electric dipole (Debye), Hirshfeld and Mulliken charges for an isolated CH_3CH_2OH molecule (C_2, H_2 = in methylene group and C_3, H_3 in methyl group; H_g = gauche hydrogens in the methyl group). Experimental values from [2].

obtained with Hartree-Fock, at the HF-MP2/6-31G** level of approximation, and differ less than 0.01 Å, 0.5^o and 0.06 D from the experimental values. The exception is the HCO angle, which is 5^o larger than the angle measured experimentally.

The electric dipole in ethanol calculated by DFT, particularly at the LDA level, (1.51 D), is closer to the experimental value (1.44 D) than the Hartree-Fock result (1.62 D), though the experimental value may show appreciable uncertainty owing to the existence of the two conformations, trans and gauche, with different dipole moments. As expected, the C_3 carbon is much more negatively charged than the C_2, though the Mulliken charges for the C_3 carbon are obviously too high, in both DFT calculations, as in methanol. For all ab-initio and partial charge methods studied in this work, the methyl hydrogens are more electropositive than the methylene ones.

Even at the single-determinant wavefunction level of theory, the Hartree-Fock method with a double-zeta basis set can usually describe reasonably well the structure of relatively simple molecules, and the data thus obtained are probably the most reliable source to compare with, when no experimental information is available.

9.4 $Si(OH)_4$ and $Si_2O(OH)_6$

Monosilicic acid, $Si(OH)_4$, is a fundamental molecule in Si chemistry, particularly in sol-gel and zeolite synthesis. However, because it is very unstable in gas-phase, no experimental data is available for the isolated molecule. The results presented in Table 9.8, for several different levels of approximation, are therefore compared with reference HF calculations. Disilicic acid, $Si_2O(OH)_6$, is the first product of condensation, probably the most important reaction of Si. The corresponding results are presented in Table 9.9.

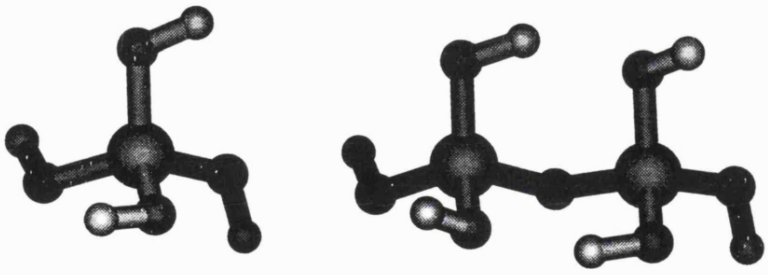


Figure 9.3: Optimised $Si(OH)_4$ and $Si_2O(OH)_6$ molecules, after ab-initio DFT-BHL/DNP energy minimisation.

The LDA method without polarisation functions (DF-BHL/DN) predicts very well the two OSiO angles in the monomer, one occuring four times (106.5^o) and the other twice (115.7^o), which match exactly the Sauers's values. The OH and SiO bond lengths, however, are respectively 0.04-0.06 Ålonger than the reference values. The calculated SiOH angle (128.2^o) is also quite far from the reference result: 118.8^o. When 3d and 4d polarisation functions are included for oxygen and silicon atoms, the SiO bond length and the SiOH angle decrease to 1.65 Å and 112.4^o, but in compensation the OH bond and the OSiO angles become slightly worse. The SiO bond length decreases again (to 1.64 Å) when 2s polarisation functions are added to the

$Si(OH)_4$

	Total	*Bond Length*			*Bond Angle*	
Method	*Energy*	SiO	OH	O- -H	OSiO(4×,2×)	SiOH
BHL/DN	-589.71495	1.68	0.98	2.97	106.5, 115.7	128.2
DND	-589.88715	1.65	0.99	2.69	105.6, 117.6	112.4
DNP	-589.89392	1.64	0.99	2.68	105.6, 117.6	112.4
IC	-589.89380	1.64	0.99	2.69	105.7, 117.3	112.3
+S	-589.89380	1.64	0.99	2.69	105.7, 117.3	112.3
+G	-589.89380	1.64	0.99	2.69	105.8, 117.1	112.2
ENP	-589.92865	1.63	0.97	2.73	106.1, 116.5	115.5
BLYP/DNP	-593.09657	1.67	0.99	2.71	105.7, 117.4	111.1
ENP	-593.13341	1.66	0.97	2.78	106.5, 115.6	116.2
TNP	-593.14211	1.65	0.97	2.78	106.6, 115.4	116.5
L443	-593.14330	1.65	0.97	2.78	106.5, 115.7	116.6
OS	-593.14329	1.65	0.97	2.78	106.4, 115.8	116.6
MP2/6-31G**	-591.76320	1.647	0.960	-	106.4, 115.9	114.9
Ref. (HF)	-	1.626	0.942	-	106.6, 115.4	118.8

	Hirshfeld			*Mulliken*		
	Si	O	H	Si	O	H
BHL/DN	0.5816	-0.3366	0.1912	1.5400	-0.8240	0.4390
DND	0.4456	-0.2870	0.1756	0.7960	-0.7280	0.5290
DNP	0.4473	-0.2842	0.1724	0.8660	-0.7620	0.5460
IC	0.4474	-0.2842	0.1723	0.8660	-0.7630	0.5465
+S	0.4474	-0.2842	0.1723	0.8660	-0.7630	0.5465
+G	0.4475	-0.2842	0.1723	0.8660	-0.7630	0.5465
ENP	0.4598	-0.2887	0.1738	0.5590	-0.3530	0.2130
BLYP/DNP	0.5087	-0.2885	0.1613	1.1510	-0.8090	0.5220
ENP	0.5215	-0.2940	0.1637	0.9130	-0.3830	0.1550
TNP	0.5267	-0.2962	0.1645	1.8220	-0.6000	0.1430
L443	0.5271	-0.2967	0.1650	1.8280	-0.6000	0.1440
OS	0.5272	-0.2967	0.1650	1.8290	-0.6000	0.1430
MP2/6-31G**	-	-	-	1.2320	-0.6593	0.3512

Table 9.8: Total energy (Hartree), bond lengths (Å), bond angles and charge distribution for an isolated $Si(OH)_4$ molecule (IC = internal coordinates, S = SCF tolerance = 10^{-7} a.u. and G = Gradient tolerance = 2×10^{-4} a.u., L443 = potential expansion for Si,O,H, OS = open shell). Reference values from [209].

$Si_2O(OH)_6$

	BHL/DN	DND	DNP	BLYP/DNP	+S+G	TNP
Energy	-1103.5615	-1103.8810	-1103.8924	-1109.7564	-1109.7566	-1109.8323
Length						
SiO_b	1.69	1.65	1.65	1.67	1.67	1.65
SiO_t	1.69	1.65	1.65	1.66-1.68	1.67-1.68	1.64-1.66
OH	0.99	0.99	0.99	0.98-0.99	0.98	0.97
O- -H (2×)	1.92	1.91	1.91	2.20	2.26	2.52
" (2×)	3.01	2.98	2.98	3.07	3.04	2.94
" (2×)	3.20	2.84	2.84	2.83	2.79	2.81
Angle						
SiOSi	121.9	118.1	118.4	123.1	124.1	132.1
OSiO	102.7-110.6	106.0-108.8	105.9-108.3	107.1-112.9	108.3-113.5	107.8-113.7
SiOH	124.2	111.6	111.8	108.7-113.4	109.8-113.4	114.1-117.7
OH- -H	140.1-141.9	146.8-147.4	146.8-147.4	144.4-145.2	142.3-142.6	134.8-138.0
Hirshfeld						
Si	0.5953	0.4576	0.4598	0.5199	0.5189	0.5367
O_b	-0.3656	-0.2774	-0.2776	-0.2982	-0.2974	-0.3036
O_t	-0.3168	-0.2714	-0.2691	-0.2796	-0.2806	-0.2902
H	0.1793	0.1651	0.1621	0.1560	0.1572	0.1619
Mulliken						
Si	1.6174	0.8900	0.9785	1.2410	1.2340	1.7615
O_b	-0.9260	-0.5488	-0.5800	-0.7070	-0.7040	-0.8260
O_t	-0.8453	-0.7442	-0.7742	-0.8178	-0.8190	-0.6006
H	0.4605	0.5390	0.5447	0.5223	0.5250	0.1511
Dipole	0.24	1.16	1.09	1.32	1.35	0.85

Table 9.9: Total energy (Hartree), bond lengths (Å), bond angles, electric dipole (Debye) and charge distribution for an isolated $Si_2O(OH)_6$ molecule (S = SCF tolerance = 10^{-7} a.u. and G = Gradient tolerance = 2×10^{-4} a.u.; t = terminal and b = bridging).

hydrogen basis set (the only noticeable refinement).

At this level of approximation, the accuracy still depends very much on the quality of the atomic basis set: a further improvement, adding respectively two and four more functions to describe the oxygens and hydrogens (DF-BHL/TNP) results in a considerable improvement in the SiO and OH bond lengths (1.63 Å and 0.97 Å), and also in the ($OSiO$ and $SiOH$) angles (106.1^o and 116.5^o). These values are very close indeed to Sauers's results, showing that, when no hydrogen bonds are present, and a good basis set is used, LDA can describe the structure of a given molecular system, with a very high accuracy.

To check the error introduced in the results by using a SCF tolerance of 10^{-5} a.u., the calculation with a double basis set was repeated with a SCF tolerance of 10^{-7} a.u.. The new bond lengths are equal to the previous ones and the bond angles are, in the worse case, 0.3^o different from before. To check the error introduced by using a gradient tolerance equal to 0.0015 a.u. in the geometry optimisation, the same calculation was repeated using a SCF tolerance of 10^{-7} a.u. and a gradient tolerance of 0.0002 a. u.. Again, the bond lengths obtained are the same as the previous ones, and the bond angles are only 0.1^o apart, which seems to justify the choice made for the SCF and gradient tolerances. However, this gradient tolerance might be too high for larger, more complicated clusters, if the corresponding potential surfaces decrease too slowly. Optimising the structure by using internal, instead of Cartesian coordinates, did not seem to change the accuracy of the minimisation algorithm-the major difference observed was a decrease of 0.3^o in the $OSiO$ angle.

At the DF-BLYP/DNP level, with non-local density, the OH bond length and the $OSiO$ angles are the same as the DF-BHL/DNP values, with the same basis set, but the SiO bond length and the SiOH bond angle become less accurate: 1.67 Å and 111.1^o. DFT tends to slightly overestimate the bond lengths, and this feature seems even to be enhanced by the introduction of non-local corrections. To increase the quality of the structural results obtained and regain the previous accuracy, a much better basis set is necessary.

Using a enhanced basis set, with the same basis functions for Si, but using a triple basis set to describe the oxygens and hydrogens, the overall structural description improves substantially. The SiO and OH bond lengths decrease to 1.66 Å and 0.97 Å and both $OSiO$ bond angles-106.5^o and 115.6^o-match the Sauer's values. In particular, the $SiOH$ angle improves considerably-to 116.2^o. A further refinement, introducing five additional basis functions for silicon to obtain what is essentially a triple basis set for all atoms, leads again to an improvement of the results obtained, which are now very close to the reference values. The $OSiO$ angles match exactly the reference values, the $SiOH$ angle is 2.3^o smaller and the SiO and OH bond lengths are only 0.02 Å and 0.03 Å, respectively, larger than in Sauer's HF study. Further calculations with a larger expansion of the model density (see chapter 6) and using a open shell treatment, did not lead to any improvement in the results, as the only differences found are certainly below the precision of the method.

The distance between adjacent hydroxyl groups is clearly too large in this cluster to allow the formation of hydrogen bonds. Consequently, no important differences were found between local DF-BHL and non-local DF-BLYP methods. For a double basis set, O- -H is equal to 2.68-2.69 Å with local DFT and 2.71 Å with non-local, whereas with the enhanced basis set, these values increased slightly to 2.73 Å and 2.78 Å, respectively. The latter is also the value predicted at the highest DF-BLYP/TNP level of approximation.

The situation changes completely in the silicate dimer, where hydrogen bonds do play a very important role. In the less ambitious $Si_2O(OH)_6$ calculation (DF-BHL/DN), the two O- -H

distances between the hydroxyl groups parallel to the *Si-O-Si* plane and the corresponding *O-O* distances are only 0.06-0.07 Å smaller than in the hydrogen bond in the gas-phase water dimer, previously discussed. The *O- -H* distances remain essentially unchanged when polarisation functions are added, at the DF-BHL/DNP level, but increase considerably, to 2.20 Å, at the DF-BLYP/DNP level, with non-local corrections for exchange and correlation energies. The *O- -H* distances increase even more at the DF-BLYP/TNP level, to 2.52 Å, which is already at the limit of what can be expected for a hydrogen-bond distance. The *O-H- -O* angle is between 134.8^o and 147.4^o for all calculations - very far therefore from the equivalent angle in the water dimer.

These differences between the results for Local and Non-Local levels of approximation suggest that, as in the water dimer, the Local Density Approximation is overestimating the strength of the hydrogen bonds. Although it was shown for the water dimer that a pure hydrogen bond depends much more on the charge distribution than on the basis set, in this cluster the two *O- -H* distances are closely related to the Si-O-Si angle, which depends very much on the quality of the basis set employed. The values obtained for these parameters are thus the result of the combination of the charge distribution in the *O- -H* distances and the atomic basis set in the Si-O-Si angle.

In the LDA calculations, the overestimated *O- -H* interactions between the two parts of the dimer force the *SiOSi* angle to decrease to values between 118.1^o and 121.9^o. With non-local density, the angle increases progressively to 123.1^o (DF-BLYP/DNP) and finally 132.1^o, in the best calculation (DF-BLYP/TNP). This last value is expected to be a very accurate and reliable result, considering the excellent agreement with experimental and theoretical data obtained for the previous systems, at this sophisticated level of approximation. The other four possible *O- -H* interactions, grouped in two pairs disposed diagonally, are too large-2.94 Å and 2.81 Å in the best calculation-to have any significant hydrogen bonding character. This is shown by the very small differences between the best local and non-local DF descriptions of the *O- -H* bond lengths: 0.04 Å in one pair and 0.03 Åin the other.

As in the monomer, the LDA calculation without polarisation functions (DF-BHL/DN) predicts values that are too large for the SiO bond length and the SiOH bond angle. When polarisation functions are added to the basis set, the *SiO* bond becomes very accurate, 1.65 Å, but the *SiOH* angle is too small: 111.8^o. As for the monomer, non-local exchange and correlation corrections increase again the *SiO* bonds (to 1.66-1.68 Å) and only when the triple basis set is used, the overall accuracy improve significantly: the *SiO* and *OH* bond lengths decrease to 1.65 Å and 0.97 Å, while the SiOH bond angle increases to 114.1-117.7^o.

Although no experimental or accurate theoretical results seem to be available for $Si_2(OH)_6$, following the results previously presented and discussed, particularly for $Si(OH)_4$ and $H_2O - -H_2O$, the *SiO* and *OH* bond lengths are probably only 0.02-0.03 Å smaller than those calculated here, while the SiOH angle will be about 119^o, 3 degrees larger than the average value calculated here. The tests carried out using different SCF and gradient tolerances, at the Non-Local Approximation level, with a DNP basis set, show small differences of about 1^o and less than 0.01 Åin the results.

The electric dipole moment is highly sensitive to the method used (in part because of the *SiOSi* angle), changing from 0.24 D to 1.09 D when the polarisation functions are added, from 1.35 D to 0.85 D when a triple instead of a double basis set is used, and from 1.09 D to 1.32 D when non-local exchange and correlation energies are added. In this respect, even the value obtained with non-local corrections and triple basis set might be not considered as totally

reliable. The electric dipole in the monomer is zero, due to its symmetry.

The condensation energy to form the dimer from the monomer ($2Si(OH)_4 + \Delta E \rightarrow Si_2O(OH)_6 + H_2O$), for the levels of theory investigated so far, is presented in Table 9.10. These results closely resemble the trends observed for the hydrogen bond energy in the water dimer H_2O--H_2O, presented in Table 9.9. This is to be expected because of the two hydrogen bonds present in $Si_2O(OH)_6$, which are not present in the reactants $Si(OH)_4$. Under the Local Density Approximation, the condensation energy is relatively large, -9.4 kcalmol^{-1}, and almost equal for all the basis sets tested, showing that, for this system, the differences in energy due to the introduction of the polarisation functions affect equally the reactants and the products.

Method	*Condensation Energy*
BHL/DN	-9.44
DND	-9.31
DNP	-9.38
BLYP/DNP	-2.84
TNP	-2.22
Ref. (HF)	-7.8

Table 9.10: $Si(OH)_4$ condensation energy (kcal/mol) after local DF-BHL and non-local DF-BLYP and HF-MP2 optimisations, compared with HF-MP2/6-31G** reference value, using numerical (DN, DND, DNP, TNP) basis sets. Reference value from [52].

The condensation energy drops considerably, however, at the DF-BLYP/DNP level, with non-local density, being calculated as -2.8 kcal mol^{-1}. When a triple basis set is applied, the energy decreases even further, to -2.2 kcal mol^{-1}, which might be a very accurate prediction for the energy of this important reaction. As in the water dimer, the Hartree-Fock/MP2 prediction, -7.8 kcal mol^{-1}, is better than the local DF-BHL/DNP, but seems to be poorer than the best Non-Local DF-BLYP/TNP. Assuming that the difference in energy between local and non-local density calculations is only due to the two intramolecular hydrogen bonds occurring in $Si_2O(OH)_6$, which is almost certainly the case, the error per hydrogen bond comitted in local density calculations can be estimated to be about -3.3 kcal mol^{-1}, smaller but not far from -4.7 kcal mol^{-1}, the corresponding difference in the water dimer. This is probably due to the $SiOSi$ angle requirements, that force the hydrogen bonds to be 0.2 Ålonger, and consequently weaker, than in the water dimer, for the same level of approximation.

9.5 $Si(OCH_3)_4$ and $Si(OCH_2CH_3)_4$

The optimised structures of tetramethoxysilane, TMOS, $Si(OCH_3)_4$ and tetraethoxysilane, TEOS, $Si(OCH_2CH_3)_4$, the most commonly used precursors in sol-gel processes, are presented in Figure 9.4. The corresponding structural and charge distribution data obtained for TEOS (at the DF-BHL/DNP level) and TMOS (at BDF-BHL/DNP and DF-BLYP/DNP levels), are presented in Table 9.11.

Because there are no hydrogen bonds in these clusters, the results obtained at the DF-BHL/DNP level of approximation are probably very accurate, but no experimental data exists

	TEOS	TMOS	
	BHL/DNP	BHL/DNP	BLYP/DNP
Energy	-901.58478	-745.68760	-750.22898
Length			
SiO	1.64	1.64	1.66
OC	1.42-1.43	1.42	1.45
CC	1.50	-	-
CH	1.10-1.11	1.10-1.11	1.10
Angle			
OSiO	107.2-109.9-111.5	107.0-111.9	106.7-109.3
SiOC	114.9-120.2	117.0-122.8	119.6-124.7
OCH	108.7-109.3	108.5-111.8	107.2-107.7
HC_3H	108.2-108.6	108.4-108.6	109.1-109.8
OCC	108.9-110.3	-	-
CCH	109.9-111.3	-	-
HC_2H	106.9-107.1	-	-
Hirshfeld			
Si	0.4612	0.4644	0.5139
O	-0.2006	-0.2050	-0.2290
C_3	-0.1337	-0.0548	-0.0182
H_3	0.0497	0.0479	0.0390
C_2	-0.0115	-	-
H_2	0.0407	-	-
Dipole	0.28	0.42	0.42
Exp. (liq)	1.63	1.71	"

Table 9.11: Total energy (Hartree), bond lengths (Å), bond angles, electric dipole (Debye) and Hirshfeld charges for isolated $Si(OCH_3)_4$ and $Si(OCH_2CH_3)_4$ molecules (C_2, H_2 = in methylene group and C_3, H_3 in methyl group). Experimental values from [42].

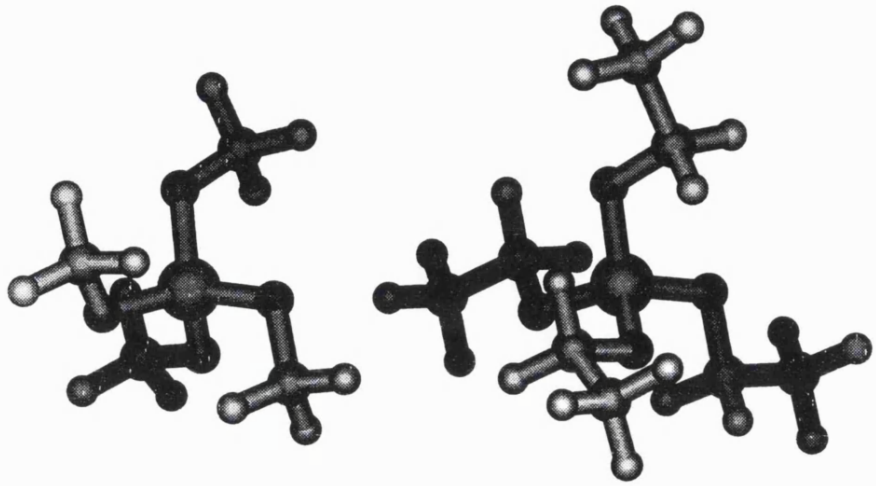


Figure 9.4: $Si(OCH_3)_4$ and $Si(OCH_2CH_3)_4$ alkoxides after ab-initio DFT-BHL/DNP energy minimisation.

to confirm this prediction. In the structures shown here, the groups CH_3CH_2OSi, CH_3OSi and $Si(OC)_4$ are disposed exactly as in the related molecules CH_3CH_2OH, CH_3OH, CH_3CH_2OH and $Si(OH)_4$. At the DF-BHL/DNP level of approximation, the OC, CH, CC and SiO bond lengths are equal to the values obtained in methanol, ethanol and monosilicic acid, at the same level of approximation, which are in good agreement with the experimental and theoretical reference data.

The small variation range of the OCH, OCC and CCH angles ($< 3.5^o$) include the values for methanol and ethanol (CCH angle) or differ very little, 0.8^o (OCH) and 1.7^o (OCC). The HC_3H and HC_2H angles also differ less than 1.0^o from the corresponding values in methanol and ethanol. In TMOS it is possible to identify two sets of OSiO angles, one between 107.0^o and 107.2^o, occurring twice, and the other between 110.1^o and 111.9^o. occurring four times. In TEOS, which is less symmetric than TMOS, three sets of OSiO angles are apparent, in the ranges 107.2^o (2×), 109.9-110.0^o (2×) and 111.5^o (2×).

The oxygen partial charges in TMOS and TEOS are only about 7 % smaller than in methanol (Table 9.6) and ethanol (Table 9.7). The carbon charges are smaller in the alkoxides and the hydrogen charges are relatively similar. Due to the TMOS and TEOS high symmetry(see chapter 14), the gas-phase electric dipoles are relatively small, particularly when compared with the experimental values in the liquid phase.

At the DF-BHL/DNP level of approximation, the calculated energies for the total TMOS and TEOS hydrolysis ($Si(OR)_4 + 4H_2O + \Delta E \rightarrow Si(OH)_4 + 4ROH, R = Me, Et$) are very small (respectively -0.4 kcalmol^{-1} and 0.7 kcalmol^{-1}), suggesting that, in gas phase, this reaction is not favoured energetically. The difference between the two energy values is probably too small to be significant and might be within the accuracy of the method. In any case, this difference is not due to an incomplete optimisation, as if this were the case, it would have greater influence on the largest and most complicated molecule, TEOS, increasing even more its hydrolysis energy.

At the DF-BLYP/DNP level of approximation, the structure prediction for TMOS becomes poorer, because the bond lengths are about 0.05 Å too long, though the bond angles remain essentially the same. The charges of the central atoms, Si and O, are slightly larger, at this

level of approximation. However, at this level of approximation the reaction energy is already significant, at least for TMOS: -4.9 kcalmol^{-1}. However, this total hydrolysis energy is the result of four individual hydrolysis reactions, each one is therefore only slightly exothermic. These reactions are studied in detail in the chapter 13.

9.6 $Al(OH)_4^-$, $Al_2O(OH)_6^{2-}$ and $AlSiO(OH)_6^-$

Although this work aims to study silica-based sol-gel processes, the smallest alumina-based clusters, $Al(OH)_4^-$, $Al_2O(OH)_6^{2-}$ and $AlSiO(OH)_6^-$, represented in Figure 9.5, have also been analysed. The main data on structure and charge distribution obtained for these clusters, at the DF-BHL/DNP level of approximation, are presented in Table 9.12.

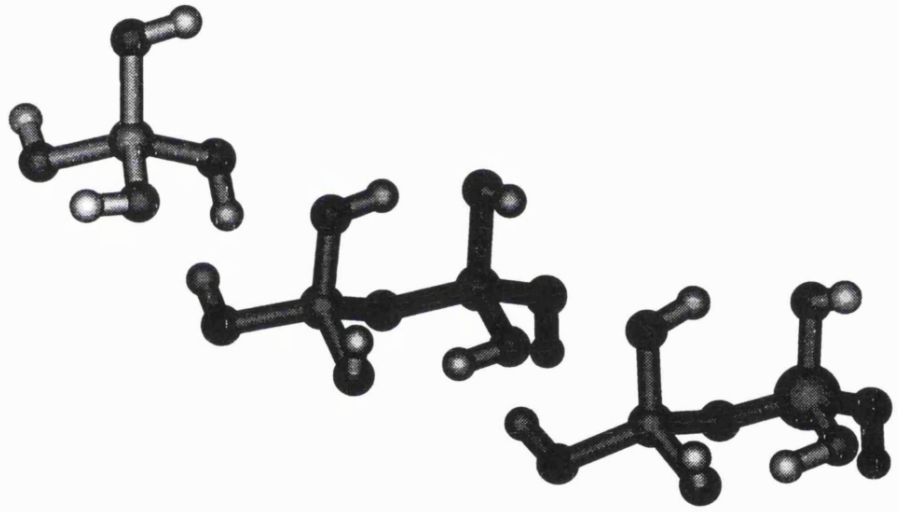


Figure 9.5: $Al(OH)_4^-$, $Al_2O(OH)_6^{2-}$ and $AlSiO(OH)_6^-$ Clusters after ab-initio DFT-BHL/DNP energy minimisation.

The key propriety of these clusters is their non-neutral total charge. The electric dipole moment becomes extremely high for the non-symmetrical species, as the additional charge results in a much more diffuse electron density distribution.

As in the silicate dimer, both $Al_2O(OH)_6^{2-}$ and $AlSiO(OH)_6^-$ have two hydrogen bonds, which we expect to be overestimated, at this level of approximation. Because the charge separation is quite large, these hydrogen bonds should be particularly strong, which is confirmed by the smallest O- -H distance in both clusters, calculated as 1.55 Å and 1.89 Å. The oxygen charges in aluminium-bonded oxygens are significantly larger than in silicon-bonded ones, which explains why, in the aluminosilicate cluster, the hydrogen bond formed by the aluminium-bonded oxygen is much stronger (1.55Å) than those formed by silicon-bonded oxygen. This result is confirmed by the corresponding OH distances in the acceptor hydroxyl groups, respectively 1.05 Å(an extremely high value, in principle overestimated) and 0.99 Å.

Like in the silicate clusters, the AlO and SiO bonds become much weaker when the oxygen

	$Al(OH)_4^-$	$Al_2O(OH)_6^{2-}$	$AlSiO(OH)_6^-$
Energy	-543.00884	-1010.0090	-1057.0357
Length			
AlO_b	-	1.75	1.79
SiO_b	-	-	1.62
AlO_t	1.78	1.79-1.81d	1.75-1.81d
SiO_t	-	-	1.65-1.68d
OH_t	0.98	0.98-1.01a	0.98-1.05a
O- -H	-	1.89-1.93	1.55_{dAl}-2.21_{dSi}
Angle			
AlOAl	-	112.0	-
AlOSi	-	-	115.0
OAlO	106.2-116.2	103.7-109.8	109.4-114.2
OSiO	-	-	103.9-109.6
AlOH	108.5	99.0-102.5	105.0-106.2
SiOH	-	-	104.4-106.2
Hirshfeld			
O_b	-	-0.4730	-0.3635
Al	0.3082	0.2928	0.3733
Si	-	-	0.3920
O_{tAl}	-0.4199	-0.3821	-0.3987
O_{dAl}	-	-0.4478	-0.3190
O_{aAl}	-	-0.4307	-0.4160
H_{tAl}	0.0928	0.0764	0.1095
H_{dAl}	-	0.0848	0.1277
H_{aAl}	-	0.0432	0.0775
O_{tSi}	-	-	-0.3116
O_{dSi}	-	-	-0.2864
O_{aSi}	-	-	-0.3470
H_{tSi}	-	-	0.1462
H_{dSi}	-	-	0.1453
H_{aSi}	-	-	0.0703
Dipole	0.00	41.1	32.8

Table 9.12: Total energy (Hartree), bond lengths (Å), bond angles, electric dipole (Debye) and Hirshfeld charges for isolated $Al(OH)_4^-$, $Al_2O(OH)_6^{2-}$ and $AlSiO(OH)_6^-$ clusters (d = in H-bond donor group, a = in H-bond acceptor group, t = in terminal group not involved in H-bonds; the heavy atom to which the hydroxyl group is attached is also indicated).

atoms form hydrogen bonds, due to the charge transference to the hydrogen atoms, resulting in longer bond lengths, 1.81Åand 1.69Å, respectively. The $AlOH$ and $SiOH$ angles are smaller in these than in the related silicate clusters, apparently due to the charge distribution. The $AlOAl$ angle is smaller than for $AlOSi$, which in turn is smaller than for $SiOSi$, for the same DF-BHL/DNP level of approximation.

At this level of theory, the condensation energy to form $Al_2O(OH)_6^{2-}$ and $AlSiO(OH)_6^-$, from $Al(OH)_4^-$ and $Si(OH)_4$, is calculated as +61.7 kcal mol^{-1} and -27.2 kcal mol^{-1}, respectively. The first reaction is highly endothermic because two species with charge -1 are transformed into a single species with charge -2, thus much less stable. The second reaction is highly exothermic because both reactants and products have a charge of -1 and this excess can be spread over a wider region in the larger product species, which becomes therefore less unstable. These results show that, in gas-phase studies of non-neutral species, their energies are essentially controlled by the charge distribution and depend very little on structural factors. This is confirmed by the results presented later in chapter 15.

9.7 Conclusions

Accuracies as high as 0.02 Å, 3^o and 1-2 kcal/mol can be currently expected for ambitious but still affordable ab-initio calculations, even for reasonably large molecular systems. Therefore, systematic calculations of the smallest silicate clusters are likely to provide reasonably accurate results.

The single determinantal Hartree-Fock method is particularly good in structural predictions, but, even at the MP2 level, it gives only modest results for energies. Furthermore, it is a particularly demanding method, that currently can only be used at present to study relatively small systems, with less than 10-15 atoms.

The Local Density Approximation methods are much faster and can be used to analyse larger systems, with more than 50 atoms, describing well systems containing only primary bonds, but failing to predict correctly the main features of hydrogen bonded systems. While the description of primary covalent bonds depend essentially on the quality of the basis set, the description of hydrogen bonds depends primarily on the quality on the exchange and correlation functional.

Density Functional Theory, at the non-local level of approximation, requires a much more complete basis set: the SCF and geometry convergence are more problematic, and the overall treatment becomes much slower than in LDA calculations. However, with a triple basis set it is a highly sophisticated method and very accurate structures and energies can be expected. In particular, it describes hydrogen bonds very well. However, even at this level of approximation, the results for double and triple basis sets still differ considerably, and further appreciable refinements might still be obtained, by increasing even further the basis set. In this case, basis sets effects should be taken into account.

The electric dipole moment is highly sensitive to the method and basis set used for the calculation, and for large molecules, very high levels of approximation seem to be necessary to obtain reliable, accurate results. Furthermore, the Mulliken partial charges, when calculated with DFT and a numerical basis set, seem to give a rather poor description of the molecular charge distribution. On the other hand, the Hirshfeld partial charges seem to give a chemically consistent description of the atomic charge distribution.

Calculations of the energies of the condensation reaction in vacuo show this to be exothermic,

with an energy about -2 to -3 kcal/mol. For the hydrolysis reaction, in the same conditions, no significant energy differences were found between reactants and products. More sophisticated calculations, applied to a wider range of alkoxides, are required to clarify these points.

Chapter 10

Different conformations

This chapter has essentially two purposes, the first is to study the structure, charge distribution and energy of some important silicate clusters, the linear trimer, $Si_3O_2(OH)_8$, the ring trimer, $Si_3O_3(OH)_6$, the linear tetramer, $Si_4O_3(OH)_{10}$, the ring tetramer, $Si_4O_4(OH)_8$, the linear pentamer, $Si_5O_4(OH)_{12}$, and the cubic cage, $Si_8O_{12}(OH)_8$. The second aim builds on the first to show the importance of analysing the various conformations of each cluster (including the monomer, monosilicic acid, $Si(OH)_4$ and the dimer, disilicic acid, $Si_2O(OH)_6$), in order to understand its chemistry, and the influence of the calculation method on the results.

10.1 Introduction

Unless a given cluster is highly symmetric, its structural optimisation by modelling methods, based on the minimisation of the energy, is extremely difficult owing to the enormous number of local minima of energy that coexist with the global minimum. To study the various conformations of a given cluster is therefore important to obtain an effective description of its energy.

Ab Initio calculations for both S_4 and D_{2d} conformations of $Si(OH)_4$, at the HF-MP2/6-31G** level, are discussed in a long review published by Sauer [209]. In particular, the energy difference between both conformations was found to be 3.21 kcalmol^{-1}, at this level of approximation. For smaller basis sets, this rotational barrier becomes 3.3 kcal mol^{-1} (6-31G*), 1.79 kcalmol^{-1} (STO-3G), 1.29 kcal mol^{-1} (STO-3G*) and 1.15 kcal mol^{-1} ((4)3-21G*). Recent work from the same group, including chains (dimer, trimer), rings (trimer, tetramer, pentamer, hexamer) and cages (prismatic hexamer, cubic octamer, hexagonal dodecamer) is reported in [171].

Ab-initio techniques, Hartree-Fock/MP2, using symmetry constraints, have been used [69] to study the interaction of silanediol molecule $SiH_2(OH)_2$ with H_2O and NH_3. Several different conformations were investigated for $SiH_2(OH)_2$, $Si(OH)_4$ and $Si(OSiH_3)_2(OH)_2$. The differences in energy between these different conformations are always between 3.5 kJmol^{-1} and 12 kJmol^{-1}.

A complete but older review of the structure of carbon-based rings, with a maximum of 10 carbons, including bridging oxygens and odd-membered rings, was presented by Dunitz [67]. The chair, crown and S-shaped conformations are recognised as the most stable for 6, 8 and 10 carbon rings. No equivalent work is known for silica-based or silicon-based cyclic structures. However,

the structure and energetics of planar rings in vitreous silica are reviewed by Galeener [79].

A complete vibrational analysis of $Si_8O_{12}H_8$, including its 78 normal modes of vibration, is presented by Bornhauser et al [38]. Its proposed structure, which is similar to that of $Si_8O_{12}(CH_3)_8$ [38], has a crown conformations for each of the face rings. Structural details, including bond lengths and bond angles, are also given in the paper.

In this chapter, the monomer and the dimer are investigated using non-local density and a triple basis set (DF-BLYP/TNP); the trimers are studied with non-local DFT and a double basis set (DF-BLYP/DNP); larger clusters are analysed at the LDA level of approximation only (DF-BHL/DNP). To save CPU time, the most promising geometries were first studied with inter-atomic potentials, submitting the system to molecular dynamics and periodically saving instantaneous geometries that were subsequently optimised by a static energy minimisation, or cooled until 0 K. In some cases semi-empirical methods (MOPAC) were also applied. The few selected geometries were then optimised fully with ab-initio DFT, using a SCF tolerance of 10^{-5} a.u. and a gradient tolerance of 0.015 a.u. for each coordinate.

The energy difference between the most important conformations and the corresponding total condensation energies (the energy to form the cluster directly from the monomer) are discussed, together with the structure and charge distribution. When determining the total condensation energy from LDA calculations, a correction factor of 3.3 kcal mol^{-1} is tentatively applied (see previous chapter) to all hydrogen bonds with O- -H distances smaller than 1.85 Å, which are in principle overestimated. The notation DF-BHL/DNP for von Berthe-Hedin-Lundqvist DF with double basis set, DF-BLYP/DNP for Becke-Lee-Yang-Parr DF with the same basis set and DF-BLYP/TNP for a triple basis set with the same functional, introduced in the previous chapter, is widely used throughout this work.

10.2 Intramolecular effects

In the case of $Si(OH)_4$, each OH group can be expected to project itself either along one of the three other SiO bonds or along the three bisector lines formed by these bonds. These corresponds to a maximum of $6^4 = 1296$ different conformations. Evidently, many of these are equal or equivalent (mirror images) and of the remaining, many are only stationary points in the Born-Oppenheimer potential surface, therefore evolving to a different conformation during the optimisation. But a undetermined number of different conformations, representing real minima of energy, still subsist.

Chemical knowledge helps to reduce this number considerably. Assuming that each OH group projects along the bisector lines formed by the SiO bonds, to minimise the electronic repulsion, but orientates relatively to other OH groups, in order to maximise hydrogen bond interactions, only two possible orientations are left for each OH group. When an SiO_4 group is seen along one of its three C_2 symmetry axes, each OH group will be disposed as either bending clockwise (+) or counterclockwise (-). The $2^4 = 16$ conformations thus found can be further reduced to only 4, applying successive symmetry transformations. It can be seen that $(abcd)$ is equal to $(-a-b-c-d)$ and $(abcd)$ is equal to $(cdab)$. Furthermore, $(abcd) \Leftrightarrow (dcba)$, because they are mirror images of each other. The conformation $(++++) = (----)$, with point symmetry S_4, is the energy global minimum in the gas phase. The conformation $(+-+-) = (-+-+)$, with point symmetry D_2d, is the most symmetric, due to its planes of symmetry. The structure and charge distribution for both conformations are presented in Figures 10.1 (DF-BHL/DNP level)

and 10.2 (DF-BLYP/TNP level).

With local-density and a double basis set, at the DF-BHL/DNP level of approximation, the energy difference between these conformations is only 0.9 kcal mol^{-1}. At the much higher DF-BLYP/TNP level of approximation, with non-local density and a triple basis set, the energy difference increases to 1.8 kcal mol^{-1}. The charges in the S_4 conformation are slightly larger but the dipole is smaller. These differences, though very small, should be significant, given the simplicity of the cluster.

Dimer

In the case of $Si_2O(OH)_6$, the number of different conformations depends on the relative orientation of the OH bonds and on the value of the SiOSi angle. At the relatively poor DF-BHL/DN level of approximation, without polarisation functions, three minima of energy were found for different SiOSi angles: 119.6°, 138.6° (+3.6 kcal mol^{-1}) and 169.7° (+4.9 $kcalmol^{-1}$). At the DF-BHL/DNP level of approximation, only two minima were found, for SiOSi angles equal to 118.4° and 164.6° (+10.0 kcal mol^{-1}). The existence of various minima of energy for the SiOSi angle reflects the soft character of this angle. It becomes harder, however, when the quality of the calculation increases, as the number of minima decreases and their energy differences are enhanced.

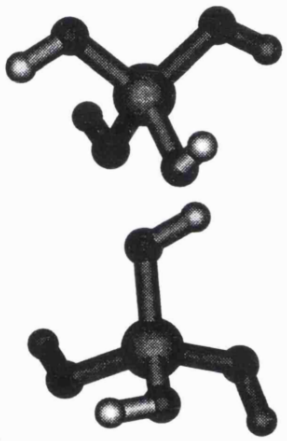
The number of conformations resulting from different arrangements of the OH bonds can be generated as in the monomer, but the complexity of the analysis increases considerably. The structure and charge distribution for the conformations with the lowest energy and the highest symmetry, respectively C_2 and C_{2v} (corresponding to the S_4 and D_2d monomer conformations) are presented in Figures 10.3 (DF-BHL/DNP level) and 10.4 (DF-BLYP/TNP level). At the DF-BHL/DNP level of approximation, the C_2 conformation is +11.0 kcal mol^{-1} more stable than the C_{2v}, while at the DF-BLYP/TNP level the difference decreases to +5.7 kcal mol^{-1}. These energy differences are substantial, even for the more sophisticated level of approximation, and show how important these conformation analysises are. The atomistic mechanisms undertaken by a given cluster depend considerably on its different conformations. Although no bond breaking is needed to transform one conformation into another, such energy barriers should be significant, particularly at low temperatures.

The charges in the C_2 conformation are influenced by the oxygen-hydrogen interactions, though these are expected to be very weak, considering the large O- -H distances and the small hydrogen bond energies, as discussed in the previous chapter. Oxygen and hydrogen atoms in donor hydroxyl groups have more positive charges, while the opposite is observed in acceptor hydroxyl groups, indicating some real charge transfer from the donor groups to the acceptors. In the C_{2v} conformation, the two terminal oxygens in the chain ends are more electronegative than the other four.

Structure

At the DF-BLYP/TNP level, the SiO bond length is slightly shorter and the OSiO and SiOH angles are slightly larger in the S_4 monomer conformation. At the same level of approximation, the bond lengths are equal in both dimer conformations. The SiOSi angle is smaller in the most stable C_2 conformation and the OSiO and SiOH angles are slightly larger.

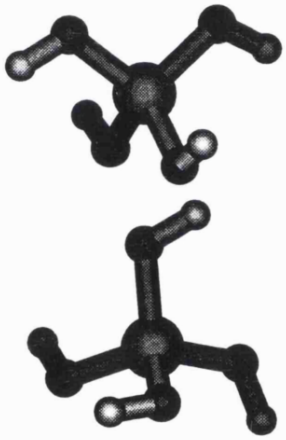
Si **4444**	SiO_b	*SiOSi*
O_b	SiO_t **1.64**	O_bSiO_b
O_t **2811**	*OH* **0.98**	O_tSiO_t **101.1-113.8**
H **1700**	*O-H*	*SiOH* **111.7**



Si **4473**	SiO_b	*SiOSi*
O_b	SiO_t **1.64**	O_bSiO_b
O_t **2842**	*OH* **0.99**	O_tSiO_t **105.6-117.6**
H **1724**	*O-H*	*SiOH* **112.4**

Figure 10.1: Bond lengths (Å), bond angles (degrees) and Hirshfeld atomic charges (0. and minus signal in O charges are omitted) for D_2d and S_4 $Si(OH)_4$ conformations, optimised at the DF-BHL/DNP level of approximation. Total energy: E = -589.89232 Ha (D_2d) and E = -589.89392 Ha (S_4).

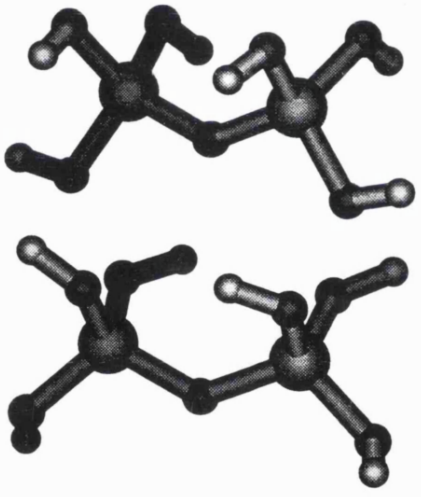
Si **5257**	SiO_b	$SiOSi$
O_b	SiO_t **1.66**	O_bSiO_b
O_t **2938**	OH **0.97**	O_tSiO_t **103.2-112.7**
H **1625**	O-H	$SiOH$ **114.6**



Si **5271**	SiO_b	$SiOSi$
O_b	SiO_t **1.65**	O_bSiO_b
O_t **2968**	OH **0.97**	O_tSiO_t **106.6-115.4**
H **1650**	O-H	$SiOH$ **116.5**

Figure 10.2: Bond lengths (Å), bond angles (degrees) and Hirshfeld atomic charges (0. and minus signal in O charges are omitted) for D_2d and S_4 $Si(OH)_4$ conformations, optimised at the DF-BLYP/TNP level of approximation. Total energy: E = -593.13921 Ha (D_2d) and E = -593.14211 Ha (S_4).

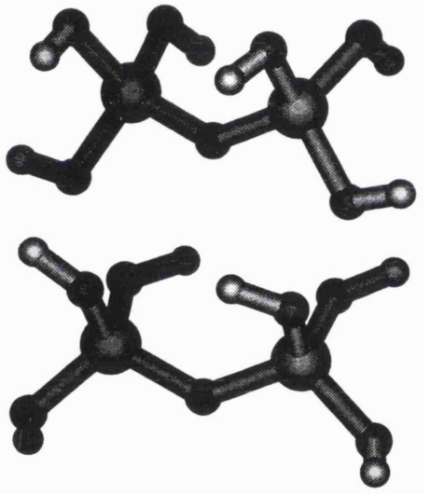
Si **4525**	SiO_b **1.64**	*SiOSi* **126.2**
O_b **2750**	SiO_t **1.64**	O_bSiO_b
O_t **2689-2832**	*OH* **0.98**	O_tSiO_t **102.0-114.6**
H **1695-1721**	*O-H*	*SiOH* **111.2-113.8**



Si **4598**	SiO_b **1.65**	*SiOSi* **118.4**
O_b **2777**	SiO_t **1.63-1.66**	O_bSiO_b
O_t **2433-2935**	*OH* **0.98-1.00**	O_tSiO_t **110.7-114.0**
H **1212-1839**	*O-H* **1.91**	*SiOH* **107.7-113.5**

Figure 10.3: Bond lengths (Å), bond angles (degrees) and Hirshfeld atomic charges (0. and minus signal in O charges are omitted) for C_{2v} and C_2 $Si_2O(OH)_6$ conformations, optimised at the DF-BHL/DNP level of approximation. Total energy: E = -1103.8749 Ha (C_{2v}) and E = -1103.8924 Ha (C_2). Dipole moment: μ = 1.49 D (C_{2v}) and μ = 1.09 D (C_2).

Si **5343**	SiO_b **1.65**	$SiOSi$ **136.6**
O_b **3030**	SiO_t **1.65-1.66**	O_bSiO_b
O_t **2863-3030**	OH **0.97**	O_tSiO_t **103.2-112.7**
H **1607-1628**	O-H	$SiOH$ **113.8-116.2**



Si **5368**	SiO_b **1.65**	$SiOSi$ **132.1**
O_b **3036**	SiO_t **1.64-1.66**	O_bSiO_b
O_t **2837-3036**	OH **0.97**	O_tSiO_t **107.8-113.7**
H **1490-1687**	O-H **2.52**	$SiOH$ **114.1-117.7**

Figure 10.4: Bond lengths (Å), bond angles (degrees) and Hirshfeld atomic charges (0. and minus signal in O charges are omitted) for C_{2v} and C_2 $Si_2O(OH)_6$ conformations, optimised at the DF-BLYP/TNP level of approximation. Total energy: E = -1109.8232 Ha (C_{2v}) and E = -1109.8323 Ha (C_2). Dipole moment: μ = 1.60 D (C_{2v}) and μ = 0.85 D (C_2).

10.3 Cyclisation effects

The linear trimer and the trimer ring are the largest silicate clusters studied in this work with non-local density. The comparison between the results obtained for DF-BHL/DNP and DF-BLYP/DNP levels of approximation is therefore important, because it helps us to estimate the accuracy of the results obtained for the larger clusters, where only DF-BHL/DNP calculations are available.

At the DF-BHL/DNP level of approximation, the best conformation found for the linear trimer is almost cyclic, with two hydrogen bonds closing the ring. This conformation is 3.0 kcal mol^{-1} more stable than the straight one, where the chain ends are far apart. The structure and charge distribution for both conformations are shown in Figures 10.5 (DF-BHL/DNP level) and 10.6 (DF-BLYP/DNP). At the DF-BLYP/DNP level (including non-local exchange and correlation), the difference in energy between these conformations decreases only slightly, to 2.2 kcal mol^{-1}.

The almost cyclic conformation may, in turn, be transformed into the trimer ring, by a intramolecular condensation reaction. The corresponding energy, though positive, is relatively small: +16.9 kcal mol^{-1} at the DF-BHL/DNP level and +13.2 kcal mol^{-1} at the DF-BLYP/DNP level. This helps to explain how a relatively strained cluster as the three-silicon ring is actually formed.

The hydrogen bonds are overestimated at the DF-BHL/DNP level of approximation, because the bond lengths O- -H are too small ($\approx$ 1.64 Å) and the OH bond lengths in the acceptor groups are too large (1.02 Å). The total condensation energy is consequently too high (-18.5 kcal mol^{-1}) when compared with the best results obtained for the dimer. Applying the energy difference between local and non-local DF found for the dimer (3.3 kcal mol^{-1} per hydrogen bond), the corrected condensation energy becomes equal to -11.9 kcal mol^{-1}, which seems more reasonable-considering the dimer results.

At the DF-BLYP/DNP level of approximation, the condensation energy becomes -7.7 kcal mol^{-1}, smaller than even the corrected DF-BHL/DNP value. For larger clusters with hydrogen bonds, which at the moment can only be studied at the DF-BHL/DNP level of approximation, the calculated condensation energies should therefore be highly overestimated and even the corrected values should be a crude upper limit for the correct results. This is due to the increasing number of weak interactions developed in these larger clusters, overestimated in local density calculations but too small to be corrected.

At the DF-LYP/DNP level, the O- -H and OH bond lengths, respectively 1.83 Å and 1.00 Å, seem to be close to the correct values. However, because non-local density calculations tend to overestimate the bond lengths, the correct SiO bond lengths, in particular, should be about 0.04 Å shorter than calculated here. The $SiOSi$, O_bSiO_b, O_tSiO_t and $SiOH$ angles are very similar in both calculations. Both calculations predict the same dipole moment for the closed conformation (0.35 D), but very different values (0.39 D and 1.55 D) for the straight one.

Linear tetramer

As in the linear trimer, the lowest energy conformation found for the linear tetramer is almost cyclic, with hydrogen bonds linking the chain ends and forming a cyclic system, where each hydrogen is covalently bonded to a oxygen and coulombically attracted to another one. At the DF-BHL/DNP level of approximation, this curved conformation is 11.6 kcal mol^{-1} more stable than the straight conformation. The structure and charge distribution for both conformations are presented in the Figure 10.7. The five hydrogen bonds in the curved conformation have an

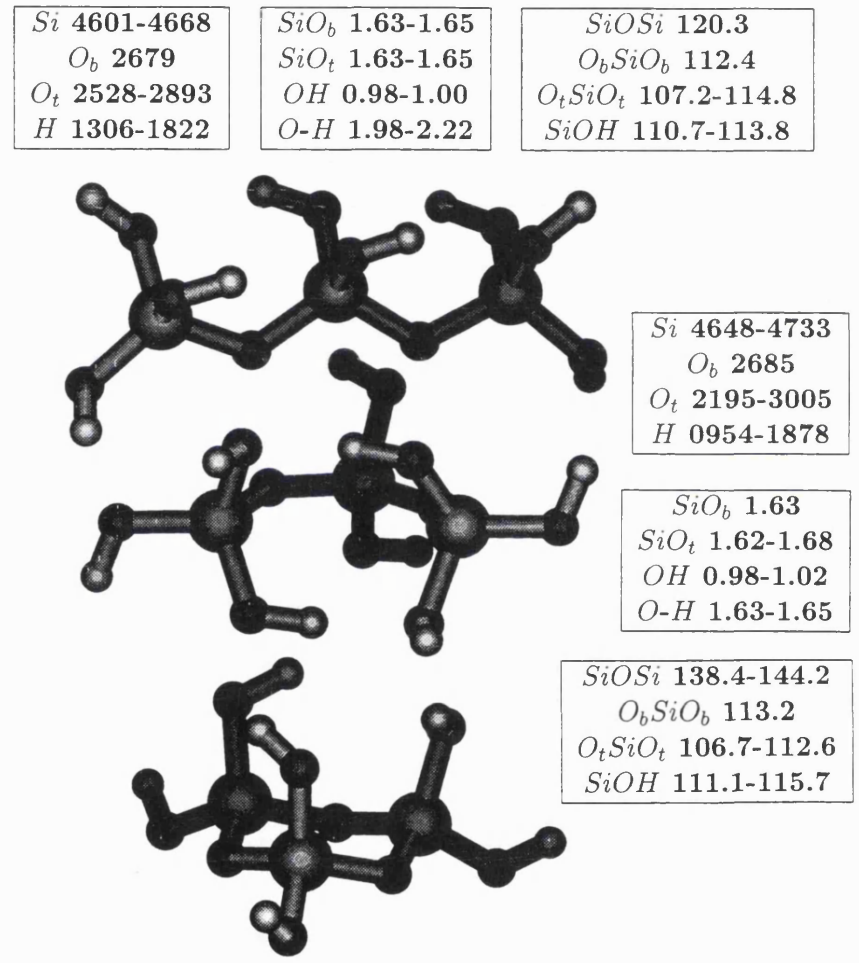


Figure 10.5: Bond lengths (Å), bond angles (degrees) and Hirshfeld atomic charges (0. and minus signal in O charges are omitted) for $Si_3O_2(OH)_8$ conformations forming $Si_3O_3(OH)_6$, optimised at the DF-BHL/DNP level of approximation. Total energy: E = -1617.8857 Ha (above), E = -1617.8905 Ha (medium) and E = -1541.9532 Ha (below). Dipole moment: μ = 0.39 D (above), μ = 0.35 D (medium) and μ = 1.68 D (below).

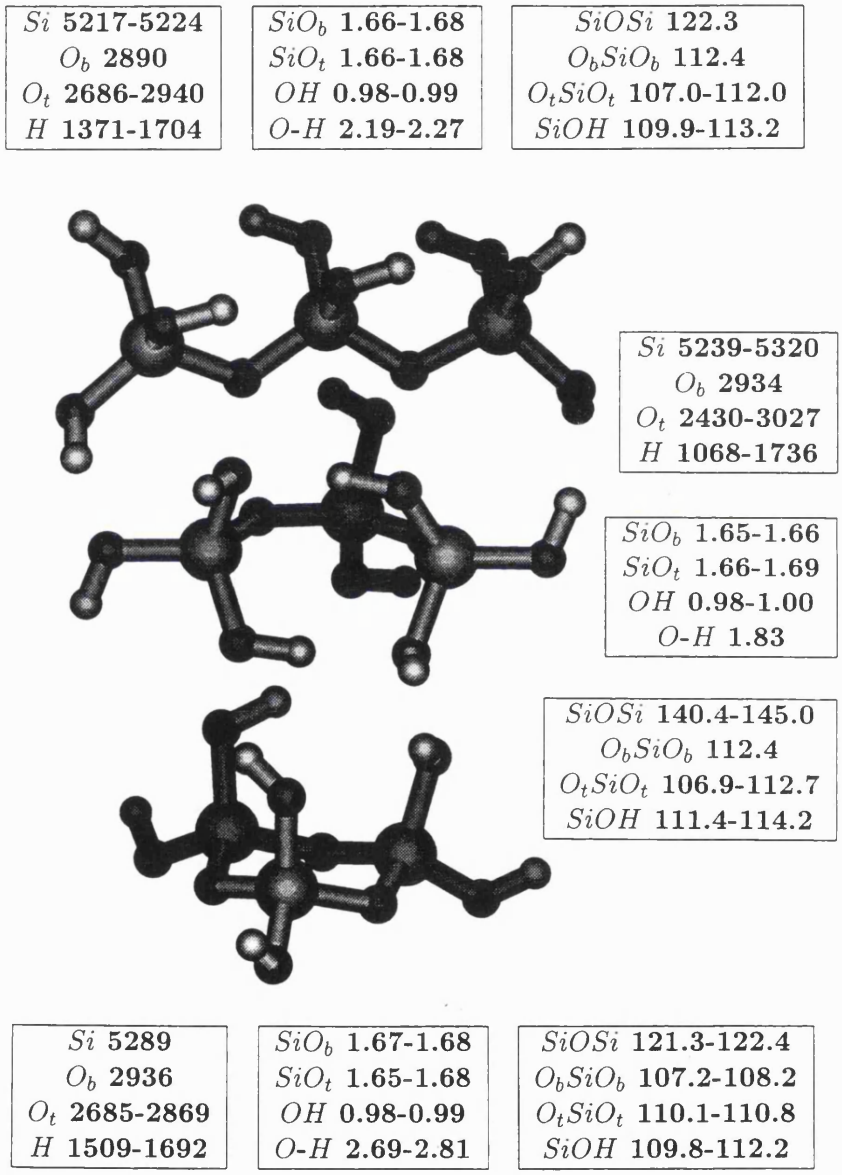


Figure 10.6: Bond lengths (Å), bond angles (degrees) and Hirshfeld atomic charges (0. and minus signal in O charges are omitted) for $Si_3O_2(OH)_8$ conformations forming $Si_3O_3(OH)_6$, optimised at the DF-BLYP/DNP level of approximation. Total energy: E = -1626.4160 Ha (above), E = -1626.4195 Ha (medium) and E = -1549.9572 Ha (below). Dipole moment: μ = 1.55 D (above), μ = 0.36 D (medium) and μ = 3.2 D (below).

O- -H distance too short (1.51-1.68 Å) and an OH distance too large (1.01-1.05 Å), while the six hydrogen bonds in the straight conformation are much weaker (with O- -H distances between 1.92 Å and 2.11 Å).

Although it is not clear what would be the results with a better level of approximation, it seems reasonable to expect that the curved conformation would be still a highly probable one, in agreement with the experimental evidence, which shows that it is relatively easy to produce four-silicon rings. The easiest way to get a four-silicon ring is probably to close a open four-silicon linear chain and that should be particularly simple starting from this almost cyclic conformation.

The total condensation energy for the curved conformation (-38.2 kcal mol^{-1}), seems too large when comparing with the best dimer calculations. Applying the correction factor estimated in the previous chapter for each overestimated hydrogen bond, the corrected condensation energy for the most stable conformation becomes equal to -21.7 kcal mol^{-1}. Even this value might be stil too negative. Because of its lower symmetry, this conformation has a higher electric dipole moment (2.75 D), than the corresponding straight conformation (2.40 D).

Linear pentamer

The lowest energy conformation found for the linear pentamer is a relatively complex structure, almost cyclic, with four hydrogen bonds closing three secondary rings: two with 8 atoms and a third one with 10. At the DF-BHL/DNP level of approximation, this conformation is 11.4 kcal mol^{-1} more stable than the straight conformation. The structure and charge distribution for both conformations are presented in the Figure 10.8.

The total condensation energy for the curved conformation is substantially negative (-43.6 kcal mol^{-1}). Even after correcting the energy, to account for the overestimation of the four hydrogen bonds, the condensation energy becomes only 1.8 kcal mol^{-1}) smaller than for the uncorrected straight conformation. It is reasonable therefore to expect that, at higher levels of approximation, the almost cyclic conformation will remain a highly stable conformation.

In spite of its complexity, this conformation is remarkable because it allows the subsequent formation of several different clusters through a single intramolecular condensation. If each of the four oxygen atoms bonded to hydrogens in different silicons (see Figure 10.8, below) react directly with these instead, in a nucleophilic attack, the five silicon ring (), the branched four silicon ring (), the branched three silicon ring (), and the double branched three silicon ring () might be formed. The O- -H distance in the four hydrogen bonds is too short (1.60-68 Å), due to the LDA overestimation of these bonds. The electric dipole moment is higher in the most stable conformation (3.23 D) than in the straight one (2.70 D), due to the highly asymmetric structure and charge distribution of the former.

Structure

In the linear trimer, the two SiO bonds bonded to hydrogen-bond donors are weaker and longer (1.67-1.68 Å) than normal, whereas the other two bonded to hydrogen-bond acceptors are stronger and shorter (1.62 Å). The primary bonds in OH donor groups are weaker due to the charge transference to the outer region, whereas the acceptor OH groups have larger OH distances because the hydrogens are attracted to the outer oxygen, but smaller SiO lengths, because the oxygen charge can be redistributed more between the oxygen and silicon atom. Hydroxyl groups acting simultaneously as donors and acceptors, where the oxygen and the hydrogen participate in different hydrogen bonds, present intermediate OH and SiO bond lengths.

In the linear tetramer, the four hydroxyl groups in equatorial positions present typical dis-

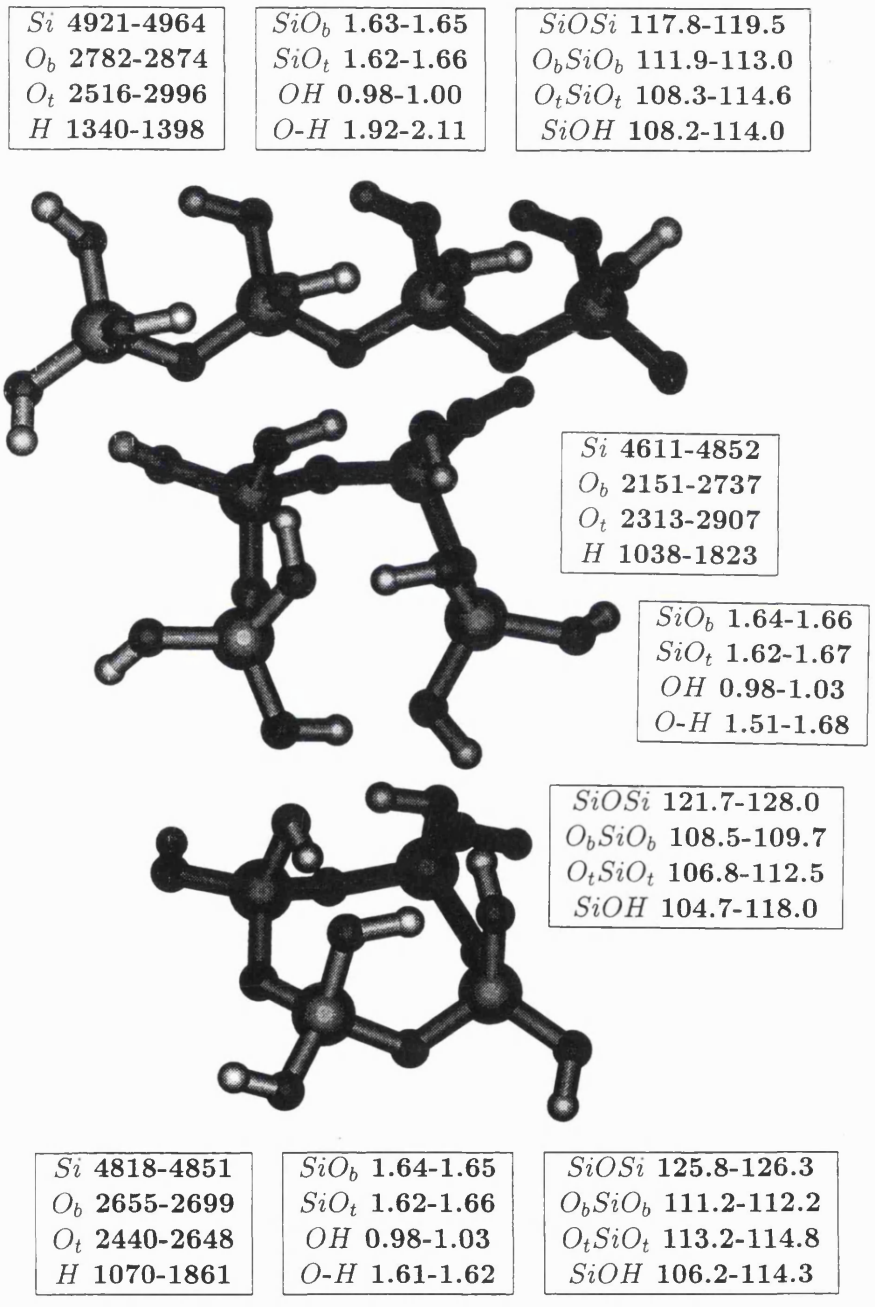
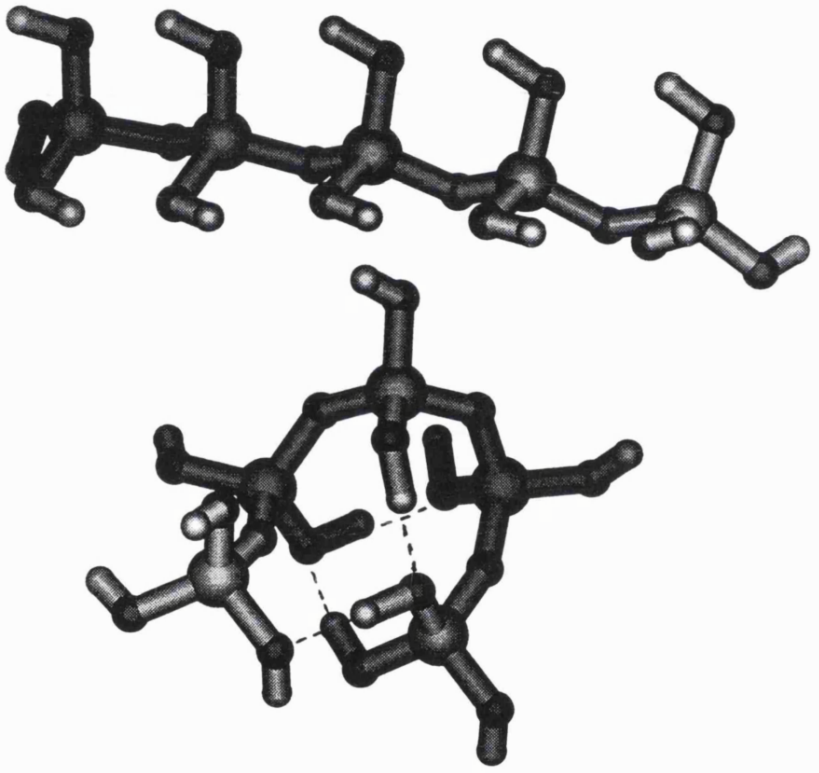


Figure 10.7: Bond lengths (Å), bond angles (degrees) and Hirshfeld atomic charges (0. and minus signal in O charges are omitted) for $Si_4O_3(OH)_{10}$ conformations forming $Si_4O_4(OH)_8$, optimised at the DF-BHL/DNP level of approximation. Total energy: E = -2131.8869 Ha (above), E = -2131.9053 Ha (medium) and E = -2055.9751 Ha (below). Dipole moment: μ = 2.40 D (above), μ = 2.75 D (medium) and μ = 0.65 D (below).

Si **4638-4678**	SiO_b **1.63-1.65**	$SiOSi$ **116.9-118.2**
O_b **2538-2636**	SiO_t **1.63-1.66**	O_bSiO_b **110.0-112.8**
O_t **2435-2887**	OH **0.98-1.00**	O_tSiO_t **108.4-115.1**
H **1291-1851**	O-H **1.95-2.07**	$SiOH$ **108.2-113.5**



Si **4579-4890**	SiO_b **1.62-1.66**	$SiOSi$ **130.4-159.2**
O_b **2559-2734**	SiO_t **1.61-1.67**	O_bSiO_b **105.8-116.1**
O_t **2120-2930**	OH **0.98-1.02**	O_tSiO_t **106.6-112.4**
H **0958-1916**	O-H **1.60-1.68**	$SiOH$ **110.0-117.7**

Figure 10.8: Bond lengths (Å), bond angles (degrees) and Hirshfeld atomic charges (0. and minus signal in O charges are omitted) for $Si_5O_4(OH)_{12}$ conformations, optimised at the DF-BHL/DNP level of approximation. Total energy: E = 2645.8794 Ha (above) and E = -2645.8975 Ha (below). Dipole moment: μ = 2.70 D (above) and μ = 2.23 D (below).

tances, for this level of approximation (SiO = 1.63-1.64 Åand OH = 0.98 Å). The SiO bond length increases slightly for the four hydroxyl groups participating in the cyclic hydrogen bond system, 1.64-1.67 Å, whereas in the (isolated) fifth hydrogen bond, SiO is equal to 1.66 Å for the donor oxygen, and 1.62 Å for the oxygen bonded to the acceptor hydrogen.

In the linear pentamer, the SiO and OH bond lengths in unconstrained outer hydroxyl groups (0.98-0.99 Åand 1.63-1.64 Å) are similar to the values calculated for other clusters. As in the linear trimer and tetramer, the two OH groups that act only as donors have larger OH and SiO distances (0.99 Å and $\approx$ 1.66 Å), whereas the two OH acceptor groups have larger OH distances (1.02 Å) but smaller Si-O lengths, 1.61-1.63 Å. The pentamer straight conformation, with weaker hydrogen bonds (O- -H equal to 1.94-2.13 Å), present intermediate values for the SiO and OH bond lengths and relatively small SiOH angles ($< 113.5^o$), due to the directionality of the hydrogen bonds.

The $SiOSi$ angles are significantly larger in the linear trimer ($\approx 141^o$) than in the dimer, due to its almost cyclic arrangement (in the trimer straight conformation, these angles are just 120.3^o). In the linear tetramer, although the O_bSiO_b angle remains almost constant, the $SiOSi$ angles still have a small range of variation due to the closing hydrogen bonds (the middle $SiOSi$ is about 6^o smaller than the other two). In the tetramer, the angles $SiOH$ change between 104.7^o (in the constrained system of four hydrogen bonds) and 118.0^o (in the equatorial free SiOH groups), almost matching Sauer's reference value for the monomer.

In the linear pentamer, the SiOH angle is very similar for terminal and constrained OH groups (111.5-115.0^o and 110.0-117.7^o) respectively. In the pentamer the O_bSiO_b angle presents significant changes along the chain (105.8-116.1^o) though the $SiOSi$ angles are clearly much softer, changing in a very large range of values (between 130.4-159.2^o), that reflects the asymmetry of this conformation. In spite of the hydrogen bonds, the O_tSiO_t angles are very similar in all these clusters (106.5-112.5^o).

10.4 Ring effects

Figure 10.9 shows the structure and charge distribution for the three most important conformations found in this work for the cyclic trimer. At the DFT-BHL/DN level, the first conformation is +5.0 kcal mol^{-1} more stable than the second, but at the DFT-BHL/DNP level, the energy of the second conformation is already 0.8 kcal mol^{-1} lower. The order in energy of these conformations changed, consequently, just by adding polarisation functions to the basis set. This was the only case throughout this work where such energy swap was observed, and in fact, the influence of the calculation method in the results is expected to decrease significantly when the level of accuracy increases. Nevertheless, for minima relatively close in energy, these effects might happen even for more sophisticated levels of approximation.

In fact, none of these planar ring conformations represent the global minimum of energy for this cluster. The third conformation represented in the Figure 10.9 is 5.3 kcal mol^{-1} more stable than the second (at the DF-BHL/DNP level) and is the lowest energy conformation that we found for the trimer ring. It has a *chair* conformation (as in 6-carbon rings), where three hydroxyl groups occupy equatorial positions, and the other three are disposed in axial positions, forming a strong system of three hydrogen bonds. At this level of approximation, the total energy of condensation is still exothermic (-1.6 kcal mol^{-1}), in spite of the strain associated with this ring.

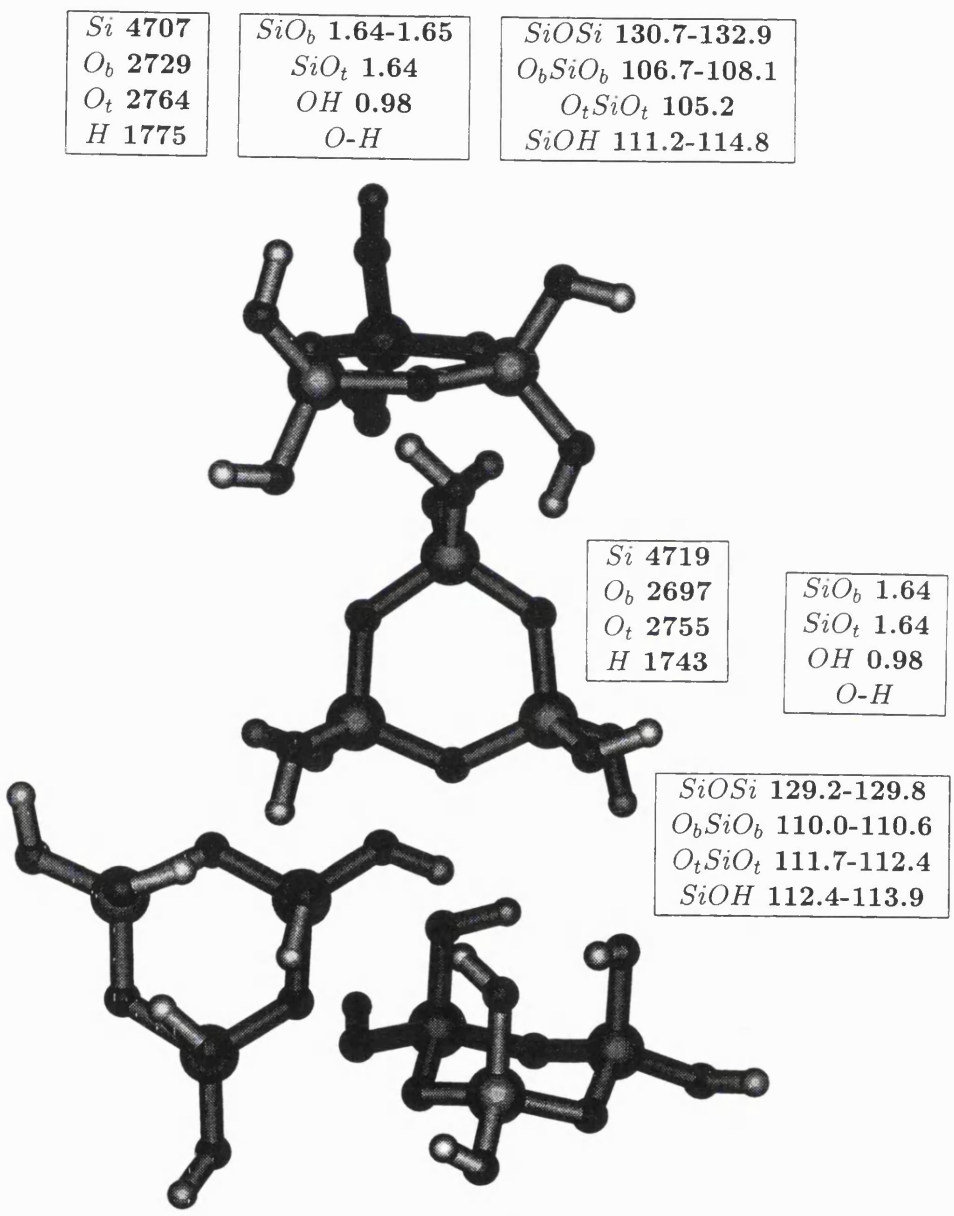


Figure 10.9: Bond lengths (Å), bond angles (degrees) and Hirshfeld atomic charges (0. and minus signal in O charges are omitted) for $Si_3O_3(OH)_6$ conformations, optimised at the DF-BHL/DNP level of approximation. Total energy: E = -1541.9434 Ha (above), E = -1541.9447 Ha (medium) and E = -1541.9532 Ha (below). Dipole moment: μ = 1.53 D (above), μ = 0.35 D (medium) and μ = 1.68 D (below).

The orientation of the equatorial *OH* groups, the same of the axial groups or the opposite one, was investigated at a higher level of approximation (DF-BLYP/DNP): the conformation with the same orientation for both axial and equatorial *OH* groups was found to be slightly more stable (+1.4 kcal mol^{-1}). This energy difference is very small (because the equatorial hydrogens are isolated) and may change for a larger basis set. At the DF-BLYP/DNP level of approximation, the total condensation energy is already positive but still small (+5.5 kcal mol^{-1}) so it can be formed in silica solutions, as experimental evidence shows, despite its internal strain.

For both levels of approximation, the axial hydrogens have smaller charges than the equatorial ones (due to the axial hydrogen bonds), but the oxygen charges are very similar. In spite of its higher symmetry, this cluster seems to have a much larger charge separation than the open trimer, apparently due to the different orientation in space of the two sets of hydroxyl groups. In fact, the dipole moment for the DF-BLYP/DNP calculation seems too high and probably will change significantly for better basis sets.

Tetramer ring

The lowest energy conformation found for the four-silicon ring is a *crown* conformation (the most stable conformation in 8-carbon rings [67]), which decreases the ring strain and allows the formation of a strong cyclic system of four hydrogen bonds, decreasing considerably the energy of the cluster. At the DF-BHL/DNP level of approximation, this conformation is 31.9 kcal mol^{-1} more stable than the planar one, highly symmetric but with relatively weak hydrogen-bond interactions. This difference in energy is the largest found throughout all this work between two conformations of the same cluster. The structure and charge of both conformations is presented in the Figure 10.10.

Although the ring strain should be considerably smaller in this cluster than in the more constrained trimer ring, the total condensation energy for the crown conformation (-25.7 $kcalmol^{-1}$) seems too negative, when compared with the non-local density results obtained for the two- and three-silicon clusters. Furthermore, it is only 5 kcal mol^{-1} higher than the corresponding value for the branched tetramer. This is due essentially to the LDA overestimation of the four hydrogen bonds, whose bond length is too small ($\approx$ 1.62 Å). Correcting the energy following the results for the dimer, the condensation energy becomes equal to -12.5 $kcalmol^{-1}$, which is much more reasonable.

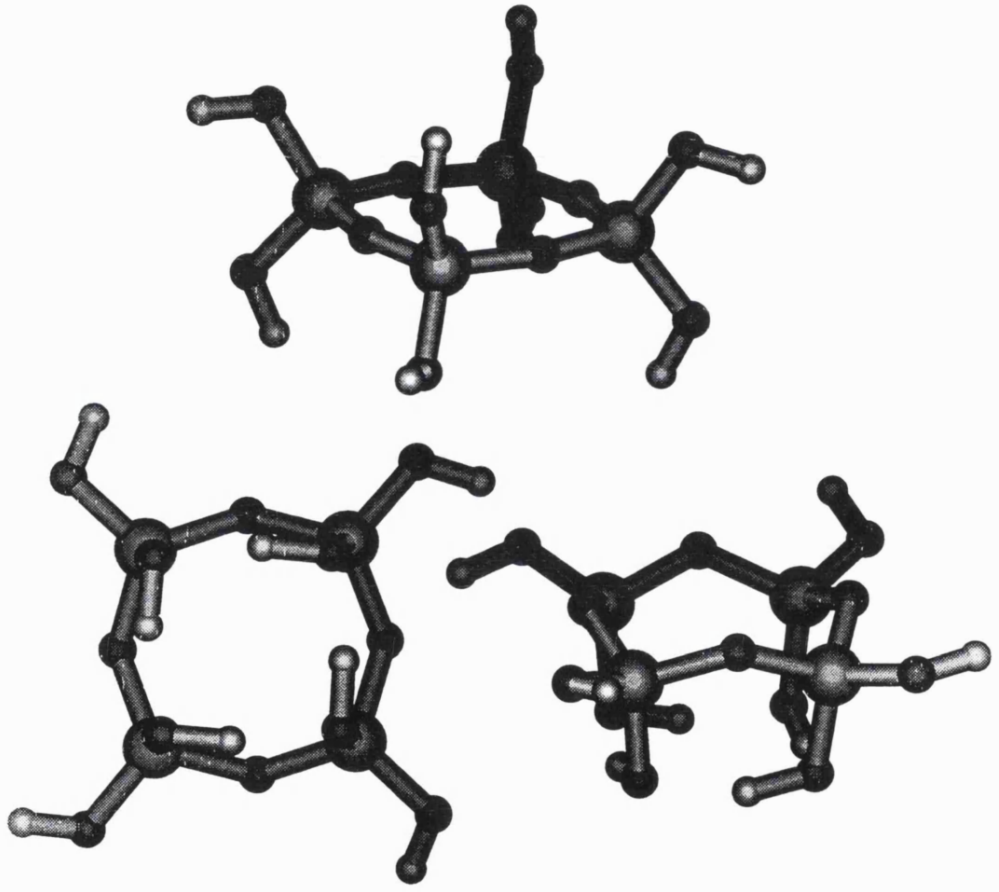
Despite the very different atomic arrangements on both sides of the ring, the cluster with a crown conformation has a relatively small electric dipole (0.65 D), much smaller than in the other four-silicon clusters (or even in the three silicon ring, with a similar hydrogen bond system). The electric dipole moment of the planar conformation is zero, as results from its symmetry.

Octamer cage

The structure and charge distribution for the most important conformations of the octamer cage (particularly important in zeolite catalysts) are shown in the Figure 10.11. These conformations differ only in the atomic arrangement of the six rings forming the cubic cage. In one conformation the rings have a crown arrangement, like in the tetramer ring, while in the other they have a non-planar hexagonal arrangement, where each oxygen is in the plane of one face of the cube and out of the plane of the face adjacent. Each ring in the cage defines a window, which is almost circular in the crown arrangement (of dimensions 3.8 Å $\times$ 3.8 Å), and rectangular in the hexagonal arrangement (of dimensions 4.2 Å $\times$ 3.1 Å).

There are no hydrogen bonds in this cluster, because the hydroxyl groups are too far apart.

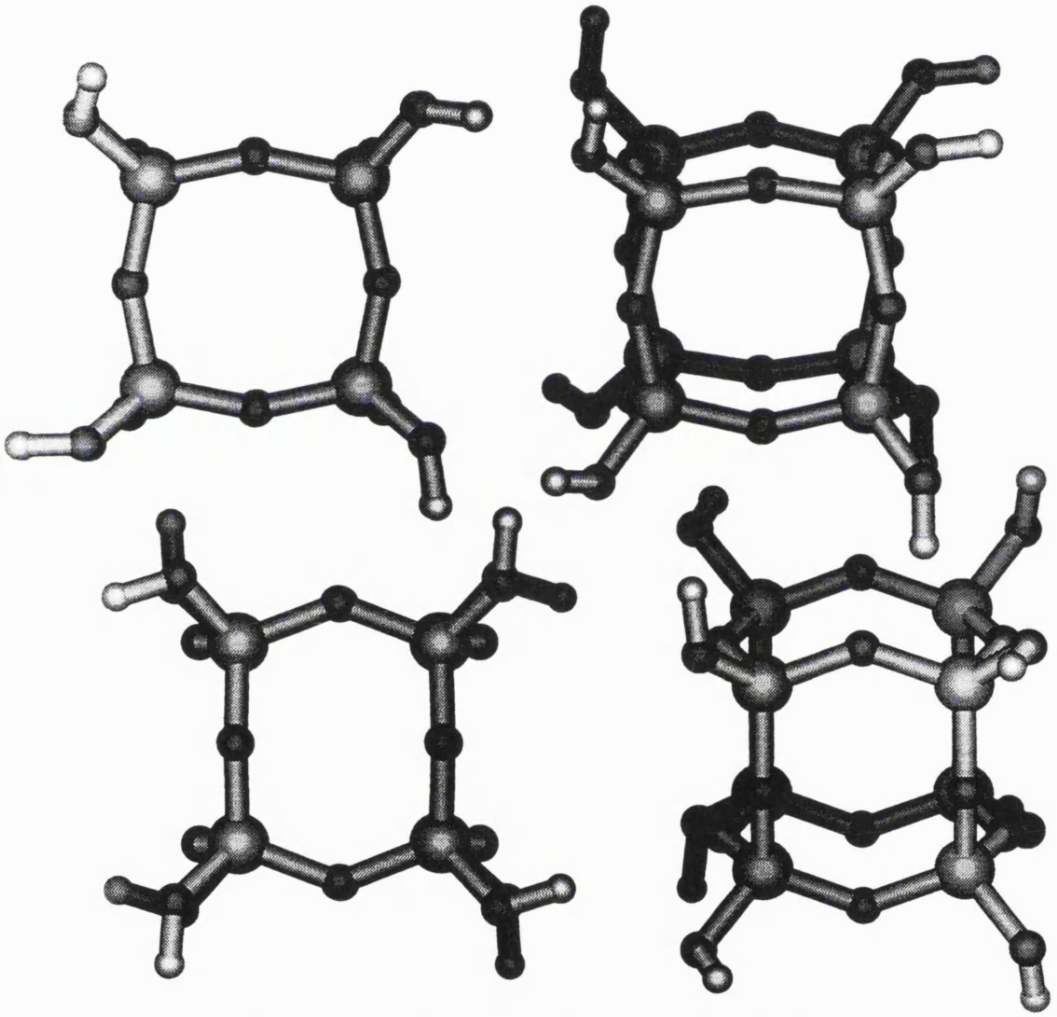
Si **4778**	SiO_b **1.62**	$SiOSi$ **160.4**
O_b **2718**	SiO_t **1.64**	O_bSiO_b **109.5**
O_t **2782-2816**	OH **0.98**	O_tSiO_t **106.0**
H **1753-1786**	O-H	$SiOH$ **112.0-114.5**



Si **4818-4851**	SiO_b **1.64-1.65**	$SiOSi$ **125.8-126.3**
O_b **2655-2699**	SiO_t **1.62-1.66**	O_bSiO_b **111.2-112.2**
O_t **2440-2648**	OH **0.98-1.03**	O_tSiO_t **113.2-114.8**
H **1070-1861**	O-H **1.61-1.62**	$SiOH$ **106.2-114.3**

Figure 10.10: Bond lengths (Å), bond angles (degrees) and Hirshfeld atomic charges (0. and minus signal in O charges are omitted) for $Si_4O_4(OH)_8$ conformations, optimised at the DF-BHL/DNP level of approximation. Total energy: E = -2055.9243 Ha (above) and E = -2055.9751 Ha (below). Dipole moment: μ = 0.01 D (above) and μ = 0.65 D (below).

Si **4871**	SiO_b **1.62-1.63**	$SiOSi$ **125.7-150.3**
O_b **2651**	SiO_t **1.63**	O_bSiO_b **108.6-112.1**
O_t **2705**	OH **0.98**	O_tSiO_t -
H **1814**	O-H	$SiOH$ **113.0-114.6**



Si **4845**	SiO_b **1.63-1.64**	$SiOSi$ **136.3-138.0**
O_b **2611**	SiO_t **1.63**	O_bSiO_b **109.6-111.2**
O_t **2703**	OH **0.98**	O_tSiO_t -
H **1817**	O-H	$SiOH$ **113.6-113.9**

Figure 10.11: Bond lengths (Å), bond angles (degrees) and Hirshfeld atomic charges (0. and minus signal in O charges are omitted) for $Si_8O_{12}(OH)_8$ conformations, optimised at the DF-BHL/DNP level of approximation. Total energy: E = -3808.2177 Ha (above) and E = -3808.2202 Ha (below).

Consequently, the energy and structure obtained with Local Density Approximation should be particularly accurate and the energy difference between the two conformations should be essentially due to the framework of the two cages. At the DFT-BHL/DNP level of approximation, the six hexagon conformation is +1.6 kcal mol^{-1} more stable than the six crown conformation. Replacing the hydroxyl groups by hydrogen atoms, the difference in energy between the two conformations decreases to only 0.5 kcal mol^{-1}.

The condensation energy for $Si_8O_{12}(OH)_8$, though positive (+4.1 kcal mol^{-1}), is still smaller than the energy of a single hydrogen bond, which helps to explain why a relatively strained cluster as this is formed in solution. As expected for such a highly symmetric conformation, the electric dipole moment is zero. The charges of the atoms forming the cage are slightly higher in the lowest energy conformation but the difference is probably too small to be significant.

Structure

In the less stable trimer ring conformation, the O_tSiO_t angle is smaller due to the interaction between adjacent hydroxyl groups. The $SiOSi$ angle is much larger in the two planar rings than in the chair conformation ($\approx$ 116.0^o). In this conformation, the $SiOSi$, O_bSiO_b and O_tSiO_t angles change very little, due to the symmetry constraints imposed by the ring and the directionality of the hydrogen bonds. The $SiOH$ angle assumes two distinct values, one for the equatorial hydroxyl groups ($\approx$ 114.5^o, as in previous clusters), and another one, which is much smaller ($\approx$ 106.8^o), for the axial hydroxyl groups, that are constrained to assume values closer to 90^o, by the directionality of the hydrogen bonds.

In general, the atoms involved in hydrogen bonds tend to form weaker primary bonds, with longer bond lengths. In the trimer ring, where each axial oxygen simultaneously donates charge to a hydrogen and is bonded to an acceptor hydrogen, the SiO_t and OH bond lengths are equal to 1.66-1.67 Å and 1.00 Å, while in the equatorial hydroxyl groups these values decrease to 1.62 Å and 0.98 Å, respectively. The SiO_b bond length in the ring is 0.02-0.03 Å larger than the corresponding bond length in the open trimer, due to the strain present in such a small ring. At the DF-BHL/DNP level of approximation, the O- -H distances (1.93-1.99 Å) are much larger than in the open trimer, because they result from the balance between the electrostatic forces that tend to move the hydroxyl groups closer and the covalent forces that tend to move them more far apart (to decrease the ring strain). At the DF-BLYP/DNP level, where hydrogen bonds are not overestimated, the O- -H distances are already much longer (2.69-3.01 Å) than in the linear trimer. The $SiOSi$ angle in the trimer ring is larger in the DF-BLYP/DNP calculation (121.3-122.4^o) than in the DF-BHL/DNP (115.7-116.1^o).

In the tetramer ring, the SiO bond length is calculated as 1.62 Å in the equatorial groups, as 1.64-1.65 Å in the ring, and as 1.66 Å in the terminal groups forming hydrogen bonds. The OH bond length is calculated as 0.98 Å in the four equatorial hydroxyl groups (a normal value for this level of approximation) but is too large in the four hydrogen bonds (1.03 Å). In the planar conformation, where hydrogen-bonds are much weaker, the SiO bond length follows exactly the opposite trend, being smaller in the ring (1.62 Å) than in the terminal groups (1.64 Å).

In the four-silicon ring the $SiOSi$ angles (125.8-126.3^o) are larger than in the three-silicon ring (115.7-116.1^o). The O_bSiO_b angles (111.2-112.2^o) are closer to the tetrahedral value than the O_tSiO_t angles (113.2-114.8^o) though these should be less constrained. The $SiOH$ angle assumes two different sets of values, one in the equatorial hydroxyl groups (113.3-114.3^o) and another much smaller in the axial hydroxyl groups ($\approx$ 106.4^o), due to the hydrogen bonds. The $SiOSi$ angle is much larger (160.4^o) in the planar conformation, reflecting the different atomic

arrangements of the two rings. The O_bSiO_b and O_tSiO_t angles are slightly smaller in the planar conformation, in the latter case because of the interactions between adjacent hydroxyl groups.

In the cubic cage, the $SiOSi$ angles are almost constant in the more stable conformation (and larger than in acyclic systems) but they change considerably in the six crown conformation. This large range of variation and the small energy difference between the two conformations shows that the $SiOSi$ angle is extremely soft. The bond lengths and O_bSiO_b and $SiOH$ bond angles are essentially constant and equal in both conformations.

To study $Si_8O_{12}H_8$ has the additional advantage of permitting us to compare the calculated values with the experimental data available for this cluster. As determined by Larsson [38], the SiH and SiO bond lengths, and $OSiH$, $OSiO$ and $SiOSi$ bond angles are respectively 1.475 Å and 1.659 Å, and 112.2°, 106.6° and 153.9°. Interestingly, the SiO bond length and Si-O-Si bond angle are relatively large.

10.5 Conclusions

The results for gas-phase species presented here show that important differences in energy (and structure and charge distribution) can be expected between different conformations of the same silicate clusters. This is essentially due to the strong intramolecular hydrogen bonds formed by the terminal hydroxyl groups, even in small silicate clusters, such as the dimer, the cyclic trimer and the cyclic tetramer. In the monomer and cubic cage, where there are no hydrogen bonds, the differences in energy are very small.

Differences in the internal frame contribute very little to the energy barrier, as can be seen in the cubic cage, because the SiOSi angle is very flexible. The chair and crown arrangements in the trimer and tetramer rings lead to very stable conformations, essentially because they allow the formation of strong systems of hydrogen bonds. (It would be interesting to study the various conformations for $Si_3O_3H_6$ and $Si_4O_4H_8$ and to compare with $C_3O_3H_6$ and $C_4O_4H_8$).

The results presented for the linear clusters (trimer, tetramer and pentamer) show that in the gas phase the straight conformations are less stable than the curved ones, where the two ends of the chain interact directly, forming almost cyclic structures. These, in turn, can react directly, by a intramolecular condensation, to form the corresponding rings. These results give important support to a two-stage mechanism for the ring formation in silicates: physical interaction followed by chemical bonding. However, the trend to adopt curved conformations is likely to be reduced in the liquid phase and further calculations are necessary to clarify this point.

The barrier of energy between two conformations depends on the level of approximation used. In extreme cases, the order of stability of two conformations can be inverted, changing only the basis set, as illustrated by the ring trimer. This dependency decreases rapidly when the level of approximation increases.

The strong hydrogen bonds formed by hydroxyl groups and the flexibility of the $SiOSi$ angle are the most important features of the chemistry of silicate clusters in vacuo. These two factors lead to the formation of many minima with considerably different energies, making the search for global energy minima particularly difficult in these clusters. Although the structure and charge distribution of different conformations can be very different, the local properties, bond lengths and partial charges change very little, unless strong hydrogen bonds are involved. In that case, the results obtained with LDA, specially the energies, need to be corrected.

Chapter 11

Silicate clusters

All silica-based clusters $Si_xO_y(OH)_z$, with a maximum of five silicon atoms and two intramolecular condensations, plus the six-silicon ring and the eight-silicon cube, are investigated in this work. Some of these 25 clusters have been discussed in previous chapters. The structure, charge distribution and energy of all the others are studied in this chapter, at the LDA level of approximation. This includes the non-cyclic four- and five-silicon chains, the branched trimer and tetramer rings, the double trimer rings, the tetramer plus trimer rings, the five and six silicon rings.

11.1 Introduction

Silicate clusters are classified in this chapter according to the NMR notation, Q_n^m, where n represents the number of silicons which are bonded to m bridging oxygens. Different groups are ordered according to the parameter n first and m second; when groups with equal m have different chemical environments they are explicitly separated (as in $Q_2^2Q_1^3Q_1^2Q_1^1$). When this notation was insufficient we used e, c, t for edge, corner, cis and trans specifications.

The most important work published to date about silica-based clusters in general are the studies of Kelts et al. [126], using ^{29}Si NMR spectroscopy, and Klemperer et al. [131, 132, 134, 133, 135], using a combined protocol to separate and measure the clusters: quenching by diazomethane, fractionation using spinning band column distillation, identification by capillary gas chromatography and structural characterisation using ^{29}Si NMR.

Klemperer identified the monomer, the dimer, the acyclic trimer, both acyclic tetramers, the cyclic tetramer, the branched cyclic tetramer, the linear and the branched acyclic pentamers and the cyclic pentamer; but the cyclic trimer, the branched cyclic trimer and the acyclic cross pentamer were not found (see Figure 11.1. The acyclic linear clusters are clearly more probable than the branched ones. For the 4-Si, 5-Si and 6-Si clusters, the ratio between linear and branched isomers was found experimentally to be equal to 0.2 (), 0.6 () and 0.008 (), in acidic conditions (0.05M HCl [134]). Under basic conditions the cluster distribution is much broader than under acidic conditions.

Knight [136] presents the structures of the 16 so-called Secondary Building Units (SBUs), the common structural subunits used to classify the 64 topologically distinct zeolite networks characterised until 1990 (the primary building units being single SiO_4 tetrahedra). These are compared with the 18 silicate anions determined by ^{29}Si NMR in organic base silicate anions,

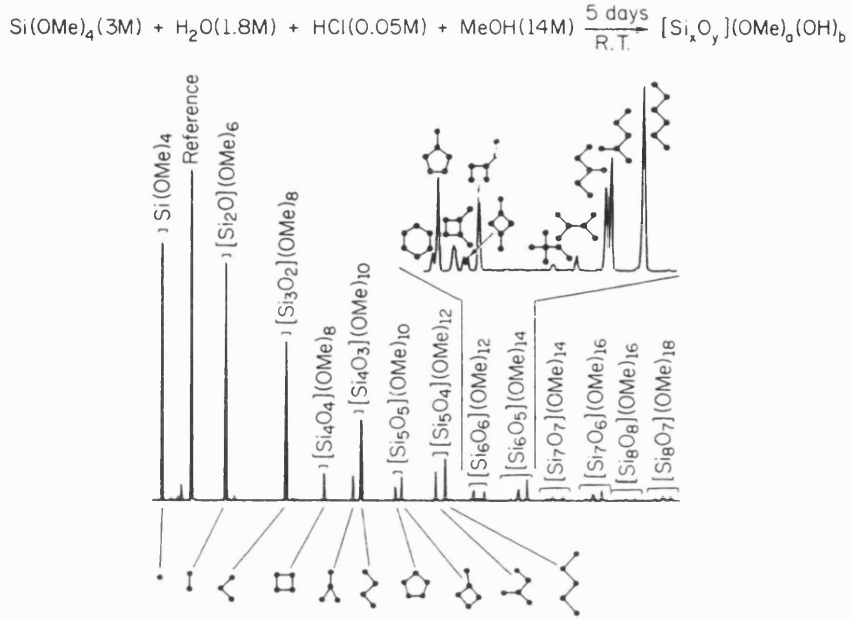


Figure 11.1: Gas chromatographic analysis of TMOS-based system [134].

and the utility of the SBU theory is questioned.

Theoretical studies using Huckel and intermediate neglect of differential overlap INDO levels of theory have been reported by West et al [244, 243], for rings and chains containing 2, 3, 4, 5 and 6 silica tetrahedra. The adsorption of a water molecule by a four silicon ring is analysed at the INDO level of theory.

Ab Initio calculations, using direct SCF with a double zeta + polarisation basis set (triple zeta + polarisation on oxygen atoms), have been done by Hill et al. [100], on silica-based chains (disilicic and trisilicic acid), rings (with 3 to 6 Si atoms) and cages (with 8, 12 and 24 Si atoms), to develop a Molecular Mechanics forcefield suitable to simulate larger zeolite (and sol-gel) structures. SCF reaction energies, per mole of SiO bonds, are presented for the formation of 3, 4, 5 and 6 Si rings, respectively -1.1 kcalmol^{-1}, -3.6 kcalmol^{-1}, -4.1 kcalmol^{-1} and -4.1 kcalmol^{-1}.

Lasaga et al. [142] also reported ab initio calculations on silicate clusters, to obtain potential surfaces for the SiO bond in silicates. These potential surfaces form the basis for extracting the key parameters in various commonly employed potential functions.

The geometry of the 5 Si cross, with hydroxyl groups replaced by hydrogens, was optimised by Pápai et al. [186], at the local DF level of theory, using the Vosko-Wilk-Nussair parameterisation, and Perdew and Wang nonlocal corrections to evaluate the energies. The energies of formation and structure of a large number of small chains and rings containing Si and Al have been calculated by Catlow et al. [51, 52], at the DF-BHL/DN level of theory.

Kelts was able to identify cyclic trimers in TEOS-based systems (see Figure 11.2) but not in those based on TMOS. When the ratio water/alkoxide decreases from 2/1 to 0.5/1 the cyclic trimer signal disappears. Kelts explains these results arguing that the probability of forming

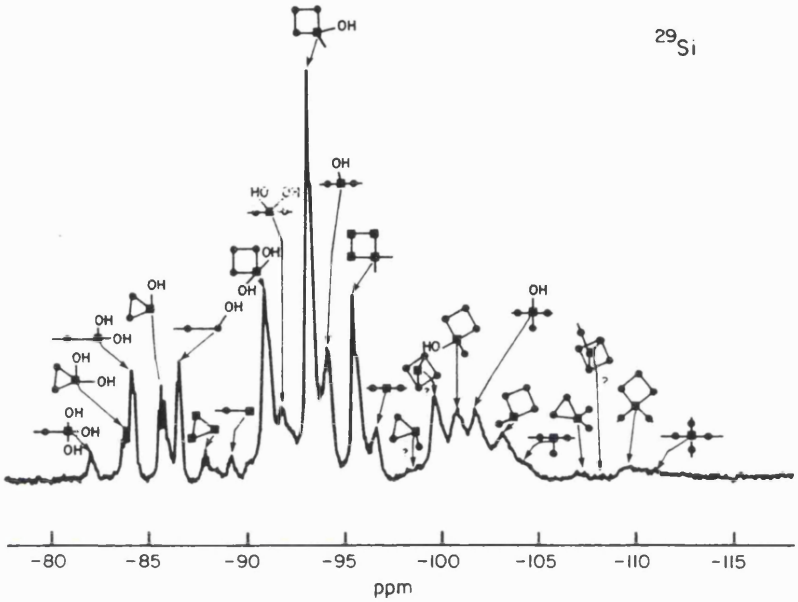


Figure 11.2: ^{29}Si NMR analysis of TEOS-based system [126].

the 3-Si ring should increase with the number of hydroxyl groups available, which in turn should increase with the amount of water available. Cyclic trimers are formed preferentially in TEOS-based systems because the hydrolysis is much faster in TEOS- than in TMOS-based systems (unless the acid concentration is very low, as the growth mechanism is affected [126].

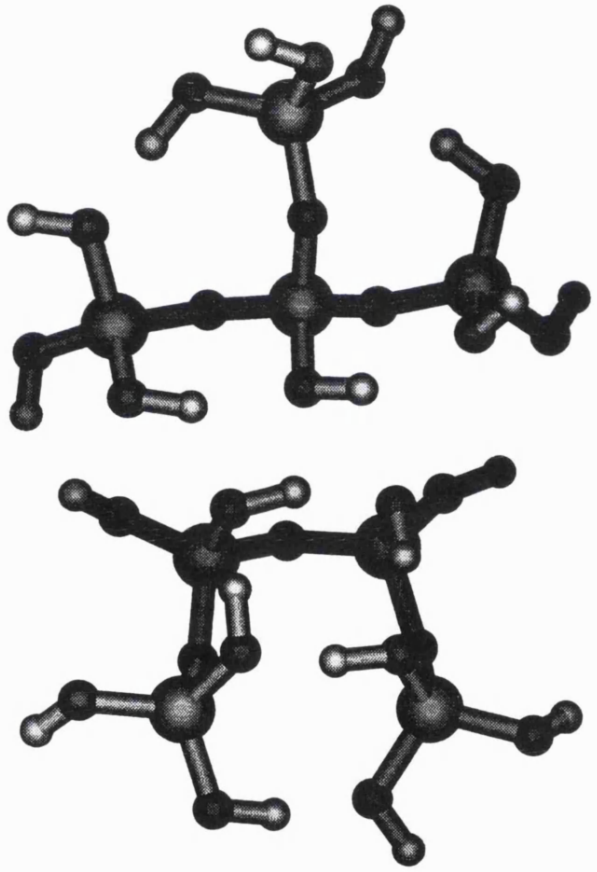
When comparing the theoretical and experimental results, two important differences should be taken into account: the terminal oxygen groups and the solvation environment. While OH groups are easier to handle in theoretical studies, OCH_3 groups are usually present in experimental work, using small amounts of water. While experimental results are obtained in liquid-state conditions, the theoretical results presented here were calculated in gas-phase conditions. Ab-initio calculations to investigate the influence of the alkoxide groups and the solvation environment in the hydrolysis and condensation reactions are presented later in this work (see chapters 13 and 14).

11.2 Branching effects

The structure and charge distribution of the non-cyclic four-silicon clusters are presented in Figure 11.5. The proposed conformation for the branched tetramer (above, in the Figure) has four hydrogen bonds: two with a reasonable O- -H distance (1.80 and 2.02 Å) and the other two overestimated (1.63-1.64 Å). The corresponding OH bond lengths seem also to be correct for the former two H-bonds (1.00 Å) but slightly large in the last two (1.01-1.02 Å).

Although the condensation energy for the branched tetramer is considerably negative (-30.6 kcal mol^{-1}), it is 7.5 kcal mol^{-1} higher than for the linear cluster (discussed in the previous chapter). This result is in agreement with the experimental evidence, which shows that it is much easier to form the linear than the branched tetramer. However, because there are five apparently overestimated H-bonds in the linear tetramer against only two in the branched tetramer, after

Si **4620-4750**	SiO_b **1.63-1.66**	$SiOSi$ **117.3-123.7**
O_b **2437-2686**	SiO_t **1.62-1.67**	O_bSiO_b **109.2-110.7**
O_t **2171-3003**	OH **0.98-1.02**	O_tSiO_t **104.4-113.7**
H **0948-1929**	O-H **1.63-2.02**	$SiOH$ **107.9-114.8**



Si **4611-4852**	SiO_b **1.64-1.66**	$SiOSi$ **121.7-128.0**
O_b **2151-2737**	SiO_t **1.62-1.67**	O_bSiO_b **108.5-109.7**
O_t **2313-2907**	OH **0.98-1.03**	O_tSiO_t **106.8-112.5**
H **1038-1823**	O-H **1.51-1.68**	$SiOH$ **104.7-118.0**

Figure 11.3: Bond lengths (Å), bond angles (degrees) and Hirshfeld atomic charges (0. and minus signal in O charges are omitted) for non-cyclic four-silicon clusters, optimised at the DF-BHL/DNP level of approximation. Total energy: E = -2131.9053 Ha ($Q_2^2Q_2^1$) and E = -2131.8933 Ha ($Q_3^1Q_1^3$). Dipole moment: μ = 2.75 D ($Q_2^2Q_2^1$) and μ = 2.60 D ($Q_3^1Q_1^3$).

applying the correction of 3.3 kcal mol^{-1} per H-bond the energy becomes lower for the branched cluster (-24.0 kcal mol^{-1}) than for the linear cluster (-21.7 kcal mol^{-1}). Although the corrected energies seem to be more reasonable, the correction is too different for both clusters, changing their relative stability, probably in a wrong way. At the LDA level of approximation, the charge separation is very similar in the linear (2.75 D) and in the branched (2.60 D) clusters.

Structure

The SiO_t bond lengths depend directly of the corresponding hydroxyl groups, changing from 1.62-1.63 Å in groups containing acceptor hydrogens, to 1.63-1.64 Å in free terminal groups, to 1.66-1.67 Å in groups with donor oxygens. The O_bSiO_b angles are almost constant but the $SiOSi$ (117.3-138.3°) and O_tSiO_t (104.4-113.7°) angles change considerably.

Non-cyclic pentamers

The structure and charge distribution of the non-cyclic five-silicon clusters are presented in Figure 11.5. The most stable conformation found for the branched five-silicon cluster (in the middle, in the Figure) has four hydrogen bonds, probably overestimated (O- -H = 1.64-1.72 Å), forming three secondary rings with 8 atoms each. The condensation energy (-40.2 kcal mol^{-1}) is 3.4 kcal mol^{-1} smaller than for the linear chain, decreasing to -27.0 kcal mol^{-1}, when corrected for the hydrogen bonds (compared with -30.4 kcal mol^{-1} for the linear chain). The corrected energy is probably a reasonable estimate, when compared with the values obtained for the previous clusters, particularly the non-cyclic ones.

The dipole moment of the branched pentamer is even larger (3.75 D) than in the five-silicon linear chain (discussed in the previous chapter). However, the calculated dipole moments (particularly for larger, less constrained and therefore more complex clusters), are probably not very reliable at this level of approximation (LDA with a double basis set), as suggested by the monomer and dimer studies shown earlier (see chapter 9).

In the pentamer cross (see Figure 11.4, above), a central silicon is attached to four bridging oxygens, each one subsequently bonded to a terminal $Si(OH)_3$, forming a highly symmetric structure, which has a almost zero dipole moment: 0.23 D. The best conformation found for this cluster has four hydrogen bonds formed by terminal hydroxyl groups, forming four secondary rings with eight atoms each. Two other hydrogen bonds formed by bridging oxygens, lead to the formation of four additional secondary rings, each one with 6 atoms. This cluster is therefore a good precursor to produce the double branched three-silicon ring, by forming an intramolecular $SiOSi$ disiloxane bond. Three of the hydrogen bonds have O- -H distances which are too short (1.76-1.83 Å), while the others are normal (O- -H = 2.04-2.14 Å) or even weak (2.57 Å).

The condensation energy for the pentamer cross, though relatively large (-32.0 kcal mol^{-1}), is still 8.2 kcal mol^{-1} smaller than for the branched chain (-40.2 kcal mol^{-1}). Taking into account the three overestimated hydrogen bonds, the corrected energy is estimated as -22.1 kcal mol^{-1}, smaller than the corrected energy (-27.0 kcal mol^{-1}) for the branched pentamer. As the condensation energy for the branched pentamer is, in turn, smaller than for the linear chain, it can be concluded that, at the LDA level of approximation, the cluster stability decreases with the degree of branching, in agreement with the experimental evidence.

The pentamer cross is the only cluster studied in this work where a silicon atom is bonded to four unconstrained bridging oxygens. It is therefore particularly interesting to compare the atomic charges in the SiO_4 central atoms with those in the terminal $Si(OH)_3$ groups and in the $Si(OH)_4$ monomer. In fact, the Hirshfeld charges are very similar for the central and terminal Si and O atoms in the cross (+0.4609 compared to [+0.4571, +0.4856] and -0.2609 compared

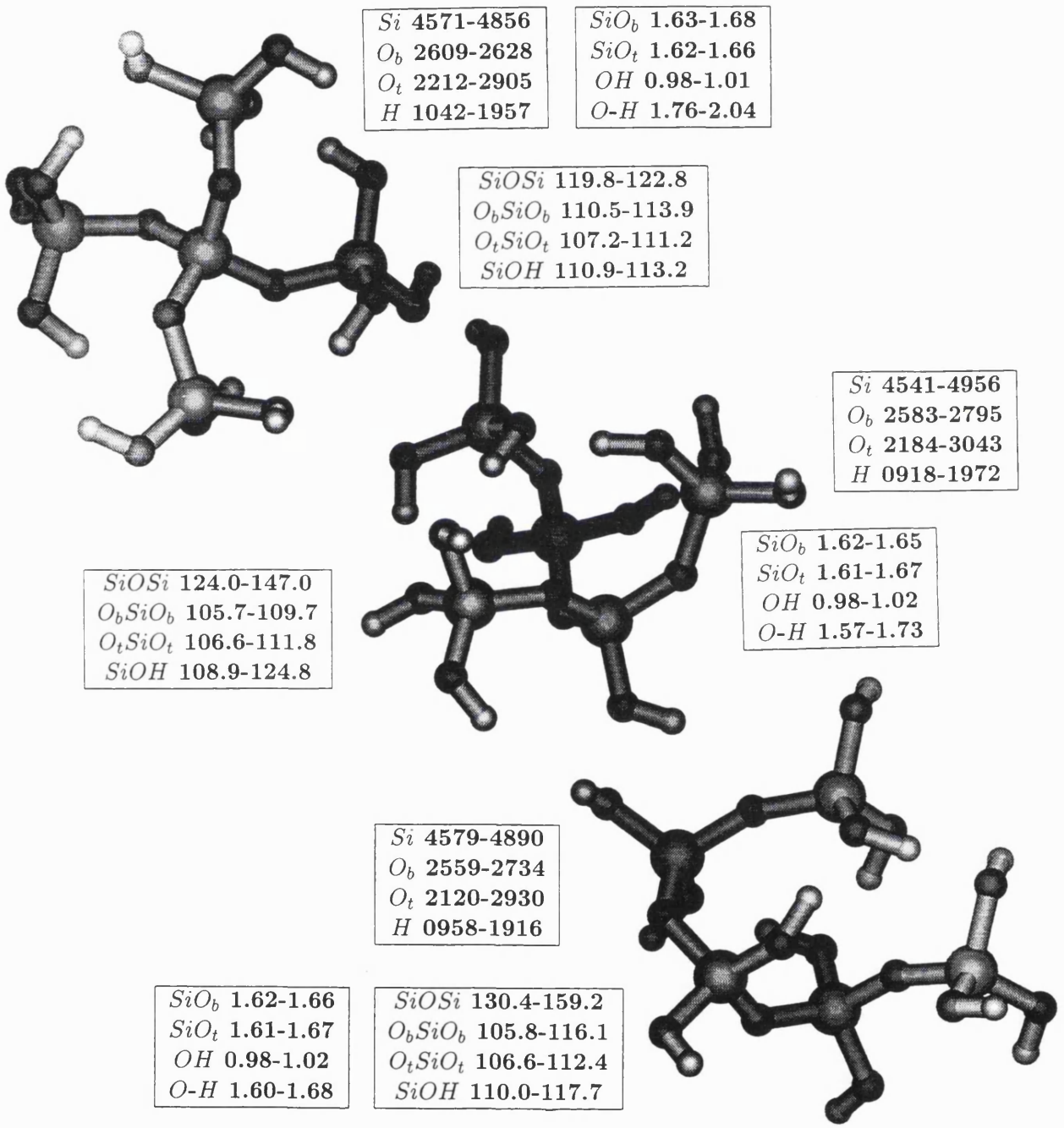


Figure 11.4: Bond lengths (Å), bond angles (degrees) and Hirshfeld atomic charges (0. and minus signal in O charges are omitted) for non-cyclic 5-silicon clusters, optimised at the DF-BHL/DNP level of approximation. Total energy: E = -2645.8975 Ha ($Q_3^2Q_2^1$), E = -2645.8921 Ha ($Q_3^1Q_1^3Q_1^2$) and E = -2645.8790 Ha ($Q_4^1Q_1^4$). Dipole moment: μ = 3.23 D ($Q_3^2Q_2^1$), μ = 3.75 D ($Q_3^1Q_1^3Q_1^2$) and μ = 0.23 D ($Q_4^1Q_1^4$).

to [-0.2249, -0.2817]). Compared with the monomer, the differences are very small: the oxygens are slightly more electronegative (-0.2842), due to the redistribution of the hydrogens charge, the same being observed with the silicons (+0.4474).

These trends are more clear when comparing the Mulliken charges, though these are less reliable (see chapter 9). The Mulliken charge in the central silicon is larger (+1.152) than in the terminal Si atoms (+0.988-1.064); the bridging oxygens have much smaller charges (-0.557-0.625) than in the terminal OH groups (-0.723-0.845). In the monomer, the Si charge decreases to +0.866, but the O charges, -0.762, do not change significantly. Nevertheless, the accuracy of these values is questionable, as the charge distribution depends very much on the level of approximation used, particularly the basis set and exchange-correlation functional.

The SiO and OH bond lengths in the different kinds of hydroxyl groups are similar to those calculated for the previous clusters. The four central SiO_b bonds are slightly shorter (1.63-1.64 Å) than the four terminal SiO_b bonds (1.64-1.68 Å), though the difference is relatively small. This seems to agree with the experimental and theoretical evidence that the SiO bond length tends to decrease in more bridged systems. The SiO bond length in alpha-quartz, for instance (1.60 Å [139]), is much smaller than the reference value for $Si(OH)_4$ in the gas-phase (about 1.62 Å [209]).

In this open, highly symmetric cluster, both $SiOSi$ (119.8-122.8°) and O_bSiO_b (110.5-113.9°) angles change very little. The $SiOSi$ angles might be about 10-15 degrees too small, taking into account the results with different basis sets obtained for the dimer (and experimental evidence on vitreous silica [174]). The O_tSiO_t and O_bSiO_b angles are very similar, while the $SiOH$ angles are almost equal for terminal (112.3-113.4°) and H-bond forming hydroxyl groups (109.8-113.8°).

Structure

In the branched pentamer, as observed for other clusters (see previous chapter), the SiO and OH bond lengths vary considerably with the bonding characteristics of the hydroxy groups, changing from 1.61-1.63 Å and 1.00-1.02 Å in acceptor groups (where the hydrogen forms an hydrogen bond, therefore receiving charge) to 1.65-1.67 Å and 0.99 Å in donor groups (where the oxygen forms an hydrogen bond, therefore giving charge). Hydroxyl groups participating simultaneously in two different hydrogen bonds (where the hydrogen accepts charge whereas the oxygen gives it) tend to present intermediate bond lengths (1.66 Å and 1.01 Å), slightly longer than in the terminal, unconstrained OH groups (1.63-1.64 Å and 0.98-0.99 Å).

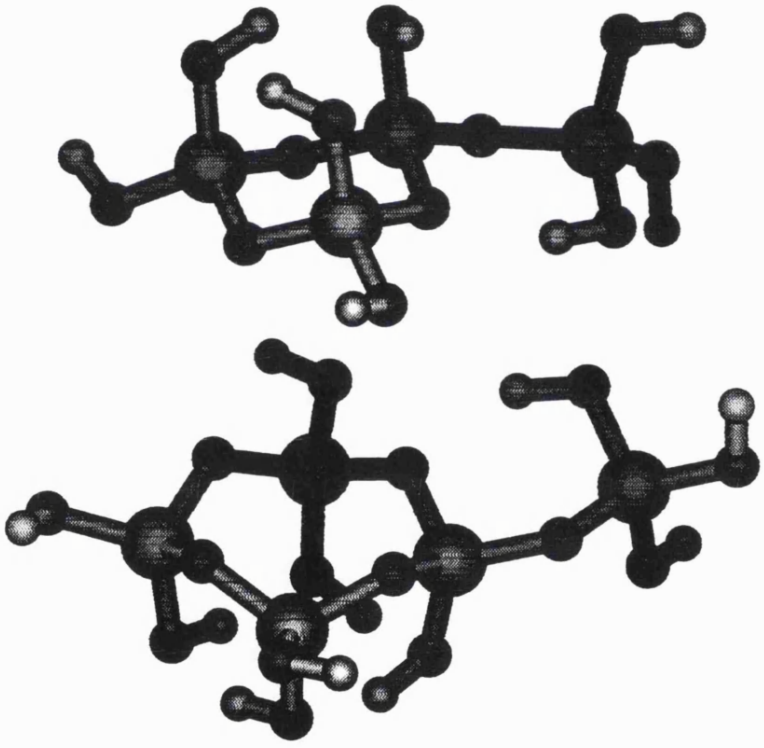
The $SiOSi$ angles change considerably along the chain (124.0-147.0°), reflecting the asymmetry of this conformation, though the relatively hard O_bSiO_b angle is almost constant (105.7-109.7°). The $SiOH$ angle presents almost the same range of variation in free and hydrogen bond constrained hydroxyl groups (respectively 110.1-113.6° and 108.9-112.7°), about six degrees smaller than the Hartree-Fock reference value for the monomer (see chapter 9).

11.3 Branched rings

The structure and charge distribution of the branched trimer and tetramer rings, are presented in Figure 11.5.

The branched trimer ring (above, in the Figure) results from the association of a trimer ring (in a chair conformation) with a monomer (in a S_4 conformation), arranged in such a way that a bridging oxygen in the ring forms a H-bond with the $Si(OH)_3$ chain. This H-bond is weaker (1.91 Å) than the three H-bonds in the ring (O- -H = 1.85-2.20 Å), which are slightly distorted

Si **4617-4861**	SiO_b **1.61-1.67**	$SiOSi$ **115.2-123.2**
O_b **2465-2701**	SiO_t **1.62-1.66**	O_bSiO_b **106.7-111.0**
O_t **2376-2913**	OH **0.98-1.01**	O_tSiO_t **113.5-115.2**
H **1224-1900**	O-H **1.85-2.20**	$SiOH$ **106.5-114.7**



Si **4601-4892**	SiO_b **1.61-1.66**	$SiOSi$ **124.7-126.6**
O_b **2417-2664**	SiO_t **1.62-1.66**	O_bSiO_b **109.1-112.5**
O_t **2353-2898**	OH **0.98-1.03**	O_tSiO_t **108.6-115.9**
H **1078-1869**	O-H **1.62-1.65**	$SiOH$ **106.2-115.1**

Figure 11.5: Bond lengths (Å), bond angles (degrees) and Hirshfeld atomic charges (0. and minus signal in O charges are omitted) for $Q_2^2Q_1^3Q_1^1$ and $Q_3^2Q_1^3Q_1^1$, optimised at the DF-BHL/DNP level of approximation. Total energy: E = -2055.9436 Ha ($Q_2^2Q_1^3Q_1^1$) and E = -2569.9670 Ha ($Q_3^2Q_1^3Q_1^1$). Dipole moment: μ = 1.93 D ($Q_2^2Q_1^3Q_1^1$) and μ = 1.88 D ($Q_3^2Q_1^3Q_1^1$).

by the influence of the lateral chain.

The condensation energy (-6.0 kcal mol^{-1}: 4.4 kcal mol^{-1} lower than for the three-silicon ring), although relatively small due to the ring strain, is negative enough to justify the significant concentration of this cluster usually found in sol-gel solutions. As in other clusters with a trimer ring, the electric dipole is relatively high (1.93 Å), an effect probably enhanced by the separation between the ring and the chain.

The branched tetramer ring (see Figure 11.5, below) is formed by associating a tetramer ring (in a crown conformation) with a S_4 monomer, thus preserving most of the features of these clusters. The lateral chain adds a further hydrogen bond ($O--H$ = 1.96 Å) to the four hydrogen bonds in the ring ($O--H$ = 1.62-1.65 Å), increasing considerably the rigidity of the cluster, as the lateral chain is not allowed to rotate anymore.

The condensation energy for this cluster (-31.0 kcal mol^{-1}: 5.3 kcal mol^{-1} lower than for the four-silicon ring) is considerably negative, due to the five H- bonds. When corrected for the four overestimated H-bonds, the energy is estimated as -17.8 kcal mol^{-1}, which is probably a more reasonable value.

The dipole moment for the branched tetramer ring(1.88 D) is much higher than in the four-silicon ring (0.65 D), which seems to confirm that a lateral chain in a ring tends to increase substantially the charge separation.

Structure

In the branched three-silicon ring, the SiO_b bonds lengths in the ring (1.65-1.67 Å) and the SiO, OH bond lengths in the chain (1.63-1.64 Å and 0.98 Å) are very close to the corresponding values in the trimer ring and in the monomer. The transition between the ring and the lateral chain is characterised by the additional hydrogen bond, which introduces a second link between the ring and the chain, this way increasing considerably the rigidity of the cluster. Quite interestingly, the SiO bond length linking the ring and the chain is much shorter (1.61 Å) than the others in the ring (1.64-167 Å) or in the chain (1.63-167 Å).

The $SiOH$ angle is smaller for OH groups forming H-bonds (106.5-111.2°) than in the terminal groups (113.0-114.7°), and the $SiOSi$ angle is smaller in the ring (115.2-116.3°) than in the chain (123.2°). As in the monomer, the O_tSiO_t angle presents two different values in the chain ($\approx$ 109.2° (2×) and 115.2° (perpendicular to the main chain), whereas it is essentially constant in the ring (113.6-114.3°).

In the branched four-silicon ring, the SiO and OH bond lengths (in hydroxyl groups) are very similar to the values obtained in the previous clusters. The SiO bond length in the ring is much smaller (1.62 Å: the Hartree-Fock value for the monomer) than the corresponding values in open chains (1.64 Å).

The $SiOSi$ angle is almost constant in this cluster and changes even less than the much harder O_bSiO_b angle, due to the high symmetry of the cluster-particularly the ring. The O_tSiO_t angle changes more in the chain (108.6-115.5°) than in the ring (112.2-115.1°), because the adjacent and opposed angles in the lateral chain are different (as in the monomer). As in all highly symmetrical rings with strong H-bond systems, the $SiOH$ angle is much larger in the free OH groups (110.9-113.7° in the chain and 112.2-115.1° in the ring) than in the OH groups involved in hydrogen bonds ($\approx$ 106.5°).

Trimer rings with two silicons in lateral chains

The structure and charge distribution of the trimer rings, with two silicon atoms in lateral chains, are presented in Figure 11.6. The trimer ring with a single two-silicon chain (above

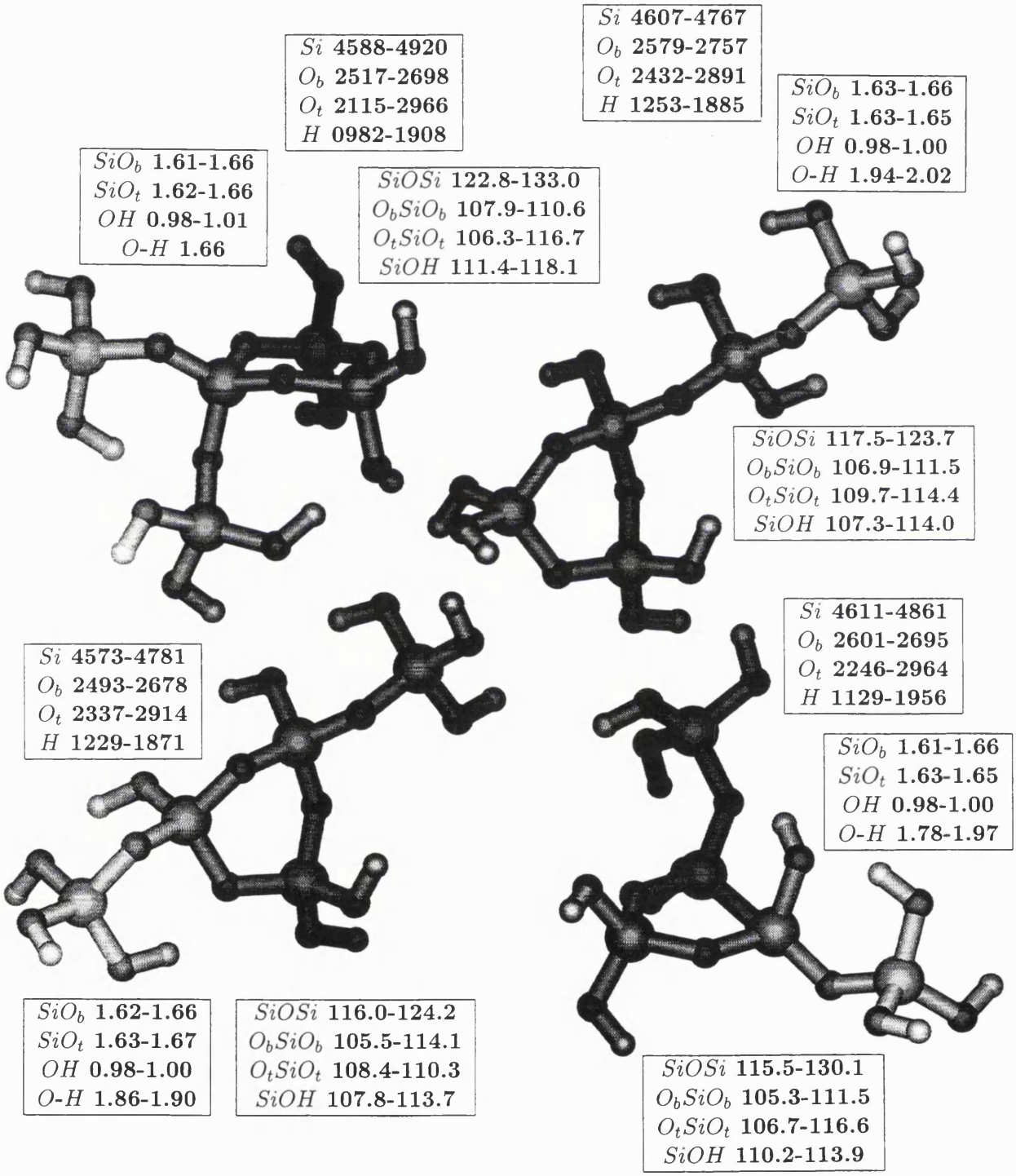


Figure 11.6: Bond lengths (Å), bond angles (degrees) and Hirshfeld atomic charges (0. and minus signal in O charges are omitted) for $Q_2^2Q_1^3Q_1^2Q_1^1$, $Q_2^2Q_2^1Q_1^4$, $Q_2^3Q_2^1Q_1^2c$ and $Q_2^3Q_2^1Q_1^2t$, optimised at the DF-BHL/DNP level of approximation. Total energy: E = -2569.9351 Ha ($Q_2^2Q_1^3Q_1^2Q_1^1$), E = -2569.9356 Ha ($Q_2^2Q_2^1Q_1^4$), E = -2569.9351 Ha ($Q_2^3Q_2^1Q_1^2c$) and E = -2569.9343 Ha ($Q_2^3Q_2^1Q_1^2t$). Dipole moment: μ = 1.78 D ($Q_2^2Q_1^3Q_1^2Q_1^1$), μ = 2.06 D ($Q_2^2Q_2^1Q_1^4$), μ = 1.28 D ($Q_2^3Q_2^1Q_1^2c$) and μ = 2.52 D ($Q_2^3Q_2^1Q_1^2t$).

left, in the Figure) is formed associating the ring (in the chair conformation) with a dimer (in the C_2 conformation), arranged in order to allow the formation of three hydrogen bonds (two in the lateral chain and one between the chain and the ring), increasing considerably the rigidity of the cluster. The corresponding O- -H distances seem to be reasonable (1.94-2.02 Å) and consequently the calculated condensation energy (-10.95 kcal mol^{-1}) is probably accurate enough not to need any correction. The dipole moment is relatively small in this cluster (1.78 D, only 0.1 D larger than in the three-silicon ring), which is surprising, as the lateral chain extends considerably the cluster size (to 11.46 Å).

In the trans-branched trimer ring (see Figure 11.6, below right), two lateral chains with one-silicon each, are attached to different silicons, in different sides of the ring. There are three hydrogen bonds in this cluster (O- -H = 1.85-1.97 Å and 1.78 Å), apparently too strong. However, the differences between the various hydroxyl groups are smaller than in previous clusters. Furthermore, the $SiOH$ anglea are almost equal for terminal and H-bond forming OH groups (111.0-113.9^o and 110.6-112.4^o).

The condensation energy for this cluster (-10.5 $kcalmol^{-1}$) is only 0.5 kcal mol^{-1} higher than in the previous cluster, but the difference increases after correcting the energy (to -7.2 $kcalmol^{-1}$), to take into account one possibly overestimated H-bond. The dipole moment is also much larger in this cluster (2.52 D), than in the previous one, apparently due to a charge separating effect provoked by the two chains on different sides of the ring.

The cis-branched trimer ring (see Figure 11.6, below left) differs from the previous cluster because the two lateral chains are on the same side of the ring, forming three H-bonds which seem reasonable (O- -H = 1.86-1.90 Å) and a fourth one very weak (O- -H = 2.74 Å).

The condensation energy for the cis-branched cluster (-10.95 kcal mol^{-1}), is almost identical to the energy calculated for the trans-branched cluster and matches exactly the energy obtained for the trimer ring with a two-silicon chain, suggesting that from the energetical point of view, the structural differences between these clusters are not relevant. The trans-cluster becomes 3.8 kcal mol^{-1}) less stable after correcting its overestimated H-bonds, but is is not clear whether the correction is accurate in this case.

The electric dipole is relatively small in this cluster (1.28 D), essentially because the relative disposition of the two chains, on each side of the ring, opposite to each other, increases considerably the whole symmetry of the cluster.

In the double branched trimer ring (see Figure 11.6, above left), two lateral chains are attached to the same silicon atom in the ring, forming two hydrogen bonds (O- -H = 1.66 Å and 1.96 Å), the first one being probably overestimated.

The condensation energy (-11.3 $kcamol^{-1}$) is calculated as or slightly more negative than in the three previous clusters, which is surprising, because only two hydrogen bonds exist in this conformation, compared with three in the previous clusters. The dipole moment (2.06 D) is in the range defined by the other three clusters.

Structure

In the single-branched trimer ring, the variations in the SiO and OH bond lengths, in terminal (1.63-1.64 Åand 0.98-0.99 Å) and hydrogen-bond forming (1.63-1.66 Åand 0.99-1.00 Å) OH groups, follow the trends observed in previous clusters. As in other branched rings, the SiO_b bond linking the ring with the chain is stronger (1.63Å) than the other SiO_b bonds (1.64-1.66 Å).

The $SiOSi$ angle is almost constant in the ring (120.1-121.7^o), changing slightly more in

the chain (117.5-123.7^o). The $SiOH$ angles are slightly larger in terminal hydroxyl groups (112.3-114.0^o) than for OH groups forming hydrogen bonds (107.3-112.8^o).

In the trans-branched trimer ring, the first SiO_b bonds in the chain (1.61-1.64 Å) are again considerably strong, particularly when compared with the second bonds, (166-1.67 Å), which are even weaker than in the ring (1.64-1.66 Å). The $SiOSi$ angles are almost equal in the chain (126.1-130.1^o) but change considerably in the ring (115.5-127.8^o) due to the distortions provoked by the lateral chains. The O_bSiO_b angles (105.3-111.5^o) are closer to the tetrahedral value than the O_tSiO_t angles (106.7-116.6^o).

In the cis-branched cluster, the SiO and OH distances are almost identical to the previous cluster: 1.00 Åand 1.63-1.64Åfor the acceptors, 1.65-1.67Åand 0.98-0.99Åfor the donors and 1.63-1.64Åand 0.98-0.99Åfor the unconstrained hydroxyl groups, not participating in hydrogen bonds. The SiO_b bonds which link the chains with the ring are very strong (1.62-1.64 Å), while the next ones are as weak (1.66-1.67 Å) as the weakest SiO_b bonds in the ring (1.64-1.67 Å).

Although the lateral chains are not symmetrically arranged and in spite of the constraints due to the ring, the $SiOSi$ angles change only slightly more in the chains (116.0-124.2^o) than in the ring (119.2-123.8^o). The O_bSiO_b angles in the chain (105.5-114.1^o) change relatively more than the O_tSiO_t angles (108.4-110.3^o). The $SiOH$ angles are almost equal for free OH groups (112.3-113.7^o) and involved in H-bonds (110.2-113.3^o).

In the double branched trimer ring, as usual, the SiO and OH bond lengths in the hydroxyl groups reflect the differences between the various chemical environments: 1.62-1.64 Å and 0.99-1.01 Å for acceptor groups, 1.66 Å and 0.99Åfor donor groups, and 1.63-1.64 Å plus 0.98-0.99 Å for unconstrained OH groups. The SiO_b bond length is again very small for the bonds connecting the two chains with the ring (1.61 Å) whereas the next bonds (1.66 Å) are even longer than in ring (1.64-1.65 Å).

The $SiOSi$ angles are larger in the chains (125.5-133.0^o) than in the ring (122.8-126.8^o), due to the constraints of the chair conformation. As usual, the O_tSiO_t angles tends to be larger than the O_bSiO_b. The SiOH angles look normal for terminal hydroxyl groups (111.4-114.3^o) but are larger than usual in the four OH groups involved in hydrogen bonds (112.8-118.1^o).

11.4 Double rings

The structure and charge distribution for the clusters with two trimer rings bonded by an edge, are presented in Figure 11.7.

The four-silicon double ring (above, in the Figure), which is never found in sol-gel solutions, is the least stable cluster discussed in this work. This is due to the substantial ring strain of the two rings (both with chair conformations), increased by the additional constraint of sharing a common $SiOSi$ edge. Furthermore, only a single hydrogen bond can be formed, at a reasonable distance (2.0 Å), as the two rings force the remaining hydroxyl groups to be too far apart to interact with each other.

The condensation energy for this cluster is consequently positive and relatively high (+6.4 kcal mol^{-1}), making its formation very improbable-in agreement with experimental evidence. The dipole moment seems to be quite large (2.82 D), a feature observed already for the trimer ring.

The second double trimer ring (see Figure 11.7, below left) results from the association of the four-silicon double ring with a monomer, in such a way that one silicon is bonded to four bridging

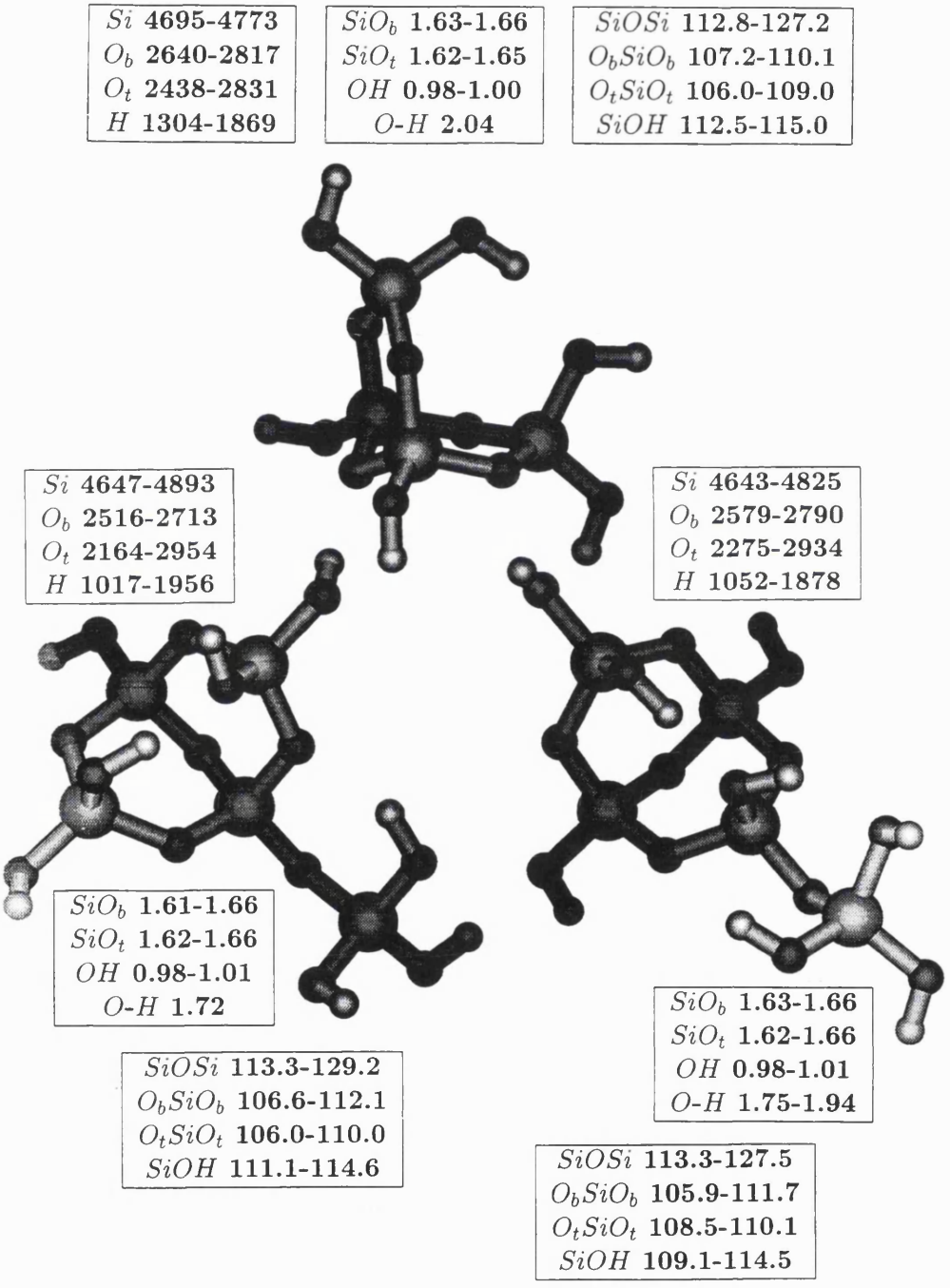


Figure 11.7: Bond lengths (Å), bond angles (degrees) and Hirshfeld atomic charges (0. and minus signal in O charges are omitted) for $Q_2^3Q_2^2$, $Q_2^3Q_1^3Q_1^2Q_1^1$ and $Q_2^2Q_1^4Q_1^3Q_1^1$, optimised at the DF-BHL/DNP level of approximation. Total energy: E = -1980.0136 Ha ($Q_2^3Q_2^2$), E = -2494.0106 Ha ($Q_2^3Q_1^3Q_1^2Q_1^1$) and E = -2494.0076 Ha ($Q_2^2Q_1^4Q_1^3Q_1^1$). Dipole moment: μ = 2.82 D ($Q_2^3Q_2^2$), μ = 2.51 D ($Q_2^3Q_1^3Q_1^2Q_1^1$) and μ = 3.36 D ($Q_2^2Q_1^4Q_1^3Q_1^1$).

oxygens. Both rings have chair conformations very similar ($SiOSi$ = 121.3-129.2^o and 113.3^o, in the common edge) to the four-silicon double ring, but more flat than in the three-silicon ring ($SiOSi$ = 116^o).

There are two hydrogen bonds in this cluster, one between OH groups in different rings (O- -H = 2.02 Å) and another between a bridging oxygen and a OH group in the lateral chain (O- -H = 1.72 Å), the latter apparently overestimated. The small condensation energy for this cluster (-0.2 kcal mol^{-1}) is again due to the ring strain, and in fact should be more positive, due to the overestimated hydrogen-bond. The corrected condensation energy, +3.1 kcal mol^{-1} seems reasonable, though perhaps slightly too high when compared with the value obtained for the four-silicon double ring (+6.4 kcalmol^{-1}), without the lateral chain and a single hydrogen bond. The dipole moment increased with the addition of the lateral chain, changing from 2.82 D in the double ring to 3.36 D in this branched double ring, perhaps due to the distance that separates the ring from the chain.

The third double trimer ring (see Figure 11.7, below right) differs from the previous one because the monomer is attached to a silicon atom belonging to a single ring, forming a system with two hydrogen bonds, with O- -H distances calculated as 1.94 Å and 1.75 Å- the latter apparently being too short.

The condensation energy (-2.1 kcal mol^{-1}) is slightly lower than for the previous cluster (-0.2 kcal mol^{-1}, which seems logical, because in the third cluster all silicon atoms are, at the maximum, attached to three bridging oxygens, whereas in the second cluster a silicon atom was bonded to four bridging oxygens, thereby increasing the cluster strain. The corrected condensation energy (+1.2kcal mol^{-1}) seems reasonable, given the strain accumulated in the double ring. The electric dipole moment is considerably smaller in the third (2.51 D) than in the second cluster (3.36 D), which is surprising, considering that the third cluster is significantly longer (10.4 Å) than the second (8.7 Å).

Structure

In the four-silicon double ring, the SiO bond length changes considerably in the constrained rings, (1.63-1.66 Å) but is quite short in terminal groups (only 1.62-1.63 Å), increasing-as expected-for groups forming hydrogen bonds (1.65 Å), as the OH bond length (0.99-1.00). Because there is only a single hydrogen-bond in this cluster, the $SiOH$ (112.5-115.0^o) and $SiOSi$ (124.6-127.2^o) angles are almost constant, except the $SiOSi$ angle in the edge common to both rings, which is much smaller (112.8^o). The constrained O_bSiO_b and terminal O_tSiO_t angles are close to the tetrahedral value.

In the second cluster, the SiO and OH distances in terminal groups are similar to the ones observed in previous clusters. The SiO distances in the rings are relatively large (1.64-1.68 Å, due to the ring strain, but the first SiO bond in the lateral chain is very strong: SiO = 1.61 Å. This interesting bonding effect is confirmed by the the observations made previously for the trimer and tetramer branched rings. The O_tSiO_t and O_bSiO_b angles are close to the tetrahedral value. The $SiOH$ angles are similar for OH groups involved in hydrogen bonds (111.1-112.6^o and for terminal ones (111.7-114.6^o).

The SiO bond lengths in the third cluster (again with chair conformations) change also considerably but are slightly shorter (1.63-1.66 Å) than in the previous cluster, confirming the smaller ring strain and higher stability of the third cluster over the second. The $SiOSi$ angles (121.8-127.5^o plus 113.3^o, in the common $SiOSi$ chain), O_tSiO_t and O_bSiO_b, are similar to the previous cluster, with differences smaller than 2 degrees, probably below the error of the

calculation. The $SiOH$ angles are similar in terminal (111.8-114.5^o) OH groups and when constrained by hydrogen-bonds (109.1-113.8^o).

Corner-bonded double trimer and trimer-tetramer rings

The structure and charge distribution of the corner-bonded double trimer ring, and of the trimer-tetramer double rings, are shown in Figure 11.8. In the corner-bonded double trimer ring (left, in the Figure), two three-silicon rings are attached to each other by a single silicon atom, instead of a $SiOSi$ edge, as in the three clusters before. The conformation proposed here is particularly favourable because it takes advantage of the chair conformation of both cycles, the less strained cyclic conformation, to allow the formation of four hydrogen bonds (O- -H = 1.72 Å, 1.86-1.88 Å and 2.60 Å), that should help considerably to stabilise the cluster.

The condensation energy obtained for this cluster (-1.6 kcal mol^{-1}) seems reasonable, though it could be expected that this cluster would be significantly more stable than the two previous ones, due to the four hydrogen bonds and because the single corner attachement instead of the shared edge between the two rings should decrease the strain. The corrected energy is already positive, +1.7 kcal mol^{-1}. The dipole moment is particularly high in this cluster, 3.84D, but the accuracy of the calculation is again questionable and it would be useful to recalculate it with a better level of approximation.

The SiO bond lengths change considerably in the double ring framework (1.62-1.67 Å), essentially due to the different chemical environment seen by the central and the outer silicon atoms. The SiO and OH bond distances in the hydroxyl groups are similar to the previous clusters.

The $SiOSi$ angle has a surprisingly small range of variation (114.7-122.8^o), considering that this is a highly strained cluster, where the central silicon atom (bonded to four bridging oxygens) has a different environment from the other four (bonded to only two bridging oxygens). As in previous clusters, the O_bSiO_b angle is about 5 degrees larger than the O_tSiO_t angle and the $SiOH$ angle is slightly larger in the free, terminal, hydroxyl groups (113.1-115.6^o) than in the OH groups forming hydrogen bonds (105.2-111.3^o).

In the edge-bonded trimer-tetramer double ring (see Figure 11.8, below left), a four-silicon ring and a three-silicon ring share a common $SiOSi$ chain, where an hydroxyl group in the three-silicon ring forms two hydrogen bonds with OH groups in the four-silicon ring, increasing even more the rigidity of the cluster. The three-silicon and four-silicon rings keep the usual chair and crown conformations, but the two hydrogen bonds seem too short: 1.62-1.63 Å.

The condensation energy obtained for this cluster, -13.6 kcalmol^{-1}, is probably too negative, even considering that this cluster is widely found in experimental sol-gel solutions. The corrected condensation energy, -7.0 kcalmol^{-1}, seems to be a more sensible value for a strained double ring like this. The electric dipole moment obtained for this cluster, 2.54D, seems reasonable, suggesting that the highly symmetrical charge distribution existent in the four silicon ring, whose dipole is only 0.65D, is not entirely destroyed by the formation of the second ring.

The corner-bonded trimer-tetramer double ring (see Figure 11.8, above left) differs from the previous one because the fragment containing the fifth silicon atom is bonded to two opposite corners of the four-silicon ring, instead of two adjacent ones, as in the cluster before. Due to this different construction, the crown configuration of the tetramer ring becomes distorted, though two hydrogen bonds are still formed (O- -H = 1.81-1.82 Å).

The corresponding total condensation energy (-8.6 kcalmol^{-1}) is considerably lower than for the edge-bonded cluster before, which seems reasonable, as to form the additional chain over

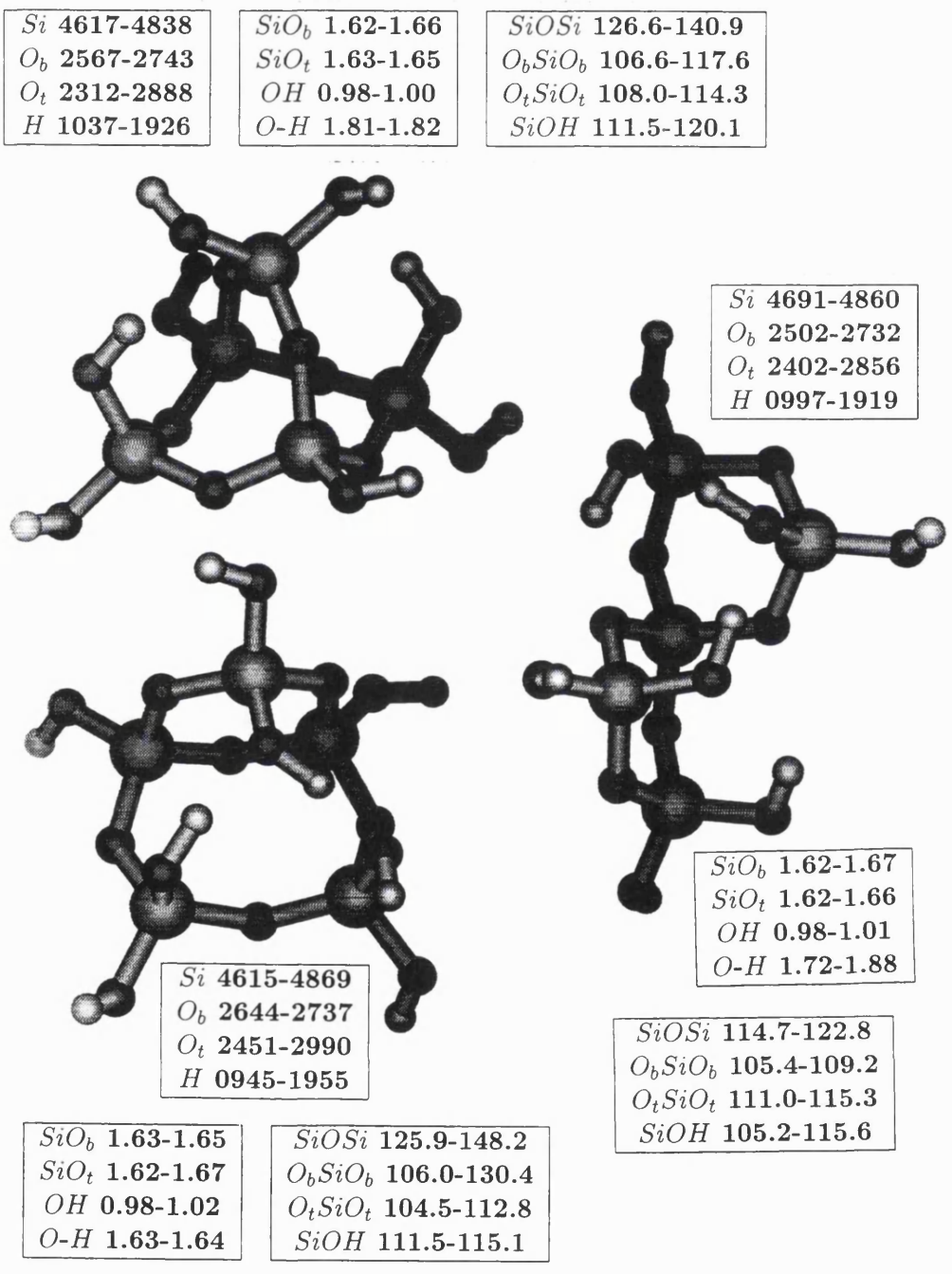


Figure 11.8: Bond lengths (Å), bond angles (degrees) and Hirshfeld atomic charges (0. and minus signal in O charges are omitted) for $Q_4^2Q_1^4$, $Q_2^2Q_2^3Q_1^2e$ and $Q_2^2Q_2^3Q_1^2c$, optimised at the DF-BHL/DNP level of approximation. Total energy: E = -2494.0098 Ha ($Q_4^2Q_1^4$), E = -2494.0289 Ha ($Q_2^2Q_2^3Q_1^2e$) and E = -2494.0209 Ha ($Q_2^2Q_2^3Q_1^2c$). Dipole moment: μ = 3.84 D ($Q_4^2Q_1^4$), μ = 2.54 D ($Q_2^2Q_2^3Q_1^2e$) and μ = 5.99 D ($Q_2^2Q_2^3Q_1^2c$).

the four-silicon ring should be energetically less favourable than to form a lateral three-silicon ring, as before. When corrected in the usual way, the energy is estimated as -2.0 kcal mol^{-1}, which seems too positive, when compared with the double trimer rings, which have almost the same energy and are much less observed in experimental work.

The strangest feature of this cluster is, however, its extremely high dipole moment (5.99 D), which is very difficult to explain. Assuming that this is not just an artifact due to the limitations of the LDA level of approximation used here, it might suggest that a lower energy conformation should exist, which would explain also the poor energy performance observed for this cluster. However, as this is a highly constrained cluster, not many degrees of freedom are left free, and major improvements to the proposed conformation seem to be unlikely.

Structure

In the edge-bonded double ring, because the hydrogen bonds are so strong the SiO and OH distances in hydroxyl groups have a significant range of variation: 1.62-1.63 Å and 0.98 Å for terminal groups, 1.62 Å and 1.02 Å for acceptor groups, 1.67 Å and 0.99 Å for donor groups, and 1.65 Å and 1.02 Å for OH groups simultaneously acceptors and donors. In particular, the OH length in the acceptors and the SiO length in the donors looks too long, while the SiO distance in the acceptors seems too short, resulting from the LDA level of approximation. The SiO_b bond length changes considerably (1.62-1.65Å), due to the three different silicon environments (Q_2^3, Q_2^2 and Q_1^2) existent in the edge-bonded cluster.

The $SiOSi$ bond angle is larger (148.2°) in the more relaxed tetramer ring edge opposite to the trimer ring (see Figure 11.8) than in the other cyclic bonds (125.9-130.4°). As before, the O_bSiO_b angles change less and are closer to the tetrahedral angle than the O_tSiO_t angles, due to the hydrogen bonds. The $SiOH$ angles for hydroxyl groups participating in hydrogen bonds are essentially constant (112.0-113.8°, and included in the range of variation of the terminal (unconstrained) OH groups: 111.5-115.1°.

In the corner-bonded cluster, the SiO and OH distances in the hydroxyl groups (1.63-1.65 Å and 0.98-1.0 Å) change less than in the edge-bonded cluster before. Interestingly, each bridging oxygen forms a shorter bond (1.62-1.63 Å), and a longer one (1.65-1.66 Å). The Q_2^3 silicons belonging to both rings have two short and one long SiO_b bond lengths (1.62 Å, 1.63 Å and 1.66 Å), while the other Q_2^2 bridging silicons have two long bonds (1.65 Å) and the fifth Q_1^2 silicon two short ones (1.62 Å).

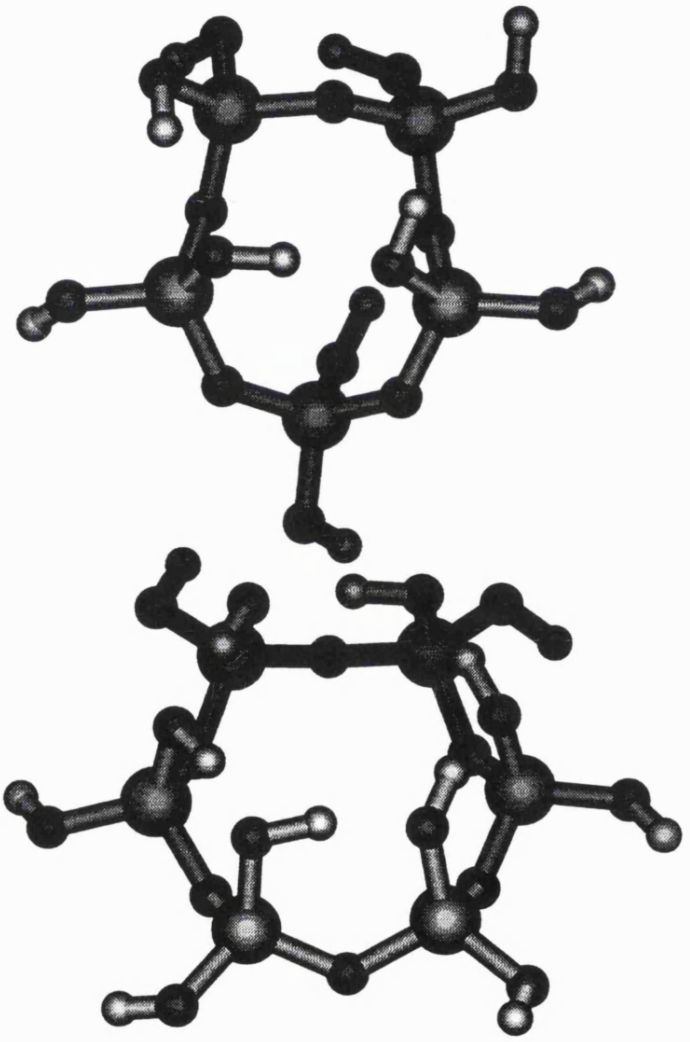
Due to the ring structure, the $SiOSi$ angles change considerably, becoming smaller in the four-silicon ring (126.6-135.5°) than in the upper chain formed by the fifth silicon atom (136.3-140.9°). The O_bSiO_b angles change also considerably in this cluster (106.6-117.6°), including the values obtained for the O_tSiO_t angle (108.0-114.3°), which is surprising for such an hard angle. The $SiOH$ angles have also larger values than usual, when hydrogen bonds are present (111.5-120.1°), even showing the values obtained for OH unconstrained groups (111.5-114.3°).

11.5 Large rings

The structure and charge distribution for the five- and six-silicon rings are presented in Figure 11.9. The five-silicon ring has the *S shape* conformation usually proposed for ten-carbon rings (see [67]). The S shape is distorted, however, by four hydrogen bonds present in this conformation (O- -H = 1.64 Å, 1.84 Å, 1.98 Å and 2.01 Å), the first two probably overestimated.

The total condensation energy for the five-silicon ring (above, in the Figure) is smaller (-

Si **4629-4893**	SiO_b **1.62-1.66**	$SiOSi$ **116.3-136.1**
O_b **2504-2786**	SiO_t **1.62-1.66**	O_bSiO_b **107.2-111.0**
O_t **2061-2824**	OH **0.98-1.02**	O_tSiO_t **103.9-115.9**
H **1033-1878**	O-H **1.64-1.84**	$SiOH$ **106.7-115.0**



Si **4816-4886**	SiO_b **1.64-1.65**	$SiOSi$ **127.1-130.0**
O_b **2615-2650**	SiO_t **1.63-1.66**	O_bSiO_b **110.5-112.3**
O_t **2380-2712**	OH **0.98-1.04**	O_tSiO_t **113.0-114.9**
H **1064-1841**	O-H **1.56-1.60**	$SiOH$ **106.4-115.3**

Figure 11.9: Bond lengths (Å), bond angles (degrees) and Hirshfeld atomic charges (0. and minus signal in O charges are omitted) for large rings, optimised at the DF-BHL/DNP level of approximation. Total energy: E = -2569.9577 Ha (Q_5^2) and E = -3083.9788 Ha (Q_6^2). Dipole moment: μ = 3.39 D (Q_5^2) and μ = 0.82 D (Q_6^2).

25.1 kcal mol^{-1}) than for the four-silicon ring (-25.7 kcal mol^{-1}), because the symmetry is much smaller, and a cyclic hydrogen-bond system is not present any longer. However, the LDA corrected energy (-18.5 kcal mol^{-1}) is already lower than the value obtained for the tetramer ring (-12.5 kcal mol^{-1}). The larger five-silicon ring allows a better relaxation of the ring strain, though stronger hydrogen bonds may be formed in the four-silicon ring, where the hydroxyl groups are closer to each other. The dipole moment in the five-silicon ring is quite large (3.39 D)-particularly when compared with the four-silicon ring (0.65 D)-due to its poor symmetry, resulting from the hydrogen-bonds distortion.

The six-silicon ring (see Figure 11.9, below) has an *extended crown* conformation, with six hydroxyl groups forming a cyclic hydrogen-bond system, that stabilises enormously the cluster. These hydrogen bonds seem to be seriously overestimated, as the O- -H bond lengths (1.56-1.60 Å) are too short, and the corresponding O-H bond lengths (1.03-1.04Å) are too large. Consequently, the total condensation energy for the six-silicon ring (-48.7 kcal mol^{-1}) is likely to be overestimated. The corrected value (-28.9 kcal mol^{-1}) seems to be a much more sensible value.

The dipole moment of the six-silicon ring is much smaller (0.88 D) than for the three- and five-silicon rings, though slightly larger than in the tetramer ring. At the LDA level of approximation, the chair conformation of the trimer ring produces a much larger charge separation than the crown or extended crown conformations proposed for the four- and six- silicon rings.

Structure

The hydrogen-bond distortions in the five-silicon ring explain the large bond length variations in bridging (SiO_b = 1.62-1.66 Å) and terminal groups (SiO_t = 1.62-1.64 Å and OH = 0.98-1.02 Å). In the six-silicon ring, the terminal groups in equatorial positions have normal OH lengths (0.98 Å) but the SiO bonds are much stronger (1.63 Å) than in the hydrogen bond system (1.65-1.66 Å).

In the five-silicon ring, the O_bSiO_b bond angles change very little, but the $SiOSi$ (116.3-136.1°) and O_tSiO_t (103.9-115.9°) bond angles vary considerably, due to the hydrogen bonds. The $SiOH$ angles are almost constant in terminal OH groups (113.3-115.0°), again changing more when constrained by hydrogen bonds (106.7-112.0°).

In the six-silicon ring, the $SiOH$ angles are also shorter in the hydrogen-bond system (106.4-108.1°) than in the terminal OH groups (111.9-115.3°). The $SiOSi$ angles (127.1-130.0°) are relatively similar to the ones in the four-silicon ring, though much larger than in the trimer ring. Although more constrained, the O_bSiO_b angles are closer to the tetrahedral value (110.5-112.3°) than the terminal O_tSiO_t angles (113.0-114.9°). This might be due to the hydrogen-bond system, which tends to attract the axial OH groups, to shorten the O- -H bonds, opening slightly the O_bSiO_b angle.

11.6 Silicate clusters data

The predicted structural data (bond lengths and bond angles), charge distribution (electric dipole moments and Hirshfeld charges) and total condensation energies (calculated and corrected energies, divided by the number of condensation reactions, and by the number of silicon atoms), for all silica clusters studied in this work, are presented in Tables 11.1, 11.2, 11.3 and 11.4.

As discussed in the previous chapters, the LDA method tends to overestimate the silicate condensation energies. This is clearly shown by the total condensation energies for the

	SiO_b	SiO_t	OH	O- -H
Q_1^0	-	1.64	0.99	-
Q_2^1	1.65	1.63-1.66	0.98-1.00	1.91
$Q_2^1Q_1^2$	1.63	1.62-1.68	0.98-1.02	1.63-1.65
Q_3^2	1.65-1.66	1.62-1.66	0.98-1.00	1.93-1.99
$Q_2^2Q_2^1$	1.64-1.66	1.62-1.67	0.98-1.03	1.51-1.68
$Q_3^1Q_1^3$	1.63-1.66	1.62-1.67	0.98-1.02	1.63-2.02
$Q_2^2Q_1^3Q_1^1$	1.61-1.67	1.62-1.66	0.98-1.01	1.85-2.20
$Q_2^3Q_2^2$	1.63-1.66	1.62-1.65	0.98-1.00	2.04
Q_4^2	1.64-1.65	1.62-1.66	0.98-1.03	1.61-1.62
$Q_3^2Q_2^1$	1.62-1.66	1.61-1.67	0.98-1.02	1.60-1.68
$Q_3^1Q_1^3Q_1^2$	1.62-1.65	1.61-1.67	0.98-1.02	1.57-1.73
$Q_4^1Q_1^4$	1.63-1.68	1.62-1.66	0.98-1.01	1.76-2.04
$Q_2^2Q_1^3Q_1^2Q_1^1$	1.63-1.66	1.63-1.65	0.98-1.00	1.94-2.02
$Q_2^2Q_2^1Q_1^4$	1.61-1.66	1.62-1.66	0.98-1.01	1.66
$Q_2^3Q_2^1Q_1^2c$	1.62-1.66	1.63-1.67	0.98-1.00	1.86-1.90
$Q_2^3Q_2^1Q_1^2t$	1.61-1.66	1.63-1.65	0.98-1.00	1.78-1.97
$Q_2^3Q_1^3Q_1^2Q_1^1$	1.63-1.66	1.62-1.66	0.98-1.01	1.75-1.94
$Q_2^2Q_1^4Q_1^3Q_1^1$	1.61-1.66	1.62-1.66	0.98-1.01	1.72
$Q_4^2Q_1^4$	1.62-1.67	1.62-1.66	0.98-1.01	1.72-1.88
$Q_3^2Q_1^3Q_1^1$	1.61-1.66	1.62-1.66	0.98-1.03	1.62-1.65
$Q_2^2Q_2^3Q_1^2e$	1.63-1.65	1.62-1.67	0.98-1.02	1.63-1.64
$Q_2^2Q_2^3Q_1^2c$	1.62-1.66	1.63-1.65	0.98-1.00	1.81-1.82
Q_5^2	1.62-1.66	1.62-1.66	0.98-1.02	1.64-1.84
Q_6^2	1.64-1.65	1.63-1.66	0.98-1.04	1.56-1.60
Q_8^3	1.63-1.64	1.63	0.98	-

Table 11.1: Bond lengths (Å) for optimised silicate clusters (O_b = bridging oxygen; O_t = terminal oxygen; O- -H = hydrogen bond).

dimer: -9.4 kcal mol^{-1} (DF-BHL/DNP), -2.8 kcal mol^{-1} (DF-BLYP/DNP) and -2.2 kcal mol^{-1} (DF-BLYP/TNP); linear trimer: -18.5 kcal mol^{-1} (DF-BHL/DNP) and -7.7 kcal mol^{-1} (DF-BLYP/DNP); and cyclic trimer: -1.6 kcal mol^{-1}) (DF-BHL/DNP) and +5.5 kcal mol^{-1} (DF-BLYP/DNP). Consequently, the DF-BHL/DNP level total condensation energies obtained in this work, for example for the linear tetramer (-38.2 kcal mol^{-1}), the tetramer ring (-25.7 kcal mol^{-1}), the linear pentamer (-43.6 kcal mol^{-1}) and the six-silicon ring (-48.7 kcal mol^{-1}), are likely to decrease considerably, when recalculated with non-local density (and a better basis set). As the condensation energies calculated for the dimer with a double basis set (-2.8 kcal mol^{-1}) and a triple basis set (-2.2 kcal mol^{-1}) are similar, the LDA energies were corrected to fit the dimer values obtained with a double instead of a triple basis set, in order to correct exclusively the non-local effects necessary to describe hydrogen bonds accurately. However, even the corrected energies are still more negative than the DF-BLYP/DNP values, as shown by the linear trimer (corrected local: -11.9 kcal mol^{-1}; non-local: -7.7 kcal mol^{-1}) and trimer ring (corrected local: -1.6 kcal mol^{-1}; non-local: +5.5 kcal mol^{-1}). This might be due to the chosen criterion of correcting only the hydrogen bonds that were more obviously overestimated, with O-

		SiOSi	O_bSiO_b	O_tSiO_t	SiOH
•	Q_1^0	-	-	105.6-117.6	112.4
—	Q_2^1	118.4	-	110.7-114.0	107.7-113.5
∧	$Q_2^1Q_1^2$	138.4-144.2	113.2	106.7-112.6	111.1-115.7
△	Q_3^2	115.7-116.1	107.9-108.8	112.9-114.4	106.6-114.8
∧∧	$Q_2^2Q_2^1$	121.7-128.0	108.5-109.7	106.8-112.5	104.7-118.0
⅄	$Q_3^1Q_1^3$	117.3-123.7	109.2-110.7	104.4-113.7	107.9-114.8
▷	$Q_2^2Q_1^3Q_1^1$	115.2-123.2	106.7-111.0	113.5-115.2	106.5-114.7
◇	$Q_2^3Q_2^2$	112.8-127.2	107.2-110.1	106.0-109.0	112.5-115.0
□	Q_4^2	125.8-126.3	111.2-112.2	113.2-114.8	106.2-114.3
⋀⋀	$Q_3^2Q_2^1$	130.4-159.2	105.8-116.1	106.6-112.4	110.0-117.7
⅄∧	$Q_3^1Q_1^3Q_1^2$	124.0-147.0	105.7-109.7	106.6-111.8	108.9-124.8
+	$Q_4^1Q_1^4$	119.8-122.8	110.5-113.9	107.2-111.2	110.9-113.2
▷∧	$Q_2^2Q_1^3Q_1^2Q_1^1$	117.5-123.7	106.9-111.5	109.7-114.4	107.3-114.0
▷◁	$Q_2^2Q_2^1Q_1^4$	122.8-133.0	107.9-110.6	106.3-116.7	111.4-118.1
△△	$Q_2^3Q_2^1Q_1^2c$	116.0-124.2	105.5-114.1	108.4-110.3	107.8-113.7
△..	$Q_2^3Q_2^1Q_1^2t$	115.5-130.1	105.3-111.5	106.7-116.6	110.2-113.9
◇▷	$Q_2^3Q_1^3Q_1^2Q_1^1$	113.3-127.5	105.9-111.7	108.5-110.1	109.1-114.5
◇◇	$Q_2^2Q_1^4Q_1^3Q_1^1$	113.3-129.2	106.6-112.1	106.0-110.0	111.1-114.6
⋈	$Q_4^2Q_1^4$	114.7-122.8	105.4-109.2	111.0-115.3	105.2-115.6
□⅄	$Q_3^2Q_1^3Q_1^1$	124.7-126.6	109.1-112.5	108.6-115.9	106.2-115.1
□▷	$Q_2^2Q_2^3Q_1^2e$	125.9-148.2	106.0-130.4	104.5-112.8	111.5-115.1
▣	$Q_2^2Q_2^3Q_1^2c$	126.6-140.9	106.6-117.6	108.0-114.3	111.5-120.1
⬠	Q_5^2	116.3-136.1	107.2-111.0	103.9-115.9	106.7-115.0
⬡	Q_6^2	127.1-130.0	110.5-112.3	113.0-114.9	106.4-115.3
⧈	Q_8^3	136.3-138.0	110.1-111.2	-	113.8-113.9

Table 11.2: Bond angles (degrees) for optimised silicate clusters (O_b = bridging oxygen; O_t = terminal oxygen).

-H distances smaller than 1.85 Å. The corrected energies will be used in almost all the discussion that follows.

The total condensation energy (from the monomer) to form a silicate cluster in the gas-phase depends essentially on its structure (hydrogen bonds, number and type of rings) and of its size. Table 11.4 shows the calculated (and corrected) condensation energies for all clusters, divided by the number of silicon atoms, and by the number of condensation reactions necessary to create them. Larger clusters should have larger condensation energies but clusters with the same silicons may need a different number of condensation reactions to occur, depending on its intramolecular condensation reactions. The most sensible way to compare the total condensation energies for the various clusters is therefore to divide the corrected energy by the number of required reactions, obtaining the so-called intrinsic condensation energy.

This intrinsic energy is small for the dimer (-2.8 kcal mol^{-1}) but increases considerably for the linear trimer (-6.0 kcal mol^{-1}), and then slowly for the linear tetramer (-7.2 kcal mol^{-1}) and the linear pentamer (-7.6 kcal mol^{-1}). Probably the dimer value is small because the hydrogen bonds tend to decrease the O- -H distances and consequently the $SiOSi$ angle also, a

	Dip.	Si	O_b	O_t	H
Q_1^0	0.00	0.8660	-	-0.7620	0.5460
Q_2^1	1.09	0.4598	-0.2777	-0.2433, -0.2935	0.1212, 0.1839
$Q_1^2Q_2^1$	0.35	0.4648, 0.4733	-0.2685	-0.2195, -0.3005	0.0954, 0.1878
Q_3^2	1.68	0.4731, 0.4764	-0.2703, -0.2734	-0.2557, -0.2643	0.1253, 0.1877
$Q_2^2Q_2^1$	2.75	0.4611, 0.4852	-0.2151, -0.2737	-0.2313, -0.2907	0.1038, 0.1823
$Q_1^3Q_3^1$	2.60	0.4620, 0.4750	-0.2437, -0.2686	-0.2171, -0.3003	0.0948, 0.1929
$Q_1^1Q_2^2Q_3^1$	1.93	0.4617, 0.4861	-0.2465, -0.2701	-0.2376, -0.2913	0.1224, 0.1900
$Q_2^2Q_2^3$	2.82	0.4695, 0.4773	-0.2640, -0.2817	-0.2438, -0.2831	0.1304, 0.1869
Q_4^2	0.65	0.4818, 0.4851	-0.2655, -0.2699	-0.2440, -0.2648	0.1070, 0.1861
$Q_2^1Q_3^2$	3.23	0.4579-0.4890	-0.2559, -0.2734	-0.2120, -0.2930	0.0958, 0.1916
$Q_1^1Q_1^2Q_3^3$	3.75	0.4541, 0.4956	-0.2583, -0.2795	-0.2184, -0.3043	0.0918, 0.1972
$Q_1^4Q_4^1$	0.23	0.4571, 0.4856	-0.2609, -0.2628	-0.2212, -0.2905	0.1042, 0.1957
$Q_1^1Q_1^2Q_2^3Q_3^1$	1.78	0.4607, 0.4767	-0.2579, -0.2757	-0.2432, -0.2891	0.1253, 0.1885
$Q_2^1Q_2^2Q_4^1$	2.06	0.4588, 0.4920	-0.2517, -0.2698	-0.2115, -0.2966	0.0982, 0.1908
$Q_1^2Q_2^3Q_3^1c$	1.28	0.4573, 0.4781	-0.2493, -0.2678	-0.2337, -0.2914	0.1229, 0.1871
$Q_1^2Q_2^3Q_3^1t$	2.52	0.4611, 0.4861	-0.2601, -0.2695	-0.2246, -0.2964	0.1129, 0.1956
$Q_1^1Q_1^2Q_2^3Q_3^1$	2.51	0.4643, 0.4825	-0.2579, -0.2790	-0.2275, -0.2934	0.1052, 0.1878
$Q_1^1Q_1^3Q_2^4Q_3^1$	3.36	0.4647, 0.4893	-0.2516, -0.2713	-0.2164, -0.2954	0.1017, 0.1956
$Q_4^2Q_4^4$	3.84	0.4691, 0.4860	-0.2502, -0.2732	-0.2402, -0.2856	0.0997, 0.1919
$Q_1^1Q_3^2Q_3^3$	1.88	0.4601, 0.4892	-0.2417, -0.2664	-0.2353, -0.2898	0.1078, 0.1869
$Q_1^2Q_2^3Q_2^3e$	2.54	0.4615, 0.4869	-0.2644, -0.2737	-0.2451, -0.2990	0.0945, 0.1955
$Q_1^2Q_2^3Q_2^3c$	5.99	0.4617, 0.4838	-0.2567, -0.2743	-0.2312, -0.2888	0.1037, 0.1926
Q_5^2	3.39	0.4629, 0.4893	-0.2504, -0.2786	-0.2061, -0.2824	0.1033, 0.1878
Q_6^2	0.82	0.4816, 0.4886	-0.2615, -0.2650	-0.2380, -0.2712	0.1064, 0.1841
Q_8^3	0.06	0.4842, 0.4847	-0.2601, -0.2705	-0.2699, -0.2707	0.1814, 0.1819

Table 11.3: Dipole moment (Debye) and Hirshfeld atomic charges for optimised silicate clusters (O_b = bridging oxygen; O_t = terminal oxygen).

energetically unfavourable change.

This evolution is similar for the straight conformations (uncorrected because the O- -H distances are longer than 1.85 Å): trimer (-7.8 kcal mol^{-1}), tetramer (-8.9 kcal mol^{-1}) and pentamer (-8.1 kcal mol^{-1}). It is possible thus to predict (for example) a total condensation energy for the six-silicon linear chain around -39.0 kcal mol^{-1} (-7.8 kcal mol^{-1} per condensation reaction) and for the corresponding straight conformation -55.0 kcal mol^{-1} (-8.2 kcal mol^{-1} per condensation reaction).

The intrinsic condensation energies for the rings show also a predictable evolution: trimer ring (-0.6 kcal mol^{-1}), tetramer ring (-3.1 kcal mol^{-1}), pentamer ring (-3.7 kcal mol^{-1}) and six-silicon ring (-4.8 kcal mol^{-1}). These energies are less negative than for the linear chains, becoming more and more negative as the ring becomes larger and more relaxed. At the corrected LDA level of approximation, it is thus possible to predict a condensation energy for the seven-silicon ring (for example) around -36.4 kcal mol^{-1} (corresponding to an intrinsic energy per reaction of -5.2 kcal mol^{-1}). For progressively larger rings, the intrinsic energy should converge to the value for linear chains (about -7.8 kcal mol^{-1}).

	Total E	CE (CE_c)	CE (CE_c)/n	CE (CE_c)/s	
Q_1^0	-589.89392	-	-	-	1 Si
Q_2^1	-1103.8924	-9.4 (-2.8)	-9.4 (-2.8)	-4.7 (-1.4)	2 Si
$Q_2^1Q_1^2$	-1617.8905	-18.5 (-11.9)	-9.3 (-6.0)	-6.2 (-4.0)	3 Si
Q_3^2	-1541.9532	-1.6 (-1.6)	-0.5 (-0.5)	-0.5 (-0.5)	
$Q_2^2Q_2^1$	-2131.9053	-38.2 (-21.7)	-12.7 (-7.2)	-9.5 (-5.4)	4 Si
$Q_3^1Q_1^3$	-2131.8933	-30.6 (-24.0)	-10.2 (-8.0)	-7.7 (-6.0)	
$Q_2^2Q_1^3Q_1^1$	-2055.9436	-6.0 (-6.0)	-1.5 (-1.5)	-1.5 (-1.5)	
$Q_2^3Q_2^2$	-1980.0136	+6.4 (+6.4)	+1.3 (+1.3)	+1.6 (+1.6)	
Q_4^2	-2055.9751	-25.7 (-12.5)	-6.4 (-3.1)	-6.4 (-3.1)	
$Q_3^2Q_2^1$	-2645.8975	-43.6 (-30.4)	-10.9 (-7.6)	-8.7 (-6.1)	5 Si
$Q_3^1Q_1^3Q_1^2$	-2645.8921	-40.2 (-27.0)	-10.1 (-6.8)	-8.0 (-5.4)	
$Q_4^1Q_1^4$	-2645.8790	-32.0 (-22.1)	-8.0 (-5.5)	-6.4 (-4.4)	
$Q_2^2Q_1^3Q_1^2Q_1^1$	-2569.9351	-11.0 (-11.0)	-2.2 (-2.2)	-2.2 (-2.2)	
$Q_2^2Q_2^1Q_1^4$	-2569.9356	-11.3 (-11.3)	-2.3 (-2.3)	-2.3 (-2.3)	
$Q_2^3Q_2^1Q_1^2c$	-2569.9351	-11.0 (-11.0)	-2.2 (-2.2)	-2.2 (-2.2)	
$Q_2^3Q_2^1Q_1^2t$	-2569.9343	-10.5 (-7.2)	-2.1 (-1.4)	-2.1 (-1.4)	
$Q_2^3Q_1^3Q_1^2Q_1^1$	-2494.0106	-2.1 (+1.2)	-0.4 (-0.2)	-0.4 (-0.2)	
$Q_2^2Q_1^4Q_1^3Q_1^1$	-2494.0076	-0.2 (+3.1)	-0.0 (+0.5)	-0.0 (+0.6)	
$Q_4^2Q_1^4$	-2494.0098	-1.6 (+1.7)	-0.3 (+0.3)	-0.3 (+0.3)	
$Q_3^2Q_1^3Q_1^1$	-2569.9670	-31.0 (-17.8)	-6.2 (-3.6)	-6.2 (-3.6)	
$Q_2^2Q_2^3Q_1^2e$	-2494.0289	-13.6 (-7.0)	-2.3 (-1.2)	-2.7 (-1.4)	
$Q_2^2Q_2^3Q_1^2c$	-2494.0209	-8.6 (-2.0)	-1.4 (-0.3)	-1.7 (-0.4)	
Q_5^2	-2569.9577	-25.2 (-18.5)	-5.0 (-3.7)	-5.0 (-3.7)	
Q_6^2	-3083.9788	-48.7 (-28.9)	-8.1 (-4.8)	-8.1 (-4.8)	6 Si
Q_8^3	-3808.2202	+4.1 (+4.1)	+0.3 (+0.3)	+0.5 (+0.5)	8 Si

Table 11.4: Total energy (Ha) and total condensation energy (kcal mol^{-1}) for optimised silicate clusters (CE = calculated; CE_c = corrected with 3.3 kcal mol^{-1} per H-bond when O- -H > 1.85 Å, see text; n = number of condensation reactions to form the cluster; s = number of silicons in the cluster).

Linear clusters seem to be more stable than branched ones, though the differences are small, as the intrinsic condensation energies show: linear pentamer (⋀⋀) (-7.6 kcal mol^{-1}), branched pentamer (人⋀) (-6.8 kcal mol^{-1}) and pentamer cross (┼) (-5.5 kcal mol^{-1}). The same is calculated for the four-silicon clusters, before the energies are corrected: the energy of the linear chain (⋀⋀) is about 7.5 kcal mol^{-1} lower than the branched one (人⋀). The order changes, however, after correcting the energies, as the intrinsic energies become calculated as -7.2 kcal mol^{-1} for the linear tetramer and -8.0 kcal mol^{-1} for the branched tetramer. In fact, the latter is the lowest intrinsic energy found in this work for a cluster, which is not justified by its structure, and should therefore result in some arbitrariness in the correction.

Introducing a lateral chain in a ring decreases the intrinsic condensation energy by about 0.5-1.0 kcal mol^{-1}: branched trimer ring (▷) (-1.5 kcal mol^{-1}) compared with the trimer ring (△) (-0.5 kcal mol^{-1}); branched tetramer ring (□) (-3.6 kcal mol^{-1}) compared with the tetramer ring (□) (-3.1 kcal mol^{-1}); branched double trimer rings (◇, ◇) (-0.2 and +0.5 kcal mol^{-1})

compared with the double ring () (+1.3 kcal mol^{-1}). The five-silicon clusters with a trimer ring and a single intramolecular condensation have essentially the same energy: -1.4 kcal mol^{-1} for the ring with two cis chains () and -2.2 kcal mol^{-1} for the rings with two trans chains (), a two silicon chain (), and two chains attached to the same silicon (). The position of the chains in the trimer ring is therefore not important for the energies of these reactions, but this may change for larger rings, as for example, the ortho-branched tetramer ring might have a lower energy than its meta isomer, where hydrogen bonds between the two lateral chains are not possible.

The three five silicon clusters with two trimer rings have also very similar condensation energies: +0.5 kcal mol^{-1} for the edge-bonded double ring with a Q^4 silicon (); -0.2 kcal mol^{-1} for the edge-bonded double ring with three Q^3 silicons () and +0.3 kcal mol^{-1} for the corner-bonded double ring (). In this case, the condensation energy seems to be almost independent of the kind of attachement of the two rings and of the position of the lateral chain. The intrinsic condensation energy changes also very little from the three-silicon ring () (-0.6 kcal mol^{-1}), to the four-silicon edge bonded double ring () (+1.3 kcal mol^{-1}), and the five silicon corner-bonded double ring () (+0.3 kcal mol^{-1}).

It is worthwhile to compare also the three pentamers with a tetramer ring: as expected, the condensation energy is significantly lower (-3.6 kcal mol^{-1}) when the fifth silicon forms just a lateral chain () than when a further intramolecular condensation () leads to the formation of a edge-bonded trimer ring (-1.2 kcal mol^{-1}). When the fifth silicon fragment is bonded to opposite corners of the tetramer ring (), straining even further the cluster and actually creating two additional four-silicon rings, the energy increases again (to only -0.3 kcal mol^{-1}). Nevertheless, these energies are still similar, given the different structures of the clusters, (the open and closed trimer energies, for example, change much more, from -6.0 kcal mol^{-1} to -0.5 kcal mol^{-1}).

As expected, the energy difference (-1.5 kcal mol^{-1}) between the strained branched trimer ring () and the tetramer ring () (-3.1 kcal mol^{-1}) is still significant, but the more relaxed branched tetramer ring () (-3.6 kcal mol^{-1}) and the five-silicon ring () (-3.7 kcal mol^{-1}) have virtually the same energy. Finally, the corrected energies obtained for the various clusters are much more consistent with the energy obtained for the cubic octamer (), the only cluster (apart from the monomer) where hydrogen bonds are not present and consequently where the LDA approximation should work well, without any need for a correction.

11.7 Conclusions

To understand the complex mechanisms of reaction, solvation and diffusion that determine the chemistry of silica in solution, it is necessary to study first the silicate clusters that participate in these processes. This study reveals a wide diversity of structures and consequently of charge distributions and energies for these clusters, that influences directly their chemical behaviour, in particular the interaction with other clusters and with the solvent.

The results presented here show that the stability of the non-cyclic clusters decreases with the degree of branching, as observed experimentally. This trend is observed for both 4-silicon and 5-silicon clusters.

All branched cyclic clusters have the ring conformation of the corresponding unbranched rings. This happens in spite of the hydrogen bonds formed between the chains and the ring that

could force a rearrangement of the cyclic frame. The SiO bond which links the ring with the lateral chain seems to be much stronger than the equivalent bonds in the ring and in the chain.

As expected, the double ring clusters are quite unstable, in particular the double trimer rings, corner-linked and edge-linked, which have essentially the same energy. The trimer-tetramer rings are easier to form, particularly the edge-linked one.

The four- and six-silicon rings seem to be more stable than the correspondent pentamer-, due to the relatively asymmetric arrangement of the latter. However, the small trimer ring, in spite of its internal strain and low stability has a low-energy, highly optimised structure. It will be interesting, in the future, to analyse the relative stability of larger rings.

Chapter 12

Silicate reactions

The purpose of this chapter is to utilise the data on silicate clusters presented in the previous chapters, in particular their energy and structure, to develop a kinetic model suitable to describe approximately the first minutes of an ideal condensation process, starting from the fully hydrolysed monomers.

12.1 Introduction

There is almost no published work concerned with the specific reactions that take place between the various silicate clusters, during the first stages of condensation. A Raman study, published by Tallant et al [226], supports the formation of three-fold and four-fold siloxane rings by intramolecular condensation of the corresponding open chains. Following Kinrade et all [128], the temperature-dependent ^{29}Si line broadening is almost entirely due to Si-Si chemical exchange, which implies involvement of a common vehicle of intermolecular Si exchange, the $Si(OH)_4$ monomer. They claim that for readily cyclisable species such as the non-cyclic trimer, cyclisation is more rapid than intermolecular condensation.

During the last 10-15 years, a considerable effort has been made to understand the kinetics of the hydrolysis and condensation reactions occurring in silica-based sol-gel processes, using a wide range of experimental techniques including ^{29}Si NMR spectroscopy [197, 196, 110, 184, 111, 27], Raman spectroscopy [226, 17, 185], ^{1}H and ^{17}O NMR spectroscopies [232, 120], Small Angle X-Ray Scattering [123, 92] or even solution volume changes [37]. Pouxviel and Boilot [197, 196] have shown that the hydrolysis rate increases with the number of hydroxyl groups and the reverse, reesterification reactions, have a significant contribution. The condensation reactions preferentially occur between the more hydrolysed monomers, with loss of water, as loss of alcohol is not very significant. The condensation rate rapidly decreases with the degree of polymerisation. For large sizes, the kinetics of the growth process is mainly controlled by the diffusion. Reviews have been presented by Brinker [41], Hench [96], Schmidt [213, 214] and others. Kinetic models for both hydrolysis and condensation reactions are discussed in chapter 3.

The total reaction energies to form the various silicate clusters directly from the monomer are presented and discussed in the previous chapters. This analysis allows a global comparison of the relative stability of the clusters but misses completely the details concerning the specific reactions occurring between these clusters. All reactions that can potentially occur between the 23 silicate clusters studied previously, with a maximum of 5 silicon atoms and 2 intramolecular

condensations, are identified in this chapter.

The situation considered here, where the chain ends are always OH groups, corresponds approximately to a highly aqueous sol-gel solution (limited by the water-alkoxide immiscibility), where the hydrolysis reaction is almost completed before the condensation starts. More than reproducing a purely ideal situation, this model aims to be a working tool, as simple as possible, which yields useful insight in the kinetic aspects of the silica growth in solution.

12.2 Silicate clusters precursors

Two types of reactions are considered here: the forward condensation, forming $SiOSi$ bonds and the reverse hydrolysis, breaking them. These reactions are either intramolecular, in the sense that a single silicate cluster is involved (producing rings by forming new $SiOSi$ bonds or breaking $SiOSi$ bonds by reaction with water) or intermolecular, where a silicate cluster reacts with a monomer or a dimer to produce larger clusters (given the five silicon limit, reactions with trimers are redundant). Reactions involving the formation or destruction of one $SiOSi$ bond (for example 2 dimers forming a 4-silicon chain), two (2 dimers forming a 4-silicon ring) or three (2 dimers forming a 4-silicon double ring) are taken into account, though the latter ones should be regarded as highly unlikely. Reactions involving more than two silicate clusters are not considered, but reverse reactions with multiple $SiOSi$ bond breaks, involving two or three water molecules, are taken into account, mostly for completeness. For each silicate cluster, all its possible precursors, identified under these rules, are presented in Table 12.1.

This Table shows also the calculated and corrected (see previous chapter) condensation energies, for all reactions. These energies were obtained at the DF-BHL/DNP level of approximation, and should be therefore overestimated, like the total condensation energies, discussed in previous chapters. The dimerisation energy, 9.1 kcal mol^{-1}, is calculated as 2.2 kcal mol^{-1} at the DF-BLYP/TNP level, while the cyclisation of the open trimer, 16.9 kcal mol^{-1} is 13.2 kcal mol^{-1}, at the DF-BLYP/DNP level. The energy of reaction of a dimer with a monomer to form an open trimer and a ring trimer, -9.1 kcal mol^{-1} and +7.7 kcal mol^{-1}, is -4.9 kcal mol^{-1} and +8.3 kcal mol^{-1} respectively, at the DF-BLYP/DNP level of approximation.

For each condensation or hydrolysis reaction, the number of different sites where the reaction can take place is analysed. This is done labeling the atoms and investigating how many different arrangements can be produced from the initial clusters. The interaction characteristics of each reaction is described by a symbol $\frac{l}{m/n}$, where $l = 0$ designates a intramolecular reaction, $l = 1$ a reaction with a monomer, $l = 2$ a reaction with a dimer, m is the number of ways the reaction can occur and n is the number of bonds formed or broken during the reaction. This interaction factor is also presented in Table 12.1 for each precursor, for both forward and reverse reactions.

Although most of the cyclic clusters can only be produced in endothermic reactions and are therefore seldom found in solution, they tend to be favoured, from the statistical point of view, because usually they can be produced by a large number of reactions occurring in different sites, while more open clusters have usually a much more restricted range of possible precursors. This is particularly evident for larger clusters, which usually have a larger range of precursors.

The most important examples of the latter are the double trimer (), with only four silicons and six identified precursors, and the five silicon cross (), which can be formed only by a single condensation reaction, between the branched four-silicon cluster () and a monomer. Additionally, for a cross to be produced, the monomer has to attack the inner, central silicon

atom, instead of one of the three outer silicons, a task which is clearly made more difficult by steric hindrance and statistical effects. The branched four silicon cluster is, in turn, less probable than the linear one (a general trend observed in the previous chapter), which makes it even more improbable that the five silicon cross will be formed. In fact, this cross was never observed in experimental work, in spite of being energetically favoured, as is the case for all non-cyclic structures.

The five silicon clusters with two rings, though highly penalised in energy due to the strain of the rings, can be produced from a large range of precursors, by both intramolecular and intermolecular reactions.

12.3 Kinetic model

We used the information contained in table 12.2 to develop a kinetic model aiming to simulate realistically the evolution with time of the concentration of the silicate clusters in solution. All forward and reverse reactions identified in Table 12.1 are considered (the six-silicon ring is ignored), corresponding to a total of 182 reactions. The model assumes that all exothermic reactions have the same activation energy G*, while the opposite, endothermic reactions, have a activation energy equal to G* plus the corresponding reaction energy E. Consequently, the energy barrier G* is equal for both condensation and hydrolysis reactions. Although different activation energies for each reaction can easily be implemented, it is important to keep the model as simple as possible, to get the maximum of science from it. Nevertheless, given the limitations of the model, it is unlikely that an increase in complexity, increasing the number of parameters, would be compensated by a increase in accuracy. Mass factors are not considered for the same reason.

The activation energy of the condensation reaction is usually believed to be between 0 and 15-20 kcal mol^{-1} (see chapter 19). In this model, the best results are obtained for G* = 15 $kcalmol^{-1}$ and G* = 20 kcal mol^{-1}, as smaller energy barriers favour by too much the most stable clusters. A temperature of 30^0C was chosen to emulate experimental conditions, as the temperature in the sol-gel solution rises quickly in the first minutes, probably due to the hydrolysis reaction. Because the reaction energies E, calculated at the DF-BHL/DNP level of approximation, appears to be overestimated, E/2 and E/3 are used instead, leading to broader, more realistic, cluster distributions. The concentration of the ring trimer, in particular, is very small when the full reaction energy E is used, which, in turn, leads to small concentrations of the various ring trimer derivatives.

A statistical factor $g = f\frac{m}{10^{n-1}}$ is used to take into account the various m reactive sites and to penalise reactions involving more than a single bond. A simple *kinetic theory of collisions* predicts a collision number f between 4×10^{10} and 4×10^{11} l $moles^{-1}s^{-1}$ [141], but these values are usually too high and numbers $10^{-1} - 10^{-2}$ smaller (sometimes 10^{-10}), are predicted by the *theory of absolute reaction rates*, in beter agreement with experiment (see Laidler [141]). In this model, f is equal to 2.0×10^9 l $moles^{-1}s^{-1}$ for G*=15 kcal mol^{-1} and 7.0×10^{12} l $moles^{-1}s^{-1}$ for G*=20 kcal mol^{-1}, in order to get a half-time of the monomer (time after which the monomer concentration becomes half of the initial value) about 4.0 min. Depending on conditions (particularly pH), experimental values are expected to be between 1-2 min and 15-25 min (see Pouxviel and Boilot [197, 196]).

For intramolecular reactions, involving a single molecule, a dimensional unit factor has to

Q_2^1	$\frac{1}{1}$ -9.4 (-2.8) $\frac{0}{1}$		
$Q_2^1Q_1^2$	$\frac{1}{2}$ -9.1(-9.1) $\frac{0}{2}$		
Q_3^2	$\frac{0}{1}$ +16.9 (+10.3) $\frac{0}{3}$	$\frac{1}{1/2}$ +7.7 (+1.1) $\frac{0}{3/2}$	
$Q_2^2Q_2^1$	$\frac{1}{2}$ -19.6 (-9.7) $\frac{0}{2}$	$\frac{2}{4}$ -19.4 (-16.1) $\frac{0}{1}$	
$Q_3^1Q_1^3$	$\frac{1}{1}$ -12.1 (-12.1) $\frac{0}{3}$		
$Q_2^2Q_1^3Q_1^1$	$\frac{0}{2}$ +32.2 (+15.7) $\frac{0}{2}$	$\frac{1}{3}$ -4.3 (-4.3) $\frac{0}{1}$	$\frac{1}{2/2}$ +12.6 (+6.0) $\frac{0}{2/2}$
	$\frac{2}{2/2}$ +12.8 (-0.4) $\frac{0}{1/2}$		
Q_4^2	$\frac{0}{1}$ +12.4 (+9.1) $\frac{0}{4}$	$\frac{1}{1/2}$ -7.2 (-0.6) $\frac{0}{4/2}$	$\frac{2}{2/2}$ -7.0 (-7.0) $\frac{0}{2/2}$
$Q_2^3Q_2^2$	$\frac{0}{2}$ +32.1 (+18.9) $\frac{0}{1}$	$\frac{0}{2}$ +12.3 (+12.3) $\frac{0}{4}$	$\frac{0}{3/2}$ +37.0 (+30.4) $\frac{0}{2/2}$
	$\frac{1}{3/2}$ +8.0 (+8.0) $\frac{0}{2/2}$	$\frac{1}{1/3}$ +24.9 +18.3 $\frac{0}{2/3}$	$\frac{2}{4/3}$ +25.1 (+11.9) $\frac{0}{2/3}$
$Q_3^2Q_{22}^1$	$\frac{1}{2}$ -5.4 (-5.4) $\frac{0}{2}$	$\frac{2}{4}$ -15.7 (-15.7) $\frac{0}{2}$	
$Q_3^1Q_1^3Q_1^2$	$\frac{1}{2}$ -2.1 (-5.4) $\frac{0}{2}$	$\frac{1}{3}$ -9.6 (-3.0) $\frac{0}{1}$	$\frac{2}{2}$ -13.0 (-12.3) $\frac{0}{1}$
$Q_4^1Q_1^4$	$\frac{1}{1}$ -1.4 (+1.9) $\frac{0}{4}$		
$Q_2^2Q_1^3Q_1^2Q_1^1$	$\frac{0}{2}$ +32.6 (+19.4) $\frac{0}{2}$	$\frac{1}{1}$ -5.0 (-5.0) $\frac{0}{1}$	$\frac{1}{2/2}$ +27.2 (+10.7) $\frac{0}{2/2}$
	$\frac{2}{6}$ +0.1 (+0.1) $\frac{0}{1}$	$\frac{2}{2/2}$ +17.0 (+3.8) $\frac{0}{1/2}$	
$Q_2^2Q_1^4Q_2^1$	$\frac{0}{6}$ +20.7 (+10.8) $\frac{0}{1}$	$\frac{0}{1}$ +28.9 (+15.7) $\frac{0}{2}$	$\frac{1}{1}$ -5.3 (-5.3) $\frac{0}{2}$
	$\frac{1}{3/2}$ +19.4 (+12.8) $\frac{0}{2/2}$	$\frac{2}{1/2}$ +16.6 (+10.0) $\frac{0}{1/2}$	
$Q_2^3Q_2^1Q_1^2c$	$\frac{0}{2}$ +29.3 (+16.1) $\frac{0}{2}$	$\frac{0}{1}$ +32.6 (+19.4) $\frac{0}{1}$	$\frac{1}{2}$ -5.3 (-5.3) $\frac{0}{2}$
	$\frac{1}{1/2}$ +27.2 (+10.7) $\frac{0}{1/2}$	$\frac{2}{4/2}$ +16.6 (+3.4) $\frac{0}{2/2}$	
$Q_2^3Q_2^1Q_1^2t$	$\frac{0}{2}$ +29.8 (+16.6) $\frac{0}{2}$	$\frac{0}{1}$ +33.1 (+19.9) $\frac{0}{1}$	$\frac{1}{2}$ -4.8 (-4.8) $\frac{0}{2}$
	$\frac{1}{1/2}$ +27.7 (+11.2) $\frac{0}{1/2}$	$\frac{2}{4/2}$ +17.1 (+3.9) $\frac{0}{2/2}$	

Table 12.1: Possible precursors for each cluster (on the left), showing the calculated (and corrected) formation energies (kcal/mol) and statistical features $\frac{l}{m/n}$ (see text) for reactions: precursor $\rightarrow$ cluster (left) and cluster $\rightarrow$ precursor (right).

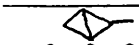
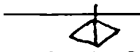
 $Q_4^2Q_1^4$	$\frac{0}{1}$ +9.7 (+13.0) $\frac{0}{2}$ $\frac{0}{1/2}$ +42.0 ((+32.1) $\frac{0}{4/2}$	$\frac{0}{1}$ +9.4 (+12.7) $\frac{0}{4}$ $\frac{1}{1/2}$ +4.4 ((+7.7) $\frac{0}{4/2}$	$\frac{0}{3/2}$ +30.4 (+23.8) $\frac{0}{1/2}$ $\frac{2}{3/2}$ +9.4 (+2.8) $\frac{0}{2/2}$
 $Q_3^2Q_1^3Q_1^1$	$\frac{0}{1}$ +9.2 (+9.2) $\frac{0}{2}$ $\frac{1}{2/2}$ +7.2 (+3.9) $\frac{0}{2/2}$	$\frac{0}{2}$ +12.6 (+12.6) $\frac{0}{2}$ $\frac{2}{4/2}$ -3.1 (-3.1) $\frac{0}{3/2}$	$\frac{1}{4}$ -5.3 (-5.3) $\frac{0}{1}$
 $Q_2^3Q_1^3Q_1^2Q_1^1$	$\frac{0}{1}$ +28.9 (+19.0) $\frac{0}{1}$ $\frac{0}{2}$ +8.9 (+8.9) $\frac{0}{2}$ $\frac{1}{2}$ -8.5 (-5.2) $\frac{0}{1}$ $\frac{2}{6/2}$ +8.9 (+12.2) $\frac{0}{1/2}$	$\frac{0}{2}$ +8.4 (+8.4) $\frac{0}{2}$ $\frac{0}{2/2}$ +38.1 (+28.2) $\frac{0}{2/2}$ $\frac{1}{1/2}$ +3.9 (+7.2) $\frac{0}{1/2}$	$\frac{0}{2}$ +8.9 (+12.2) $\frac{0}{2}$ $\frac{0}{2/2}$ +41.5 (+31.6) $\frac{0}{2/2}$ $\frac{1}{2/3}$ +36.1 (+22.9) $\frac{0}{2/3}$
 $Q_2^2Q_1^4Q_1^3Q_1^1$	$\frac{0}{1}$ +30.8 (+20.9) $\frac{0}{1}$ $\frac{0}{2}$ +11.1 (+14.4) $\frac{0}{2}$ $\frac{0}{2/2}$ +43.4 (+33.5) $\frac{0}{2/2}$ $\frac{2}{6/3}$ +27.7 (+17.8) $\frac{0}{3/3}$	$\frac{0}{2}$ +10.2 (+10.2) $\frac{0}{2}$ $\frac{0}{12/2}$ +31.8 (+25.2) $\frac{0}{1/2}$ $\frac{1}{2}$ -6.6 (-3.3) $\frac{0}{1}$	$\frac{0}{2}$ +10.7 (+14.0) $\frac{0}{2}$ $\frac{0}{1/2}$ +40.0 (+30.1) $\frac{0}{2}$ $\frac{1}{2/2}$ +5.7 (+9.0) $\frac{0}{2/2}$
 $Q_2^3Q_2^2Q_1^2e$	$\frac{0}{2}$ +17.4 (+10.8) $\frac{0}{2}$ $\frac{1}{4}$ +12.1 (+5.5) $\frac{0}{1/2}$ $\frac{2}{4/3}$ +14.3 (+7.7) $\frac{0}{2/3}$	$\frac{0}{2}$ -2.6 (+4.0) $\frac{0}{2}$ $\frac{1}{2/3}$ +24.6 (+14.7) $\frac{0}{2/3}$	$\frac{0}{2/2}$ +30.0 (+23.4) $\frac{0}{2/2}$ $\frac{2}{6/2}$ -2.6 (-2.6) $\frac{0}{1/2}$
 $Q_2^3Q_2^2Q_1^2c$	$\frac{0}{1}$ +22.4 (+15.8) $\frac{0}{2}$ $\frac{2}{4/3}$ +19.4 (+12.8) $\frac{0}{4/3}$	$\frac{1}{2/2}$ +17.2 (+10.6) $\frac{0}{1/2}$	$\frac{1}{3/3}$ +22.1 (+22.1) $\frac{0}{2/3}$
 Q_5^2	$\frac{0}{1}$ +18.5 (+11.9) $\frac{0}{5}$	$\frac{1}{1/2}$ +13.0 (+3.1) $\frac{0}{5/2}$	$\frac{2}{2/2}$ +2.8 (-3.8) $\frac{0}{5/2}$
Q_6^2	$\frac{0}{1}$ $\frac{0}{6}$	$\frac{1}{1/2}$ -5.1 (+1.5) $\frac{0}{6/2}$	$\frac{2}{2/2}$ -1.2 (-4.5) $\frac{0}{6/2}$

Table 12.2: Possible precursors for each cluster (on the left), showing the calculated (and corrected) formation energies (kcal/mol) and statistical features $\frac{l}{m/n}$ (see text) for reactions: precursor $\rightarrow$ cluster (left) and cluster $\rightarrow$ precursor (right) (*Continuation*).

be considered, to keep correct dimensionality. For reactions involving breaking several $SiOSi$ bonds, a single water term [w] is considered, though the whole process implies the participation of two or three water molecules.

As large silicate clusters cannot be studied in this work, the kinetic model is constrained to the initial stages of the silica growth, when the concentration of clusters with more than 5 silicon atoms is still relatively unimportant. For larger times, boundary effects will become relevant, as the 5 silicon clusters are not allowed to react further, and reverse reactions will become artificially important. In this work the total simulation time was set to 15 min.

To simulate typical experimental sol-gel solutions, molar ratios water/alkoxide = 4 and alcohol/alkoxide = 8 are considered, corresponding to a TMOS concentration of 1.8 mol/l, in a methanol-based solution. Assuming that the hydrolysis of the alkoxide is completed before the condensation starts, and that volume variations are negligible during the whole process, water and monomer concentrations, in the beginning of the condensation, will be respectively zero and 1.8 mol/l. The full set of kinetic equations is presented below. They were solved numerically, by a iterative process, using a timestep of 10^{-4} s:

$$[\bullet] = [\bullet]_0 - \{\, 2[\text{—}] + 3([\wedge] + [\triangle]) + 4([\text{⋀}] + [\text{⅄}] + [\text{▷—}] + [\square] + [\diamond]) + 5([\text{⋀⋀}] + [\text{⅄⅄}] + [\text{+}] + [\text{▷⋀}] + [\text{▷▷}] + [\text{⋮▷}] + [\text{⋈}] + [\square\!\!/] + [\diamond\!\!-]) + [\diamond\!\!\triangleright] + [\square\!\!\triangleright] + [\square\!\!\!/] + [\diamond\!\!\!\!\bigcirc] \,\} \quad (12.1)$$

$$[w] = [w]_0 + \{\, [\text{—}] + 2[\wedge] + 3([\triangle] + [\text{⋀}] + [\text{⅄}]) + 4([\text{▷—}] + [\square] + [\text{⋀⋀}] + [\text{⅄⅄}] + [\text{+}]) + 5([\diamond] + [\text{▷⋀}] + [\text{▷▷}] + [\text{⋮▷}] + [\square\!\!/] + [\diamond\!\!\!\!\bigcirc]) + 6([\text{⋈}] + [\diamond\!\!-] + [\diamond\!\!\triangleright] + [\square\!\!\triangleright] + [\square\!\!\!/]) \,\} \quad (12.2)$$

$$2\frac{d[\text{—}]}{dt} = g_1^1 e^{-\frac{G^*}{RT}}[\bullet]^2 - g_0^1 e^{-\frac{G^*+9.4}{RT}}[\text{—}][w] - g_2^1 e^{-\frac{G^*}{RT}}[\text{—}][\bullet] + g_2^0 e^{-\frac{G^*+9.1}{RT}}[\wedge][w] \quad (12.3)$$
$$-g_{1/2}^1 e^{-\frac{G^*+7.7}{RT}}[\text{—}][\bullet] + g_{3/2}^0 e^{-\frac{G^*}{RT}}[\triangle][w] - g_4^2 e^{-\frac{G^*}{RT}}[\text{—}]^2 + g_1^0 e^{-\frac{G^*+19.4}{RT}}[\text{⋀}][w]$$
$$-g_{2/2}^2 e^{-\frac{G^*+12.8}{RT}}[\text{—}]^2 + g_{1/2}^0 e^{-\frac{G^*}{RT}}[\text{▷—}][w] - g_{2/2}^2 e^{-\frac{G^*}{RT}}[\text{—}]^2 + g_{2/2}^0 e^{-\frac{G^*+7.0}{RT}}[\square][w]$$
$$-g_{4/3}^2 e^{-\frac{G^*+25.1}{RT}}[\text{—}]^2 + g_{2/3}^0 e^{-\frac{G^*}{RT}}[\diamond][w] - g_4^2 e^{-\frac{G^*}{RT}}[\wedge][\text{—}] + g_2^0 e^{-\frac{G^*+15.7}{RT}}[\text{⋀⋀}][w]$$
$$-g_2^2 e^{-\frac{G^*}{RT}}[\wedge][\text{—}] + g_1^0 e^{-\frac{G^*+12.3}{RT}}[\text{⅄}][w] - g_6^2 e^{-\frac{G^*+0.1}{RT}}[\triangle][\text{—}] + g_1^0 e^{-\frac{G^*}{RT}}[\text{▷⋀}][w]$$
$$-g_{2/2}^2 e^{-\frac{G^*+17.0}{RT}}[\wedge][\text{—}] + g_{1/2}^0 e^{-\frac{G^*}{RT}}[\text{▷⋀}][w] - g_{1/2}^2 e^{-\frac{G^*+16.6}{RT}}[\wedge][\text{—}] + g_{1/2}^0 e^{-\frac{G^*}{RT}}[\text{⋈}][w]$$
$$-g_{4/2}^2 e^{-\frac{G^*+16.6}{RT}}[\wedge][\text{—}] + g_{2/2}^0 e^{-\frac{G^*}{RT}}[\text{⋮▷}][w] - g_{4/2}^2 e^{-\frac{G^*+17.1}{RT}}[\wedge][\text{—}] + g_{2/2}^0 e^{-\frac{G^*}{RT}}[\text{⋮▷}][w]$$
$$-g_{3/2}^2 e^{-\frac{G^*+9.4}{RT}}[\triangle][\text{—}] + g_2^0 e^{-\frac{G^*}{RT}}[\text{⋈}][w] - g_{2/2}^2 e^{-\frac{G^*}{RT}}[\wedge][\text{—}] + g_{2/2}^0 e^{-\frac{G^*+3.1}{RT}}[\square\!\!/][w]$$
$$-g_{6/2}^2 e^{-\frac{G^*+8.9}{RT}}[\triangle][\text{—}] + g_{1/2}^0 e^{-\frac{G^*}{RT}}[\diamond\!\!-][w] - g_{6/3}^2 e^{-\frac{G^*+27.7}{RT}}[\wedge][\text{—}] + g_{3/3}^0 e^{-\frac{G^*}{RT}}[\diamond\!\!\triangleright][w]$$
$$-g_{6/2}^2 e^{-\frac{G^*}{RT}}[\triangle][\text{—}] + g_{1/2}^0 e^{-\frac{G^*+2.6}{RT}}[\square\!\!\triangleright][w] - g_{4/3}^2 e^{-\frac{G^*+14.3}{RT}}[\wedge][\text{—}] + g_{4/3}^0 e^{-\frac{G^*}{RT}}[\square\!\!\triangleright][w]$$
$$-g_{4/3}^2 e^{-\frac{G^*+19.4}{RT}}[\wedge][\text{—}] + g_{2/3}^0 e^{-\frac{G^*}{RT}}[\square\!\!/][w] - g_{2/2}^2 e^{-\frac{G^*+2.8}{RT}}[\wedge][\text{—}] + g_{5/2}^0 e^{-\frac{G^*}{RT}}[\diamond\!\!\!\!\bigcirc][w]$$

$$3\frac{d[\wedge]}{dt} = g_2^1 e^{-\frac{G^*}{RT}}[\text{—}][\bullet] - g_2^0 e^{-\frac{G^*+9.1}{RT}}[\wedge][w] - g_1^0 e^{-\frac{G^*+16.9}{RT}}[\wedge] + g_3^0 e^{-\frac{G^*}{RT}}[\triangle][w] \quad (12.4)$$
$$-g_2^1 e^{-\frac{G^*}{RT}}[\wedge][\bullet] + g_2^0 e^{-\frac{G^*+19.6}{RT}}[\text{⋀}][w] - g_1^1 e^{-\frac{G^*}{RT}}[\wedge][\bullet] + g_3^0 e^{-\frac{G^*+12.1}{RT}}[\text{⅄}][w]$$

$$-g^1_{2/2}e^{-\frac{G^*+12.6}{RT}}[\wedge][\cdot\,]+g^0_{2/2}e^{-\frac{G^*}{RT}}[\,\dot{\triangle}\,][w]-g^1_{1/2}e^{-\frac{G^*}{RT}}[\wedge][\,\bullet\,]+g^0_{4/2}e^{-\frac{G^*+7.2}{RT}}[\square][w]$$
$$-g^1_{1/3}e^{-\frac{G^*+24.9}{RT}}[\wedge][\cdot\,]+g^0_{2/3}e^{-\frac{G^*}{RT}}[\diamond][w]-g^2_4e^{-\frac{G^*}{RT}}[\wedge][-]+g^0_2e^{-\frac{G^*+15.7}{RT}}[\wedge\!\!\wedge][w]$$
$$-g^2_2e^{-\frac{G^*}{RT}}[\wedge][-]+g^0_1e^{-\frac{G^*+12.3}{RT}}[\,\dot{\wedge}\,][w]-g^2_{2/2}e^{-\frac{G^*+17.0}{RT}}[\wedge][-]+g^0_{1/2}e^{-\frac{G^*}{RT}}[\triangleright\!\!\!-][w]$$
$$-g^2_{1/2}e^{-\frac{G^*+16.6}{RT}}[\wedge][-]+g^0_{1/2}e^{-\frac{G^*}{RT}}[\bowtie][w]-g^2_{4/2}e^{-\frac{G^*+29.8}{RT}}[\wedge][-]+g^0_{2/2}e^{-\frac{G^*}{RT}}[\,\dot{\triangleright}\,][w]$$
$$-g^2_{4/2}e^{-\frac{G^*+17.1}{RT}}[\wedge][-]+g^0_{2/2}e^{-\frac{G^*}{RT}}[\,\ddot{\triangleright}\,][w]-g^2_{2/2}e^{-\frac{G^*}{RT}}[\wedge][-]+g^0_{2/2}e^{-\frac{G^*+3.1}{RT}}[\square\!\!\!/][w]$$
$$-g^2_{6/3}e^{-\frac{G^*+27.7}{RT}}[\wedge][-]+g^0_{3/3}e^{-\frac{G^*}{RT}}[\diamond][w]-g^2_{4/3}e^{-\frac{G^*+14.3}{RT}}[\wedge][-]+g^0_{2/3}e^{-\frac{G^*}{RT}}[\square\!\!\triangleright][w]$$
$$-g^2_{4/3}e^{-\frac{G^*+19.4}{RT}}[\wedge][-]+g^0_{2/3}e^{-\frac{G^*}{RT}}[\square\!\!\!/][w]-g^2_{2/2}e^{-\frac{G^*+2.8}{RT}}[\wedge][-]+g^0_{5/2}e^{-\frac{G^*}{RT}}[\pentagon][w]$$

$$3\frac{d[\triangle]}{dt} = g^0_1e^{-\frac{G^*+16.9}{RT}}[\wedge]+g^1_{1/2}e^{-\frac{G^*+7.7}{RT}}[-][\cdot\,]-g^0_3e^{-\frac{G^*}{RT}}[\triangle][w]-g^0_{3/2}e^{-\frac{G^*}{RT}}[\triangle][w] \quad (12.5)$$
$$-g^1_3e^{-\frac{G^*}{RT}}[\triangle][\cdot\,]+g^0_1e^{-\frac{G^*+4.3}{RT}}[\,\dot{\triangle}\,][w]-g^1_{3/2}e^{-\frac{G^*+8.0}{RT}}[\triangle][\cdot\,]+g^0_{2/2}e^{-\frac{G^*}{RT}}[\diamond][w]$$
$$-g^2_6e^{-\frac{G^*+0.1}{RT}}[\triangle][-]+g^0_1e^{-\frac{G^*}{RT}}[\triangleright\!\!\!-][w]-g^2_{3/2}e^{-\frac{G^*+9.4}{RT}}[\triangle][-]+g^0_{2/2}e^{-\frac{G^*}{RT}}[\bowtie][w]$$
$$-g^2_{6/2}e^{-\frac{G^*+12.2}{RT}}[\triangle][-]+g^0_{1/2}e^{-\frac{G^*}{RT}}[\diamond\!\!-][w]-g^2_{6/2}e^{-\frac{G^*}{RT}}[\triangle][-]+g^0_{1/2}e^{-\frac{G^*+2.6}{RT}}[\square\!\!\triangleright][w]$$

$$4\frac{d[\wedge\!\!\wedge]}{dt} = g^1_2e^{-\frac{G^*}{RT}}[\wedge][\,\bullet\,]+g^2_4e^{-\frac{G^*}{RT}}[-]^2-g^0_2e^{-\frac{G^*+19.6}{RT}}[\wedge\!\!\wedge][w]-g^0_1e^{-\frac{G^*+19.4}{RT}}[\wedge\!\!\wedge][w]$$
$$-g^0_2e^{-\frac{G^*+32.2}{RT}}[\wedge\!\!\wedge]+g^0_2e^{-\frac{G^*}{RT}}[\triangle][w]-g^0_1e^{-\frac{G^*+9.1}{RT}}[\wedge\!\!\wedge]+g^0_4e^{-\frac{G^*}{RT}}[\square][w]$$
$$-g^1_2e^{-\frac{G^*}{RT}}[\wedge\!\!\wedge][\,\bullet\,]+g^0_2e^{-\frac{G^*+5.4}{RT}}[\wedge\!\!\wedge][w]-g^1_2e^{-\frac{G^*}{RT}}[\wedge\!\!\wedge][\,\bullet\,]+g^0_1e^{-\frac{G^*+2.1}{RT}}[\,\dot{\wedge}\,][w]$$
$$-g^1_{2/2}e^{-\frac{G^*+27.0}{RT}}[\wedge\!\!\wedge][\,\bullet\,]+g^0_{1/2}e^{-\frac{G^*}{RT}}[\triangleright\!\!\!-][w]-g^1_{1/2}e^{-\frac{G^*+27.2}{RT}}[\wedge\!\!\wedge][\,\bullet\,]+g^0_{1/2}e^{-\frac{G^*}{RT}}[\,\dot{\triangleright}\,][w]$$
$$-g^1_{1/2}e^{-\frac{G^*+27.7}{RT}}[\wedge\!\!\wedge][\,\bullet\,]+g^0_{1/2}e^{-\frac{G^*}{RT}}[\,\ddot{\triangleright}\,][w]-g^1_{2/2}e^{-\frac{G^*+7.2}{RT}}[\wedge\!\!\wedge][\,\bullet\,]+g^0_{2/2}e^{-\frac{G^*}{RT}}[\square\!\!\!/][w]$$
$$-g^1_{2/3}e^{-\frac{G^*+36.1}{RT}}[\wedge\!\!\wedge][\,\bullet\,]+g^0_{2/3}e^{-\frac{G^*}{RT}}[\diamond\!\!-][w]-g^1_{2/3}e^{-\frac{G^*+24.6}{RT}}[\wedge\!\!\wedge][\,\bullet\,]+g^0_{2/3}e^{-\frac{G^*}{RT}}[\square\!\!\triangleright][w]$$
$$-g^1_{1/2}e^{-\frac{G^*+13.0}{RT}}[\wedge\!\!\wedge][\,\bullet\,]+g^0_{5/2}e^{-\frac{G^*}{RT}}[\pentagon][w] \quad (12.6)$$

$$4\frac{d[\,\dot{\wedge}\,]}{dt} = g^1_1e^{-\frac{G^*}{RT}}[\wedge][\,\bullet\,]-g^0_3e^{-\frac{G^*+12.1}{RT}}[\,\dot{\wedge}\,][w]-g^0_{3/2}e^{-\frac{G^*+37.0}{RT}}[\,\dot{\wedge}\,]+g^0_{2/3}e^{-\frac{G^*}{RT}}[\diamond][w]$$
$$-g^1_3e^{-\frac{G^*}{RT}}[\,\dot{\wedge}\,][\,\bullet\,]+g^0_1e^{-\frac{G^*+9.6}{RT}}[\,\dot{\wedge}\,][w]-g^1_{3/2}e^{-\frac{G^*+19.4}{RT}}[\,\dot{\wedge}\,][\,\bullet\,]+g^0_{2/2}e^{-\frac{G^*}{RT}}[\bowtie][w]$$
$$-g^1_{3/3}e^{-\frac{G^*+22.1}{RT}}[\,\dot{\wedge}\,][\,\bullet\,]+g^0_{2/3}e^{-\frac{G^*}{RT}}[\square\!\!\!/][w] \quad (12.7)$$

$$4\frac{d[\,\dot{\triangle}\,]}{dt} = g^0_2e^{-\frac{G^*+32.2}{RT}}[\wedge\!\!\wedge]+g^1_3e^{-\frac{G^*}{RT}}[\triangle][\,\bullet\,]+g^1_{2/2}e^{-\frac{G^*+12.6}{RT}}[\wedge][\,\bullet\,]+g^2_{2/2}e^{-\frac{G^*+12.8}{RT}}[-]^2 \quad (12.8)$$
$$-g^0_2e^{-\frac{G^*}{RT}}[\,\dot{\triangle}\,][w]-g^0_1e^{-\frac{G^*+4.3}{RT}}[\,\dot{\triangle}\,][w]-g^0_{2/2}e^{-\frac{G^*}{RT}}[\,\dot{\triangle}\,][w]-g^0_{1/2}e^{-\frac{G^*}{RT}}[\,\dot{\triangle}\,][w]$$
$$-g^0_2e^{-\frac{G^*+12.3}{RT}}[\,\dot{\triangle}\,]+g^0_4e^{-\frac{G^*}{RT}}[\diamond][w]-g^1_1e^{-\frac{G^*}{RT}}[\,\dot{\triangle}\,][\,\bullet\,]+g^0_1e^{-\frac{G^*+5.0}{RT}}[\triangleright\!\!\!-][w]$$
$$-g^1_1e^{-\frac{G^*}{RT}}[\,\dot{\triangle}\,][\,\bullet\,]+g^0_2e^{-\frac{G^*+5.3}{RT}}[\bowtie][w]-g^1_1e^{-\frac{G^*}{RT}}[\,\dot{\triangle}\,][\,\bullet\,]+g^0_2e^{-\frac{G^*+5.3}{RT}}[\,\dot{\triangleright}\,][w]$$

$$-g_1^1 e^{-\frac{G^*}{RT}}[\,\text{}\,][\,\cdot\,] + g_2^0 e^{-\frac{G^*+4.8}{RT}}[\,\text{  }\,][w] - g_{1/2}^1 e^{-\frac{G^*+4.4}{RT}}[\,\text{}\,][\,\cdot\,] + g_{4/2}^0 e^{-\frac{G^*}{RT}}[\,\text{  }\,][w]$$
$$-g_{1/2}^1 e^{-\frac{G^*+3.9}{RT}}[\,\text{}\,][\,\cdot\,] + g_{1/2}^0 e^{-\frac{G^*}{RT}}[\,\text{}\,][w] - g_{2/2}^1 e^{-\frac{G^*+5.7}{RT}}[\,\text{}\,][\,\cdot\,] + g_{2/2}^0 e^{-\frac{G^*}{RT}}[\,\text{}\,][w]$$

$$4\frac{d[\,\text{}\,]}{dt} = g_1^0 e^{-\frac{G^*+12.4}{RT}}[\,\text{  }\,] + g_{1/2}^1 e^{-\frac{G^*}{RT}}[\,\text{  }\,][\,\cdot\,] + g_{2/2}^2 e^{-\frac{G^*}{RT}}[\,-\,]^2 - g_4^0 e^{-\frac{G^*}{RT}}[\,\text{}\,]\;[w]$$
$$-g_{4/2}^0 e^{-\frac{G^*+7.2}{RT}}[\,\text{}\,][w] - g_{2/2}^0 e^{-\frac{G^*}{RT}}[\,\text{}\,][w] - g_2^0 e^{-\frac{G^*+32.1}{RT}}[\,\text{}\,] + g_1^0 e^{-\frac{G^*}{RT}}[\,\text{  }\,][w]$$
$$-g_4^1 e^{-\frac{G^*}{RT}}[\,\text{}\,][\,\cdot\,] + g_1^0 e^{-\frac{G^*+5.3}{RT}}[\,\text{}\,][w] - g_4^1 e^{-\frac{G^*+12.1}{RT}}[\,\text{}\,][\,\cdot\,] + g_{1/2}^0 e^{-\frac{G^*}{RT}}[\,\text{  }\,][w]$$
$$-g_{2/2}^1 e^{-\frac{G^*+17.2}{RT}}[\,\text{}\,][\,\cdot\,] + g_{1/2}^0 e^{-\frac{G^*}{RT}}[\,\text{  }\,][w] \qquad (12.9)$$

$$4\frac{d[\,\text{}\,]}{dt} = g_2^0 e^{-\frac{G^*+32.1}{RT}}[\,\text{}\,] + g_2^0 e^{-\frac{G^*+12.3}{RT}}[\,\text{}\,] + g_{3/2}^0 e^{-\frac{G^*+37.0}{RT}}[\,\text{}\,] + g_{3/2}^1 e^{-\frac{G^*+8.0}{RT}}[\,\text{  }\,][\,\cdot\,]$$
$$+g_{1/3}^1 e^{-\frac{G^*+24.9}{RT}}[\,\text{  }\,][\,\cdot\,] + g_{4/3}^2 e^{-\frac{G^*+25.1}{RT}}[\,-\,]^2 - g_1^0 e^{-\frac{G^*}{RT}}[\,\text{  }\,][w] - g_4^0 e^{-\frac{G^*}{RT}}[\,\text{}\,][w]$$
$$-g_{2/3}^0 e^{-\frac{G^*}{RT}}[\,\text{}\,][w] - g_{2/2}^0 e^{-\frac{G^*}{RT}}[\,\text{}\,][w] - g_{2/3}^0 e^{-\frac{G^*}{RT}}[\,\text{}\,][w] - g_{2/3}^0 e^{-\frac{G^*}{RT}}[\,\text{}\,][w]$$
$$-g_2^1 e^{-\frac{G^*}{RT}}[\,\text{}\,][\,\cdot\,] + g_1^0 e^{-\frac{G^*+8.5}{RT}}[\,\text{}\,][w] - g_2^1 e^{-\frac{G^*}{RT}}[\,\text{}\,][\,\cdot\,] + g_1^0 e^{-\frac{G^*+6.6}{RT}}[\,\text{  }\,][w] \qquad (12.10)$$

$$5\frac{d[\,\text{  }\,]}{dt} = g_2^1 e^{-\frac{G^*}{RT}}[\,\text{}\,][\,\cdot\,] + g_4^2 e^{-\frac{G^*}{RT}}[\,\text{}\,][\,-\,] - g_2^0 e^{-\frac{G^*+5.4}{RT}}[\,\text{}\,][w] - g_2^0 e^{-\frac{G^*+15.7}{RT}}[\,\text{}\,][w]$$
$$-g_2^0 e^{-\frac{G^*+32.6}{RT}}[\,\text{}\,] + g_2^0 e^{-\frac{G^*}{RT}}[\,\text{  }\,][w] - g_1^0 e^{-\frac{G^*+32.6}{RT}}[\,\text{}\,] + g_1^0 e^{-\frac{G^*}{RT}}[\,\text{}\,][w]$$
$$-g_1^0 e^{-\frac{G^*+33.1}{RT}}[\,\text{}\,] + g_1^0 e^{-\frac{G^*}{RT}}[\,\text{  }\,][w] - g_{2/2}^0 e^{-\frac{G^*+41.5}{RT}}[\,\text{}\,] + g_{2/2}^0 e^{-\frac{G^*}{RT}}[\,\text{}\,][w]$$
$$-g_{2/2}^0 e^{-\frac{G^*+43.4}{RT}}[\,\text{}\,] + g_{2/2}^0 e^{-\frac{G^*}{RT}}[\,\text{  }\,][w] - g_{2/2}^0 e^{-\frac{G^*+30.0}{RT}}[\,\text{}\,] + g_{2/2}^0 e^{-\frac{G^*}{RT}}[\,\text{}\,][w]$$
$$-g_1^0 e^{-\frac{G^*+18.5}{RT}}[\,\text{}\,] + g_5^0 e^{-\frac{G^*}{RT}}[\,\text{  }\,][w] \qquad (12.11)$$

$$5\frac{d[\,\text{}\,]}{dt} = g_2^1 e^{-\frac{G^*}{RT}}[\,\text{  }\,][\,\cdot\,] + g_3^1 e^{-\frac{G^*}{RT}}[\,\text{}\,][\,\cdot\,] + g_2^2 e^{-\frac{G^*}{RT}}[\,\text{}\,][\,-\,] - g_2^0 e^{-\frac{G^*+2.1}{RT}}[\,\text{}\,][w]$$
$$-g_1^0 e^{-\frac{G^*+9.6}{RT}}[\,\text{}\,][w] - g_1^0 e^{-\frac{G^*+12.3}{RT}}[\,\text{}\,][w] - g_1^0 e^{-\frac{G^*+28.9}{RT}}[\,\text{}\,] + g_2^0 e^{-\frac{G^*}{RT}}[\,\text{  }\,][w]$$
$$-g_2^0 e^{-\frac{G^*+29.3}{RT}}[\,\text{}\,] + g_2^0 e^{-\frac{G^*}{RT}}[\,\text{}\,][w] - g_2^0 e^{-\frac{G^*+29.8}{RT}}[\,\text{}\,] + g_2^0 e^{-\frac{G^*}{RT}}[\,\text{  }\,][w]$$
$$-g_1^0 e^{-\frac{G^*+9.2}{RT}}[\,\text{}\,] + g_2^0 e^{-\frac{G^*}{RT}}[\,\text{  }\,][w] - g_{2/2}^0 e^{-\frac{G^*+38.1}{RT}}[\,\text{}\,] + g_2^0 e^{-\frac{G^*}{RT}}[\,\text{  }\,][w] \qquad (12.12)$$

$$5\frac{d[\,\text{  }\,]}{dt} = g_1^1 e^{-\frac{G^*}{RT}}[\,\text{}\,][\,\cdot\,] - g_4^0 e^{-\frac{G^*+1.4}{RT}}[\,\text{}\,][w] - g_6^0 e^{-\frac{G^*+20.7}{RT}}[\,\text{}\,] + g_1^0 e^{-\frac{G^*}{RT}}[\,\text{}\,][w]$$
$$-g_{3/2}^0 e^{-\frac{G^*+30.4}{RT}}[\,\text{}\,] + g_{1/2}^0 e^{-\frac{G^*}{RT}}[\,\text{}\,][w] - g_{12/2}^0 e^{-\frac{G^*+31.8}{RT}}[\,\text{}\,] + g_{1/2}^0 e^{-\frac{G^*}{RT}}[\,\text{}\,][w] \qquad (12.13)$$

$$5\frac{d[\,\text{}\,]}{dt} = g_2^0 e^{-\frac{G^*+32.6}{RT}}[\,\text{}\,] + g_{2/2}^1 e^{-\frac{G^*+27.2}{RT}}[\,\text{  }\,][\,\cdot\,] + g_1^1 e^{-\frac{G^*+5.0}{RT}}[\,\text{}\,][\,\cdot\,] + g_6^2 e^{-\frac{G^*+0.1}{RT}}[\,\text{}\,][\,\text{  }\,]$$
$$+g_{2/2}^2 e^{-\frac{G^*+17.0}{RT}}[\,\text{}\,][\,\text{}\,] - g_2^0 e^{-\frac{G^*}{RT}}[\,\text{  }\,][w] - g_2^0 e^{-\frac{G^*}{RT}}[\,\text{}\,][w] - g_1^0 e^{-\frac{G^*}{RT}}[\,\text{}\,][w]$$
$$-g_1^0 e^{-\frac{G^*}{RT}}[\,\text{}\,][w] - g_{1/2}^0 e^{-\frac{G^*}{RT}}[\,\text{}\,][w] - g_1^0 e^{-\frac{G^*+9.4}{RT}}[\,\text{}\,] + g_4^0 e^{-\frac{G^*}{RT}}[\,\text{}\,][w]$$

$$-g_2^0 e^{-\frac{G^*+8.9}{RT}}[\,]+g_2^0 e^{-\frac{G^*}{RT}}[\,][w]-g_2^0 e^{-\frac{G^*}{RT}}[\,]+g_2^0 e^{-\frac{G^*+2.6}{RT}}[\,][w] \tag{12.14}$$

$$\begin{aligned}5\frac{d[\,]}{dt} &= g_6^0 e^{-\frac{G^*+20.7}{RT}}[\,]+g_1^0 e^{-\frac{G^*+28.9}{RT}}[\,]+g_1^1 e^{-\frac{G^*}{RT}}[\,][\,\cdot\,]+g_{3/2}^1 e^{-\frac{G^*+19.4}{RT}}[\,][\,\cdot\,]\\ &+g_{1/2}^2 e^{-\frac{G^*+16.6}{RT}}[\,][-\,]-g_1^0 e^{-\frac{G^*}{RT}}[\,][w]-g_2^0 e^{-\frac{G^*}{RT}}[\,][w]-g_2^0 e^{-\frac{G^*+5.3}{RT}}[\,][w]\\ &-g_{2/2}^0 e^{-\frac{G^*}{RT}}[\,][w]-g_{1/2}^0 e^{-\frac{G^*}{RT}}[\,][w]-g_1^0 e^{-\frac{G^*+9.7}{RT}}[\,]+g_2^0 e^{-\frac{G^*}{RT}}[\,][w]\\ &-g_2^0 e^{-\frac{G^*+11.1}{RT}}[\,]+g_2^0 e^{-\frac{G^*}{RT}}[\,][w]\end{aligned} \tag{12.15}$$

$$\begin{aligned}5\frac{d[\,]}{dt} &= g_1^0 e^{-\frac{G^*+32.6}{RT}}[\,]+g_2^0 e^{-\frac{G^*+29.3}{RT}}[\,]+g_2^1 e^{-\frac{G^*}{RT}}[\,][\,\cdot\,]+g_{1/2}^1 e^{-\frac{G^*+27.2}{RT}}[\,][\,\cdot\,]\\ &+g_{4/2}^2 e^{-\frac{G^*+16.6}{RT}}[\,][-\,]-g_1^0 e^{-\frac{G^*}{RT}}[\,][w]-g_2^0 e^{-\frac{G^*}{RT}}[\,][w]-g_2^0 e^{-\frac{G^*+5.3}{RT}}[\,][w]\\ &-g_{1/2}^0 e^{-\frac{G^*}{RT}}[\,][w]-g_{2/2}^0 e^{-\frac{G^*}{RT}}[\,][w]-g_2^0 e^{-\frac{G^*+8.9}{RT}}[\,]+g_2^0 e^{-\frac{G^*}{RT}}[\,][w]\\ &-g_2^0 e^{-\frac{G^*+10.7}{RT}}[\,]+g_2^0 e^{-\frac{G^*}{RT}}[\,][w]\end{aligned} \tag{12.16}$$

$$\begin{aligned}5\frac{d[\,]}{dt} &= g_1^0 e^{-\frac{G^*+33.1}{RT}}[\,]+g_2^0 e^{-\frac{G^*+29.8}{RT}}[\,]+g_2^1 e^{-\frac{G^*}{RT}}[\,][\,\cdot\,]+g_{1/2}^1 e^{-\frac{G^*+27.7}{RT}}[\,][\,\cdot\,]\\ &+g_{4/2}^2 e^{-\frac{G^*+17.1}{RT}}[\,][-\,]-g_1^0 e^{-\frac{G^*}{RT}}[\,][w]-g_2^0 e^{-\frac{G^*}{RT}}[\,][w]-g_2^0 e^{-\frac{G^*+4.8}{RT}}[\,][w]\\ &-g_{1/2}^0 e^{-\frac{G^*}{RT}}[\,][w]-g_{2/2}^0 e^{-\frac{G^*}{RT}}[\,][w]-g_2^0 e^{-\frac{G^*+8.4}{RT}}[\,]+g_2^0 e^{-\frac{G^*}{RT}}[\,][w]\\ &-g_2^0 e^{-\frac{G^*+10.3}{RT}}[\,]+g_2^0 e^{-\frac{G^*}{RT}}[\,][w]\end{aligned} \tag{12.17}$$

$$\begin{aligned}5\frac{d[\,]}{dt} &= g_{3/2}^0 e^{-\frac{G^*+30.4}{RT}}[\,]+g_{1/2}^0 e^{-\frac{G^*+42.0}{RT}}[\,]+g_1^0 e^{-\frac{G^*+9.7}{RT}}[\,]+g_1^0 e^{-\frac{G^*+9.4}{RT}}[\,]\\ &+g_{1/2}^1 e^{-\frac{G^*+4.4}{RT}}[\,][\,\cdot\,]+g_{3/2}^2 e^{-\frac{G^*+9.4}{RT}}[\,][-\,]-g_{1/2}^0 e^{-\frac{G^*}{RT}}[\,][w]-g_{4/2}^0 e^{-\frac{G^*}{RT}}[\,][w]\\ &-g_2^0 e^{-\frac{G^*}{RT}}[\,][w]-g_4^0 e^{-\frac{G^*}{RT}}[\,][w]-g_{4/2}^0 e^{-\frac{G^*}{RT}}[\,][w]-g_{2/2}^0 e^{-\frac{G^*}{RT}}[\,][w]\end{aligned} \tag{12.18}$$

$$\begin{aligned}5\frac{d[\,]}{dt} &= g_1^0 e^{-\frac{G^*+9.2}{RT}}[\,]+g_2^0 e^{-\frac{G^*+12.6}{RT}}[\,]+g_4^1 e^{-\frac{G^*}{RT}}[\,][\,\cdot\,]+g_{2/2}^1 e^{-\frac{G^*+7.2}{RT}}[\,][\,\cdot\,]\\ &+g_{4/2}^2 e^{-\frac{G^*}{RT}}[\,][-\,]-g_2^0 e^{-\frac{G^*}{RT}}[\,][w]-g_2^0 e^{-\frac{G^*}{RT}}[\,][w]-g_1^0 e^{-\frac{G^*+5.3}{RT}}[\,][w]\\ &-g_{2/2}^0 e^{-\frac{G^*}{RT}}[\,][w]-g_{2/2}^0 e^{-\frac{G^*+3.1}{RT}}[\,][w]-g_1^0 e^{-\frac{G^*+28.9}{RT}}[\,]+g_1^0 e^{-\frac{G^*}{RT}}[\,][w]\\ &-g_1^0 e^{-\frac{G^*+30.8}{RT}}[\,]\qquad+g_1^0 e^{-\frac{G^*}{RT}}[\,][w]-g_2^0 e^{-\frac{G^*+17.4}{RT}}[\,]+g_2^0 e^{-\frac{G^*}{RT}}[\,][w]\\ &-g_1^0 e^{-\frac{G^*+22.4}{RT}}[\,]+g_1^0 e^{-\frac{G^*}{RT}}[\,][w]\end{aligned} \tag{12.19}$$

$$\begin{aligned}5\frac{d[\,]}{dt} &= g_1^0 e^{-\frac{G^*+28.9}{RT}}[\,]+g_2^0 e^{-\frac{G^*+8.9}{RT}}[\,]+g_2^0 e^{-\frac{G^*+8.4}{RT}}[\,]+g_2^0 e^{-\frac{G^*+8.9}{RT}}[\,]\\ &+g_{2/2}^0 e^{-\frac{G^*+38.1}{RT}}[\,]+g_{2/2}^0 e^{-\frac{G^*+41.5}{RT}}[\,]+g_2^1 e^{-\frac{G^*}{RT}}[\,][\,\cdot\,]+g_{2/3}^1 e^{-\frac{G^*+36.1}{RT}}[\,][\,\cdot\,]\\ &+g_{1/2}^1 e^{-\frac{G^*+3.9}{RT}}[\,][\,\cdot\,]+g_{6/2}^2 e^{-\frac{G^*+8.9}{RT}}[\,][-\,]-g_1^0 e^{-\frac{G^*}{RT}}[\,][w]-g_2^0 e^{-\frac{G^*}{RT}}[\,][w]\end{aligned}$$

$$-g_2^0 e^{-\frac{G^*}{RT}}[\text{  }][w] - g_2^0 e^{-\frac{G^*}{RT}}[\text{}][w] - g_{2/2}^0 e^{-\frac{G^*}{RT}}[\text{}][w] - g_{2/2}^0 e^{-\frac{G^*}{RT}}[\text{}][w]$$
$$-g_1^0 e^{-\frac{G^*+8.5}{RT}}[\text{}][w] - g_{2/3}^0 e^{-\frac{G^*}{RT}}[\text{}][w] - g_{1/2}^0 e^{-\frac{G^*}{RT}}[\text{}][w] - g_{1/2}^0 e^{-\frac{G^*}{RT}}[\text{}][w] \quad (12.20)$$

$$5\frac{d[\text{}]}{dt} = g_{12/2}^0 e^{-\frac{G^*+31.8}{RT}}[\text{}] + g_{1/2}^0 e^{-\frac{G^*+40.0}{RT}}[\text{}] + g_{2/2}^0 e^{-\frac{G^*+43.4}{RT}}[\text{}] + g_2^0 e^{-\frac{G^*+11.1}{RT}}[\text{}]$$
$$+g_2^0 e^{-\frac{G^*+10.7}{RT}}[\text{}] + g_2^0 e^{-\frac{G^*+10.2}{RT}}[\text{}] + g_1^0 e^{-\frac{G^*+30.8}{RT}}[\text{}] + g_2^1 e^{-\frac{G^*}{RT}}[\text{}][\cdot\ ]$$
$$+g_{2/2}^1 e^{-\frac{G^*+5.7}{RT}}[\text{}][\cdot\ ] + g_{6/3}^2 e^{-\frac{G^*+27.7}{RT}}[\text{}][-\ ] - g_{1/2}^0 e^{-\frac{G^*}{RT}}[\text{}][w] - g_{1/2}^0 e^{-\frac{G^*}{RT}}[\text{}][w]$$
$$-g_{2/2}^0 e^{-\frac{G^*}{RT}}[\text{}][w] - g_2^0 e^{-\frac{G^*}{RT}}[\text{}][w] - g_2^0 e^{-\frac{G^*}{RT}}[\text{}][w] - g_2^0 e^{-\frac{G^*}{RT}}[\text{}][w]$$
$$-g_1^0 e^{-\frac{G^*}{RT}}[\text{}][w] - g_1^0 e^{-\frac{G^*+6.6}{RT}}[\text{}][w] - g_{2/2}^0 e^{-\frac{G^*}{RT}}[\text{}][w] - g_{2/3}^0 e^{-\frac{G^*}{RT}}[\text{}][w] \quad (12.21)$$

$$5\frac{d[\text{}]}{dt} = g_2^0 e^{-\frac{G^*+17.4}{RT}}[\text{}] + g_2^0 e^{-\frac{G^*}{RT}}[\text{}] + g_{2/2}^0 e^{-\frac{G^*+30.0}{RT}}[\text{}] + g_4^1 e^{-\frac{G^*+12.1}{RT}}[\text{}][\cdot\ ]$$
$$+g_{2/3}^1 e^{-\frac{G^*+24.6}{RT}}[\text{}][\cdot\ ] + g_{6/2}^2 e^{-\frac{G^*}{RT}}[\text{}][-\ ] + g_{4/3}^2 e^{-\frac{G^*+14.3}{RT}}[\text{}][-\ ] - g_2^0 e^{-\frac{G^*}{RT}}[\text{}][w]$$
$$-g_2^0 e^{-\frac{G^*+2.6}{RT}}[\text{}][w] - g_{2/2}^0 e^{-\frac{G^*}{RT}}[\text{}][w] - g_{1/2}^0 e^{-\frac{G^*}{RT}}[\text{}][w] - g_{2/3}^0 e^{-\frac{G^*}{RT}}[\text{}][w]$$
$$-g_{1/2}^0 e^{-\frac{G^*+2.6}{RT}}[\text{}][w] - g_2^0 e^{-\frac{G^*}{RT}}[\text{}][w] \quad (12.22)$$

$$5\frac{d[\text{}]}{dt} = g_1^0 e^{-\frac{G^*+22.4}{RT}}[\text{}] + g_{2/2}^1 e^{-\frac{G^*+17.2}{RT}}[\text{}][\cdot\ ] + g_{3/3}^1 e^{-\frac{G^*+22.1}{RT}}[\text{}][\cdot\ ] + g_{4/3}^2 e^{-\frac{G^*+19.4}{RT}}[\text{}][-\ ]$$
$$-g_2^0 e^{-\frac{G^*}{RT}}[\text{}][w] - g_{1/2}^0 e^{-\frac{G^*}{RT}}[\text{}][w] - g_{2/3}^0 e^{-\frac{G^*}{RT}}[\text{}][w] - g_{4/3}^0 e^{-\frac{G^*}{RT}}[\text{}][w] \quad (12.23)$$

$$5\frac{d[\text{}]}{dt} = g_1^0 e^{-\frac{G^*+18.5}{RT}}[\text{}] + g_{1/2}^1 e^{-\frac{G^*+13.0}{RT}}[\text{}][\cdot\ ] + g_{2/2}^2 e^{-\frac{G^*+2.8}{RT}}[\text{}][-\ ] - g_5^0 e^{-\frac{G^*}{RT}}[\text{}][w]$$
$$-g_{5/2}^0 e^{-\frac{G^*}{RT}}[\text{}][w] - g_{5/2}^0 e^{-\frac{G^*}{RT}}[\text{}][w] \quad (12.24)$$

12.4 Silicate clusters evolution

The results obtained for the two sets of parameters are shown in the Figures 12.1 to 12.4. They seem to be very reasonable and in qualitative agreement with the experimental results obtained by Pouxwiell, Kelts, Klemperer and others.

A quantitative comparison is difficult, however, because the huge number of clusters with different combinations of alkoxy and hydroxyl groups that can be formed, is not considered in this model. In particular, the progressive formation of $Si(OH)_4$, that takes place in real sol-gel solutions, is not taken into account in the model, where $Si(OH)_4$ is therefore considered as the initial reactant.

On the other side, as clusters with more than 5 silicon atoms were not considered, there is a cumulative effect for these clusters in the boundary, which in turn increases artificially the rate of their reverse reactions. Eventually, a equilibrium is reached between the rate of formation and elimination for each cluster. The results obtained, in particular for the non-cyclic 4 and 5 silicon clusters, show that, even after the full time considered, 15 min, the system is still far from reaching that artificial equilibrium. This is confirmed by the evolution of the water concentration,

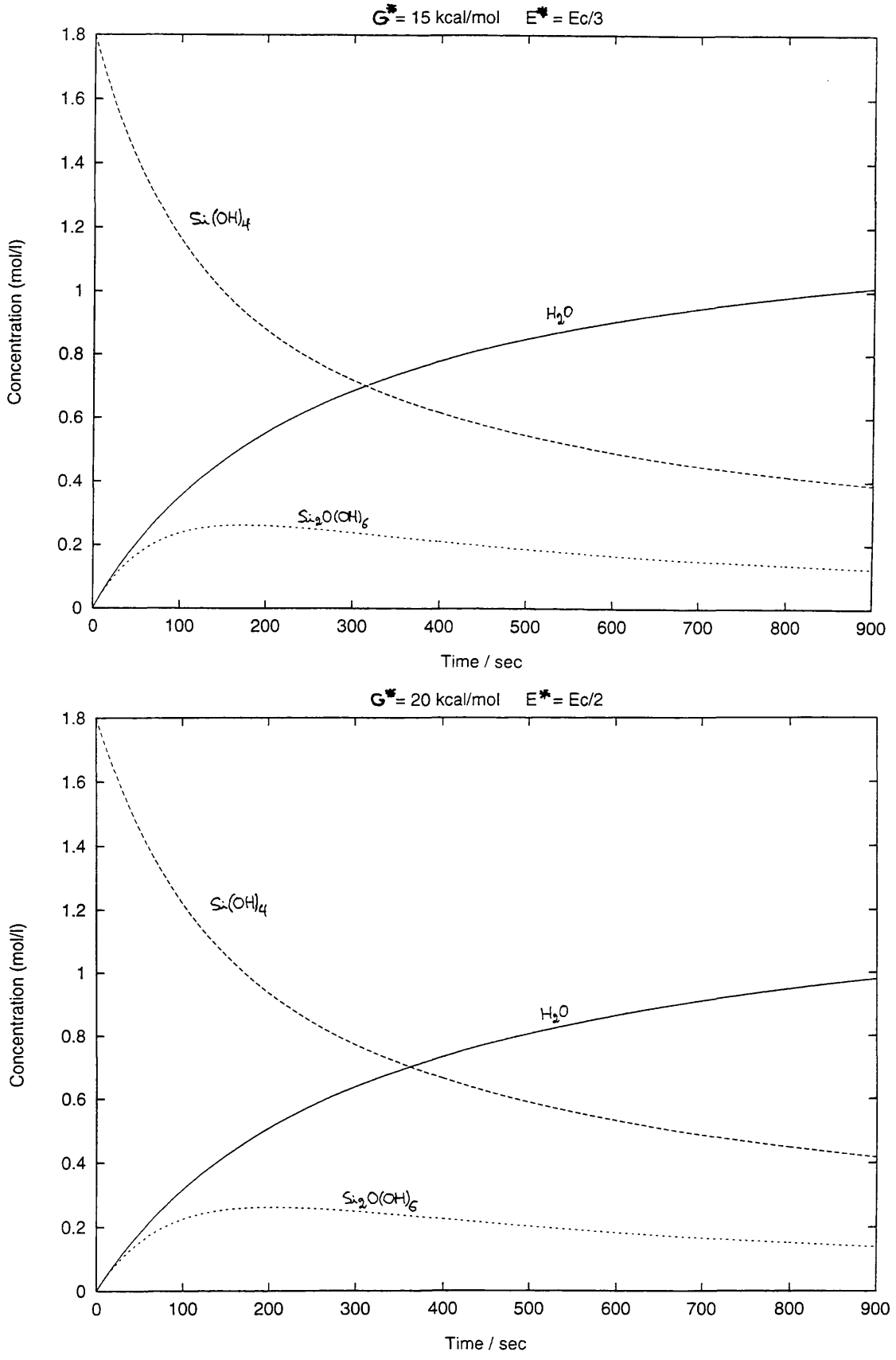


Figure 12.1: Water, monomer and dimer kinetic evolution with time, for G* = 15 kcal/mol and E* = E/3 (above) and G* = 20 kcal/mol and E* = E/2 (below).

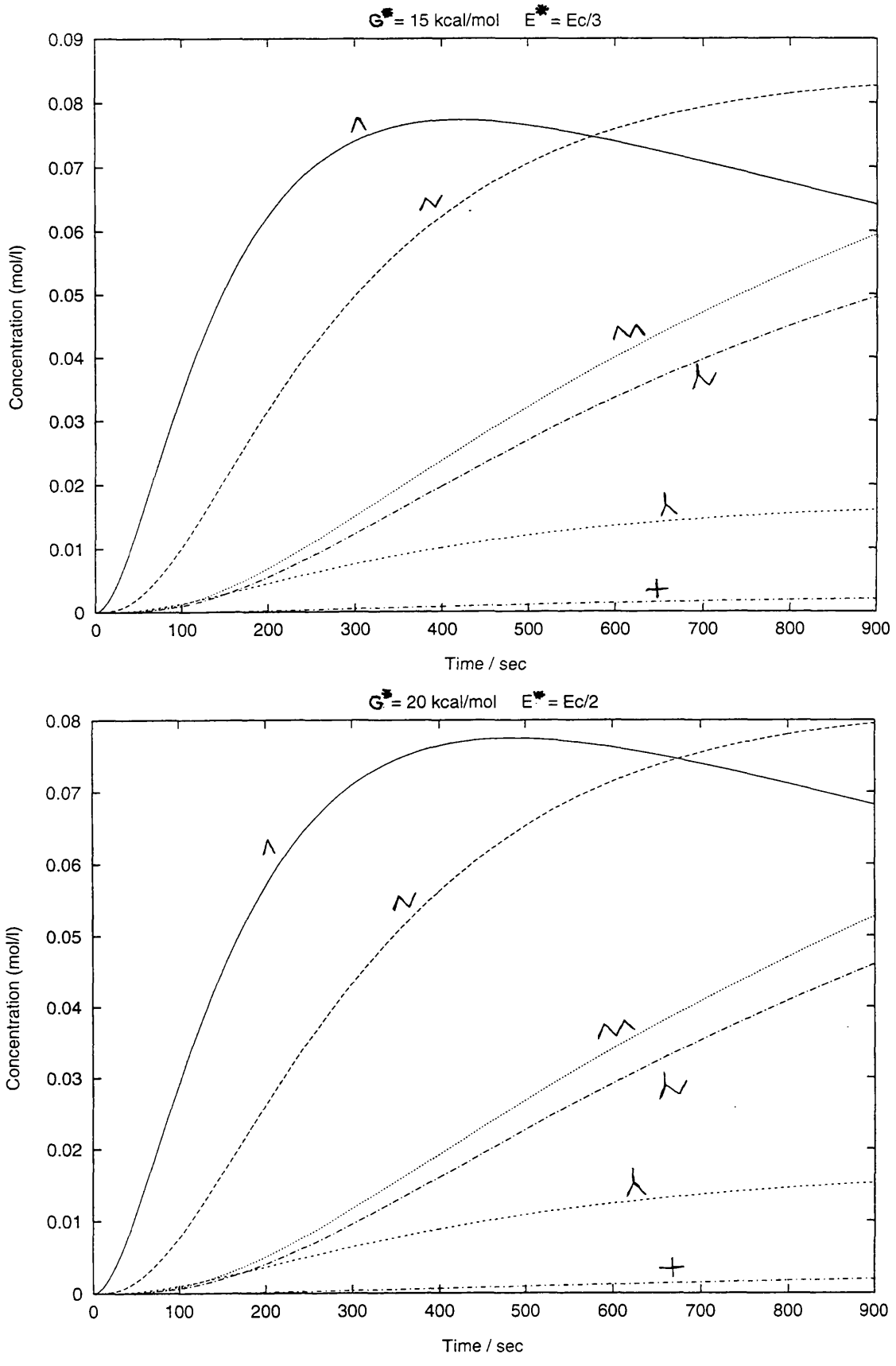


Figure 12.2: Non-cyclic clusters kinetic evolution with time, for G* = 15 kcal/mol and E* = E/3 (above) and G* = 20 kcal/mol and E* = E/2 (below).

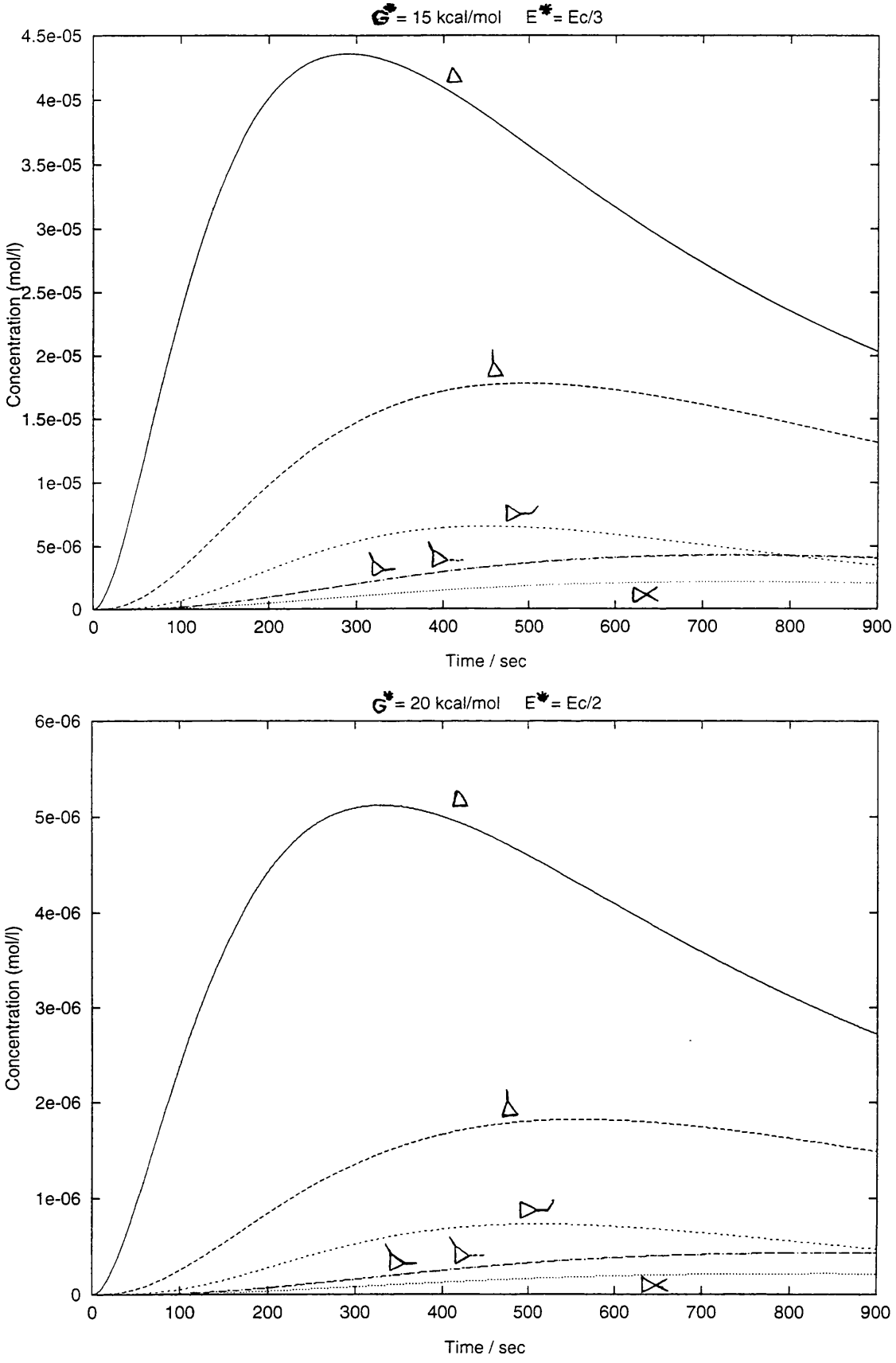


Figure 12.3: Trimer rings kinetic evolution with time, for G* = 15 kcal/mol and E* = E/3 (above) and G* = 20 kcal/mol and E* = E/2 (below).

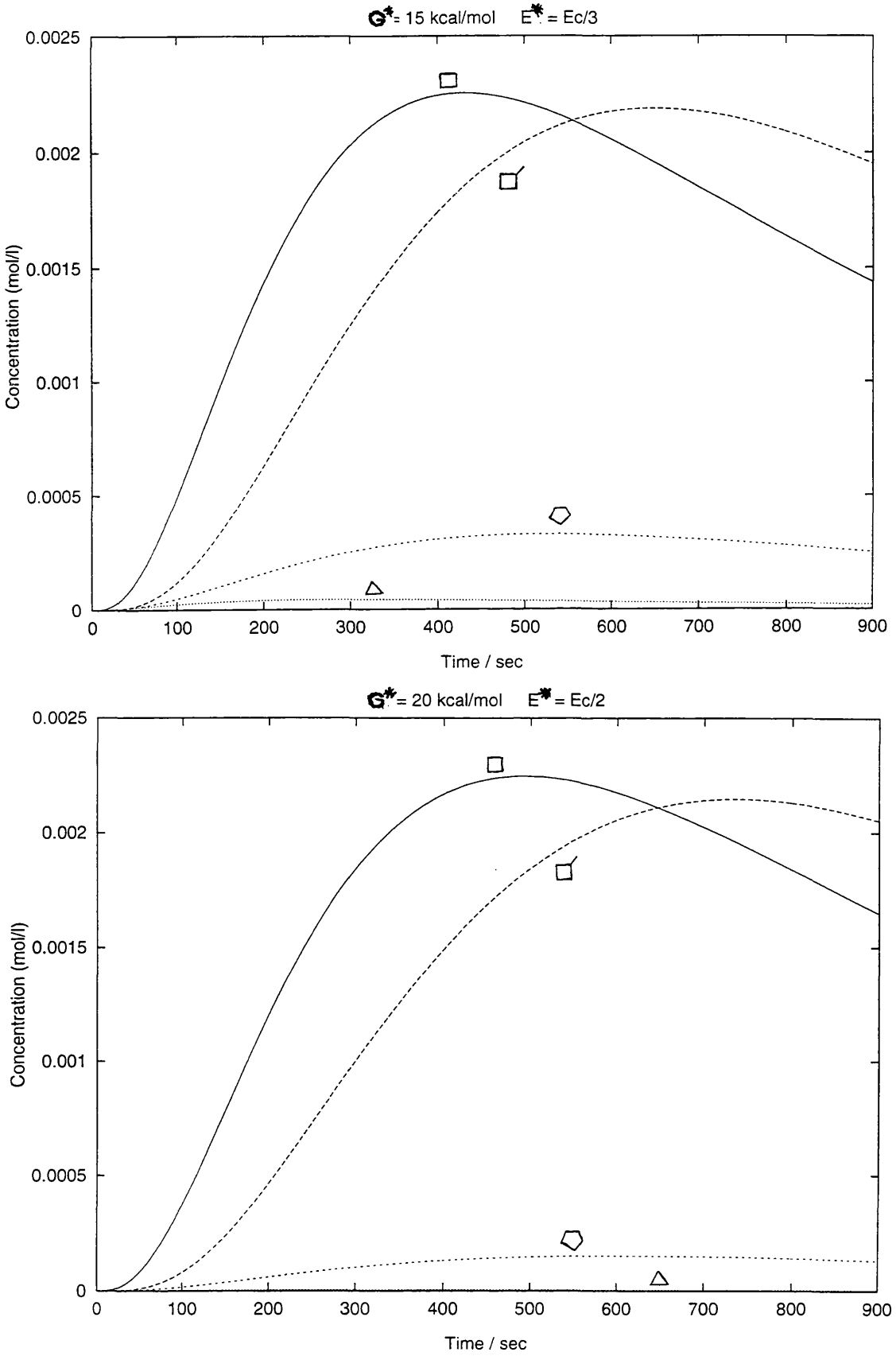


Figure 12.4: Tetramer and pentamer rings kinetic evolution with time, for G* = 15 kcal/mol and E* = E/3 (above) and G* = 20 kcal/mol and E* = E/2 (below).

which is still increasing after 15 min. Because water is formed in all condensation reactions and is consumed in all hydrolysis reactions, it can be used as a general reaction coordinate, to follow the global degree of silica growth.

As expected, the dimer concentration increases with time, until its rate of formation from the monomer is surpassed by the rate of formation of larger, more stable clusters, in particular the non-cyclic ones. In real sol-gel solutions, the $Si(OH)_4$ concentration is always much smaller than in this model, because it has to be formed first from the alkoxide precursor, after successive hydrolysis reactions.

The concentration of the trimer () and pentamer () rings is much smaller than the concentration of the tetramer () and branched tetramer () rings, reflecting the lower ring strain and stronger hydrogen-bond systems of the latter clusters. The concentration of the trimer ring is particularly small in the treatment with G* = 20 kcal/mol and E* = E/2. This is the main difference between the two treatments shown in this work. In the treatment with G* = 15 kcal/mol and E* = E/3, the smaller energy barrier emphasises the calculated energies, which thus have to be divided by 3, to avoid a cluster distribution that is too narrow, around the more stable non-cyclic clusters. This difference between the two treatments might be interesting, because the trimer ring has been detected in some experiments but not in others, and it is not clear in which conditions it can be formed in significant amounts. As expected, the concentration of the branched trimer rings ( , ,  and) is even smaller than for the trimer ring itself, from which they are formed. The branched trimer rings are, in turn, precursors for other clusters, often with two intramolecular condensations, formed by condensation reactions, which are usually endothermic.

The time evolution of the non-cyclic clusters shows a clear predominance of the linear structures over the branched ones, as discussed earlier. The concentration of clusters containing rings, with 3, 4 or even 5 silicon atoms, tends to decrease after some time, to form the more stable non-cyclic clusters with 4 and 5 silicons.

All clusters taken into account in this study but not represented in the graphs observed in the figures have concentrations that are too small to have any significant contribution to the overall results. These include the double trimer rings (,  and ) and the tetramer plus trimer rings (and).

12.5 Conclusions

The results presented here show that it is possible to construct a reasonable kinetic model, using only ab-initio information, to study complex systems, involving many reactions, which cannot be analysed separately by experimental techniques. A model like this can be used to study temperature effects, mass effects, the relative importance of the reverse reactions, and in general to get a deeper insight in the relation between macroscopic kinetics and atomic reactions.

At present, the model is limited by the quality of the ab-initio data, calculated in the gas-phase, at the LDA level of approximation only, and by the range of transformations studied, ignoring the hydrolysis reactions occurring before the one-silicon clusters and the condensation reactions occurring after the five-silicon clusters. With accurate DFT calculations, in a solvated environment, for a larger range of clusters and key activation energies for both forward and reverse reactions, excellent results might be obtained.

However, to simulate a real sol-gel process, the hydrolysis reaction has to be considered,

which increases enormously the complexity of the treatment, due to the huge number of possible clusters, with both hydroxyl and alkoxy terminal groups attached. This general study is not difficult, but demands considerable human and computing resources.

The simplest approach, which may be reasonable, is to admit that both the reaction and activation energies involved in the replacement of a alkoxy by a hydroxyl group are constant for all hydrolysis reactions. This way, a full kinetic study involving all real sol-gel clusters, until a given size limit, can be undertaken performing ab-initio calculations for only the small subset of fully hydrolysed clusters. The energy data thus obtained is subsequently used to estimate the energy of all other clusters containing alkoxy groups.

Chapter 13

Sol-Gel clusters

The purpose of this chapter is to investigate the influence of alkoxy groups on the structure, charge and energy of silicate clusters. In the previous chapters, the terminal groups of the silicate clusters were always hydroxyl groups. Non-local DFT, with a double basis set, is used in this study.

13.1 Introduction

During the last two decades, a wide range of experimental work has shown that the final structure and properties of sol-gel systems depend, to a great extent, on the structural and kinetic events taking place in the solution, during the first stages of the reaction process. The hydrolysis rate of TMOS as a function of the molar ratio TMOS/H_2O, temperature and pH, is investigated in Su et al. [225]. The variation of the gel time in TEOS-based sol-gel solutions as a function of the TEOS/H_2O ratio is presented in [88].

In particular, from the sequence of the experimental work of Yoldas, Kelts and Klemperer, it seems important to study the clusters initially formed during the hydrolysis-condensation process, in order to have a better understanding of the fundamental aspects governing the chemistry of sol-gel processes, like diffusion, solvation, hydrolysis, condensation and the reverse reactions.

To simplify this study as much as possible, reducing it to its essential aspects, the smallest alkoxide was chosen, $Si(OCH_3)_4$ (TMOS), and only clusters with a maximum of two silicon atoms were considered. Ab-initio Density Functional Theory could thus be used to optimise these clusters, at a high level of approximation, with non-local exchange (Becke) and correlation (Lee-Yang-Parr) energies and a double numerical basis set. Throughout this chapter, each functional group $Si(OCH_3)_X(OH)_Y(OSi)_Z$ will be represented as $[XYZ]$, with $X+Y+Z=4$, so TMOS will be designated as [400], $Si(OH)_4$ as [040] and $Si_2O(OH)_6$ as [031][031].

Essentially three series of clusters are considered in this work: 1) one-silicon clusters $[XY0]$, represented in Figure 13.1, asymmetrical (one side fully-hydrolysed) two-silicon clusters $[XY1][031]$, represented in Figure 13.2 and symmetrical two-silicon clusters $[XY1][XY1]$, represented in Figure 13.3. In each of these series, clusters are successively hydrolysed, so X methoxyl groups are progressively replaced by Y hydroxyl groups: in the first series, [400] $\rightarrow$ [310] $\rightarrow$ [220] $\rightarrow$ [130] $\rightarrow$ [040]; in the second, [301][031] $\rightarrow$ [211][031] $\rightarrow$ [121][031] $\rightarrow$ [031][031] and in the third, [301][301] $\rightarrow$ [211][211] $\rightarrow$ [121][121] $\rightarrow$ [031][031]. The data for [400], [040] and

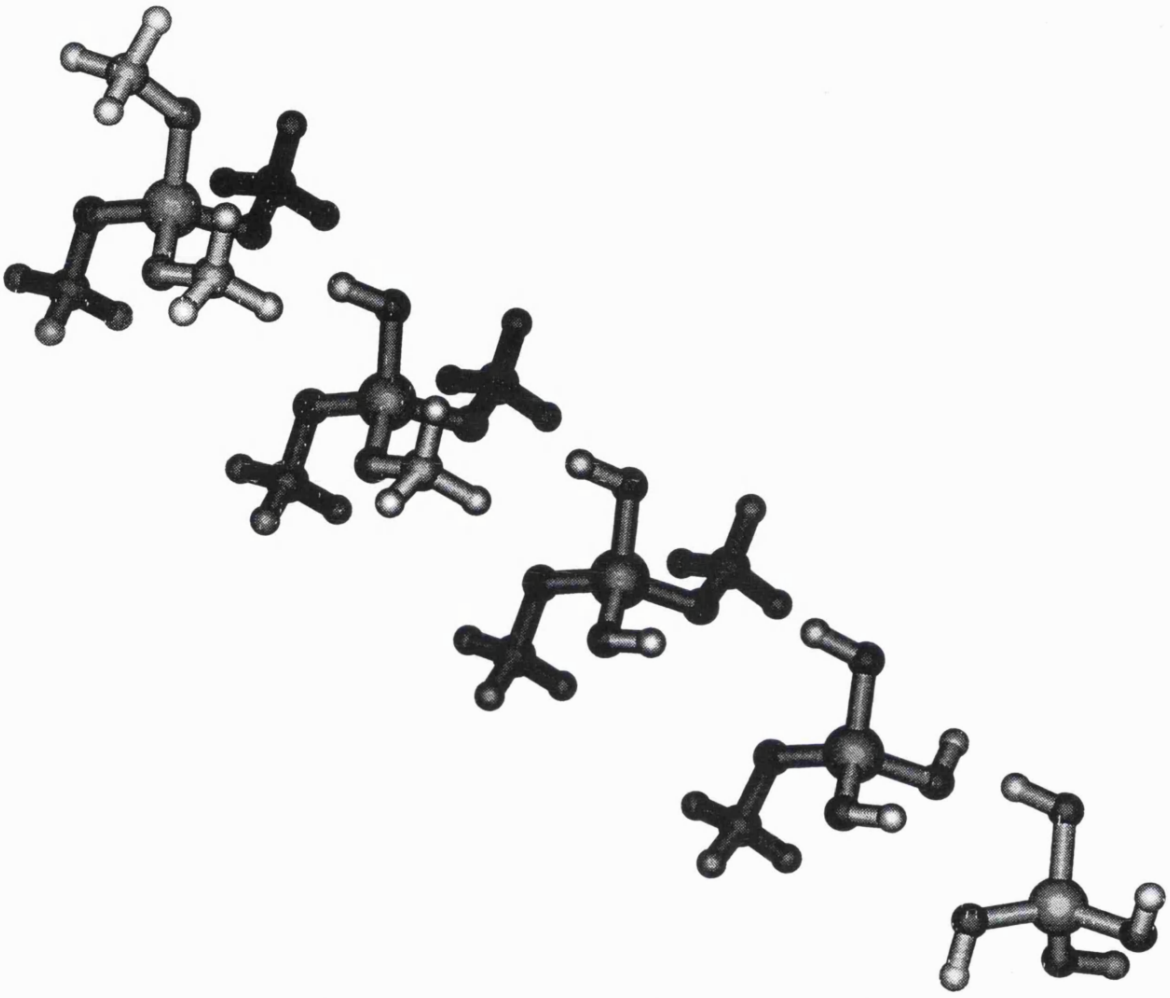


Figure 13.1: Optimised $[XY0]$ silicate clusters, after non-local DFT energy minimisation.

[031][031] is repeated here, for comparison.

13.2 Structure

The structural data of clusters $[XY0]$, $[XY1][031]$ and $[XY1][XY1]$ are presented in Tables 13.1, 13.2 and 13.3. The bond lengths are essentially those calculated for methanol, ethanol, $Si(OH)_4$, $Si_2O(OH)_6$ and $Si(OCH_3)_4$, at the same level of approximation. As discussed previously, these values are systematically too large, by about 0.04-0.06Å for SiO, 0.04 Å for OC, 0.03 Å for OH and 0.01 Å for CH. As shown before, these differences can be considerably reduced by increasing the quality of the basis set (using a triple instead of a double basis set), but given the complexity of some of these clusters, the difficulty of the calculation increases significantly.

In all clusters the $SiOH$, $SiOC$ and OCH angles are consistently close to 112^o, 122^o and $107\text{-}111^o$ (trans-gauche), with variations which rarely exceed 2^o. These results are also in good agreement with the structural data obtained, at the same level of approximation, for TMOS and the fully hydrolysed one-silicon and two-silicon clusters, and the comments then made (see chapter 9) about its accuracy should remain valid.

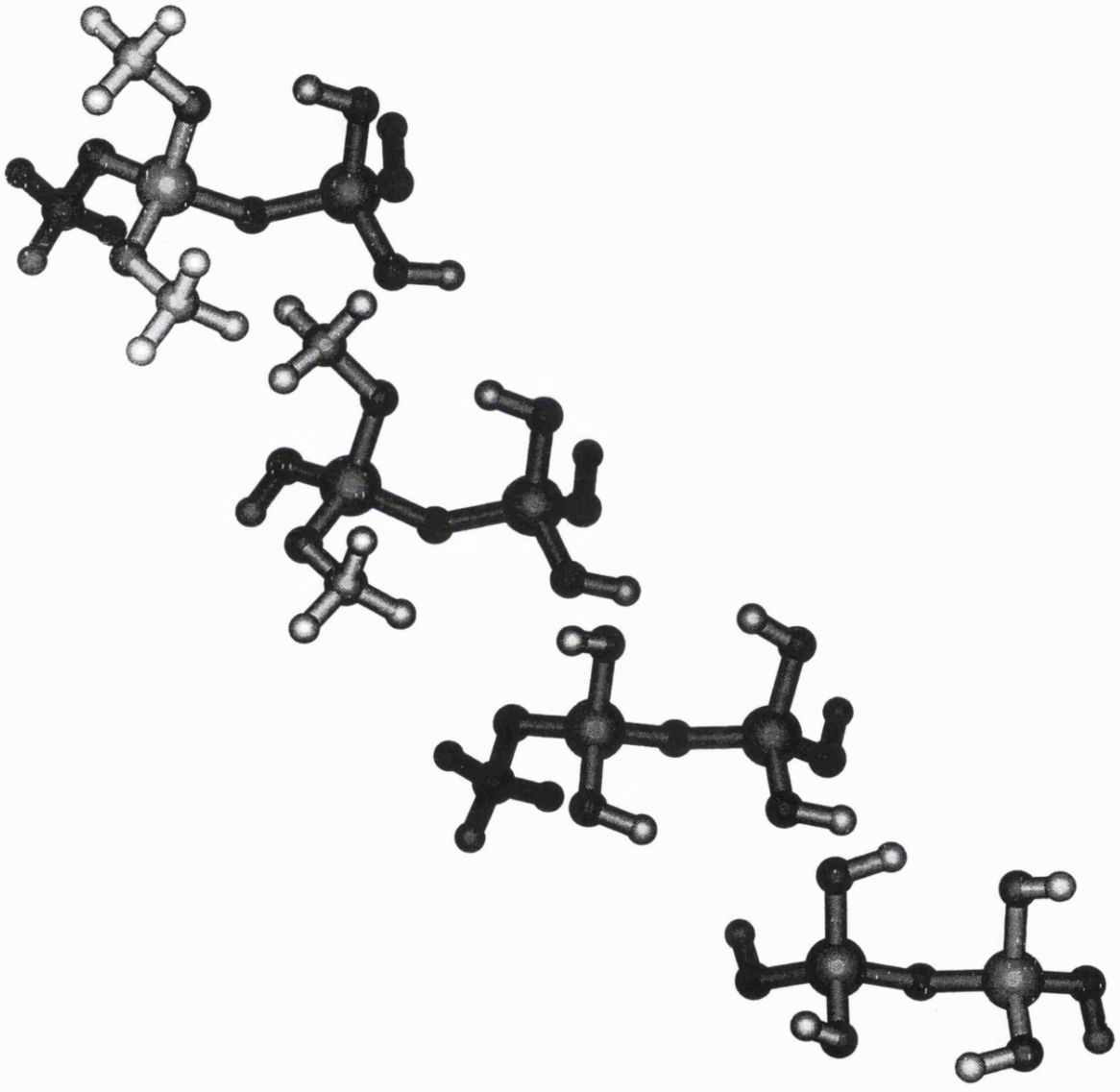


Figure 13.2: Optimised $[XY1][031]$ silicate clusters, after non-local DFT energy minimisation.

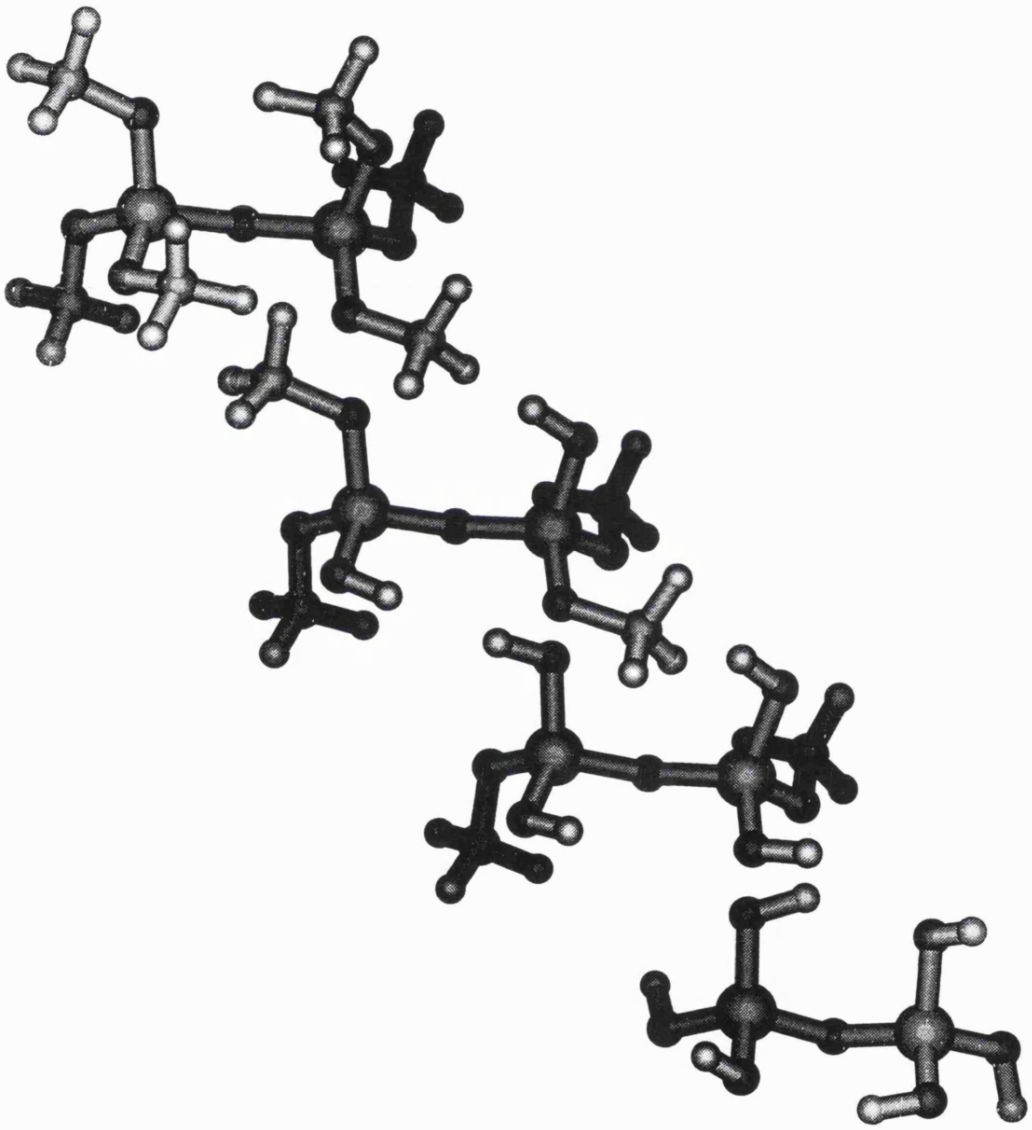


Figure 13.3: Optimised $[XY1][XY1]$ silicate clusters, after non-local DFT energy minimisation.

	[400]	[310]	[220]	[130]	[040]
Energy	-750.22898	-710.94624	-671.66254	-632.37895	-593.09657
Length					
Si-O_H	-	1.67	1.67	1.67	1.67
Si-O_C	1.66	1.66	1.66	1.66	-
O-C	1.45-1.46	1.45-1.46	1.45-1.46	1.45	-
C-H	1.10	1.10	1.10	1.10	-
O-H	-	0.98	0.98	0.98	0.99
Angle					
O-Si-O	106.7-113.4	107.1-113.5	106.8-113.5	105.8-115.0	105.7-117.4
Si-O-H	-	112.4	112.0-113.3	111.9-112.9	111.1
Si-O-C	119.6-124.7	121.0-123.2	122.0-122.4	126.0	-
O-C-H	107.2-111.3	107.2-111.0	106.7-113.5	107.3-115.0	-

Table 13.1: Total energy (Hartree), bond lengths (Å) and bond angles, for $[XY0]$ one-silicon clusters, after non-local DFT energy minimisation.

All $[XY0]$ clusters have two different values for the $OSiO$ angle, as found previously for $Si(OH)_4$ (105.7° and 117.4°, at this level of approximation). While the smaller angle (occurring four times), remains essentially constant, the larger angle (occurring twice), seems to increase slightly when methoxy groups are replaced by hydroxyl groups. In the two-silicon clusters, a similar range of variation is observed for the $O_{Si}SiO_C$ and $O_{Si}SiO_H$ angles.

In contrast, the $SiOSi$ angle depends considerably on the substituent groups attached to the silicon atoms. In the asymmetrical clusters $[XY1][031]$, the angle decreases steadily from 136.6° to 123.1° when methoxy are progressively replaced by hydroxyl groups, which promote stronger electrostatic interactions between the two silicon regions. In the symmetrical clusters $[XY1][XY1]$, the angle is larger and almost constant, about 145°, for all clusters except the fully-hydrolysed [031][031]. These values are consistent with the broad distribution found experimentally by Mozzi et al. [174] for this angle in vitreous silica, with a maximum at 144°.

The smaller $OSiO$ angle of the asymmetrical clusters is partly due to a hydrogen-bond formed in the [301][031] and [211][031] clusters , with an O- -H distance of 1.95 Å and 1.86 Å, respectively. Due to the soft potential associated with this angle, the optimised structure can change considerably due to small chemical modifications, and several similar minima of energy are likely to exist, which makes the determination of the global minimum more difficult.

The [211][211] cluster, in particular, has several different conformations, shown in Figure 13.4 and Table 13.4, which we should consider. In the more stable conformation (on the left), the hydroxyl groups act as acceptors relatively to the adjacent methoxy groups, while in the less stable conformation (+4.2 kcalmol^{-1}, on the right) they act as donors. In the conformation with intermediate energy (+3.5 kcalmol^{-1}), the hydroxyl groups occupy the trans positions, further apart.

Although the $SiOSi$ angle is essentially the same in all clusters, dramatic differences were found in the electric dipole moment. The O- -H distance, corresponding to potential hydrogen-bonds, indicate that these are not present in the more stable conformation and are relatively weak in the other two. The differences between these three conformations show how difficult it is to extract safe conclusions when comparing different clusters.

	[301][031]	[211][031]	[121][031]	[031][031]
Energy	-1227.6071	-1188.3227	-1149.0394	-1109.7564
Length				
Si-O_{Si}	1.66-1.67	1.65-1.67	1.66-1.67	1.67
Si-O_H	1.66-1.67	1.66-1.67	1.66-1.68	1.66-1.68
Si-O_C	1.65-1.68	1.66-1.68	1.65	-
O-C	1.46	1.45-1.46	1.46	-
C-H	1.10	1.10	1.10	-
O-H	0.98-0.99	0.98-0.99	0.98-0.99	0.98-0.99
O- -H	1.95-3.09	1.86-3.12	2.55	2.20
Angle				
Si-O-Si	136.6	135.8	131.9	123.1
O_{Si}-Si-O_H	105.4-112.9	105.0-112.2	104.6-112.6	107.1 - 112.9
O_{Si}-Si-O_C	105.1-112.3	104.0-111.4	110.1	-
Si-O-H	110.1-111.8	109.2-112.9	111.1-113.6	108.7-113.4
Si-O-C	121.8-124.5	122.2-123.6	121.7	-
O-C-H	106.9-110.5	107.2-111.2	107.0-110.1	-

Table 13.2: Total energy (Hartree), bond lengths (Å) and bond angles, for $[XY1][031]$ assymetrical two-silicon clusters, after non-local DFT energy minimisation.

	[301][301]	[211][211]	[121][121]	[031][031]
Energy	-1345.4500	-1266.8875	-1188.3201	-1109.7564
Length				
Si-O_{Si}	1.66	1.66	1.65-1.66	1.67
Si-O_H	-	1.67	1.67	1.66-1.68
Si-O_C	1.65-1.66	1.66	1.65-1.66	-
O-C	1.45-1.46	1.46	1.46	-
C-H	1.10	1.10	1.10	-
O-H	-	0.99	0.98	0.98-0.99
O- -H	2.27-2.30	2.91-3.03	3.14-3.20	2.20
Angle				
Si-O-Si	145.1	145.3	148.1	123.1
O_{Si}-Si-O_H	-	109.6-109.7	105.6-111.8	107.1-112.9
O_{Si}-Si-O_C	105.6-112.3	107.6-110.0	110.7-111.0	-
Si-O-H	-	111.8-112.2	112.2-113.4	108.7-113.4
Si-O-C	123.1-124.5	118.5-121.1	122.0-123.1	-
O-C-H	106.9-111.3	107.5-111.1	107.0-110.9	-

Table 13.3: Total energy (Hartree), bond lengths (Å) and bond angles, for $[XY1][XY1]$ symmetrical two-silicon clusters, after non-local DFT energy minimisation.

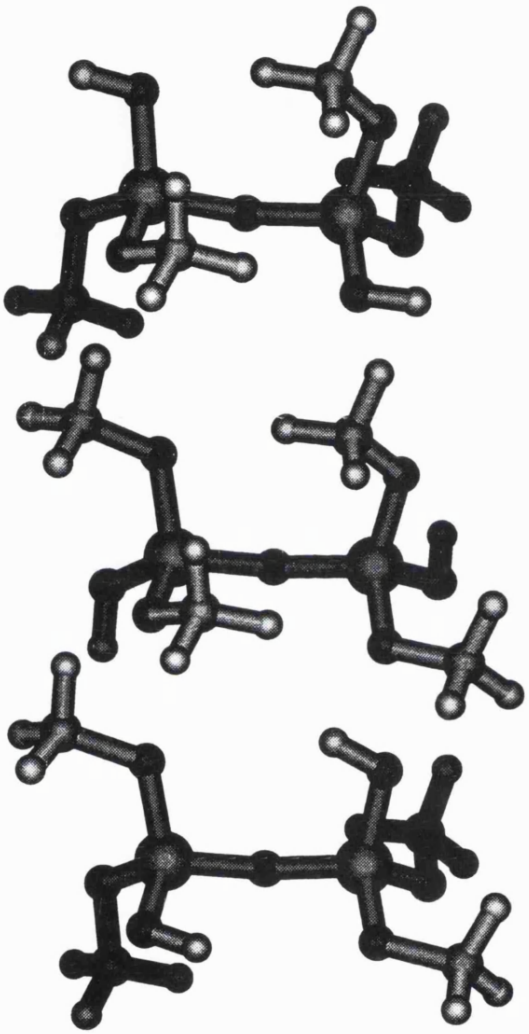


Figure 13.4: Different conformations for the [211][211] silicate cluster, after non-local DFT energy minimisation.

	[211][211]-a	[211][211]-b	[211][211]-c
Energy	-1266.8875	-1266.8820	-1266.8808
Dipole	0.29	2.50	1.33
O- -H bond	2.91-3.03	2.34	2.22-2.26
SiOSi angle	145.3	147.2	146.5
charges O	-0.2329	-0.2177	-0.2667
H	0.1530	0.0263	0.0240

Table 13.4: Energy (Hartree), dipole (Debye), hydrogen-bond length (Å), bridging angle and Hirshfeld charges, for different conformations of the [211][211] silicate cluster, after non-local DFT energy minimisation.

	[400]	[310]	[220]	[130]	[040]
Dipole	0.42	0.43	0.66	0.83	0.01
Charges					
Si	0.5139	0.5126	0.5101	0.5103	0.5087
C	-0.0185	-0.0185	-0.0172	-0.0151	-
O_C	-0.2290	-0.2311	-0.2323	-0.2335	-
O_H	-	-0.2848	-0.2892	-0.2896	-0.2885
H_C	0.0397	0.0401	0.0411	0.0423	-
H_O	-	0.1599	0.1602	0.1600	0.1614

Table 13.5: Electric dipole (Debye) and Hirshfeld charges for $[XY0]$ one-silicon clusters, after non-local DFT energy minimisation.

13.3 Charge distribution

The electric dipole moment and Hirshfeld partial charges calculated for the $[XY0]$, $[XY1][031]$ and $[XY1][XY1]$ clusters are presented in Tables 13.5, 13.6 and 13.7, respectively. Hirshfeld charges were chosen because they are in much better agreement with the chemical evidence than the Mulliken charges, as seen before (see chapter 9). The dipole moment is very sensitive to the cluster geometry (as seen for [211][211]) and to the level of approximation used (as seen for [031][031]), so further refinements might lead to considerable changes in the values presented here.

The dipole moment is relatively small for the one-silicon clusters and similar to the values obtained for water, methanol and ethanol. In $[XY0]$ species, the dipole moment increases with Y, essentially because a hydroxyl group has a larger charge separation than an alkoxy group. For the [220] cluster, for example, a charge of +0.160 for H(O) compares with only +0.106 for CH_3(O), whereas a charge of -0.289 for O(H) compares with only -0.232 for O(CH_3). This is consistent with both DFT and HF methanol results, where the charge of H(O) is always more positive than the charge of CH_3(O).

However, according to these results, the relative inductive effect of the OH and OCH_3 groups depends on the particular cluster considered. In [310], the charge in OCH_3 is -0.129 compared with -0.125 in OH, whereas in [130] the charge in OCH_3 is -0.122 compared with -0.130 in OH. The silicon atom becomes slightly less electropositive as methoxy groups are replaced by hydroxyl groups. As discussed before, the dipole of [040] is zero, due to its high symmetry.

The dipole moment is much less predictable in the two-silicon clusters, due to its increased complexity. The [301][301] cluster, with only OCH_3 groups, has a larger dipole moment than [031][031], with only OH groups, due to considerations of symmetry (as in [400] versus [040]). Asymmetrical $[XY1][031]$ clusters tend to have higher dipole moments than the corresponding symmetrical ones $[XY1][XY1]$. Bridging oxygens O_{Si} have slightly bigger charges than terminal ones O_H, but the differences are very small. In both asymmetrical and symmetrical clusters, OH groups are more electronegative than OCH_3.

Nevertheless, in spite of that, the Si charge systematically decreases when OCH_3 groups are replaced by OH groups. This tendency is clearly visible in the symmetrical clusters $[XY1][XY1]$ but is even clearer in the asymmetrical ones $[XY1][031]$. The charge on the left Si decreases with successive hydrolysis, approaching progressively the charge of the right, fully hydrolysed Si,

	[301][031]	[211][031]	[121][031]	[031][031]
Dipole	1.86	2.17	0.42	1.32
Charges				
Si_l	0.5286	0.5293	0.5205	0.5199
Si_r	0.5171	0.5172	0.5182	"
C	-0.0136	-0.0134	-0.0137	-
O_{Si}	-0.2928	-0.2932	-0.2945	-0.2981
O_C	-0.2199	-0.2140	-0.2283	-
O_H	-0.2937	-0.2907	-0.2848	-0.2796
H_C	0.0435	0.0445	0.0438	-
H_O	0.1457	0.1492	0.1581	0.1560

Table 13.6: Electric dipole (Debye) and Hirshfeld charges for $[XY1][031]$ asymetrical two-silicon clusters, after non-local DFT energy minimisation.

	[301][301]	[211][211]	[121][121]	[031][031]
Dipole	1.62	0.29	0.52	1.32
Charges				
Si	0.5262	0.5230	0.5204	0.5199
C	-0.0190	-0.0167	-0.0147	-
O_{Si}	-0.2893	-0.2887	-0.2876	-0.2981
O_C	-0.2239	-0.2302	-0.2310	-
O_H	-	-0.2880	-0.2877	-0.2796
H_C	0.0386	0.0417	0.0424	-
H_O	-	0.1530	0.1597	0.1560

Table 13.7: Electric dipole (Debye) and Hirshfeld charges for $[XY1][XY1]$ symmetrical two-silicon clusters, after non-local DFT energy minimisation.

which remains almost unchanged. This is surprising, as it is usually believed that the substitution of OCH_3 by more electronegative OH groups, should increase the electrophilic character of the silicon atom. These differences are, however, very small, and at this level of approximation, it seems reasonable to conclude that inductive effects caused by the substituent groups should have a minor role in the chemistry of these clusters.

13.4 Reaction energies

The reaction energies obtained for the various monomer and dimer hydrolyses are presented in Tables 13.8 and 13.9, respectively. In the gas phase conditions where these studies were carried out, the hydrolysis reaction seems to be a slightly exothermic process, with reaction energies ranging from -0.4 to -2.7 kcal mol^{-1}. Experimental evidence, however, shows that the hydrolysis of silicon alkoxides in solution is a highly exothermic process, resulting in significant increases of temperature in the first minutes after the reactants are added (a definitive enthalpy of reaction seems difficult to measure, as many reactions occur simultaneously). These differences between

H_2O +	Reactant	+ $\Delta E/kcalmol^{-1}$ $\longrightarrow$	Product	+ CH_3OH
	[400]	-1.46	[310]	
	[310]	-0.86	[220]	
	[220]	-0.92	[130]	
	[130]	-1.68	[040]	

Table 13.8: Reaction energies for the monomer hydrolysis, from non-local DFT calculations.

H_2O +	Reactant	+ $\Delta E/kcalmol^{-1}$ $\longrightarrow$	Product	+ CH_3OH
	[301][031]	-0.42	[211][031]	
	[211][031]	-1.10	[121][031]	
	[121][121]	-2.74	"	
	[121][031]	-1.30	[031][031]	

Table 13.9: Reaction energies for the dimer hydrolysis, from non-local DFT calculations.

theoretical and experimental results should therefore be accounted for by solvations effects, which seem to stabilise preferentially hydroxyl compared with alkoxyl groups.

Due to its energetic importance, hydrogen-bonds should play a major role in these stabilisation effects. As hydrogen-bonds are essentially electrostatic interactions, and partial charges are much smaller in OR than in OH groups, only extremely weak hydrogen-bond interactions may result from interactions with alkoxy groups. This is confirmed by the structural and energetic results above discussed for the two-silicon clusters, in particular the [211][211] isomers. Therefore, each time hydrolysis takes place, three hydrogen-bond sites, in the reactant water molecule, are replaced by four, two in the product alcohol molecule and two in the OH group thus formed. The full hydrolysis of a [400] molecule to form a [040] monomer, would thus result, in a total stabilisation energy of -4.9 kcal mol^{-1} from the reaction itself plus about 4×-4.5 kcal mol^{-1} from hydrogen-bond solvation effects, giving an estimate of -22.9 kcal mol^{-1}. This crude estimate is probably a reasonable upper limit for the reaction energy. In future years, accurate ab-initio and classical molecular dynamics will certainly provide satisfactory answers for this difficult problem.

The calculated energies are very similar for all the monomer and dimer hydrolysis reactions considered. This shows that the energy of the hydrolysis reaction does not depend in a significant way on the structure of the reacting cluster, in particular on its previous degree of hydrolysis Y and condensation Z. A tendency for hydrolysis to become slightly more exothermic in clusters with larger Y may be noticed, but the differences are probably too small to be relevant.

The [211][031] cluster, with two methoxyl groups attached to the same silicon atom, are about 1.5 kcal mol^{-1} more stable than its isomer [121][121], where each methoxyl group is attached to a different silicon atom. This difference is due to the hydrogen bond present in the first cluster and also to the Van der Waals interactions between the two adjacent CH_3 groups, which are too far apart in the second cluster to interact. The effect may not be significant, however, resulting only from the soft character of the SiOSi angle, which is larger in the [121][121] cluster, not allowing the formation of hydrogen bonds.

The energies calculated for the water forming condensation reaction, presented in Tables 13.10 and 13.11, show that this is an exothermic process. The reaction energies, usually in the

Reactant1	+	Reactant2	+	$\Delta E/kcalmol^{-1}$	$\longrightarrow$	Product	+	H_2O
[310]		[040]		-3.48		[301][031]		
[220]		[040]		-3.04		[211][031]		
[130]		[040]		-3.23		[121][031]		
[040]		[040]		-2.84		[031][031]		

Table 13.10: Reactional energies for the water forming asymmetrical condensation, from non-local DFT calculations.

Reactant1	+	Reactant2	+	$\Delta E/kcalmol^{-1}$	$\longrightarrow$	Product	+	H_2O
[310]		[310]		+0.77		[301][301]		
[220]		[220]		-2.31		[211][211]		
[130]		[130]		-2.17		[121][121]		
[040]		[040]		-2.84		[031][031]		

Table 13.11: Reactional energies for the water forming symmetrical condensation, from non-local DFT calculations.

range -2 to -5 kcal mol^{-1}, are larger than in the hydrolysis reaction, and depend considerably on the structure of the reactant clusters, in particular of their terminal groups.

Applying the same solvation analysis discussed previously for hydrolysis, the number of possible hydrogen-bonds seems, in this case, to remain the same before and after the reaction, as each of the two OH reactant groups can participate in two hydrogen-bonds, whereas the water molecule formed can participate in three and the new siloxane group OSi in one. As shown above, the charge bridging oxygens is even higher than in terminal ones, so they are expected to form strong hydrogen bonds in solution. Therefore, the energies calculated for the condensation reaction in gas phase, are probably a reasonable estimate of the equivalent reaction energies in the liquid phase.

The results obtained show that, when symmetrical condensation takes place, the reaction energy becomes less negative when the number of alkoxyl groups in both silicon atoms increases. In particular, the condensation of two bulky [310] monomers to form a [301][301] dimer, with no OH groups, is already an endothermic process. These energetic considerations are likely to be reinforced by a kinetic analysis, as the probability of two $[XY0]$ clusters interacting with the right relative orientation to form $[X(Y-1)1][X(Y-1)1]$ should decrease substantially with the number of X groups, due to statistical and spatial reasons.

In compensation, the condensation reactions forming asymmetrical $[XY1][031]$ clusters seem to have a reaction energy that is slightly more negative and tends to be more exothermic when the number of alkoxy groups in the bulky $[XY0]$ cluster increases. Unlike the symmetrical condensation, no interactions between bulky groups are created here during the condensation process, as they all are already present in the $[XY0]$ monomer, and the Van der Waals interactions formed between the hydrolysed [031] and the bulky $[XY1]$ sites may help to stabilise the second group. As one of the monomers is fully hydrolysed, the kinetic factors should also depend much less on the number of alkoxy groups X in the bulky monomer. These important differences between symmetrical and asymmetrical condensation are expected to be enhanced when larger alkyl groups are considered, like isopropyl and t-butyl groups.

Reactant1	+	Reactant2	+	$\Delta E/kcalmol^{-1}$	$\longrightarrow$	Product	+	CH_3OH
[310]		[130]		-5.17		[301][031]		
[400]		[040]		-4.94		"		
[220]		[130]		-4.73		[211][031]		
[310]		[040]		-3.90		"		
[130]		[130]		-4.91		[121][031]		
[220]		[040]		-4.15		"		
[220]		[040]		-4.52		[031][031]		

Table 13.12: Reactional energies for the methanol forming asymmetrical condensation, from non-local DFT calculations.

Reactant1	+	Reactant2	+	$\Delta E/kcalmol^{-1}$	$\longrightarrow$	Product	+	CH_3OH
[310]		[400]		-0.70		[301][301]		
[220]		[310]		-3.17		[211][211]		
[130]		[220]		-3.10		[121][121]		
[040]		[130]		-4.52		[031][031]		

Table 13.13: Reactional energies for the methanol forming symmetrical condensation, from non-local DFT calculations.

The energies of methanol forming condensation reactions, forming asymmetrical and symmetrical clusters, are presented in Tables 13.12 and 13.13, respectively. The methanol forming condensation is kinetically much less probable than the water forming condensation, but from the energetic point of view, it can be always represented by the sum of a hydrolysis and a water forming condensation reaction. For example, the methanol forming condensation [220] + [310] $\longrightarrow$ [211][211] can be decomposed as the sum of the hydrolysis [310] $\longrightarrow$ [220] plus the subsequent water forming condensation [220] + [220] $\longrightarrow$ [211][211]. The energy of the methanol forming condensation (-3.17 kcal mol^{-1}), is thus equal to the sum of -0.86 kcal mol^{-1} for the hydrolysis plus -2.31 kcal mol^{-1} for the corresponding water forming condensation.

As both hydrolysis and water forming condensation are usually exothermic reactions, it follows that the methanol forming (and in general any alcohol forming) condensation reaction has to be even more exothermic. The difference between the water forming condensation energies, in Tables 13.10 and 13.11, and the methanol forming condensation energies, in Tables 13.12 and 13.13, is the energy of the corresponding hydrolysis reaction. The same general trends are consequently observed in the energetics of water and methanol forming condensation. In symmetrical condensation the energy decreases with the number of X groups in the reactants but in asymmetrical condensation the energy increases with the number of X groups in the bulky monomer.

In the methanol forming asymmetrical condensation it can be seen that, for the same final cluster, the reaction energy is systematically more negative when the reacting methoxy comes from the monomer with less methoxy groups (smaller X). However, the energy differences involved may be too small to be significant.

13.5 Conclusions

In spite of the large differences observed between the various [211][211] conformations, several clear trends can be established for the three series of clusters $[XY0]$, $[XY1][031]$ and $[XY1][XY1]$ studied here.

With the exception of the SiOSi angle, which decreases when OCH_3 groups are replaced by smaller OH groups, thereby forming stronger electrostatic interactions, all bond lengths and angles remain essentially unaltered by changes in the chemical environment. In particular, the SiO_4 and OCH_3 groups keep the same structure as in $Si(OH)_4$ and CH_3OH.

As expected, the charge separation is much larger in the OH than OCH_3 groups, but surprisingly, the silicon charges decrease when hydroxyl replace methoxy groups.

Of greater concern is our finding that, although many reactions can take place, the predicted hydrolysis energies are very small. It is difficult to measure experimentally a single enthalpy of reaction, because there are many sol-gel reactions occurring at the same time, but it is well known that the temperature of the solution tends to increase in the first minutes, when the hydrolysis is taking place. Solvation effects, not accounted in these gas-phase calculations, are probably the principal cause of these apparent differences between calculated and experimental results.

The water condensation energies are also small and decrease noticeably with the number of methoxy groups attached to both silicon atoms. Certainly, it will be enlightening to repeat these calculations with different methods, particularly Hartree-Fock, trying also to take into account solvent effects.

Chapter 14

Solvated clusters

The purpose of this chapter is to study the influence of the solvent in otherwise gas-phase calculations, by applying a dielectric continuum model, COSMO, to the non-local DFT optimisations of some key sol-gel clusters: water, methanol, $Si(OCH_3)_4$, $Si(OH)_4$ and $Si_2O(OH)_6$, in water and methanol environments.

14.1 Introduction

Due to the enormous importance of solvation effects in chemistry, the proper handling of the solvation in Molecular Mechanics and particularly in Ab Initio methods is a field of active research [130]. Ab Initio quantum mechanical methods are capable of correctly describing the electronic and geometrical structures of solute molecules, including polarisation effects, due to the presence of the solvent, by considering explicitly solvent molecules. However, this approach is severely restricted by the rapid scaling of computer time with the size of the system.

To overcome these difficulties, several models have been proposed during the last 15 years, usually classified as dielectric continuum models, where the solute molecule is embedded in a dielectric continuum of permittivity ε. The solute forms therefore a cavity within the dielectric, and a surface charge distribution if formed on this interface between the solute and the solvent-the *solvent accessible surface*-as the response of the homogeneous dielectric continuum to the charge distribution of the solute. For an arbitrarily shaped surface, these screening charge densities, that result from the polarisation of the dielectric medium, cannot be obtained by analytical means [130]. To solve this problem, fast and efficiently, is therefore the ultimate goal of the various models that have been proposed to date.

A method has been developed to calculate the surface charge distribution iteratively but it implies a double iterative procedure within a single SCF-cycle and consequently it is computationally very expensive. For spherical and ellipsoidal cavities the problem can be solved analytically [130], and various models have been built assuming this type of cavity. They are very fast and probably very informative, from the theoretical point of view, but as they can be applied only to ellipsoid-like conformations of the solute, their range of applications is obviously restricted to a few cases.

A Green function solution has been developed, assuming a general treatment of anisotropic dielectric media [130], which allows us to express the screening charge distribution as a linear function of the charge distribution of the solute. The Conductor-like Screening Model, COSMO,

is based in a similar but simplified approach, which allows the calculation of the energy gradients without relevant additional costs, as soon as the screen charges are obtained, allowing reasonably fast geometry optimisations.

The first implementation of COSMO in a DFT code, presented by Andzelm et al. [16] and used in this work, allows the direct determination of the surface charges within the SCF procedure, using only the electrostatic potentials, and the accurate calculation of the gradients with respect to the solute coordinates, without any restriction on the shape of the cavity. Typically, COSMO increases the CPU time needed for a gas-phase calculation by less than 10-20%.

Dielectric continuum models are certainly not a unique nor even the ultimate solution to describe solvation effects and several other approaches have been tried so far. Hydration energies have been calculated by Catlow et al. [51, 52], using Molecular Mechanics calculations based on standard forcefields and these energies are subsequently added to the Ab Initio reaction energies, accounting for solvation effects.

The adsorption of a water molecule by a four silicon ring was analysed at the INDO level of theory by West [244, 243]. A small expansion was predicted when water is bonded to the silica cluster.

In this work, the structure, charge distribution and energy of the clusters are compared in the gas-phase and COSMO environments. The COSMO dielectric energy (included in the total energy) is presented for all structures. The more stable gas-phase conformations for the three silicate clusters, respectively S_4, S_4 and C_2, are compared with the extended, more symmetrical D_2d, D_2d and C_{2v} conformations. The hydrolysis and condensation energies are then presented for both sets of conformations, in gas and COSMO environments.

14.2 Solvated water and methanol

The total energy, structure and charge distribution for a molecule of water and methanol in the gas phase, water and methanol environments are presented in Tables 14.1 and 14.2. The total energy of the water decreases by 8.3 kcal mol^{-1} from gas phase to the methanol environment and a further 0.3 kcal mol^{-1} to the water environment. The methanol total energy decreases 8.6 kcal mol^{-1} in the methanol environment plus 0.2 kcal mol^{-1} in water. These values compare reasonably well with the enthalpy of vaporisation of water and methanol, respectively 9.71 and 8.41 kcal mol^{-1} (see chapter 16). It should be noticed that, for all systems analysed, the difference in energy between the gas-phase and the COSMO calculations is smaller than the electrostatic solvation energy, that results from the interaction of the solute with the screening charges. The COSMO total energy minus the electrostatic interaction energy is thus higher than the gas-phase value, showing that, as expected, the solute is slightly distorted by the screening charges.

For both molecules, the structure is essentially the same in all three environments, which is surprising, because the molecular charge distribution is considerably affected by the dielectric properties of the medium. As expected, the atomic charges are larger in a polar liquid, such as methanol, than in gas phase, increasing even slightly more in water, with a higher dielectric constant ($\epsilon = 78.54$ for water, $\epsilon = 32.63$ for methanol). As expected for polar methanol, the hydrogen atomic charge increases more in the polar hydroxyl group than in the non-polar methyl group.

The calculated electric dipole moment of water and methanol in the liquid phase (in both

	Gas	*Water*	*Methanol*
Energy			
Total	-76.441266	-76.454912	-76.454475
Dielectric	-	-0.016158	-0.015556
Length			
OH	0.99	0.99	0.99
Angle			
HOH	103.8	103.4	103.4
Charges			
O	-0.2867	-0.3353	-0.3338
H	0.1433	0.1677	0.1669
Dipole	1.80	2.33	2.31

Table 14.1: Total and dielectric energy (Hartree), bond lengths (Å), bond angles, Hirshfeld charges and electric dipole moment (Debye), for water, in gas-phase and COSMO (water and methanol) environments.

cases 2.3 D), agree with the experimental predictions, in the range 2.0-3.0D (see chapter 16). Due to charge inductive effects, these values are much larger than in gas phase, respectively 1.85 D and 1.70 D, in excellent agreement with the calculated results, as seen before.

14.3 Solvated TMOS

Two different conformations are considered for $Si(OCH_3)_4$, S_4 and D_2d, equivalent to the S_4 and D_2d conformations studied for $Si(OH)_4$, but with OCH_3 terminal groups. In the gas phase, the S_4 conformation is more stable, because it allows the formation of weak O- -H interactions, which are not possible in the more open, straight, D_2d conformation. In the solvated environment, however, the outer groups can interact with the environment and therefore, particularly in more polar environments, more extended conformations like the D_2d might be more stable. The results obtained for both conformations are presented in Table 14.3. The D_2d conformation is 0.13 kcal mol^{-1} more stable in water, but 0.32 kcal mol^{-1} less stable in methanol. These differences are probably too small to be significant.

As for water and methanol, the TMOS structure remains almost unchanged when placed in a water or methanol environment, though SiO and OC bond lengths tend to increase slightly. In both water and methanol environments, the Si and C atomic charges decrease, while the O and H charges increase. In fact, atomic charges in polar groups are likely to be strongly enhanced in strongly polar solvents, particularly when it is possible to form hydrogen bonds, but it is not clear why the non-polar Si and C charges decrease. As the extended D_2d conformation is more affected by solvation effects, there is a slight enhancement of the charges in this conformation, compared with the S_4, with stronger intramolecular interactions.

For both conformations, the electric dipole moment remains very small, when solvation effects are considered, due to its almost tetrahedral symmetry.

	Gas	*Water*	*Methanol*
Energy			
Total	-115.72633	-115.73705	-115.73669
Dielectric	-	-0.01279	-0.01229
Length			
CH	1.10	1.10	1.10
CO	1.45	1.46	1.46
OH	0.99	0.99	0.99
Angle			
H_gCH_g	109.8	109.8	109.8
H_tCO	106.1	106.8	106.8
COH	107.2	106.9	106.9
Charges			
C	-0.0285	-0.0305	-0.0306
O	-0.2238	-0.2714	-0.2698
H_C	0.0380	0.0457	0.0454
H_O	0.1431	0.1649	0.1642
Dipole	1.63	2.27	2.25

Table 14.2: Total and dielectric energy (Hartree), bond lengths (Å), bond angles, Hirshfeld charges and electric dipole moment (Debye), for methanol, in gas-phase and COSMO (water and methanol) environments.

14.4 Solvated monomer

The results obtained for both S_4 and D_2d $Si(OH)_4$ conformations are presented in Table 14.4. Although the S_4 conformation is clearly more stable in the gas phase, as discussed previously (at the DF-BLYP/TNP level of approximation), in COSMO water and methanol simulated environments the energy of the D_2d conformation is respectively 1.7 kcal mol^{-1} and 0.3 kcal mol^{-1} lower than in the S_4 conformation. As in $Si(OCH)_3)_4$, the extended D_2d conformation allows a better interaction of the cluster with the solvent, particularly in water.

The difference in energy between the cluster in the gas phase and the cluster in the solvated environments is quite significant, respectively 15.6 kcalmol^{-1} and 16.4 kcal mol^{-1}, for water and methanol. It is surprising that the energy of the S_4 conformation is 0.8 kcal mol^{-1} lower in methanol, whereas the energy of the D_2d conformation is 0.6 kcal mol^{-1} lower in water. Again, these differences in energy are probably too small to be significant.

The $Si(OH)_4$ structure remains essentially unchanged when the simulated solvent is added to the gas-phase calculation. The electric dipole moment also remains zero, due to the symmetry of the cluster. As in $Si(OCH)_3)_4$, the O and H atomic charges increase and the Si charge decreases in both solvated environments.

14.5 Solvated dimer

The results obtained for the most important dimer conformations, C_2 and C_{2v}, corresponding to the S_4 and D_2d monomer conformations, are presented in Table 14.5. As in the monomer, the

	Gas	*Water*	*Methanol*	*Water*	*Methanol*
Energy					
Total	-750.22898	-750.24500	-750.24450	-750.24521	-750.24399
Dielectric	-	-0.01960	-0.01881	-0.02323	-0.02245
Length					
SiO	1.66	1.66	1.66	1.67	1.67
OC	1.45	1.47	1.47	1.47	1.47
CH	1.10	1.10	1.10	1.10	1.10
Angle					
OSiO	106.7-109.3	106.8-113.2	106.8-113.2	101.3113.8	100.9-113.9
SiOC	119.6-124.7	120.0-122.6	120.2-122.3	119.0-119.9	119.8-120.9
OCH	107.2-107.7	107.1-110.5	107.1-110.6	107.0-107.3	106.9-107.2
HCH	109.1-109.8	109.6-110.0	109.7-110.0	109.6-109.7	109.7-110.0
Charges					
Si	0.5139	0.4938	0.4942	0.4886	0.4890
O	-0.2290	-0.2543	-0.2535	-0.2576	-0.2567
C	-0.0182	-0.0153	-0.0153	-0.0148	-0.0143
H	0.0390	0.0487	0.0484	0.0501	0.0495
Dipole	0.42	0.39	0.40	0.27	0.18

Table 14.3: Total and dielectric energy (Hartree), bond lengths (Å), bond angles, Hirshfeld charges and electric dipole moment (Debye), for S_4 (left) and D_2d (right) TMOS conformations, in gas-phase and COSMO (water and methanol) environments.

	Gas	*Water*	*Methanol*	*Water*	*Methanol*
Energy					
Total	-593.09657	-593.12136	-593.12265	-593.12407	-593.12317
Dielectric	-	-0.02965	-0.02945	-0.03336	-0.03203
Length					
SiO	1.67	1.67	1.67	1.67	1.67
OH	0.99	0.99	0.99	0.99	0.99
O- -H	2.71	2.79	2.85	3.27	3.27
Angle					
OSiO	105.7-117.4	106.5-115.6	107.0-114.6	101.2-113.8	101.3-113.7
SiOH	111.1	113.3	112.7	112.0	111.8
Charges					
Si	0.5087	0.5067	0.5056	0.5050	0.5054
O	-0.2885	-0.3100	-0.3099	-0.3110	-0.3102
H	0.1613	0.1833	0.1834	0.1847	0.1838
Dipole	0.00	0.00	0.01	0.01	0.00

Table 14.4: Total and dielectric energy (Hartree), bond lengths (Å), bond angles, Hirshfeld charges and electric dipole moment (Debye), for S_4 (left) and D_2d (right) monomer conformations, in gas-phase and COSMO (water and methanol) environments.

differences in energy between the gas-phase and the methanol and water solvated calculations are quite substantial, 20.5 kcal mol^{-1} and 21.5 kcal mol^{-1}, respectively.

In both solvation environments, the hydrogen-bond forming C_2 conformation, that is more stable in the gas-phase, is 2.4 kcal mol^{-1} higher than the C_{2v} extended conformation, where the weaker intramolecular interactions are more than compensated by larger interactions with the solvent. In fact, the two hydrogen bonds that stabilise the C_2 conformation in the gas-phase, do not exist anymore when this conformation is solvated in methanol and water, resulting in a much more open SiOSi angle-158.4^o instead of 123.1^o-at this DF-BLYP/DNP level of approximation. In general, intramolecular hydrogen bonds will become less and less important in progressively polar solvents, being replaced by strong interactions with the sovent, resulting in substantial differences in the molecular structure.

The differences between the SiO bond lengths for the C_2 non-extended conformation, registered in Table 14.5, are essentially due to whether intramolecular hydrogen bonds are present. When these bonds are not involved, the molecular structure remains essentially unaltered by COSMO solvation effects.

As in the previous molecules, the charges of the terminal O and H atoms are considerably enhanced by the solvation environment. In particular, the charges of the terminal oxygen atoms are considerably more enhanced by water and methanol solvation than the charges of bridging oxygens, that are less exposed to the solvent. As in TMOS and in the monomer, the Si charge decreases when the solvent is considered. Because the extended conformation interacts more with the solvent, it has larger O and H atomic charges (and smaller Si charges) than the other conformation.

The electric dipole moment is very different in the two conformations, though it remains almost constant when water is replaced by methanol as solvent. The difference in the dipole between the gas phase and the solvated calculations, for the hydrogen-bond forming conformation (respectively 1.32D and 4.12-4.16D), is simply because these bonds do not exist any longer in the solvated environments.

14.6 Energy

The energy of the complete hydrolysis, $Si(OCH_3)_4 + 4H_2O \rightarrow Si(OH)_4 + 4CH_3OH$ and dimerisation, $2Si(OH)_4 \rightarrow Si_2O(OH)_6 + H_2O$, calculated in gas-phase, water and methanol environments, is presented in Table 14.6, for both contracted and extended conformations. Clearly the reaction energies are fairly similar in the gas-phase and in the COSMO solvated environments, as the differences are usually smaller than 1.0 kcal mol^{-1}.

Nevertheless, it seems significant that both hydrolysis and condensation energies become systematically more negative when the solvated, extended conformations are considered. As these conformations interact more with the solvent, both hydrolysis and condensation reactions become therefore more exothermic when solvents effects are considered, in better agreement with the experimental evidence.

14.7 Conclusions

The COSMO solvation model undoubtedly introduces important changes in the results of ab-initio optimisations of neutral species. Although the structure of the molecules tested here

	Gas	*Water*	*Methanol*	*Water*	*Methanol*
Energy					
Total	-1109.7564	-1109.7906	-1109.7891	-1109.7944	-1109.7930
Dielectric	-	-0.0533	-0.0513	-0.0531	-0.0512
Length					
SiO_b	1.67	1.65	1.65	1.67	1.67
SiO_t	1.66-1.68	1.66-1.67	1.66-1.67	1.67	1.67
OH	0.98-0.99	0.99	0.99	0.99	0.99
Angle					
SiOSi	123.1	158.4	158.4	130.4	130.4
OSiO	107.1-112.9	106.8-114.2	106.8-114.2	113.4-114.4	113.4-114.4
SiOH	108.7-113.4	110.9-112.8	110.9-112.8	111.9-112.7	111.9-112.7
Charges					
Si	0.5199	0.5181	0.5182	0.5114	0.5114
O_b	-0.2982	-0.2998	-0.2997	-0.3094	-0.3091
O_t	-0.2796	-0.3085	-0.3077	-0.3057	-0.3049
H	0.1560	0.1858	0.1849	0.1868	0.1859
Dipole	1.32	4.16	4.12	2.34	2.31

Table 14.5: Total and dielectric energy (Hartree), bond lengths (Å), bond angles, Hirshfeld charges and electric dipole moment (Debye), for C_2 (left) and C_{2v} (right) dimer conformations, in gas-phase and COSMO (water and methanol) environments.

	Gas	*Water*	*Methanol*	*Water*	*Methanol*
Hydrolysis	-4.9	-3.1	-4.4	-3.9	-5.8
Condensation	-2.8	-1.8	+1.1	-2.5	-3.2

Table 14.6: Hydrolysis and condensation energies, for $S_4 \xrightarrow{Hyd.} S_4 \xrightarrow{Con.} C_2$ (left) and $D_2d \xrightarrow{Hyd.} D_2d \xrightarrow{Con.} C_{2v}$ (right) conformations, in gas-phase and COSMO (water and methanol) environments.

remains, in most cases, virtually unchanged when using the COSMO environment, this tends to stabilise more the open, extended structures, which allow a wider contact with the solvent, than the more closed arrangements, with important non-bonded intramolecular interactions.

Consequently, the monomer D_2d and dimer C_{2v} conformations become more stable in COSMO than the S_4 and C_2 conformations, the respective global minima in gas-phase. These changes are highly likely to occur in several other silicate clusters previously studied. It is important to emphasise that both results are very reasonable and almost certainly correct. They are different because they correspond to different physical situations, a cluster surrounded by a polar continuum solvent and a cluster in vacuo. In particular, the agreement between the experimental enthalpy of vaporisation and the difference between the gas-phase and COSMO total energies is very encouraging.

With the COSMO model, the partial charges of the outside atoms, interacting more with the solvent, tend to increase, while the charges of the inside atoms decrease. However, because the COSMO environment stabilises simultaneously the reactants and the products, the hydrolysis and condensation energies become very similar to the corresponding gas-phase results.

Although dielectric continuum models cannot describe the particular solvation effects, at the atomistic level, they are a invaluable tool to account solvation effects in liquid systems, particularly in ab-initio calculations, where the inclusion of solvation shells, is very time-consuming. COSMO, in particular, is extremely fast and combined with ab-initio methods may well prove to be a powerful tool in the atomistic study of liquid systems.

Chapter 15

Reaction mechanisms

The purpose of this chapter is to study the mechanisms of the simplest condensation and hydrolysis reactions: 1) $2Si(OH)_4 \rightarrow Si_2O(OH)_6 + H_2O$, 2) $Si(OH)_3OCH_3 + H_2O \rightarrow Si(OH)_4 + CH_3OH$ and 3) $Si(OCH_3)_4 + H_2O \rightarrow Si(OCH_3)_3(OH) + CH_3OH$, with acid catalysis, in both the gas-phase and COSMO environments.

15.1 Introduction

To know and control the fundamental events governing sol-gel processes, it is necessary to have a full understanding, at the atomistic level, of the hydrolysis and condensation reaction mechanisms. Although a completely accurate treatment requires a dynamic quantum mechanical approach, to take into account the rapid atomic vibrations, these methods are only now becoming available and a static energy analysis can provide extremely valuable information about these reactions, most importantly activation energies, intermediate species and transition states.

Since 1985, Burggraf and co-workers [62, 61] have been publishing theoretical calculations, essentially semiempirical (MNDO and AM1), of several aspects of the chemistry of silicon in solution. Calculated acidities and silane affinities have been reported for the reactions $XH_n \rightarrow XHn-1^- + H^+$ and $XH_{n-1}^- + SiH_4 \rightarrow [SiH_4XH_{n-1}]^-$, where X = C, N, O, F, Si, P, S and Cl [84]. The anion affinities have been computed for 91 pentacoordinate silicon anions (siliconates), most of them were found to be stable [59].

Semiempirical MNDO studies of the polymerisation of silanol in basic conditions seem to show that the formation of both $Si(OH)_5^-$ and $Si(OH)_3^-$ anions is essentially a non-activated process [44, 60]. $Si(OH)_5^-$ is apparently very stable, but the subsequent water elimination has a large activation energy, which is not required in the $Si(OH)_3^-$ mechanism and much higher than the experimental estimate for the activation energy (of about 15 kcal mol^{-1} [45]) for the base-catalysed polymerisation. Equivalent studies with F^- showed also the existence of very stable $Si(OH)_4F^-$ five pentacoordinated intermediates, again requiring a large activation energy to eliminate water.

The reverse reaction $Si-O-Si+H_2O \rightarrow Si-OH+HO-Si$ was studied by Lasaga et al. [143], to explain the surface dissolution of quartz. Based on ab-inition calculations, a simple mechanism was proposed (see Figure 15.1), with a estimated activation energy of 21.9 kcal mol^{-1}, very close to the experimental energy barrier for silicate and quartz dissolution. A study of calculations of transition states and activation energies with non-local Density, applied

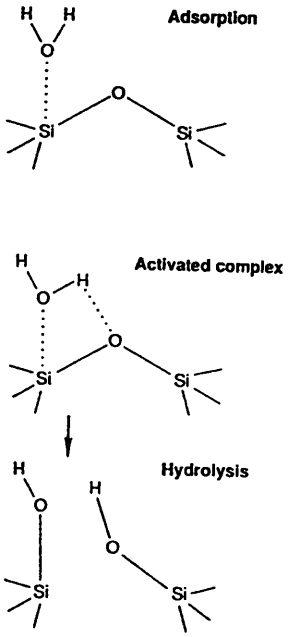


Figure 15.1: Reaction mechanism proposed by Lasaga, to explain the surface hydrolysis in quartz, in neutral pH conditions.

to organic chemistry, is given by Fan et al [68].

The hydrolysis and condensation reactions are studied in this chapter, using non-local DFT with a double numerical basis set (DF-BLYP/DNP). All atomic arrangements considered here are first optimised in the gas-phase and subsequently recalculated with the COSMO model, as a single energy point, without reoptimisation. A methanol environment (instead of water, for example) was chosen for COSMO calculations, to fit better the electrostatic conditions found in real sol-gel solutions, where the alcohol is usually the main component (typical compositions, water/alkoxide = 2-4 and alcohol/alkoxide = 4-10). Acid catalysis is considered throughout this work, corresponding to pH < 3, the conditions mostly found in current experimental sol-gel work.

The structure, charge distribution and protonation energy of the key species, $Si(OH)_3H_2O^+$, $Si_2OH(OH)_6^+$, $Si(OH)_3HOCH_3^+$, $Si(OCH_3)_3HOCH_3^+$, $Si(OCH_3)_3(H_2O)^+$ are first investigated. The transformation of the protonated reactants into the protonated products is then analysed in detail for the condensation reaction, considering an S_N2 and a *Lateral Attack* mechanisms. Several possible intermediates for an S_N2 hydrolysis reaction mechanismn are then considered, to estimate the energy change during this reaction. Special emphasis is given to the study of the condensation reaction, due to its major importance in silica-based sol-gel processes and in the chemistry of silica in general.

15.2 Data on protonated species

The energy, structure and charge distribution of the protonated species $Si(OH)_3(H_2O)^+$ and $Si_2OH(OH)_6^+$, which are the most important in the condensation reaction, are presented in the Table 15.1.

	$Si(OH)_3(H_2O)^+$	$Si_2OH(OH)_6^+$
Energy	-593.39059	-1110.0560
Length		
Si-O	1.63	1.63-1.66
O-H	0.99	0.99
Si-O^+-	1.88	1.82-1.83
-O^+-H	1.00	0.99
Angle		
O-Si-O	115.5-121.5	112.2-118.7
Si-O-H	116.7-118.3	113.2-116.8
Si-O^+-Si	-	121.5
Si-O^+-H	112.0-113.2	114.5
Charges		
Si	0.6291	0.6027
O	-0.2355	-0.2387
H	0.2114	0.2066
H_a	-	0.1572
O^+	-0.0628	-0.1439
(O^+)H	0.2529	0.2298
Dipole	5.4	0.6

Table 15.1: Energy (Hartree), bond lengths (Å), bond angles, Hirshfeld charges and electric dipole moment (Debye), for $Si(OH)_3(H_2O)^+$ and $Si_2OH(OH)_6^+$. H_a represents acceptor hydrogens in hydrogen-bonds (H_a = in hydrogen bonds).

Assuming that the reaction occurs by the attack of a monomer on a second protonated monomer, the proton remaining after the water molecule has left should be attached to the oxygen that initiated the nucleophilic attack: the bridging oxygen. The consequent redistribution of charge due to this proton, weakens considerably both $Si\text{-}O_b^+$- bonds, which become almost 0.2 Å longer than in the neutral dimer: 1.83 Å. This effect is even more pronounced in the protonated monomer, where only one silicon atom is available to compensate the redistributed charge, resulting into a even weaker $Si\text{-}O^+$- bond: 1.88 Å. The protonated oxygen and the silicon in the charged monomer become thus more electropositive than the protonated oxygen and the silicons in the charged dimer.

The $-O^+\text{-}H$ distance, however, remains almost unaltered ($\approx$ 1.00 Å) by the redistribution of charge, perhaps due to the appreciable ionic character of this bond. In fact, in contrast with the oxygen O^+ charges, the proton $(O^+)H$ charges are very similar in the protonated monomer and dimer.

It is important to notice that the protonation effects are predominantly local, affecting very little the structure and charge of the first and second neighbours. Significant differences from this pattern might occur, however, after a full COSMO optimisation, as the dielectric medium probably helps to spread the charge.

The energy, structure and charge distribution of the protonated species $Si(OCH_3)_3(HOCH_3)^+$, $Si(OH)_3(HOCH_3)^+$ and $Si(OCH_3)_3(H_2O)^+$, which play a key role in the hydrolysis reaction, are presented in the Table 15.2. For all these species, the atomic charges are, to a first approximation, relatively similar to the ones obtained for $Si(OH)_3(H_2O)^+$ and $Si_2OH(OH)_6^+$, in equivalent conditions. However, the electron-donor inductive effect of the methyl groups help considerably to stabilise the positive charge and to spread it over a much larger region of space. This happens even for $Si(OH)_3(HOCH_3)^+$, with just one methoxy group, though the Si, C and O^+ charges are already higher, due to the electron-withdrawing effect of the three hydroxyl groups.

The $Si\text{-}O^+$- bond distances are similar and show the same trends registered for $Si(OH)_3(H_2O)^+$ and $Si_2OH(OH)_6^+$. In particular, the Si-O^+ distance is larger (1.90 Å) in $Si(OCH_3)_3(H_2O)^+$, because the protonated oxygen is not attached to a electron-donor methoxy group. However, the Si-O distances are surprisingly short, apparently due to the transference of charge from the methyl groups to the SiO_4 central core, which leads to stronger Si-O bonds and weaker O-C bonds.

15.3 Formation of protonated species

The auto-ionisation of water, to form H_3O^+ and OH^- ions, influences decisively all reaction processes happening in aqueous solution. In chapter 9 we used this reaction to check the accuracy provided by several ab-initio levels of approximation. In Table 15.3 the influence of the environment in the auto-ionisation energy is analysed.

As expected, the ionisation energy is much higher in the gas phase than in a continuous dielectric medium, where charged species are considerably more stabilised. The ionisation energy is higher in a methanol-like dielectric environment than in the more polar water, but the difference of 5.2 kcal mol^{-1} is relatively small. While the energy of a water molecule decreases only 8.6 kcal mol^{-1} when the gas-phase is replaced by a water COSMO environment, the energy of the H_3O^+ and OH^- ions decrease as much as 98.3 kcal mol^{-1} and 91.2 kcal mol^{-1},

	$Si(OMe)_3(HOMe)^+$	$Si(OH)_3(HOMe)^+$	$Si(OMe)_3(H_2O)^+$
Energy	-750.55324	-632.69004	-711.25633
Length			
Si-O	1.62	1.63-1.64	1.61-1.63
O-C	1.48	-	1.48
C-H	1.09-1.10	1.09	1.09-1.10
O-H	-	0.99	-
Si-O^+-	1.86	1.84	1.90
-O^+-C	1.52	1.53	-
-O^+-H	0.99	0.99	1.00
Angle			
O-Si-O	112.9	112.4	119.4
Si-O-C	127.2-130.6	-	127.4-130.6
Si-O-H	-	117.6-118.1	-
O-C-H	107.4-109.7	-	107.1-110.1
H-C_3-H	109.8-110.6	112.0-112.6	110.4-111.0
Si-O^+-H	111.8	111.5	108.7-111.0
C-O^+-H	110.4	110.1	-
Charges			
Si	0.5832	0.6129	0.5975
O	-0.2061	-0.2401	-0.2076
C	0.0182	0.0520	0.0142
H_C	0.0665	0.0868	0.0638
H_O	-	0.2066	-
O^+	-0.0601	-0.0573	-0.0729
(O^+)H	0.2247	0.2325	0.2404
Dipole	16.1	36.1	4.9

Table 15.2: Energy (Hartree), bond lengths (Å), bond angles, Hirshfeld charges and electric dipole moment (Debye), for $Si(OMe)_3(HOMe)^+$, $Si(OH)_3(HOMe)^+$ and $Si(OMe)_3(H_2O)^+$.

	Water Ionisation					
	$2H_2O$	+	ΔE	$\longrightarrow$	H_3O^+	+ OH^-
Gas	-76.441266		+222.7		-76.705321	-75.822320
Methanol	-76.454475		+55.2		-76.857587	-75.963414
Water	-76.454912		+50.4		-76.861895	-75.967578

Table 15.3: Total energy (Hartree) and energy of ionisation (kcal mol^{-1}) for water in gas phase and COSMO (water and methanol) environments.

					Protonated Species Formation		*Gas COSMO*
$Si(OMe)_4$	+	H_3O^+	+	ΔE	$\longrightarrow$	$Si(OMe)_3(HOMe)^+$	+ H_2O
-750.22898		-76.705321		-37.8		-750.55324	-76.441266
-750.24387		-76.857131		+0.7		-750.64549	-76.454459
$Si(OMe)_3(OH)$	+	H_3O^+	+	ΔE	$\longrightarrow$	$Si(OMe)_3(H_2O)^+$	+ H_2O
-710.94624		-76.705321		-28.9		-711.25633	-76.441266
-710.96355		-76.857131		+6.4		-711.35595	-76.454459
$Si(OH)_3(OMe)$	+	H_3O^+	+	ΔE	$\longrightarrow$	$Si(OH)_3(HOMe)^+$	+ H_2O
-632.37895		-76.705321		-29.5		-632.69004	-76.441266
-632.40156		-76.857131		+2.3		-632.80057	-76.454459
$Si(OH)_4$	+	H_3O^+	+	ΔE	$\longrightarrow$	$Si(OH)_3(H_2O)^+$	+ H_2O
-593.09657		-76.705321		-18.8		-593.39059	-76.441266
-593.12187		-76.857131		+7.4		-593.51277	-76.454459
$Si_2O(OH)_6$	+	H_3O^+	+	ΔE	$\longrightarrow$	$Si_2OH(OH)_6^+$	+ H_2O
-1109.7564		-76.705321		-22.3		-1110.0560	-76.441266
-1109.7900		-76.857131		+12.9		-1110.1721	-76.454459

Table 15.4: Formation energies for $Si(OMe)_4H^+$, $Si(OMe)_3(OH)H^+$, $Si(OH)_3(OMe)H^+$, $Si(OH)_4H^+$ and $Si_2O(OH)_6H^+$, in gas-phase and COSMO (methanol) environments (E/Ha and ΔE/kcal mol^{-1}).

respectively. These differences in energy between gas-phase and COSMO environments have important consequences for all reactions involving charged species.

The protonation energy for several key molecules in sol-gel processes is analysed in Table 15.4. In all cases, the protonation reaction is exothermic in the gas-phase and endothermic in the COSMO (methanol) environment. In gas-phase calculations, the key factor is always the location of the additional charge, which becomes easier for larger systems, with more atoms and basis functions. Consequently, the side of the equilibrium where the charge is hosted by a larger species tends to have a lower energy, not reflecting the real energetics of the reaction.

The gas-phase results show this trend, with one exception. The methoxyl protonation of $Si(OH)_3(OCH_3)$ is slightly more exothermic than that for the hydroxyl protonation of the much larger $Si(OCH_3)_3(OH)$. This shows that in a partially hydrolysed alkoxide, the protonation of a alkoxy group is a process energetically more favourable than the protonation of a hydroxyl group. This result is confirmed by COSMO results. While $Si(OCH_3)_4$ and $Si(OH)_3(OCH_3)$ have very small methoxy protonation energies, +0.7 and +2.3 kcal mol^{-1}, the hydroxyl protonation of $Si(OCH_3)_3(OH)$ is already +6.4 kcal mol^{-1}. Therefore, in acid conditions, assuming that the reactions start with the protonation of the neutral molecules, the forward hydrolysis reaction is favoured when compared with the reverse reesterification reaction.

In the COSMO environment, the charge stabilisation effect observed in the gas-phase seems to be non existent or at least much less important. The protonation of TMOS, where the charge moves from a 4-atom (15 basis functions) to a 34-atom (95 basis functions) system is still endothermic. It requires more energy to protonate the $Si_2O(OH)_6$ dimer than the $Si(OH)_4$ monomer.

The protonation energies calculated with COSMO agree with the basicity trends reviewed

		Protonated Species Reactions						*Gas COSMO*
H_2O	+	$Si(OMe)_3(HOMe)^+$	+	ΔE	$\longrightarrow$	$Si(OMe)_3(H_2O)^+$	+	$MeOH$
-76.441266		-750.55324		+7.4		-711.25633		-115.72633
-76.454459		-750.64549		+4.7		-711.35595		-115.73647
H_2O	+	$Si(OH)_3(HOMe)^+$	+	ΔE	$\longrightarrow$	$Si(OH)_3(H_2O)^+$	+	$MeOH$
-76.441266		-632.69004		+9.0		-593.39059		-115.72633
-76.454459		-632.80057		+3.6		-593.51277		-115.73647
$Si(OH)_4$	+	$Si(OH)_3(H_2O)^+$	+	ΔE	$\longrightarrow$	$Si_2OH(OH)_6^+$	+	H_2O
-593.09657		-593.39059		-6.3		-1110.0560		-76.441266
-593.12187		-593.51277		+5.1		-1110.1721		-76.454459

Table 15.5: Hydrolysis and condensation reactions involving $Si(OMe)_4H^+$, $Si(OMe)_3(OH)H^+$, $Si(OH)_3(OMe)H^+$, $Si(OH)_4H^+$ and $Si_2O(OH)_6H^+$, in gas-phase and COSMO (methanol) environments (E/Ha and ΔE/kcal mol^{-1}).

by Brinker et al. [42] and discussed in chapter 3. The most basic is $Si(OCH_3)_4$, due to the electron-providing effect of the four alkyl groups. Replacing three of these by hydroxyl groups, $Si(OH)_3(OCH_3)$, the OCH_3 basicity decreases slightly. The OH basicity in $Si(OCH_3)_3(OH)$ is even smaller, in spite of the three alkyl groups as first neighbours. When these are replaced by hydroxyl groups, in $Si(OH)_4$, the basicity decreases slightly again. Due to the electron-withdrawing effect of OSi groups, the bridging O, in $Si_2O(OH)_6$, is the least basic site analysed. Assuming that these trends apply for larger clusters, it means that, in acid conditions, the hydrolysis rate decreases with progressive substitution and in the condensation, larger, neutral species attack the smaller, protonated monomers, as predicted before.

15.4 Reactions of protonated species

The energies of some key reactions occurring in sol-gel solutions, in acid conditions, are presented in Table 15.5. The gas-phase results are again dominated by charge effects. The first and last hydrolysis reactions, where the products are larger than the reactants, both have positive energies, while the condensation energy is negative, because the dimer is larger than the monomer. In the COSMO environment, where these charge effects are unimportant, all reactions are endothermic, essentially because in all three cases, the protonated products have groups more electron withdrawing than the reactants.

15.5 Condensation S_N2 and *Lateral Attack* mechanisms

To study in detail the mechanism of condensation, from the protonated reactants to the protonated products, it is important to establish a bridge between reactants and products-a common atomic arrangement that can be reached from both sides-not necessarily a transition state or an intermediate. Outside the interaction region the atomic arrangement should change to the optimised isolated species.

In $Si_2OH(OH)_6^+$, the bridging Si-O_b^+- distance is 1.83 Å and in $Si(OH)_3(H_2O)^+$ the single

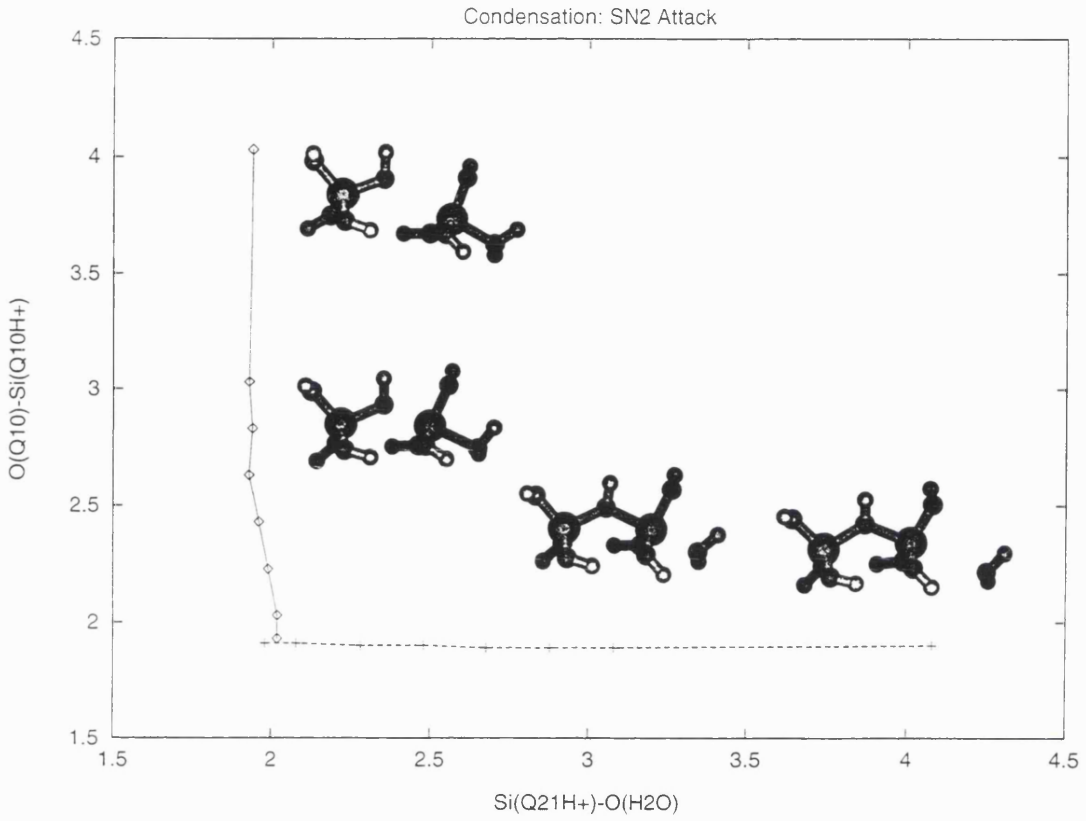


Figure 15.2: S_N2 mechanism for the condensation reaction $Si(OH)_4 + Si(OH)_4H^+ + \rightarrow Si_2O(OH)_6H^+ + H_2O$.

Si-O^+- distance is 1.88 Å, so the two key distances in the atomic arrangement $Si(OH)_3OH - Si(OH)_3 - H_2O^+$, between the oxygen performing the nucleophilic attack and the silicon, and between this and the leaving water molecule, were kept constant to 1.83 Åand 1.88 Å, respectively. The two optimised atomic arrangements, formed from the reactants and the products, aim to be exactly the same. In fact, for both the S_N2 and the *Lateral Attack* mechanisms, the maximum differences found between the two arrangements are approximately 0.25 kcal mol^{-1}, 0.01 Å, 1.2 ^{o} and 0.25% for the charges.

The reaction path from the reactants until the products is subsequently generated from these two arrangements increasing progressively the O-Si bridging distance in one, until reaching the reactants and the water-leaving Si-O distance in the other, until reaching the products. The second key distance is left free to change during the subsequent optimisation. The general procedure is shown in Figures 15.2 and 15.3, for the S_N2 and the Lateral Attack mechanisms, respectively. The corresponding results are presented in Tables 15.6 and 15.7 and in Figure 15.4.

The S_N2 and *Lateral Attack* reaction paths, optimised in the gas-phase, are very different. While the S_N2 path is composed of two almost straight lines, suggesting a negligible activation energy, the *Lateral Attack* path exhibits a pronounced curvature, showing that there is a significant repulsion in this area. The different energy evolution of the two mechanisms, in the gas phase, is evident in Figure 15.4. While in the S_N2 mechanism, the energy in the intermediate region is much lower than in the reactants or the products, indicating a strong charge effect, in

S_N2
Mechanism

before				after			
O-Si	Si-O	Gas	COS	O-Si	Si-O	Gas	COS
9.03	1.88	0.0	0.0	1.91	1.98	-21.5	-3.4
4.03	1.94	-0.7	2.5	1.91	2.08	-22.0	-3.1
3.03	1.93	-6.0	2.0	1.90	2.28	-21.3	-1.3
2.83	1.94	-9.0	0.0	1.90	2.48	-19.6	0.4
2.63	1.93	-10.1	1.8	1.89	2.68	-18.2	2.0
2.43	1.96	-13.9	0.0	1.89	2.88	14.7	5.5
2.23	1.99	-17.2	-1.5	1.89	3.08	12.3	6.8
2.03	2.02	-19.6	-2.0	1.90	4.08	-4.8	11.3
1.93	2.02	-20.4	-2.1	1.83	9.08	-6.9	5.1

Table 15.6: Key bond distances O(Q_1^0)-Si(($Q_1^0H^+$) and Si($Q_2^1H^+$)-O(H_2O) (Å) and energy (kcal mol^{-1}) evolution, during a S_N2 condensation mechanism, in gas phase and COSMO (methanol) environments.

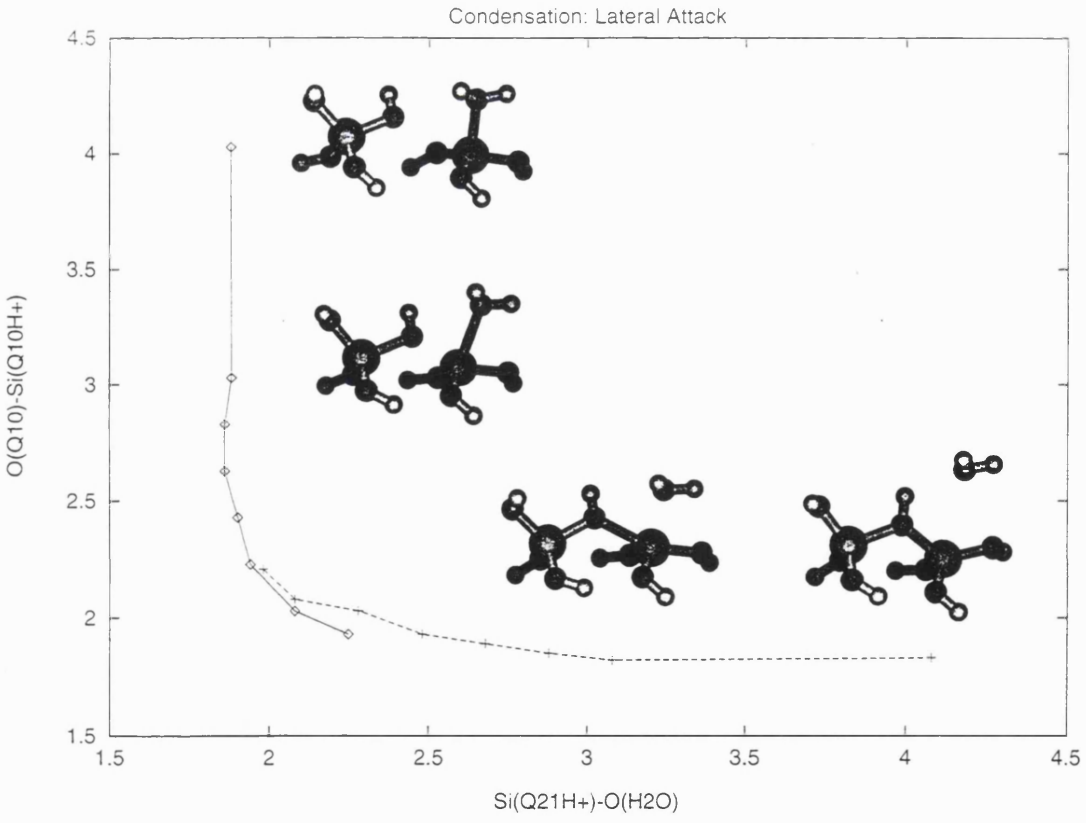


Figure 15.3: *Lateral Attack* mechanism for the condensation reaction $Si(OH)_4 + Si(OH)_4H^+ + \rightarrow Si_2O(OH)_6H^+ + H_2O$.

Lateral Attack Mechanism

before				after			
O-Si	Si-O	Gas	COS	O-Si	Si-O	Gas	COS
9.03	1.88	0.0	0.0	2.21	1.98	-10.6	5.3
4.03	1.88	-4.6	2.5	2.08	2.08	-9.9	7.7
3.03	1.88	10.3	1.9	2.03	2.28	-6.8	12.5
2.83	1.86	-11.2	1.9	1.93	2.48	-3.6	17.3
2.63	1.86	-11.7	2.4	1.89	2.68	-6.3	15.1
2.43	1.90	-13.0	2.7	1.85	2.88	-8.7	12.8
2.23	1.94	-11.5	5.3	1.82	3.08	-9.6	11.9
2.03	2.08	-10.4	7.8	1.83	4.08	-9.7	8.7
1.93	2.25	-7.3	12.2	1.83	9.08	-6.9	5.1

Table 15.7: Key bond distances O(Q_1^0)-Si(($Q_1^0H^+$) and Si($Q_2^1H^+$)-O(H_2O) (Å) and energy (kcal mol^{-1}) evolution, during a *Lateral Attack* condensation mechanism, in gas phase and COSMO (methanol) environments.

the *Lateral Attack* mechanism the energy seems to be the combination of two factors: the charge effect, decreasing the energy as before, and a process energy, responsible for the important peak appearing in the middle. For *Si-O* = 2.43 Å, the peak position, the energy difference between the two mechanisms (-19.6 and -3.6 kcal mol^{-1}) is equal to 16 kcal mol^{-1}, a first indication of the activation energy difference between the two mechanisms.

In the COSMO environment, the energy evolution along the S_N2 reaction path shows first a small energy barrier of 2.5 kcal mol^{-1} before decreasing to a five-silicon intermediate, which is 3.4 kcal mol^{-1} more stable than the reactants, with *O-Si* = 1.91 Å and *Si-O* = 1.98 Å. The small 1.8 kcal mol^{-1} peak at *O-Si* = 2.63 Å, before the intermediate, seems to be a side-effect of the gas-phase optimisation, resulting in a decrease of the Si-O distance, due to some charge effect and hydrogen-bond attraction. A second energy barrier of 11.3 kcal mol^{-1}, the largest in the whole reaction process, occurs later, when the *Si-O* distance is already 4.08 Å.

In the *Lateral Attack* mechanism, after the first 2.5 kcal mol^{-1} energy barrier, a 5-silicon intermediate occurs at O-Si = 2.83 Åand Si-O = 1.86 Å(1.9 kcal mol^{-1} less stable than the reactants). As in the gas phase, a pronounced peak occurs at *Si-O* = 2.48 Å, forming the largest energy barrier in the overall mechanism: 17.3 kcal mol^{-1} (6 kcal mol^{-1} larger than in the S_N2 mechanism).

Figure 15.5, represents the energy evolution along the diagonal O-Si = Si-O distance (for both atomic arrangements, before and after), for the *Lateral Attack* and shows that important differences between the gas-phase reaction path and the COSMO environment path should not be expected, at least if the same conformations are considered. However, differences of about 2-3 kcal mol^{-1} in energy can easily be expected between gas-phase optimisations followed by COSMO single-point calculations and complete COSMO optimisations.

The global energy evolution from the neutral reactants to the neutral products is depicted in Figure 15.6. Due to the strategy utilised in this study, a gas-phase optimisation followed by a COSMO energy calculation, the difference in energy between reactants and products is rather small-only -0.4 kcal mol^{-1}. On optimising both reactants and products in the COSMO

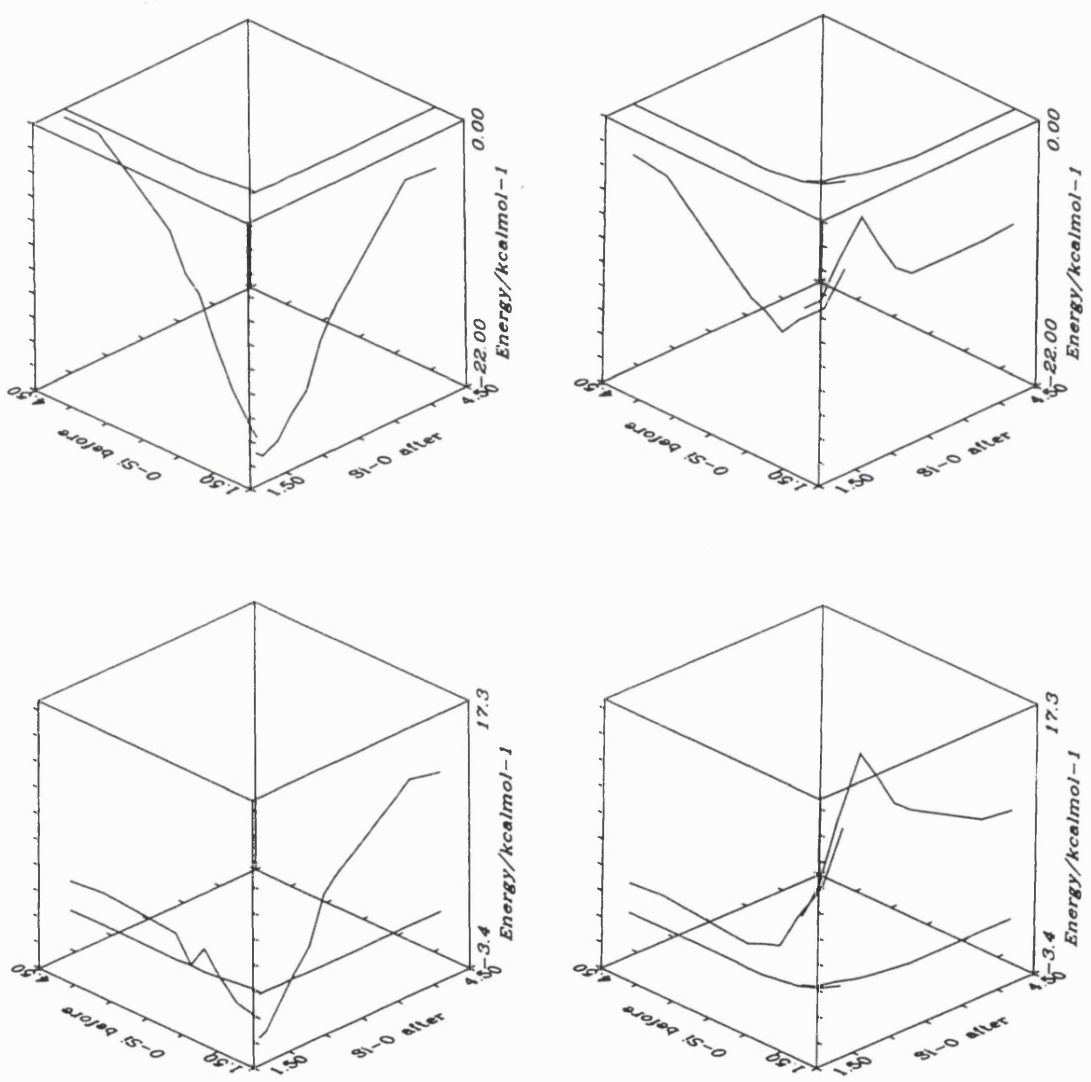


Figure 15.4: Gas-phase (top) and COSMO (bottom) energy evolution during S_N2 (left) and *Lateral Attack* (right) mechanisms, for the $Si(OH)_4$ condensation, from non-local DFT/COSMO calculations.

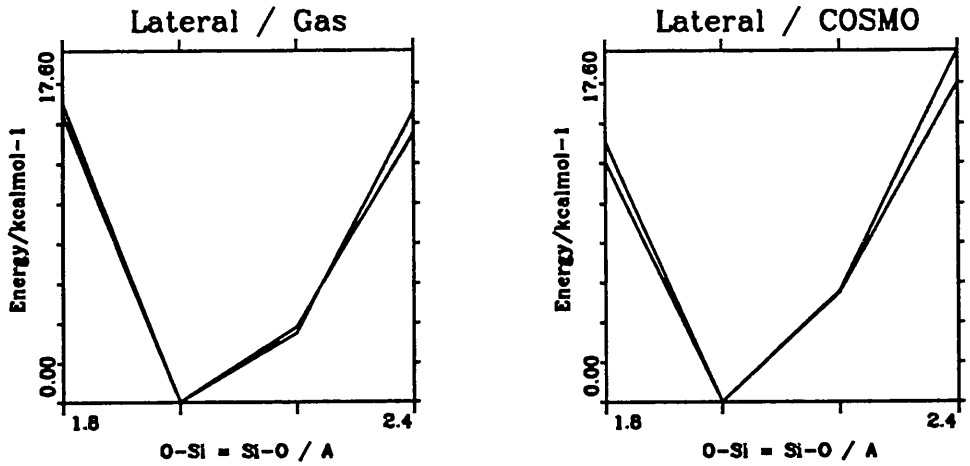


Figure 15.5: Energy evolution across the valley, along the diagonal O(monomer)-Si(protonated monomer) = Si(protonated dimer)-O(water), for gas-phase (left) and COSMO (right) DFT calculations, in the *Lateral Attack* condensation mechanism.

environment, as discussed in the previous chapter, this difference increases to -3.2 kcal mol^{-1}, which is still surprisingly small.

15.6 Hydrolysis S_N2 mechanism

The hydrolysis mechanism is studied in the gas-phase and the COSMO environment, by considering several different cases, shown in table 15.8, which help us to understand the energetics involved in this reaction. In all cases, an S_N2 mechanism is assumed and a distance of 1.98 Åis fixed for both key distances: the O-Si interaction between water and silicon and the Si-O interaction between this and methanol.

This distance was chosen because the condensation S_N2 path passes through the point 2.03-2.02 and Figure 15.5 shows that in the *Lateral Attack* the minimum along the diagonal O-Si = Si-O occurs for 2.03-2.08 Å and is already about 12 kcal mol^{-1} higher for 1.83-1.88 Å and 6 kcal mol^{-1} higher for 2.23-2.28 Å. Steric repulsion effects should be smaller in the hydrolysis than in the condensation reaction and the O-Si-O distance can be expected to be smaller in an S_N2 interaction than in a *Lateral* one. In any case, it is better to use distances that are slighty too short, leading to activation energies that are too high, than the opposite case. The chosen distance should therefore be a reasonable estimate for the intermediate arrangement on the reaction path of the hydrolysis reaction.

All species were optimised in the gas-phase, using a maximum gradient of 0.0010 a.u. for reactants and products and 0.0015 a.u. for the intermediate atomic arrangements, and subsequently recalculated with the COSMO environment (methanol).

The first two cases analyse the interaction between neutral species, a water molecule approaching $Si(OH)_3(OCH_3)$ (direct reaction) and a methanol molecule approaching $Si(OH)_4$ (reverse reaction). Because only neutral species are involved, gas-phase and COSMO results are almost equal, leading to an energy barrier of 13.9 kcal mol^{-1} for the hydrolysis reaction and 15.6 kcal mol^{-1} for the reverse reaction.

The third and fourth cases represent the same kind of interactions, but for protonated

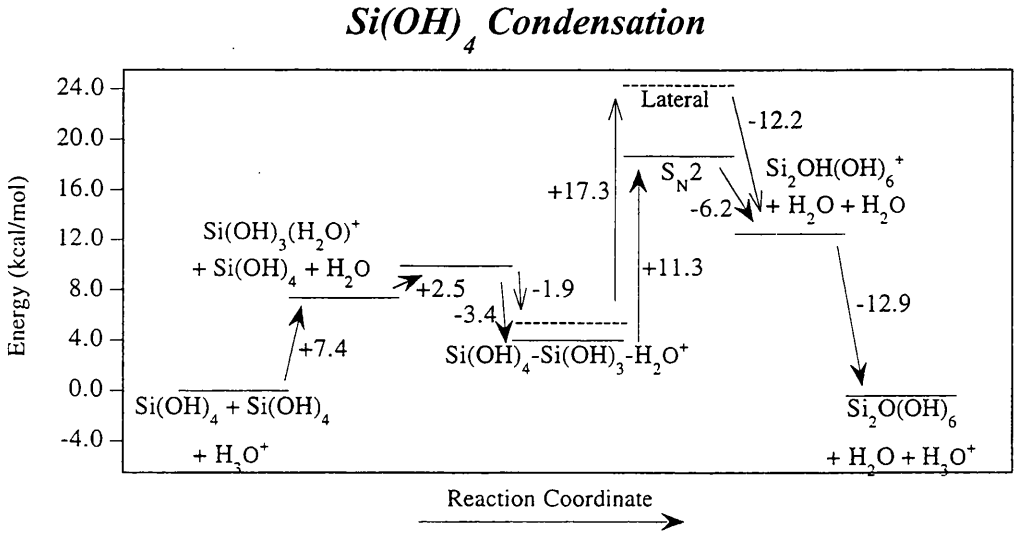


Figure 15.6: Energy evolution (kcal mol^{-1}) during the $Si(OH)_4$ condensation reaction, for both S_N2 and *Lateral Attack* mechanisms, from non-local DFT/COSMO calculations.

species. The results calculated with the COSMO environment show that the energy barriers are substantially smaller for the protonated species than for the neutral ones. In the first, TMOS hydrolysis (case 3), to reach the intermediate atomic arrangement from $Si(OCH_3)_3(HOCH_3)^+$ the increase in energy is only 4.1 kcal mol^{-1}, followed by an additional 0.6 kcal mol^{-1} to reach $Si(H_2O)(OCH_3)_3^+$. In the last TMOS hydrolysis (case 4), where steric hindrance effects should be much smaller, the intermediate atomic arrangement is lower in energy than the protonated reactants and products, $Si(OH)_3(HOCH_3)^+$ and $Si(H_2O)(OH)_3^+$, respectively.

Cases 5, 6 and 7 are less important and are considered here essentially for completeness. In all of them, additional species are added, always at a distance of 1.2 Å, for specific purposes. Case 5 is like case 4 but with a OH^- group, to guarantee charge neutrality. In case 6, additional H_2O and H_3O^+ clusters are considered, one receiving a proton from the attacking water molecule, the other giving a proton to the leaving methanol molecule. Case 7 is like case 6 but with an OH^- group, to guarantee charge neutrality. The addition of an OH^- group, in cases 5 and 7, increases considerably the charge separation and consequently the energy of the intermediate, even in COSMO environment. Furthermore, the intermediate energy seems to be sensitive to the position of the OH^- group, making these results not reproducible. Reducing the distance of the OH^- group to the main cluster, in a effort to decrease the charge separation and maintain a neutral system, is not compatible with an acid catalysis model. Case 6 seems more hopeful, but in fact the small increase in energy for the intermediate in gas phase, 12-14 kcal mol^{-1}, is essentially due to the poor stabilisation of the H_3O^+ cation, in the reactants and products, as the corresponding COSMO calculations clearly show.

The global energy evolution, from the neutral reactants to the neutral products, for both the first and the last hydrolysis of TMOS, are represented in Figures 15.7 and 15.8, respectively. In both cases the intermediate 5-Si species seem to be stable, particularly $H_2O--Si(OH)_3^+--HOCH_3$. In fact, the energy calculated for this species is even slightly lower than the energy of the final neutral products. This might due to the gas-phase optimisation, penalising more the products than the intermediate, after the COSMO recalculation, or to a residual charge effect

S_N2 *hydrolysis intermediates*

	Gas	*COSMO*
1)	$H_2O + Si(OH)_3(OCH_3)$	
	ΔE = +13.9 $\downarrow$	ΔE = +13.9
	$H_2O--Si(OH)_3(OCH_3)$	
2)	$Si(OH)_4--HOCH_3$	
	ΔE = -15.8 $\downarrow$	ΔE = -15.6
	$Si(OH)_4 + CH_3OH$	
3)	$H_2O + Si(OCH_3)_3(HOCH_3)^+$	
	ΔE = +0.5 $\downarrow$	ΔE = +4.1
	$H_2O--Si(OCH_3)_3^+--HOCH_3$	
	ΔE = +6.9 $\downarrow$	ΔE = +0.6
	$Si(H_2O)(OCH_3)_3^+ + CH_3OH$	
4)	$H_2O + Si(OH)_3(HOCH_3)^+$	
	ΔE = -10.1 $\downarrow$	ΔE = -4.4
	$H_2O--Si(OH)_3^+--HOCH_3$	
	ΔE = +19.1 $\downarrow$	ΔE = +8.1
	$Si(H_2O)(OH)_3^+ + CH_3OH$	
5)	$H_2O + Si(OH)_3(HOCH_3)^+ ----OH^-$	
	ΔE = +72.6 $\downarrow$	ΔE = +52.3
	$H_2O--Si(OH)_3^+(----OH^-)--HOCH_3$	
	ΔE = -74.3 $\downarrow$	ΔE = -53.8
	$OH^- ----Si(H_2O)(OH)_3^+ + CH_3OH$	
6)	$H_2O + H_2O + Si(OH)_3(OCH_3) + H_3O^+$	
	ΔE = +12.4 $\downarrow$	ΔE = +61.5
	$H_2O----H_2O--Si(OH)_3^+--HOCH_3----H_2O$	
	ΔE = -14.1 $\downarrow$	ΔE = -63.0
	$H_3O^+ + Si(OH)_4 + CH_3OH + H_2O$	
7)	$H_2O + H_2O + Si(OH)_3(OCH_3) + H_3O^+ ----OH^-$	
	ΔE = +177.9 $\downarrow$	ΔE = +150.5
	$H_2O----H_2O--Si(OH)_3^+(----OH^-)--HOCH_3----H_2O$	
	ΔE = -179.6 $\downarrow$	ΔE = -152.0
	$OH^- ----H_3O^+ + Si(OH)_4 + CH_3OH + H_2O$	

Table 15.8: Hydrolysis and condensation reactions involving $Si(OH)_3(OCH_3)H^+$, $Si(OH)_4H^+$ and $Si_2O(OH)_6H^+$, in gas-phase and COSMO (methanol) environments (E/Ha and ΔE/kcal mol^{-1}). (--) and (----) distances are equal to 1.98 Å and 1.2 Å, respectively.

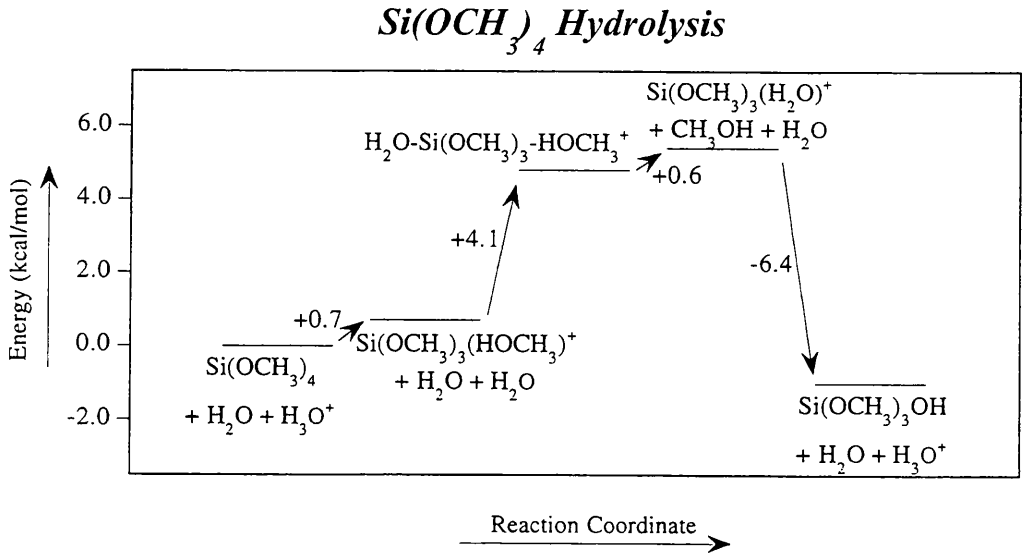


Figure 15.7: Energy evolution (kcal mol^{-1}) during the first $Si(OMe)_4H^+$ hydrolysis reaction, for a S_N2 mechanism, from non-local DFT/COSMO calculations.

occurring in the COSMO calculations. Even for the bulky $H_2O--Si(OCH_3)_3^+--HOCH_3$, the calculated energy is still lower than the energy of the protonated products.

Assuming that this intermediate exists, two additional energy barriers, before and after it, might be found, as in the condensation reaction. The energy barriers calculated so far are smaller than for the condensation reaction, in agreement with the experimental evidence that hydrolysis is a faster process than condensation. For both the first and the last TMOS hydrolysis, the protonation energy is much smaller than the largest barrier of energy, 4.1 and 8.1 kcal mol^{-1}, respectively. In fact, in these reactions steric effects are expected to play a role that is more important than inductive effects.

As the energy required to protonate the hydrolysis reactants is smaller than the corresponding energy to protonate the condensation reactants, the hydrolysis rate is likely to increase faster with the $[H^+]$ concentration (below pH = 2, the isoelectric point), than the condensation rate.

15.7 Conclusions

The protonation energy of charged silicate clusters is substantially different in the gas-phase and COSMO environments. While in the gas-phase, the size of an ion determines its capacity to accommodate the charge excess and consequently its relative stability, the results obtained with COSMO seem to agree with the inductive trends predicted experimentally for these clusters in solution. As expected, ionic species are much more stable in the COSMO environment than in the gas-phase. The water auto-ionisation reaction, in particular, requires much less energy in solution. The charge redistribution resulting from the gas-phase protonation of silicate clusters seems to be significant near the protonated oxygens only, though it is not clear if this local rearrangement will persist in the liquid-phase.

The study of the mechanisms of hydrolysis and condensation in the gas-phase, with acid catalysis (and presumably with basic catalysis) leads to reductions in the energy for the larger (charged) intermediates. This effect is not observed with the COSMO environment and the

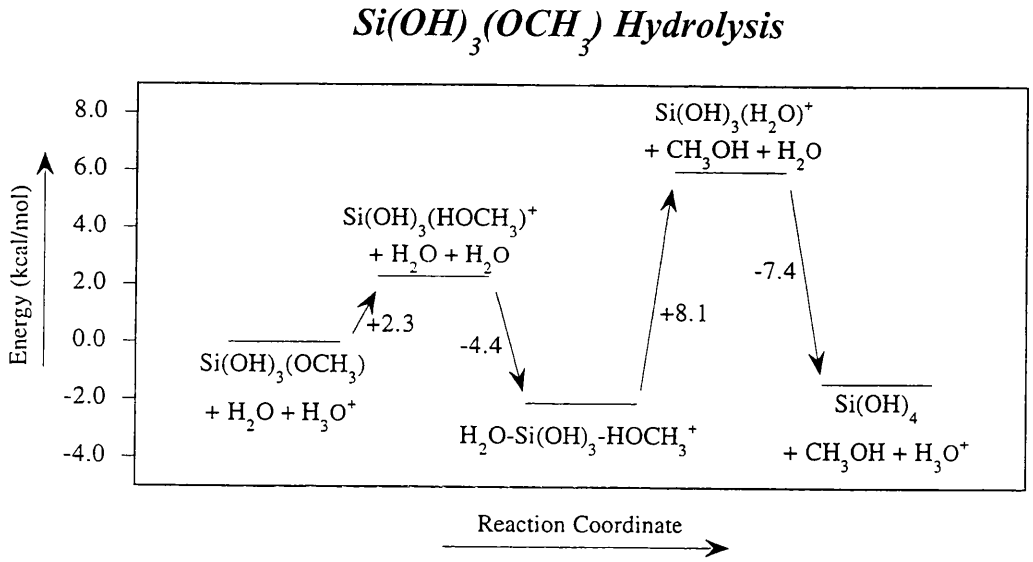


Figure 15.8: Energy evolution (kcal mol^{-1}) during the last $Si(OH)_3(OMe)H^+$ hydrolysis reaction, for a S_N2 mechanism, from non-local DFT/COSMO calculations.

values thus obtained for the activation energy of the various mechanisms seem to be reasonable. However, as the COSMO results for all intermediate arrangements are obtained for single point calculations after gas-phase optimisations, the energy barriers are likely to decrease after performing full geometry optimisations with COSMO.

These results show that both the condensation and the hydrolysis reactions have a very small activation energy. This is smaller for the hydrolysis than for the condensation, as expected from experimental kinetic studies ($k_{Hyd} > k_{Con}$). The estimate of the hydrolysis activation energies presented here should be regarded as a first approximation only. Although the determination of the transition states is important in understanding the reaction mechanism, a step-by-step analysis gives valuable information, such as the evolution of the charge distribution, which is fundamental in understanding the full transformation from the reactants to the products and to develop a physically realistic potential to describe it.

For both reactions, the S_N2 mechanism seems to be a easy way to convert the reactants into the products. However, as the study for the *Lateral Attack* shows, several other mechanisms that are energetically and statistically less favourable, should still be possible and may occurr simultaneously in the solution.

Clearly, a DFT implementation coupled with a COSMO model seems to offer a powerful tool to study, step by step, the various mechanisms occurring in sol-gel hydrolysis and condensation reactions, although more conclusive tests need yet to be done, to check the accuracy of the COSMO model, in studies of charged species.

Part IV

Molecular Mechanics studies

Chapter 16

Cutoff-based liquids

The purpose of this chapter is to develop a Molecular Dynamics model to simulate, in an NPT ensemble, the liquids most commonly used in sol-gel processes - water, methanol, ethanol, TMOS and TEOS - applying always the same methodology and potentials, so these can be used to describe more complex sol-gel solutions, where experimental data is not available to test the accuracy of the model.

16.1 Introduction

In 1969, in one of the first simulations of molecular liquids, Barker et al. [28] calculated the energy, specific heat and radial distribution function of liquid water, using a Monte Carlo technique, with a intermolecular pair potential determined by Rowlinson from the properties of ice and steam. Two years later, Rahman et al. [200] used Molecular Dynamics to study, for the first time, the static structure and kinetic properties of water, including radial distribution functions and self-diffusion coefficients, using the so-called Ben-Naim and Stillinger potentials, BNS. At the same time, Narten et al [178] derived from X-ray diffraction the molecular correlation functions in water, at progressively higher temperatures. A revised potential, ST2, was proposed by Stillinger et al. [219], who compared the molecular structure and thermodynamic properties in water for the three sets of potentials proposed so far, R, BNS and ST2. In 1975 Stillinger published an ambitious 100 page review on the molecular description of water [220].

All these potentials use a four charge description for each water molecule, considered as a unique body, and a cutoff to truncate the long range interactions. In Watt's model for water, applied by McDonald [159], the charges are already in the nucleus and a Morse potential is used to describe the OH hydrogen bond.

Since 1980, using Monte Carlo techniques coupled with NVT and NPT conditions, Metropolis sampling and a long-range cutoff, Jorgensen carried out an extensive set of simulations of liquid water [117, 118], methanol [116], ethanol [115] and other organic liquids [113, 114, 112], applying the so-called transferable intermolecular potential functions, TIPS potentials.

By this time, the Ewald sum was already progressively replacing the Coulombic cutoff as the preferred method to describe the long-range interactions, though very similar thermodynamic and structural properties have been found for both methods, for cutoffs not larger than 6 Å [14]. The SPC potentials, presented and developed, since 1981, by Berendsen et al. [33], are a particularly simple but successful description of liquid water, with point charges on the oxygen and

hydrogen positions, as in the models studied in this work.

The work presented in this chapter and in the next one was done with Discover 2.9, from Molecular Simulations Inc. [5]. We used a cubic cell containing 408 molecules of water, methanol, ethanol or 51 of TMOS, TEOS, with PBC conditions, a minimum image convention, a group-based method and a 9 Å cutoff. The equations of motion are integrated with a Verlet leapfrog algorithm, using a 1 fs (10^{-15} s) timestep and the NPT conditions are simulated by a Berendsen algorithm, using 1 fs and 50 fs for temperature and pressure relaxation times.

To avoid overlaps between the molecules and to allow them to move freely to equilibrium positions, all liquid systems were initialised disposing the molecules first along cubic lattice positions inside a cubic cell with low density, ca. 0.25 g/cm^{-3}. Each system is then submitted to NPT Molecular Dynamics, using ambient temperature and very high pressure, usually 10,000 bar, to force the molecules to interact and to come closer, to speed up all the process, before finally decreasing the pressure to 1 bar and allowing the system to relax to ambient conditions.

Densities, enthalpies of vaporisation, radial distribution functions and self-diffusion coefficients are calculated for three thermodynamic conditions: 20°C and 1 bar, 20°C and 10,000 bar, and 80°C and 1 bar. The equilibration and sampling times were set to 19.5 ps and 0.5 ps, respectively. Preliminary MD tests covering intramolecular energy, forcefield, cutoff, run time, system size, timestep and CPU time are also presented.

16.2 Density versus partial charges

From the theoretical point of view, the micro canonical ensemble is the natural choice to simulate a molecular system and it may be used to calculate fluctuation dependent properties, like, for example, specific heats. In practise, as we live in a constant temperature and pressure world, the NPT ensemble is becoming increasingly important in molecular simulation studies and several methods have been developed for such simulations. Density was chosen as one of the test properties in this work, due to its importance and the extensive range of experimental data available, as a function of temperature and pressure. It is easy to calculate in a periodic boundary system and simultaneously provides a good test of the intermolecular forces, the cutoff and the NPT method used.

The most representative results obtained for the density of water, methanol, ethanol and TMOS, for several conditions of temperature and pressure, are presented in Table 16.1. These results were obtained using an NPT group-based method, with a cff91 forcefield, and two sets of charges, the standard cff91 and the Hirshfeld, previously calculated. The results presented for ethanol and methanol at 80°C are extrapolations, as both are already gases at this temperature (see Table 3.3). Under ambient conditions, the agreement with experiment is good, particularly for the set with Hirshfeld charges, where the scaling factor is always the same. However, at high pressure and high temperature the calculated densities tend to be significantly lower than the experimental values, particularly for the alcohols.

The magnitudes of the partial charges used are absolutely fundamental to simulate adequately the intermolecular interactions in condensed matter. For simulations with cvff (empirical) and cff91 (ab-initio) forcefields, the most promising sets of partial charges found during this work (see chapter 9) are presented in Table 16.2, for water, methanol and ethanol.

The Mulliken partial charges, when multiplied by 0.85, seem to give reasonable results for the density, but the charges of the apolar groups, namely of the CH_3 carbon atom are unrealistically

	Density (ρ/gcm^{-3})					
	Pt		pt		pT	
Charges	cal.	exp.	cal.	exp.	cal.	exp.
			Water			
1.0*F	1.217	1.246	1.033	0.998	0.954	0.972
2.6*H	1.204	"	1.009	"	0.946	"
			Methanol			
1.1*F	0.998	1.052	0.729	0.791	0.662	0.736
2.6*H	0.996	"	0.747	"	0.694	"
			Ethanol			
1.1*F	0.987	1.050	0.735	0.789	0.686	0.737
2.6*H	0.984	"	0.730	"	0.649	"
			Tmos			
1.0*F	1.226	-	1.002	1.02	0.931	-
2.6*H	1.229	"	1.042	"	1.013	"

Table 16.1: Calculated and experimental density of water, methanol, ethanol and TMOS, at 10,000 bar and 20°C (Pt), 1 bar and 20°C (pt), and 1 bar and 80°C (pT), obtained after group-based simulations with a Coulombic cutoff, using cff91 (F) and Hirshfeld (H) partial charges multiplied by a scaling factor (1.0-2.6). Experimental values from [1] and [63].

	Partial Charges / a. u.			
atom	cvff	cff91	0.85*Mulliken	2.6*Hirshfeld
		water		
O	-0.8200	-0.7982	-0.7580	-0.7868
H	0.4100	0.3991	0.3790	0.3934
		methanol		
C	-0.2700	-0.0457	-0.5930	-0.1752
H_3	0.1000	0.0530	0.2440	0.1139
O	-0.3800	-0.5374	-0.5530	-0.5723
H_o	0.3500	0.4241	0.4140	0.4058
		ethanol		
C_3	-0.3000	-0.1590	-0.8400	-0.3523
H_3	0.1000	0.0530	0.2840	0.1274
C_2	-0.1700	0.0073	-0.3390	-0.0603
H_2	0.1000	0.0530	0.2400	0.0920
O	-0.3800	-0.5374	-0.5700	-0.5569
H_o	0.3500	0.4241	0.4170	0.4033

Table 16.2: Sets of partial charges used in NPT group-based simulations with a Coulombic cutoff: cvff and cff91 from MSI forcefields [5], Mulliken and Hirshfeld from DFT-BHL/DNP ab-initio calculations.

	Dipole / Debye		
Charges	cal.		exp.
		water	1.85 (gas)
2.6H	2.27		2.01-3.00 (liq)
1.0F	2.30		"
1.0V	2.32		"
0.85M	2.18		"
		methanol	
2.6H	2.11		1.70 (gas)
1.1F	2.12		"
1.0V	1.56		"
0.85M	2.34		"
		ethanol	trans-gauche
2.6H	1.67-2.29		1.44-1.68 (gas)
1.1F	2.10-2.14		"
1.0V	1.52-1.60		"
0.85M	1.80-2.83		"
		TMOS	
2.6H	0.00		1.71 (liq)
1.0F	-		"
		TEOS	
2.6H	0.001-1.66		1.63 (liq)
1.0F	-		"

Table 16.3: Experimental and calculated dipole moments of a single molecule water, methanol, ethanol, TMOS and TEOS, with Hirshfeld (H), cff91 (F), cvff (V) and Mulliken (M) partial charges, multiplied by a scaling factor (0.85-2.6). Experimental values from [122], [42] and [2].

high, from a chemical point of view. In compensation, the cff91 partial charges, for the same atoms, seem to be too low.

The Hirshfeld partial charges, when multiplied by 2.6, are similar to the cff91 charges for the polar hydroxyl atoms and to cvff charges for the apolar methyl atoms. Thus, they seem to be a reasonable compromise between the charge description of both forcefields, although the calculated densities for methanol and ethanol are still slightly lower than those observed.

16.3 Dipoles versus partial charges

The simplest way of checking the physical plausibility of a proposed set of partial charges is probably to use them to calculate the electric dipole moment for each of the molecular aggregates in which we are interested. We did this for the sets of partial charges investigated so far, for some of the reagents and solvents which are more common in sol-gel systems of silicates. The electric dipoles obtained for the most relevant sets, together with the experimental values published in the literature, are presented in Table 16.3.

The calculated values were obtained after a long period of equilibration (typically 100ps), followed by a static energy minimisation. The electric dipole moment for ethanol was calculated

	Energy ($kcalmol^{-1}$) *10,000 bar 20°C*					
Charges	Tot.	ΔTot.	Pot.	ΔPot.	Kin.	ΔKin.
			water			
1.0F	-2591.0	8.2	-3662.5	18.1	1071.5	18.6
2.6H	-2422.3	11.2	-3495.0	15.9	1072.7	13.9
			methanol			
1.1F	3417.3	7.1	1278.4	20.6	2138.9	20.3
2.6H	7096.2	8.7	4956.5	25.4	2139.6	25.5
			ethanol			
1.1F	-2105.9	12.1	-5314.4	27.6	3208.5	25.9
2.6H	-2807.5	9.9	-6021.1	28.2	3213.6	26.9
			TMOS			
1.0F	3407.7	6.3	2487.9	14.1	919.8	14.6
2.6H	5414.1	15.0	4496.5	15.3	917.6	3.3

Table 16.4: Total, potential and kinetic energies, and standard deviations, for water, methanol, ethanol and TMOS, at 10,000 bar and 20°C, with cff91 (F) and Hirshfeld (H) partial charges (multiplied by a factor n).

for both trans and gauche conformations. For Mulliken and Hirshfeld partial charges, we present only the values obtained for the converted sets which reproduce better the experimental densities, without leading to unrealistic values for μ_{cal}.

In the liquid phase, the electrostatic induction of an atom on each other, tends to increase the electric dipole moment, as can be seen for water. This enhancement effect is correctly described by the various sets of charges proposed to simulate liquid water, methanol and ethanol. Although the electric dipole of TEOS and TMOS should be very small in the gas state, due to symmetry considerations, as is corroborated by our values, it is reported to be quite high in the liquid state, due to important polarisability effects.

16.4 Energy versus partial charges

To simulate properly a given molecular system, the proposed forcefield should be able not only to describe its static and dynamic features but also its thermodynamic properties, which is indeed one of the more severe tests of any forcefield. Due to its physical importance and simplicity of calculation, the enthalpy of vaporisation and the specific heat are probably the most usually tested. Here we start by presenting the total, potential and kinetic energies, together with the respective standard deviations, that were obtained for the various conditions of temperature and pressure already described above.

As can be seen in Tables 16.4, 16.5 and 16.6, the standard deviations are very high, which is probably due, together with the intrinsic complexity of the systems under study, to the group based (instead of atom based) criteria used by Discover 2.95 (discussed in chapter 7) to decide if a given atom is inside the cut-off region and which are the nearest atoms.

Furthermore, the Berendsen method, with the relaxation times used, does not seem to be describing correctly an NPT ensemble, as the standard deviations of energy for the potential

	Energy (kcalmol^{-1}) *1 bar 20°C*					
Charges	Tot.	ΔTot.	Pot.	ΔPot.	Kin.	ΔKin.
			water			
1.0F	-2428.3	7.9	-3496.0	16.9	1067.6	15.9
2.6H	-2255.0	12.8	-3322.2	22.6	1067.1	18.3
			methanol			
1.1F	3669.9	9.083	1532.8	23.490	2137.2	23.1
2.6H	7380.4	13.0	5238.9	26.9	2141.5	25.9
			ethanol			
1.1F	-1843.2	19.3	-5053.0	34.1	3209.8	31.0
2.6H	-2441.3	9.5	-5646.8	29.9	3205.5	29.7
			TMOS			
1.0F	3471.7	6.0	2554.7	15.5	917.0	15.2
2.6H	5449.0	23.7	4531.5	23.9	917.5	3.4

Table 16.5: Total, potential and kinetic energies, and standard deviations, for water, methanol, ethanol and TMOS, at 1 bar and 20°C, with cff91 (F) and Hirshfeld (H) partial charges (multiplied by a factor n).

	Energy (kcalmol^{-1}) *1 bar 80°C*					
Charges	Tot.	ΔTot.	Pot.	ΔPot.	Kin.	ΔKin.
			water			
1.0F	-1839.6	9.3	-3130.2	21.3	1290.7	19.1
2.6H	-1664.1	7.7	-2952.6	18.3	1288.4	17.7
			methanol			
1.1F	4727.6	9.2	2151.7	28.5	2575.9	27.3
2.6H	8453.8	19.2	5876.2	37.5	2577.6	33.0
			teos			
1.1F	-280.4	17.3	-4135.7	30.9	3855.3	32.8
2.6H	-684.9	17.2	-4545.8	37.7	3860.8	33.7
			TMOS			
1.0F	3894.5	9.4	2786.1	20.8	1108.4	19.7
2.6H	5836.8	24.5	4731.6	24.6	1105.3	4.7

Table 16.6: Total, potential and kinetic energies, and standard deviations, for water, methanol, ethanol and TMOS, at 1 bar and 80°C, with cff91 (F) and Hirshfeld (H) partial charges (multiplied by a factor n).

	Molecular Energy		*Internal Energy*			
Charges	t	T	Pt	pt	pT	ΔH_v (T_b)
			water			
1.0F	2.585	3.110	11.56	11.15	10.78	9.71
2.6H	2.583	3.108	11.15	10.73	10.34	"
			methanol			
1.1F	14.231	15.324	11.10	10.47	10.05	8.41
2.6H	21.857	22.944	9.71	9.02	8.54	"
			ethanol			
1.1F	-4.150	-2.668	8.88	8.23	7.47	9.21
2.6H	-8.869	-7.538	5.89	4.97	3.60	"

Table 16.7: Energy of an isolated molecule, internal energy per molecule and experimental enthalpy of vaporisation ΔH_v (kcalmol^{-1}) for water, methanol and ethanol, with cff91 (F) and Hirshfeld (H) partial charges, multiplied by a scaling factor (1.0-2.6), for t = 20°C or T = 80°C, and p = 1 bar or P = 10,000 bar. Experimental values from [1] and [191].

and kinetic energies are similar for each system, and much bigger than the standard deviations for the total energy. This can be attenuated by decreasing further the relaxation time, but it will seriously disturb the trajectory determined by the integration algorithm, producing instabilities and leading, for example, to incorrect predictions of the mean square displacement of the atoms in a system.

To determine the internal energy for the systems and conditions described above, which can be related directly to the enthalpy of vaporisation, the energy per molecule in the bulk system was compared with the energy of a single molecule, completely isolated, with a kinetic energy corresponding to the same temperature. Clearly, the internal energy of a bulk system, defined in this way, is not equal to its intermolecular energy, as the intramolecular energy of a single molecule in a bulk system is not equal to the energy of a isolated molecule, due to the distortions caused by the other molecules.

As the accuracy of the total calculation for the internal energy strongly depends on the precision obtained for the energy of a single molecule, and considering that, as will be seen later, the time necessary to properly equilibrate a single isolated molecule can be unexpectedly long, we equilibrated the molecules during 1.5 ns before collecting their average energies during 1 ns. The results presented in Table 16.7, although encouraging, are not entirely satisfactory when compared with the experimental values for ΔH_v.

The energies obtained with the 2.6*Hirshfeld charges are systematically lower than those obtained with the corrected cff91 partial charges, which supports the first set. Unfortunately, the internal energy obtained for ethanol with 2.6*Hirshfeld partial charges, for all conditions of temperature and pressure, is very low.

Probably this is related to the existence of different trans and gauche conformations for ethanol, and to a strong stabilisation of the gauche conformation in the isolated molecule, for the 2.6*Hirshfeld set of charges. In fact, for this set of charges, the trans conformation was never obtained by molecular dynamics or energy minimisation, and its energy seems to be relatively high, when compared with the equivalent value for the 1.1*cff91 partial charges set. As expected, the internal energy increases with pressure and decreases with temperature, for all the systems.

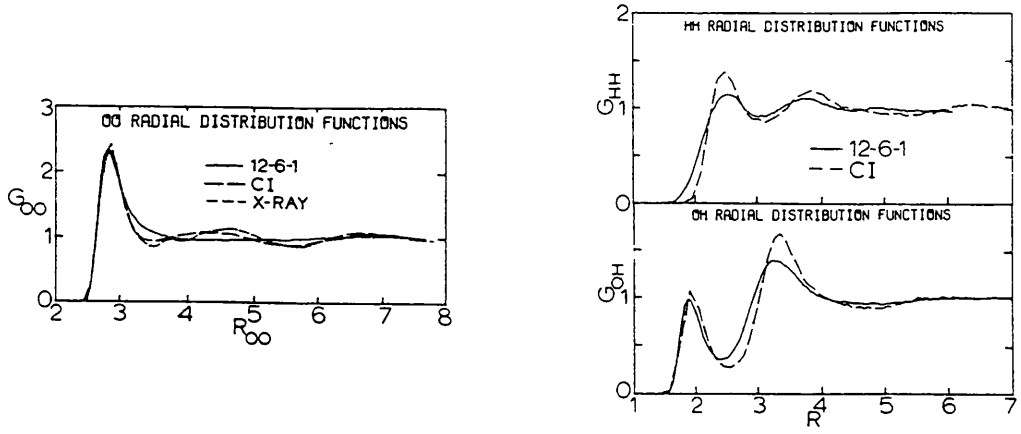


Figure 16.1: Intermolecular radial distribution functions in water, as calculated by Jorgensen [117], using TIP and CI potentials.

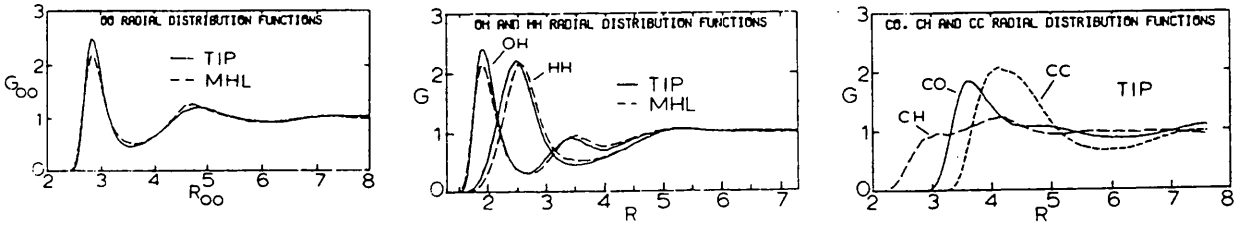


Figure 16.2: Intermolecular radial distribution functions in methanol, as calculated by Jorgensen [116], using TIP potentials.

Clearly, it is important to study more deeply the behaviour of these systems under microcanonical conditions, to check the energy conservation and the liquid dynamics, using a atom-based criterion to check the cutoff distance and the boundaries of the cell, as discussed above. In particular, specific heats can be calculated directly in an NVE ensemble, as a function of the fluctuations of the system.

16.5 RDF versus partial charges

The pair radial distribution functions are one of the most informative ways to describe the static structure of a given liquid or amorphous system, and thus they are calculated here for water, methanol, ethanol and TMOS. As the total number of possible pair functions is quite large, only the most important are presented here, as in Jorgensen's work. As a cutoff of 9.0 Å, with a switching function width of 1.0 Å, has been used in all simulations, RDFs are calculated up to a maximum distance of 8.0 Åfor water, methanol and ethanol, and 10.0 Åfor TMOS, due to its larger molecules.

Due to the significant amount of information present in the 25x3x2 = 150 functions here displayed and the lack of accurate experimental information available, only a general discussion of the results is made here. It will be important for this project to obtain reliable experimental information, particularly from recent neutron-diffraction data, for the various pair functions calculated here.

Generally speaking, these seem to compare fairly well with these obtained by Jorgensen, for

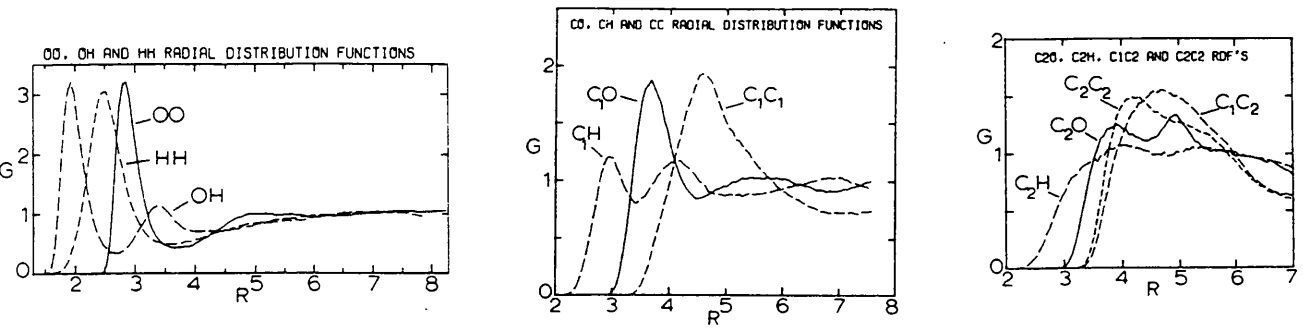


Figure 16.3: Intermolecular radial distribution functions in ethanol, as calculated by Jorgensen [115], using TIP potentials.

g_{O-O}, g_{O-H}, g_{H-H}, g_{O-C_1}, g_{O-C_2}, $g_{C_1-C_1}$, $g_{C_2-C_2}$, $g_{C_1-C_2}$, g_{C_1-H} and g_{C_2-H} in ethanol, for g_{O-O}, g_{O-H}, g_{H-H}, g_{O-C}, g_{C-C} and g_{C-H} in methanol, and for g_{O-H} in water.

However, the second peak in the g_{O-O} pair function in water is at the position of 5.5 Å instead of 4.5 Å, which is a cause of particular concern as this peak is usually recognised as being the most characteristic peak of water structure.

Different sets of partial charges seem to introduce important structural changes in the system, even if the global density does not change significantly, as can be seen particularly in the bigger systems, TMOS and ethanol. As expected, for higher temperatures and lower pressures, the peaks present in these radial distribution functions become less defined as their height decreases and their distance increases.

16.6 MSD versus partial charges

All the properties presented so far depend essentially on the static structure of the systems, and do not help very much in understanding their dynamic behaviour. The mean square displacement is probably the most simple dynamic property that can be calculated by molecular dynamics, being directly related to the self-diffusion coefficient, available experimentally from a large number of techniques [109]. The mean square displacements obtained for water, methanol, ethanol and TMOS, as a function of time, are presented in Figures 16.13 to 16.16, for different pressures and temperatures.

Clearly, most of the curves obtained do not show a linear increase of the total displacement with time, as they should if the system were properly equilibrated; indeed there is a negative second derivative, indicative of a progressive slow down of the movement of the atoms. This is relatively surprising, because the times used to equilibrate the systems, 19500 timesteps of 1 fs each, seemed to be already sufficient, and consequently, such a large variation in the dynamic conditions of the systems was not expected, at least in the comparatively small sampling time of just 500 timesteps used in these calculations.

The results obtained for the mean square displacement, as a function of time, can be used to determine the corresponding self-diffusion coefficients, given by a Einstein equation (see chapter 7):

$$2tD = \frac{1}{3} < |\vec{r}_i(t) - \vec{r}_i(0)|^2 > .$$

Due to the curvature existent in most of the graphs presented here, the calculated average

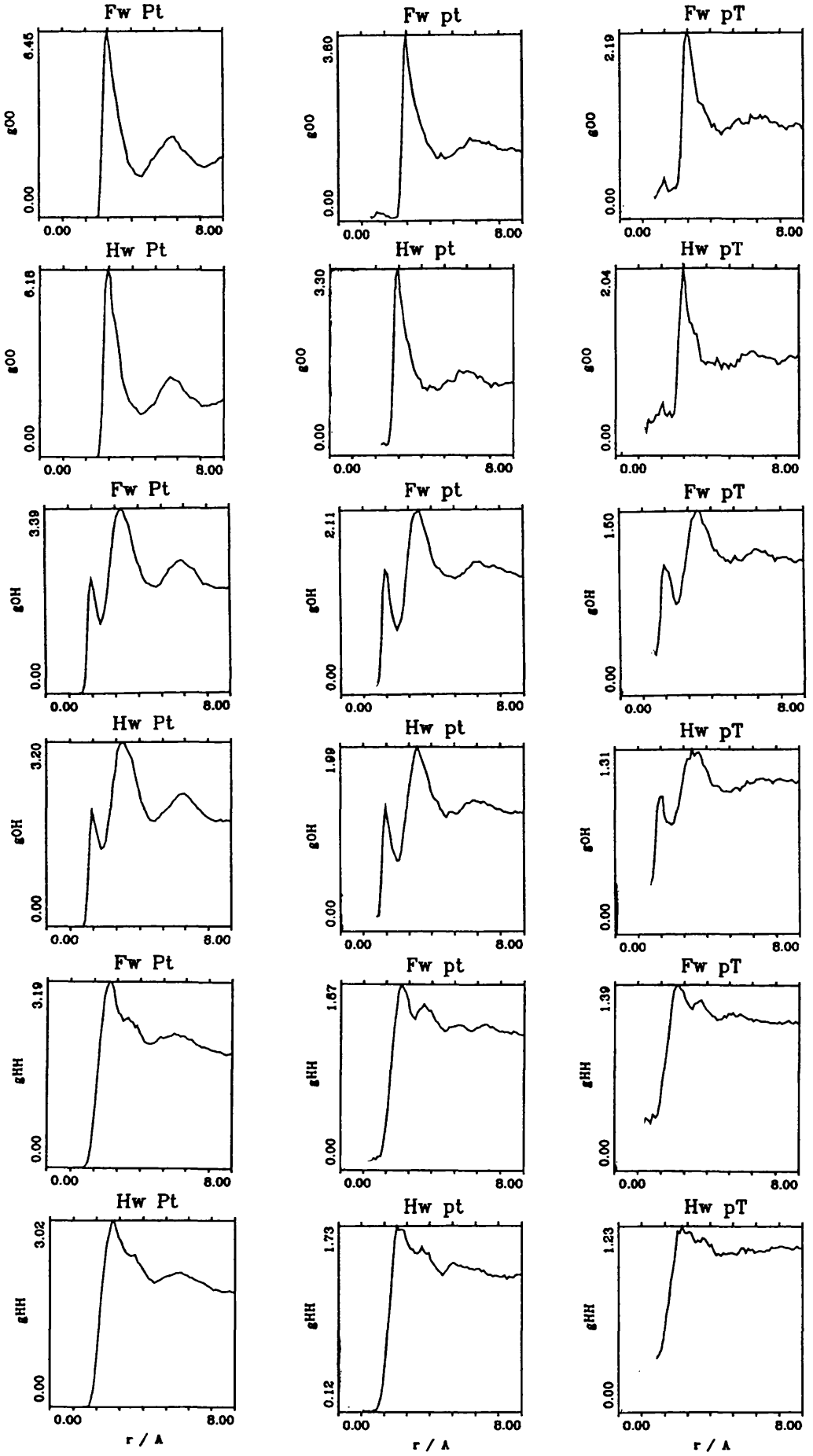


Figure 16.4: RDFs in water, for P = 10,000 bar or p = 1 bar and t = 20°C or T = 80°C, employing group-based simulations with a Coulombic cutoff, using cff91 (F) and 2.6*Hirshfeld (H) partial charges.

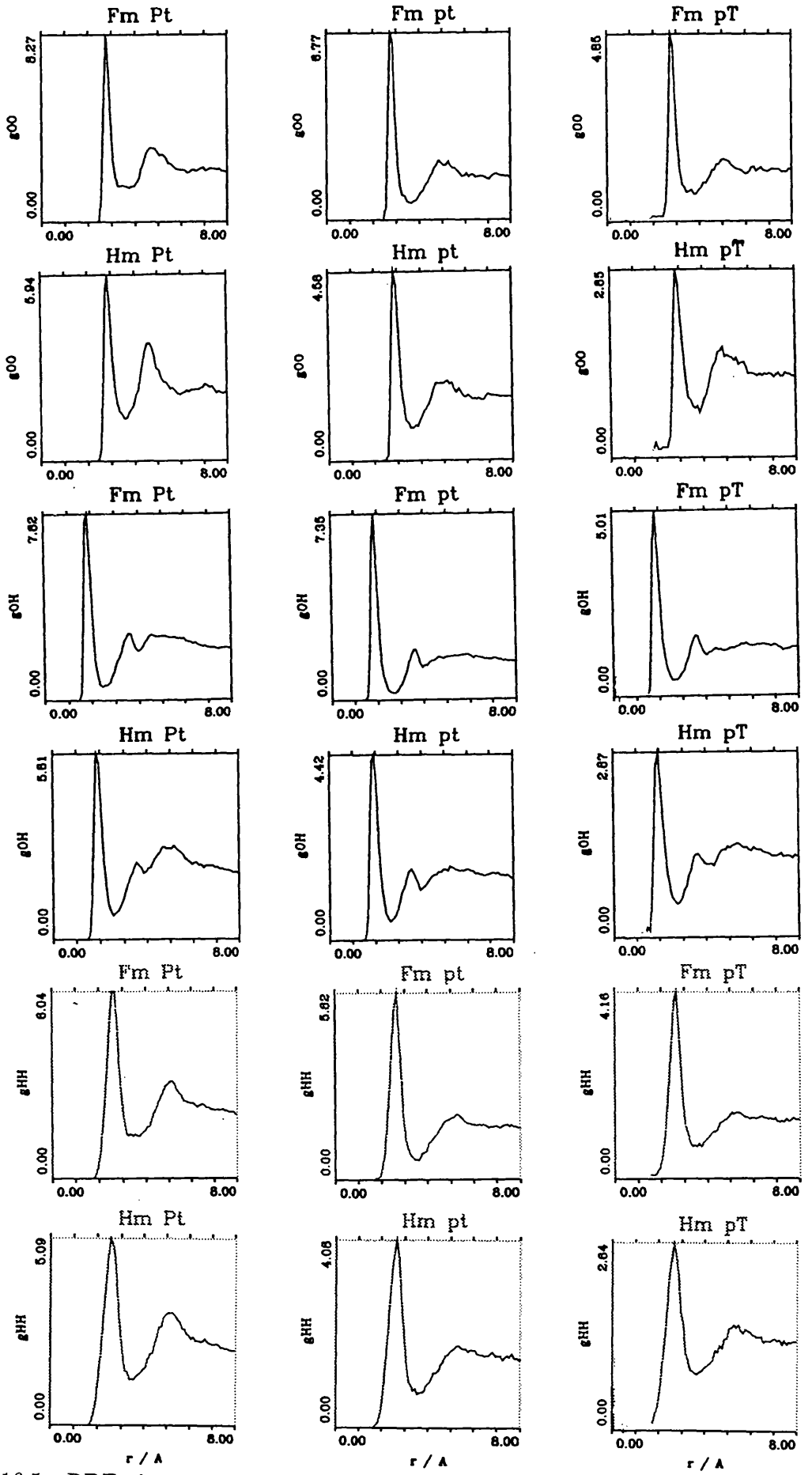


Figure 16.5: RDFs in methanol, for P = 10,000 bar or p = 1 bar and t = 20°C or T = 80°C, employing group-based simulations with a Coulombic cutoff, using 1.1*cff91 (F) and 2.6*Hirshfeld (H) partial charges.

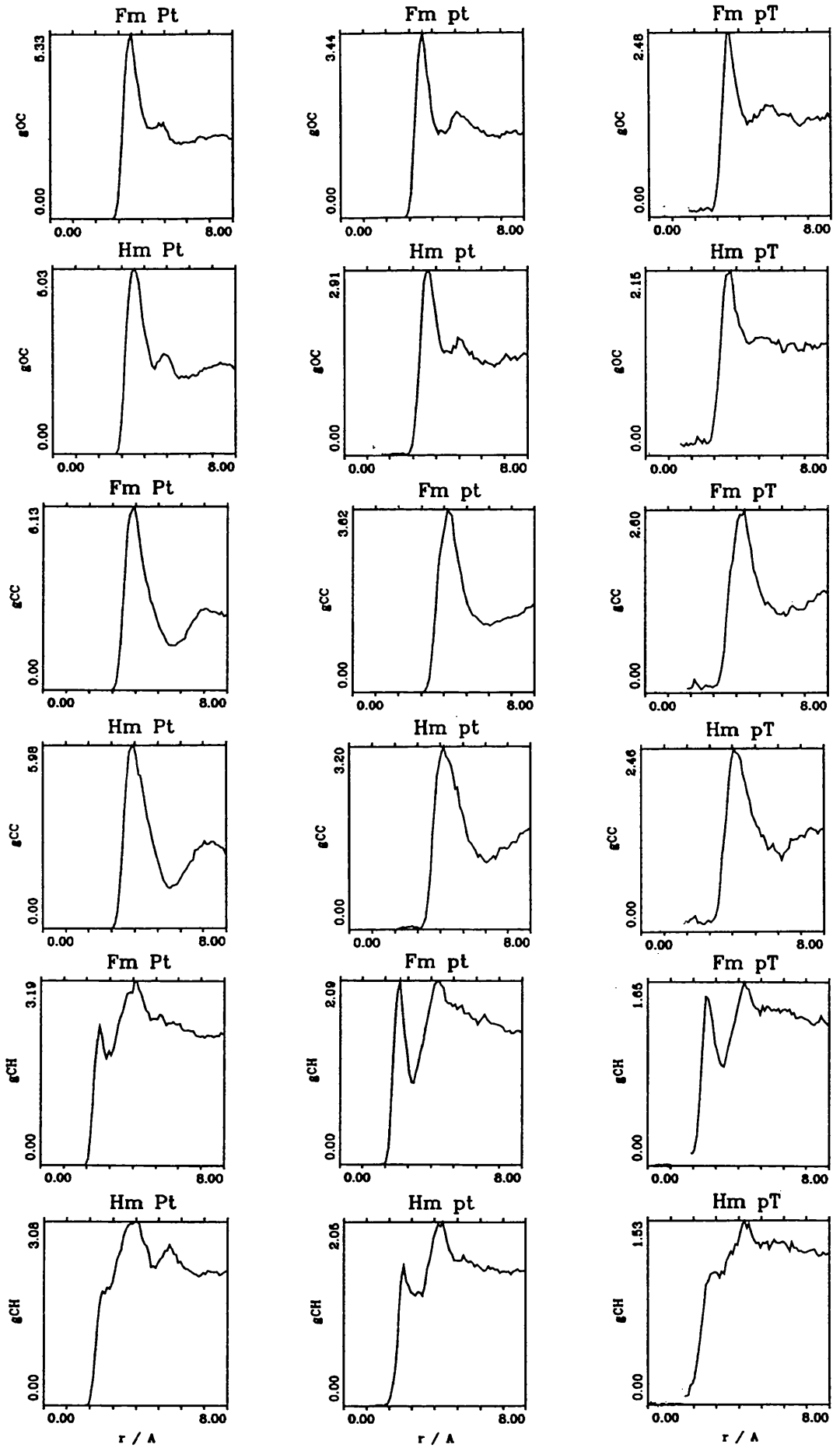


Figure 16.6: RDFs in methanol, for P = 10,000 bar or p = 1 bar and t = 20°C or T = 80°C, employing group-based simulations with a Coulombic cutoff, using 1.1*cff91 (F) and 2.6*Hirshfeld (H) partial charges (*continuation*).

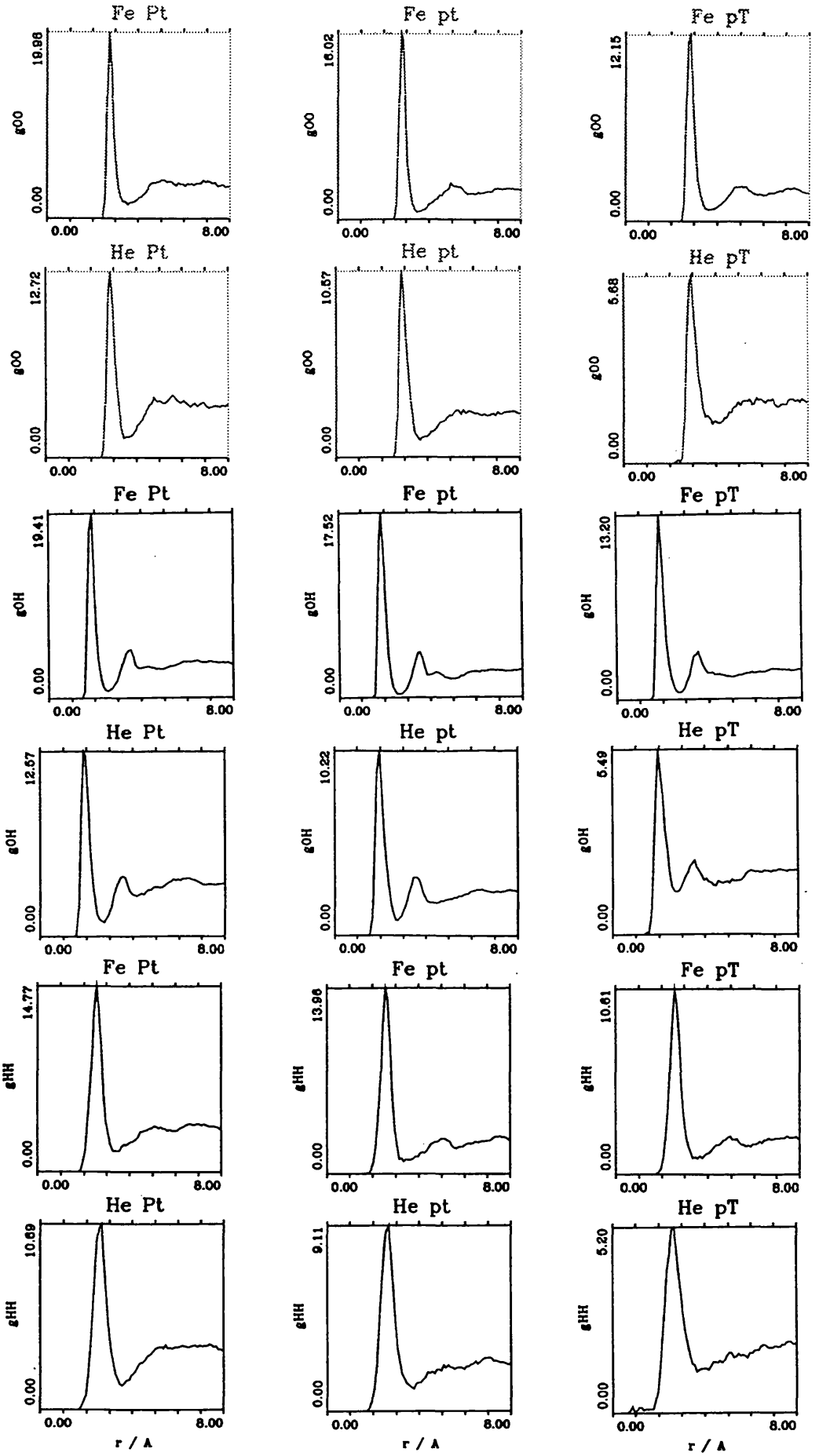


Figure 16.7: RDFs in ethanol, for P = 10,000 bar or p = 1 bar and t = 20°C or T = 80°C, employing group-based simulations with a Coulombic cutoff, using 1.1*cff91 (F) and 2.6*Hirshfeld (H) partial charges.

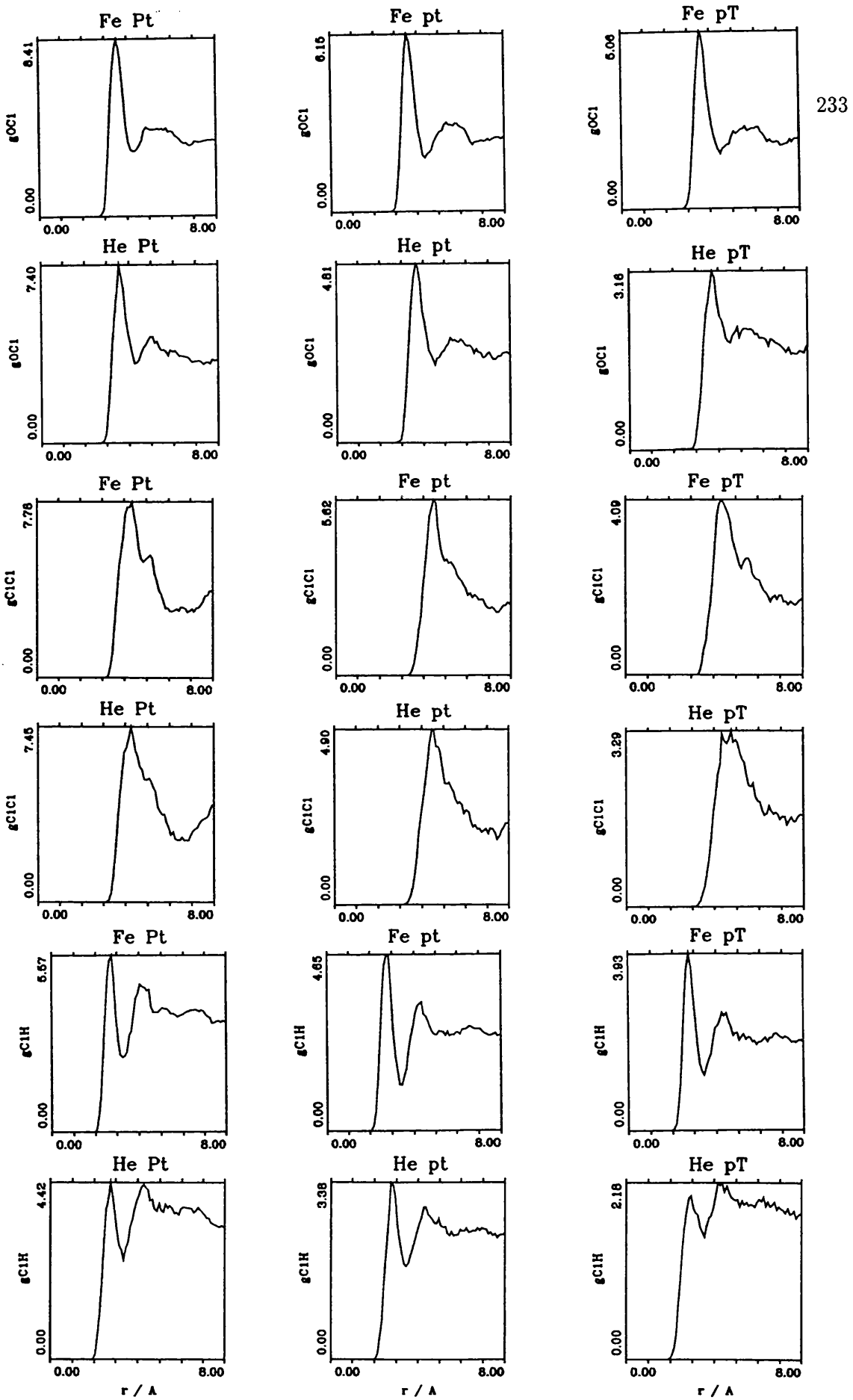


Figure 16.8: RDFs in ethanol, for P = 10,000 bar or p = 1 bar and t = 20°C or T = 80°C, employing group-based simulations with a Coulombic cutoff, using 1.1*cff91 (F) and 2.6*Hirshfeld (H) partial charges (*continuation*).

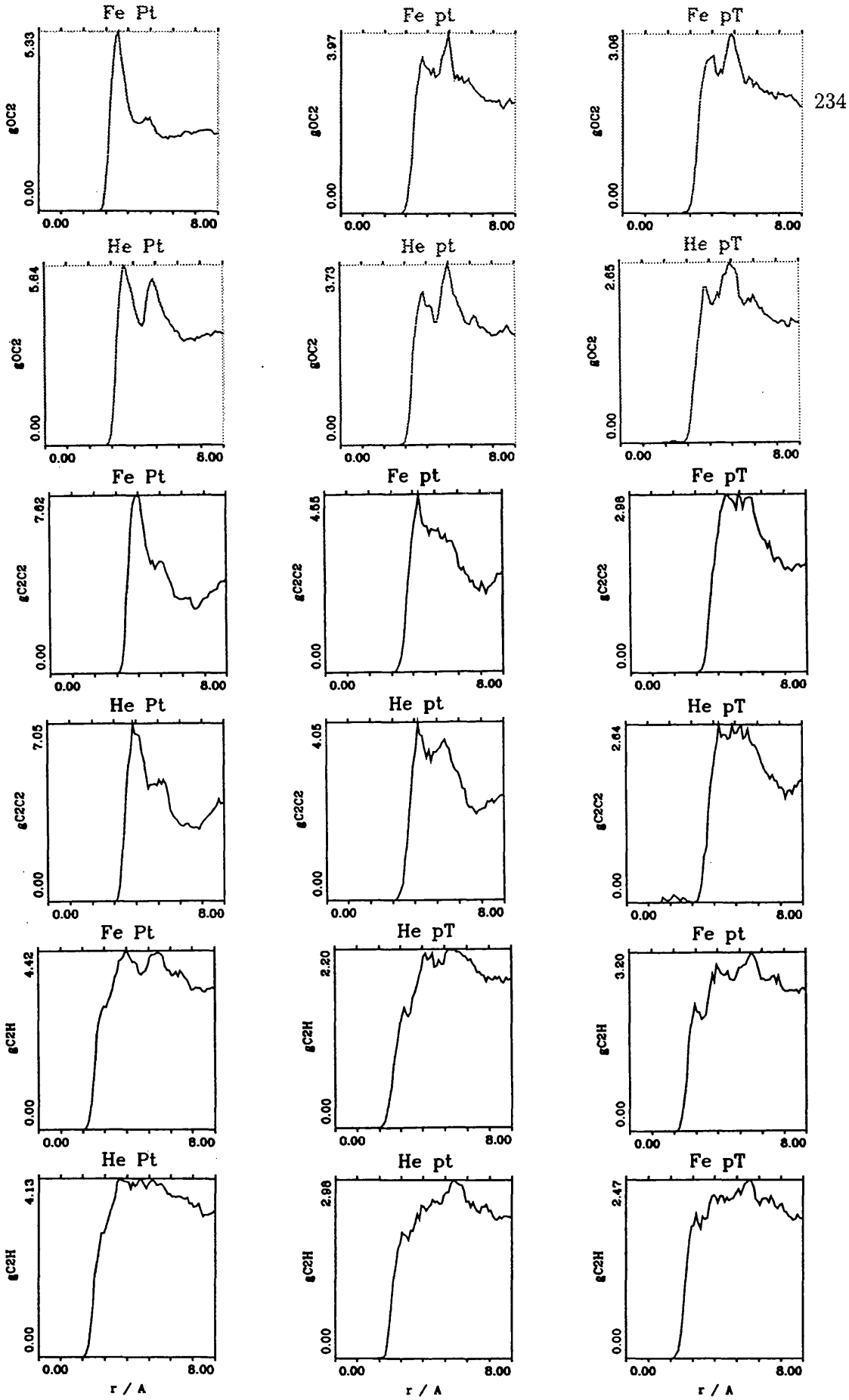


Figure 16.9: RDFs in ethanol, for P = 10,000 bar or p = 1 bar and t = 20°C or T = 80°C, employing group-based simulations with a Coulombic cutoff, using 1.1*cff91 (F) and 2.6*Hirshfeld (H) partial charges (*continuation*).

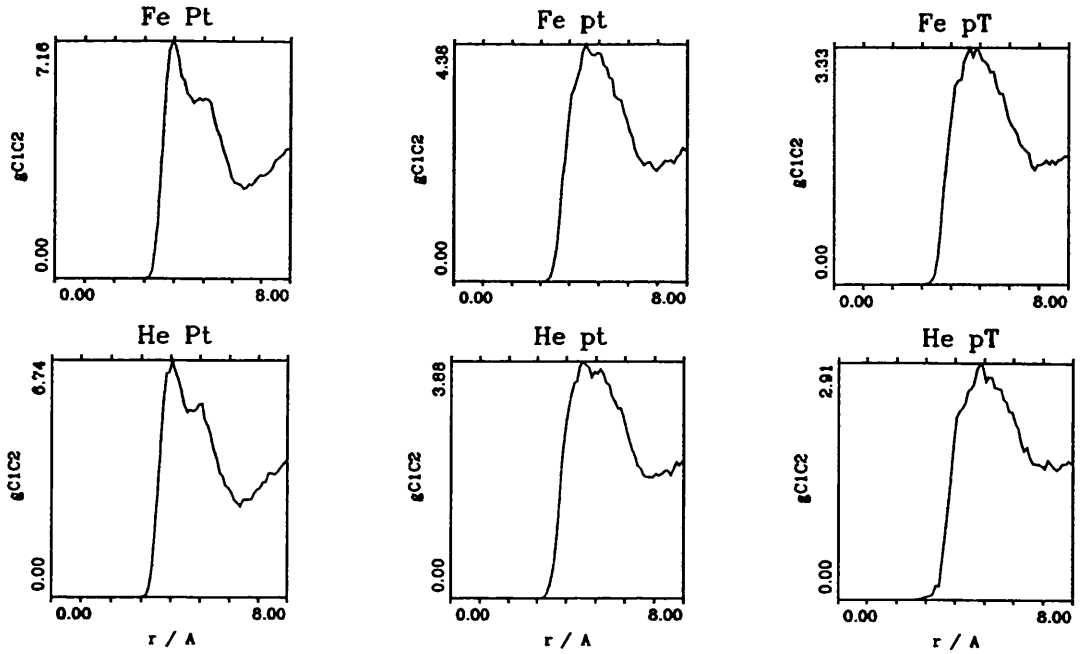


Figure 16.10: RDFs in ethanol, for P = 10,000 bar or p = 1 bar and t = 20°C or T = 80°C, employing group-based simulations with a Coulombic cutoff, using 1.1*cff91 (F) and 2.6*Hirshfeld (H) partial charges (*continuation*).

values for D, presented in Table 16.8, are substantially higher than the values obtained in the limit when t $\rightarrow$ 0.5 ps and consequently should be considered as a maximum limit for the self-diffusion coefficient in equilibrium conditions. This is probably one of the reasons why the calculated values are considerably higher than the experimental ones, presented in the review of Johnson et al. [109].

16.7 Intramolecular equilibration

To choose the minimum amount of time necessary to equilibrate properly a given molecular system, without wasting computer time, is one of the most difficult and important decisions to be taken in a molecular dynamics or Monte Carlo simulation. The importance of a good choice for this equilibration period clearly increases when complicated systems, like molecular liquids, and more sophisticated techniques, like free energy calculations, Ewald summation, and Nose and Parrinello thermostat and barostat are used. The intramolecular equilibration is studied here, monitoring the energy evolution with time of a single molecule of water, methanol, ethanol, TMOS and TEOS, as shown in figures 16.17 to 16.21.

These simulations used different sets of partial charges and temperatures to make it possible to obtain conclusions about the influence of these parameters and to make comparisons with the same conditions used in bulk liquid systems.

Although the results presented are not exactly transferable to a bulk system, where each molecule interacts with many others, they clearly reveal significant trends. Although a water molecule seems to be equilibrated after 1 ps and a methanol molecule after 20ps, for a ethanol molecule much longer equilibration periods seems to be needed, even if the action of the surrounding molecules tends to substantially decrease this time.

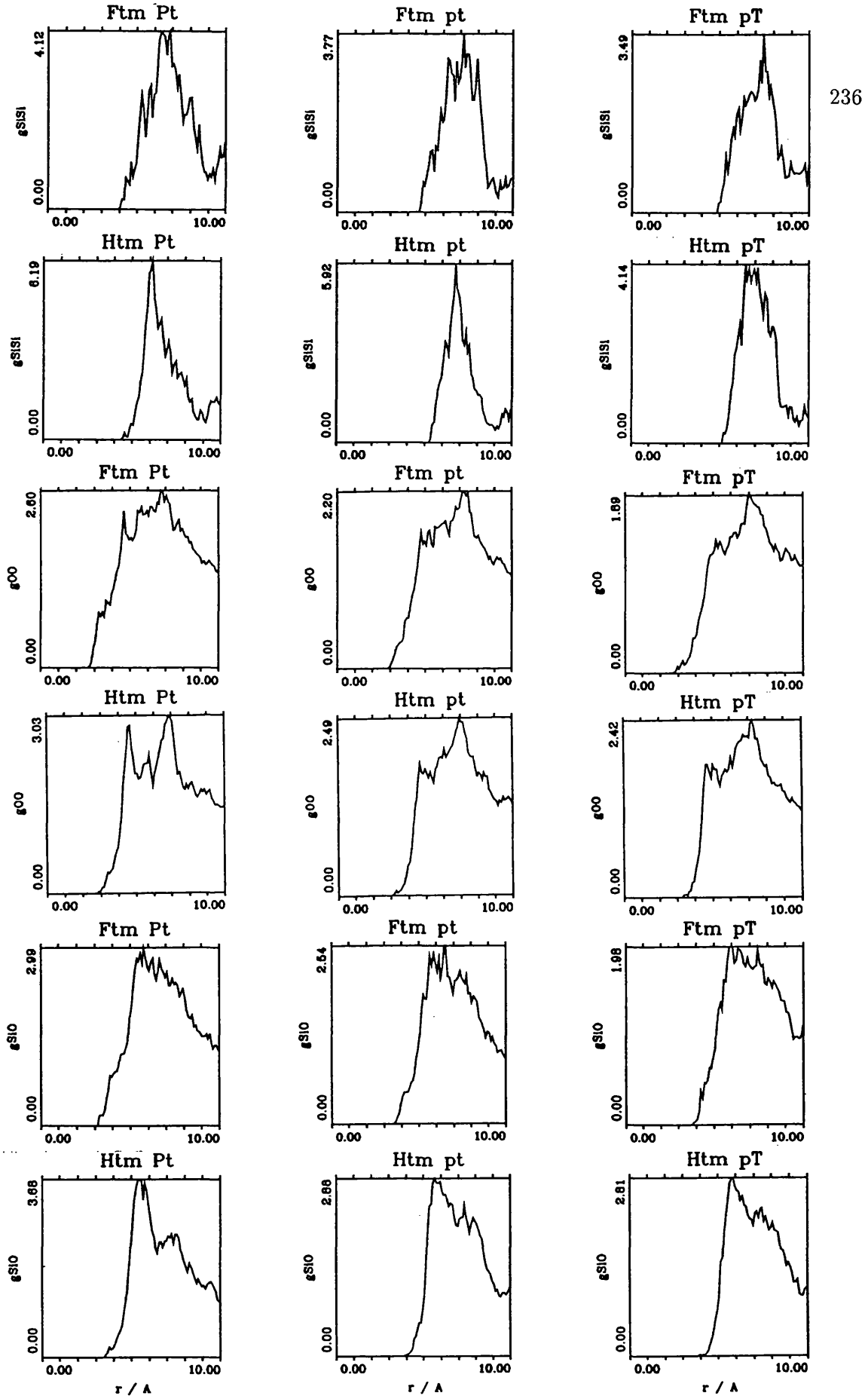


Figure 16.11: RDFs in TMOS, for P = 10,000 bar or p = 1 bar and t = 20°C or T = 80°C, employing group-based simulations with a Coulombic cutoff, using cff91 (F) and 2.6*Hirshfeld (H) partial charges.

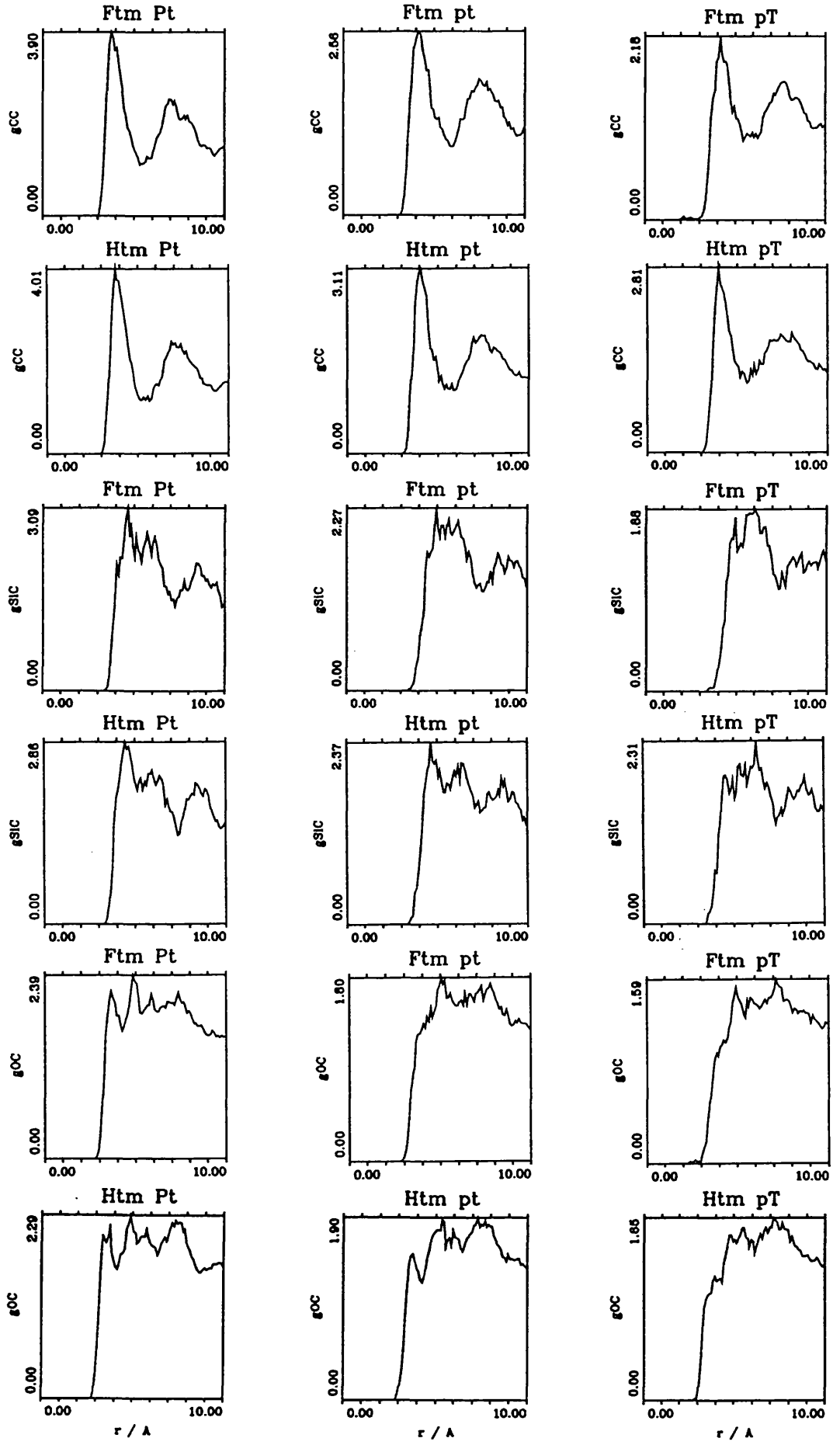


Figure 16.12: RDFs in TMOS, for P = 10,000 bar or p = 1 bar and t = 20°C or T = 80°C, employing group-based simulations with a Coulombic cutoff, using cff91 (F) and 2.6*Hirshfeld (H) partial charges (*continuation*).

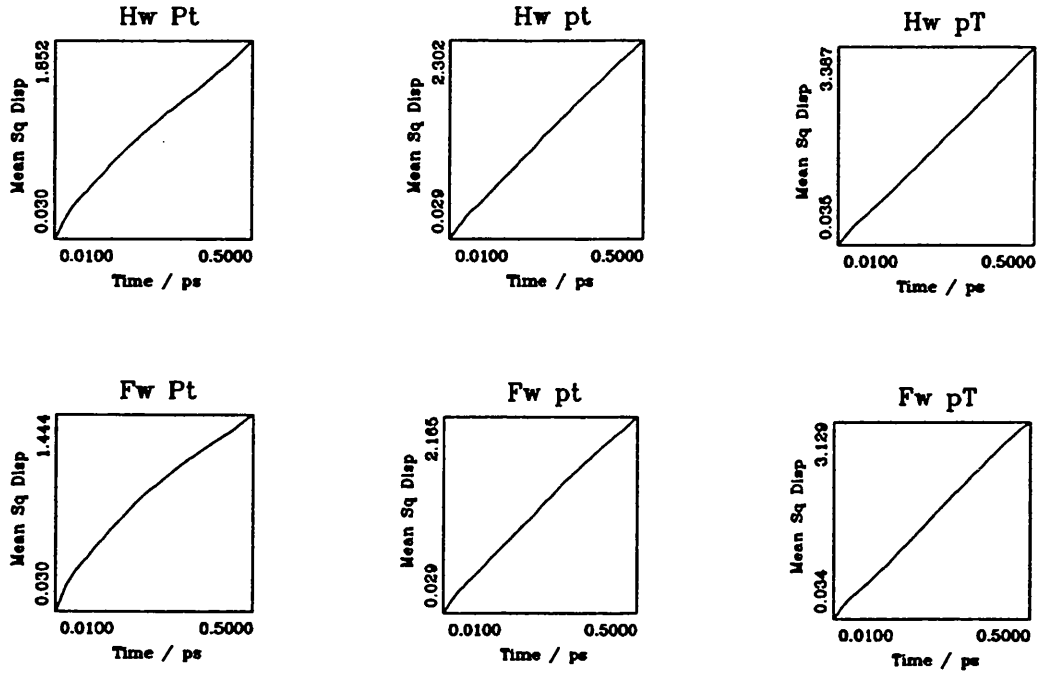


Figure 16.13: MSDs in water, as a function of time (ps), for P = 10,000 bar or p = 1 bar and t = 20°C or T = 80°C, employing group-based simulations with a Coulombic cutoff, using cff91 (F) and 2.6*Hirshfeld (H) partial charges.

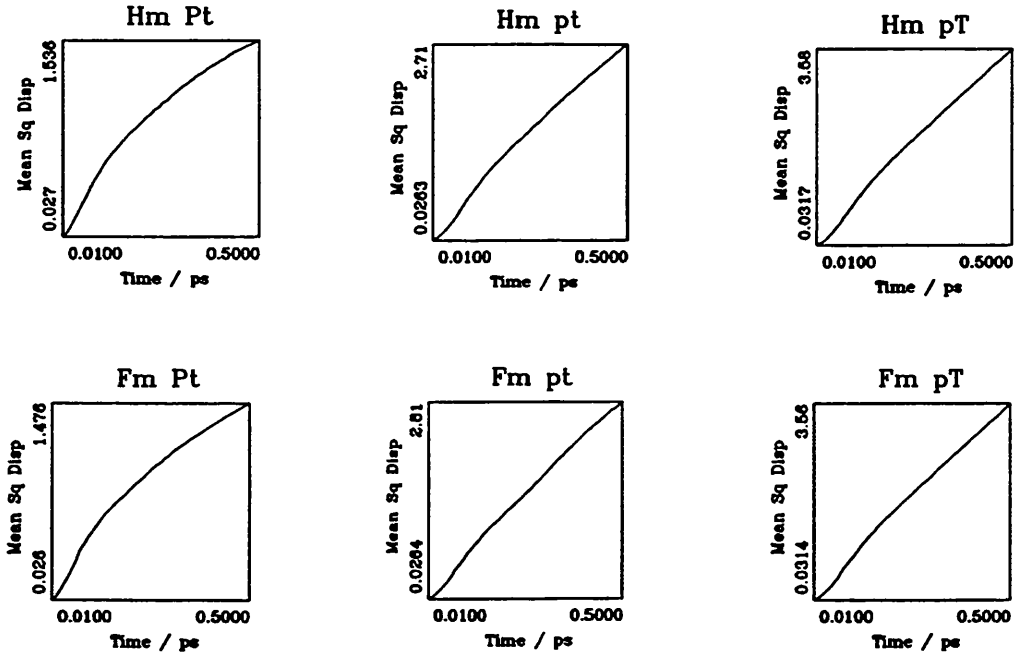


Figure 16.14: MSDs in methanol, as a function of time (ps), for P = 10,000 bar or p = 1 bar and t = 20°C or T = 80°C, employing group-based simulations with a Coulombic cutoff, using 1.1*cff91 (F) and 2.6*Hirshfeld (H) partial charges.

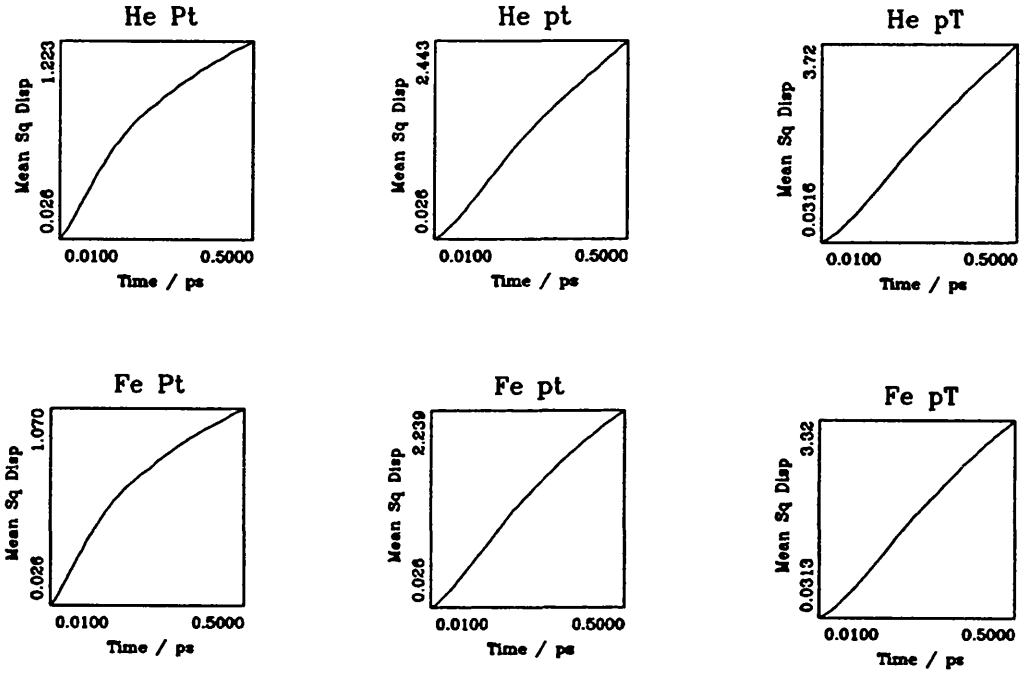


Figure 16.15: MSDs in ethanol, as a function of time (ps), for P = 10,000 bar or p = 1 bar and t = 20°C or T = 80°C, employing group-based simulations with a Coulombic cutoff, using 1.1*cff91 (F) and 2.6*Hirshfeld (H) partial charges.

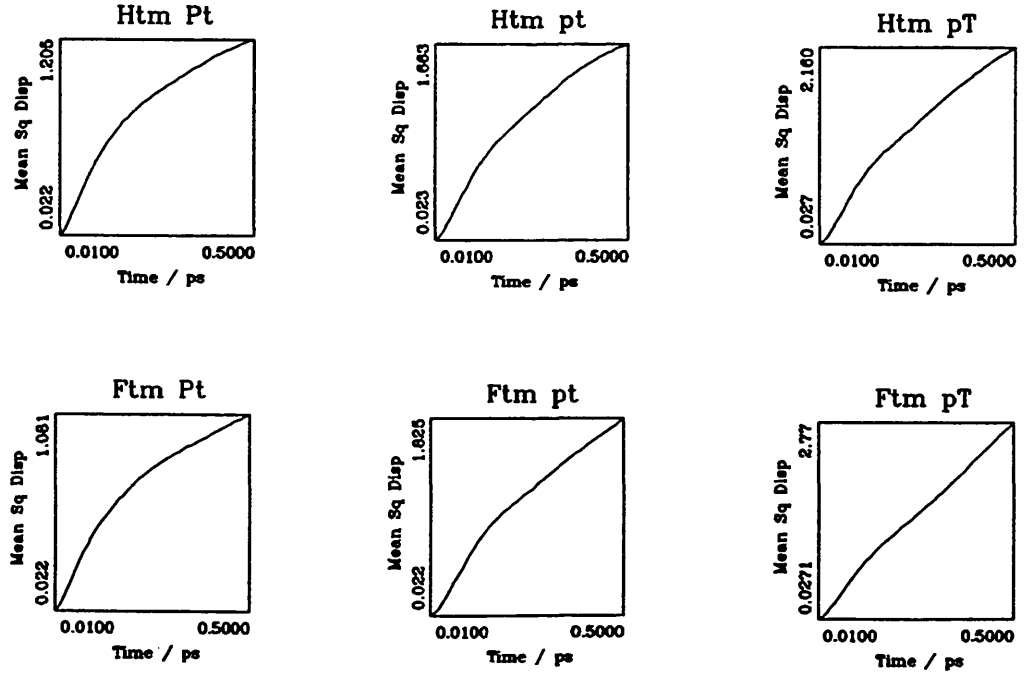


Figure 16.16: MSDs in TMOS, as a function of time (ps), for P = 10,000 bar or p = 1 bar and t = 20°C or T = 80°C, employing group-based simulations with a Coulombic cutoff, using cff91 (F) and 2.6*Hirshfeld (H) partial charges.

	Self-diffusion Coefficient $(10^{-5} cm^2 s^{-1})$					
	Pt		pt		pT	
Charges	cal.	exp.	cal.	exp.	cal.	exp.
			water			
1.0F	4.81	0.50	7.22	2.15	10.43	6.20
2.6H	6.17	"	7.67	"	11.29	"
			methanol			
1.1F	4.92	-	9.37	2.10	11.87	-
2.6H	5.12	"	9.03	"	11.93	"
			ethanol			
1.1F	3.57	-	7.46	0.95	11.07	3.00
2.6H	4.08	-	8.14	"	12.40	"
			tmos			
1.0F	3.60	-	6.08	-	9.23	-
2.6Htm	4.02	-	5.54	-	7.20	-

Table 16.8: Calculated and experimental self-diffusion coefficients $(10^{-5} cm^2 s^{-1})$ of water, methanol, ethanol and TMOS, for t = 20°C or T = 80°C, and p = 1 bar or P = 10,000 bar, employing group-based simulations with a Coulombic cutoff. Hirshfeld H and cff91 F partial charges were used, multiplied by a scaling factor (1.0-2.6). Experimental values from [109].

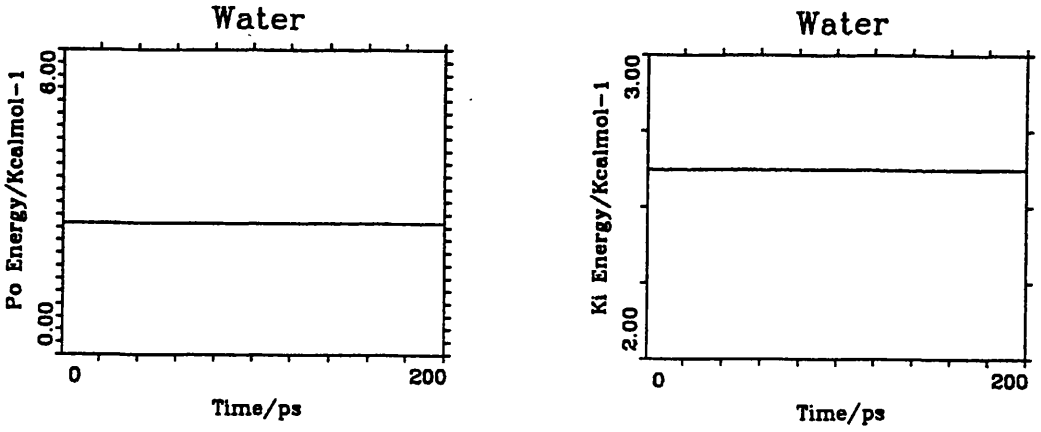


Figure 16.17: Potential Po and Kinetic Ki Energies of a single molecule of water, using 2.6*Hirshfeld partial charges, at 20°C, for 200 ps of sampling time, after 100 ps of equilibration time. Each point in the graphs represents an average over 1 ps, corresponding to 1000 timesteps.

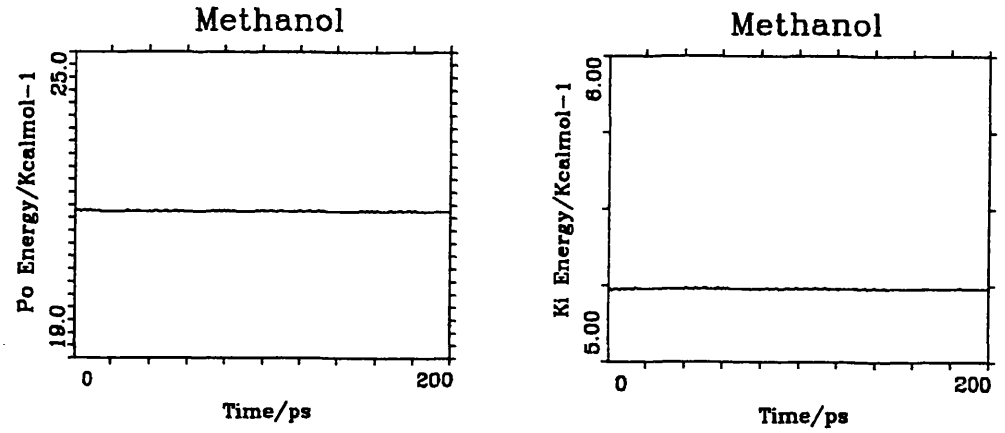


Figure 16.18: Potential Po and Kinetic Ki Energies of a single molecule of methanol, using 2.6*Hirshfeld partial charges, at 20°C, for 200 ps of sampling time, after 100 ps of equilibration time. Each point in the graphs represents an average over 1 ps, corresponding to 1000 timesteps.

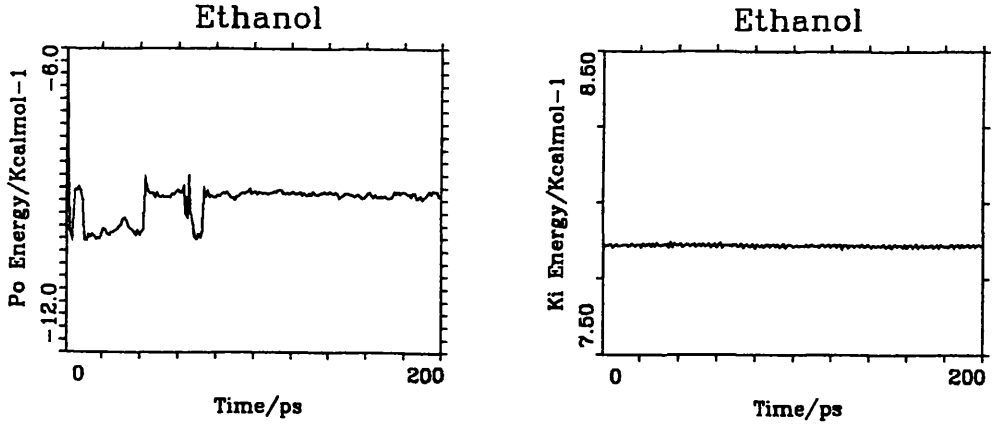


Figure 16.19: Potential Po and Kinetic Ki Energies of a single molecule of ethanol, using 2.6*Hirshfeld partial charges, at 20°C, for 200 ps of sampling time, after 100 ps of equilibration time. Each point in the graphs represents an average over 1 ps, corresponding to 1000 timesteps.

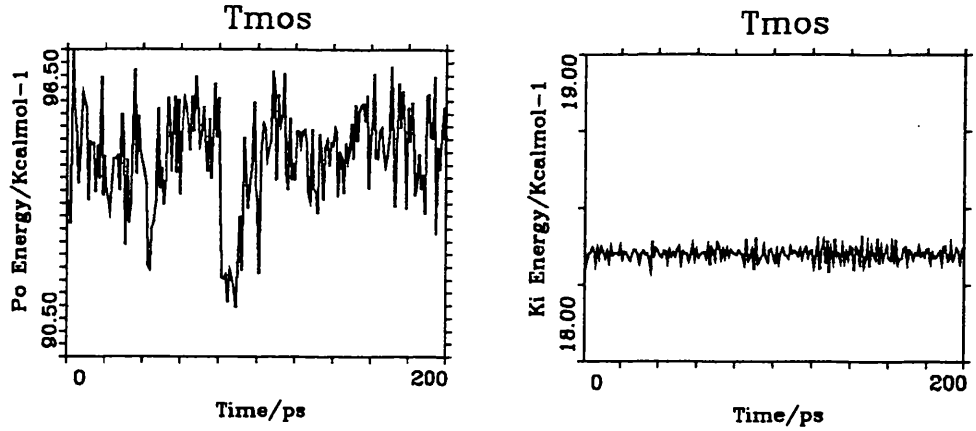


Figure 16.20: Potential Po and Kinetic Ki Energies of a single molecule of TMOS, using 2.6*Hirshfeld partial charges, at 20°C, for 200 ps of sampling time, after 100 ps of equilibration time. Each point in the graphs represents an average over 1 ps, corresponding to 1000 timesteps.

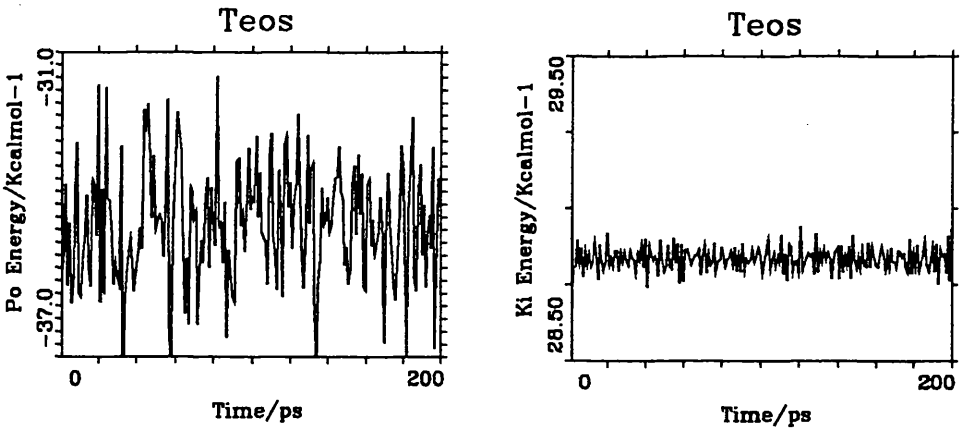


Figure 16.21: Potential Po and Kinetic Ki Energies of a single molecule of TEOS, using 2.6*Hirshfeld partial charges, at 20°C, for 200 ps of sampling time, after 100 ps of equilibration time. Each point in the graphs represents an average over 1 ps, corresponding to 1000 timesteps.

	Density (ρ/gcm^{-3})					
	Pt		pt		pT	
Charges	cal.	exp.	cal.	exp.	cal.	exp.
			Water			
V(v)	1.235	1.246	1.047	0.998	0.983	0.972
F(f)	1.195	"	1.030	"	1.007	"
			Methanol			
V(v)	1.032	1.052	0.884	0.791	0.834	0.736
F(f)	0.964	"	0.736	"	-	"
F(1.1f)	0.978	"	0.740	"	-	"
			Ethanol			
V(v)	1.005	1.050	0.887	0.789	-	0.737
F(1.1f)	0.943	"	0.728	"	-	"

Table 16.9: Calculated and experimental densities of water, methanol and ethanol, for t = 20°C or T = 80°C, and p = 1 bar or P = 10,000 bar, employing group-based simulations with a Coulombic cutoff, using the cvff forcefield (V) with cvff partial charges (v) and the cff91 forcefield (F) with cff91 partial charges (f), multiplied by a scaling factor (1.0-1.1), with a equilibration time of 1.5 ps.

This behaviour is probably due to the interchange between the trans and the gauche conformations existent in ethanol and similar behaviour can be expected for larger molecules, like TMOS, TEOS and the silicate aggregates we will simulate in this project. These results also show that partial charges and temperature strongly influence the required intramolecular equilibration period and the same is probably true for pressure.

16.8 Forcefield dependence of density

All the MD and EM calculations reported so far were done using both cvff and cff91 MSI forcefields. The latter, which is a second generation forcefield, clearly behaves better than the former, which is a first generation, empirically based, forcefield. Furthermore, new sets of parameters, determined from ab-initio calculations, are being published for this forcefield. Some data relevant for this comparison is presented in Table 16.9.

Clearly, for methanol and ethanol, the densities obtained with the cvff forcefield are too high and the ones obtained with cff91 are slightly low. The partial charges for the cff91 forcefield can be increased, because the dipoles are not too high, but the partial charges for the cvff forcefield cannot decrease, because the calculated dipoles would become unrealistically low. Improved results (for longer run times), with the cff91 forcefield, for methanol and ethanol, have been presented before, in Table 16.1.

To know better the behaviour of these liquid systems when submitted to both forcefields, water, methanol and ethanol were tested with cvff and cff91 forcefields, using exactly the same set of Mulliken partial charges, calculated with Dmol. The results obtained for density, with both forcefields, using this exaggerated set of charges, depicted in figure 16.10, clearly corroborate our previous considerations, showing that cvff tends to create more compressed systems than cff91. For each system, when the density at ambient conditions increases, the compressibility

	Density (ρ/gcm^{-3})					
	Pt		pt		pT	
Charges	cal.	exp.	cal.	exp.	cal.	exp.
			Water			
V(m)	1.269	1.246	1.131	0.998	1.067	0.972
F(m)	1.245	"	1.111	"	1.072	"
			Methanol			
V(m)	1.082	1.052	0.987	0.791	0.984	0.736
F(m)	1.019	"	0.875	"	0.851	"
			Ethanol			
V(m)	Unstable	1.050	-	0.789	-	0.737
F(m)	0.992	"	0.847	"	-	"

Table 16.10: Calculated and experimental densities of water, methanol and ethanol, for t = 20°C or T = 20°C, and p = 1 bar or P = 10,000 bar, employing group-based simulations with a Coulombic cutoff, using the cvff (V) and the cff91 (F) forcefields with Mulliken partial charges (m), with a equilibration time of 1.5 ps.

(ρ_{Pt}/ρ_{pt}) at high pressure decreases, as expected. To get definitive conclusions, however, longer equilibration periods will be necessary.

When optimising the structure of different clusters, the cff91 forcefield usually allowed to obtain lower energy minima than the cvff, probably due to its improved flexibility.

16.9 Density versus cutoff

Because the calculation of the medium- and long-range interactions cannot usually be undertaken for distances greater than, say, 10-15 Å, done, due to obvious cpu time limitations, it is important to know, as exactly as possible, what is the magnitude of the error introduced when they are ignored. This is particularly important in this work, because the partial charges assume significant values in the polar liquids studied here, and because all the present calculations were still done without considering a Ewald sum to account for the long range electrostatic interactions.

When using a Ewald sum, the influence of the partition factor and of the real space and reciprocal space cutoffs should be investigated with great attention. The values presented in table 16.11 show that the density and consequently the magnitude of the forces changes rapidly, when cutoffs smaller than 9 Å are considered. The non monotonic increase of density for larger cutoffs, particularly for water, can be attributed to a obviously insufficient equilibration.

16.10 Density versus equilibration time

Since this work started, essentially three different periods of equilibration have been tried, 1.5 ps, 4.5 ps and 20.0 ps, when simulating NPT ensembles with the Berendsen thermostat and barostat. The necessary time of equilibration strongly depends on the system, the integration algorithm, the thermostat and barostat used and consequently it is not possible to derive general conclusions on this point.

		Pt			pt	
Cutoff/Å	*water*	*methanol*	*ethanol*	*water*	*methanol*	*ethanol*
11.0	1.233	1.045	1.020	1.040	0.872	0.900
10.0	1.216	1.033	1.005	1.006	0.883	0.902
9.0	1.235	1.032	1.005	1.047	0.884	0.887
8.0	1.227	1.033	-	1.047	0.862	-
7.0	1.215	1.025	-	1.037	0.850	-
6.0	1.288	1.009	0.993	1.075	0.839	0.838

Table 16.11: Density as a function of the cutoff, in water, methanol and ethanol, for t = 20°C and p = 1 bar or P = 10,000 bar, employing group-based simulations with a Coulombic cutoff, using cvff forcefield and cvff partial charges, with a equilibration time of 1.5 ps.

		Pt			pt	
System	1.5 ps	4.5 ps	20.0 ps	1.5 ps	4.5 ps	20.0 ps
water						
2.5H	0.9985	0.9928	-	1.1744	1.2009	-
2.6H	-	-	1.009	-	-	1.2040
methanol						
2.5H	0.7405	0.7474	-	0.9623	0.9986	-
2.6H	-	- 0.7470 -	-	0.9960		
ethanol						
2.5H	-	0.7300	-	0.9452	0.9792	-
2.6H	-	-	0.7300 -	-	0.9840	

Table 16.12: Density as a function of the equilibration time, in water, methanol and ethanol, for t = 20°C and p = 1 bar or P = 10,000 bar, employing group-based simulations with a Coulombic cutoff, using Hirshfeld partial charges (H), multiplied by a scaling factor (2.5-2.6).

The results presented in Table 16.12 show that, for the particular set of conditions used here, 1.5 ps is clearly insufficient, as the density at high pressure changes considerably when the run time is increased. Although significant differences cannot be detected between the values obtained after 4.5 ps and 20.0 ps, more detailed analysis are required. Furthermore, density is not the best test variable, because it is a relatively stable quantity, when compared with energy fluctuations or mean square displacements, for example.

16.11 Density versus system size

This topic has not been studied carefully, because until now only systems with 51 and 408 molecules have been considered, and in the former case the test is severely limited by the short cutoff (around 6.0Å) allowed by the minimum image convention. Nevertheless, comparing the results of the Table 16.13, and considering that the silicate aggregate used for the systems with 400 solvent molecules is heavier, there is no obvious size effect.

System	ρ/gcm^{-3} *water*	*methanol*	*ethanol*
50 + $Si(OH)_4$	1.07	0.83	0.88
50 + $Si_2O(OH)_6$	1.11	0.90	0.88
400 + 8 $Si_3O_3(OH)_6$	1.18	0.93	0.93

Table 16.13: Calculated density for 50 solvent molecules with $Si(OH)_4$, 50 solvent molecules with $Si_2O(OH)_6$ and 400 solvent molecules with 8 $Si_3O_3(OH)_6$, after 1.5 ps of equilibration at room temperature and pressure with Berendsen thermostat and barostat, using cvff forcefield and cvff partial charges.

timesetp	$< \Delta E^2 >^{1/2}$
0.1	0.153
0.2	0.341
0.5	0.985
1.0	1.574
2.0	5.496

Table 16.14: Standard deviation of energy $< \Delta E^2 >^{1/2}$ (kcal mol^{-1}), as a function of timestep (fs), for a system comprising 50 water molecules and one $Si(OH)_4$, at room temperature and pressure, using a Leafrog integration algorithm.

16.12 Energy fluctuation versus timestep

A detailed study of this important topic has not been undertaken yet. The only results obtained so far, for a system with 50 water molecules and an $Si(OH)_4$ monomer, in a NVT ensemble, with a Leapfrog integration algorithm, are presented in Table 16.14 and Figure 16.22. As expected for this algorithm, the standard deviation of energy increases as $< \Delta E^2 >^{1/2} = \mathrm{K}\ \Delta T^m$, with m = 1.4, instead of 2, as predicted. This factor m should be a function of temperature and pressure as well, increasing, for example, when temperature increases. Clearly, with these systems it is not possible to use timesteps bigger than 1.0 fs.

16.13 Execution time versus cutoff

Some run times are presented in Table 16.15, obtained for systems with 408 molecules, as a function of the cutoff distance and of the Verlet neighbour list width, for a given number of time steps, at ambient pressure, using the cff91 forcefield. The time seems to be increasing almost linearly with cutoff, mainly for the smallest system, water, which is satisfactory.

On the other hand, Table 16.16 shows that a Verlet neighbour list is a very useful tool to decrease substantially the cpu time and it is worth spending more time optimising the choice for VNL width. Similar results were obtained for a cvff forcefield.

At higher pressures, 10,000 bar, the times can increase by more than 15-25 %, for the bigger system, ethanol, as the number of atoms inside the cutoff region increases. All these results were obtained using a Leapfrog Verlet integration algorithm, a ensemble coupling Berendsen algorithm

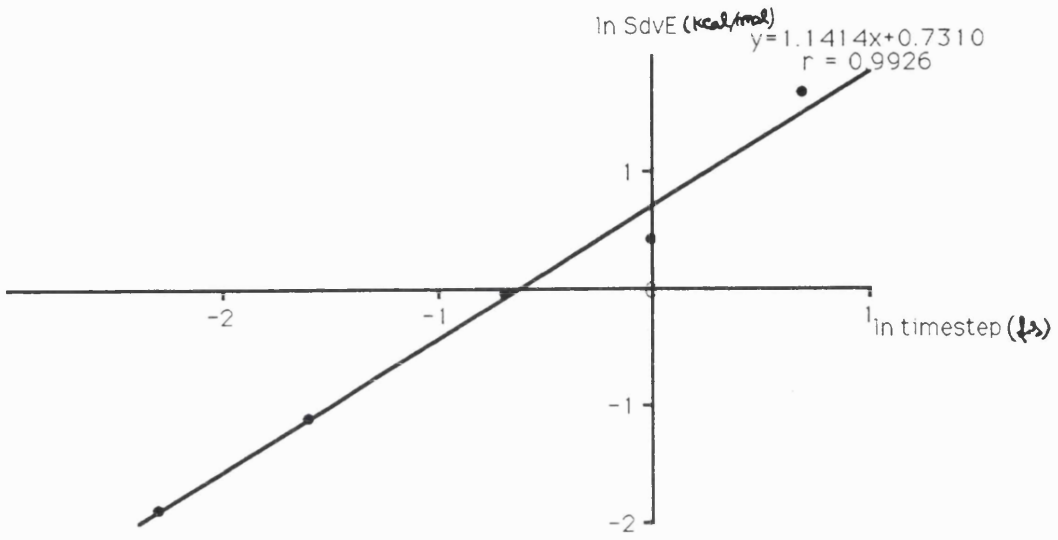


Figure 16.22: $\ln < \Delta E^2 >^{1/2}$, as a function of $\ln \Delta T$, for a system constituted by 50 water molecules and one $Si(OH)_4$, at room temperature and pressure, using a Leafrog integration algorithm.

Cutoff/Å	*water*	*methanol*	*ethanol*
11.0	$1.76t_w$	$1.62t_m$	$1.54t_e$
10.0	$1.39t_w$	$1.36t_m$	$1.12t_e$
9.0	t_w	t_m	t_e
8.0	$0.77t_w$	$0.77t_m$	-
7.0	$0.59t_w$	$0.56t_m$	-
6.0	$0.43t^w$	$0.46t_m$	-

Table 16.15: Execution times corresponding to runs of 375 timesteps at room temperature and pressure for 408 molecules of water, methanol and ethanol, using a Verlet neighbour list width of 1.0 Å, for several cutoff distances.

Width/Å	Time
0.0	$1.23t_o$
1.0	t_o
2.0	$1.05t_o$
3.0	$1.14t_o$

Table 16.16: Execution time versus buffer width in the Verlet neighbour list method, for runs of 50 timesteps at room temperature and pressure of 400 molecules of water and 8 $Si_3O_3(OH)_6$ rings, using a cutoff of 11.5 Å.

and a single cutoff for all intermolecular interactions. The time used increases considerably when more sophisticated integration and coupling algorithms are used, particularly when the long range interactions are calculated with an Ewald sum.

16.14 Conclusions

The results presented here show that it is possible to develop a general methodology to simulate, by Molecular Dynamics or Monte Carlo, the most notorious properties of simple liquids, for a wide range of thermodynamic conditions.

For water, the alcohols and TMOS, the structural properties, density and radial distribution functions are well simulated and in accord with the limited experimental data available, while the enthalpy of vaporisation, the only quantity directly related to energetics, seems to be in reasonable agreement with experience.

The self-diffusion coefficients, the only dynamic property investigated here, are too high by a factor of two, considering the results obtained from experimental measurements. The curvature observed in the MSDs for most systems also suggests a insufficient equilibration. The dynamic conditions in the liquids are the aspect of the simulations that needs further to be improved. Self-diffusion coefficients are very sensitive to the medium conditions, particularly temperature, and are difficult to simulate or even to measure experimentally.

In general, the agreement between simulated and experimental results seems extremely encouraging, considering that the methodology is the same, the Van der Waals and the bond potentials for each atom are the same, the charges are obtained in the same way and the thermodynamic conditions vary from ambient to very high pressure and/or temperature.

In particular, this sucess should allow us to prepare automatically solutions formed by the mixture of simple liquids, without requiring systematic expensive analysis-a key result to assist further studies of complex sol-gel solutions or indeed of any liquid mixture.

Some technical difficulties still remain however. TEOS could not be studied, because the simulation becomes unstable, due to the group-based algorithm. The long-range Coulombic forces, for distances larger than the cutoff, are totally neglected-a approximation particularly significant in polar liquids, as water, alcohols and sol-gel solutions. A Berendsen NPT algorithm, simple but describing incorrectly the dynamic fluctuations, is used throughout this study. A more sophisticated method is required, though it can be anticipated that it will not change significantly the static results presented here, which depend essentially on the interaction potentials.

Chapter 17

Cutoff-based solutions

This chapter has two main purposes: the first is to investigate how the MD model, developed before, describes the mixture of the different components in a sol-gel solution, the first step in any real sol-gel process; the second is to investigate how this MD model describes the aggregation of the silicate clusters in solution, a necessary step before the condensation can occur.

17.1 Introduction

The first Molecular Dynamics simulations related to sol-gel processes were published by Garofalini et al. in 1986 [82, 80] and consisted, in a first stage, in the simulation of the monomer, dimer and water molecules, using a modified Born-Mayer-Huggins (BMH) potential to describe all Si-Si, Si-O and O-O pairs in the non-water molecules and a revised Rahman-Stillinger-Lemberg (RSL2) potential to describe all O-H, H-H and O-O pairs in the water molecules.

They found that changing only the BMH potential, both silicic and disilicic acids can be reasonably described and an accurate energy can be obtained for the deprotonation of $Si(OH)_4$ into $SiO_4H_3^-$, in agreement with previous quantum mechanical calculations. Simulations of two silicic acid monomers to describe the condensation reaction were less successful. Although the clusters attracted each other, a water molecule was not formed during the reaction; merely association of the two clusters occurred instead of a true condensation reaction.

Simulation of solvation and mixing effects in liquids attracted progressively more attention from the scientific community in the second half of the '80s. Fleischman et al. used Molecular Dynamics coupled with Thermodynamic-Cycle-Perturbation Theory [73], to calculate relative Helmholtz free energies of hydration for methanol, ethanol, ethane and propane.

Equimolar mixtures of methanol and water have been studied by Stouten et al. [222], using NPT Molecular Dynamics, in the sequence of previous simulations of liquid water and methanol. They concluded that both the volume contraction and the excess enthalpy of the solution can be well described with the SPC and OM2 potentials developed for pure water and methanol. Results like these help to support the assumption that sol-gel solutions can be simulated with the methodologies and potentials developed for pure liquids.

The effect of different initial sites for water molecules in crystal hydrates have been studied by Howell et al. [103], comparing MC simulations started from random and experimental configurations. It was found that the overall hydrogen-bond structure could be reproduced in both cases, but some differences still subsist after 600,000 configurations.

The effect of the molecular separation of the reacting species on the polycondensation of $Si(OCH_2CH_3)_4$ was studied by Yoldas [249], using a combination of Size-Excluded Liquid Chromatography (SEC) and ^{29}Si NMR. It was shown that the mean value and distribution of the molecular weight of the resultant organosiloxane polymers depends considerably on the molecular separation between the reacting TEOS molecules in the initial solution. The molecular structure and molecular size distribution in sol-gel processes are thus determined primarily by chemical encounter rates and the diffusion process.

Two compositions are considered in this work, one with 200 water molecules plus 200 methanol molecules plus 8 monomers $Si(OH)_4$, and another with 200 water molecules plus 200 ethanol molecules plus 8 trimer rings $Si_3O_3(OH)_6$. Methanol and ethanol were chosen because they are the most commonly used solvents in sol-gel processes. Three initial configurations are considered: one with all the water molecules on one side and the alcohol molecules on the other; a second with water and alcohol molecules occupying alternate octant cubes of the cell and finally a third with all water and alcohol molecules alternating their positions in the initial configurations. The silicate clusters are uniformly distributed in all configurations.

Large trimer rings were chosen to decrease diffusion and increase the stringency of the mixture conditions. Highly dilute solutions were chosen to increase the stringency of the aggregation conditions. After a initial NVT run, at low temperature, of 10 ps, to eliminate intramolecular residual tensions, all simulations were prepared compressing first at 10,000 atm during 10 ps, before relaxing to ambient conditions, during 20 ps. Successive configurations were then collected, every 100 ps, until completing 500 ps. G_{SiSi} RDFs were measured for these configurations, which then ran for more 10 ps, to collect the density and energetic data. A smaller timestep, 0.5 fs, was used in the ethanolic solutions, due to some unstability created by the large trimer rings. The instantaneous radial distribution functions were collected during 10 timesteps of 0.001 fs each. The MD methodology used is described in the previous chapter.

17.2 Forcefield

All liquids simulated in this work are described by potentials containing bond, VdW and Coulombic terms (see chapter 7). The bond terms in silicate clusters, including bond length, bond angle and dihedral interactions, are described by the zeolite parameters, published by Hill et all. in 1994 [100]. The bond terms in Si-O-C metalorganic interactions have been obtained from the LDA calculations presented before (bond lengths and bond angles), and from geometric averages of the force constants for Si-O-Si and C-O-C interactions. The other bond terms and all VdW terms are obtained from MSI cff91 ab-initio forcefield [5]. The partial charges, shown in Table 17.1, come from the LDA optimisation of each molecule, multiplying the Hirshfeld charges by a golden number, 2.6 in Coulombic cutoff, group-based, simulations.

While bond terms and the repulsive VdW potentials describe short-range interactions, particularly the molecular vibrations, the VdW dispersion terms and principally the charge interactions are responsible for the medium- and long-range intermolecular effects, which influences diffusion aspects and control the mixture and aggregation in solution. The silicon charges, in both alkoxides and silicate clusters, are much larger than the oxygen charges in water and silicate clusters, which, in turn, are much larger than all the others, including oxygen charges in alkoxides and alcohols.

Atomic arrangements with large charge separations, immersed in a medium formed by species

2.6 x Hirshfeld
Partial Charges

H_2O	O	H				
	-0.7868	0.3934				
CH_3OH	C	O	H_3	H_o		
	-0.1752	-0.5723	0.1139	0.4058		
CH_3CH_2OH	C_3	C_2	O	H_3	H_2	H_o
	-0.3523	-0.0603	-0.5569	0.1274	0.0920	0.4033
$Si(OCH_3)_4$	Si	C	O	H		
	1.2076	-0.1424	-0.5330	0.1245		
$Si(OCH_2CH_3)_4$	Si	C_3	C_2	O	H_3	H_2
	1.1992	-0.3476	-0.0299	-0.5215	0.1292	0.1058
$Si(OH)_4$	Si	O	H			
	1.1628	-0.7389	0.4482			
$Si_2O(OH)_6$	Si	O_b	O_t	H		
	1.1955	-0.7218	-0.6997	0.4215		
$Si_3O_3(OH)_6$	Si	O_b	O_t	H		
	1.2346	-0.7062	-0.6747	0.4105		

Table 17.1: Partial charges used throughout this work, in atom-based simulations with a Coulombic cutoff, of simple liquids and sol-gel solutions.

with much smaller charges, are likely to attract each other, forming aggregates, to decrease the energy (and enthalpy) of the system. Consequently, the silicate clusters in a sol-gel solution can be expected to aggregate and the same is likely to occur, for example, to water molecules in a solvent as methanol. It would be enlightening to test this electrostatic aggregation effect, studying the behaviour of a few solute molecules with extremely large charges, in a solvent with no charges at all. Because larger silicate clusters have larger Si atomic charges and the probability of interaction also increases, aggregation effects between trimer rings should be more effective than between monomers.

17.3 Mixture effects

The mixture of water and methanol or ethanol is a irreversible phenomena, which leads to a substantial increase in entropy, because the number of molecules is relatively large for both constituents. If the concentration of water in ethanol increases, the entropy contribution becomes more important, and particularly for these small molecules, a effective mixture should occur, in spite of the electrostatic effect. The opposing effects of aggregation, favoured by energy, and mixture, favoured by entropy factors, can be studied as a function of temperature, with the MD mdel applied here, as shown in the previous chapter. For higher temperatures, the electrostatic effect on aggregation should be less important, but in compensation, the diffusion coefficients should increase exponentially.

The initial configurations of the six solutions, containing water, an alcohol and a silicate cluster, specifically designed to study mixture and aggregation effects in sol-gel processes, are

presented in Figure 17.1.

To study the mixture of various species with Molecular Dynamics is important for two reasons. First, it is necessary to guarantee that the results obtained for MD simulations of relatively complex sol-gel solutions are independent of the initial configuration chosen. This only happens if the mixture of the various components occurs effectively, in a reasonable amount of time, after which no bias or signal of the initial configuration can be observed. The second reason is more physical. The first step in any sol-gel process is always the mixture of its constituents and consequently, a realistic simulation should be able to describe the mixture of completely separated components, to form a homogeneous solution.

The MD solutions for which the formation of a mixture should be more difficult, i.e. the two initially unmixed (one containing water, methanol and monomers and the other, water, ethanol and trimer rings), are illustrated in Figures 17.2 to 17.5, for t = 0, after the initial equilibration, and t = 500 ps, in the end of the simulation.

Although both solutions are clearly unmixed after the 30 ps of equilibration needed to prepare the solutions at ambient conditions, 500 ps later the mixture of alcohol and water seems to be completed and neither of the two solutions show signals of their initial unmixed condition. This evidence is particularly remarkable for the ethanolic solution, where the diffusion and mixture mechanisms should be slower, due to the larger size of the ethanol and trimer ring molecules. To make the analysis easier, the molecules are shown without using the periodic boundary conditions to generate their replicas inside the cell.

These results, which were also obtained for the other four solutions, which were initially mixed or partially mixed, should be a consequence only of the potentials used, and therefore should remain valid in more sophisticated MD or MC simulations. However, the dynamic trajectories used to reach these results are likely to be different, in particular, because the diffusion coefficients are currently too high, as shown in the previous chapter, so the times of mixture should increase for more accurate simulations.

17.4 Aggregation effects

This visual analysis is confirmed by the instantaneous Si-Si intermolecular radial distribution functions, calculated for the same solutions and times, presented in Figures 17.6 and 17.7. Instantaneous RDFs were chosen for this study, instead of averages over time, as the structure of the solution changes progressively with time, due to the mixture of the various components.

While, for t = 0, the radial distribution functions are very different for the mixed, partially mixed and unmixed solutions, for t = 500 ps, the RDFs become very similar for the three solutions. Furthermore, while for t = 0, the distribution of Si-Si peaks seems to be relatively erratic, with groups of peaks separated by gaps, for t = 500 ps, the peak distribution becomes relatively uniform, showing that a reasonable degree of homogeneity has apparently been achieved in the solutions. For t = 0, the distance of the first Si-Si peaks decreases with the degree of mixture for the solutions with rings and increases for the solutions with monomers. These opposite trends, which should be attributed to the lack of equilibration in these solutions, are not observed for t = 500 ps. For both methanol- and ethanol-based systems, all solutions seem thus to be reasonably mixed and equilibrated, at the end of the simulations. These results might be even be more clear in more concentrated solutions, as in experimental sol-gel solutions, where the statistical weight of the Si-Si interactions is higher.

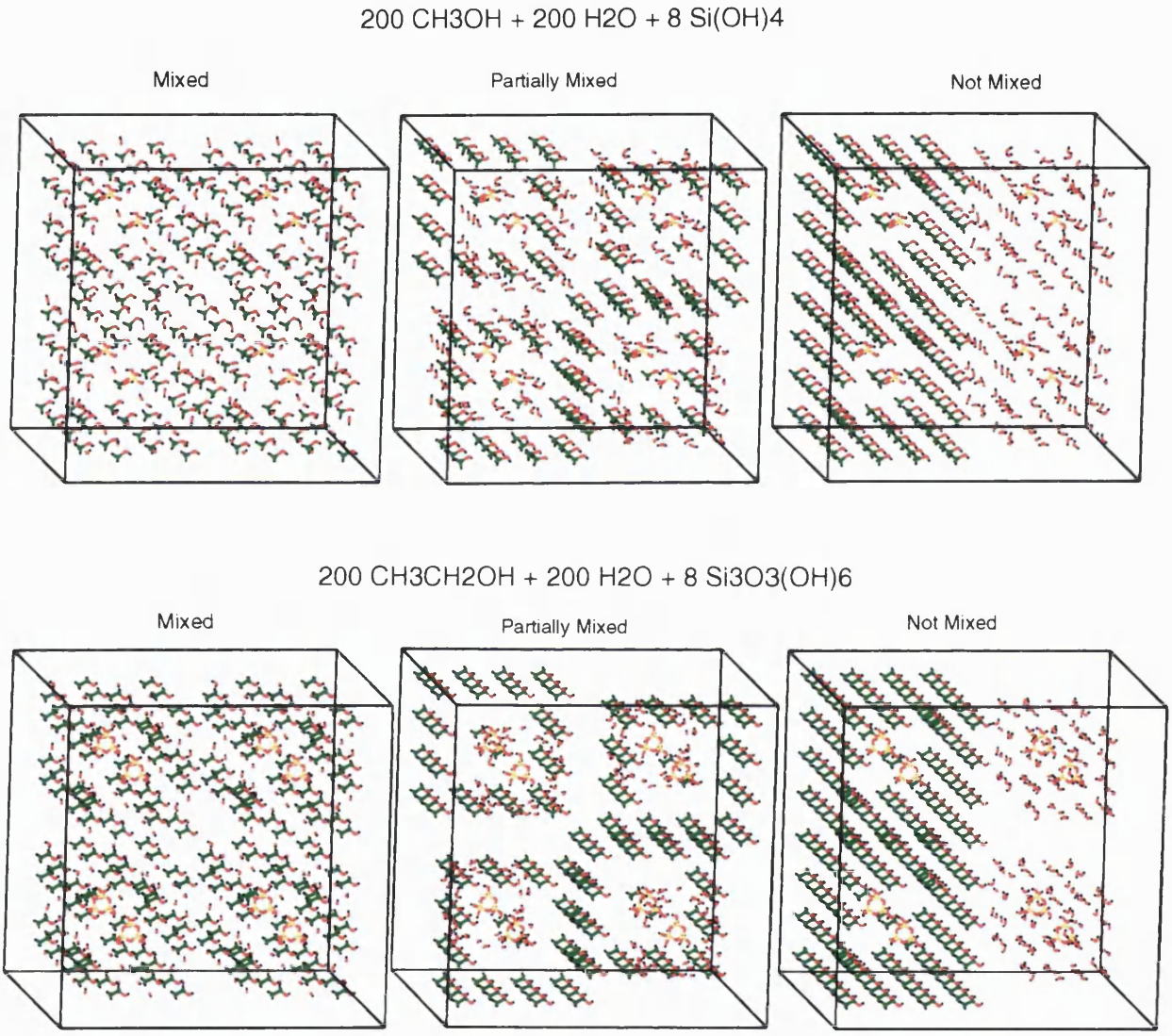


Figure 17.1: Initial configurations, mixed, partially mixed and unmixed, for methanolic solutions, containing methanol, water and monomers and ethanolic solutions, containing ethanol, water and trimer rings.

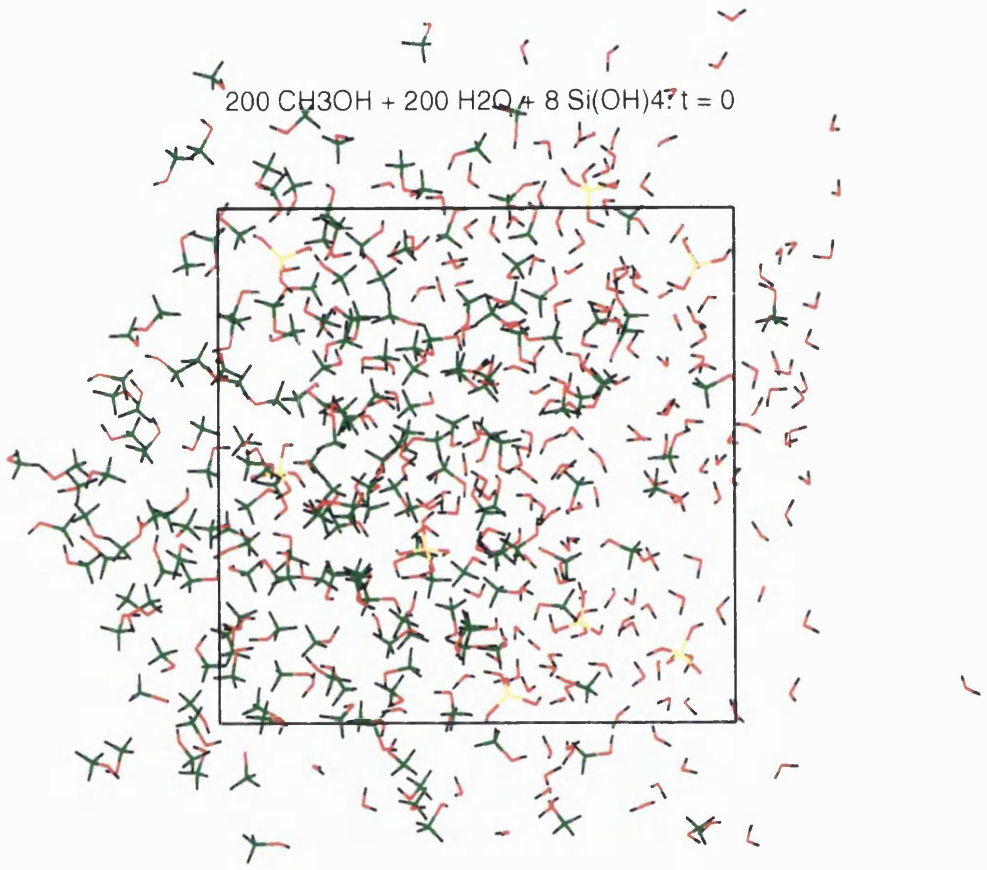


Figure 17.2: Methanolic solution, initially unmixed, after preparation, for t = 0.

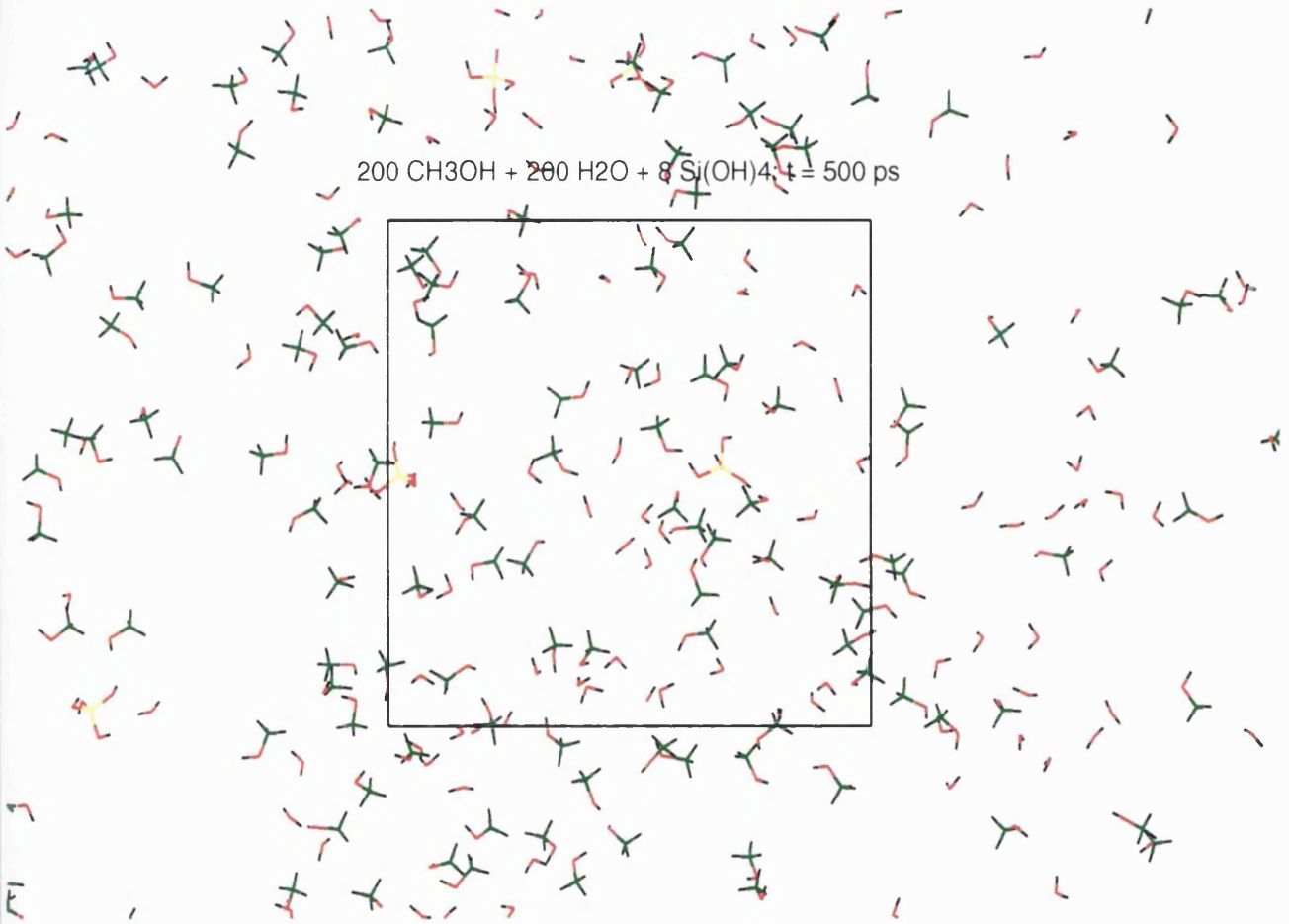


Figure 17.3: Methanolic solution, initially unmixed, after simulation, for t = 500 ps.

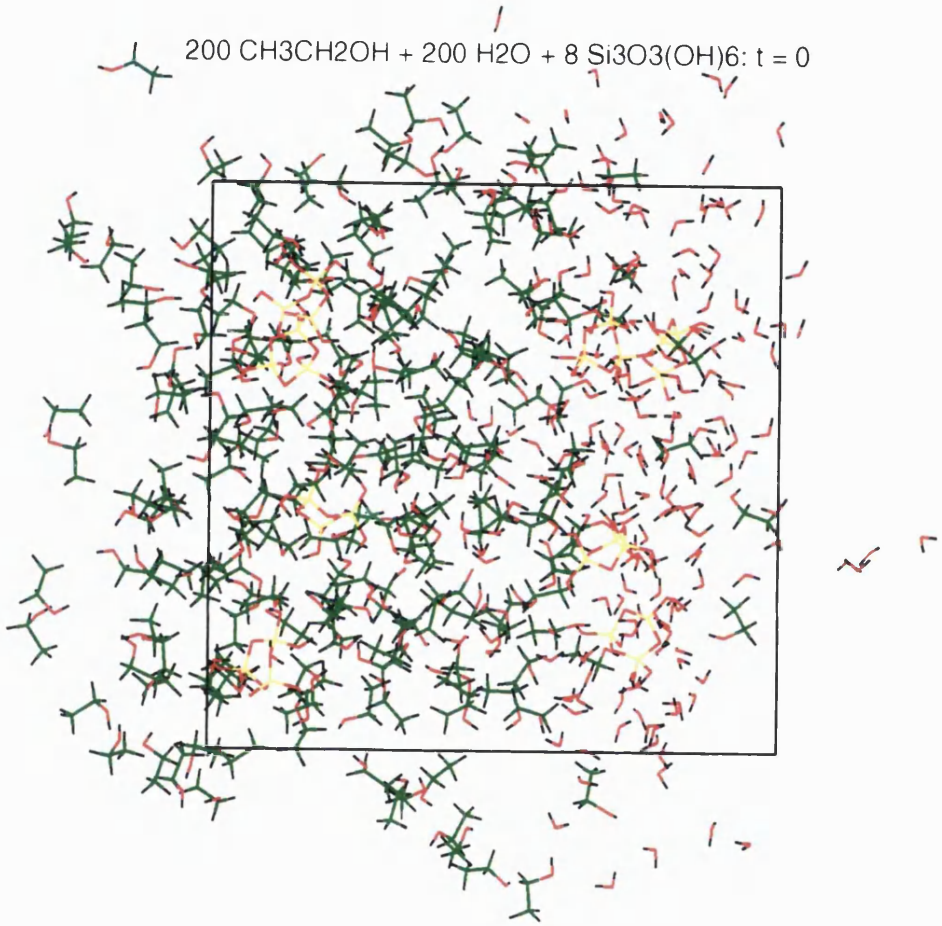


Figure 17.4: Ethanolic solution, initially unmixed, after preparation, for t = 0.

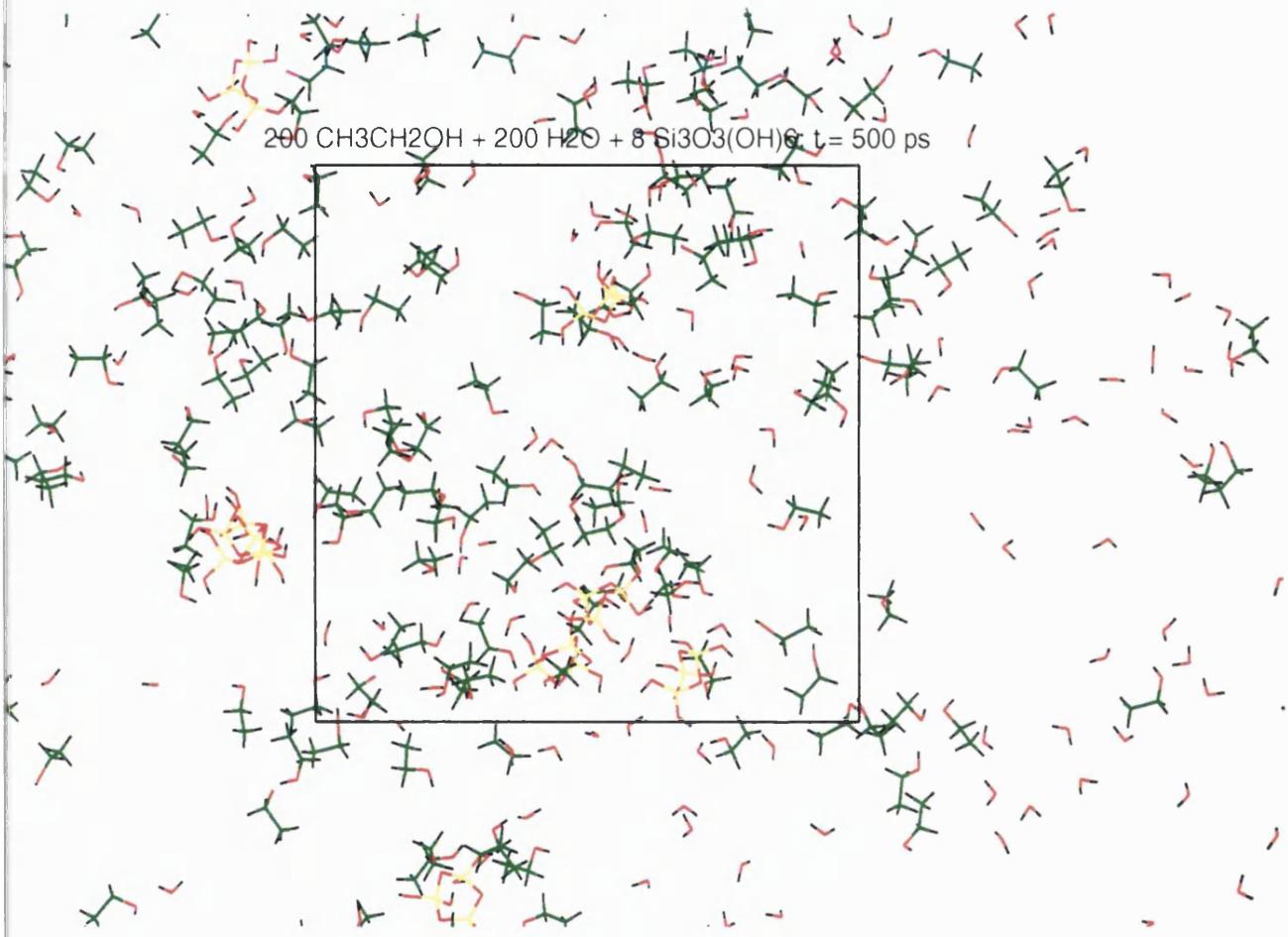


Figure 17.5: Ethanolic solution, initially unmixed, after simulation, for t = 500 ps.

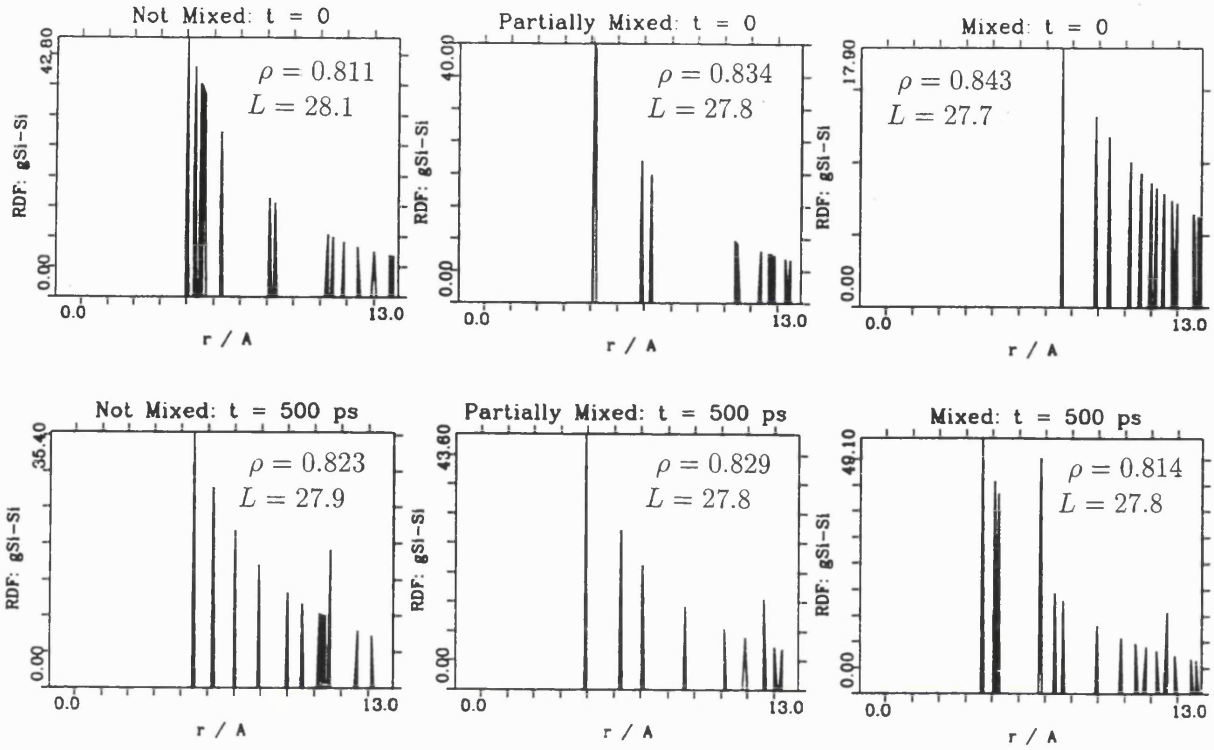


Figure 17.6: Instantaneous Si-Si pair distributions between monomers, in methanolic solutions, initially mixed, partially mixed and unmixed, after 500 ps of run time. The density (g/cm^3) and cell length (Å) are indicated for each solution.

Surprisingly, the differences between the various solutions cannot be observed in any other RDF interaction, even for t = 0. In particular, the radial distribution function between the oxygens in alcohol and water, which might be expected to provide a effective way to follow the progressive water-alcohol mixture, is almost equal in the three solutions, even for t = 0. This happens because, even in the unmixed solutions, there are large water-alcohol interfaces, that assure a significant interaction between the two molecular types.

The analysis of the Si-Si radial distribution functions shows also that, during the MD simulation, the silicate clusters tend to approach each other, with the first Si-Si peaks becoming progressively more important and shifted to smaller distances, until a minimum of 4.5 Å. As the cell length in methanolic and ethanolic solutions is about 28 Å and 31 Å, respectively, the distance between the monomers and between the rings would be about 14 Å and 15.5 Å, if the silicate clusters were completely separated, corresponding in both cases, to 14 Å between the silicon atoms. Although Si-Si first peaks between 14 Å and, say, 8 Å might result only from the thermal Brownian motions inside the solutions, the much smaller Si-Si distances observed in all solutions studied show that, in fact, the silicate clusters are aggregating. This effect is confirmed by visual inspection of the six final solutions, after removing the water and alcohol molecules, as shown in Figure 17.8.

The interaction of the silicate clusters seems to be even more important for the larger trimer rings than for the monomers, probably due to the larger scattering cross section of the rings and the larger charge of the ring silicon atoms, as discussed earlier.

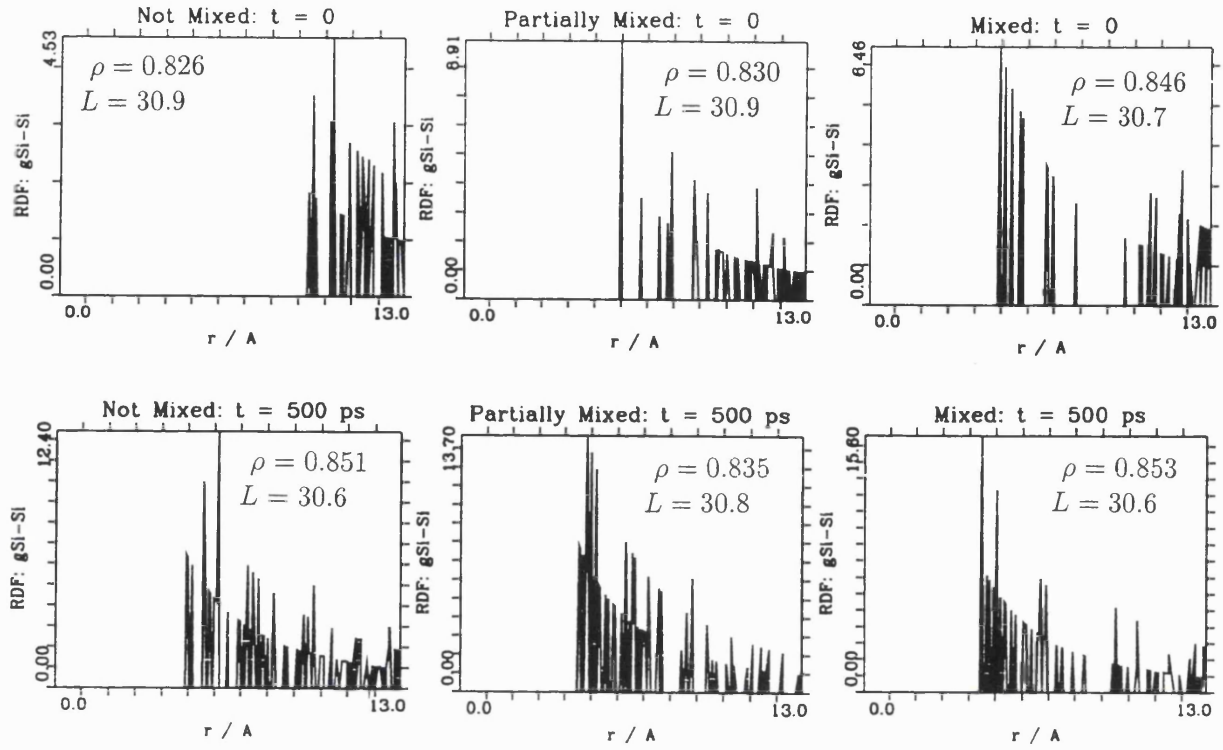


Figure 17.7: Instantaneous Si-Si pair distributions between trimer rings, in ethanolic solutions, initially mixed, partially mixed and unmixed, after 500 ps of run time. The density (g/cm^3) and cell length (Å) are indicated for each solution.

17.5 Density and energy

The mean values and fluctuations of energy, temperature, pressure and density, for all run times and mixing conditions, are shown in Tables 17.2 and 17.3, for the methanolic and ethanolic solutions, respectively. Although the potential energy seems to decrease from 0 to 500 ps, particularly for the more bulky ethanolic solutions, where equilibration should take more time, no clear trend can be observed. What is more, no visible trends can be found between the results of the mixed, partially mixed and unmixed solutions. In fact, the energy, density and pressure differences between the various solutions, are less than the relatively significant time oscillations observed for these quantities.

Even for the ethanolic solutions, where differences should be more noticeable, the partially mixed solution has the highest energy for t = 0, the lowest for t = 100 ps and the highest again for t = 200 ps. Definitely, no clear trends can be observed for different solutions or times after the short initial period of compression (10 ps) and relaxation (20 ps) to ambient conditions. This is quite surprising, because the visual inspection of the solutions or the analysis of the Si-Si RDFs show that significant differences between the various solutions still persist after 200-300 ps, and even after 500 ps, the history of the solutions has not been totally forgotten yet.

The observed oscillations are not erratic, however, and show strong correlation between energy, density and pressure, which is common in MD simulations with Columbic cutoff, group-based, Berendsen NPT algorithms. When the density increases, the molecules become closer and the energy decreases, but the repulsion terms also become more important and the pressure

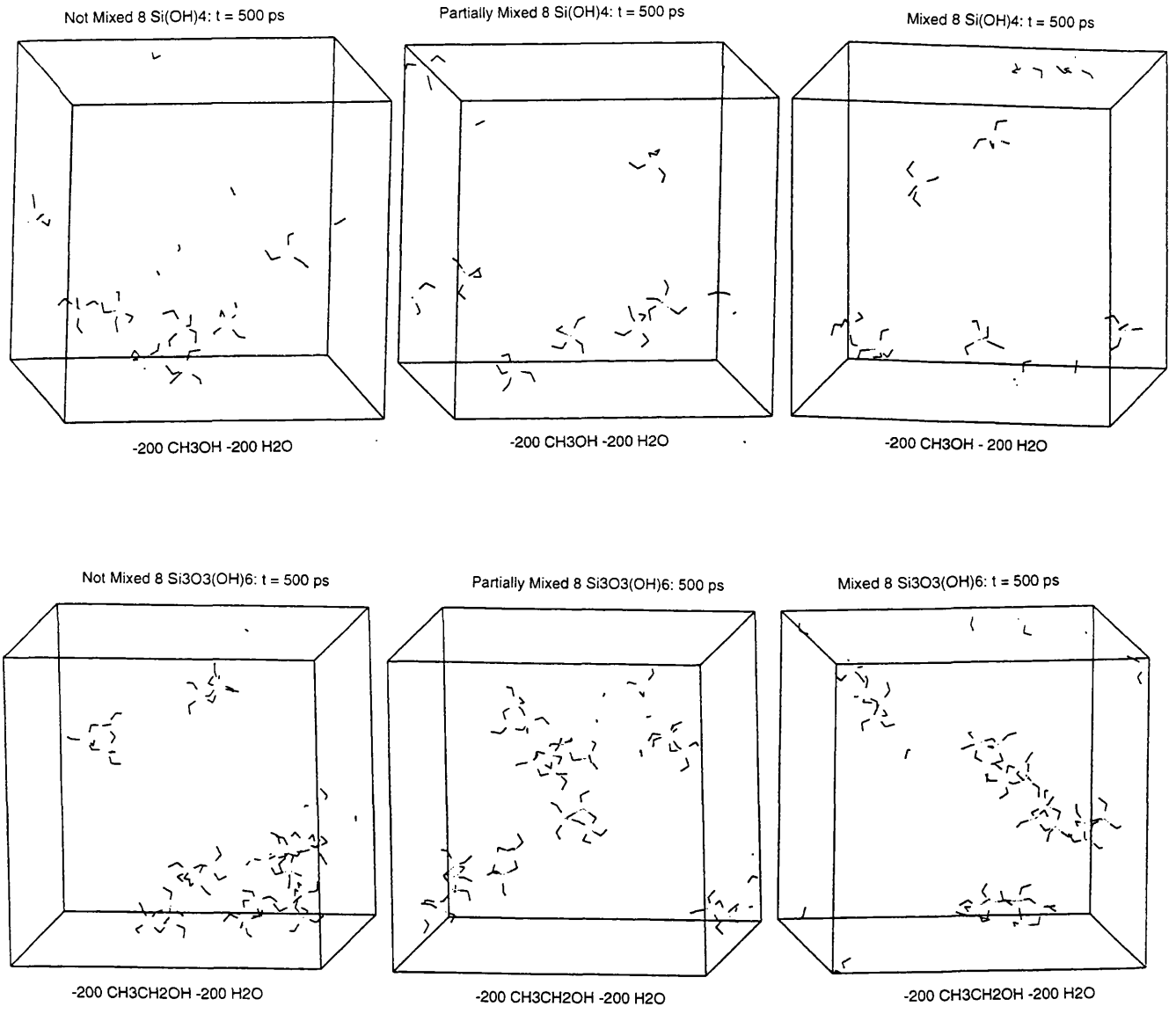


Figure 17.8: Methanolic and ethanolic solutions, initially mixed, partially mixed and unmixed, showing only the silicate monomers and trimer rings, after 500 ps of run time.

Methanolic Solutions
$200H_2O + 200CH_3OH + 8Si(OH)_4$

Time	Sol	E	ΔE	T	ΔT	P	ΔP	ρ	$\Delta\rho$
	not	350.1	35.6	293.0	1.1	-14.3	191.8	0.830	0.005
0	par	329.6	28.6	293.0	1.0	-8.2	173.0	0.850	0.004
	mix	312.6	35.9	293.0	1.0	0.3	193.5	0.848	0.004
	not	303.5	25.9	293.0	0.9	-4.9	164.0	0.845	0.003
100	par	342.6	27.1	293.0	0.9	-17.3	164.7	0.839	0.006
	mix	329.2	25.2	293.0	1.0	5.4	213.5	0.841	0.008
	not	365.9	29.1	293.0	1.0	-16.2	187.8	0.829	0.004
200	par	319.8	38.2	293.0	1.0	-21.2	196.7	0.843	0.006
	mix	309.4	29.0	293.0	0.9	-12.4	177.4	0.845	0.005
	not	326.2	35.7	293.0	1.0	-12.5	175.9	0.844	0.005
300	par	362.5	31.2	293.0	1.0	-22.1	196.5	0.832	0.004
	mix	329.7	26.7	293.0	1.0	10.9	187.6	0.846	0.010
	not	345.4	42.2	293.0	1.0	-8.2	187.8	0.832	0.008
400	par	311.5	30.9	293.0	1.0	19.5	169.8	0.846	0.006
	mix	328.8	31.1	293.0	1.1	-16.1	178.2	0.835	0.006
	not	333.8	34.0	293.0	1.0	-10.1	160.4	0.837	0.008
500	par	307.1	36.9	293.0	1.0	-9.5	177.5	0.848	0.005
	mix	342.7	30.0	293.0	1.0	-34.4	181.6	0.837	0.008

Table 17.2: Total energy (kcalmol^{-1}), temperature (^oC), pressure (bar) and density (gcm^{-3}), as a function of time (ps), for mixed (mix), partially mixed (par) and not mixed (not) methanol-based solutions.

rises progressively, eventually forcing the system to expand, until the pressure becomes negative again and the contraction restarts.

While the temperature variations are very small, due to the short temperature relaxation time used, pressure oscillations are relatively large, due to the low statistical weight of these solutions (a given moment, a majority of atoms hit the cell walls, increasingly suddenly the pressure, while the next instant they retreat, decreasing again).

17.6 Conclusions

The MD simulations presented here are the logical extension, to ideal sol-gel solutions, of the work presented before for pure liquids. The results obtained help to clarify two important problems related to diffusion in sol-gel liquid solutions. First, the progressive equilibration of a solution formed by initially unmixed species is effectively described by an MD simulation, occurring in a time short enough to be followed by this method. This behaviour is observed

Ethanolic Solutions

$200H_2O + 200CH_3CH_2OH + 8Si_3O_3(OH)_6$

Time	Sol	E	ΔE	T	ΔT	P	ΔP	ρ	$\Delta\rho$
	not	-10,017.7	38.0	293.0	0.9	-23.9	232.5	0.846	0.007
0	par	-9,994.3	28.8	293.0	0.9	-2.7	190.7	0.840	0.006
	mix	-10,013.0	30.2	293.0	0.9	6.1	191.9	0.848	0.005
	not	-10,015.5	33.3	293.0	0.9	10.5	192.3	0.852	0.003
100	par	-10,045.9	31.3	293.0	0.9	-8.5	161.2	0.856	0.004
	mix	-10,020.1	35.7	293.0	0.9	-25.1	205.0	0.842	0.006
	not	-10,028.7	36.1	293.0	0.9	3.5	169.8	0.851	0.004
200	par	-10,001.7	43.8	293.0	0.9	-0.8	190.3	0.846	0.006
	mix	-10,034.5	32.6	293.0	0.9	-6.1	185.5	0.858	0.005
	not	-9,999.6	50.0	293.0	0.9	7.0	215.3	0.850	0.004
300	par	-9,981.7	33.8	293.0	0.8	-3.1	186.7	0.832	0.004
	mix	-10,017.9	37.0	293.0	0.9	5.0	176.6	0.847	0.003
	not	-10,020.8	35.5	293.0	0.8	-14.2	170.4	0.841	0.004
400	par	-10,037.7	38.3	293.0	0.9	-2.6	169.2	0.859	0.004
	mix	-10,053.1	32.0	293.0	0.8	3.8	168.5	0.859	0.004
	not	10,042.9	34.8	293.0	0.9	-1.2	193.3	0.856	0.006
500	par	-10,045.8	34.9	293.0	0.9	-20.0	197.3	0.848	0.006
	mix	-10,077.0	36.2	293.0	0.9	-5.1	171.3	0.862	0.005

Table 17.3: Total energy ($kcalmol^{-1}$), temperature (^oC), pressure (bar) and density (gcm^{-3}), as a function of time (ps), for mixed (mix), partially mixed (par) and not mixed (not) ethanolic solutions.

even in the most difficult conditions, with initial configurations that are very far from equilibrium and with relatively large molecules, for which the diffusion is slow.

In particular, the total energy, density and even RDFs, of solutions with different degrees of initial mixing become essentially equal (within the uncertainty of the method), after relatively short MD run times. These observations guarantee that the initial configuration is not critical in obtaining accurate results in the simulation of very complex solutions, where the mixture of the various molecular species is a very important factor as the first step of a sol-gel process is always the mixture of the various components.

The second problem analysed in this study was the aggregation of the various silicate species in solution, a necessary step for both hydrolysis and condensation reactions to occur. Our results show that this aggregation indeed occurs and apparently seems to be more effective in larger clusters. It would be interesting to repeat this analysis considering simultaneously small and large silicate clusters in solution and to observe which interactions occur preferentially, small cluster-small cluster, small cluster-large cluster or, as appears to be the case, large cluster-large cluster.

The results thus obtained, for very dilute solutions, show that after large but affordable simulation times, the silicate clusters tend to interact directly with each other, without other molecules between them, with a key O-Si intermolecular distance that can be smaller than 3 Å. This is a remarkable result, if confirmed by other MD or even MC simulations, and is essential to construct a theoretical model able to perform realistic simulations of silica-based sol-gel processes.

However, as seen in the previous chapter, the diffusion coefficients are currently too high, so a slower dynamics may lead to a decrease in the mixing and aggregation rates. This will increase the times involved (in same way as a decrease in temperature), but should not change the final results, which depend essentially on the potentials employed. The conclusions concerning mixing and aggregation will remain valid.

Chapter 18

Ewald sum-based liquids

The purpose of this chapter is to refine the Molecular Dynamics model developed before, simulating water, heavy water, methanol, ethanol, TMOS and TEOS, with almost the same potentials as before, but with an Ewald sum and atom-based methods replacing the previous Coulombic cutoff and group-based approaches.

18.1 Introduction

The Molecular Dynamics simulations of liquid water published by Stillinger et al. [221], using a revised central force model, are among the first simulations carried out in liquids with an Ewald sum. The comparisons between SPC, ST2, TIPS2 and TIP4P potentials, made by Jorgensen et al. [119], for the structure and self-diffusion coefficients of water, were also done using an Ewald sum.

The optimisation of the Ewald sum in order to minimise the cutoff error is discussed by Fincham et al. [72] and Kolafa et al. [138]. A extensive set of measurements, to determine the plateau region of the Ewald energy, similar to the ones presented in our work, is presented by Rycerz et al. [205, 204], for ionic systems, such as $NaCl$ and Bi_2O_3.

Monte Carlo simulations in the NVT ensemble, using SPC, TIP4P and TIPS2 potentials have been undertaken by Strauch et al. [223], to calculate the internal energy, dielectric constant and radial distribution functions of water. The SPC model, similar to the models used in this work, gives the best dielectric constant description, according to experiment. Monte Carlo simulations of water have recently been done by K. Hona et al. [102], using a new potential, and various thermodynamic properties, including heat capacity and compressibility, are reported.

Cell size effects in liquid methanol have been studied by Csulleras et al. [49]. No significant changes were observed for the short and intermediate time translation motion but the molecular mobility and the dielectric constant were reported to increase noticeably in the long time regime.

New potentials to reproduce liquid water and ice 1h, using Molecular Dynamics, have been proposed by Kumagai et al. [140] and Brodholt et al. [43]. Extensive MD simulations of the structure and thermodynamic properties of water at high pressures and temperatures have been reported by Brodholt et al. [43], using TIP4P, SPC/E, WK and Belonoshko and Saxena potentials. Both TIP4P and SPC/E seem to reproduce well the experimental data for these thermodynamic conditions, while the WK model is accurate only for densities close to 1 gcm^{-3}. and the volumes predicted by Belonoshko and Saxena potentials, for high pressures, are within

0.3 cm^3mol^{-1} of those predicted with TIP4P.

The work presented in this chapter and in the next one was done with Dl_poly 1.1, from Daresbury Laboratories. As before, we used a cubic cell contained 408 molecules of water, heavy-water, methanol, ethanol, or 51 of TMOS and TEOS, with PBC conditions, a minimum image convention, a Verlet leapfrog integration algorithm and a Berendsen NPT ensemble. A cutoff of 11.0 Åfor the real space contributions and a timestep of 0.5 fs were chosen for these simulations.

Densities, enthalpies of vaporisation, radial distribution functions, self-diffusion coefficients and specific heat estimates were calculated for three thermodynamic states, 20°C and 1 atm, 20°C and 10,000 atm, and boiling temperature and 1 atm. The initial configurations, prepared with low density (about 0.25 gcm^{-3}), to avoid overlaps and make the equilibration easier, are compressed to 10,000 atm, relaxed to ambient conditions and heated until reaching the boiling temperature. The equilibration and sampling times were set to 24.0 ps and 1.0 ps, respectively.

18.2 Forcefield

As a result of the tests previously discussed (see chapter 16), the cff91 forcefield developed by Molecular Simulations Inc. from ab-initio calculations in the gas-phase, with the Hirshfeld partial charges obtained from the ab-initio Dmol optimisations presented before (see chapter 9), were chosen as a working basis for the following MD Ewald-based calculations. The zeolite parameters published by Hill et al. [100] are used in the silicate clusters.

In these calculations, the long range Coulombic energy and forces are calculated using an Ewald sum. The long range VdW interactions are calculated using a cutoff criterion and the remaining residual interactions are estimated by a long range contribution, affecting both energy and pressure (see [11]), which assumes that the corresponding radial distribution function converged already for 1 (which is certainly the case for water but not for TEOS).

The partial charges used in all Ewald-based MD simulations are presented in Table 18.1. These were obtained multiplying the Hirshfeld charges resulting from ab-initio Dmol optimisations of each single molecule, by a golden factor, 2.7. Hirshfeld charges were used because they present the right trends, from the chemical and physical point of view, though they are too small. To fit the experimental densities and enthalpies of vaporisation, the golden factor applied in these calculations is slightly larger than in the previous cutoff-based MD calculations, 2.6. The charges presented here are very similar to the cvff and cff91 charges discussed earlier and to charges previously reported by Jorgensen [118] and Berendsen [33].

Clearly, oxygens in silicates are much more electronegative than in alcohols, in fact almost as much as in water. In compensation, all hydroxyl hydrogens have very similar charges, which are slightly smaller than in water. Methyl carbons are significantly more electronegative than those of methylene groups, while methyl hydrogens are slightly more electropositive than those in methylene groups. The charges on silicon atoms are high, compared with the others, and increase with the degree of aggregation of the cluster.

Bond interactions are described by a quartic bond length and a quartic bond angle (the first three terms of a Taylor series) and a trigonometric dihedral angle (the first three terms of a Fourier series). Cross terms are not allowed in the present version 1.1 of Dl_poly and are not considered. Not only is the influence of these terms small and their accuracy questionable, but they make calculations more complex and slower. However, they might be important in

*2.7*Hirshfeld*
Partial Charges

H_2O	ohh: -0.8170	ho: 0.4085
CH_3OH	c3: -0.1820	h3:0.1183
	o: -0.5943	ho: 0.4214
CH_3CH_2OH	c3: -0.3660	h3: 0.1323
	c2: -0.0626	h2: 0.0956
	o: -0.5783	ho: 0.4188
$Si(OCH_3)_4$	sz4: 1.2540	osc: -0.5535
	c3: -0.1479	h3: 0.1293
$Si(OCH_2CH_3)_4$	sz4: 1.2452	osc: -0.5416
	c3: -0.3610	h3: 0.1342
	c2: -0.0311	h2: 0.1099
$Si(OH)_4$	osh: -0.7673	hos: 0.4655
	sz0: 1.2072	
$Si_2O(OH)_6$	osh : -0.7266	hos: 0.4377
	sz1: 1.2415	oss: -0.7496

Table 18.1: 2.7*Hirshfeld partial charges used throughout this work, in atom-based simulations with a Ewald sum, of simple liquids and sol-gel solutions.

vibrational studies, which are not considered in this work.

As before, a 9-6-1 instead of a 12-6-1 non-bond potential is applied in these simulations because it is usually believed that it fits better simultaneously gas-phase and crystallographic data. The full set of parameters applied throughout this work is presented by MSI [5].

Five different sets of potentials are used for oxygen atoms: o, used in hydroxyl groups in methanol and ethanol, ohh, used only in water (essentially for historical reasons), oss, used in bridging oxygens in silicates, osh, used in terminal oxygens in silicates, and osc, used to simulate the metal-oxygen-carbon metalorganic bond in alkoxides. Bond lengths and bond angles in osc were obtained from ab-initio optimisations presented in this work and the corresponding force constants were obtained directly or after geometric averages of other values (the force constant in Si-O and O-C was made equal to previous si-o and o-c interactions, whereas the force constant in Si-O-C was obtained from the geometric average of Si-O-Si and C-O-C force constants).

Three different sets of potentials are used for hydrogen atoms: ho, used in water and hydroxyl groups in alcohols, h2 or h3, used in methylene and methyl groups, and hos, used in hydroxyl groups in silicates. h2 and h3 are exactly the same and different names are used only to facilitate the analysis of the results.

One set of potentials is used to simulate all carbon atoms: c2 (in the methylene groups) and c3 (in methyl groups). One set of potentials is used to simulate all silicon atoms: sz0, sz1, sz2, sz3 and sz4 (where the number represents the number of bridging oxygens, as in the NMR notation). In both cases, different names are given only to facilitate the analysis of the results.

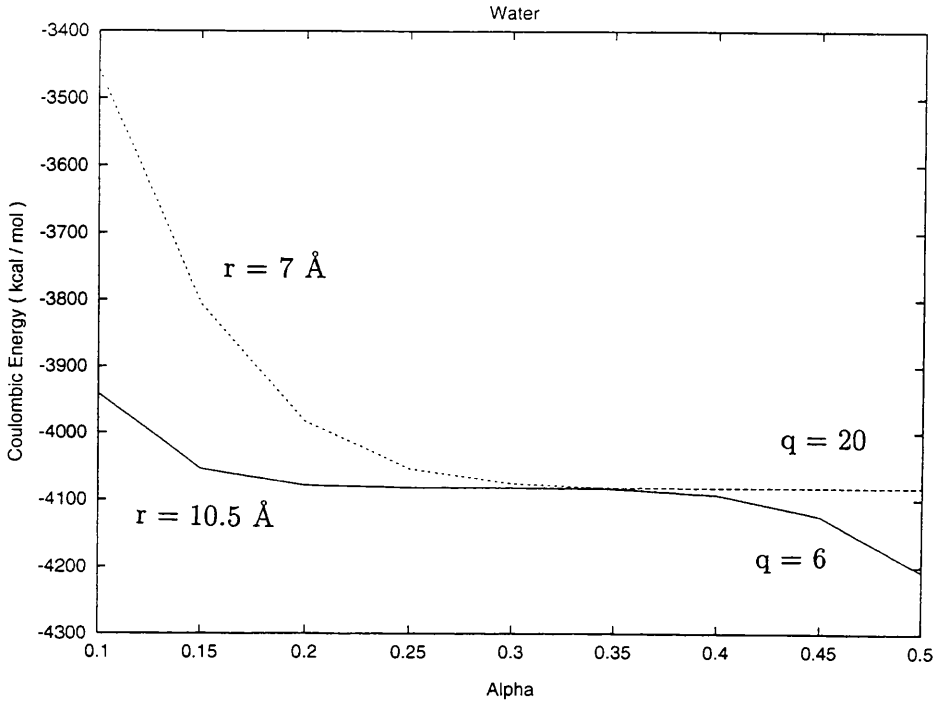


Figure 18.1: Coulombic energy of water at ambient conditions, as a function of the Ewald sum parameter α, for a real space cutoff of 7.0 Å or 10.5 Å and a reciprocal space cutoff of 6 or 20 vectors.

18.3 Ewald sum

The Coulombic energy of water, methanol, ethanol, tmos and teos, as a function of the Ewald sum parameter α, is presented in Figures 18.1-18.3, at ambient conditions. Clearly, a flat plateau is observed for all these systems, where the Coulombic energy does not change with the value of the parameter α. What is more, this plateau occurs exactly in the same region for all systems. In this region, the Ewald sum achieves convergence, as it does not change with small modifications in α, r_{max} or q_{max}.

For a large reciprocal space cutoff, $q_{max} = 20$, the flat region seems to extend indefinitely for large values of α. For a large real space cutoff, $r_{max} = 11.0$ Å, the flat region becomes much larger for small values of α. This means that for larger values of α, the convergence of the reciprocal space sum becomes more difficult and more reciprocal space vectors are needed, while for smaller values of α it is the real space sum which becomes more problematic, requiring larger real cutoffs.

Fortunately, for all systems studied, the same Coulombic energy (and presumably forces) can be obtained applying much smaller direct and reciprocal space cutoffs, if a suitable value is chosen for the α parameter. For this optimised range of the α parameter, the Ewald sum converges rapidly and much smaller calculations are required, decreasing significantly the computational times and costs, without compromising the accuracy of the results. This is particularly important because the calculation of the Ewald sum is usually one of the most time-consuming steps in MD simulations.

In practise, the Van der Waals interactions and the real space Ewald sum are usually calcu-

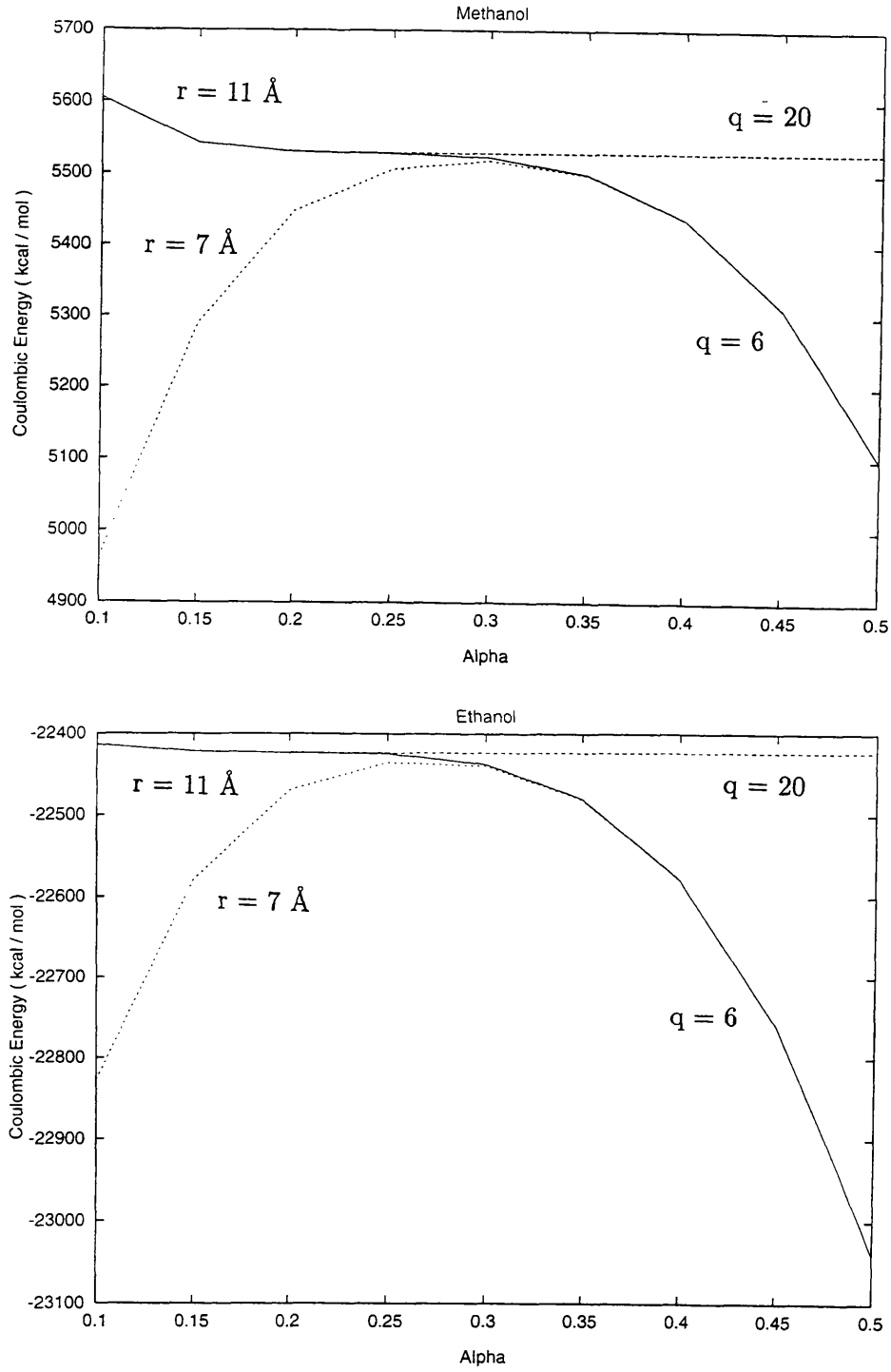


Figure 18.2: Coulombic energy of methanol and ethanol at ambient conditions, as a function of the Ewald sum parameter α, for a real space cutoff of 7.0 Å or 11.0 Å and a reciprocal space cutoff of 6 or 20 vectors.

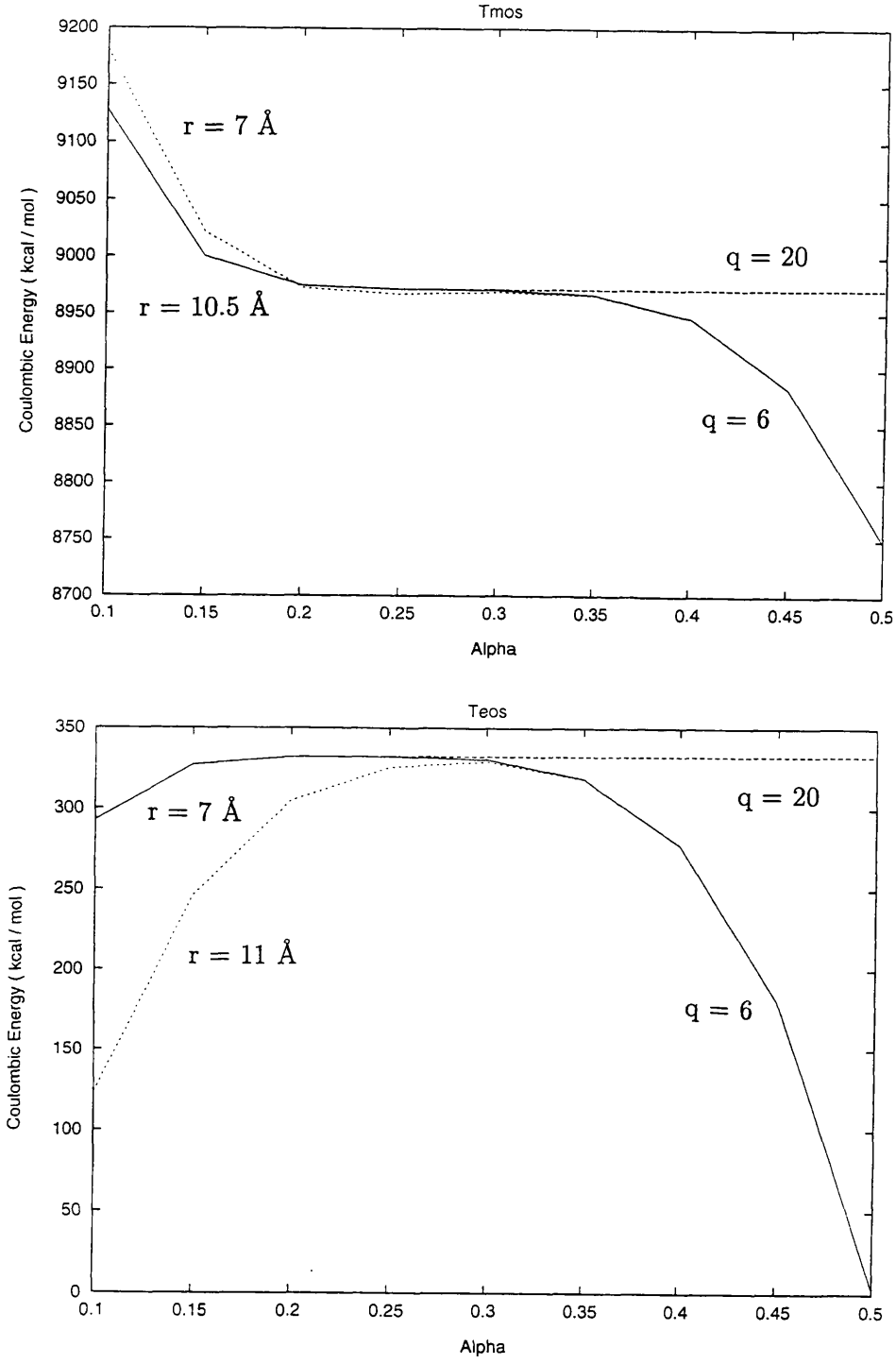


Figure 18.3: Coulombic energy of TMOS and TEOS at ambient conditions, as a function of the Ewald sum parameter α, for a real space cutoff of 7.0 Å or 11.0 Å (10.5 Å in TMOS) and a reciprocal space cutoff of 6 or 20 vectors.

lated together, to save time, therefore using the same real space cutoff. To account effectively the VdW interactions, a relatively large real space cutoff is used in this work, 11.0Å, together with 6 reciprocal space vectors for the reciprocal space cutoff. As a result of the minimum image convention applied throughout this work, water and tmos have to be simulated using a slightly smaller cutoff, 10.5Å, due to the smaller size of their cell boxes.

The fact that the optimised range of the α parameter is essentially the same for all systems studied means that the same α, r_{max} and q_{max} parameters can be used for all these systems and, in principle, for any mixture of them. This is true for systems as different as 408 molecules of polar water with 3 atoms each and 51 molecules of apolar teos with 33 atoms each, which in fact are so different that they immiscible. From the technical point of view, this is a major result for Molecular Dynamics simulations in liquids. Not only does it mean that MD simulations in solutions with very different compositions can be done without spending valuable efforts finding the right Ewald parameters, but it solves one of the potential problems in using classic Molecular Dynamics to simulate chemical reactions in solution, where the composition necessarily changes with time.

The variation of the Coulombic energy with the α parameter is presented in Figures 18.4-18.6, for the same liquid systems, for ambient conditions, very high pressure and very high temperature. Although the Coulombic energy is obviously different for different thermodynamic conditions, decreasing with the degree of condensation of the system, the flat region occurs always in the same range of α. This is another important result for Molecular Dynamics simulations of liquids in real conditions, where temperature and pressure effects are obviously very important. Not only does it show that totally different conditions of pressure and temperature can be studied using the same Ewald sum parameters, but it also allows us to study accurately irreversible processes involving heat and momentum transport, in conditions where updating constantly the Ewald sum parameters would be difficult.

18.4 Density

The calculated densities of water, methanol, ethanol, tmos, teos and heavy water, for several different conditions of pressure and temperature, are presented in Table 18.2, after MD-NPT(B)-EA/cff91 simulations with 45,000 timesteps (22.5 ps) of equilibration time and 2,000 timesteps (1 ps) of collection time. The agreement between calculated and experimental values is very good for all systems and thermodynamic conditions, which is particularly exciting, because exactly the same methodology was used in all cases.

All parameters are the same at ambient conditions, high pressure and high temperature. The partial charges were obtained multiplying the ab-initio charges always by the same factor, in a completely general procedure. Hirshfeld charges were used because they are implemented in Dmol, but it is believed that similar results would be obtained with other ab-initio charges, provided they present the right trends. A single set of potentials was used for carbon and silicon, though three and four different environments were considered for hydrogen and oxygen, respectively. Even these could probably be reduced to a single one also, without compromising the quality of the results.

In fact, when using a Molecular Mechanics forcefield, essentially composed of intramolecular, VdW intermolecular and Coulombic intermolecular interactions, the density of a liquid is likely to be essentially determined by the short and medium range Coulombic interactions and the

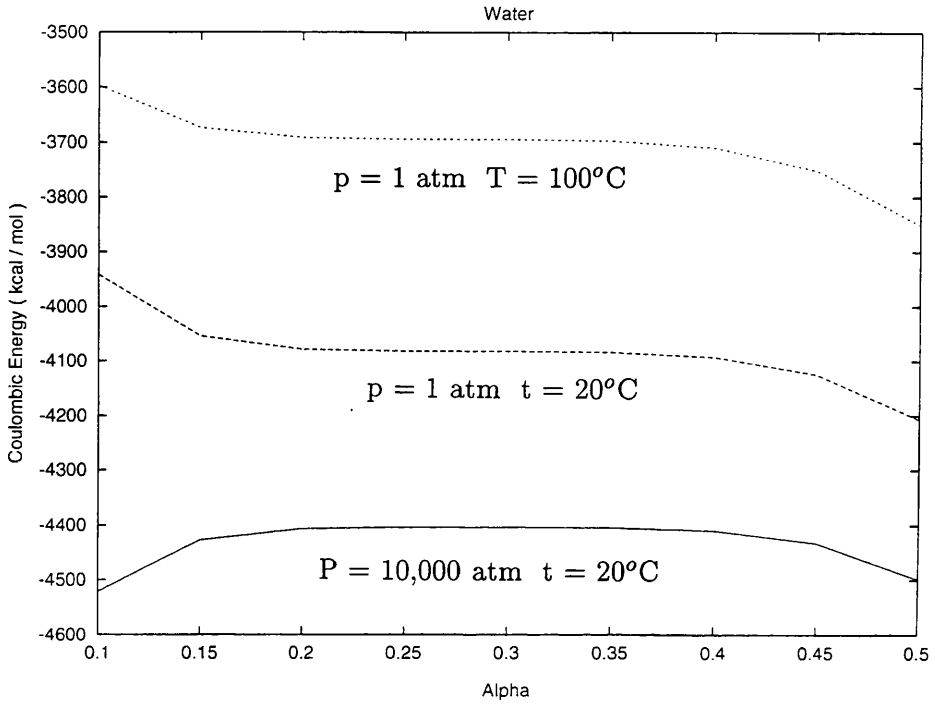


Figure 18.4: Coulombic energy of water at several different conditions of pressure and temperature, as a function of the Ewald sum parameter α, for r_{max} = 10.5 Å and q_{max} = 6.

very short range VdW repulsions, with a comparatively smaller contribution from the bond interactions (at high pressure, due to compactation effects, and at high temperature, due to vibrational effects).

The results presented here show a small but significant improvement over those discussed earlier, using group-based and cutoff criteria for all long-range interactions. Simulations of liquid TEOS, previously too unstable, are undertaken for the first time, thanks to the atom-based criteria. However, because the species considered with this criteria are charged, artificial charge effects tend to occur when Coulombic cutoffs are tried. This artifact, which is particularly important in systems with large charges, small molecules and high pressures, even leads to volume oscillations as in water at 10,000 atm and is avoided by using an Ewald sum instead, to take into account the long-range Coulombic interactions.

The densities of methanol and ethanol, both underestimated before, are much closer now to the experimental values. In general, the densities at high pressure (10,000atm) and high temperature (T_b) increased and are now noticeably closer to the experimental reported values. The largest difference between calculated and experimental values (MetOH at 10,000 atm) is now 0.045g/cm^3, corresponding to a relative error of 4.2%, which is remarkable, considering the large range of conditions and liquids simulated with the same systematic approach.

18.5 Potential and kinetic energy

The detailed analysis of the intramolecular and intermolecular energy contributions is presented for all systems and conditions studied, in Tables 18.3 to 18.7. This specific information is needed to understand the most fundamental aspects of these simulations, particularly how the

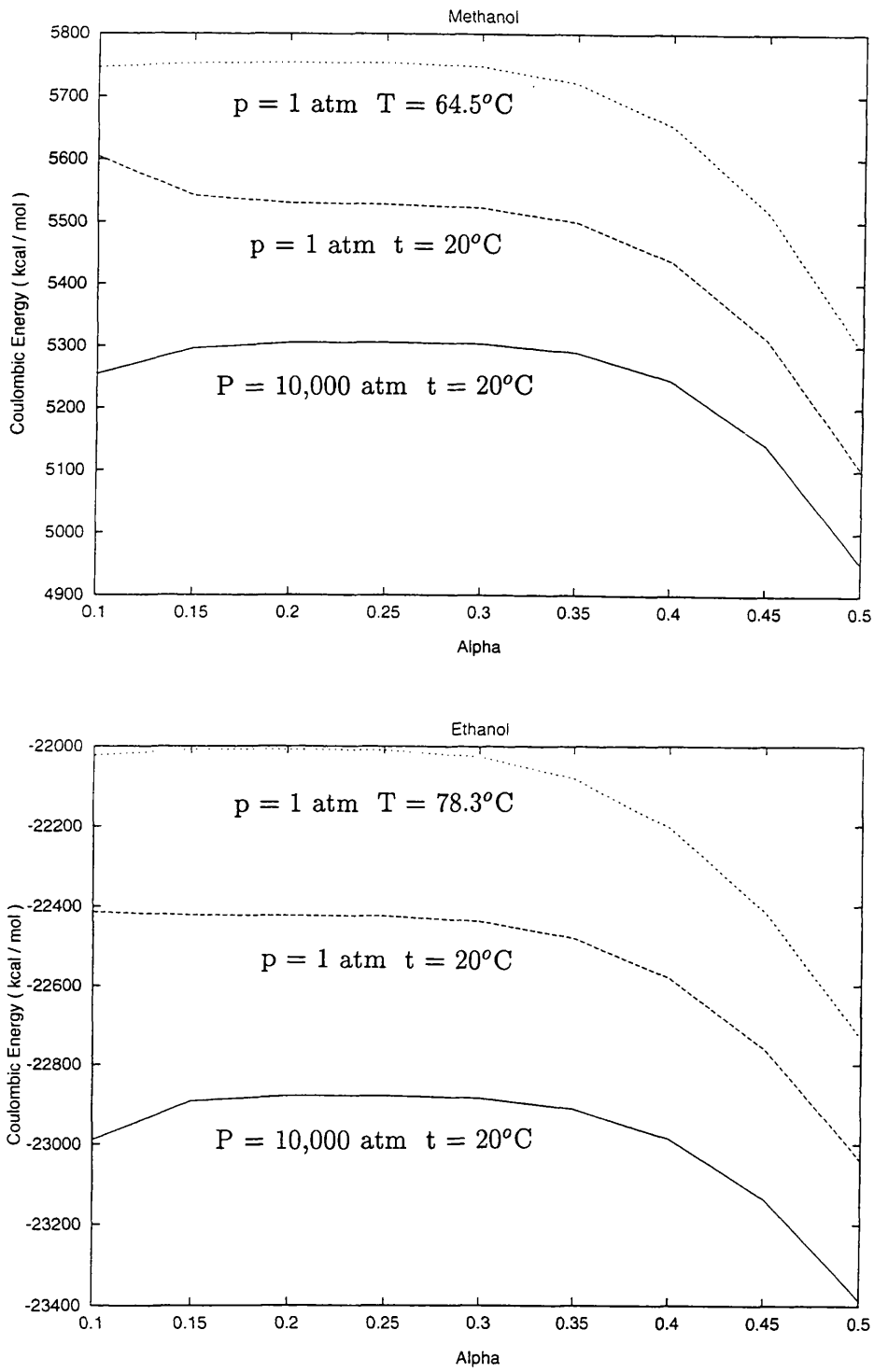


Figure 18.5: Coulombic energy of methanol and ethanol at several different conditions of pressure and temperature, as a function of the Ewald sum parameter α, for r_{max}=11.0 and q_{max} = 6.

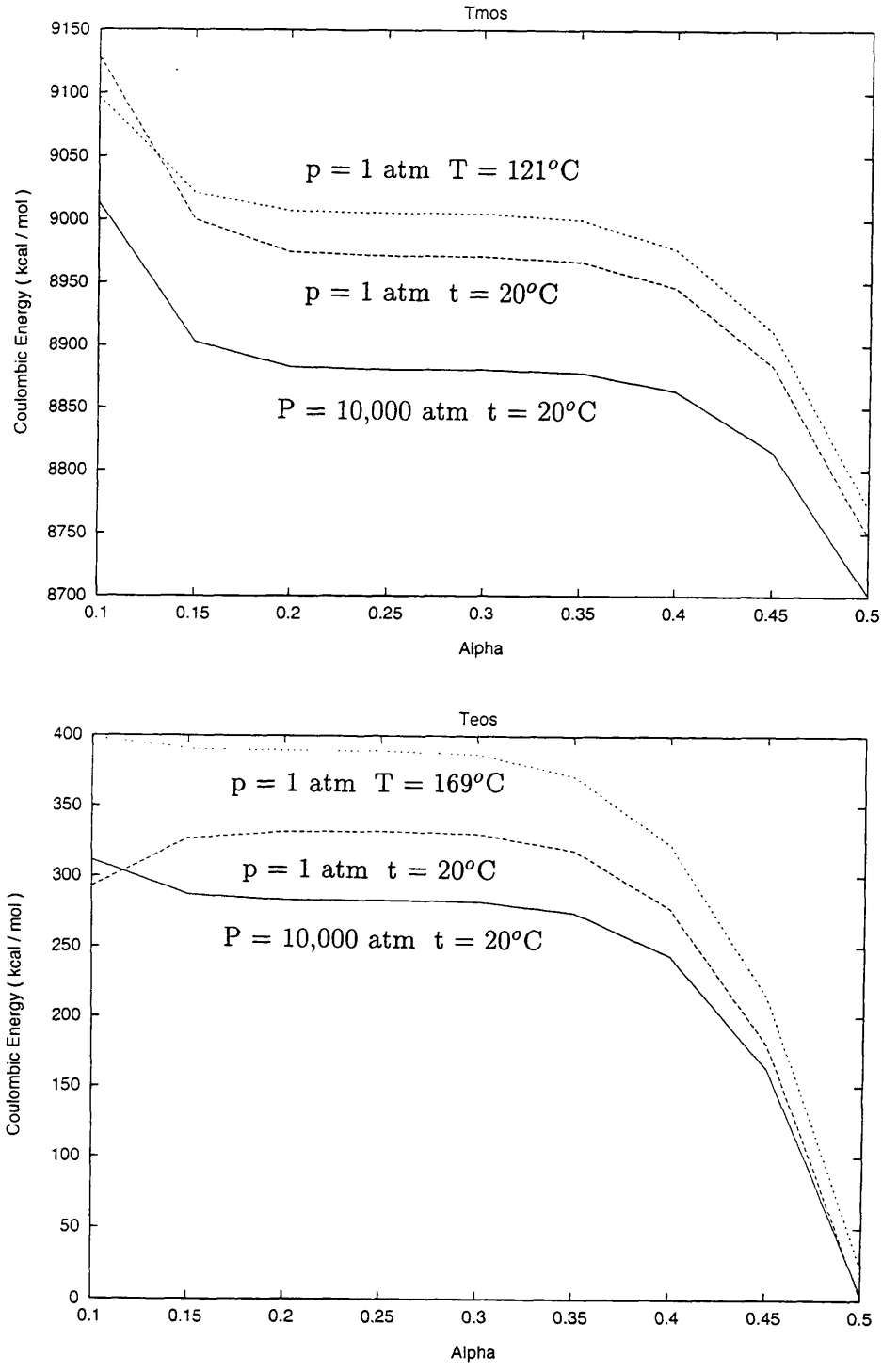


Figure 18.6: Coulombic energy of TMOS and TEOS at several different conditions of pressure and temperature, as a function of the Ewald sum parameter α, for r_{max}=11.0 Å (10.5 Å in TMOS) and $q_{max} = 6$.

	Density (gcm^{-3})			*Cal.* *Exp.*		
	H_2O	MeOH	EtOH	$Si(OMe)_4$	$Si(OEt)_4$	D_2O
20.0° C	1.215	1.007	1.006	1.277	1.191	-
10,000 atm	1.245	1.052	1.050	-	-	-
20.0° C	1.020	0.773	0.773	1.040	0.941	1.145
1.0 atm	0.998	0.791	0.789	1.02	0.93	1.105
T_b	0.947	0.733	0.705	0.933	0.788	-
1.0 atm	0.958	0.753	0.735	-	-	-
(T_b/°C)	(100.0)	(64.5)	(78.3)	(121)	(169)	-

Table 18.2: Calculated and experimental density of water, methanol, ethanol, tmos, teos and heavy water, for several conditions of pressure and temperature, obtained from atom-base simulations with a Ewald sum, after 24.0 ps of equilibration and 1.0 ps of collecting time. Experimental values from [1], [63] and [42].

various terms of the energy (and the corresponding forces) depend on the molecular systems and thermodynamic conditions involved. The comparison between the energy in the liquid-phase and gas-phase allows us to calculate the internal energy, which is directly related to the enthalpy of vaporisation. The comparison between the energy at ambient and high temperatures allows us to calculate, to a first approximation, the specific heat at constant pressure.

The energy contributions presented for the gas-phase simulations are the total intramolecular contributions only, because, by construction, the cutoff used is large enough to guarantee that all intramolecular interactions are accounted and small enough to guarantee that no intermolecular interactions are possible. This allows us to analyse separately the intramolecular and intermolecular Coulombic and Van der Waals interactions in the corresponding condensed systems. This comparison is only approximate, because the intramolecular energies can be noticeably different in condensed and gas-phase states, as can be seen by inspection of the bond, angle and dihedral energies.

In water at normal conditions, the intermolecular Coulombic contribution is 4067.4 kcal mol^{-1} (per cell), accounting for 99.2% of the intermolecular energy. In the alcohols, methanol and ethanol, this contribution decreases to 2597.6 kcal mol^{-1} and 2098 kcal mol^{-1}, accounting for 75.3% and 57.6% of the intermolecular energy. In the alkoxides, tmos and teos, this contribution is 257.8 and 98.4 $kcalmol^{-1}$, corresponding only to 31.4% and 12.0% of the total intermolecular energy. This is in agreement with experimental evidence, as water is much more polar than methanol and ethanol, due to its charges and permanent dipole, while these alcohols are much more polar than tmos and teos, where induced dipoles should be more important than permanent ones, due to their almost spherical symmetry. In fact, both tmos and teos are immiscible in water, due to their apolar characteristics, though both are miscible in methanol and alcohol. These results predict also, correctly, that ethyl-based are less polar than methyl-based molecules, due to the size of the apolar alkyl groups.

As expected, the energy fluctuations and the total energy are slightly lower in heavy water

than in water, as the heavier deuterium atoms tend to slow down the dynamics in the liquid. However, only the Coulombic energy is lower in heavy water, all other contributions are higher, meaning that on average its molecules are more distorted. As the vibrational frequencies decrease, due to the mass increase, the dominant Coulombic forces have more time to control the intermolecular interactions and the overall structure of the liquid, at the price of larger molecular shifts from the equilibrium.

The same behaviour is observed to some extent, for all systems, at high pressure. Although the total energy and the dominant Coulombic energy are systematically lower in these conditions, the bond and Van der Waals contributions usually increase. The apolar TMOS and TEOS, where the Coulombic interactions are not dominant, are the only systems where the VdW energy decreases at high pressure. Therefore, in all other systems, at 10,000 atm, the interatomic distances are already smaller than the distance of the minimum of the 9-6 VdW potential. In water this happens even at ambient conditions, because its VdW energy is lower at the boiling temperature, after the interatomic distances increased. This is due again to the small influence of the VdW interactions in water, compared with the Coulombic terms (96.6% at 10,000 atm and 98.5% at the boling temperature). The corresponding O VdW potential is used only in water, essentially for historical reasons, and it will be desirable to replace it by a more general oxygen potential.

In condensed-phase systems, the energy fluctuations essentially increase with the total number of atoms, and consequently only small differences are discernible between the systems discussed here, all with similar number of atoms. However, in gas-phase systems, where each molecule is completely isolated from the others, the energy fluctuations depend instead on the number of atoms in each molecule. They are consequently very small for water, increasing steadily for methanol, ethanol, TMOS and TEOS. In this last system, the gas-phase and condensed-phase fluctuations are almost identical.

18.6 Enthalpy of vaporisation

The enthalpy of vaporisation is the easiest energy dependent experimental property to compare, and is certainly one of the most important, because it allows us to check directly the intermolecular energy of the system, responsible for its state of aggregation. Experimental values for the enthalpy of vaporisation are usually obtained either at 1 atm and the boiling temperature or at the equilibrium vapor pressure for lower temperatures (in vacuum, therefore). Table 18.8 shows the calculated and experimental enthalpies of vaporisation of water, methanol, ethanol, TMOS and TEOS, at boiling temperature and 1.0 atm, at 20.0^o C and at the equilibrium vapour pressure and finally at 20.0^o C and 1.0 atm. Clearly, the latter is a non-physical situation, because in a one-component two-phase equilibrium, only one degree of freedom is available, as stated by the Gibbs's phase rule. This situation is used here only as a test.

For water, methanol and ethanol, the agreement between calculated and experimental values is good, both at the boiling temperature and at the vapour pressure. The maximum difference, for ethanol at the equilibrium vapour pressure, is 0.71 kcal mol^{-1}, corresponding to a relative error of 7.1 %, which is certainly very encouraging, when considering the general approach used in these simulations. Unfortunately, the agreement is much less satisfying for both alkoxides, where the difference between calculated and experimental data amounts to 4.6 kcal mol^{-1} and 4.4 kcalmol^{-1}, for tmos and teos, respectively. However, the difference between the two calculated

	Energy ($kcalmol^{-1}$)			*Mean value* *Fluctuation*		
H_2O:	Pt	pt	pT	Vt	VT	D_2O: pt
Bond	207.7	252.8	327.7	83.5	105.4	262.4
	3.3	3.6	4.6	1.2	1.9	4.0
Angle	250.6	224.3	247.0	97.7	109.1	239.2
	12.9	12.5	9.0	2.1	2.9	8.8
Dihed.	0.0	0.0	0.0	0.0	0.0	0.0
	0.0	0.0	0.0	0.0	0.0	0.0
Coul.	-4389.2	-4067.4	-3722.9	0.0	0.0	-4117.6
	34.8	34.5	26.3	0.0	0.0	25.9
VdW	149.4	-32.2	-56.6	0.0	0.0	-23.9
	17.1	16.6	12.7	0.0	0.0	15.5
Poten.	-3781.6	-3622.5	-3204.8	181.2	214.5	-3640.0
	26.5	26.8	26.5	2.5	3.4	21.5
Kinet.	1068.7	1068.7	1360.3	1068.7	1360.3	1068.7
	2.7	2.7	3.1	1.0	1.5	2.2
Total	-2712.9	-2553.9	-1844.5	1249.9	1574.8	-2571.3
	26.4	26.7	26.4	2.3	3.1	21.5

Table 18.3: Energy contributions in 408 molecules of water and heavy water, employing atom-based simulations with an Ewald sum, in condensed phase (Pt, pt and pT) and in gas phase (Vt and VT), for a pressure P=10,000 atm or p=1 atm and a temperature t=20°C or T=100°C, with a collection time of 2000 timesteps (1 ps).

	Energy ($kcalmol^{-1}$)			*Mean value* *Fluctuation*	
MeOH :	Pt	pt	pT	Vt	VT
Bond	574.8	607.3	721.8	424.7	491.6
	9.1	10.3	11.0	6.4	9.3
Angle	809.5	805.2	914.5	665.5	739.7
	13.2	13.4	11.9	10.8	14.8
Dihed.	-678.4	-681.9	-670.4	-551.7	-554.8
	7.5	7.1	8.0	7.8	9.1
Coul.	5253.3	5525.6	5747.6	8123.2	8122.6
	29.4	29.7	29.7	82.6	12.0
VdW	-816.0	-852.5	-824.7	0.4	0.4
	20.2	18.0	16.9	0.1	0.1
Poten.	5143.3	5403.7	5888.8	8662.0	8799.5
	28.1	37.3	31.7	13.3	15.5
Kinet.	2138.2	2138.2	2462.9	2138.2	2462.8
	4.5	4.6	5.2	3.6	4.4
Total	7281.5	7541.9	8351.6	10800.0	1126.2
	27.7	37.0	31.3	12.7	14.9

Table 18.4: Energy contributions in 408 molecules of methanol, employing atom-based simulations with an Ewald sum, in condensed phase (Pt, pt and pT) and in gas phase (Vt and VT), for a pressure P=10,000 atm or p=1 atm and a temperature t=20°C or T=64.5°C, with a collection time of 2000 timesteps (1 ps).

		Energy $(kcalmol^{-1})$		*Mean value* *Fluctuation*	
EtOH :	Pt	pt	pT	Vt	VT
Bond	984.9	978.2	1166.7	1161.2	1354.2
	17.5	18.1	22.6	20.6	25.7
Angle	1531.1	1523.9	1762.2	1845.0	2076.4
	26.4	21.5	28.1	28.0	37.0
Dihed.	-2090.9	-2100.2	-2080.0	-2097.2	-2054.4
	18.5	15.1	18.9	21.7	13.6
Coul.	-22862.0	-22439.0	-21996.0	-20341.0	-20298.0
	41.2	25.8	36.6	33.9	41.6
VdW	-587.5	-591.6	-457.8	953.3	966.9
	28.8	20.1	35.4	21.4	23.1
Poten.	-23024.0	-22628.0	-21604.0	-18479.0	-17954.0
	39.2	38.5	41.3	38.7	42.9
Kinet.	3207.8	3207.8	3845.7	3207.8	3845.7
	6.7	6.4	8.9	8.7	9.1
Total	-19816.0	-19421.0	-17759.0	-15271.0	-14109.0
	38.6	38.0	40.4	37.7	41.9

Table 18.5: Energy contributions in 408 molecules of ethanol, employing atom-based simulations with an Ewald sum, in condensed phase (Pt, pt and pT) and in gas phase (Vt and VT), for a pressure P=10,000 atm or p=1 atm and a temperature t=20°C or T=78.3°C, with a collection time of 2000 timesteps (1 ps).

	Energy ($kcalmol^{-1}$)			*Mean value* *Fluctuation*	
$Si(OMe)_4$:	Pt	pt	pT	Vt	VT
Bond	331.2	346.1	448.7	342.5	463.7
	8.7	10.0	13.0	10.6	16.1
Angle	688.9	705.4	824.9	737.0	879.5
	16.6	14.6	17.1	27.1	25.4
Dihed.	-524.5	-527.3	-508.9	-510.5	-493.4
	7.1	6.8	5.8	6.9	5.4
Coul.	8885.5	8948.3	9009.3	9206.1	9207.3
	14.9	13.7	15.1	21.3	18.4
VdW	-647.9	-632.2	-546.2	-69.9	-62.7
	9.9	6.9	12.5	8.2	8.8
Poten.	8733.2	8840.4	9227.9	9705.1	9994.4
	20.3	17.9	26.7	17.6	22.2
Kinet.	935.0	935.0	1257.1	935.0	1257.1
	3.4	2.9	4.2	3.5	4.7
Total	9668.2	9775.4	10485.0	10640.0	11252.0
	20.0	17.6	26.5	17.2	21.7

Table 18.6: Energy contributions in 51 molecules of TMOS, employing atom-based simulations with an Ewald sum, in condensed phase (Pt, pt and pT) and in gas phase (Vt and VT), for a pressure P=10,000 atm or p=1 atm and a temperature t=20°C or T=121°C, with a collection time of 2000 timesteps (1 ps).

	Energy ($kcalmol^{-1}$)			*Mean value* *Fluctuation*	
$Si(OEt)_4$:	Pt	pt	pT	Vt	VT
Bond	474.7	483.7	714.1	496.0	748.3
	12.1	11.6	17.8	13.3	20.5
Angle	924.3	918.5	1252.9	963.5	1330.3
	19.7	18.7	25.3	24.7	29.9
Dihed.	-1264.2	-1261.1	-1186.5	-1226.2	-1171.9
	10.0	11.3	10.5	10.4	11.6
Coul.	268.3	336.7	382.8	435.1	440.9
	9.9	9.3	11.9	12.4	13.0
VdW	-742.1	-683.8	-498.8	38.6	55.2
	15.0	10.4	15.1	17.6	12.8
Poten.	-339.1	-205.9	664.5	707.1	1402.8
	25.3	23.7	37.3	23.7	31.9
Kinet.	1469.8	1469.7	2216.8	1469.7	2216.9
	4.7	4.6	7.2	4.7	8.2
Total	1130.7	1263.8	2881.3	2176.8	3619.7
	24.9	23.3	36.6	23.2	30.8

Table 18.7: Energy contributions in 51 molecules of TEOS, employing atom-based simulations with an Ewald sum, in condensed phase (Pt, pt and pT) and in gas phase (Vt and VT), for a pressure P=10,000 atm or p=1 atm and a temperature t=20°C or T=169°C, with a collection time of 2000 timesteps (1 ps).

	Enthalpy of Vaporisation ($kcalmol^{-1}$)			*Cal.* *Exp.*	
	H_2O	MeOH	EtOH	$Si(OMe)_4$	$Si(OEt)_4$
T_b	9.12	7.80	9.64	15.82	15.37
1.0 atm	9.72	8.42	9.41	11.5	11.0
(T_b/°C)	(100.0)	(64.5)	(78.3)	(121)	(169)
20.0° C	9.90	8.51	10.73	-	-
P_v	10.54	8.96	10.02	-	-
(P_v/atm)	(0.023)	(0.141)	(0.065)	-	-
20.0° C	9.91	8.57	10.75	17.54	18.48
1.0 atm	-	-	-	-	-

Table 18.8: Calculated and experimental enthalpy of vaporisation of water, methanol, ethanol, TMOS and TEOS, for several conditions of pressure and temperature, obtained from atom-based simulations with an Ewald sum. Experimental values from [1], [191], [42], [3] and [4].

values, 0.45 kcal mol^{-1}, matches almost exactly the difference between the two experimental values, 0.50 kcal mol^{-1}.

The enthalpies at 20.0° were not calculated, because the corresponding vapour pressures are not known, but they might be very similar to the ones calculated for 20.0° C and 1.0 atm conditions. In fact, for water, methanol and ethanol, changing the pressure from 1.0 atm to the vapour pressure did not lead to appreciable differences in the enthalpy of vaporisation (which is surprising but reflects the relative insensitivity of MD simulations to low pressures).

The reasons for such large calculated enthalpies of vaporisation, for TMOS and TEOS, can be found by analysing separately the various components of the intermolecular energy. While in methanol and ethanol, the Van der Waals contributions for the internal energy are equal to 2.1 $kcalmol^{-1}$ and 3.8 $kcalmol^{-1}$ (after dividing by the number of molecules in the cell), in TMOS and TEOS the same contributions become 11.0 $kcalmol^{-1}$ and 14.16 $kcalmol^{-1}$, respectively.

18.7 Specific heat

The specific heats at constant pressure, presented in Table 18.9, were obtained applying directly the definition, for the temperature variation from 20°C to the boiling temperature, the two temperature states studied here:

$$C_P = (\frac{\delta H}{\delta T})_P \approx \frac{E_{T_b} + PV_{T_b} - E_{20} - PV_{20}}{T_b - 20}$$

These values should therefore be considered as estimates only of the average specific heat in this large range of temperatures.

The specific heat for water is only slightly higher than the experimental result but the values obtained for the other liquids are clearly too large. For progressively larger molecular liquids,

Specific Heat
$(calmol^{-1}K^{-1})$

	H_2O	MeOH	EtOH	$Si(OMe)_4$	$Si(OEt)_4$
Cond. (pt $\rightarrow$ pT)	21.7	44.6	69.9	138	213
Cond/3nR	1.21	1.25	1.30	1.10	1.08
Gas (Vt $\rightarrow$ VT)	10.0	25.4	48.9	119	190
Kin.	8.9	17.9	26.8	62.5	98.3
Exp.	18.02	19.77	28.61	-	-
($T_{avg}/^oC$)	(60)	(40)	(41)	-	-

Table 18.9: Condensed and gas-phase specific heat (and kinetic contribution), compared with experimental values at average temperatures, for water, methanol, ethanol, TMOS and TEOS, obtained from atom-based simulations with an Ewald sum. Experimental values from [191] and [42].

with increasingly important vibrational framework, the quantum effects are likely to be very significant and the characteristic temperatures very high.

When the calculated values are compared with the classical limit, 3nR (n = atoms per molecule), the agreement becomes much better. Certainly, the calculated values are still too high, from 8 % to 30 %, but these differences are already reasonable, considering the poor accuracy of these estimates. What is relevant is the common trend observed for all liquids, from water to TEOS, to have a classical limit for C_P about 20% lower than the estimated specific heat. It should be possible, thus, to correct these differences to the classic limit. However, to describe the experimental C_Ps, a more sophisticated treatment needs to be developed.

The calculated values of C_Vs in the gas-phase, between the same temperatures, presented in the same table, are much smaller, showing the importance of the intermolecular potential energy in the specific heat. It can be seen also that the difference in kinetic energy alone is almost as large as the specific heat, for methanol, ethanol, and probably the alkoxides as well.

18.8 Radial distribution function

The intermolecular radial distribution functions are a invaluable tool to study the liquid structure, and therefore they have been calculated here, for all liquids and thermodynamic conditions studied. In water and heavy water, the three O-O, O-H, H-H interactions are presented (Figure 18.7), while in methanol and ethanol, the six O-O, O-H_o, H_o-H_o, C-C, C-O, C-H_o and ten O-O, O-H_o, H_o-H_o, C_2-C_2, C_3-C_3, C_2-C_3, O-C_2, O-C_3, C_2-H_o, C_3-H_o interactions are shown (Figures 18.9, 18.10 and 18.11), as in Jorgensen's work. In TMOS and TEOS, the six Si-Si, Si-O, O-O, C-C, C-O, O-H and six Si-Si, Si-O, O-O, C_3-C_3, C_3-O, O-H_3 interactions are presented here (Figures 18.12 and 18.13).

In general, the present results, obtained with an Ewald sum, atom-based, method, are very similar to the results calculated before, with a Coulombic cutoff, group-based, algorithm. The O-O first peak in water is well positioned, between 2.9 Åand 3.0 Å, and is lower than before,

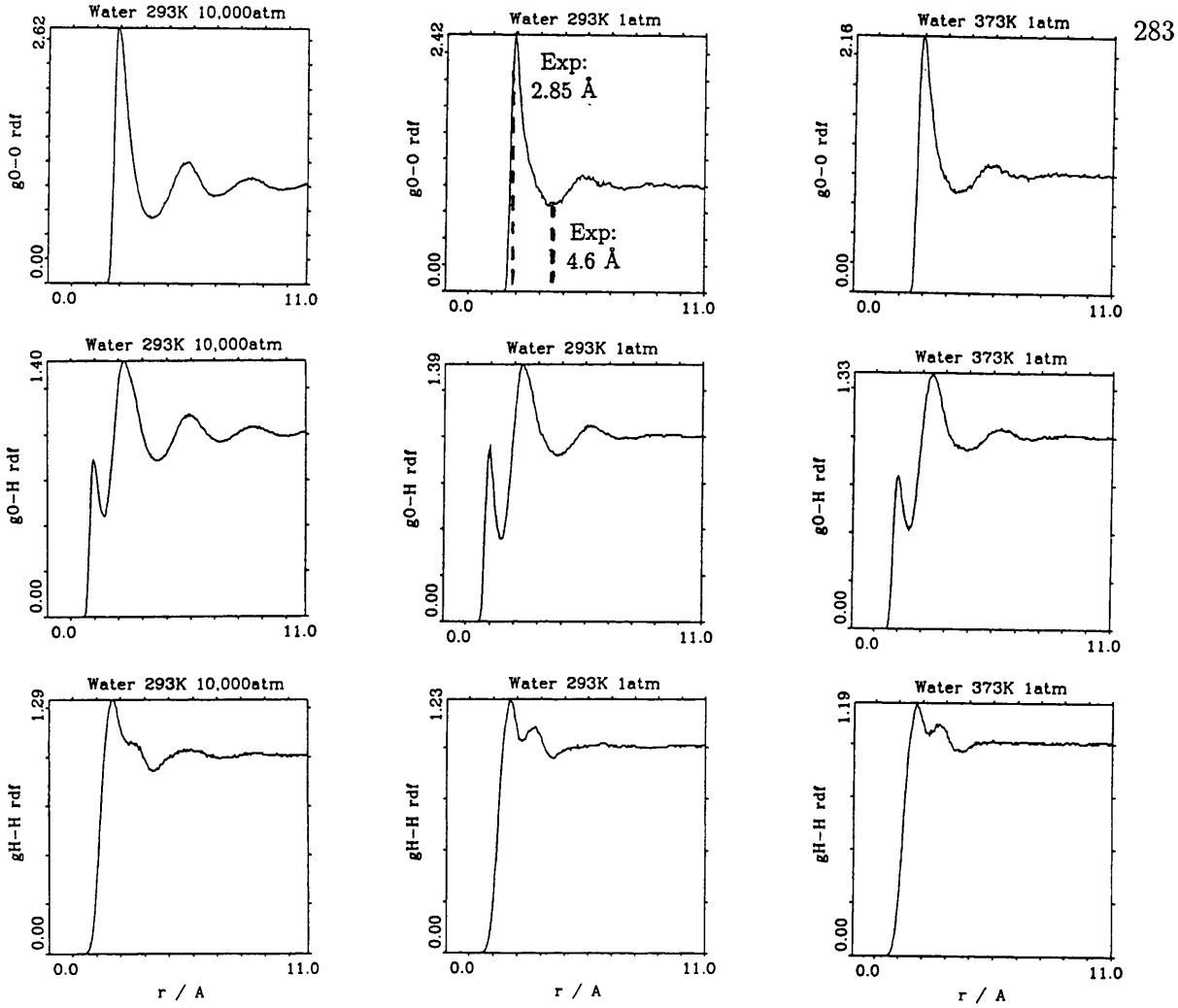


Figure 18.7: Intermolecular pair distribution functions in water, for a pressure of 10,000 atm or 1 atm and a temperature of 20°C or 100°C, from atom-based simulations with an Ewald sum, after 24.0 ps of equilibration time and 1.0 ps of collecting time. X-ray data from [118].

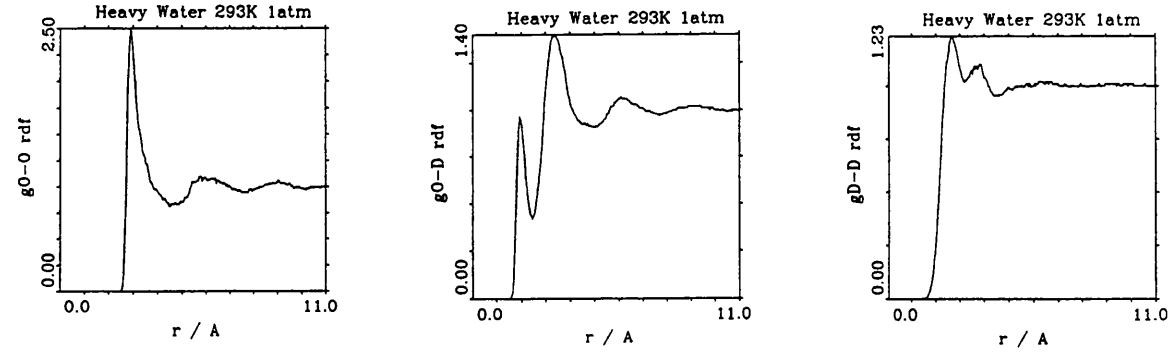


Figure 18.8: Intermolecular pair distribution functions in heavy water, for a pressure of 1 atm and a temperature of 20°C, from atom-based simulations with an Ewald sum, after 24.0 ps of equilibration time and 1.0 ps of collecting time.

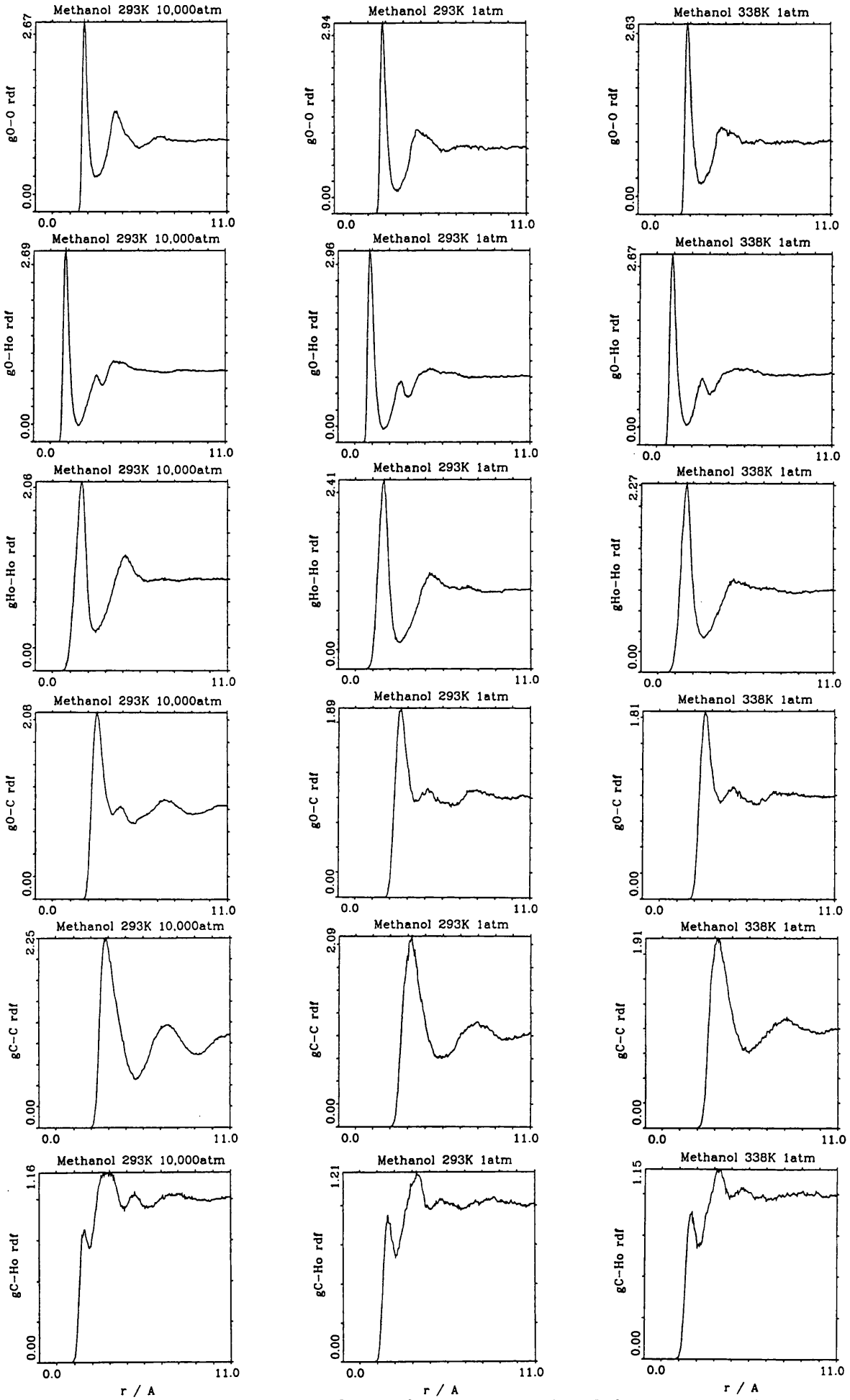


Figure 18.9: Intermolecular pair distribution functions in methanol, for a pressure of 10,000 atm or 1 atm and a temperature of 20°C or 64.5°C, from atom-based simulations with an Ewald sum, after 24.0 ps of equilibration time and 1.0 ps of collecting time.

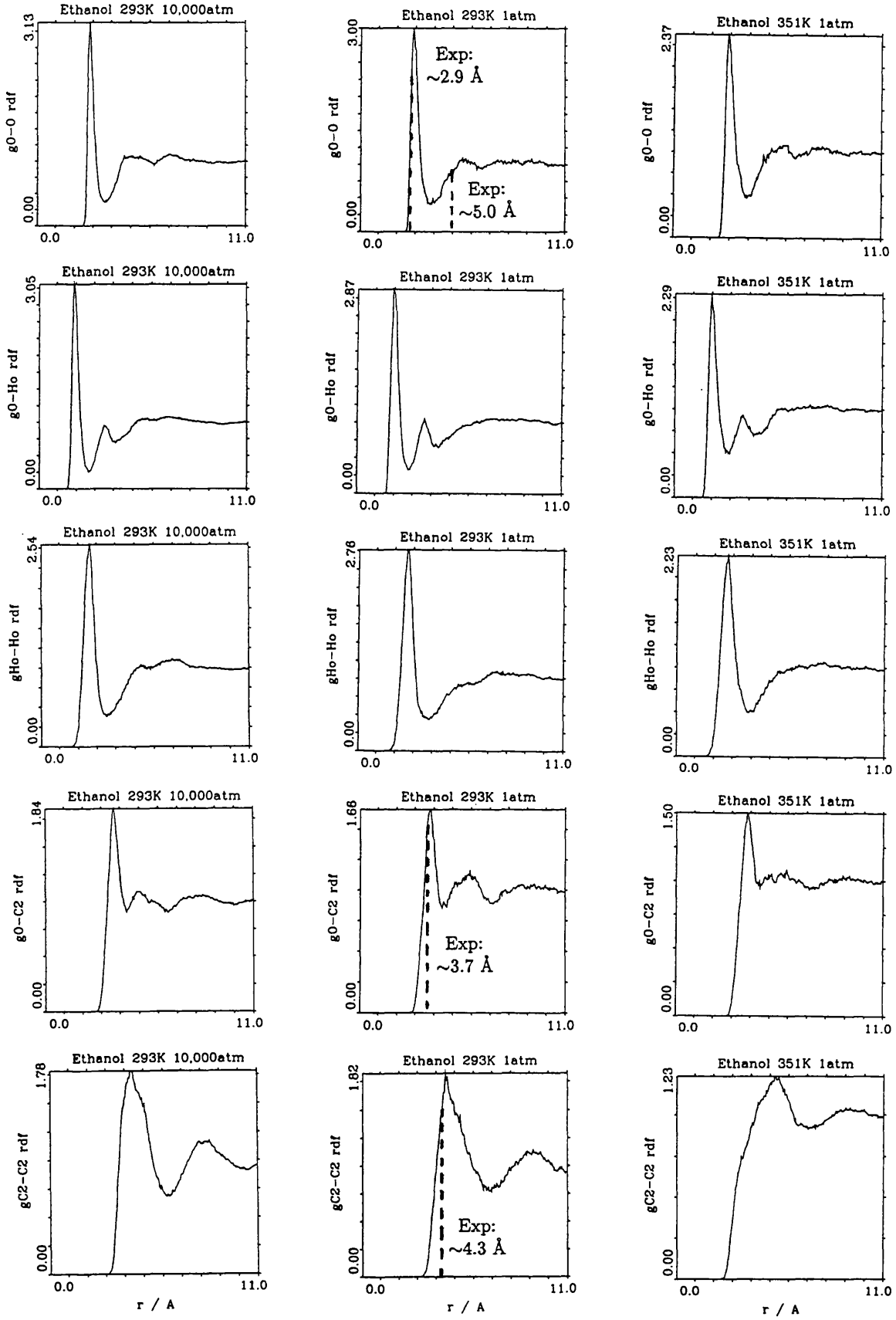


Figure 18.10: Intermolecular pair distribution functions in ethanol, for a pressure of 10,000 atm or 1 atm and a temperature of 20°C or T=78.3°C, from atom-based simulations with an Ewald sum, after 24.0 ps of equilibration time and 1.0 ps of collecting time. X-ray data from [115].

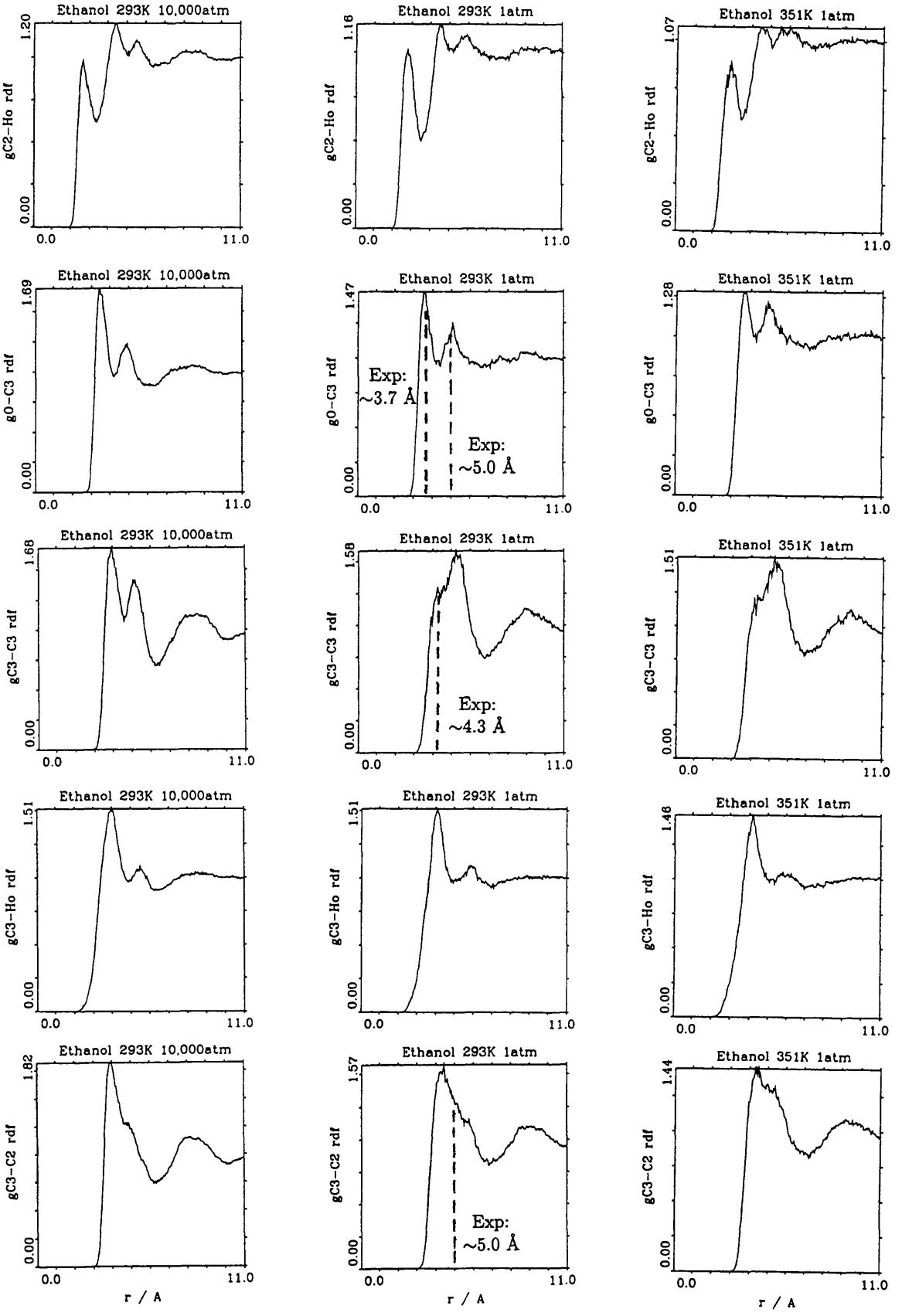


Figure 18.11: Intermolecular pair distribution functions in ethanol, for a pressure of 10,000 atm or 1 atm and a temperature of 20°C or 78.3°C, from atom-based simulations with an Ewald sum, after 24.0 ps of equilibration time and 1.0 ps of collecting time. X-ray data from [115] (*continuation*).

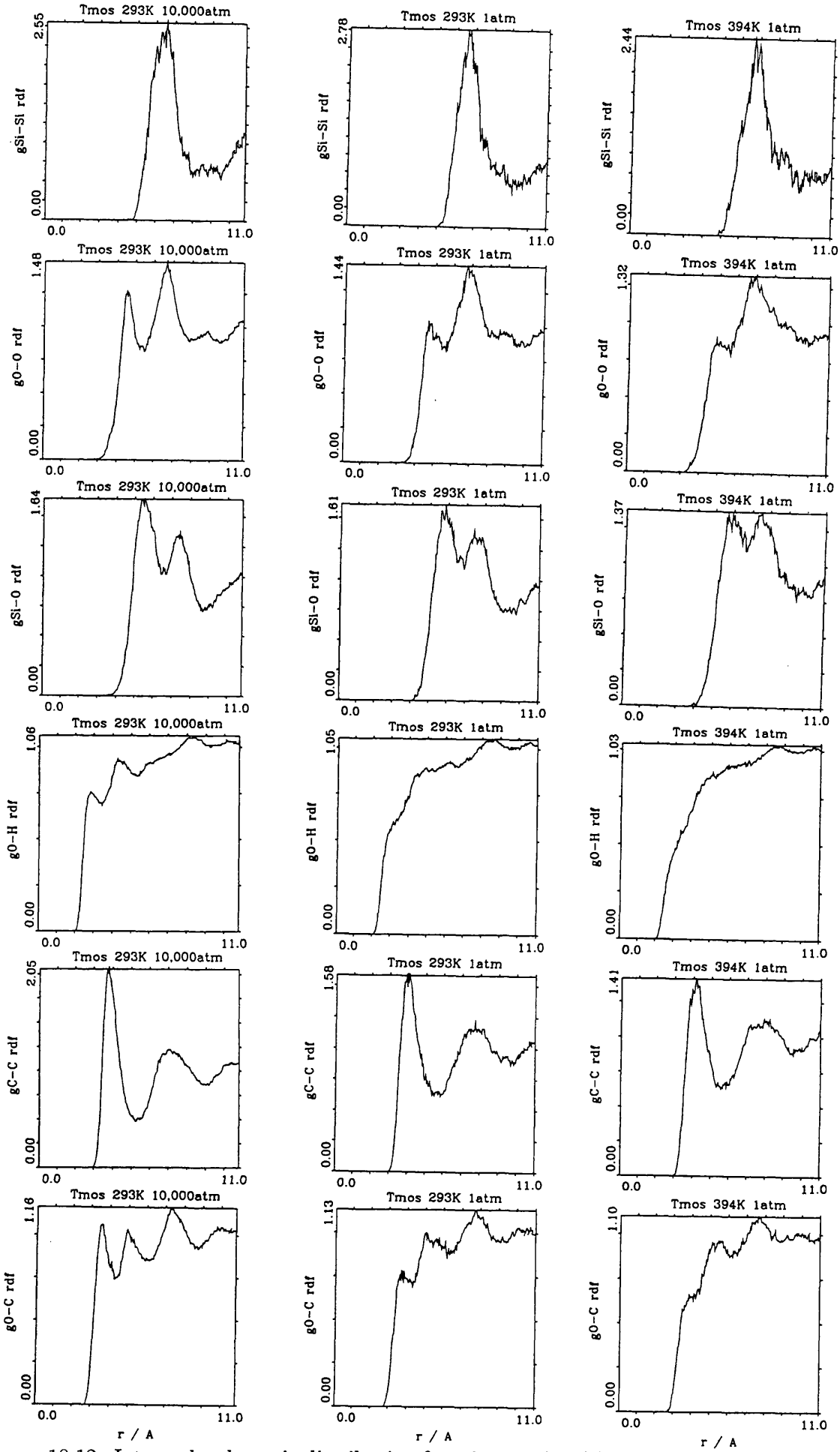


Figure 18.12: Intermolecular pair distribution functions in TMOS, for a pressure of 10,000 atm or 1 atm and a temperature of 20°C or 121°C, from atom-based simulations with an Ewald sum, after 24.0 ps of equilibration time and 1.0 ps of collecting time.

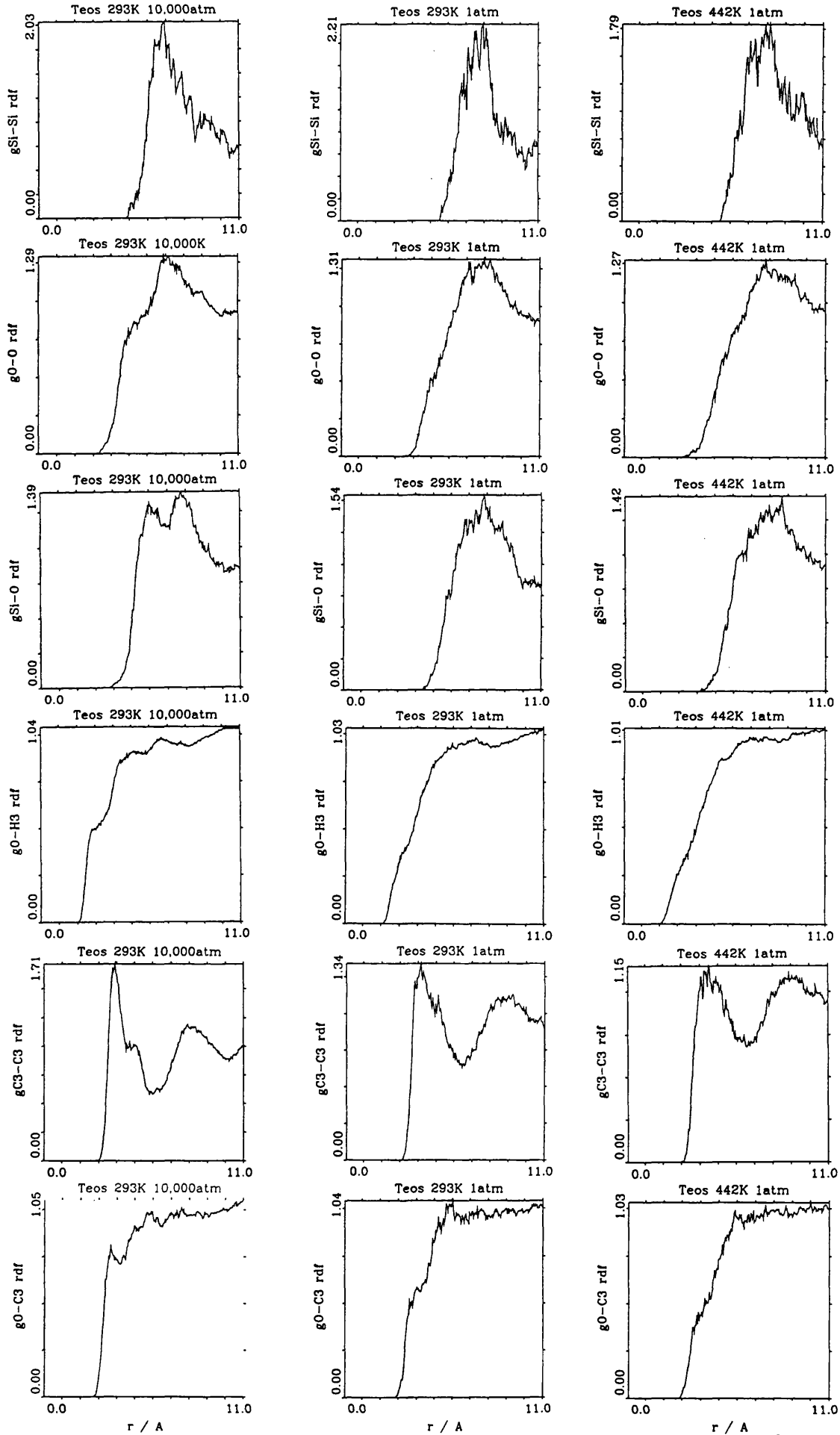


Figure 18.13: Intermolecular pair distribution functions in TEOS, for a pressure of 10,000 atm or 1 atm and a temperature of 20°C or 169°C, from atom-based simulations with an Ewald sum, after 24.0 ps of equilibration time and 1.0 ps of collecting time.

in better agreement with experiment, but the position of the second peak, at about 5.7 Å, is still greater than experiment. At the boiling temperature, the second peak is still visible, while at high pressure, a third peak appears at 8.5 Å. In heavy water, the liquid structure is more defined, due to the lower deuterium velocities; the third peak is already visible, but the first two peaks are almost equal as in water.

In methanol and ethanol, the O-O first peak appears at the same position, though it is higher than in water. In both alcohols, there is a pronounced valley between 3.5 Å and 4.5 Å, before the second peak, at about 4.8 Å in methanol and 5.2 Å in ethanol. At high pressure, the second peaks are shifted to smaller distances, an effect particularly visible in ethanol. In fact, temperature and pressure variations are likely to cause greater changes in the structures of liquids with larger molecules. For both alcohols, a third peak can be seen at about 7.0 Å, at high pressure.

The O-H (O-D) interactions in water, heavy water, methanol and ethanol show two important peaks, the first between 1.9 Å and 2.0 Å and the second at about 3.5 Å. However, while in water and heavy water the second peak is more important, in the alcohols this is relatively small and the first peak is predominant. This first peak represents the hydrogen-bonds, which in water, in the gas-phase, occur at 1.98 Å(as shown before for the water dimer). Although these distributions are in agreement with Jorgensen's results, it is unclear why the hydrogen-bond peak is so weak in water. A third peak appears in water and heavy-water at about 6.0 Å, which is visible in methanol at 5.0 Å, and cannot be seen in ethanol.

Because the H-H interactions are, in general, much weaker, due to the smaller charges and VdW repulsion and dispersion, the corresponding RDFs could be expected to show much less structure. This is the case in water and heavy water, but definitely not in the alcohols. In water and heavy water, there are very small peaks, at 2.5 Å and 4.0 Å, the second one becoming just a shoulder, at high pressure. In the alcohols, the first peak appears at 2.5 Å, but it is very pronounced, and the second peak, even at high pressure, appears only at 5.0 Å. These features are also in agreement with Jorgensen's results.

These interactions between hydroxyl groups may be compared with interactions between alkyl groups, in methanol and ethanol. The C-C interaction in methanol shows a pronounced peak at about 4.2 Å and a well defined second peak at about 8.0 Å, so an important structural distribution exists between the more apolar alkyl groups. The C_3-C_3, C_3-C_2 and C_2-C_2 interactions in ethanol are all very similar, at ambient conditions, and fairly close to the corresponding C-C interaction in methanol, though the first peak is less defined and the second is displaced to 9.0 Å. The relatively broad C_3-C_3 first peak in ethanol splits, at high pressure, in two perfectly separated peaks, at 4.0 Å and 5.0 Å, an effect which is not observed in methanol. Additionally, the structure of the C_2-C_2 interaction in ethanol becomes poor at high temperature.

These C-C interactions in methanol and ethanol are very similar to the equivalent C-C and C_3-C_3 interactions in TMOS and TEOS. In both cases, the first peak appears at 4.2 Å, but is smaller in the alkoxides. The second peak occurs at about 8.0 Å in TMOS and 9.0 Å in TEOS, as in methanol and ethanol, respectively. As can be seen by the peak and shoulder appearing at high pressure, the first C_3-C_3 peak in TEOS is in fact formed by two peaks, one at about 3.9 Å and a second at about 4.0 Å, as in the same interaction in ethanol. The CH_3-CH_3 interactions are thus almost equal in $Si(OCH_3)_4$ and CH_3OH, and in $Si(OCH_2CH_3)_4$ and CH_3CH_2OH, but are slightly different in $Si(OCH_3)_4$ and $Si(OCH_2CH_3)_4$ or between CH_3OH and CH_3CH_2OH, showing that these interactions depend more of the alkyl groups than on the chemical characteristics of the molecules.

The interactions between hydroxyl and alkyl groups can be analysed, looking at the C-O, C-H_o interactions in methanol and C_2-O, C_3-O, C_2-H_o, C_3-H_o, in ethanol. In all three C-O interactions, the first peak occurs at about 3.5 Å, but the second, at about 5.0 Å, is very weak in methanol and is displaced to 6.0 Å, in ethanol, in the C_2-O interaction. At 10,000 atm, these three interactions become very similar and even a broad third peak can be seen, at 7.5 Å in methanol and 8.0 Å in ethanol.

The C-H_o and C_2-H_o interactions, in methanol and ethanol, are very similar, particularly at high pressure, showing four well defined peaks, all systematically displaced for shorter distances in methanol, at about 0.5 Å, compared with ethanol. Surprisingly, the C_3-H_o ethanol interaction is considerably different, showing only the second and third peaks, and a incipient fourth one. The second peak is much more important than in the other two interactions, and the first peak definitely does not exist. In both C-H_o and C_2-H_o interactions, the carbon atom is bonded to a hydroxyl oxygen, which might attract closer the H_o hydrogen, due to its important charge, this way splitting the strong first peak observed in the C_3-H_o interaction, into two much smaller ones, the first occurring at only 2.5-2.8 Å.

The O-C, O-H and O-C_3, O-H_3 interactions in TMOS and TEOS, should be very different from the O-C, O-H interactions discussed so far for water, methanol and ethanol, because the oxygen atom is in a metalorganic group, instead of a hydroxyl group. As expected, in both alkoxides, the O-H interactions start at shorter distances, of about 2.2 Å, compared with the O-C, starting at 2.8 Å. The almost absence of structure, until the cutoff distance of 11.0 Å, for all four interactions, show that, probably due to steric hindrance, the interaction of the inner oxygen atoms with the outer alkyl groups is not particularly important, even at high pressure.

The O-O interactions in both alkoxides show two peaks: the first is only visible in TEOS at high pressure; they occur at fairly large distances, of 4.5 Å and 5.5 Å, in TMOS and TEOS, respectively. The Si-O RDFs for both alkoxides show also two distinct peaks, at 6.0-6.5 Å, which again, in the case of TEOS is only visible at high pressure.

The Si-Si distance in pure TEOS is reported by Yoldas to be slightly over 7 Å. Although the signal/noise ratio is not particularly good for the Si-Si RDFs calculated here, due to the small number (only 51) of Si atoms contained in these simulations, the agreement with experiment is good. In TMOS the corresponding first peak occurs at a slightly smaller distance, of about 6.5 Å.

In general, in all radial distribution functions discussed here, the compression and expansion effects due to the high pressure and temperature can clearly be seen.

18.9 Mean square displacement

Figures 18.14 to 18.19 show the total and partial x, y, z displacements, as a function of time, for water, heavy water, methanol, ethanol, Tmos and Teos, at ambient conditions, boiling temperature and high pressure. To represent better the molecular diffusion, only the oxygen atoms in water, heavy water, methanol, ethanol and the silicon atoms in TMOS, TEOS, were considered in this analysis.

At ambient conditions (20°C and 1 atm), the results look reasonable, given the size of the liquid molecules. The MSD increase with time is linear in water and heavy water, but already shows a curvature in methanol and particularly in ethanol. The results for the alkoxides, with much larger molecules, are very encouraging, perhaps even slightly better than in ethanol, with

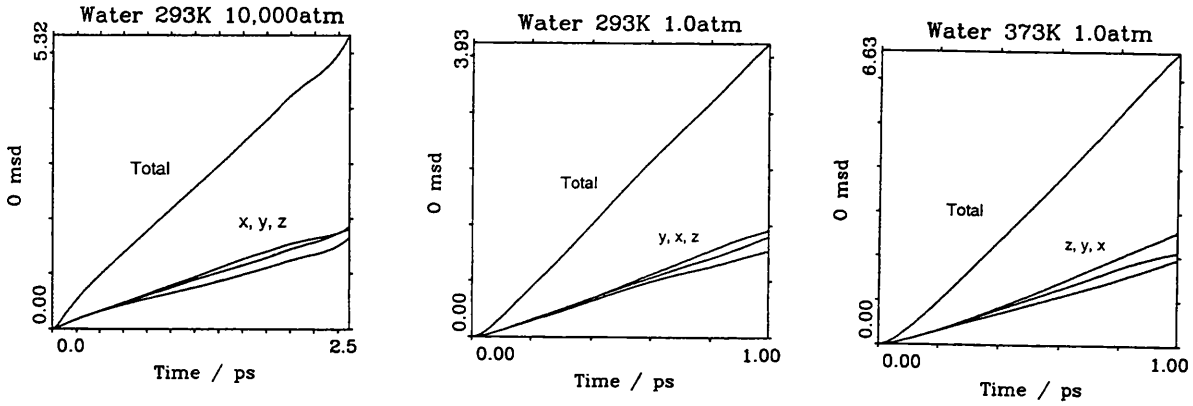


Figure 18.14: Mean Square Displacement (Å^2) as a function of time (ps) in water, for a pressure of 10,000 atm or 1 atm and a temperature of 20°C or 100°C, after 24.0 ps of equilibration time, from atom-based simulations with an Ewald-sum.

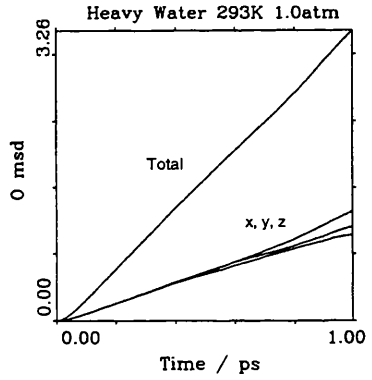


Figure 18.15: Mean Square Displacement (Å^2) as a function of time (ps) in heavy water, for a pressure of 1 atm and a temperature of 20°C, after 24.0 ps of equilibration time, from atom-based simulations with an Ewald sum.

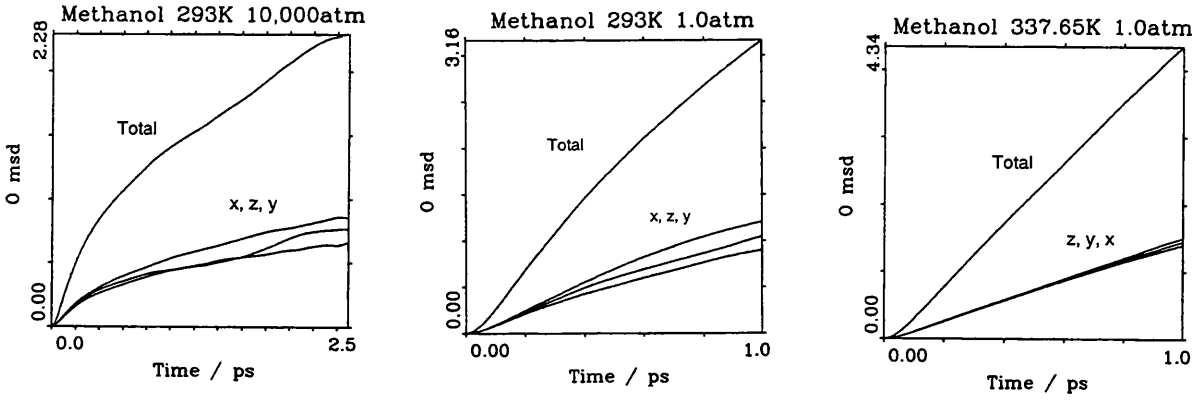


Figure 18.16: Mean Square Displacement (Å^2) as a function of time (ps) in methanol, for a pressure of 10,000 atm or 1 atm and a temperature of 20°C or 64.5°C, after 24.0 ps of equilibration time, from atom-based simulations with an Ewald sum.

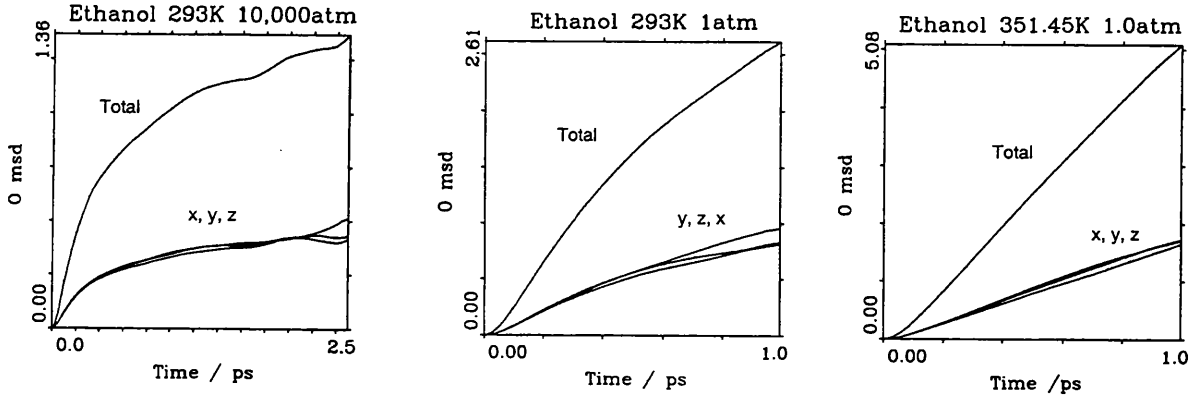


Figure 18.17: Mean Square Displacement ($Å^2$) as a function of time (ps) in ethanol, for a pressure of 10,000 atm or 1 atm and a temperature of 20°C or 78.3°C, after 24.0 ps of equilibration time, from atom-based simulations with an Ewald sum.

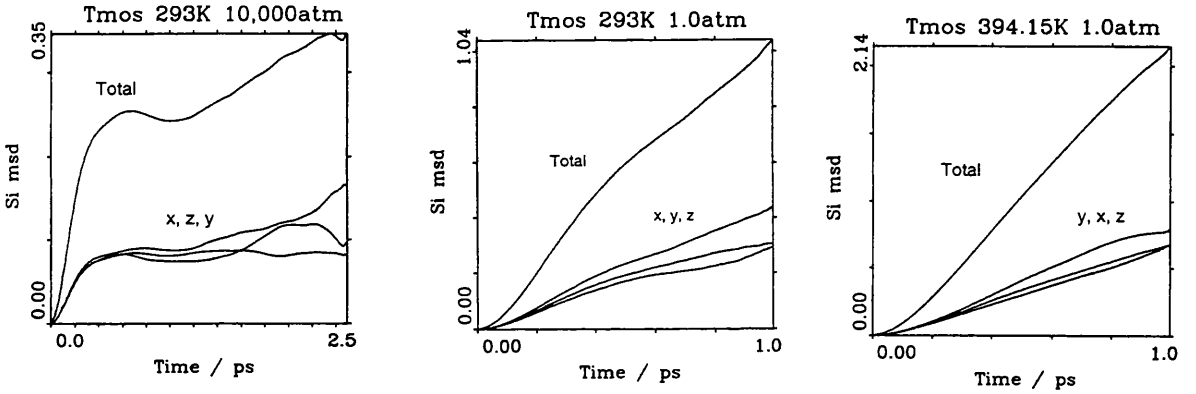


Figure 18.18: Mean Square Displacement ($Å^2$) as a function of time (ps) in TMOS, for a pressure of 10,000 atm or 1 atm and a temperature of 20°C or 121°C, after 24.0 ps of equilibration time, from atom-based simulations with an Ewald sum.

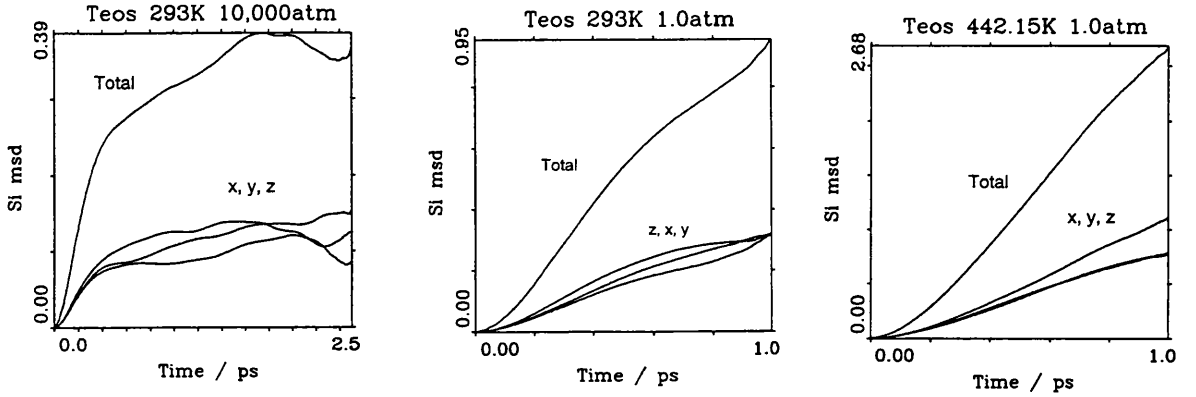


Figure 18.19: Mean Square Displacement ($Å^2$) as a function of time (ps) in TEOS, for a pressure of 10,000 atm or 1 atm and a temperature of 20°C or 169°C, after 24.0 ps of equilibration time, from atom-based simulations with an Ewald sum.

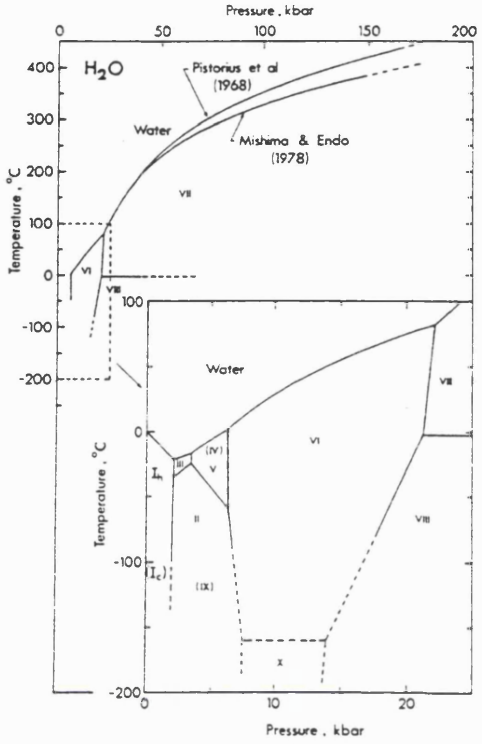


Figure 18.20: Phase diagram of H_2O [148].

just a hint of some oscillation.

For all liquids, the partial x, y, z MSD are fairly similar, showing that no overall translational motion is occurring during the liquid simulation. The MSDs in heavy water are almost as small as in methanol, while the values obtained for Tmos and Teos are very similar, despite the different alkyl groups.

At high temperatures, the results are significantly better, because the kinetic energy contribution increases considerably, so the dynamic trajectories become less distorted by the system specificities, described by the potential energy. In these conditions, no curvature is observed in the results for both alcohols and even in the alkoxides, the total MSDs show a very reasonable, almost liner, evolution with time. The partial MSDs in both alkoxides show that the movement in one direction is slightly faster than in the other two. This effect is most probably caused by the small statistical weight of the Si atoms in these liquids, but might also show that some translation motion is occurring at these high temperatures.

At very high pressures, of 10000 atm and 20^oC, even increasing the sampling time from 2000 to 5000 timesteps (2.5 ps), the results look very poor. Even in water, the MSD evolution shows some distortion, while in the alcohols and alkoxides (particularly the latter), the distortion is very large and the system motion approaches the behaviour which might be expected for, say, a glass. In fact, all these systems are solid at this very high pressure, even water (ice VI, see Figure 18.20). However, in spite of the oscillations and distortions observed in these conditions, no significant differences are observed between the partial MSDs, even in the alkoxides.

Because the average medium- and long-range interactions affecting a molecule, are isotropic, increasing the pressure reduces residual differences between the partial MSDs, while on increasing

the temperature these differences tend to increase and kinetic translation motion becomes more probable. Clearly, both temperature and pressure affect very much the molecular displacement in liquids and the effect increases with the size of the molecules.

18.10 Diffusion coefficient

The self-diffusion coefficients for water, heavy-water, methanol, ethanol, TMOS and TEOS, at ambient conditions, high pressure and high temperature, are presented in Table 18.10 and compared with experimental data. The total D_t and partial D_x, D_y, D_z diffusion coefficients were calculated using the Einstein equation (see chapter 7).

For all cases considered, the calculated values are substantially higher than the experimental results. This is surprising, particularly in water, which has been simulated in the last two decades, with much better results for the diffusion coefficients. In particular, the Berendsen SPC model, with atomic charges very similar to the ones applied here, is reported to give good results for the self-diffusion coefficient of water at ambient conditions. The differences between the results obtained with the two models, are most likely due to the intramolecular potentials, the NPT algorithm and the temperature relaxation time.

Intramolecular potentials, aiming to simulate the atomic vibrational motions, like the ones used here, should increase the atomic movements and therefore the diffusion coefficients. The NPT ensemble algorithm has clearly a important influence on the dynamic trajectories. However, less constrained simulations, with larger Berendsen relaxation times or more sophisticated NPT algorithms (Parrinello-Rahman or Nose-Hoover), which produce important pressure and temperature fluctuations, are likely to increase even more the diffusion coefficients, rather than to decrease, as wished.

The investigation of the dynamic behaviour of the NPT algorithms proposed so far, compared with the NVE ensemble, is one of the most important tasks for the future. The fact that the same trends are observed for all liquids and conditions studied, a excess of about 3-5 x 10^{-5} cm^2s^{-1} in all self-diffusion coefficients, is however very encouraging. It shows that the identification and correction of the problem in, say, water in ambient conditions, will also lead to good dynamic properties for all liquids and thermodynamic conditions, a extremely important goal in this project. Of course, reliable and accurate self-diffusion coefficients rely on the rigorous calculations of the mean square displacements or velocity autocorrelation functions, which is still a difficult task for liquids with large molecules, like the alkoxides, or even ethanol.

18.11 Conclusions

The results obtained with an atom-based criterion and a Ewald sum confirm and extend the results previously calculated with a group-based criterion and a Coulombic cutoff.

The densities and enthalpies of vaporisation are now slightly more accurate. The radial distribution functions are essentially the same as before, but the self-diffusion coefficients are still about twice as high as the experimental values.

Despite its large molecules, TEOS can now be simulated for any conditions of pressure and temperature, due to the atom-based criterion applied. Liquid heavy-water was also studied, as it might provide a way to investigate in future isotopic effects in sol-gel solutions.

	Self-diffusion Coefficient ($10^{-5} cm^2 s^{-1}$) *Cal.* *Exp.*					
	H_2O	MeOH	EtOH	$Si(OMe)_4$	$Si(OEt)_4$	D_2O
20.0° C	3.55	1.52	0.91	0.23	0.26	-
10,000 atm	0.50	-	-	-	-	-
20.0° C	6.55	5.27	4.35	1.73	1.58	5.43
1.0 atm	2.15	2.10	0.95	-	-	-
T_b	11.05	7.23	8.47	3.57	4.47	-
1.0 atm	6.60	-	3.00	-	-	-
(T_b/°C)	(100.0)	(64.5)	(78.3)	(121)	(169)	-

Table 18.10: Calculated and experimental self-diffusion coefficients of water, methanol, ethanol, TMOS, TEOS and heavy water, for a pressure of 10,000 atm or 1 atm and a temperature of 293 K or T_b, obtained from atom-based simulations with an Ewald sum. Experimental values from [109].

The similarity of the results obtained for the two methods, for a whole range of liquids and thermodynamic conditions, show the basic strength and correctness of the potentials and general methodology adopted in these studies. The fact that the same Ewald sum parameters can be used in a wide range of liquids and thermodynamic conditions is a major result in itself, opening enormous opportunities for the future.

It is certainly encouraging that such a range of different liquids, thermodynamic conditions, properties, namely RDF pair functions, can be simulated with reasonable accuracies, always using the same potentials and procedures.

However, this should be regarded as only a beginning: the specific heats are higher than even the classic limit; a key aspect of these simulations, the liquid dynamics, needs to be seriously improved, as shown by the exaggerated diffusion coefficients. This overestimation happens equally for all liquids and temperatures, and according to published results, is not observed in the similar SPC potentials, making the problem soluble.

It is probably closely related to the choice of the NPT algorithm. The Berendsen algorithm used throughout this work is reliable, but it does not simulate properly the thermodynamic fluctuations of an isothermic-isobaric system. Furthermore, the temperature relaxation time used in this work is very small, tighthnening too much the temperature oscillations. Exhaustive tests need to be done with NVE and NPT ensembles, with more sophisticated algorithms, such as Parrinello-Rahman and Nose-Hoover.

Chapter 19

Ewald sum-based solutions

This chapter has two purposes: the first is to investigate, for realistic sol-gel solutions, how the improved MD model, presented in the previous chapter, describes the aggregation of the silicate clusters and the key interactions that allow the forward and reverse sol-gel reactions to occur. The second purpose is to study directly the chemical environment around the silica clusters, by visual inspection of these realistic solutions, a invaluable tool to understand solvation and reaction mechanisms.

19.1 Introduction

The first successful simulations of sol-gel condensation reactions were reported by Feuston et al. in 1990 [71], using only two- and three-body potentials. The Si-Si, O-O and O-Si interactions are represented by a modified Born-Mayer-Huggins (BMH) potential, while Si-H, O-H and H-H interactions are described by BMH potentials plus additional terms taken from the Rahman-Stillinger-Lemberg potential (RSL2). The O-Si-O, Si-O-Si, H-O-H and Si-O-H angular distributions are controlled by a combined bond angle-bond length potential.

The Si-Si, O-O, Si-O, O-Si-O and Si-O-Si potentials have been derived before to simulate vitreous silica [70] and give a reasonable description of the radial distribution function and structure factor of the glass, in particular, reducing the distribution of tetrahedral angles and the concentration of bond defects to ~1-2%. The O-O interaction is therefore the same in the water and silica subsystems.

For temperatures above 1500 K this model is able to simulate the onset of polymerisation, leading to the formation of oligomers as large as six-silicon chains, in less than 20 ps. An OH group is first deprotonated, leaving a negatively charged Si-O^- group, which subsequently attacks another monomer, forming a unstable pentaccordinated silicon, that finally relaxes by the dissociation of a OH^- group.

This empirical model was studied later [81] for longer run times, about 120 ps, showing that the chains formed during the early stages of the simulation can close to form rings, with 3 to, at least, 8 silicon atoms. The activation energy for formation of branching Q_m^n species (12 kcal/mol) is consistent with the experimental data of 12 kcal/mol for gelation and compares well with the activation enthalpy of condensation between two monomers, predicted experimentally [81]: 15 kcal/mol.

The importance and complexity of the reverse transesterification is shown by the experimen-

tal work of Uhlmann et al. [235]. When the TEOS hydrolysis is carried out in iPOH, the iPOH concentration initially decreases, due to ester exchange, and then increases toward its original value as hydrolysis proceeds. When TEOS is solvated in MeOH or iPOH, no exchange can be detected. Furthermore, TEOS hydrolyses much faster in MeOH than in EtOH reflecting also ester exchange.

The modelling of glass systems (since the first MD simulation of glass formation, carried out by Woodcock in 1971, who cooled molten KCl) is discussed in the 1982 review of glass tructure and diffusion in glass published by Soules [217]. Later MD simulations of silica-based glasses include the wok of Vessal et al. [238], proposing three different potential models to describe vitreous silica, Newel et al. [179] and Zirl et al. [255], developing models to simulate sodium trisilicate and sodium aluminosilicate glasses, respectively. Ab-initio interatomic potentials proposed by Tsuneyuki for silicon dioxide have been tested for α-quartz under pressure, by Chelikowsky et al. [56]. Molecular Dynamics simulations of SiO_2 melt and glass have been carried out by Kubicki et al. [139] using two sets of ionic and covalent interatomic potentials. Monte Carlo simulations of amorphous silicon have been done by Dereli [65], using two-body and three-body Stillinger-Weber potentials (the potentials are fully described).

The hydrolysis and condensation reactions are not described yet in the purely classical simulations carried out in this work. Three ideal stages of the sol-gel process are therefore considered, for real sol-gel solutions with composition water/alkoxide = 4 and alcohol/alkoxide = 8:

1) before the hydrolysis, with 30 molecules of alkoxide plus 120 molecules of water plus 240 molecules of alcohol, 2) after the full hydrolysis but before the condensation, with 30 molecules of monosilicic acid plus 360 molecules of alcohol and 3) after the first stage of condensation, with 15 molecules of disilicic acid plus 15 molecules of water and 360 molecules of alcohol. Two sets of solutions were investigated, one containing methanol and TMOS, the other containing ethanol and TEOS, resulting in a total of six sol-gel solutions.

All simulations were done applying the MD model described in the previous chapter. The low density initial configurations were compressed first to 10,000 atm and 20°C, for 20,000 timesteps (10 ps), and then relaxed for ambient conditions, at 1 atm and 20°C, for more 20 ps, to equilibrate the solutions. After this initial procedure, the configuration of each of the six solutions was collected for analysis, after every 50 ps, until reaching a run time of 500 ps.

Densities and energies are presented for every 50 ps configurations, after 1 ps of collecting time. Densities, energies and key radial distribution functions, for forward and reverse reactions, are presented for 100 ps, 300 ps and 500 ps MD run times, after 5 ps of collecting time. The aggregation of the silicate clusters and the chemical environment surrounding each silicate cluster are analysed for the same run times, by visual inspection of the solutions.

19.2 Reactive interactions

A chemical reaction in solution is a three-stage process, involving, first, the diffusion of the reactants to each other, second, the replacement of reactant-solvent by reactant-reactant interactions, and finally, the chemical transformation itself, when the orientation and energy of the reactants is adequate. While the first stage depends essentially on the concentration of the solution, on the size of the reactant molecules and on the strength of the reactant-solvent interactions, the second stage depends mainly on the relative strength of the concurrent reactant-solvent and reactant-reactant interactions.

To study these non-reactive aggregation steps, the liquid structure should be investigated, as a function of time. In sol-gel processes, where the analysis is made more difficult by the large number of reactions and species involved, the simulation of ideal solutions simplifies considerably the task, focusing on its essential aspects.

The first two solutions studied here, containing 30 molecules of alkoxide (TMOS or TEOS), 120 molecules of water and 240 molecules of alcohol (MeOH or EtOH, respectively) emulate realistic sol-gel solutions, before the hydrolysis reaction starts. HCl was not added to the solutions because, even for pH = 1, the corresponding 10^{-1}M concentration of H^+ corresponds to only 2.6 ions per cell. Because the reactions are actually not simulated, acid catalysis effects in solution cannot be studied yet. In these conditions, the only possible reaction is the hydrolysis of the alkoxides, replacing an alkoxyl by an hydroxyl group:

$$Si(OR)_4 + H_2O \longrightarrow Si(OR)_3OH + ROH.$$

The reverse reaction can then occur, replacing an hydroxyl by an alkoxy group-a reesterification. In principle, these reactions are promoted by O(water)→Si(alkoxide) and O(alcohol)→Si(alkoxide) nucleophilic attacks. The radial distribution functions for these key interactions, as a function of time, are presented in Figure 19.1, for methanol- and ethanol-based solutions, respectively. Strictly speaking, the O(alcohol)-Si(alkoxide) interaction calculated here describes the transesterification reaction, the replacement of a alkoxy group OR by another OR'. Since the Si environment remains almost the same after removing the first OR group, that interaction describes also the reesterification.

Clearly, the O(water)-Si interaction, favouring the forward reaction, is much stronger than the O(alcohol)-Si interaction, favouring the reverse process. Although there are, in solution, twice as much molecules of alcohol than molecules of water, these latter are much smaller and have larger oxygen charges, which helps them to avoid the outer alkyl groups and to come closer to the inner silicons, with large positive charges. As the comparison of the results for methanolic and ethanolic solutions show, larger alkyl groups in alkoxides and alcohols increase the O(water)-Si and decrease the O(alcohol)-Si interactions. As can be seen for both solutions, time also favours the forward reaction. While the O(alcohol)-Si interactions are relatively stable, there is an increase of the O(water)-Si first peak (around 4 Å), accompanied by a decrease of the second peak (around 6 Å).

The next two solutions, containing 360 molecules of alcohol (MeOH or EtOH) and 30 molecules of monosilicic acid, are obtained from the first, assuming that the hydrolysis reaction was completed:

$$30Si(OR)_4 + 120H_2O + 240ROH \longrightarrow 30Si(OH)_4 + 360ROH$$

In these solutions, two reactions can occur, the forward condensation reaction, replacing two hydroxyl groups by a disiloxane bond:

$$Si(OH)_4 + Si(OH)_4 \longrightarrow Si_2O(OH)_6 + H_2O$$

and the reverse reesterification:

$$Si(OH)_4 + ROH \longrightarrow Si(OH)_3OR + H_2O$$

Assuming again that both reactions are promoted by nucleophilic O(monomer)→Si(monomer) and O(alcohol)→Si(monomer) attacks, the corresponding RDFs for these interactions are presented in Figure 19.2, for methanol- and ethanol-based solutions.

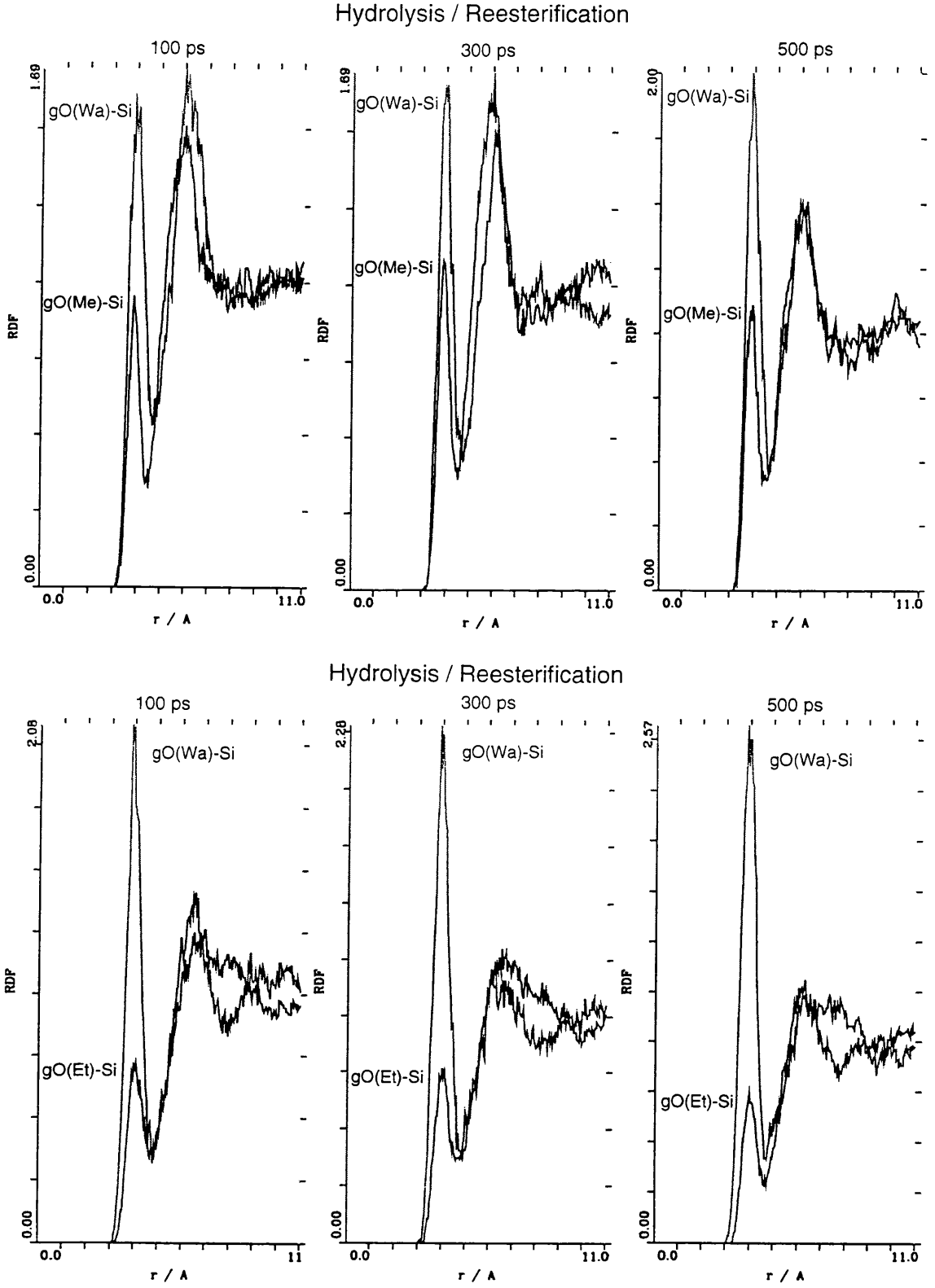


Figure 19.1: O(water)-Si(alkoxide) and O(alcohol)-Si(alkoxide) pair distributions, in methanolic (above) and ethanolic (below) solutions, before hydrolysis, for 100 ps, 300 ps and 500 ps of run time and 5 ps of collecting time.

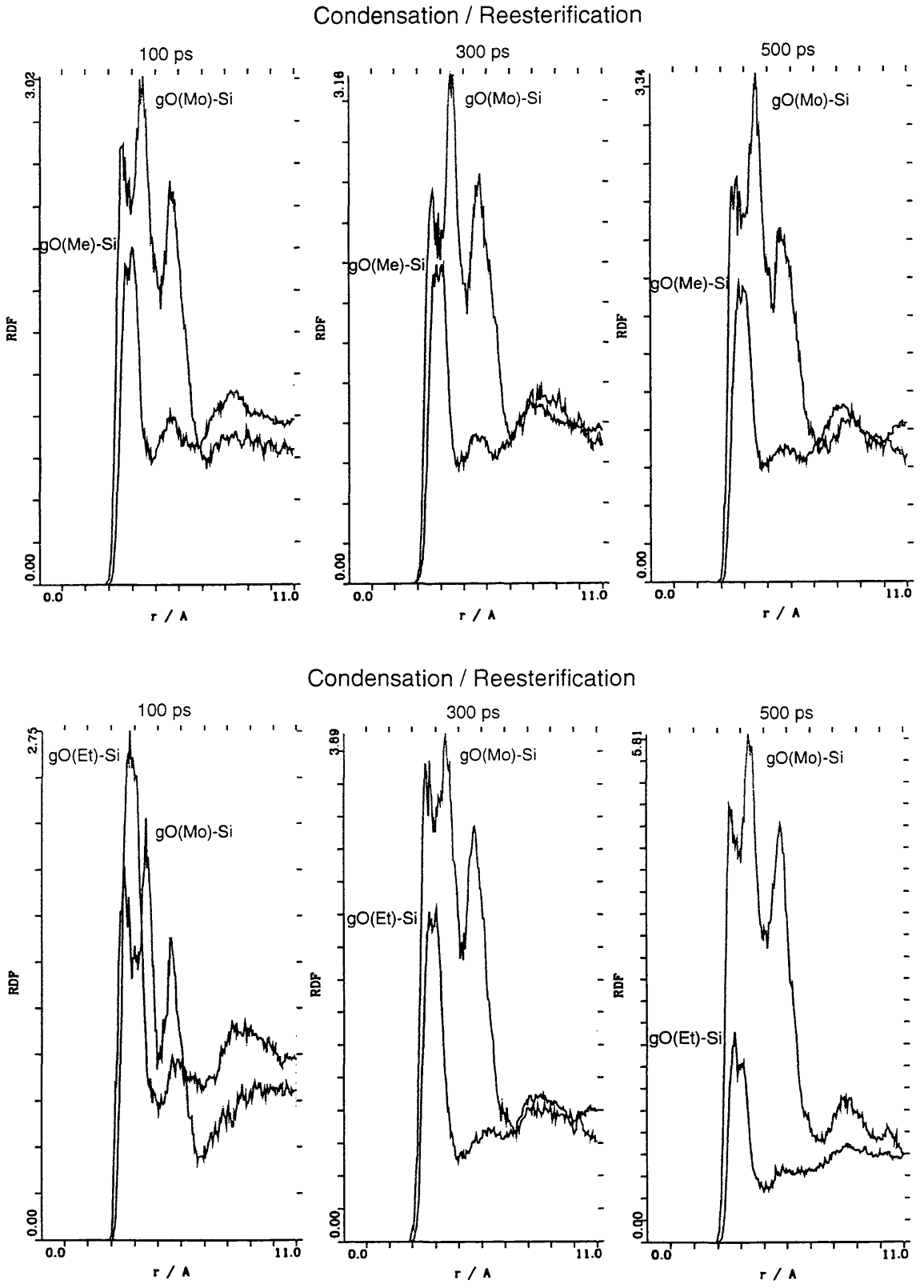


Figure 19.2: O(monomer)-Si(monomer) and O(alcohol)-Si(monomer) pair distributions, in methanolic (above) and ethanolic (below) solutions, after hydrolysis but before condensation, for 100 ps, 300 ps and 500 ps of run time and 5 ps of collecting time.

In both cases, the O(monomer)-Si interaction becomes stronger for longer times, while the O(alcohol)-Si interaction remains stable in the methanolic and decreases in the ethanolic solution (due to the larger alkyl groups). In both solutions, after 300 ps, the O(monomer)-Si interactions, favouring the forward condensation reaction, become much stronger than the O(alcohol)-Si interactions, promoting the reverse reesterification. This result is particularly impressive taking into account that there are 360 alcohol molecules in solution and only 30 monomers. Clearly, the monomers are much more attracted to each other than by the solvent, methanol or ethanol. While the O-Si interactions with the alkoxides started at 3.2 Å, with the monomers they start at 3.0 Å or even less, as in O(monomer)-Si interactions.

The last two solutions, containing 360 molecules of alcohol (MeOH) or EtOH) and 15 molecules of disilicic acid, are obtained from the second solutions, assuming that all the monomers reacted to form dimers, by a water condensation reaction:

$$30Si(OH)_4 + 360ROH \longrightarrow 15Si_2O(OH)_6 + 15H_2O + 360ROH.$$

Four different reactions can be considered in these solutions: first the forward condensation:

$$2Si_2O(OH)_6 \longrightarrow Si_4O_2(OH)_{12} + H_2O,$$

second the reverse reesterification:

$$Si_2O(OH)_6 + ROH \longrightarrow Si_2O(OH)_5OR + H_2O,$$

third the reverse hydrolysis:

$$Si_2O(OH)_6 + H_2O \longrightarrow 2Si(OH)_4,$$

and fourth the reverse alcoholysis:

$$Si_2O(OH)_6 + ROH \longrightarrow Si(OH)_4 + Si(OH)_3OR.$$

Assuming, as before, that all reactions start with a O→Si nucleophilic attack, the corresponding key interactions O_t(dimer)→Si, O(alcohol)→Si and O(water)→Si are analysed in Figure 19.3, for methanol- and ethanol-based solutions.

In both cases, the O(dimer)-Si interactions considerably increase with time and the O(water)-Si interactions drop substantially. The O(alcohol)-Si interactions decrease also in the methanolic but remain stable in the ethanolic solution. In both solutions, for 500 ps, the O(dimer)-Si interaction, favouring the forward condensation reaction, is already more important than the other two, that promote the reverse reactions. Again, these results are even more convincing when taking into account that there are only 15 dimers in solution, against 360 alcohol molecules. There are also only 15 water molecules, but their small size and higher charges should help the O(water)-Si interactions.

19.3 Monomer and dimer aggregation

An important aggregation effect is observed in these solutions, between both the monomers and the dimers. This aggregation of the silicate clusters in solution can indeed be seen, by visual inspection of the final configurations of the six solutions, conveniently stripped of the water and

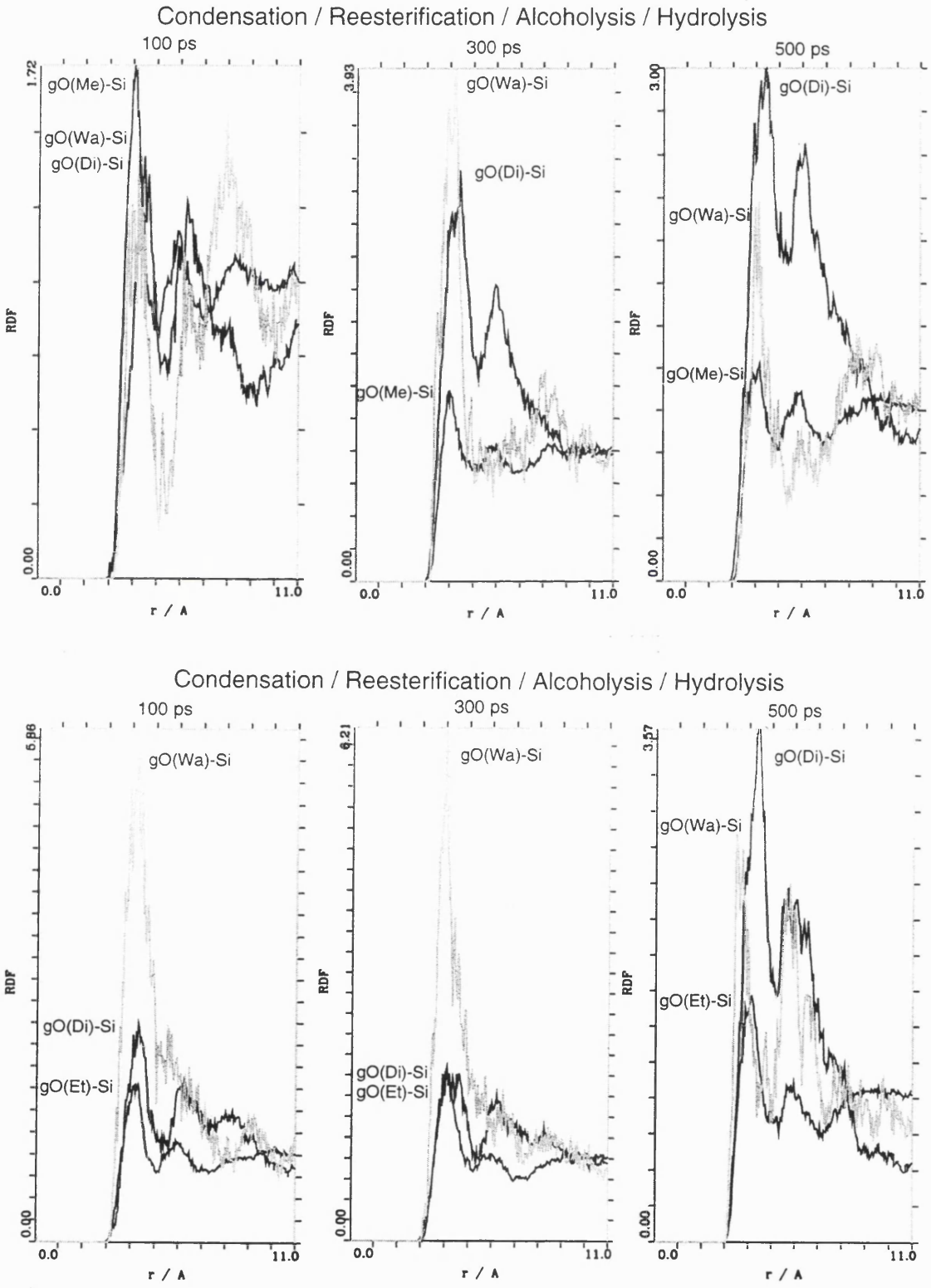


Figure 19.3: O(dimer)-Si(dimer), O(water)-Si(dimer) and O(alcohol)-Si(dimer) pair distributions, in methanolic (above) and ethanolic (below) solutions, after condensation, for 100 ps, 300 ps and 500 ps of run time and 5 ps of collecting time.

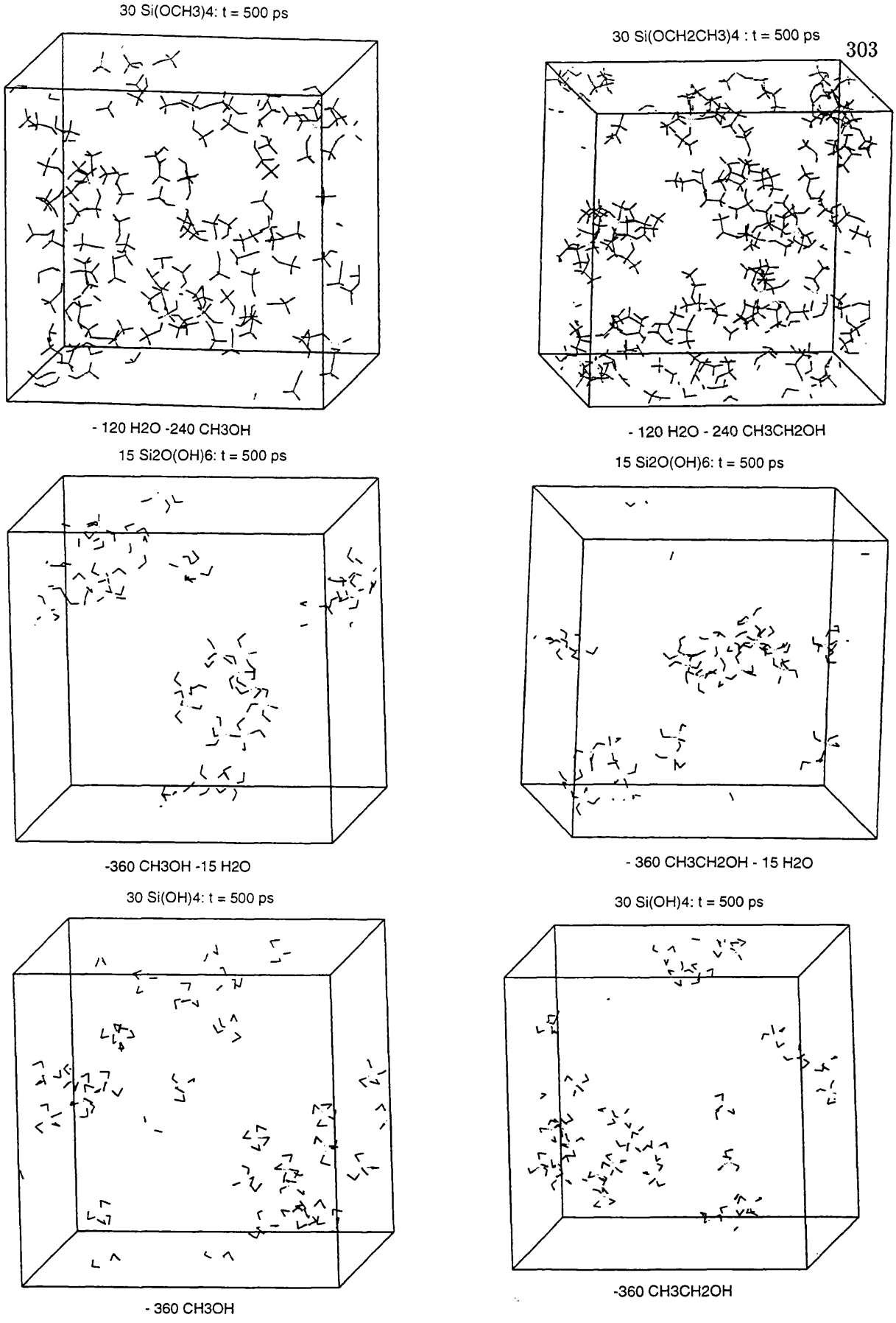


Figure 19.4: Methanolic (left) and ethanolic (right) solutions: 1) before hydrolysis; 2) after hydrolysis but before condensation; 3) after condensation, showing only the alkoxide, monomer and dimer molecules, after 500 ps of run time.

alcohol molecules as represented in Figure 19.4. Clearly, relatively dense clouds of monomers can be seen in several parts of the cell. This effect is particularly visible taking into account the periodic boundary conditions of the system, so molecules in opposite sides of the cell are actually interacting directly with each other.

The dimer aggregation seems to be even more evident, with large regions of the space completely empty of silicate clusters, which are concentrated in just a small number of regions across the cell. The few dimers that seem to remain completely isolated, would aggregate, probably, with the continuation of the run.

Aggregation effects between the alkoxides can hardly be seen, due to the numerous alkyl groups present, which complicate too much the image. These alkyl groups, which are relatively large and with positive charges in all the outer hydrogens, are likely to make O(alkoxide)-Si interactions very difficult. Although these interactions are not particularly important in sol-gel processes, because no chemical reaction is involved, they might give an indication of the difficulty for a mono-hydrolysed alkoxide to attack another alkoxide in a alcohol-forming condensation:

$$Si(OR)_3(OH) + Si(OR)_4 \longrightarrow Si_2O(OR)_6 + ROH$$

A quantitative description of the aggregation of the silicate clusters is given by the Si-Si radial distribution functions, as a function of time, presented in Figure 19.5, for all six solutions.

Alkoxide aggregation is definitely not occurring, as the Si-Si first peak is relatively weak in both initial solutions and occurs at relatively large distances (6.5 Å(methanol-based) to 7.5 Å(ethanol-based)) and does not show any increase with time. In compensation, the monomer-monomer aggregation is demonstrated by the steadly increase, with time, of the first Si-Si peak, in both methanolic and ethanolic solutions. These results confirm entirely the O-Si RDF analysis and the visual observations discussed before, for this one-centre silicate clusters.

The Si-Si RDF analysis for the dimers is less clear, partially because the statistical weight is now considerably smaller, 15 instead of 30, and because these are two-centre molecules, so the relative orientation of the interacting dimers can interfere with the results. Nevertheless, the dimer aggregation is still visible, as the Si-Si first peak is much higher for 500 ps than for 100 ps or 300 ps, in the ethanolic solution, and is much higher for 300 ps and 500 ps than for 100 ps, in the methanolic solution. Clearly, the alkoxide molecules do not attract each other, but as soon as the alkoxy are replaced by hydroxyl groups, the silicate clusters start to aggregate, making possible the subsequent condensation reaction.

19.4 Density and energy

The density and energy contributions for the six sol-gel solutions, collected simultaneously with the radial distribution functions discussed above, are presented in Tables 19.1 and 19.2.

In all solutions, the density remains constant with time, as the small differences observed are below the uncertainties of the method. The structural changes occurring with time, in all solutions, are thus not reflected in their total volume. This ideal behaviour is confirmed by the densities of the initial solutions, which match exactly the predicted values for ideal solutions. In particular, water-alcohol contraction effects are not observed.

Furthermore, the density also remains unchanged with the progression of the sol-gel process, though a very small increase might be noticeable, after the hydrolysis, in the methanolic solutions. During sol-gel processes, the density increases substantially, but certainly that effect

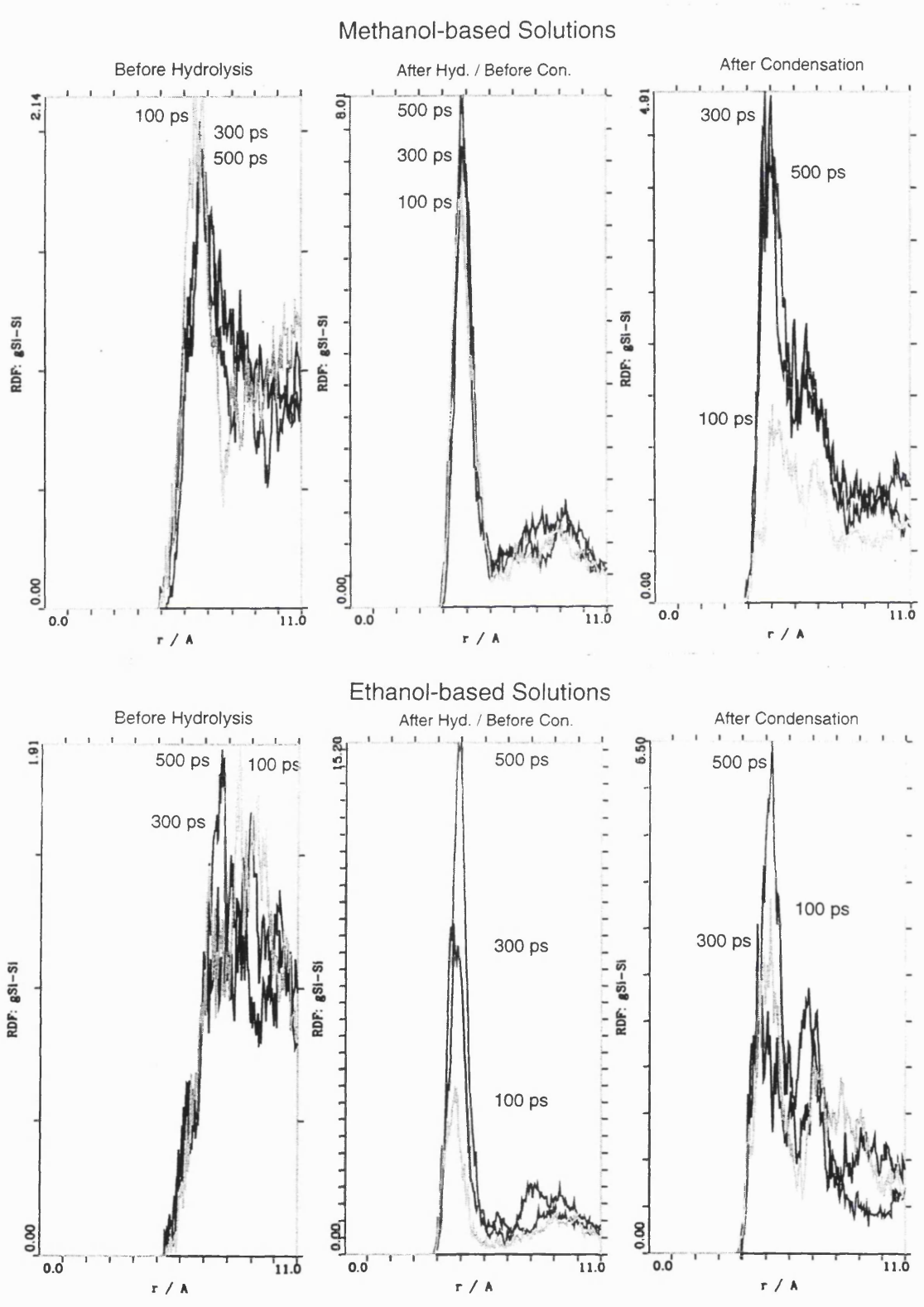


Figure 19.5: Si-Si pair distributions, in methanolic and ethanolic solutions, before hydrolysis, after hydrolysis but before condensation, and after condensation, for 500 ps of run time and 5 ps of collecting time.

	$Density/gcm^{-3}$					
Time/ps	H_2O $MeOH$ $Si(OMe)_4$	$MeOH$ $Si(OH)_4$	H_2O $MeOH$ $Si_2O(OH)_6$	H_2O $EtOH$ $Si(OEt)_4$	$EtOH$ $Si(OH)_4$	H_2O $EtOH$ $Si_2O(OH)_6$
100	0.872	0.879	0.892	0.845	0.848	0.851
300	0.871	0.890	0.880	0.841	0.858	0.851
500	0.869	0.896	0.884	0.860	0.859	0.851
Ideal	0.876	-	-	0.844	-	-

Table 19.1: Calculated and ideal-solution density for methanolic and ethanolic sol-gel solutions, before hydrolysis, after hydrolysis and before condensation, and after condensation. All values represent averages over 5 ps.

cannot be observed by analysing only the very beginning of the sol-gel process, the alkoxide hydrolysis and the monomer condensation. Additionally, in a real sol-gel experiment, this increase in density is also due to water and alcohol evaporation during the long time needed to reach the gel-point: a mass transfer effect which is not simulated here.

The equal densities observed for the various stages of the sol-gel process show also that the charges and zeolite parameters used to describe the monomer and dimer, are very reasonable, an important test which widely confirms the reliability of the methodology previously developed, to simulate liquids by Molecular Dynamics.

Like the density, the total and partial energies of each solution remain virtually constant with the time, during the whole MD run. This is a surprising result, which means that the total energy and its components do not depend on the structure of the liquid and on the particular interactions occurring there. This ideal behaviour in energy confirms the ideal behaviour in volume discussed above and fully corroborates identical conclusions obtained for the dilute sol-gel solutions, simulated with a Coulombic cutoff, group-based method.

For methanol- and ethanol-based solutions, the total energy decreases considerably from the first to the second solutions (during Hydrolysis) and increases from the second to the third solutions (during the Condensation). Although these differences are not particularly important in the dynamic and structural studies done here, as the 6 sol-gel solutions are independent, they are absolutely critical to develop a realistic MD or MC model of the hydrolysis and condensation reactions. For both methanol- and ethanol-based solutions, the total energy decreases about 42,500-45,000 kcal/mol from the first to the second solution (during the Hydrolysis) and increases about 30,000 kcal/mol from the second to the third solutions (during the Condensation). These differences correspond to MD hydrolysis and condensation energies of 44,000/(30x4) $\approx$ 370 kcal/mol and 30,000/15 $\approx$ 2,000 kcal/mol, clearly too high, when compared with the ab-initio values calculated before, about 1 kcal/mol and 3 kcal/mol, respectively.

Because these differences in energy are essentially the same in methanolic and ethanolic solutions, they are independent of the alkyl groups in the alkoxide and alcohol. A closer look at the energies, presented in Table 19.2, shows that they originate from the Coulombic contributions. These enormous differences cannot be due to intermolecular Coulombic interactions, because these are similar in the various solutions. The differences are the result of the short-range

		Energy ($kcalmol^{-1}$)							
Sol.	*Time*	*Bond*	*Angle*	*Dihed.*	*Coul.*	*VdW*	*Poten.*	*Kinet.*	*Total*
Me:									
	100	624.5	930.3	-706.6	7,352.8	-882.2	7,318.8	2,122.5	9,441.3
b. H.	300	609.2	948.4	-705.7	7,347.0	-876.1	7,322.7	2,122.5	9,445.2
	500	612.3	949.4	-706.2	7,318.7	-869.2	7,305.0	2,122.5	9,427.5
	100	1,738.2	6,107.4	485.1	-44,927	1,467.4	-35,129	2,122.5	-33,006
a. H.	300	1,762.1	6,151.8	483.8	-45,004	1,456.5	-35,150	2,122.5	-33,027
b. C.	500	1,759.1	6,127.5	483.1	-44,998	1,443.2	-35,185	2,122.5	-33,062
	100	789.2	1,342.7	155.0	-6,619.9	-846.8	-5,179.7	2,122.5	-3,057.2
a. C.	300	761.8	1,352.8	156.7	-6,559.4	-846.2	-5,134.3	2,122.5	-3,011.8
	500	749.5	1,362.3	154.6	-6,563.4	-845.2	-5,142.2	2,122.5	-3,019.7
Et:									
	100	926.4	1,472.3	-1,970.6	-14,149	-771.7	-14,492	3,066.2	-11,426
b. H.	300	910.2	1,486.8	-1,965.4	-14,134	-775.3	-14,477	3,066.3	-11,411
	500	919.1	1,501.0	-1,968.8	-14,198	-808.8	-14,556	3,066.3	-11,489
	100	2,078.9	6,747.9	-778.0	-69,654	1,721.5	-59,884	3,066.2	-56,817
a. H.	300	2,078.5	6,792.7	-777.1	-69,727	1,698.8	-59,934	3,066.2	-56,867
b. C.	500	2,076.4	6,760.4	-772.6	-69,724	1,689.5	-59,971	3,066.2	-56,904
	100	1,088.5	1,971.1	-1,085.5	-31,205	-618.6	-29,850	3,066.3	-26,783
a. C.	300	1,077.1	1,971.1	-1,088.9	-31,198	-620.5	-29,859	3,066.3	-26,793
	500	1,076.0	1,983.8	-1,093.6	-31,235	-616.2	-29,885	3,066.3	-26,814

Table 19.2: Energy of methanolic (Me) and ethanolic (Et) sol-gel solutions, before Hydrolysis (b. H.), after Hydrolysis but before Condensation (a. H. b. C.), and after Condensation (a. C.). All values represent averages over 5 ps.

electrostatic interactions in $Si(OR)_4$, $Si(OH)_4$ and $Si_2O(OH)_6$.

Because 1-3 and 1-4 interactions are set-up to 0 and 1 respectively, each $Si(OH)_4$ cluster has 12 strong O-H interactions (hydrogen bonds) compensated only by 12 much weaker H-H interactions. In $Si_2O(OH)_6$, there are only 6 O-H (and (H-H) short-range interactions per Si atom. In $Si(OR)_4$, the charges are smaller and the repulsive O-C and Si-H interactions compensate the attractive Si-C and O-H interactions. Because intramolecular Coulombic interactions are so important in $Si(OH)_4$ and $Si_2O(OH)_6$, they distort these molecules and the bond, angle and dihedral energies increase accordingly, as can be seen in the same table.

Although thse intramolecular effects and the corresponding differences in total energy between the various solutions are not particularly important in the dynamic and solvation studies done here, they are fundamental to describe correctly the energetics of chemical reactions by MD or MC. In particular, the scaling factors for 1-2, 1-3, 1-4, 1-5, etc... interactions, usually an undervaluated aspect of MD and MC simulations, need to be chosen very carefully, to get consistent results for the different chemical arrangements.

19.5 Short data collection times

The density and energy results discussed so far were obtained after a run time of 100ps, 300ps and 500ps, and a collecting time of 5 ps. Equivalent results covering every 50 ps of run time, with a collection time of 0.5 ps, are presented in Tables 19.3 and 19.4. As before, no differences in density and energy are observed during the whole range of times analysed. The density and total energy for t = 100 ps, 300 ps, and 500 ps are also very similar (for all six solutions) to the values presented above, with a collecting time ten times larger. This shows that, for properly equilibrated solutions, sampling times as small as 0.5 ps can produce reliable, essentially correct, results, even if the signal/noise ratio is poor.

19.6 Short run times

The results discussed so far have been obtained after long MD run times. The density and total energy in the very beginning of the simulations, for t = 0, 5 ps and 10 ps (20,000 timesteps) are presented in Table 19.5. A comparison with the results of the Tables 19.3 and 19.4 shows that for shorts run times the densities tend to be slightly lower (and the energies slightly higher than in the fully equilibrated solutions, but the differences are usually very small, in some cases below the uncertainty of the method. Consequently, the results presented in the previous chapter for the pure liquids, after 22.5 ps of equilibration time and 2.5 ps of collection time, should remain almost unaltered after arbitrarily long run times or better data sampling.

19.7 Solvation effects

Figures 19.6, 19.7 and 19.8 show the solvation environments around some of the silicate clusters, observed at the end of the simulations. Because these solutions emulate real sol-gel solutions, the images should be realistic representations of the liquid structure around the reactant clusters, therefore providing a valuable tool for studying the chemistry of the reactions and for developing realistic potentials to simulate them, using purely classic techniques.

	$Density/gcm^{-3}$					
Time/ps	H_2O $MeOH$ $Si(OMe)_4$	$MeOH$ $Si(OH)_4$	H_2O $MeOH$ $Si_2O(OH)_6$	H_2O $EtOH$ $Si(OEt)_4$	$EtOH$ $Si(OH)_4$	H_2O $EtOH$ $Si_2O(OH)_6$
100	0.861	0.886	0.895	0.853	0.851	0.850
150	0.885	0.899	0.884	0.865	0.852	0.853
200	0.887	0.873	0.881	0.849	0.851	0.851
250	0.874	0.888	0.884	0.845	0.848	0.857
300	0.875	0.892	0.882	0.843	0.857	0.854
350	0.885	0.882	0.895	0.849	0.856	0.844
400	0.876	0.898	0.893	0.853	0.852	0.854
450	0.871	0.892	0.883	0.845	0.849	0.857
500	0.859	0.896	0.874	0.858	0.861	0.857

Table 19.3: Density, as a function of time (ps), for methanolic and ethanolic solutions, before hydrolysis, after hydrolysis but before condensation, and after condensation. All values represent averages over 1 ps.

	Total Energy/kcalmol^{-1}					
Time/ps	H_2O *MeOH* $Si(OMe)_4$	*MeOH* $Si(OH)_4$	H_2O *MeOH* $Si_2O(OH)_6$	H_2O *EtOH* $Si(OEt)_4$	*EtOH* $Si(OH)_4$	H_2O *EtOH* $Si_2O(OH)_6$
100	9,446.9	-33,039	-3,075.2	-11,458	-56,836	-26,773
150	9,386.1	-33,026	-3,020.7	-11,497	-56,882	-26,801
200	9,391.8	-32,978	-3,019.4	-11,438	-56,800	-26,826
250	9,445.4	-33,028	-3,050.2	-11,442	-56,834	-26,832
300	9,460.2	-32,992	-3,008.7	-11,431	-56,804	-26,812
350	9,393.9	-33,007	-3,038.8	-11,432	-56,794	-26,787
400	9,433.8	-33,084	-3,033.6	-11,454	-56,889	-26,812
450	9,430.0	-33,073	-2,986.8	-11,437	-56,894	-26,826
500	9,440.0	-33,066	-3,029.4	-11,488	-56,916	-26,831

Table 19.4: Total energy, as a function of time, for methanolic and ethanolic solutions, before hydrolysis, after hydrolysis but before condensation, and after condensation. All values represent averages over 1 ps.

Density/gcm^{-3}
Total Energy/kcalmol^{-1}

Time/ps	H_2O *MeOH* $Si(OMe)_4$	*MeOH* $Si(OH)_4$	H_2O *MeOH* $Si_2O(OH)_6$	H_2O *EtOH* $Si(OEt)_4$	*EtOH* $Si(OH)_4$	H_2O *EtOH* $Si_2O(OH)_6$
0	0.845	0.866	0.872	0.844	0.848	0.848
	9,523.5	-32,788	-2,901.2	-11,419	-56,599	-26,781
5	0.854	0.862	0.864	0.844	0.850	0.848
	9,522.6	-32,782	-2,927.6	-11,408	-56,623	-26,783
10	0.869	0.875	0.862	0.843	0.851	0.842
	9,477.7	-32,816	-2,980.1	-11,409	-56,599	-26,763

Table 19.5: Density and total energy, after a short run time (ps), for methanolic and ethanolic solutions, before hydrolysis, after hydrolysis but before condensation, and after condensation. All values represent averages over 1 ps.

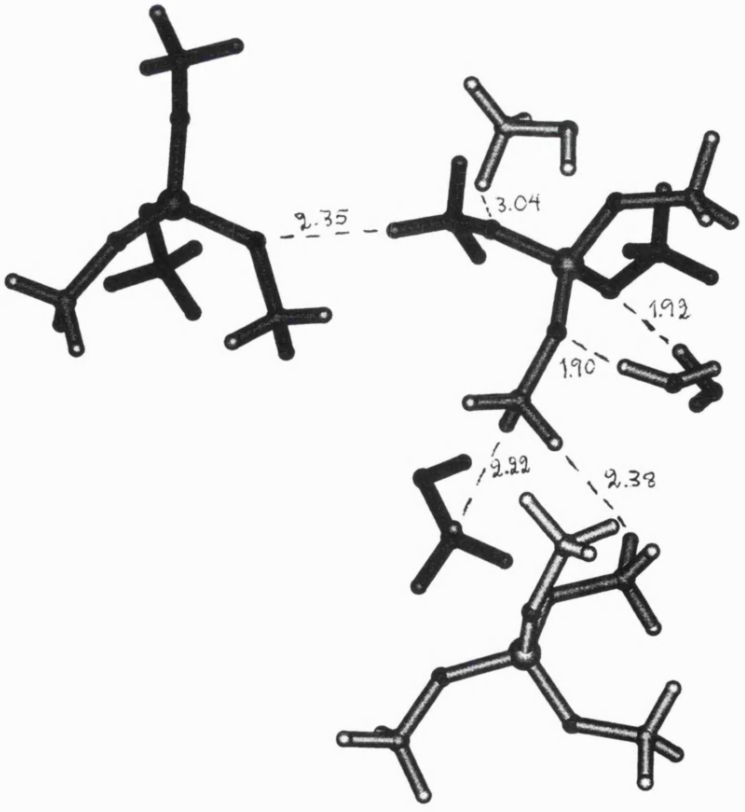


Figure 19.6: Solvation environment around a alkoxide, in a methanolic solution before hydrolysis, showing all clusters at a distance smaller than 2.5 Å.

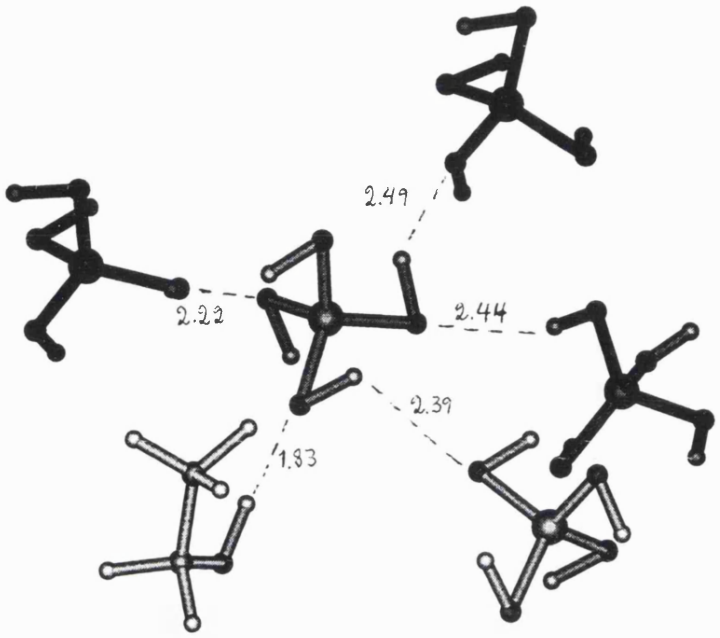


Figure 19.7: Solvation environment around a monomer, in a ethanolic solution between hydrolysis and condensation, showing all clusters at a distance smaller than 2.5 Å.

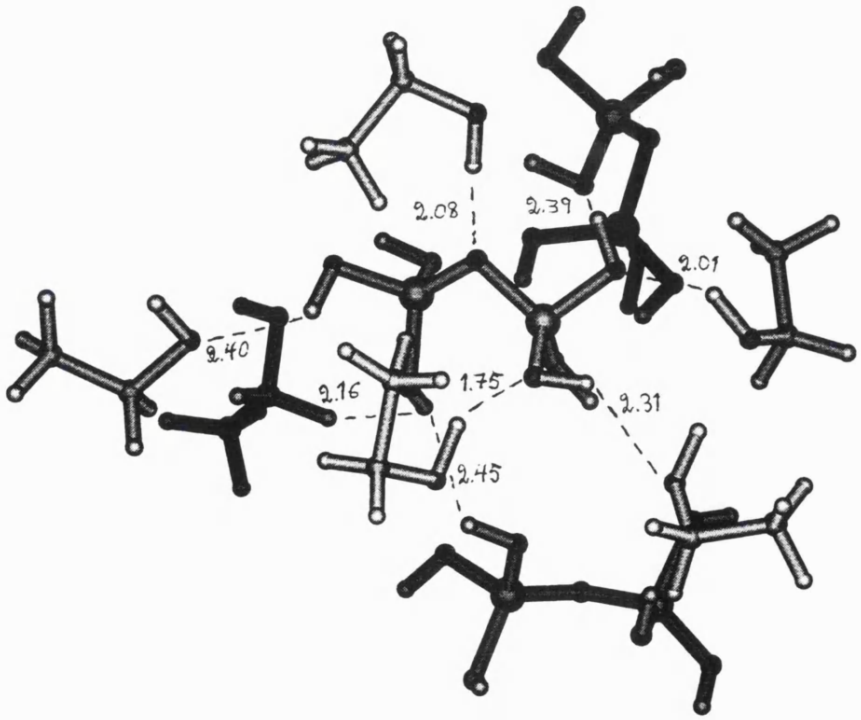


Figure 19.8: Solvation environment around a dimer, in a ethanolic solution after condensation, showing all clusters at a distance smaller than 2.5 Å.

In particular, the monomer surrounded by four other monomers, found in the ethanolic solution, after hydrolysis but before condensation (Figure 19.7), shows that small rings might be formed directly from aggregated monomers.

19.8 Conclusions

The models of liquid solutions studied here aim to be simulations, as closely as possible, of real sol-gel solutions, matching compositions commonly used in experimental work. At the present stage of the global project, chemical reactions cannot be modelled, in these purely classical simulations, so ideal solutions, representing ideal stages of the sol-gel process, have to be considered.

The results obtained show that in all solutions considered, the silicate clusters tend to aggregate after a relatively long time. This aggregation effect confirms entirely the observations made previously for sol-gel solutions simulated with a Coulombic cutoff, group-based, method. As before, the aggregation seems to be more pronounced between larger silicate clusters. The fact that these aggregation effect have been observed with 2 different MD methods, implemented in 2 different codes, for many different solutions, containing various different silicates, is very significant.

This aggregation effect is corroborated by the analysis of the intermolecular radial distribution functions, for the key interactions that govern the forward and reverse reactions. For all solutions studied, the mechanism of diffusion favours always the interactions leading to the forward reactions, which become systematically more important, for long run times, than the interactions leading to the reverse reactions.

These diffusion effects, favouring cluster aggregation and the forward reactions, are crucial to simulate the global sol-gel processes, and constitute therefore a major result of this work. The diffusion times should be longer than observed here, however, because the diffusion coefficients are still too high, as seen before.

Despite these structural changes, no significant variations with time are observed for the energy and density of these solutions. This somewhat surprising result corroborates the observations made before with the Coulombic cutoff, group-based method, for more dilute sol-gel solutions.

The simulation of sol-gel solutions, with compositions used in experimental work, provides also a useful tool for studying the local environment of the silicate clusters in solution, by direct observation of the atomic arrangements around each cluster. In particular, this analysis will prove valuable in the development of potentials, to simulate accurately the competing mechanisms of reaction and solvation that take place in sol-gel solutions. The successful completion of these simulations will provide a firm basis for understanding and controlling these important and exciting systems.

Part V

Final Remarks

Chapter 20

Discussion

20.1 Chemistry of silica in solution

The aim of this project is to understand and simulate the chemistry of silica in solution. Described in this generality, it is the task of a lifetime. The work now presented is thus a first contribution to explore the enormous possibilities of atomistic modelling in the study of these processes. The general approach is to profit from the specific advantages of each technique to investigate the different aspects of the problem.

Ab-initio methods cannot be used to investigate large atomic systems but they provide the means to understand the fundamental atomic features of small aggregates and to obtain atomistic information required by molecular mechanics methods. The latter cannot be used to investigate fundamental atomic properties, but they provide the means to understand the macroscopic behaviour of large systems observed in experimental work. This duality between ab-initio and molecular mechanics methods, establishing a bridge between atomic and macroscopic analysis, is the basis of this project.

The dispute concerning the relative merits of Hartree-Fock and Density Functional methods continues. This discussion can only be fruitful, but the wisest approach is certainly to recognise that both models are important and to apply one or the other according to their relative advantages.

Hartree-Fock calculations have been used to only a limited extension in this work because they proved to be too demanding for computer facilities currently available. Even the relatively small molecules of $Si(OCH_3)_4$ and $Si_2O(OH)_6$ could not be optimised with a 6-31G** basis set. These two Hartree-Fock calculations are vital because they allow us to obtain reference energies for the hydrolysis and condensation reactions, to compare with the DFT results. These, in turn, were obtained using always the same code, with a numerical basis set. It is necessary to repeat also these DFT calculations with different programs and preferentially with Gaussian basis sets, to assess the influence of the method, basis set and program on the final results. When a direct comparison with experimental data is possible, the DFT results, particularly the energy values, prove to be very accurate, in fact more than those from the HF techniques. However, this trend might change for larger clusters, where experimental evidence is not available.

In particular, the exothermic hydrolysis and condensation energies calculated in this work are very small, in contrast with HF results proposed by other authors. Experimentally, a silica-based sol-gel solution warms up significantly in the first minutes, cooling down subsequently to

the ambient temperature. Definitely, further theoretical and experimental evidence is necessary to clarify this point.

To understand the complex mechanisms occurring in sol-gel solutions, it is necessary to know first their isolated constituents. One of the main aims of this project was therefore to study individually the smallest silicate clusters and other molecules and ions present in solution. To make the study feasible yet relevant, a limit of five silicon atoms and two intramolecular condensations was established for the range of clusters analysed. Initially, only LDA calculations with a DN basis set could be undertaken, without raising unrealistically the CPU time required. In the late stages of the work, sophisticated improvements such as the use of non-local DFT, triple basis sets and continuum dielectric environments could be applied already, at least for the smallest silicate clusters.

The results presented in this work for the twenty five silicate clusters studied, corresponding to more than one hundred different conformations analysed, are undoubtedly a significant contribution to a full understanding of these clusters, which requires knowledge of the structure, charge distribution and energy of their most important conformations. Several experimental observations are confirmed and clarified by the ab-initio results obtained in this work, as the superiority of branched over linear clusters, the stability of the trimer ring, a explanation for the easy formation of small rings and the unstability of double rings. Furthermore, part of the vast information thus acquired - the Hirshfeld charges and the *Si-O-C* structural information - has been successfully combined with a standard ab-initio forcefield, playing a key role in the Molecular Dynamics simulations of sol-gel solutions.

However, these results are far from being complete. All clusters with more than 2 silicon atoms have been optimised in the gas-phase only and all clusters with more than 3 silicon atoms have been optimised with a Local Density Approximation only. As the COSMO results for different conformations of the monomer and dimer show, the strong gas-phase intramolecular interactions, like hydrogen-bonds, tend to be partially replaced in a liquid by cluster-solvent interactions. These changes should be particularly important in highly polar solvents, such as the alcohols and water used in sol-gel solutions. As this work and that of other authors show, LDA calculations seriously overestimate the strength of hydrogen bonds, decreasing their bond length and increasing their energy substantially. The combination of gas-phase specificities and LDA limitations is likely to change noticeably the liquid-phase atomic properties of the 3, 4 and 5 silicon clusters discussed in this work. Other authors have also reported an appreciable bias of the molecular grid in the results.

Fortunately, the future is very exciting for these studies. The computational and scientific progress of the last years, together with the experience acquired with this work, provide the basis to extend much further the ab-initio study of the silicate clusters and other molecules involved in sol-gel processes. It is not a dream anymore to study all clusters with a maximum of, say, eight silicon atoms, with non-local DFT, a triple basis set, a fine grid and a COSMO solvation model.

The investigation of the mechanisms of the hydrolysis and condensation reactions is essential to understand and to simulate the corresponding sol-gel processes. These reactions are catalysed by acid or basic conditions, and charged species should therefore be involved in the most favourable mechanisms. As this work shows, the differences between vacuum and solvated ab-initio results increase dramatically for charged species. An ab-initio study in vacuo of a liquid reaction involving charged species leads invariably to incorrect results. The COSMO results show that both hydrolysis and condensation reactions can easily occur in a one-step

transformation, with small activation energies. This agrees with published semi-empirical results and is probably correct, as stable pentacoordinated silicon clusters have been reported before. The COSMO model may represent a satisfactory environment to study these reactions. Secure conclusions cannot, however, be drawn without doing exhaustive tests before. Two-step mechanisms, involving the removal of a OH group and the formation of a tricoordinated silicon cation as intermediate, have not been investigated yet.

Continuum dielectric models are of course not the only or even the best way of describing solvent effects. Clearly they represent a crude approximation to real complex solute-solvent atomic interactions. There are at least three other alternatives. The first and simplest, is to dispose a layer of solvent molecules around the solute molecule and to study this global cluster in vacuum. A natural extension is to use periodic boundary conditions, to take into account not only the short-range but also the medium- and long-range interactions of the solvent with the solute. Of course the CPU time requirements will increase considerably. However, the real difficulties are physical: the energy of a system like this will depend considerably on the position and orientation of the solvents molecules, because the statistical weight is very small. Generating automatically successive different solvent layers (for example, allocating randomly the solvent molecules around the solute with classic MC and optimising the system with ab-initio DFT) and taking the average results will decrease considerably the uncertainty in the energy but the CPU time and the complexity of the treatment will increase considerably. These approaches should work much better in apolar liquids, like CCl_4, where strong, localised, hydrogen-bonds do not exist.

A key physical limitation still persists, however, which cannot be solved by the two approaches depicted above. All ab-initio methods considered so far ignore completely the dynamics of the system. They generate atomic displacements over the hyperdimensional Born-Oppenheimer surface, to reach a minimum or a saddle point, but not the real atomic movements due to the vibrational, rotational and translational modes of the system. These atomic movements, in particular the vibrations, should obviously needed to explain the diffusion and reaction mechanisms occurring in sol-gel processes and indeed in any reactional liquid system. The methods of Carr-Parrinello, where classical molecular dynamics is combined with a quantum mechanical determination of the forces, is probably the most suitable technique to investigate small clusters in solution, particularly with PBC conditions, but at a price, as the CPU times involved are extremely large. Although calculations of this type are probably possible already with LDA, they cannot be afforded with higher ab-initio levels of approximation.

In spite of all their usefulness and potential accuracy, ab-initio methods will never be able to describe the full reality of complex macroscopic systems. However, interatomic potential-based methods, like Molecular Dynamics, Monte Carlo, Lattice Dynamics and Energy Minimisation, are well suited to simulate macroscopic solids, liquids and gases. The empirical potentials, the weak point in these methods, can be obtained either from experimental data (the traditional way) or from ab-initio calculations, which are the more elegant way, because only theoretical data are needed, potentially more systematic and accurate. The interatomic potentials used in this work have all been obtained by ab-initio means only, either from standard forcefields or from our own calculations.

Molecular Dynamics is usually more appealing than the other methods, because it allows the simulation of the atomic trajectories. However, its major advantage is also its major weakness. To simulate properly the fastest vibrational modes and avoid instabilities, extremely small timesteps have to be used, which seriously limit the total simulation time and the phase-space

sampling. Monte Carlo methods, with clever configuration sorting techniques, allow, in principle, a better sampling of the phase-space, but the sampling trajectory itself lacks physical meaning, making it difficult to extract quantitative results from the dynamic aspects of these simulations.

Furthermore, MD and MC simulations, with a charge distribution based on atomic charges only, are far from being satisfactory. The obvious extension of the electrostatic potential development to include higher terms, dipoles, quadrupoles, etc..., is generally too costly, at the moment, because the number of interactions to consider increases rapidly but also because the long-range interactions become even more difficult to calculate. To include charge-dipole and dipole-dipole interactions within the cutoff region used to calculate the real space charge-charge interactions is perhaps a reasonable compromise. Of course, reliable ab-initio data are necessary to feed these extended potentials. The shell model used in Lattice Dynamics provide a easy way to simulate polarisability effects, displacing the shells from the cores. Unfortunately, it involves a time consuming energy minimisation, which can be done in a single-point LD analysis but is very expensive after each timestep of a MD simulation. The description of the charge distribution remains a open question in Molecular Dynamics and Monte Carlo simulations.

Twenty years ago, MD and MC were used to simulate atomic Lennard-Jones liquids, like Ar, Kr and Xe. Today, the ultimate goal of this project is to simulate the diffusion, solvation and reaction mechanisms in complex solutions, in order to reproduce, by realistic MD or MC, the fractal growth observed in experimental sol-gel work. To achieve this, many requirements have to be fulfilled first.

1. *PBC conditions have to be used.* In principle this is straightforward. There is no other solution to describe properly the medium- and long-range interactions present in bulk conditions. For large cell boxes, the distortion in the long-range forces due to the periodic repetition of the central cell should be very small. Every time the image used in a interaction changes, there is a discontinuity in the forces, but these interactions, corresponding to half the cell size, are very small for large cell boxes. A difficulty remains, however. During the silica growth process, new bonds will be formed across the boundaries and the reaction mechanisms should still work in these edge conditions. In principle this is not a problem but needs to be handled carefully.

2. *Atomic-based conditions have to be used.* The group-based method of choosing the side of the cutoff or boundary for whole neutral groups is much faster and avoids the charge effects that can be observed with the atom-based method. However, it is conceptually unsatisfactory because it leads to arbitrary discriminations between the atoms and cannot be reasonably applied in simulations involving chemical reactions, where the individual atoms have to be considered. Furthermore, increasingly larger groups lead rapidly to energy instabilities. The results obtained in this work for simple liquids, with small molecules, without chemical reactions, are very similar for both group-based and atom-based methods. However, with a group-based method, the simulation of liquid TMOS and of the solutions containing trimer rings became unstable and liquid TEOS could not be simulated at all. To decrease the size of the groups is not a solution because they become usually non-neutral. The atom-based criteria avoids all these problems: liquids with large molecules, like TEOS, can be easily simulated and reactions can be described effectively. Effects due to the charge of the atoms make it impossible, however, to use a Coulombic cutoff with this method. Using only a Coulombic cutoff with an atom-based criterion, artificial charge layers tend to be created on the cutoff surface, because longer range interactions are not considered. This distorts completely the simulation and can produce odd resonance oscillations of the whole cell box.

3. *Long-range forces need to be considered.* A Ewald sum proved to be effective avoiding this problem and, for liquids with small molecules, the results obtained are very similar to the ones observed with a Coulombic cut-off, group-based method. From the theoretical point of view, the main problem of the Ewald summation method is the difficulty in calculating the error thus introduced in the simulation. Comparisons between optimised Ewald sum and Coulombic cutoff results, with larger and larger cutoffs, will allow us to clarify the convergence of the two methods. From the practical point of view, the evaluation of the Ewald summation is usually one of the slowest steps in MD simulations.

4. *NPT conditions should be used.* From the theoretical point of view, the microcanonical ensemble is ideal for performing MD or MC simulations and many more tests need to be done under NVE conditions. However, in real life, temperature and pressure are approximately constant but volume and energy are not. To simulate a realistic environment, NPT conditions are required. However, so far there has been no definitive solution for the problem of simulating NPT conditions, in spite of the many methods proposed already. The Berendsen method used throughout this work does not describe properly the fluctuations of the system, but is simple and reliable, and therefore very convenient for all the test work. The results of this work show that with these conditions it is possible to simulate accurately the structure and internal energy of a liquid, its density, radial distribution functions and enthalpy of vaporisation, for a wide range of temperatures and pressure. This is fundamental to simulate the experimental sol-gel conditions and to study the influence of pressure and temperature on the final structure of the gel.

To replace the Berendsen algorithm by a Parrinello-Rahman, Nose-Hoover or other more accurate NPT algorithm may be necessary in future work. However, these methods have also two degrees of freedom, which can control pressure and temperature fluctuations. The theory of Molecular Mechanics simulations in NPT conditions needs to be clarified and probably improved. Ideally, the same algorithms, with minor alterations, should be applied in both MD and MC simulations.

5. *The same simulation parameters should be used in all conditions.* This is essential if we are to simulate a wide range of solutions and thermodynamic conditions occurring in sol-gel processes, without optimising each time the parameters, which might not even be possible. During the simulation of the silica growth, the composition of the solution changes continuously and because the chemical reactions involve liberation or consumption of energy, the temperature changes also continuously during the process.

The results obtained in this work, with both the Coulombic cutoff, group-based method and the Ewald sum, atom-based method, show that it is possible to achieve a good agreement with the experimental evidence, for very different temperatures, pressures and types of liquids, using always the same algorithm and parameters, such as relaxation times and long-range cutoffs. In particular, it was shown that the same Ewald sum parameters can be used in liquids as different as water or TEOS, at 20°C or 169°C, at 1 atm or 10,000 atm. These are major results, extremely important for the future of this project and of MD and MC in liquids in general.

6. *The potentials should be obtained in a automatic way and to be valid in all conditions*- obviously a challenging and very difficult task. To develop an extremely accurate potential, with many adjustable parameters, which can be used only to describe a specific situation, might help to solve a difficult technological problem but is unlikely to contribute to increase the overall scientific understanding. It is not possible to simulate the complex, continuously changing, sol-gel solutions applying different specific potentials for each individual system.

This work shows that it is possible to develop general potentials which are able to describe a wide range of thermodynamic conditions and chemical environments, with a reasonable accuracy. The Van der Waals potentials describing the hydrogen atoms in methanol at 10,000 atm and in TEOS at 169°C are the same. The charges describing water at ambient conditions and high temperature or pressure are the same and obtained exactly in the same way as the charges used to describe TEOS in those conditions. Although these results are of considerable use, they need further improvement, however, as significant inaccuracies are still present (the second peak of g_{OO} in water is at too large a distance, the enthalpies of vaporisation of TMOS and TEOS, the diffusion coefficients and the specific heats are all too high).

7. *The liquid dynamics have to be accurately described.* The most important aspect in a MD simulation of a liquid solution is to model accurately the movements of all its constituents. However, to simulate the dynamics of a liquid is more difficult than to simulate its structure.

The dynamic description obtained so far for the pure liquids is not entirely satisfactory because the diffusion coefficients are too high, and the same happens certainly in the sol-gel solutions. Consequently, the dynamical conditions of these liquids correspond to temperatures that are much higher than the real one and the diffusion times are shorter than they are in reality. To improve the dynamic aspects of the liquid simulations is one of the major tasks for future work in this field.

8. *The initial configuration should not be important.* Sol-gel solutions are formed initially by at least four components and their complexity increases even more as the hydrolysis and condensation reactions take place. To simulate these solutions, by MD or MC, a endless number of initial configurations can therefore be proposed and it is essential to guarantee that the results obtained are independent of the way the simulation starts.

The results presented here show that even for initial configurations with the various components completely separated, mixing is effective after a relatively short equilibration time, that can be handled in MD or MC simulations. The energy and structural data, like RDFs, are even less affected by the mixing conditions. Initial configurations with the components completely separated are actually very close to the real starting conditions in sol-gel processes where the liquids are added to each other. The first step in a sol-gel process is always the mixture of the various components and future realistic simulations might need to take this into account.

9. *The reactions should have a small activation energy.* In conventional equilibrium molecular dynamics, where the atom velocities are expected to follow a normal distribution, a transformation requiring a high activation energy is unlikely to occur, except at very high temperatures. Fortunately, the results obtained in this work and by other authors show that both hydrolysis and condensation reactions can occur via a one-step transformation with a small activation energy. This result is vital for the continuation of the whole project, as these are the ideal conditions to simulate chemical reactions by classical molecular dynamics or Monte Carlo techniques. A simulation of a two-step mechanism poses severe problems related to solvation, diffusion and charge neutrality which do not exist or can be minimised in a purely local, one-step mechanism.

10. *The simulation has to reproduce the clusters aggregation.* To simulate the silica growth in sol-gel processes it is not enough to guarantee that the reactions involved can be modelled. The clusters cannot react unless they interact with each other. The model has to be able to simulate the aggregation of the silicate clusters, even in dilute sol-gel solutions.

The results obtained in this work with the Coulombic cutoff, group-based method for dilute solutions and with the Ewald sum, atom-based method for real solutions show that indeed this is the case. What is more, time seems to favour the forward sol-gel reactions. These results

provide fundamental information necessary to simulate silica growth in solution and are a great encouragement for the future of the whole project.

11. *A realistic potential is needed to simulate accurately the reactions.* The fulfillment of all conditions listed so far is indispensable to simulate silica-based sol-gel processes by classical methods. This work has shown that all these conditions can be satisfied. However, the most exciting part is still to be done: To develop a potential suitable to simulate, in a realistic way, the hydrolysis and condensation reactions, including catalysis effects.

One of the key aspects to consider is the charge distribution. The same atom has different charges in different molecules and consequently the charges have to change progressively during the reactions. The charges cannot be constant anymore; they have to be a function of the chemical environment. But the requirement for charge neutrality makes it very hard to treat charge alterations at a local level. To simulate chemical reactions, in a realistic way, using MD or MC techniques, all atomic charges have to change every timestep. These dynamic potentials will make simulations slower and perhaps more unstable, but do not introduce any further conceptual difficulty.

Another important aspect to consider are the transferences of energy occurring in reacting systems. The reaction potentials have to describe, step by step, the evolution of the potential energy (and charge distribution and structure) from the reactants to the products. Because hydrolysis and condensation reactions are both exothermic, the temperature rises in the beginning to decrease later on, due to the laboratory thermal reservoir. The reaction potentials have therefore to describe the conversion of chemical energy into kinetic energy, whereas the thermostat has to regulate the transference of kinetic energy into heat transfered to the outside.

The forcefield used in this work describes bond lengths and bond angles potentials in terms of fourth-power developments of the potential function around the equilibrium positions. In a reacting liquid, these have to be replaced by more realistic descriptions, that allow the bonds to break, like Morse potentials. These alterations should not affect in any essential way the results obtained in this work for densities, RDFs, enthalpies of vaporisation, Ewald sum parameters, which depend essentially on the partial charges and Van der Waals parameters used.

The potentials used so far in this work, involve a maximum of four atoms, to describe dihedral interactions. Assuming that both hydrolysis and condensation reactions can occur in a simple one-step mechanism, as the results obtained in this work seem to show, a minimum of six atoms is likely to be involved in the reaction potentials: a silicon, the four oxygens attached to it and the attacking oxygen. Clearly, the success of the attack depends very much on the number and position of the oxygens formerly attached to the silicon. Less than four makes the attack extremely probable, while more than four makes it extremely difficult.

Needless to say, the potentials have to describe simultaneously forward and reverse reactions. Although different mechanisms may be considered for each direction, it seems very reasonable, at least to a first approximation, to treat forward and reverse reactions in exactly the same way, as reversible transformations, for the sake of simplicity.

12. *Large size simulations are required.* All MD simulations done so far in this project have been consecrated to the development of new methodologies, to obtain potentials and to test the conditions necessary to simulate silica-based sol-gel processes, in a realistic way. Consequently, less than 5,000 atoms have been used in all these simulations, which is considered enough to get accurate conclusions.

However, to simulate the silica growth occurring in sol-gel processes, much larger simulations are required. For typical ethanolic sol-gel solutions, as the ones studied in this work, there are

30 silicons in a total of 3510 atoms. To simulate the silica fractal growth, a minimum of, say, 200 silicon atoms is required, corresponding, for the same composition, to 23,400 atoms in a simulation cell with less than 70 Å of length. These simulations are feasible today. More ambitious simulations, containing about 2000 silicon atoms in a total of 234,000 atoms, in a cell with more than 140 Å of length, requiring very large memory and CPU time, can be expected to be possible in the future.

Methanolic solutions are easier to simulate, although less used in practise (due to the toxicity of methanol), as a consequence of which there is less experimental data with which to compare. More concentrated solutions should also be considered, limited only by the water-alkoxide immiscibility. However, before trying such large simulations, size effects have to be studied carefully, even if important alterations have not been detected in preliminary tests carried out in this work and by other authors.

13. *Extremely long simulation times are required.* The most difficult problem faced by the simulation of the silica growth in solution is, however, the huge difference between the characteristic times of sol-gel processes and atomistic simulation methods. Typical silica-based sol-gel solutions, for instance, can take hours or even days before reaching the gel point, but the corresponding MD simulations have to be done with a timestep not larger, probably smaller, than one femtosecond. Consequently, simulations of several seconds, not to say hours, are impossible.

The solution lies in the fact that, like the simulation time, the portion of solution to be simulated is also very small. Simulated solutions, like the ones above discussed, with about $10^4 - 10^5$ atoms, are $10^{19} - 10^{18}$ smaller in volume than a real solution, typically with a Avogadro number of atoms. The length dimensions of the simulation cell are therefore 10^6 times smaller than the dimensions of a real dimension. Admitting, to a first approximation, that the silica growth progresses steadly with time along each direction, a continuous solid phase across the simulation cell is likely to occur after a time 10^6 smaller than the gel-time observed in real solutions. If the real gel-time is reached in 10^4 s, the gel-time for the small simulated cell should occur in about 10^{-2} s. If the sol-gel conditions are pushed to accelerate the reaction process, increasing the silicon concentration, decreasing the pH, if necessary increasing the temperature, the real gel-time can certainly be of the order of 10^2 s. Consequently, the gel-time in the simulation cell will be about 10^{-4} s, which is thus the shortest time in which a continuous silica skeleton can be expected to be formed, traversing the simulation cell from one side to the other. To follow the complete gelification of the simulation cell, it will be necessary then to run solutions with 20,000 to 200,000 atoms for 10^{11} fs, a time 10^5 longer than the longest simulations carried out during this work, for systems with less than 5,000 atoms.

Technically speaking, simulations of this size are not possible today, and they are so hugely expensive that even with the predictable evolution in computer technology it is unlikely that they will be done in the near future. In any circumstances, it is not reasonable to try these simulations before having a really good model description of the basic phenomena occurring in solution. In the next few years this project should aim to simulate more and more accurately the growth of aggregates with, say, ten or twenty silicon atoms, but not more.

14. *Evaporation effects should be considered.* The alcohol and water evaporation that takes place during the long reaction time has not been considered so far, because is is difficult to simulate and is not essential to understand the chemical transformations occurring before the gel point. However, these mass transfer effects should considerably influence the microstructure of the dried gel and consequently its optical and mechanical properties. A possible solution is to implement 2D simulations, using the third dimension to simulate the liquid-gas equilibrium

and allowing the molecules to escape through the interface.

This work is the first contribution to the whole project of simulating the chemistry of silica in solution. As more it is known about these processes, better simulations can be prepared and consequently more can be learnt from them. Atomistic modelling is in rapid evolution and that is apparent in every chapter of this work. Non-local exchange and correlation energies in DFT and Ewald sum in MD became available only during the course of the work and the COSMO model and Nose-Parrinnelo NPT algorithms almost towards the end of it. The computing capacity available increased more than 20 times in the last three years.

This evolution promises to continue in the future. Is is very important therefore to explore new possibilities, to develop new and ambitious methodologies, that will work when more computer power will be available. We need to explore the present but it is even more important to prepare the future.

Several research topics should be considered or given more importance in the future of the project. Ab-initio calculations of the vibrational and electronic spectra for small molecules provide extremely important information, which can be compared with experimental spectroscopic data, when available. The influence of the MD relaxation times and the DF numerical grids should be investigated. We need to increase the diversity and quality of the experimental data available to compare with our theoretical results.

Free energy calculations are essential to have a quantitative description of the thermodynamics of many-particle systems, but in spite of the many methods proposed so far, it remains a open question, because the results are very sensitive to the phase-space sampling. Definitely, the accurate calculation of differences of free energy by MD or MC simulations is one of the most important challenges for atomistic modelling in the future.

The establishment of a bridge between liquid and crystal treatments is another challenge left for the future. Although the structure of crystals like alpha- and beta-quartz, alpha- and beta-cristobalite and beta-trydimite, can be reasonably described by Lattice Dynamics and Energy Minimisation techniques, by applying the same potentials and methodology used in liquids, the elastic and dielectric constants do not match the superior results obtained with the shell model and much simpler Buckingham potentials.

20.2 Atomistic modelling

Modern atomistic modelling, with its revolutionary approach to the investigation of physical and chemical sciences, is now twenty years old. During this time the progress has been tremendous, due to the rapid development of computer hardware and software, but also due to the enormous effort in developing new modelling techniques and better sets of atomic basis and interaction potentials, allowing us to tackle a ever growing range of more difficult problems with better accuracies. While experimentation aims to discover Nature interacting directly with it, modelling aims to understand Nature by imitating it in an ideal laboratory - the computer.

Every result in computer modelling can always be repeated and analysed in a completely quantitative basis, without any uncertainty (though sometimes it is difficult to estimate the corresponding accuracy). Atomistic modelling can also play an important role in the education of physical-chemical sciences, because the theoretical concepts relating to these disciplines can be seen working together, in practise. Atomistic modelling is so recent, however, that several problems still remain, which urge to solve in order to guarantee its general acceptance and

application.

To write a sophisticated atomistic modelling code is to develop a piece of high technology. The ultimate task of writing the code is actually the less difficult part of the job. What is really demanding is to develop the theoretical and numerical algorithms and to design the general lay-out of the program, including effective input/output interfaces. A good lay-out means a program that is easy to read, where the information is exchanged efficiently, and flexible enough to allow easy alterations and incorporation of new modules.

Usually, this task is accomplished by large teams, with different persons working simultaneously on different parts of the code and preparing successively new code releases. Experience shows that this approach is far from ideal. The most important sources of bugs in large atomistic modelling codes are probably lack of communication between different programmers and late modifications to the program.

Ideally, the study of the algorithms and the design of the lay-out should be completed in every detail, including the names of the variables and routines, before writing a single line of code. This approach aims to minimise the work of code writing, isolating it as much as possible from the scientific aspects of the program. Therefore, while the algorithms and the lay-out may have to be developed by a large research group, the code itself can be written by a single programmer. A program developed in this way can incorporate the most modern science, that can be provided only by a large research group, and the homogeneity and uniformity of style that can be provided only by a single code writer.

This strategy in software development is rarely applied in practise, due to the pressure to produce visible results (the code), as soon as possible. The universities and similar research institutions are the right place to develop long term projects in software development. Unfortunately, perhaps because writing software is such a new activity, it tends to be considered as technical instead of scientific work. Modern universities tend to praise mainly the publication of scientific papers, which contributes to explain why many of the major advances in software in the last 30 years have been done in the commercial sector. In a world where each aspect of life is more and more controlled by software, it would be desirable if Universities could encourage more its development.

A key aspect to ensure the scientific credibility of atomistic modelling is to guarantee the correctness of the results produced by the increasing range of programs available. Atomistic modelling is particularly sensitive to this question because, in last instance, only the right application of hundreds of theoretical models and numerical methods and the right implementation of tens of thousands of lines of code can guarantee the accuracy of the final results. Every program has to be checked in full detail, but ultimately, the final test is to investigate how it behaves with real problems previously studied by other programs.

To ensure a fast and reliable validation of atomistic modelling software, a set of well known scientific problems should be defined as standard tests that every program should pass before being considered reliable and good for scientific purposes. These tests, designed to help both the programmer and the user, should cover a range of scientific areas and conditions as wide as possible. Articles based in unvalidated software should be refused. Currently, each paper based on a given code is cross-examined by usually two referees, but none checks the ultimate source of the information contained in these papers - the code. The examination of programs by referees could be very similar to the current examination of papers for publication, in a way designed to be as simple and rapid as possible.

Because atomistic modelling is so recent, the codes currently available, written by scientists,

seldom by programmers, are essentially concerned with the correct application of the scientific algorithms. In the future, it will be very important to define worldwide standards, for both input and output files, in order to maximise efficiency and reliability. As less time is wasted with programming problems, like compatibility between programs or operating systems, more time (and more tools) are left to study real scientific problems. In particular, in a world made smaller by fast communications, contacts between different research groups, using different computers and codes, can be expected to increase substantially, with obvious advantages for atomistic modelling and science in general.

This problem is particularly important for molecular mechanics codes, where the number of atoms involved is usually very large, requiring often large input files. The comparison of the results produced by different codes, using the same data, becomes an extremely costly operation, which is usually avoided, this way discarding the best chance of spotting algorithm errors and learning from the different results produced by different methods. Additionally, the conversion of large but not repetitive amounts of information (which are therefore difficult to handle by a program) from a format to another, often involving the recalculation of the data, as is the case in the conversion of classical forcefields, is clearly a potential source of appreciable data errors, with far-reaching consequences. The output information should also be written in a standard way, to take advantage of the large range of data processing software currently available to produce graphs, pictures and build molecules.

To find a suitable standard is not an easy task, mainly because a bad one would be much worse than none at all. In a permanently changing environment like scientific research, these standard specifications have to be extremely flexible. In particular, they have to support completely new techniques and data structures that might be proposed in the future. Such a degree of flexibility can only be achieved by creating a command language, to be used simultaneously in ab initio, molecular mechanics and other kinds of atomistic modelling techniques. A standard control language and standard formats for input and output data, would help enormously the programmers to prepare the codes and the users to prepare the files.

Currently, most molecular mechanics codes accept only a predefined set of potential functions. In the future, it will be important to allow the user to define his own functions, perhaps as combinations of simple functions linked by simple algebraic operations. Equivalence tables relating different atom types are very important to avoid unnecessary repetitions and to increase the program utilisation flexibility. Equivalence tables might be useful also in describing atoms of the same element with slightly different atomic basis functions. A code should always be regarded as part of a system, which also includes the documentation produced to help using and modifying it. Unfortunately, even in commercial packages, the quality of the manuals is relatively poor. A lot more needs to be done in this field in the future.

Important points to clarify are the commercial aspects related to the development of atomistic modelling software. Currently, many of the codes used by the scientific community are controlled by commercial enterprises, that developed or bought them, from the universities. These enterprises played an important role in the worldwide dissemination of atomistic modelling, particularly among the powerful chemical and materials industries. These enterprises helped to establish the basis of atomistic modelling, but they may constraint its development in the future.

To keep control of the code, avoiding its parallel distribution and development, some enterprises supply the executable but not the source code. It is not possible therefore to study the code, to learn with it, to check its correctness, and to change it. One of the main advantages of

atomistic modelling, the capacity to do research in a completely controlled environment, where everything can be analysed, repeated and altered, is therefore lost and the ideal laboratory transformed into a black box. Software houses should be strongly encouraged to supply their source codes.

Even when the source code is accessible, the details of the scientific algorithms and the numerical tricks used to speed up the calculations are not clarified, for commercial reasons. The earnings of these software houses is primarily from big companies, not from the universities. Consequently their research and development work is primarily directed to fulfill the requirements of these customers, which are essentially interested in creating new products and improving their quality. It would be desirable if the universities could invest more in software development, to produce state-of-the art programs to compete with the commercial packages and boost the interest in computer modelling among the scientific community.

In practise, the progress of atomistic modelling will depend directly on the technological evolution in hardware and software. New architectures, processors, compilers and operating systems will shape the future of computing sciences. In particular, they will clarify key options currently under discussion in large scientific projects, between mainframes and workstation networks and between serial and parallel processing. Languages such as C++ and LISP are likely to play an increasing role in atomistic modelling, in writing efficient scientific code and flexible input interfaces. Small increases in CPU time due to the increased complexity of the input interface are completely negligible when compared with the CPU time required for calculations.

Mainframes usually mean more security, easier maintenance, more memory available, and generally speaking, a more efficient utilization of the computing resources. In compensation, workstations are more flexible, have optimised graphic interfaces and generally speaking run much better software. In the last ten years, the gap between personal computers and workstations essentially disappeared and the gap between workstations and mainframes has been considerably reduced. Medium size jobs, particularly molecular mechanics applications, will run efficiently on personal workstations in the next future. However, scientific ambition will increase proportionately to computing power and large scientific calculations will demand ever increasing amounts of expensive memory, a key advantage of mainframes over workstations. Supercomputers are a completely different matter. They require highly sophisticated maintenance, and because they are so costly, their access requires considerable organisation. These state-of-the art computers should be used only in the most demanding calculations, which cannot be done on a mainframe.

In spite of the past frustrating experiences with parallel processing, it will certainly have an ever increasing role in the future. The incredible progress in serial hardware observed in the last twenty years cannot continue forever and parallel processing is the only solution to increase computing power substantially. However, the tremendous difficulties of parallel software have transformed this beautifully simple concept in one of the most thrilling technological challenges for the next century.

Finally, atomistic modelling needs to be teached. Certainly it deserves a place in courses of physical-chemical sciences. More important, it is necessary to prepare books, describing the various aspects of theory, exemplified by full pieces of real code, in the good tradition of classic books as *Numerical Recipes in C* and *Operating Systems, Design and Implementation.* Such work, covering ab-initio, molecular mechanics and other mixed methods, written by leading experts, would certainly boost the interest in atomistic modelling, and would help it occupying its proper place in modern science.

Bibliography

[1] *International Critical Tables*, 1st ed., vol. III and V. 1928.

[2] *Macmillan's Chemical and Physical Data.* Macmillan Press Ltd., 1992.

[3] *Handbook of Chemistry and Physics.* CRC Press, 1994.

[4] *Silicon, Germanium, Tin and Lead Compounds, Metal Alkoxides, Diketonates and Carboxylates: A Survey of Properties and Chemistry.* Gelest Inc., ABCR GmbH + Co., 1995.

[5] *Discover manual.* Molecular Simulations Inc., 1996.

[6] *Dmol manual.* Molecular Simulations Inc., 1996.

[7] ADAMS, D. J. On the Use of the Ewald Summation in Computer Simulation. *J. Chem. Phys. 78*, 5 (1983), 2585.

[8] AHLRICHS, R., BÄR, M., AND HÄSER, M. Nonempirical direct SCF calculations on sodalite and double six-ring models of SiO_2 and $AlPO_4$ minerals: $H_{24}Si_{24}O_{60}$, $H_{12}Si_{12}O_{30}$, $H_{12}Al_6P_6O_{30}$. *Chemical Physics Letters 164*, 2-3 (1989), 199.

[9] ALDER, B. J., AND WAINWRIGHT, T. E. Phase Transition for a Hard Sphere System. *J. Chem. Phys. 27* (1957), 1208.

[10] ALDER, B. J., AND WAINWRIGHT, T. E. Studies in Molecular Dynamics. I. General Method. *J. Chem. Phys. 31*, 2 (1959), 459.

[11] ALLEN, M. P., AND TILDESLEY, D. J. *Computer Simulation of Liquids.* Oxford Science Publications, 1987.

[12] ALTMANN, J. A. A Study of the Perfomance of Numerical Basis Sets in DFT Calculations on Sulfur-containing Molecules. preprint, 1994.

[13] ANDERSEN, H. C. Molecular Dynamics Simulations at Constant Pressure and/or Temperature. *J. Chem. Phys. 72*, 4 (1980), 2384.

[14] ANDREA, T. A., SWOPE, W. C., AND ANDERSEN, H. C. The Role of Long Ranged Forces in Determining the Structure and Properties of Liquid Water. *J. Chem. Phys. 79*, 9 (1983), 4576.

[15] ANDZELM, J., AND KÖLMEL, C. Incorporation of solvent effects into density functional calculations of molecular energies and geometries. *J. Chem. Phys. 103*, 21 (1995), 9312.

[16] ANDZELM, J., AND WIMMER, E. Density Functional Gaussian-type-orbital approach to Molecular Geometries, Vibrations and Reaction Energies. *J. Chem. Phys. 96*, 2 (1992), 1280.

[17] ARTAKI, I., BRADLEY, M., ZERDA, T. W., JONAS, J., ORCEL, G., AND HENCH, L. L. NMR, Raman Study of the Effect of Formamide on the Sol-Gel Process. In *Science of Ceramic Chemical Processing*, L. L. Hench and D. R. Ulrich, Eds. John Wiley & Sons, Inc., 1986, ch. 6, p. 73.

[18] ASSINK, R. A., AND KAY, B. D. Sol-Gel Kinetcis: III. Test of the Statistical Reaction Model. *Journal of Non-Crystalline Solids 107* (1988), 35.

[19] ASSINK, R. A., AND KAY, B. D. Sol-Gel Kinetics: ^{29}Si NMR and a Statistical Reaction Model. In *Better Ceramics Through Chemistry III*, C. J. Brinker, D. E. Clark, and D. R. Ulrich, Eds., vol. 121 of *Materials Research Society.* Elsevier Science Publishing Co., Inc., 1988, p. 25.

[20] ASSINK, R. A., AND KAY, B. D. Sol-Gel Kinetics: I. Functional Group Kinetics. *Journal of Non-Crystalline Solids 99* (1988), 359.

[21] AVNIR, D. Fractal Aspects of Surface Science-An Interim Report. In *Better Ceramics Through Chemistry II*, C. J. Brinker, D. E. Clark, and D. R. Ulrich, Eds., vol. 73 of *Materials Research Society.* Elsevier Science Publishing Co., Inc., 1986, p. 321.

[22] BAKER, J. An Algorithm for the Location of Transition States. *Journal of Computational Chemistry 7*, 4 (1986), 385.

[23] BAKER, J. Geometry Optimization in Cartesian Coordinates: Constrained Optimization. *Journal of Computational Chemistry 13*, 2 (1992), 240.

[24] BAKER, J. Techniques for Geometry Optimization: A Comparison of Cartesian and Natural Internal Coordinates. *Journal of Computational Chemistry 14*, 9 (1993), 1085.

[25] BAKER, J., AND BERGERON, D. Constrained Optimization in Cartesian Coordinates. *Journal of Computational Chemistry 14*, 11 (1993), 1339.

[26] BAKER, J., AND HEHRE, W. J. Geometry Optimization in Cartesian Coordinates: The End of the Z-Matrix? *Journal of Computational Chemistry 12*, 5 (1991), 606.

[27] BALFE, C. A., AND MARTINEZ, S. L. Studies of the Initial Steps in Sol-Gel Processing of $Si(OR)_4$: ^{29}Si NMR of Alkoxysilane and Alkoxysiloxane Solutions. In *Better Ceramics Through Chemistry II*, C. J. Brinker, D. E. Clark, and D. R. Ulrich, Eds., vol. 73 of *Materials Research Society.* Elsevier Science Publishing Co., Inc., 1986, p. 27.

[28] BARKER, J. A., AND WATTS, R. O. Structure of Water: A Monte Carlo Calculation. *Chemical Physics Letters 3*, 3 (1969), 144.

[29] BECKE, A. D. Density-Functional Exchange Energy Approximation with Correct Asymptotic Behavior. *Physical Review A 38*, 6 (1988), 3098.

[30] BECKE, A. D. A Multicenter Numerical Integration Scheme for Polyatomic Molecules. *J. Chem. Phys. 88*, 4 (1988), 2547.

[31] BEEMAN, D. Some Multistep Methods for Use in Molecular Dynamics Calculations. *Journal of Computational Physics 20* (1976), 130.

[32] BELL, R. L., AND TRUONG, T. N. Direct Ab Initio Dynamics Studies of Proton Transfer in Hydrogen-Bond Systems. *J. Chem. Phys. 101*, 12 (1994), 10442.

[33] BERENDSEN, H. J. C., GRIGERA, J. R., AND STAATSMA, T. P. The Missing Term in Effective Pair Potentials. *J. Phys. C: Solid State Phys. 91* (1987), 6269.

[34] BERENDSEN, H. J. C., POSTMA, J. P. M., VAN GUNSTEREN, W. F., DINOLA, A., AND HAAK, J. R. Molecular Dynamics with Coupling to an External Bath. *J. Chem. Phys. 81*, 8 (1984), 3684.

[35] BERENDSEN, H. J. C., AND VAN GUNSTEREN, W. F. Molecular Dynamics Simulations: Techniques and Approaches. In *Molecular Liquids, Dynamics and Interaction*, A. J. Barnes, W. J. Orville-Thomas, and J. Yarwood, Eds., C135. NATO ASI Series, Reidel, 1984, p. 475.

[36] BLEIBER, A., AND SAUER, J. The vibrational frequency of the donor *OH* group in the H-bonded dimers of water, methanol and silanol. Ab initio calculations including anharmonicities. *Chemical Physics Letters 238* (1995), 243.

[37] BOGUSH, G. H., DICKSTEIN, G. L., C.), P. L. K., AND C. F. ZUKOSKI, I. Studies of the Hydrolysis and Polymerization of Silicon Alkoxides in Basic Alcohol Solutions. In *Better Ceramics Through Chemistry III*, C. J. Brinker, D. E. Clark, and D. R. Ulrich, Eds., vol. 121 of *Materials Research Society*. Elsevier Science Publishing Co., Inc., 1988, p. 57.

[38] BORNHAUSER, P., AND CALZAFERRI, G. Normal coordinate analysis of $H_8Si_8O_{12}$. *Spectrochimica Acta 46A*, 7 (1990), 1045.

[39] BRADLEY, D. C. Chemistry and Reactions of Metal Alkoxides. In *Ultrastructure Processing of Advanced Materials*, D. R. Uhlmann and D. R. Ulrich, Eds. John Wiley & Sons, Inc., 1992, ch. 1, p. 3.

[40] BRAND, H. V., CURTISS, L. A., AND ITON, L. E. Computational Studies of Acid Sites in ZSM-5: Dependence on Cluster Size. *J. Phys. C: Solid State Phys. 96* (1992), 7725.

[41] BRINKER, C. J. Hydrolysis and Condensation of Silicates: Effects on Structure. In *Fourth International Workshop on Glasses and Glass Ceramics from Gels*, S. Sakka, Ed., vol. 100 of *Journal of Non-Crystalline Solids*. North-Holland Publishing Company, 1988, p. 31.

[42] BRINKER, C. J., AND SCHERER, G. W. *Sol-Gel Science: The Physics and Chemistry of Sol-Gel Processing*. Academic Press, Inc., 1989.

[43] BRODHOLT, J., AND WOOD, B. Simulations of the Structure and Thermodynamic Properties of Water at High Pressures and Temperatures. *Journal of Geophysical Research 98*, B1 (1993), 519.

[44] BURGGRAF, L. W., AND DAVIS, L. P. A Theoretical Study of Silanol Polymerization. In *Better Ceramics Through Chemistry II*, C. J. Brinker, D. E. Clark, and D. R. Ulrich, Eds., vol. 73 of *Materials Research Society*. Elsevier Science Publishing Co., Inc., 1986, p. 529.

[45] BURGGRAF, L. W., DAVIS, L. P., AND GORDON, M. S. Neutral and Anionic Hypervalent Silicon Complexes in Silanol Polymerization. In *Ultrastructure Processing of Advanced Materials*, D. R. Uhlmann and D. R. Ulrich, Eds. John Wiley & Sons, Inc., 1992, ch. 4, p. 47.

[46] BUTHER, I. S., AND HARROD, J. F. *Inorganic Chemistry Principles and Applications*. The Benjamin Publishing Company, 1989.

[47] CALVERT, P. Biomimetic Processing of Ceramics and Composites. In *Ultrastructure Processing of Advanced Materials*, D. R. Uhlmann and D. R. Ulrich, Eds. John Wiley & Sons, Inc., 1992, ch. 14, p. 149.

[48] CAR, R., AND PARRINELLO, M. Unified Approach for Molecular Dynamics and Density-Functional Theory. *Physical Review Letters 55*, 22 (1985), 2471.

[49] CASULLERAS, J., AND GUARDIA, E. Computer Simulations of Liquid Methanol II. System Size Effects. *Molecular Simulation 8* (1992), 273.

[50] CATLOW, C. R. A., AND FREEMAN, C. M. Computers, Molecules and Materials. *Royal Institution Proceedings 63* (1991), 57.

[51] CATLOW, C. R. A., GEORGE, A. R., AND FREEMAN, C. M. Ab-initio and molecular-mechanics studies of aluminosilicate fragments, and the origin of Lowenstein's rule. preprint.

[52] CATLOW, C. R. A., GEORGE, A. R., PEREIRA, J. C., AND FREEMAN, C. M. Ab-initio and molecular mechanics studies of silica fragments. preprint.

[53] CATLOW, C. R. A., AND NORGETT, M. J. Lattice Structure and Stability of Ionic Materials. Private memorandum, 1976.

[54] CHAPUT, F., BOILOT, J. P., DEVREUX, F., BRUN, M. C. A., AND GEORGES, P. Des Gels Pour Í Optique. *Pour la Science*, 191 (September 1993), 46.

[55] CHARACTERIZATION OF PRECURSORS TO CHEMICALLY DERIVED CERAMICS, N. J. D. Basil and C-C. Lin. In *Better Ceramics Through Chemistry III*, C. J. Brinker, D. E. Clark, and D. R. Ulrich, Eds., vol. 121 of *Materials Research Society*. Elsevier Science Publishing Co., Inc., 1988, p. 49.

[56] CHELIKOWSKY, J. R., H. E. KING, J., AND GLINNEMANN, J. Interatomic Potentials and the Structural Properties of Silicon Dioxide Under Pressure. *Physical Review B 41*, 15 (1990), 10866.

[57] CHIALVO, A. A., AND DEBENEDETTI, P. G. An Automated Verlet Neighbor List Algorithm with a Multiple Time-Step Approach for the Simulation of Large Systems. *Computer Physics Communications 70* (1992), 467.

[58] COLTRAIN, B. K., MELPOLDER, S. M., AND SALVA, J. M. Effect of Hydrogen Ion Concentration on Gelation of Tetrafunctional Silicate Sol-Gel Systems. In *Ultrastructure Processing of Advanced Materials*, D. R. Uhlmann and D. R. Ulrich, Eds. John Wiley & Sons, Inc., 1992, ch. 6, p. 69.

[59] DAMRAUER, R., BURGGRAF, L. W., DAVIS, L. P., AND GORDON, M. S. Gas-Phase and Computational Studies of Pentacoordinate Silicon. *J. Am. Chem. Soc. 110*, 20 (1988), 6601.

[60] DAVIS, L. P., AND BURGGRAF, L. W. A Theoretical Study of the Silanol Polymerization Mechanism. In *Ultrastructure Processing of Advanced Ceramics*, J. D. Mackenzie and D. R. Ulrich, Eds. John Wiley & Sons, Inc., 1988, ch. 27, p. 367.

[61] DAVIS, L. P., BURGGRAF, L. W., AND GORDON, M. S. Theoretical Study of the Decomposition of Five-Coordinate Silicon Anions. *J. Am. Chem. Soc. 110* (1988), 3056.

[62] DAVIS, L. P., BURGGRAF, L. W., GORDON, M. S., AND BALDRIDGE, K. K. A Theoretical Stdy of Fluorine Atom and Fluoride Ion Attack on Methane and Silane. *J. Am. Chem. Soc. 107* (1985), 4415.

[63] DEAN, J. A. *Lange's Handbook of Chemistry*, 14th ed. 1992.

[64] DELLEY, B. An All-electron Numerical Method for Solving the Local Density Functional for Polyatomic Molecules. *J. Chem. Phys. 92*, 1 (1990), 508.

[65] DERELI, G. Stillinger-Weber Type Potentials in Monte Carlo Simulation of Amorphous Silicon. *Molecular Simulation 8* (1992), 351.

[66] DISLICH, H., AND HINZ, P. History and Principles of the Sol-Gel Process, and Some New Multicomponent Oxide Coatings. In *International Workshop on Glasses and Glass Ceramics From Gels*, V. Gottardi, Ed., vol. 48 of *Journal of Non-Crystalline Solids*. North-Holland Publishing Company, 1982, p. 11.

[67] DUNITZ, J. D., AND IBERS, J. A. *Perspectives in Structural Chemistry*, vol. II. John Wiley & Sons, Inc., 1968.

[68] FAN, L., AND ZIEGLER, T. Nonlocal Density Functional Theory as a Pratical Tool in Calculations on Transition States and Activation Energies. Applications to Elementary Reaction Steps in Organic Chemistry. *J. Am. Chem. Soc. 114* (1992), 10890.

[69] FERRARI, A. M., UGLIENGO, P., AND GARRONE, E. Geminal Silica Hydroxyls as Adsorbing Sites: An Ab Initio Study. *J. Phys. C: Solid State Phys. 97* (1993), 2671.

[70] FEUSTON, B. P., AND GAROFALINI, S. H. Empirical three-body potential for vitreous silica. *J. Chem. Phys. 89*, 9 (1988), 5818.

[71] FEUSTON, B. P., AND GAROFALINI, S. H. Oligomerization in Silica Sols. *J. Phys. C: Solid State Phys. 94* (1990), 5351.

[72] FINCHAM, D. Optimisation of the Ewald Sum for Large Systems. *Molecular Simulation 13* (1994), 1.

[73] FLEISCHMAN, S. H., AND III, C. L. B. Thermodynamics of Aqueous Solvation: Solution Properties of Alcohols and Alkanes. *J. Chem. Phys. 87*, 5 (1987), 3029.

[74] FLORY, P. J. *Principles of Polymer Chemistry.* Cornell Univ. Press, 1953.

[75] FRICKE, J. Aerogels and Their Applications. In *Sixth International Workshop on Glasses and Glass Ceramics from Gels*, L. Esquivias, Ed., vol. 147 & 148 of *Journal of Non-Crystalline Solids.* North-Holland Publishing Company, 1992, p. 356.

[76] FRICKE, J., AND CAPS, R. Aerogels-A Fascinating Class of Porous Solids. In *Ultrastructure Processing of Advanced Ceramics*, J. D. Mackenzie and D. R. Ulrich, Eds. John Wiley & Sons, Inc., 1988, ch. 45, p. 613.

[77] GALE, J. D. A Density Functional Study of Molecular Adsorption in Zeolites. preprint.

[78] GALE, J. D., CATLOW, C. R. A., AND CARRUTHERS, J. R. An Ab Initio Study of Methanol Adsorption in Zeolites. preprint.

[79] GALEENER, F. L. Planar Rings in Vitreous Silica. In *Sixth University Conference on Glass Science*, C. G. P. G. E. Rindone and W. B. White, Eds., vol. 49 of *Journal of Non-Crystalline Solids.* North-Holland Publishing Company, 1982, p. 53.

[80] GAROFALINI, S. H. Simulation of the Sol-Gel Process. In *Sol-Gel Technology For Thin Films, Fibers, Preforms, Electronics, and Specialty Shapes*, L. C. Klein, Ed., Materials Science and Process Technology. Noyes Publications, New Jersey, 1988, p. 16.

[81] GAROFALINI, S. H., AND MARTIN, G. Molecular Simulations of the Polymerization of Silicic Acid Molecules and Network Formation. *J. Phys. C: Solid State Phys. 98* (1994), 1311.

[82] GAROFALINI, S. H., AND MELMAN, H. Applications of Molecular Dynamics Simulations to Sol-Gel Processing. In *Better Ceramics Through Chemistry II*, C. J. Brinker, D. E. Clark, and D. R. Ulrich, Eds., vol. 73 of *Materials Research Society.* Elsevier Science Publishing Co., Inc., 1986, p. 497.

[83] GIBBS, G. V., AND BOISEN, M. B. Molecular Mimicry of Structure and Electron Density Distributions in Minerals. In *Better Ceramics Through Chemistry II*, C. J. Brinker, D. E. Clark, and D. R. Ulrich, Eds., vol. 73 of *Materials Research Society.* Elsevier Science Publishing Co., Inc., 1986, p. 515.

[84] GORDON, M. S., DAVIS, L. P., BURGGRAF, L. W., AND DAMRAUER, R. Theoretical Studies of the Reactions $XH_n \longrightarrow XH_{n-1}^- + H^+$ and $XH_{n-1}^- + SiH_4 \longrightarrow [SiH_4XH_{n-1}]^-$. *J. Am. Chem. Soc. 108*, 25 (1986), 7889.

[85] GORDON, M. S., AND PEDERSON, L. A. Thermal Decomposition Processes for Silanol. *J. Phys. C: Solid State Phys. 94* (1990), 5527.

[86] GORDON, R. G. Correlation Functions for Molecular Motion. *Adv. Magn. Reson. 3* (1968), 1.

[87] GOTTARDI, V. Glasses of the Same Composition but Different Properties. In *Sixth University Conference on Glass Science*, C. G. P. G. E. Rindone and W. B. White, Eds., vol. 49 of *Journal of Non-Crystalline Solids*. North-Holland Publishing Company, 1982, p. 461.

[88] GOTTARDI, V., GUGLIELMI, M., BERTOLUZZA, A., FAGNANO, C., AND MORELLI, M. A. Further Investigations on Raman Spectra of Silica Gel Evolving Toward Glass. In *Second International Workshop on Glasses and Glass Ceramics from Gels*, H. Scholze, Ed., vol. 63 of *Journal of Non-Crystalline Solids*. North-Holland Publishing Company, 1984, p. 71.

[89] GREENWOOD, N. N., AND GARNSHAW, A. *Chemistry of the Elements*. Pergamon Press, 1984.

[90] GUBBINS, K. E. The Role of Computer Simulation in Studying Fluid Phase Equilibria. *Molecular Simulation 2* (1989), 223.

[91] GUGLIELMI, M., AND CARTURAN, G. Precursors for Sol-Gel Preparations. In *Fourth International Workshop on Glasses and Glass Ceramics from Gels*, S. Sakka, Ed., vol. 100 of *Journal of Non-Crystalline Solids*. North-Holland Publishing Company, 1988, p. 16.

[92] HARDMAN-RHYNE, K. A., COYLE, T. D., AND LEWIS, E. P. Kinetic Investigations of Alkoxysilane Sol-Gel Processing. In *Better Ceramics Through Chemistry II*, C. J. Brinker, D. E. Clark, and D. R. Ulrich, Eds., vol. 73 of *Materials Research Society*. Elsevier Science Publishing Co., Inc., 1986, p. 173.

[93] HEANRY, P. J., PREWITT, C. T., AND GIBBS, G. V. The Elusive *SiO* bond. In *Silica, Physical Behavior, Geochemistry and Materials Applications*, P. H. Ribbe, Ed., vol. 29 of *Reviews in Mineralogy*. Mineralogical Society of America, 1994, p. 331.

[94] HEDIN, L., AND LUNDQVIST, B. I. Explicit Local Exchange-Correlation Potentials. *J. Phys. C: Solid State Phys. 4* (1971), 2064.

[95] HENCH, L. L. Concepts of Ultrastructure Processing. In *Ultrastructure Processing of Ceramics, Glasses, and Composites*, L. L. Hench and D. R. Ulrich, Eds. John Wiley & Sons, Inc., 1984, ch. 1, p. 3.

[96] HENCH, L. L., AND WEST, J. K. The Sol-Gel Process. *Chem. Rev. 90* (1990), 33.

[97] HENCH, L. L., WILSON, M. J. R., BALABAN, C., AND NOGUÈS, J. L. Sol-Gel Processing of Large Silica Optics. In *Ultrastructure Processing of Advanced Materials*, D. R. Uhlmann and D. R. Ulrich, Eds. John Wiley & Sons, Inc., 1992, ch. 15, p. 159.

[98] HENCHE, L. L., AND ORCEL, G. Physical-Chemical and Biochemical Factors in Silica Sol-Gels. Section I: Gel Formation. In *Third International Workshop on Glasses and Glass Ceramics from Gels*, J. Zarzycki, Ed., vol. 82 of *Journal of Non-Crystalline Solids*. North-Holland Publishing Company, 1986, p. 1.

[99] HEYES, D. M. Molecular Dynamics at Constant Pressure and Temperature. *Chemical Physics 82* (1983), 285.

[100] HILL, J., AND SAUER, J. Molecular Mechanics Potential for Silica and Zeolite Catalysts Based on Ab Initio Calculations. I. Dense and Microporous Silica. *J. Phys. C: Solid State Phys. 98* (1994), 1238.

[101] HOHENBERG, P., AND KOHN, W. Inhomogeneous Electron Gas. *Physical Review 136*, 3B (1964), B864.

[102] HONDA, K., KITAURA, K., AND NISHIMOTO, K. Monte Carlo Simulation of Liquid Water and an Evaluation of Thermodynamic Properties. *Molecular Simulation 6*, 4-6 (1991), 275.

[103] HOWELL, P. L., AND GOODFELLOW, J. M. Effect of Initial Positions on the Simulation of Water Networks in Crystal Hydrates. *Molecular Simulation 1* (1988), 333.

[104] HUZINAGA, S., ANDZELM, J., KTOBUKOWSKI, M., RADZIO-ANDZELM, E., SAKAI, Y., AND TATEWAKI, H., Eds. *Gaussian Basis Sets for Molecular Calculations*, vol. 16 of *Physical Sciences Data.* Elsevier, 1984.

[105] ILER, R. K. *The Chemistry of Silica.* John Wiley & Sons, 1979.

[106] ISHIKAWA, T., WANG, P. Y., WAKUI, K., AND YABE, T. A Method for the High-speed Generation of Random Numbers with Arbitrary Distributions. *Computer Physics Communications 70* (1992), 501.

[107] JACKSON, J. D. *Classical Electrodynamics.* John Wiley & Sons, 1975.

[108] JACKSON, R. A., AND CATLOW, C. R. A. Studies of Zeolite Structure. *Molecular Simulation 1* (1988), 207.

[109] JOHNSON, P. A., AND BABB, A. L. Liquid Diffusion of Non-Electrolytes. *Chem. Rev. 56* (1956), 387.

[110] JONAS, J. Kinetics and Mechanism of Sol-Gel Polymerization. In *Science of Ceramic Chemical Processing*, L. L. Hench and D. R. Ulrich, Eds. John Wiley & Sons, Inc., 1986, ch. 5, p. 65.

[111] JONAS, J. Molecular-Level Understanding of the Sol-Gel Process. In *Ultrastructure Processing of Advanced Materials*, D. R. Uhlmann and D. R. Ulrich, Eds. John Wiley & Sons, Inc., 1992, ch. 2, p. 13.

[112] JORGENSEN, W. Pressure Dependence of the Structure and Properties of Liquid *n*-Butane. *J. Am. Chem. Soc. 103* (1981), 4721.

[113] JORGENSEN, W., AND IBRAHIM, M. Structures and Properties of Organic Liquids: n-Alkyl Ethers and their Conformational Equilibria. *J. Am. Chem. Soc. 103* (1981), 3976.

[114] JORGENSEN, W., R. C. BINNING, J., AND BIGOT, B. Structures and Properties of Organic Liquids: *n*-Butane and 1,2-Dichloroethane and their Conformational Equilibria. *J. Am. Chem. Soc. 103* (1981), 4393.

[115] JORGENSEN, W. L. Simulation of Liquid Ethanol Including Internal Rotation. *J. Am. Chem. Soc. 103* (1981), 345.

[116] JORGENSEN, W. L. Transferable Intermolecular Potential Functions. Application to Liquid Methanol Including Internal Rotation. *J. Am. Chem. Soc. 103* (1981), 341.

[117] JORGENSEN, W. L. Transferable Intermolecular Potential Functions for Water, Alcohols, and Ethers. Application to Liquid Water. *J. Am. Chem. Soc. 103* (1981), 335.

[118] JORGENSEN, W. L. Revised TIPS for Simulations of Liquid Water and Aqueous Solutions. *J. Chem. Phys. 77*, 7 (1982), 4156.

[119] JORGENSEN, W. L., CHANDRASEKHAR, J., AND MADURA, J. D. Comparison of Simple Potential Functions for Simulating Liquid Water. *J. Chem. Phys. 79*, 2 (1983), 926.

[120] KAY, B. D., AND ASSINK, R. A. High Field ^1H NMR Studies of Sol-Gel Kinetics. In *Better Ceramics Through Chemistry II*, C. J. Brinker, D. E. Clark, and D. R. Ulrich, Eds., vol. 73 of *Materials Research Society*. Elsevier Science Publishing Co., Inc., 1986, p. 157.

[121] KAY, B. D., AND ASSINK, R. A. Sol-Gel Kinetics: II. Chemical Speciation Modeling. *Journal of Non-Crystalline Solids 104* (1988), 112.

[122] KAYE, G. W. C., AND LABY, T. H., Eds. *Tables of Physical and Chemical Constants*, 14th ed. 1973.

[123] KEEFER, K. D. The Effect of Hydrolysis Conditions on the Structure and Growth of Silicate Polymers. In *Better Ceramics Through Chemistry*, C. J. Brinker, D. E. Clark, and D. R. Ulrich, Eds., vol. 32 of *Materials Research Society*. Elsevier Science Publishing Co., Inc., 1984, p. 15.

[124] KEEFER, K. D. Growth and Structure of Fractally Rough Silica Colloids. In *Better Ceramics Through Chemistry II*, C. J. Brinker, D. E. Clark, and D. R. Ulrich, Eds., vol. 73 of *Materials Research Society*. Elsevier Science Publishing Co., Inc., 1986, p. 295.

[125] KEEFER, K. D. A model for the Growth of Fractal Silica Polymers. In *Science of Ceramic Chemical Processing*, L. L. Hench and D. R. Ulrich, Eds. John Wiley & Sons, Inc., 1986, ch. 14, p. 131.

[126] KELTS, L. W., AND AMSTRONG, N. J. A Silicon-29 NMR Study of the Structural Intermediates in Low pH Sol-Gel Reactions. *J. Mater. Res. 4*, 2 (1989), 423.

[127] KINGERY, W. D. Some Aspects of the History of Ceramic Procesing. In *Ultrastructure Processing of Advanced Ceramics*, J. D. Mackenzie and D. R. Ulrich, Eds. John Wiley & Sons, Inc., 1988, p. 1.

[128] KINRADE, S. D., AND SWADDLE, T. W. Silicon-29 NMR Studies of Aqueous Silicate Solutions. 2. Transverse ^{29}Si Relaxation and the Kinetics and Mechanism of Silicate Polymerization. *Inorg. Chem. 27* (1988), 4259.

[129] KITTEL, C. *Solid-State Physics*. John Wiley & Sons, 1986.

[130] KLAMT, A., AND SCHÜÜRMANN. COSMO: A New Approach to Dielectric Screening in Solvents with Explicit Expressions for the Screening Energy and its Gradient. *J. Chem. Soc. Perkin Trans. 2* (1993), 799.

[131] KLEMPERER, W. G., MAINZ, V. V., AND MILLAR, D. M. A Molecular Building-Block Approach to the Synthesis of Ceramic Materials. In *Better Ceramics Through Chemistry II*, C. J. Brinker, D. E. Clark, and D. R. Ulrich, Eds., vol. 73 of *Materials Research Society.* Elsevier Science Publishing Co., Inc., 1986, p. 3.

[132] KLEMPERER, W. G., MAINZ, V. V., AND MILLAR, D. M. A Solid State Multinuclear Magnetic Resonance Study of the Sol-Gel Process Using Polysilicate Precursors. In *Better Ceramics Through Chemistry II*, C. J. Brinker, D. E. Clark, and D. R. Ulrich, Eds., vol. 73 of *Materials Research Society.* Elsevier Science Publishing Co., Inc., 1986, p. 15.

[133] KLEMPERER, W. G., MAINZ, V. V., RAMAMURTHI, S. D., AND ROSENBERG, F. S. Structural Characterization of Polysilicate Intermediates Formed During Sol-Gel Polymerization. In *Better Ceramics Through Chemistry III*, C. J. Brinker, D. E. Clark, and D. R. Ulrich, Eds., vol. 121 of *Materials Research Society.* Elsevier Science Publishing Co., Inc., 1988, p. 15.

[134] KLEMPERER, W. G., AND RAMAMURTHI, S. D. Molecular Growth Pathways in Silica Sol-Gel Polymerization. In *Better Ceramics Through Chemistry III*, C. J. Brinker, D. E. Clark, and D. R. Ulrich, Eds., vol. 121 of *Materials Research Society.* Elsevier Science Publishing Co., Inc., 1988, p. 1.

[135] KLEMPERER, W. G., AND RAMAMURTHI, S. D. A Flory-Stockmayer Analysis of Silica Sol-Gel Polymerization. In *Fifth International Workshop on Glasses and Glass Ceramics from Gels*, M. A. Aegerter, Ed., vol. 121 of *Journal of Non-Crystalline Solids.* North-Holland Publishing Company, 1990, p. 16.

[136] KNIGHT, C. T. G. Are Zeolite Secondary Building Units Really Red Herrings? *Zeolites 10* (February 1990), 140.

[137] KOHN, W., AND SHAM, L. J. Self-Consistent Equations Including Exchange and Correlation Effects. *Physical Review 140*, 4A (1965), A1133.

[138] KOLAFA, J., AND PERRAM, J. W. Cutoff Errors in the Ewald Summation Formulae for Point Charge Systems. *Molecular Simulation 9*, 5 (1992), 351.

[139] KUBICKI, J. D., AND LASAGA, A. C. Molecular Dynamics Simulations of SiO2 Melt and Glass: Ionic and Covalent Models. *American Mineralogist 73* (1988), 941.

[140] KUMAGAI, N., KAWAMURA, K., AND YOKOKAWA, T. An Interatomic Potential Model for H_2O: Applications to Water and Ice Polymorphs. *Molecular Simulation 12*, 3-6 (1994), 177.

[141] LAIDLER, K. J. *Chemical Kinetics.* McGraw-Hill Ltd., 1980.

[142] LASAGA, A. C., AND GIBBS, G. V. Applications of Quantum Mechanical Potential Surfaces to Mineral Physics Calculations. *Phys. Chem. Minerals 14* (1987), 107.

[143] LASAGA, A. C., AND GIBBS, G. V. Ab-Initio Quantum Mechanical Calculations of Water-Rock Interactions: Adsorption and Hydrolysis Reactions. *American Journal of Science 290* (1990), 263.

[144] LAWLEY, K. P. *Ab Initio Methods in Quantum Chemistry: Part I.* Cambridge University Press, 1987.

[145] LAWLEY, K. P. *Ab Initio Methods in Quantum Chemistry: Part II.* Cambridge University Press, 1987.

[146] LEE, C., YANG, W., AND PARR, R. G. Development of the Colle-Salvetti correlation-energy formula into a functional of the electron density. *Physical Review B 37*, 2 (1988), 785.

[147] LIMTRAKUL, J., AND TANTANAK, D. Structures, energetics and vibrational frequencies of zeolitic catalysts: a comparison between density functional and post-Hartree-Fock approaches. *Journal of Molecular Structure (Theochem) 358* (1995), 179.

[148] LIU, L., AND BASSETT, W. A. *Elements, Oxides, and Silicates: High-Pressure Phases with Implications for the Earth's Interior*, oxford university press ed. 1986.

[149] LIVAGE, J., AND SANCHEZ, C. Sol-Gel Chemistry. In *Third International Symposium on Aerogels*, J. Fricke, Ed., vol. 145 of *Journal of Non-Crystalline Solids.* North-Holland Publishing Company, 1992, p. 11.

[150] LUKE, B. T. An Ab Initio Investigation of the Lowest Potential Energy Surface of Disiloxane. *J. Phys. C: Solid State Phys. 97* (1993), 7505.

[151] LÜSCHER, M. A Portable High-quality Random Number Generator for Lattice Field Theory Simulations. *Computer Physics Communications 79* (1994), 100.

[152] MACGOWAN, D., AND HEYES, D. M. Large Timesteps in Molecular Dynamics Simulations. *Molecular Simulation 1* (1988), 277.

[153] MACKENZIE, J. D. Glasses From Melts and Glasses from Gels, a Comparison. In *International Workshop on Glasses and Glass Ceramics from Gels*, V. Gottardi, Ed., vol. 48 of *Journal of Non-Crystalline Solids.* North-Holland Publishing Company, 1982, p. 1.

[154] MACKENZIE, J. D. Applications of Sol-Gel Methods For Glass and Ceramics Processing. In *Ultrastructure Processing of Ceramics, Glasses, and Composites*, L. L. Hench and D. R. Ulrich, Eds. John Wiley & Sons, Inc., 1984, ch. 3, p. 15.

[155] MACKENZIE, J. D. Applications of the Sol-Gel Method: Some Aspects of Initial Processing. In *Science of Ceramic Chemical Processing*, L. L. Hench and D. R. Ulrich, Eds. John Wiley & Sons, Inc., 1986, ch. 12, p. 113.

[156] MACKENZIE, J. D. Amorphous Oxides From Gels. In *Ultrastructure Processing of Advanced Ceramics*, J. D. Mackenzie and D. R. Ulrich, Eds. John Wiley & Sons, Inc., 1988, ch. 43, p. 589.

[157] MACKENZIE, J. D. Applications of the Sol-Gel Process. In *Fourth International Workshop on Glasses and Glass Ceramics from Gels*, S. Sakka, Ed., vol. 100 of *Journal of Non-Crystalline Solids.* North-Holland Publishing Company, 1988, p. 162.

[158] MANDELBROT, B. B. *The Fractal Geometry of Nature.* W. H. Freeman, 1983.

[159] McDonald, I. R., and Klein, M. L. Intermolecular Potentials and The Simulation of Liquid Water. *J. Chem. Phys. 68*, 11 (1978), 4875.

[160] Meakin, P. Formation of Fractal Clusters and Networks by Irreversible Diffusion-Limited Aggregation. *Physical Review Letters 51*, 13 (1983), 1119.

[161] Meakin, P. Computer Simulation of Growth and Aggregation Processes. In *On Growth and Form*, H. E. Stanley and N. Ostrowski, Eds. Martinus-Nijhoff, Boston, 1986, p. 111.

[162] Meakin, P. Models for Colloidal Aggregation. *Ann. Rev. Phys. Chem. 39* (1988), 237.

[163] Medenbach, O., and Fornefeld, C. S. *Minerais.* Editorial Publica, 1983.

[164] Mehrotra, R. C. Synthesis and Reactions of Metal Alkoxides. In *Fourth International Workshop on Glasses and Glass Ceramics from Gels*, S. Sakka, Ed., vol. 100 of *Journal of Non-Crystalline Solids.* North-Holland Publishing Company, 1988, p. 1.

[165] Mehrotra, R. C. Chemistry of Alkoxide Precursors. In *Fifth International Workshop on Glasses and Glass Ceramics from Gels*, M. A. Aegerter, Ed., vol. 121 of *Journal of Non-Crystalline Solids.* North-Holland Publishing Company, 1990, p. 1.

[166] Mehrotra, R. C. Precursors for Aerogels. In *Third International Symposium on Aerogels*, J. Fricke, Ed., vol. 145 of *Journal of Non-Crystalline Solids.* North-Holland Publishing Company, 1992, p. 1.

[167] Melchionna, S., Ciccotti, G., and Holian, B. L. Hoover *NPT* Dynamics for Systems Varying in Shape and Size. *Molecular Physics 78*, 3 (1993), 533.

[168] Metropolis, N., Rosenbluth, A. W., Rosenbluth, M. N., and Teller, A. H. Equation of State Calculations by Fast Computing Machines. *J. Chem. Phys. 21*, 6 (1953), 1087.

[169] Møller, C., and Plesset, M. S. Note on an Approximation Treatment for Many-Electron Systems. *Physical Review 46* (1934), 618.

[170] Morales, J. J., and Toxvaerd, S. The Cell-neighbour Table Method in Molecular Dynamics Simulations. *Computer Physics Communications 71* (1992), 71.

[171] Moravetski, V., Hill, J., Eichler, U., Cheetham, A. K., and Sauer, J. ^{29}Si NMR Chemical Shifts of Silicate Species: Ab Initio Study of Environment and Structure Effects. *J. Am. Chem. Soc. 118* (1996), 13015.

[172] Mortier, W. J., Sauer, J., Lercher, J. A., and Noller, H. Bridging and Terminal Hydroxyls. A Structural Chemical and Quantum Chemical Discussion. *J. Phys. C: Solid State Phys. 88* (1984), 905.

[173] Moruzzi, V. L., Janak, J. F., and Schwarz, K. Calculated Thermal Properties of Metals. *Physical Review B 37*, 2 (1988), 790.

[174] Mozzi, R. L., and Warren, B. E. The Structure of Vitreous Silica. *J. Appl. Cryst. 2* (1969), 164.

[175] MUKHERJEE, S. P. A Comparison of Structures and Crystallization Behavior of Gels, Gel-Derived Glasses, and Conventional Glasses. In *Better Ceramics Through Chemistry II*, C. J. Brinker, D. E. Clark, and D. R. Ulrich, Eds., vol. 73 of *Materials Research Society.* Elsevier Science Publishing Co., Inc., 1986, p. 443.

[176] MULLIKEN, R. S. Electronic Population Analysis on LCAO-MO Molecular Wave Functions. I. *J. Chem. Phys. 23*, 10 (1955), 1833.

[177] NAKANO, A., VASHISHTA, P., AND KALIA, R. K. Parallel Multiple-time-step Molecular Dynamics with Three-body Interaction. *Computer Physics Communications 77* (1993), 303.

[178] NARTEN, A. H., AND LEVY, H. A. Liquid Water: Molecular Correlation Functions from X-ray Diffraction. *J. Chem. Phys. 55*, 5 (1971), 2263.

[179] NEWELL, R. G., FEUSTON, B. P., AND GAROFALINI, S. H. The Structure of Sodium Trisilicate Glass via Molecular Dynamics Employing Three-Body Potentials. *J. Mater. Res. 4*, 2 (1989), 434.

[180] NICHOLAS, J. B., WINANS, R. E., HARRISON, R. J., ITON, L. E., AND CURTIS, L. A. Ab Initio Molecular Orbital Study of the Effects of Basis Set Size on the Calculated Structure and Acidity of Hydroxyl Groups in Framework Molecular Sieves. *J. Phys. C: Solid State Phys. 96* (1992), 10247.

[181] NOSE, S. A Unified Formulation of the Constant Temperature Molecular Dynamics Methods. *J. Chem. Phys. 81*, 1 (1984), 511.

[182] NOSE, S., AND KLEIN, M. L. A Study of Solid and Liquid Carbon Tetrafluoride Using the Constant Pressure Molecular Dynamics Technique. *J. Chem. Phys. 78*, 11 (1983), 6929.

[183] ONSAGER, L. Electric Moments of Molecules in Liquids. *J. Am. Chem. Soc. 58* (1936), 1486.

[184] ORCEL, G., AND HENCH, L. Effect of Formamide Additive on the Chemistry of Silica Sol-Gels. Part I: NMR of Silica Hydrolysis. *Journal of Non-Crystalline Solids 79* (1986), 177.

[185] ORCEL, G., HENCH, L. L., ARTAKI, I., JONAS, J., AND ZERDA, T. W. Effect of Formamide Additive on the Chemistry of Silica Sol-Gels: II. Gel Structure. *Journal of Non-Crystalline Solids 105* (1988), 223.

[186] PÁPAI, I., GOURSOT, A., AND FAJULA, F. Density Functional Calculations on Model Clusters of Zeolite-β. *J. Phys. C: Solid State Phys. 98* (1994), 4654.

[187] PARR, R. G., AND YANG, W. *Density-Functional Theory of Atoms and Molecules.* Oxford University Press, 1989.

[188] PARRINELLO, M., AND RAHMAN, A. Polymorphic Transitions in Single Crystals: A new Molecular Dynamics Method. *J. Appl. Phys. 52*, 12 (1981), 7182.

[189] PEPPAS, N. A., SCRANTON, A. B., TSOU, A. H., AND EDWARDS, D. E. Branching Theory in Sol-Gel Processing. In *Better Ceramics Through Chemistry III*, C. J. Brinker, D. E. Clark, and D. R. Ulrich, Eds., vol. 121 of *Materials Research Society*. Elsevier Science Publishing Co., Inc., 1988, p. 43.

[190] PÉREZ-JORDÁ, J. M. A simple, efficient and more reliable scheme for automatic numerical integration. *Computer Physics Communications 77* (1993), 46.

[191] PERRY, R. H. *Chemical Engineers Handbook*, 5th ed. 1969.

[192] PHILIPP, G., AND SCHMIDT, H. The Reactivity of TiO_2 and ZrO_2 in Organically Modified Silicates. In *Third International Workshop on Glasses and Glass Ceramics from Gels*, J. Zarzycki, Ed., vol. 82 of *Journal of Non-Crystalline Solids*. North-Holland Publishing Company, 1986, p. 31.

[193] POIRIER, R., KARI, R., AND CSIZMADIA, I. G., Eds. *Handbook of Gaussian Basis Sets*, vol. 24 of *Physical Sciences Data*. Elsevier, 1985.

[194] POPKIE, H., KISTENMACHER, H., AND CLEMENTI, E. Study of the Structure of Molecular Complexes. IV. The Hartree-Fock Potential for the Water Dimer and its Application to the Liquid State. *J. Chem. Phys. 59*, 3 (1973), 1325.

[195] POPLE, J. A. *Ab-Initio Molecular Orbital Theory*. John Wiley & Sons, 1986.

[196] POUXVIEL, J. C., AND BOILOT, J. P. Kinetic Simulations and Mechanisms of the Sol-Gel Polymerization. *Journal of Non-Crystalline Solids 94* (1987), 374.

[197] POUXVIEL, J.-C., AND BOILOT, J. P. Kinetics Study of the Acidic Catalyzed Polymerization of Tetraehoxysilane by ^{29}Si NMR. In *Better Ceramics Through Chemistry III*, C. J. Brinker, D. E. Clark, and D. R. Ulrich, Eds., vol. 121 of *Materials Research Society*. Elsevier Science Publishing Co., Inc., 1988, p. 37.

[198] PRATT, L. R., AND HANN, S. W. Effects of Periodic Boundary Conditions on Equilibrium Properties of Computer Simulated Fluids. I. Theory. *J. Chem. Phys. 74*, 3 (1981), 1864.

[199] PRESS, W. H., FLANNERY, B. P., TEUKOLSKY, S. A., AND VETTERLING, W. T. *Numerical Recipes in C: the Art of Scientific Computing*. University Cambridge Press, 1988.

[200] RAHMAN, A., AND STILLINGER, F. Molecular Dynamics Study of Liquid Water. *J. Chem. Phys. 55*, 7 (1971), 3336.

[201] RE, N. Kinetics of Bicomponent Sol-Gel Processes. *Journal of Non-Crystalline Solids 142* (1992), 1.

[202] RITTGER, E. Handling Three-body Potentials in Computer Simulation. *Computer Physics Communications 67* (1992), 412.

[203] RODGER, P. M. On the Accuracy of Some Common Molecular Dynamics Algorithms. *Molecular Simulation 3* (1989), 263.

[204] RYCERZ, Z. A. Calculation of the Coulomb Interactions in Condensed Matter Simulation. *Molecular Simulation 9*, 5 (1992), 327.

[205] RYCERZ, Z. A., AND JACOBS, P. W. M. Ewald Summation in the Molecular Dynamics Simulation of Large Ionic Systems: The Cohesive Energy. *Molecular Simulation 8* (1992), 197.

[206] SAKKA, S., KOZUKA, H., AND KIM, S.-H. Various Factors Affecting the Conversion of Silicon Alkoxide Solutions to Gels. In *Ultrastructure Processing of Advanced Ceramics*, J. D. Mackenzie and D. R. Ulrich, Eds. John Wiley & Sons, Inc., 1988, ch. 10, p. 159.

[207] SAKKA, S., TANAKA, Y., AND KOKUBO, T. Hydrolysis and Polycondensation of Dimethyldiethoxysilane and Methyltriethoxysilane as Materials for Sol-Gel Process. In *Third International Workshop on Glasses and Glass Ceramics from Gels*, J. Zarzycki, Ed., vol. 82 of *Journal of Non-Crystalline Solids*. North-Holland Publishing Company, 1986, p. 24.

[208] SANCHEZ, C., AND IN, M. Molecular Design of Alkoxide Precursors for the Synthesis of Hybrid Organic-Inorganic Gels. In *Sixth International Workshop on Glasses and Glass Ceramics from Gels*, L. Esquivias, Ed., vol. 147 & 148 of *Journal of Non-Crystalline Solids*. North-Holland Publishing Company, 1992, p. 1.

[209] SAUER, J. Molecular Models in Ab Initio Studies of Solids and Surfaces: From Ionic Crystals and Semiconductors to Catalysts. *Chem. Rev. 89* (1989), 199.

[210] SCHAEFER, D. W., AND KEEFER, K. D. Fractal Geommetry of Silica Condensation Polymers. *Physical Review Letters 53*, 14 (1984), 1383.

[211] SCHAEFER, D. W., AND KEEFER, K. D. Fractal Aspects of Ceramic Synthesis. In *Better Ceramics Through Chemistry II*, C. J. Brinker, D. E. Clark, and D. R. Ulrich, Eds., vol. 73 of *Materials Research Society*. Elsevier Science Publishing Co., Inc., 1986, p. 277.

[212] SCHMIDT, H. Organically Modified Ceramics-Materials With "History" or "Future"? In *Ultrastructure Processing of Advanced Materials*, D. R. Uhlmann and D. R. Ulrich, Eds. John Wiley & Sons, Inc., 1992, ch. 38, p. 409.

[213] SCHMIDT, H., SCHOLZE, H., AND KAISER, A. Contribution to the Kinetics of Glass Formation From Solutions. In *International Workshop on Glasses and Glass Ceramics from Gels*, V. Gottardi, Ed., vol. 48 of *Journal of Non-Crystalline Solids*. North-Holland Publishing Company, 1982, p. 65.

[214] SCHMIDT, H., SCHOLZE, H., AND KAISER, A. Principles of Hydrolysis and Condensation Reaction of Alkoxysilanes. In *Second International Workshop on Glasses and Glass Ceramics from Gels*, H. Scholze, Ed., vol. 63 of *Journal of Non-Crystalline Solids*. North-Holland Publishing Company, 1984, p. 1.

[215] SCULLY, J. L., AND HERMANS, J. Multiple Time Steps: Limits on the Speedup of Molecular Dynamics Simulations of Aqueous Systems. *Molecular Simulation 11* (1993), 67.

[216] SMITH, W. A Replicated Data Molecular Dynamics Strategy for the Parallel Ewald Sum. *Computer Physics Communications 67* (1992), 392.

[217] SOULES, T. F. Molecular Dynamic Calculations of Glass Structure and Diffusion in Glass. In *Sixth University Conference on Glass Science*, C. G. P. G. E. Rindone and W. B. White, Eds., vol. 49 of *Journal of Non-Crystalline Solids*. North-Holland Publishing Company, 1982, p. 29.

[218] STAVE, M. S., AND NICHOLAS, J. B. Density Functional Study of Cluster Models of Zeolites. 1. Structure and Acidity of Hydroxyl Groups in Disiloxane Analogs. *J. Phys. C: Solid State Phys. 97* (1993), 9630.

[219] STILLINGER, F. H. Improved Simulation of Liquid Water by Molecular Dynamics. *J. Chem. Phys. 60*, 4 (1974), 1545.

[220] STILLINGER, F. H. Theory and Molecular Models for Water. *Adv. Chem. Phys. 31* (1975), 1.

[221] STILLINGER, F. H., AND RAHMAN, A. Revised Central Force Potentials for Water. *J. Chem. Phys. 68*, 2 (1978), 666.

[222] STOUTEN, P. F. W., AND KROON, J. Computation Confirms Contraction: A Molecular Dynamics Study of Liquid Methanol, Water and a Methanol-Water Mixture. *Molecular Simulation 5* (1990), 175.

[223] STRAUCH, H. J., AND CUMMINGS, P. T. Computer Simulation of the Dielectric Properties of Liquid Water. *Molecular Simulation 2* (1989), 89.

[224] STULL, D. R., AND ET AL., H. P., Eds. *Thermochemical Tables*, 2nd ed. JANAF, 1970.

[225] SU, S. R., AND ONORATO, P. I. K. Synthesis of High Purity Silica Glass From Metal Alkoxide. In *Better Ceramics Through Chemistry II*, C. J. Brinker, D. E. Clark, and D. R. Ulrich, Eds., vol. 73 of *Materials Research Society*. Elsevier Science Publishing Co., Inc., 1986, p. 237.

[226] TALLANT, D. R., BUNKER, B. C., BRINKER, C. J., AND BALFE, C. A. Raman Spectra of Rings in Silicate Materials. In *Better Ceramics Through Chemistry II*, C. J. Brinker, D. E. Clark, and D. R. Ulrich, Eds., vol. 73 of *Materials Research Society*. Elsevier Science Publishing Co., Inc., 1986, p. 261.

[227] THOMAS, I. M. Multicomponent Glasses From the Sol-Gel Process. In *Sol-Gel Technology For Thin Films, Fibers, Preforms, Electronics, and Specialty Shapes*, L. C. Klein, Ed., Materials Science and Process Technology. Noyes Publications, New Jersey, 1988, p. 2.

[228] TILDESLEY, D. J. Towards a More Complete Simulation of Small Polyatomic Molecules. In *Molecular Liquids, Dynamics and Interactions*, A. J. Barnes, W. J. Orville-Thomas, and J. Yarwood, Eds. D. Reidel Publishing Company, 1984, p. 519.

[229] TORAL, R., AND CHAKRABARTI, A. Generation of Gaussian Distributed Random Numbers by Using a Numerical Inversion Method. *Computer Physics Communications 74* (1993), 327.

[230] TOSSELL, J. A., AND VAUGHAM, D. J. *Theoretical Geochemistry: Applications of Quantum Mechanics in the Earth and Mineral Sciences.* Oxford University Press, 1992.

[231] TSCHINKE, V., AND ZIEGLER, T. Gradient Corrections to the Hartree-Slater exchange and their Influence on Bond Energy Calculations. *Theor. Chim. Acta 81* (1991), 65.

[232] TURNER, C. W., AND FRANKLIN, K. J. A Multinuclear (^1H, ^{29}Si, ^{17}O) NMR study of the Hydrolysis and Condensation of Tetraethylorthosilicate (TEOS). In *Science of Ceramic Chemical Processing*, L. L. Hench and D. R. Ulrich, Eds. John Wiley & Sons, Inc., 1986, ch. 7, p. 81.

[233] UGLIENGO, P., SAUNDERS, V., AND GARRONE, E. Silanol as a Model for the Free Hydroxyl of Amorphous Silica: Ab Initio Calculations of the Interaction with Water. *J. Phys. C: Solid State Phys. 94* (1990), 2260.

[234] UHLMANN, D. R. Microstructure of Glasses: Does it Really Matter? In *Sixth University Conference on Glass Science*, C. G. P. G. E. Rindone and W. B. White, Eds., vol. 49 of *Journal of Non-Crystalline Solids.* North-Holland Publishing Company, 1982, p. 439.

[235] UHLMANN, D. R., ZELINSKI, B. J., SILVERMAN, L., WARNER, S. B., FABES, B. D., AND DOYLE, W. F. Kinetic Processes in Sol-Gel Processing. In *Science of Ceramic Chemical Processing*, L. L. Hench and D. R. Ulrich, Eds. John Wiley & Sons, Inc., 1986, ch. 19, p. 173.

[236] UMEYAMA, H., AND MOROKUMA, K. The Origin of Hydrogen Bonding. An Energy Decomposition Study. *J. Am. Chem. Soc. 99*, 5 (1977), 1316.

[237] VAN GUNSTEREN, W. F., BERENDSEN, H. J. C., AND RULLMANN, J. A. C. Inclusion of Reaction Fields in Molecular Dynamics: Application to Liquid Water. *Faraday Discuss. Chem. Soc. 66* (1978), 58.

[238] VESSAL, B., LESLIE, M., AND CATLOW, C. R. A. Molecular Dynamics Simulation of Silica Glass. *Molecular Simulation 3* (1989), 123.

[239] VON BARTH, U., AND HEDIN, L. A Local Exchange-Correlation Potential for the Spin Polarized Case: I. *J. Phys. C: Solid State Phys. 5* (1972), 1629.

[240] VOSKO, S. H., WILK, L., AND NUSAIR, M. Accurate Spin-dependent Electron Liquid Correlation Energies for Local Spin Density Calculations: A Critical Analysis. *Can. J. Phys. 58* (1980), 1200.

[241] WEEKS, J. D., CHANDLER, D., AND ANDERSEN, H. C. Role of Repulsive Forces in Determining the Equilibrium Structure of Simple Liquids. *J. Chem. Phys. 54*, 12 (1971), 5237.

[242] WEINBERG, M. C. Are Gel-Derived Glasses Different From Ordinary Glasses? In *Better Ceramics Through Chemistry II*, C. J. Brinker, D. E. Clark, and D. R. Ulrich, Eds., vol. 73 of *Materials Research Society.* Elsevier Science Publishing Co., Inc., 1986, p. 431.

[243] WEST, J. K., WALLACE, S., HENCH, L. L., AND LISHAWA, C. R. Quantum Calculations on Sol-Gel Silica Clusters. In *Ultrastructure Processing of Advanced Materials*, D. R. Uhlmann and D. R. Ulrich, Eds. John Wiley & Sons, Inc., 1992, ch. 11, p. 111.

[244] WEST, J. K., ZHU, B. F., CHENG, Y. C., AND HENCH, L. L. Quantum Chemistry of Sol-Gel Silica Clusters. In *Fifth International Workshop on Glasses and Glass Ceramics from Gels*, M. A. Aegerter, Ed., vol. 121 of *Journal of Non-Crystalline Solids*. North-Holland Publishing Company, 1990, p. 51.

[245] WHEELER, G. E., AND FLEMING, S. A. Modulus of Rupture for Room-Temperature Gels Derived From Methyltrimethoxysilane. In *Ultrastructure Processing of Advanced Materials*, D. R. Uhlmann and D. R. Ulrich, Eds. John Wiley & Sons, Inc., 1992, ch. 30, p. 327.

[246] WILSON, S. Basis Sets. In *Ab Initio Methods in Quantum Chemistry I*, K. P. Lawley, Ed., vol. LXVII of *Adv. Chem. Phys.* John Wiley & Sons Ltd., 1987, p. 439.

[247] WOIGNIER, T., PHALIPPOU, J., AND ZARZYCKI, J. Monolithic Aerogels in the Systems $SiO_2 - B_2O_3$, $SiO_2 - P_2O_5$, $SiO_2 - B_2O_3 - P_2O_5$. In *Second International Workshop on Glasses and Glass Ceramics from Gels*, H. Scholze, Ed., vol. 63 of *Journal of Non-Crystalline Solids*. North-Holland Publishing Company, 1984, p. 117.

[248] WOODCOCK, L. V., ANGELL, C. A., AND CHEESEMAN, P. Molecular Dynamics Studies of the Vitreous State: Simple Ionic Systems and Silica. *J. Chem. Phys. 65* (1976), 1565.

[249] YOLDAS, B. E. Effect of Molecular Separation on the Hydrolytic Polycondensation of $Si(OC_2H_5)_4$. In *Third International Workshop on Glasses and Glass Ceramics from Gels*, J. Zarzycki, Ed., vol. 82 of *Journal of Non-Crystalline Solids*. North-Holland Publishing Company, 1986, p. 11.

[250] ZALLEN, R. *The Physics of Amorphous Solids*. John Wiley & Sons, 1983.

[251] ZARZYCKI, J. Physical-Chemical Factors in Sol-Gel Processes. In *Science of Ceramic Chemical Processing*, L. L. Hench and D. R. Ulrich, Eds. John Wiley & Sons, Inc., 1986, ch. 2, p. 21.

[252] ZARZYCKI, J. Sonogels-Development and Perspectives. In *Ultrastructure Processing of Advanced Materials*, D. R. Uhlmann and D. R. Ulrich, Eds. John Wiley & Sons, Inc., 1992, ch. 13, p. 135.

[253] ZIEGLER, T. Approximate Density Functional Theory as a Pratical Tool in Molecular Energetics and Dynamics. *Chem. Rev. 91* (1991), 651.

[254] ZIMAN, J. M. *Principles of the Theory of Solids*. Cambridge University Press, 1964.

[255] ZIRL, D. M., AND GAROFALINI, S. H. Structure of Sodium Aluminosilicate Glasses. *J. Am. Ceram. Soc. 73*, 10 (1990), 2848.